

# Molecular Clouds and Star Formation: A Multiwavelength Study of Perseus, Serpens, and Ophiuchus

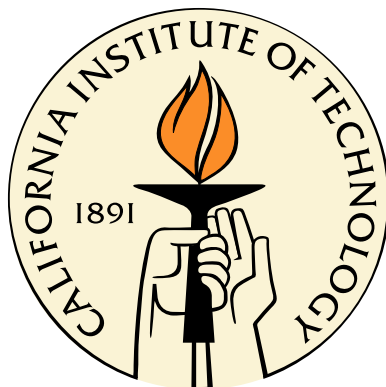
Thesis by

Melissa L. Enoch

In Partial Fulfillment of the Requirements

for the Degree of

Doctor of Philosophy



California Institute of Technology

Pasadena, California

2008

(Defended June 8, 2007)

© 2008

Melissa L. Enoch

All Rights Reserved

# Acknowledgements

Having at last reached the end of this long and often daunting expedition, I find myself at somewhat of a loss as to how to adequately express my appreciation for all of the help, support, and guidance that has gotten me here. But if graduate school has taught me anything, it is to just put pen to paper (or fingers to keyboard) and hope for the best.

This thesis could not have been completed without the help and collaboration of many people. Over the years that I have worked with her, my advisor, Anneila Sargent, has always forced me to focus on the larger picture, for which I am eternally grateful. I know that the lessons she has taught me will continue to improve my work, my papers, and my presentations for many years.

Working on the earliest phases of star formation at Caltech can be a lonely venture at times, but I have been lucky enough to have a number of collaborators at other institutions who have taken interest in my work, particularly Neal Evans at the University of Texas and Jason Glenn at the University of Colorado. I can safely say that this thesis would not exist without our many useful discussions, telecons, emails, and sometimes even battles. Being involved with the “Cores to Disks” *Spitzer* Legacy project has been an invaluable resource, not only for the wealth of data but for the collaborations it has generated. The c2d group meetings have sparked some of my most productive work, and the discussions, questions, and suggestions of many c2d members helped to keep me excited about my research.

I am indebted to the many members of the Bolocam instrument team, in particular Sunil Golwala, Jack Sayers, and Glenn Laurent, who patiently answered questions and helped me to develop the iterative mapping routine used for reduction of the Bolocam

data presented here. The analysis of the Ophiuchus Bolocam data would not have been possible without the help of Kaisa Young, who completed the data reduction and initial analysis. I am grateful to John Carpenter, who never kicked me out of his office when I insisted on pestering him with stupid questions. Thank you to my committee members, Nick Scoville, Re'em Sari, John Carpenter, and Sunil Golwala, for useful comments and questions that helped to focus my research, and for not giving me too much grief about the length of this thesis.

On a more personal note, my fellow classmates, Laura, Cathy, Stuartt, Milan, Margaret, and Elina, have been my lifeline here at Caltech, keeping me afloat through our first year and sharing the many ups and downs of the following five. To everyone else who helped to make grad school bearable in the tough times and fun in the not so tough; thanks to Dave for the pizza and movies, Dan for the gossip, the girls for the cosmos, and the boys for the forties.

My family is a consistent and unwavering source of support, always providing a much needed sanctuary for escape and regeneration. Knowing that they would have supported me even if I had run away to cooking school somehow made it easier to carry on. Although she probably doesn't realize it, my sister Paige is a constant inspiration. My love and appreciation to all of you. Finally, thanks to Monica, who will always be my oldest friend, for stubbornly believing that I could do anything, even graduate. And to Tom, for keeping me (mostly) sane.

# Abstract

In this thesis I utilize large-scale millimeter and mid- to far-infrared surveys to address a number of outstanding questions regarding the formation of low mass stars in molecular clouds. Continuum  $\lambda = 1.1$  mm maps completed with Bolocam at a resolution of  $31''$  cover the largest areas observed to date at millimeter or submillimeter wavelengths in three molecular clouds:  $7.5 \text{ deg}^2$  in Perseus ( $140 \text{ pc}^2$  at the adopted distance of  $d = 250 \text{ pc}$ ),  $10.8 \text{ deg}^2$  ( $50 \text{ pc}^2$  at  $d = 125 \text{ pc}$ ) in Ophiuchus, and  $1.5 \text{ deg}^2$  ( $30 \text{ pc}^2$  at  $d = 125 \text{ pc}$ ) in Serpens. These surveys are sensitive to dense substructures with mean density  $n \gtrsim 2 - 3 \times 10^4 \text{ cm}^{-3}$ . A total of 122 cores are detected in Perseus, 44 in Ophiuchus, and 35 in Serpens above mass detection limits of  $0.1 - 0.2 M_{\odot}$ . Combining with *Spitzer* mid- and far-infrared maps from the c2d Legacy program provides wavelength coverage from  $\lambda = 1.25 - 1100 \mu\text{m}$ , and enables the assembly of an unbiased, complete sample of the youngest star forming objects in three environments. This sample includes 108 prestellar cores, 43 Class 0 sources and 94 Class I sources.

The approximately equal number of starless cores and embedded protostars in each cloud implies a starless core lifetime of  $2 - 4 \times 10^5 \text{ yr}$ , only a few free-fall timescales. This timescale, considerably shorter than the timescale predicted by the classic scenario of magnetic field support in which core evolution is moderated by ambipolar diffusion, suggests that turbulence is the dominant process controlling the formation and evolution of dense cores. However, dense cores in all three clouds are found only at high cloud column densities, where  $A_V \gtrsim 7 \text{ mag}$ , and the fraction of cloud mass in these cores is less than 10%, indicating that magnetic fields must play some role as well. Measured angular deconvolved sizes of the majority of starless

cores are consistent with radial density profiles substantially flatter than  $\rho \propto r^{-2}$ , or with Bonnor-Ebert spheres. The prestellar core mass distribution (CMD) has a slope of  $\alpha = -2.5 \pm 0.2$  for  $M > 0.8 M_{\odot}$ , remarkably similar to recent measurements of the slope of the stellar initial mass function:  $\alpha = -2.3$  to  $-2.8$ . While this result does not rule out the importance of feedback or competitive accretion, it provides support for the hypothesis that stellar masses are determined during the core formation process.

The lifetime of the Class 0 phase is estimated to be  $1 - 2 \times 10^5$  yr in Perseus and Serpens, or approximately half that of the Class I phase, arguing against a very rapid early accretion phase. In Ophiuchus the fraction of Class 0 sources is much smaller, consistent with previous measurements of a short ( $\sim 10^4$  yr) Class 0 phase in that cloud. A large population of low luminosity Class I sources that cannot be explained by constant or monotonically decreasing accretion rates is observed in each cloud. This result strongly suggest that accretion during the Class I phase is episodic, with sources spending approximately 25% of the Class I lifetime in a quiescent state.

Finally, I investigate the environmental dependence of star formation by comparing the dense core populations of the three clouds. Cores are found at considerably higher cloud column densities in Ophiuchus than in Perseus or Serpens; more than 75% of cores occur at visual extinctions of  $A_V \gtrsim 8$  mag in Perseus,  $A_V \gtrsim 15$  mag in Serpens, and  $A_V \gtrsim 20 - 23$  mag in Ophiuchus. Cloud CMDs are well characterized by power-law fits ( $dN/dM \propto M^{\alpha}$ ) above their empirically derived 50% completeness limits, resulting in slopes of  $\alpha = -2.1 \pm 0.1$  in Perseus,  $\alpha = -2.1 \pm 0.3$  in Ophiuchus, and  $\alpha = -1.6 \pm 0.2$  in Serpens. Measured slopes for Perseus and Ophiuchus broadly agree with turbulent fragmentation, but the relative shapes of the observed cloud CMDs are inconsistent with detailed simulations of the dependence of CMD shape on Mach number.

# Contents

<b>1</b>	<b>Introduction</b>	<b>1</b>
1.1	A Star is Born . . . . .	1
1.1.1	Working Model for Isolated Star Formation . . . . .	2
1.1.2	Outstanding Questions . . . . .	5
1.1.3	Global Processes: Magnetic Fields versus Turbulence . . . . .	6
1.1.4	Core Initial Conditions . . . . .	10
1.1.5	Early Protostellar Evolution . . . . .	16
1.1.6	Effects of Environment . . . . .	19
1.2	Observations . . . . .	22
1.2.1	Millimeter Surveys . . . . .	22
1.2.1.1	Prestellar Cores . . . . .	23
1.2.1.2	Masses . . . . .	24
1.2.2	Infrared Surveys . . . . .	26
1.2.2.1	“Cores to Disks” Legacy Program . . . . .	27
1.3	Thesis Goals and Outline . . . . .	28
	Bibliography . . . . .	31
<b>2</b>	<b>Bolocam Survey for 1.1 mm Dust Continuum Emission in the Perseus Molecular Cloud</b>	<b>37</b>
	Abstract . . . . .	37
2.1	Introduction . . . . .	38
2.2	Observations . . . . .	42
2.3	Data Reduction . . . . .	45

2.3.1	Pointing . . . . .	45
2.3.2	Removal of Sky Noise . . . . .	46
2.3.3	Mapping and Calibration . . . . .	48
2.3.4	Iterative Mapping . . . . .	50
	2.3.4.1 Method . . . . .	50
	2.3.4.2 Performance . . . . .	51
2.4	Results . . . . .	56
	2.4.1 Source Identification . . . . .	56
	2.4.2 Comparison to Molecular and $A_V$ Maps . . . . .	61
	2.4.3 Source Statistics . . . . .	67
2.5	Discussion . . . . .	83
	2.5.1 Completeness and the Mass versus Size Distribution . . . . .	83
	2.5.2 The 1.1 mm Mass Function . . . . .	87
	2.5.3 Clustering . . . . .	92
	2.5.4 An Extinction Threshold for 1.1 mm Cores . . . . .	95
	2.5.5 Comparison to c2d Observations: B1 Ridge . . . . .	97
2.6	Summary . . . . .	99
	Acknowledgments . . . . .	100
	Bibliography . . . . .	102
<b>3</b>	<b>Bolocam Survey for 1.1 mm Dust Continuum Emission in the Ophi-</b>	
	<b>uchus Molecular Cloud</b>	<b>107</b>
	Abstract . . . . .	107
	3.1 Introduction . . . . .	108
	3.2 Observations . . . . .	109
	3.3 Data Reduction . . . . .	111
	3.3.1 Pointing and Flux Calibration . . . . .	111
	3.3.2 Iterative Mapping . . . . .	112
	3.3.3 Source Identification . . . . .	112
	3.4 Results . . . . .	113

3.4.1	General Cloud Morphology . . . . .	113
3.4.2	Source Properties . . . . .	119
3.4.2.1	Positions and Photometry . . . . .	119
3.4.2.2	Sizes and Shapes . . . . .	126
3.4.2.3	Masses, Densities, and Extinctions . . . . .	128
3.5	Discussion . . . . .	130
3.5.1	Completeness . . . . .	130
3.5.2	The Core Mass Distribution . . . . .	132
3.5.3	Clustering . . . . .	135
3.5.4	Extinction threshold . . . . .	138
3.6	Summary . . . . .	142
	Acknowledgments . . . . .	143
	Bibliography . . . . .	144
<b>4</b>	<b>Bolocam Survey for 1.1 mm Dust Continuum Emission in the Serpens Molecular Cloud</b>	<b>147</b>
	Abstract . . . . .	147
4.1	Introduction . . . . .	147
4.2	Observations and Data Reduction . . . . .	149
4.2.1	Observations . . . . .	149
4.2.2	Pointing and Flux Calibration . . . . .	151
4.2.3	Cleaning and Mapping . . . . .	151
4.2.4	Source Identification . . . . .	152
4.3	Results . . . . .	155
4.3.1	Comparison to Visual Extinction . . . . .	157
4.3.2	Source Properties . . . . .	159
4.3.2.1	Positions and Photometry . . . . .	159
4.3.2.2	Sizes and Shapes . . . . .	164
4.3.2.3	Masses, Densities, and Extinctions . . . . .	165
4.4	Summary . . . . .	167

Acknowledgments . . . . .	168
Bibliography . . . . .	169
<b>5 Comparing Star Formation on Large Scales in the c2d Legacy Clouds: Bolocam Surveys of Serpens, Perseus, and Ophiuchus</b>	<b>171</b>
Abstract . . . . .	171
5.1 Introduction . . . . .	172
5.2 Three-Cloud Sample . . . . .	174
5.3 What is a Core? . . . . .	174
5.4 Distance Effects . . . . .	178
5.5 Discussion . . . . .	181
5.5.1 Physical Implications of Source Sizes and Shapes . . . . .	181
5.5.2 Densities and the Mass versus Size Distribution . . . . .	185
5.5.3 Fragmentation and the Core Mass Distribution . . . . .	188
5.5.4 Clustering . . . . .	192
5.5.5 Relationship to Cloud Column Density . . . . .	196
5.5.6 Efficiency of Forming Cores . . . . .	198
5.6 Summary . . . . .	201
Acknowledgments . . . . .	204
Bibliography . . . . .	205
<b>6 Prestellar Cores and Deeply Embedded Protostars with Spitzer and Bolocam: Properties of the Youngest Objects in Perseus, Serpens, and Ophiuchus</b>	<b>207</b>
Abstract . . . . .	207
6.1 Introduction . . . . .	208
6.2 Combining Bolocam and Spitzer c2d Data . . . . .	212
6.3 Identifying Cold Protostars . . . . .	219
6.3.1 Association with a 1.1 mm Core . . . . .	222
6.3.2 Separating Starless and Protostellar Cores . . . . .	224
6.4 Comparing the Starless and Protostellar 1.1 mm Core Populations . . . . .	226

6.4.1	Sizes and Shapes . . . . .	227
6.4.2	Core Densities . . . . .	230
6.4.3	The Mass versus Size Distribution . . . . .	234
6.4.4	Core Mass Distributions . . . . .	237
6.4.5	Relationship to Cloud Column Density . . . . .	239
6.4.6	Clustering . . . . .	241
6.5	The Prestellar Core Mass Distribution . . . . .	243
6.6	Properties of Cold Protostars . . . . .	249
6.6.1	Bolometric Luminosity and Temperature . . . . .	249
6.6.2	Envelope Mass . . . . .	250
6.6.3	Completeness . . . . .	250
6.6.4	Individual Sources . . . . .	255
6.6.4.1	IRAS 03292+3039 . . . . .	255
6.6.4.2	Pers-Bolo 102 . . . . .	257
6.6.4.3	Serp-Bolo 33 and Other Class II Objects . . . . .	259
6.7	Comparison of Classification Methods . . . . .	262
6.7.1	Alternative Classifications . . . . .	269
6.8	Protostellar Evolution . . . . .	271
6.9	Lifetimes . . . . .	280
6.9.1	Timescale of the Class 0 Phase . . . . .	280
6.9.2	Timescale of the Prestellar Phase . . . . .	283
6.10	Conclusions . . . . .	285
	Acknowledgments . . . . .	287
6.11	Appendix: Calculating the bolometric luminosity and temperature . .	289
	Bibliography . . . . .	294
<b>7</b>	<b>Summary and Future work</b>	<b>299</b>
7.1	Summary . . . . .	299
7.2	The Future . . . . .	305
7.2.1	Main Accretion Phase Lifetime . . . . .	306

7.2.2	Tracing Structure Near the Protostar . . . . .	306
7.2.3	Timescale for Disk Formation and the Disk Mass Fraction . . .	308
	Bibliography . . . . .	311

# List of Figures

1.1	Standard schematic picture of how an isolated low mass star forms . . .	3
1.2	Correlation between measured core lifetime and mean density . . . . .	9
1.3	Core mass distribution for extinction-identified cores in the Pipe Nebula	13
1.4	Correlation between source angular size and density profile index . . .	15
1.5	Simple protostellar evolution models for an exponentially decreasing ac- cretion rate . . . . .	18
1.6	Core mass distributions resulting from turbulent fragmentation simula- tions . . . . .	21
2.1	Observational coverage of Bolocam and IRAC maps in Perseus, overlaid on an integrated intensity $^{13}\text{CO}$ map . . . . .	44
2.2	Iterative mapping performance: NGC 1333 . . . . .	52
2.3	Iterative mapping performance: Fractional lost peak flux density . . .	54
2.4	Iterative mapping performance: Fractional lost integrated flux density	55
2.5	Bolocam 1.1 mm map of the Perseus molecular cloud . . . . .	57
2.6	Bolocam map of Perseus, with high source density regions magnified and sources identified . . . . .	59
2.7	Examples of new millimeter detections in Perseus . . . . .	60
2.8	Comparison of 1.1 mm emission and visual extinction in Perseus . . . .	63
2.9	Comparison of 1.1 mm emission and $^{13}\text{CO}$ integrated intensity in Perseus	64
2.10	$A_V$ calculated from the 1.1 mm emission in Perseus . . . . .	65
2.11	Distribution of source peak and total flux densities in Perseus . . . . .	80
2.12	Distribution of source minor and major axis FWHM sizes in Perseus . .	81
2.13	Distribution of source axis ratios in Perseus . . . . .	82

2.14	Total mass versus FWHM size for sources in Perseus, with empirically derived completeness curves . . . . .	84
2.15	Total mass versus size at the $3\sigma$ contour for sources in Perseus . . . . .	86
2.16	Differential mass distribution for sources in Perseus . . . . .	88
2.17	Characterization of the dependence on dust temperature of the core mass distribution . . . . .	90
2.18	Two-point correlation function for sources in Perseus . . . . .	94
2.19	Probability of finding a 1.1 mm core as a function of $A_V$ for sources in Perseus . . . . .	96
2.20	Comparison of Bolocam and Spitzer maps in the B1 Ridge . . . . .	98
3.1	Observational coverage of Bolocam and IRAC maps in Ophiuchus, overlaid on a visual extinction map . . . . .	110
3.2	Bolocam 1.1 mm map of the Ophiuchus molecular cloud . . . . .	114
3.3	Map of the $1\sigma$ rms noise in Ophiuchus . . . . .	115
3.4	Bolocam map of Ophiuchus, with high source density regions magnified and sources identified . . . . .	116
3.5	MIPS three-color image of the eastern streamer in Ophiuchus, with 1.1 mm contours . . . . .	118
3.6	Comparison of 1.1 mm emission and visual extinction in Ophiuchus . . . . .	120
3.7	Distribution of source peak and total flux densities in Ophiuchus . . . . .	127
3.8	Distribution of source minor and major axis FWHM sizes in Ophiuchus . . . . .	128
3.9	Total mass versus FWHM size for sources in Ophiuchus, with empirically derived completeness curves . . . . .	131
3.10	Differential mass distribution for sources in Ophiuchus . . . . .	133
3.11	Two-point correlation function for sources in Ophiuchus . . . . .	137
3.12	Probability of finding a 1.1 mm core as a function of $A_V$ for sources in Ophiuchus . . . . .	139
3.13	Flux density, size, and mass versus $A_V$ for sources in Ophiuchus . . . . .	140

4.1	Observational coverage of Bolocam, IRAC, and MIPS maps in Serpens, overlaid on a visual extinction map . . . . .	150
4.2	Bolocam 1.1 mm map of the Serpens molecular cloud . . . . .	153
4.3	Map of the $1\sigma$ rms noise in Serpens . . . . .	154
4.4	Bolocam map of Serpens, with high source density regions magnified and sources identified . . . . .	156
4.5	Comparison of 1.1 mm emission and visual extinction in Serpens . . .	158
4.6	Distribution of source peak and total flux densities in Serpens . . . . .	163
4.7	Distribution of source minor and major axis FWHM sizes in Serpens .	164
4.8	Differential mass distribution for sources in Serpens . . . . .	166
5.1	Completeness as a function of linear deconvolved source size in Serpens, Perseus, and Ophiuchus . . . . .	176
5.2	Comparison of source properties for the original and degraded-resolution Ophiuchus samples: sizes, shapes, masses, and densities . . . . .	179
5.3	Ratio of angular deconvolved size to beam size for the original and degraded-resolution Ophiuchus samples . . . . .	180
5.4	Comparison of linear and angular deconvolved source sizes in Serpens, Perseus, and Ophiuchus . . . . .	182
5.5	Comparison of source axis ratios in Serpens, Perseus, and Ophiuchus .	184
5.6	Comparison of core mean densities measured at the half-maximum and $4\sigma$ contours in Serpens, Perseus, and Ophiuchus . . . . .	186
5.7	Total mass versus angular deconvolved size for sources in Serpens, Perseus, and Ophiuchus . . . . .	187
5.8	Comparison of the core mass distributions for Serpens, Perseus, and Ophiuchus . . . . .	189
5.9	Comparison of the two-point correlation function for Serpens, Perseus, and Ophiuchus . . . . .	194
5.10	Cumulative fraction of 1.1 mm cores as a function of cloud $A_V$ for Serpens, Perseus, and Ophiuchus . . . . .	197

6.1	three-color Spitzer images (8.0, 24, 160 $\mu\text{m}$ ) of selected starless cores in Perseus, Serpens, and Ophiuchus . . . . .	214
6.2	three-color Spitzer images (8.0, 24, 70 $\mu\text{m}$ ) and SEDs of selected protostellar cores in Perseus . . . . .	216
6.3	three-color Spitzer images and SEDs of selected protostellar cores in Serpens . . . . .	217
6.4	three-color Spitzer images and SEDs of selected protostellar cores in Ophiuchus . . . . .	218
6.5	Selection criteria for the cold protostar samples . . . . .	220
6.6	Protostellar selection criteria applied to galaxy candidates . . . . .	221
6.7	Distribution of the distance from cold protostar candidates in Perseus to the nearest core position, compared to a random distribution . . . .	223
6.8	Angular deconvolved sizes of starless and protostellar cores in Perseus, Serpens, and Ophiuchus . . . . .	228
6.9	Axis ratios of starless and protostellar cores . . . . .	229
6.10	Peak column densities of protostellar and starless cores . . . . .	232
6.11	Mean densities of protostellar and starless cores . . . . .	233
6.12	Mass versus size for starless and protostellar cores in Perseus . . . . .	235
6.13	Mass versus size for protostellar and starless cores in Serpens and Ophiuchus . . . . .	236
6.14	Mass distributions of protostellar and starless cores in Perseus, Serpens, and Ophiuchus . . . . .	238
6.15	Cumulative fraction of starless and protostellar cores as a function of cloud $A_V$ . . . . .	240
6.16	Two-point correlation function for protostellar and starless cores . . . .	242
6.17	Combined prestellar core mass distribution . . . . .	245
6.18	Combined protostellar core mass distribution . . . . .	247
6.19	three-color <i>Spitzer</i> image (3.6, 24, 70 $\mu\text{m}$ ) of IRAS 03292+3039 (Pers-Cold 2) . . . . .	257
6.20	three-color <i>Spitzer</i> image (8, 24, 70 $\mu\text{m}$ ) of Pers-Bolo 102 . . . . .	258

6.21	three-color <i>Spitzer</i> image of Serp-Cold 33 . . . . .	260
6.22	Bolometric temperature versus spectral index $\alpha_{IR}$ for cold protostar candidates in Perseus, Serpens, and Ophiuchus . . . . .	263
6.23	Distribution of $T_{bol}$ as a function of distance to the nearest 1.1 mm core for cold protostar candidates in Perseus, Serpens, and Ophiuchus . . .	264
6.24	Distribution of $\alpha_{IR}$ as a function of distance to the nearest 1.1 mm core	265
6.25	Average spectra for Class 0, Class I, and Class II . . . . .	266
6.26	Results of fitting Ophiuchus source SEDs to average Class 0 and Class I spectra . . . . .	268
6.27	Average spectra for designated $T_{bol}$ bins: “early Class 0,” “late Class 0,” etc. . . . .	270
6.28	Results of fitting cold protostar candidate SEDs to template average spectra . . . . .	272
6.29	$L_{bol}$ versus $T_{bol}$ for cold protostars, compared to evolutionary models .	274
6.30	Average spectra for “non-envelope Class I,” and low- $L_{bol}$ sources . . . .	277
6.31	$M_{env}$ versus $T_{bol}$ for cold protostars, compared to evolutionary models .	279
6.32	Comparison of methods for calculating $T_{bol}$ . . . . .	290
6.33	Characterization of sampling errors for $T_{bol}$ and $L_{bol}$ . . . . .	291
6.34	Characterization of errors in $T_{bol}$ for missing 160 $\mu\text{m}$ fluxes . . . . .	292
7.1	Example of using IRS spectra to probe small-scale envelope structure .	307
7.2	Example of separating disk and envelope contributions in an embedded protostar . . . . .	309



# List of Tables

1.1	Millimeter and submillimeter bolometer arrays . . . . .	23
2.1	Identified sources in Perseus . . . . .	69
2.2	Photometry, masses, sizes, and morphology for sources in Perseus . . .	73
3.1	Identified sources in Ophiuchus . . . . .	121
3.2	Photometry, masses, sizes, and morphology for sources in Ophiuchus .	123
3.3	Cumulative mass as a function of extinction for sources in Ophiuchus	141
4.1	Identified sources in Serpens . . . . .	160
4.2	Photometry, masses, sizes, and morphology for sources in Serpens . .	161
5.1	Cumulative mass as a function of extinction for sources in Serpens, Perseus, and Ophiuchus . . . . .	199
6.1	Statistics of 1.1 mm cores in the three clouds . . . . .	226
6.2	Bolometric temperatures, luminosities, and envelope masses of cold pro- tostars in Perseus . . . . .	251
6.3	Bolometric temperatures, luminosities, and envelope masses of cold pro- tostars in Serpens . . . . .	253
6.4	Bolometric temperatures, luminosities, and envelope masses of cold pro- tostars in Ophiuchus . . . . .	255
6.5	Class II sources detected at 1.1 mm in Perseus, Serpens, and Ophiuchus	260
6.6	Relative numbers of starless, Class 0, and Class I sources . . . . .	280



# Chapter 1

## Introduction

### 1.1 A Star is Born

*“Stars are the fundamental objects of astronomy; thus, the formation of stars constitutes one of the basic problems of astrophysics.”*

So began the seminal paper on the theory of isolated low mass star formation by Shu, Adams, & Lizano (1987). Understanding how stars form has consequences not only for the current generation of star birth in our own Galaxy, but also for the existence of planets suitable for life, the evolution of galaxies, and the creation of the first heavy elements.

Our current general picture of how an isolated low mass star is born was driven largely by the work of Shu et al. (1987), which provided one of the first coherent paradigms detailing the formation of a star, beginning with the dense parent core and continuing until the young stellar object becomes optically visible as it evolves onto the main sequence. Despite significant progress over the last few decades, however, the formation of stars in our Galaxy remains one of the basic problems of astrophysics. The lack of a more complete understanding, especially regarding the earliest phases from the formation of dense cores through the end of the main accretion phase, is due in large part to the difficulty of observing stellar systems in their prenatal and infant phases, and to the complexity of the environments in which they form.

The basic framework on which we hope to build a more complete picture is summarized below in §1.1.1. It may be thought of as the pencil sketch of an unfinished

painting; important structural features are in place, but the details, subtleties, and true coherence of the image have yet to be completed. In fact, this general outline by no means represents a complete picture of low mass star formation; the majority of stars do not form in isolation, but in groups and clusters in molecular clouds. The formation of stars must be understood in the context of their birth sites, and to be complete our picture must include the formation of prestellar cores from the cloud medium. In §1.1.2 I outline a few of the most outstanding questions regarding the formation of low mass stars in molecular clouds. In the remainder of this chapter I discuss approaches for attacking those questions, and summarize the goals and outline of this thesis.

### 1.1.1 Working Model for Isolated Star Formation

What has become the standard schematic picture of how an isolated low mass star forms (Shu, Adams, & Lizano, 1987; Lada, 1987; André, Ward-Thompson, & Barsony, 1993), is shown in figure 1.1. Characteristic spectral energy distributions (SED) of the observationally defined classifications for Class 0 (André et al., 1993), Class I, II, and III (Lada & Wilking, 1984), are plotted on the left as  $\log(\lambda F_\lambda)$  versus  $\lambda$ . In the center column are schematic depictions of what those SEDs may correspond to physically. Note that a direct association between Class 0 through Class II and a true evolutionary sequence remains a subject of debate (e.g. Jayawardhana, Hartmann, & Calvet, 2001), and timescales listed to the far right are highly uncertain, especially for the earliest phases (e.g. Visser, Richer, & Chandler, 2002).

Classes I–III were originally defined empirically by Lada & Wilking (1984) based on the SED shapes of infrared sources in the Ophiuchus molecular cloud. More specifically, objects were grouped into classes based on their near-infrared to mid-infrared spectral index. These morphological classifications were soon interpreted in terms of a physical evolutionary sequence (Adams, Lada, & Shu, 1987), based on the theoretical models of Adams & Shu (1986). Class I sources are associated in this evolutionary sequence with protostars during their main infall stage, surrounded by

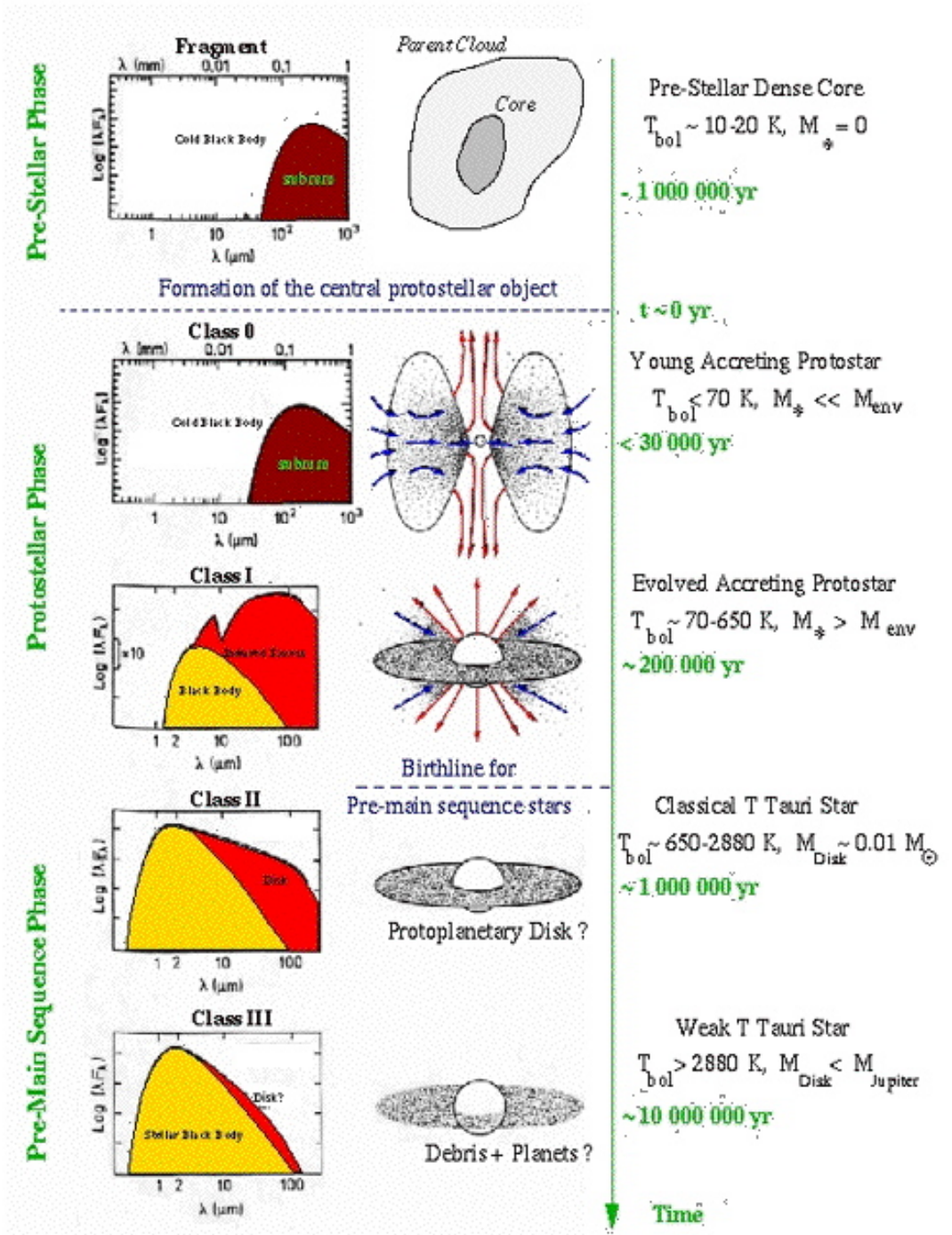


Figure 1.1 Standard schematic picture of how an isolated low mass star forms, originally adapted from André (1994), Shu et al. (1987), and Wilking (1989). Observationally classified SEDs are shown on the left, with the proposed physical interpretations (Adams et al., 1987; André et al., 1993) in the center column. Evolution proceeds from top to bottom, but the associated timescales are highly uncertain.

a rotating disk and infalling dusty envelope (Adams et al., 1987). More recently, Class I sources have been associated with an evolutionary state in which the mass of the accreting protostar exceeds the mass of the infalling envelope:  $M_* > M_{env}$  (André & Montmerle, 1994). The Class I SED shown in figure 1.1 arises primarily as a result of reprocessed emission from the disk and envelope.

Accretion from the envelope onto the protostar occurs through a rotating accretion disk (e.g., Shu et al., 1993). The dissipation of kinetic energy of infalling material in an accretion shock at the hydrostatic surface of the protostar provides the primary source of luminosity:

$$L_{acc} \sim \frac{GM_*\dot{M}}{R_*}, \quad (1.1)$$

where  $M_*$ ,  $R_*$  are the mass and radius of the central protostar, and  $\dot{M} = dM/dt$  is the mass accretion rate (Shu et al., 1987). Class I sources are observed to have well-collimated bipolar outflows, which create a cavity in the envelope and interact with the surrounding cloud medium to produce large-scale molecular outflows (Bachiller, 1996).

When infall is terminated by a widening stellar wind or outflow, the object becomes optically visible and enters Class II, with a passive nebular disk reprocessing emission from the pre-main sequence star (Adams et al., 1987). Class II or classical T Tauri stars are characterized by an SED that peaks in the near-infrared and resembles a stellar photosphere with excess emission from a remnant disk at longer wavelengths. After removal of the nebular disk, the SED of the Class III or weak T Tauri star is that of a reddened photosphere (Lada, 1987).

Later, observations of submillimeter condensations (cores) revealed a population of such cores that were invisible in the near-infrared but showed indirect evidence for a central protostar, such as a compact radio continuum source, collimated bipolar outflow, or a source of internal heating (e.g., André, 1996). Thus the Class 0 phase was added to the classification scheme to accommodate sources with SEDs peaking at long wavelengths but evidence of a protostellar nature (André et al., 1993). André & Montmerle (1994) interpreted Class 0 sources as a younger stage than Class I, when

the mass of the central protostar is still less than that of the surrounding envelope ( $M_* < M_{env}$ ), although the validity of this interpretation has not been verified. The Class 0 SED is shown in figure 1.1 as a cold blackbody peaking at  $\lambda \sim 100 - 200\mu\text{m}$ , with all emission from the hot protostar absorbed by the dense envelope and re-emitted at long wavelengths. Recent *Spitzer* Space Telescope observations have shown that some Class 0 sources are detectable at  $3.6 - 8\mu\text{m}$ , however (e.g., Jørgensen et al., 2006).

Submillimeter cores similar to Class 0 sources but with no evidence for a central protostar likely represent the earliest prestellar phase, prior to core collapse and protostellar formation (Ward-Thompson et al., 1994). Shown at the top of figure 1.1, dense prestellar cores have no internal source of luminosity; they are heated from the outside by the interstellar radiation field, and the SED resembles that of a cold blackbody, peaking in the far-infrared (e.g., Myers & Benson, 1983). The lifetime of this prestellar phase depends strongly on the core formation process and the dominant physics in the cloud (e.g., Ward-Thompson et al., 2007).

The more evolved Class II and III sources, or pre-main sequence stars, are fairly well understood, as they do not have an obscuring envelope and thus are directly observable. In this thesis I will focus on the earlier stages, from prestellar cores to Class I, where I sometimes refer to Class 0/I as the “main accretion phase.”

### 1.1.2 Outstanding Questions

In spite of the general framework described above, there remain a number of outstanding questions regarding the formation and early evolution of low mass stars. In reality, the star formation process begins on scales much larger than an individual core. The majority of stars are born in molecular clouds (e.g., Lada & Lada, 2003, and references therein), and their formation is governed by global physics such as turbulence and magnetic fields (e.g., Evans, 1999), as well as local processes such as outflows and rotation (e.g., Shu et al., 1987). The relative importance of these processes are still not well understood. Details of the early evolution of protostel-

lar sources are extremely uncertain, including mass accretion rates during the Class 0 and Class I phases. In addition, measurements of the timescales associated with the earliest stages vary considerably, ranging from  $10^5$  to  $10^7$  yr for prestellar cores (Ward-Thompson et al., 2007) and from  $10^4$  to a few  $\times 10^5$  yr for Class 0 (André & Montmerle, 1994; Visser et al., 2002). In fact, the association of Class 0 and Class I with distinct evolutionary stages is still a matter of debate (e.g., Jayawardhana et al., 2001).

The primary questions that will be investigated in this thesis are:

- (1) What are the global physical processes controlling the formation and support of prestellar cores and their subsequent collapse into protostars?
- (2) What are the initial conditions of star formation, as traced by the prestellar core populations of molecular clouds?
- (3) After core collapse, how do protostars evolve through the earliest phases, including mass accretion rates and timescales?
- (4) How does the star formation process depend on environmental factors such as average cloud density or the strength of turbulence?

### 1.1.3 Global Processes: Magnetic Fields versus Turbulence

The mass and spatial distributions of prestellar cores retain imprints of their formation process, and the lifetime of those cores is extremely sensitive to the dominant physics controlling their formation. Understanding the properties of prestellar cores on cloud scales, and how they vary with environment, provides insight into the global physical processes controlling star formation in molecular clouds.

It has long been accepted that Galactic molecular clouds cannot be in free-fall collapse (Zuckerman & Palmer, 1974). Given the typical masses of clouds ( $M > 10^4 M_\odot$ ), together with the Jeans mass for average cloud conditions ( $M_J \lesssim 80 M_\odot$ ), this conclusion implies that some additional means of support beyond thermal pressure is required (see Evans 1999 for a review). Magnetic fields and large-scale turbulence are the most likely candidates for this additional support, and both provide mechanisms

for the formation of self-gravitating cores, and subsequent collapse (Shu et al., 1987; Mac Low & Klessen, 2004). In a general sense, magnetic fields are associated with the slow, quasi-static evolution of prestellar cores, while turbulence is associated with a more rapid, dynamic evolution.

In the Shu et al. (1987) paradigm (hereafter the Shu model), magnetic fields dominate the support of molecular clouds on large scales, and low mass star formation takes place in magnetically sub-critical clouds. The relevant parameter is the ratio of magnetic field energy density to gravitational potential energy:  $E_B/E_G$ . For  $E_B/E_G = 1$  the region will be magnetically critical, while  $E_B/E_G < 1$  and  $E_B/E_G > 1$  indicate sub-critical and super-critical regions, respectively. In the highly sub-critical case, ambipolar diffusion moderates the quasi-static contraction of prestellar cores with masses exceeding the local Jeans mass (Shu et al., 1987):

$$M_J = \frac{a^3}{\rho^{1/2}G^{3/2}}, \quad (1.2)$$

where  $a$  is the thermal sound speed and  $\rho$  is the mass density (Jeans, 1928).

Neutral particles are supported against self-gravity only by their friction with ionized particles, which are tied to the magnetic field; ambipolar diffusion refers to the process by which neutrals slip relative to the ions (Spitzer, 1968). The relevant timescale is the ambipolar diffusion timescale:

$$t_{AD} = \frac{3}{4\pi G\rho\tau_{n_i}} \simeq 7.3 \times 10^{13} x_e \text{ yr}, \quad (1.3)$$

where  $\tau_{n_i}$  is the ion-neutral collision time and  $x_e$  is the ionization fraction (e.g., Evans, 1999). For typical cloud conditions,  $t_{AD} \sim 10t_{ff}$  (Nakano, 1998), where  $t_{ff}$  is the free-fall timescale (Spitzer, 1978):

$$t_{ff} = \sqrt{\frac{3\pi}{32G\rho}}. \quad (1.4)$$

Although slow, quasi-static evolution of prestellar cores toward collapse is typically associated with magnetic field support, the gradual dissipation of low level turbulence

can also lead to quasi-static evolution (Myers, 1998).

Molecular clouds are known to be turbulent, with supersonic line widths (e.g., McKee & Zweibel, 1992), and the idea that turbulence dominates the star formation process has gained prevalence in recent years. This is due in part to a number of observations that seem to be inconsistent with the standard Shu model, including the measured density profiles of cores, and the inferred lifetimes of various protostellar phases (see Mac Low & Klessen 2004 for a review). Furthermore, simulations of turbulent fragmentation have had some success reproducing the shape of the initial mass function of stars (e.g., Padoan & Nordlund, 2002; Li et al., 2004). If highly turbulent processes dominate molecular cloud evolution, then detailed models suggest that the lifetime of prestellar cores should be short, approximately  $1 - 2 t_{ff}$  (Ballesteros-Paredes, Klessen, & Vázquez-Semadeni, 2003; Vázquez-Semadeni et al., 2005). Even if magnetic fields are present, cores will collapse on approximately the free-fall timescale as long as the region is super-critical.

Thus, the lifetime of prestellar cores should be a strong discriminator of core formation mechanisms. Published measurements of the prestellar core lifetime vary by two orders of magnitude, however. For example, based on the fraction of optically selected cores with mean densities of  $6 - 8 \times 10^3 \text{ cm}^{-3}$  observed by Lee & Myers (1999) to be starless, a core lifetime of  $6 \times 10^5 \text{ yr}$  was suggested. This is a factor of  $\sim 20$  shorter than the ambipolar diffusion timescale. The fraction of starless isolated globules detected in  $\text{NH}_3$  by Bourke et al. (1995) implies a lifetime of  $2 \times 10^6 \text{ yr}$ . By contrast, Jessop & Ward-Thompson (2000) find a lifetime of  $10^7 \text{ yr}$ , similar to the ambipolar diffusion timescale, for low density cores detected from column density maps based on IRAS far-infrared observations. Most recently, using SCUBA and *Spitzer* maps of Perseus, Jørgensen et al. (2007); Hatchell et al. (2007) both find starless core lifetimes of a few  $\times 10^5 \text{ yr}$ .

The implications of these results can be seen in figure 1.2, from Ward-Thompson et al. (2007), which compares the inferred starless core lifetime from earlier published studies with the mean volume density for each sample. In this figure, the lower dashed line represents the free-fall timescale  $t_{ff}$  as a function of mean density, and the upper

line indicates  $10 t_{ff}$ , approximately the ambipolar diffusion timescale. Most points fall between these two extremes, suggesting that (a) starless cores have some additional means of support beyond thermal pressure, and (b) that cores are unlikely to be highly magnetically sub-critical. Uncertainties in the contributing measurements are large, however, and the number of studies for cores with mean densities greater than approximately  $10^4 - 10^5 \text{ cm}^{-3}$  are relatively few. Cores with densities less than  $10^4 \text{ cm}^{-3}$  may not be truly prestellar, so lifetime arguments based on such objects may be biased.

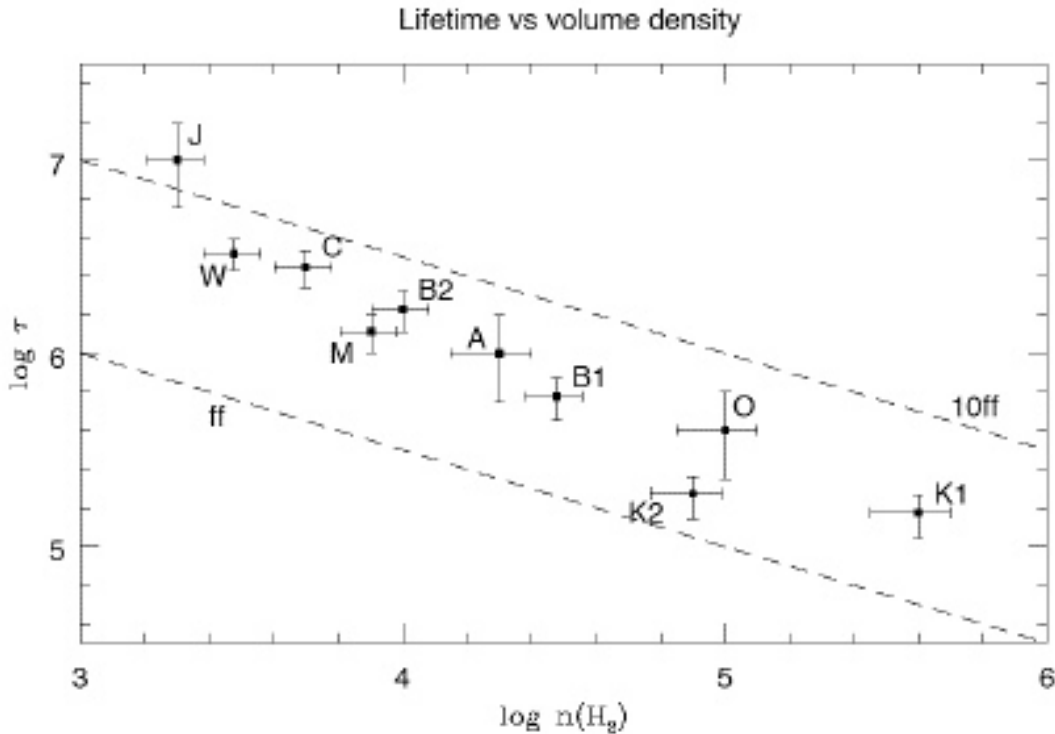


Figure 1.2 Correlation between measured starless core lifetime and the mean density of the sample for a number of studies published before 2006, from Ward-Thompson et al. (2007). Dashed lines indicate the free fall timescale (lower), and  $10t_{ff}$ , or approximately the ambipolar diffusion timescale (upper). The distribution of measurements suggests that cores have some non-thermal support, but are not highly sub-critical.

Another possible discriminator of global cloud physics is the existence of a column density, or  $A_V$ , threshold for star formation. Scenarios in which magnetic fields are the dominant force in molecular clouds naturally accommodate such a threshold, since the support of cloud material by magnetic fields requires the presence of ionized

particles. Core collapse cannot occur if the ionization fraction is too high, but in cloud interiors where material is shielded from cosmic rays, the lower ionization fractions allow for the formation and collapse of cores via ambipolar diffusion. McKee (1989) estimates that star formation requires a minimum column density of  $A_V \sim 4 - 8$  mag, while Shu et al. (1987) suggest  $A_V > 4(B/30\mu G)$  mag. While a few authors claim to have observed such an  $A_V$  threshold (Palla & Stahler, 2002; Johnstone, DiFrancesco, & Kirk, 2004), the supporting evidence is hardly robust, and further observations are required. As noted by Johnstone et al. (2004), it is not clear how turbulent models of star formation could produce an  $A_V$  threshold, so confirmation of such a threshold would provide support for the importance of magnetic fields in the star formation process.

#### 1.1.4 Core Initial Conditions

The initial conditions of dense star-forming cores depend strongly on the physical processes leading to their formation (§1.1.3). In turn, core properties help to determine the evolution of newly formed protostars, as will be demonstrated in §1.1.5. One of the most important diagnostics of initial conditions is the mass distribution of prestellar cores. In addition to being a testable prediction of core formation models, a comparison of the core mass distribution (CMD) to the stellar initial mass function (IMF) may reveal what process is responsible for determining stellar masses (e.g., Meyer et al., 2000).

We focus on three possible processes in the determination of a star's final mass, the value of which fixes its subsequent evolution: (1) In the Shu paradigm, a star determines its own destiny. Cores evolve toward a singular isothermal sphere (SIS) configuration before collapse, and the accreting protostar has, by definition, an infinite mass supply. Accretion is self-regulating, halted by a stellar wind or outflow that is triggered by the onset of thermonuclear burning and clears out the remaining envelope material. The final mass of the star depends primarily on the accretion rate (Shu,

1977):

$$\dot{M} = m_0 a^3 / G, \quad (1.5)$$

and thus on the sound speed in the initial core, since  $a$  is the effective sound speed and  $m_0$  is a constant of order unity. (2) In the competitive accretion picture (e.g., Bonnell et al., 2001), the mass accretion of sources in clusters is a dynamic process. Sources that form earlier or are closest to the cluster center, where the gas density is higher, will have the highest accretion rates and thus the largest final masses. A strong similarity between the prestellar CMD and the final stellar IMF is not necessarily expected for either competitive accretion or the self-regulating Shu model. (3) Alternatively, the final mass of a star may be established during core formation, presumably by the fragmentation process. In crowded regions where the mass reservoir of any given protostar is limited to the core in which it formed, the final stellar mass will depend on the initial core mass. If this fraction is relatively universal, then the shape of the emergent IMF should mirror that of the CMD. The idea that cloud fragmentation leads directly to the IMF is by no means new, but the original idea of the formation of cores by hierarchical fragmentation (Hoyle, 1953) has largely been replaced by turbulent fragmentation (e.g., Mac Low & Klessen, 2004; Ballesteros-Paredes et al., 2006).

Of course, all three of these processes probably play some role. Given the current observational capabilities, we can realistically hope to test the hypothesis that the stellar IMF is entirely determined by the core fragmentation process, based on a comparison of the prestellar CMD to the IMF. While a direct link between the two cannot be definitively determined by comparing the mass distribution shapes, it is possible to either rule out or build evidence for such a link. Most often, the shape of both the IMF and CMD are approximated either by a power law:

$$\frac{dN}{dM} \propto M^\alpha, \quad (1.6)$$

where  $dN/dM$  is the differential mass distribution and  $\alpha$  is the power law slope, or

by a lognormal function:

$$\frac{dN}{d \log M} = A \exp \left[ \frac{-(\log M - \log M_0)^2}{2\sigma^2} \right], \quad (1.7)$$

where

$$\frac{dN}{dM} = \frac{1}{(\ln 10)M} \frac{dN}{d \log M}, \quad (1.8)$$

$M_0$  is the characteristic mass, and  $\sigma$  is the width of the distribution.

There is some evidence that the stellar IMF is universal within our Galaxy (e.g., Kroupa, 2002), but individual measurements of the IMF shape can vary significantly, and uncertainties remain large (e.g., Scalo, 2005). The classic value for the IMF slope is the ‘‘Salpeter IMF’’:  $\alpha = -2.35$  (Salpeter, 1955), while Scalo (1986) found a steeper slope ( $\alpha \sim -2.7$ ) for sources with mass  $M \gtrsim 1 M_\odot$ . More recently, Reid, Gizis, & Hawley (2002) find  $\alpha \sim -2.5$  above  $0.6 M_\odot$ , and  $\alpha \sim -2.8$  above  $1 M_\odot$ , while Schröder & Pagel (2003) find  $\alpha \sim -2.7$  for  $1.1 < M < 1.6 M_\odot$  and  $\alpha \sim -3.1$  for  $1.6 < M < 4 M_\odot$ . Thus an IMF slope within the range  $\alpha = -2.3$  to  $-2.8$  appears to be a reasonable choice for  $M > 1 M_\odot$ .

Much recent work has focused on lower masses, where the IMF becomes flatter than the Salpeter or Scalo values, and may be better characterized by a lognormal function. Kroupa (2002) suggests a three-component power law:  $\alpha = -2.3$  for  $0.5 < M < 1 M_\odot$ ,  $\alpha = -1.3$  for  $0.08 < M < 0.5 M_\odot$ , and  $\alpha = -0.3$  for  $0.01 < M < 0.08 M_\odot$ , while Chabrier (2005) finds that a lognormal distribution with  $\sigma = 0.55$  and  $M_0 = 0.25 M_\odot$  is a good fit for  $M < 1 M_\odot$ . The system IMF, for which multiple systems are not resolved, is appropriate for comparison to core studies and peaks at approximately  $0.2 - 0.3 M_\odot$  (e.g., Chabrier, 2005; Luhman et al., 2003). To date, a few studies have found similarities between the shapes of the IMF and CMD, providing support for the idea that stellar masses in clusters are determined by the fragmentation of turbulent clouds. Testi & Sargent (1998) measured the mass distribution of millimeter cores in the Serpens main core with the OVRO interferometer, finding a power law slope of  $\alpha = -2.1$  above  $0.4 M_\odot$ , similar to the Salpeter IMF. Similarly, Motte et al. (1998) found  $\alpha = -2.5$  for submillimeter cores with  $M > 0.5 M_\odot$  in the  $\rho$  Ophiuchi main

cloud, while Onishi et al. (2002) measured a slope for the mass distribution of starless  $\text{H}^{13}\text{CO}^+$   $J = 1 - 0$  condensations in Taurus of  $\alpha = -2.5$  for  $M > 3.5 M_{\odot}$ .

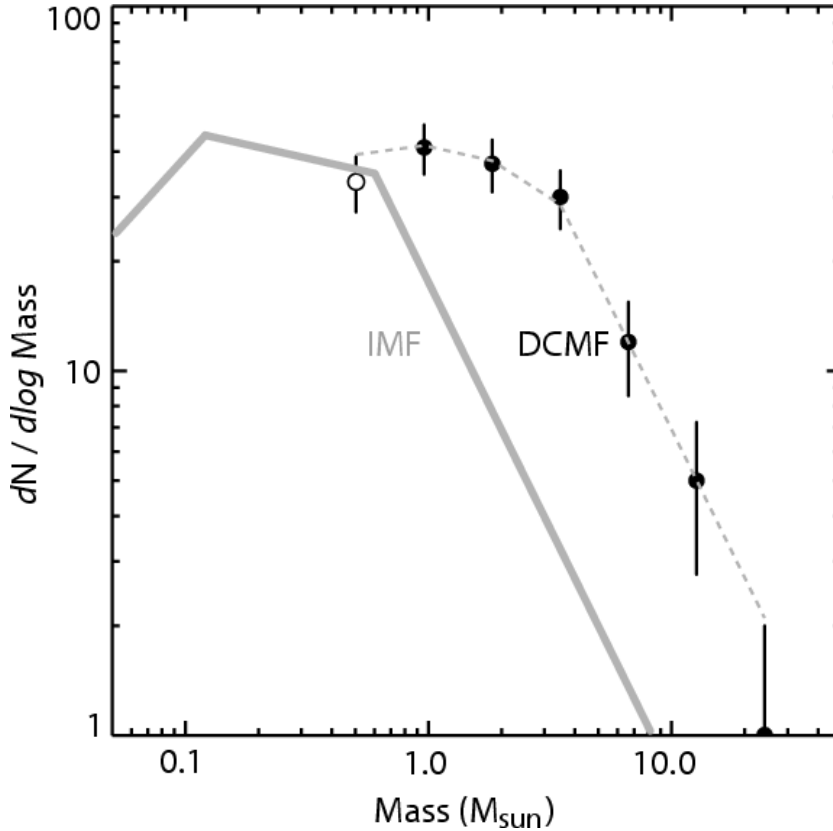


Figure 1.3 Mass distribution of cores in the Pipe nebula identified by dust extinction, from Alves et al. (2007). The shape of the CMD is remarkably similar to the shape of the stellar IMF measured by Muench et al. (2002) for the Trapezium cluster, with the CMD shifted to higher masses by approximately a factor of four.

More recently, Alves, Lombardi, & Lada (2007) used dust extinction toward the Pipe nebula to derive a CMD that is characterized by a two-component power law above  $1 M_{\odot}$ , with a break at about  $2.5 M_{\odot}$  (figure 1.3). The Pipe Nebula CMD appears remarkably similar to the stellar IMF for the Trapezium cluster (Muench et al., 2002), with the CMD shifted to higher masses by approximately a factor of four. Alves et al. (2007) interpret this similarity as evidence that the stellar IMF is a direct product of the CMD, with a uniform core-to-star efficiency of  $30\% \pm 10\%$ . The mean densities of the extinction-identified cores in this study ( $5 \times 10^3 - 2 \times 10^4 \text{ cm}^{-3}$ ) are lower than those of typical cores traced by dust (sub)mm emission ( $\gtrsim 10^4 \text{ cm}^{-3}$ ; chap-

ter 5), however, and the cores may not be truly prestellar. Furthermore, extinction measurements are sensitive to all material along the line of sight, and may confuse dense cores with more extended structures.

Large samples of prestellar cores are important for further addressing this problem, as is a more reliable separation of prestellar, protostellar, and unbound starless cores. Molecular line or extinction surveys often trace relatively low density material ( $10^3 - 10^4 \text{ cm}^{-3}$ ), leaving the possibility that such cores may never collapse to form stars. In addition, most previous studies base the identification of protostellar versus starless cores on near-infrared data, which is not sensitive to the most embedded protostars, or on low resolution and poor sensitivity IRAS maps. The first issue can be remedied by using millimeter or submillimeter surveys; (sub)mm emission traces dense ( $n > 10^4$ ) material, and detection at (sub)mm wavelengths tends to correlate well with other indications of a true prestellar nature, such as in-falling motions (Gregersen & Evans, 2000). *Spitzer* provides significant progress on the second, with substantially superior resolution and sensitivity compared to IRAS, making the identification of prestellar cores much more secure.

Another revealing measure of core initial conditions is the radial density profile of prestellar cores. In the Shu model, cores forming via ambipolar diffusion evolve toward the radial density profile of a singular isothermal sphere, characterized by  $\rho(r) \propto r^{-2}$ , just before collapse. There are many possible initial configurations, however. Isothermal cores confined by external pressure, or Bonnor-Ebert spheres (Bonnor, 1956; Ebert, 1955), have a maximum density contrast from the center to the outer edge of 14, and an inner density profile that is significantly shallower than the SIS. The logotropic equation of state considered by McLaughlin & Pudritz (1997) corresponds to initial cores with  $\rho(r) \propto r^{-1}$ .

Two complementary methods may be employed to understand the density profiles of prestellar cores: high resolution studies of individual cores, or statistical arguments based on large samples. A number of recent studies using high resolution observations at (sub)mm wavelengths and radiative transfer modeling have found evidence for flattened inner density profiles, similar to BE spheres (Di Francesco et al., 2007). It

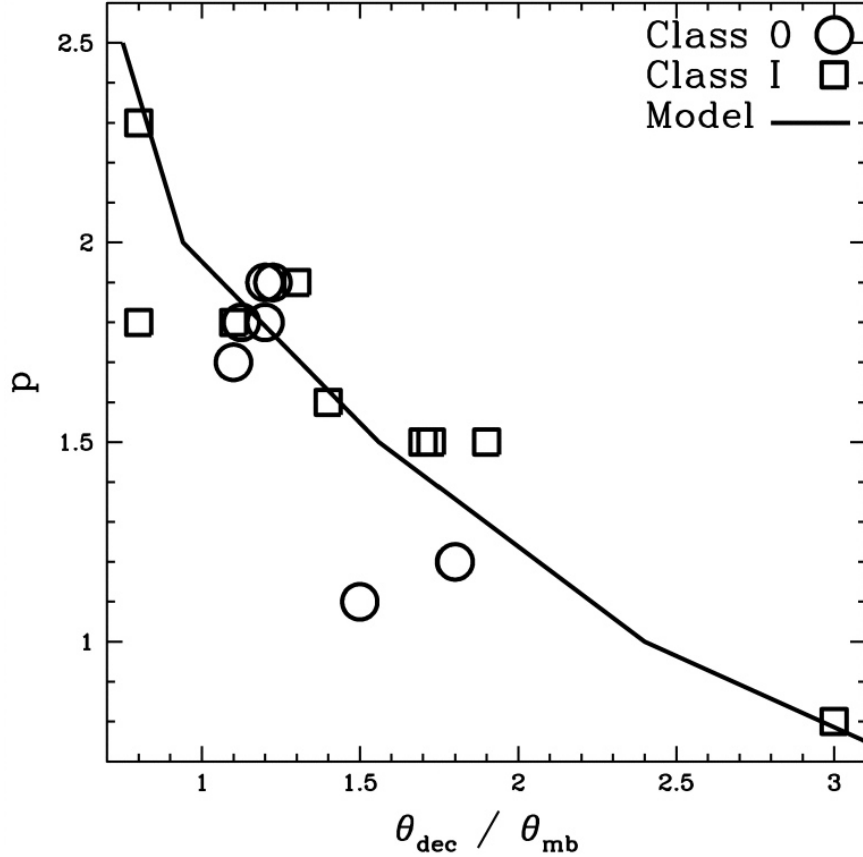


Figure 1.4 Correlation between source angular size and density profile, from Young et al. (2003). The density power law index  $p$ , inferred from radiative transfer modeling of Class 0 and Class I sources, is shown versus the measured angular deconvolved size, together with the relation predicted by dust emission models (solid line). This correlation provides a method for probing source density profiles with only marginally resolved data.

may also be possible to probe the density profile of starless cores with only marginally resolved data, if a sufficient sample size is assembled. Young et al. (2003) have shown that the measured angular deconvolved sizes  $\theta_{dec}$  of sources with power law density profiles are inversely proportional to the index of the power law  $p$ . This is demonstrated in figure 1.4, from Young et al. (2003), where  $\theta_{mb}$  is the beam full-width at half-maximum, and the observed  $p$  values for Class 0 and Class I sources were determined from radiative transfer modeling of SCUBA data. The solid line represents dust emission models with  $0.5 < p < 2.5$ . Using the correlation between  $p$  and  $\theta_{dec}$  shown in figure 1.4, it is feasible to infer the average density power law index

of a large sample of sources based on their observed sizes. Although this analysis requires the assumption of a power law density profile, it is nonetheless possible to test the Shu model prediction that  $p = 2$  for prestellar cores close to collapse.

### 1.1.5 Early Protostellar Evolution

Protostellar evolution is directly tied to initial conditions of cores, and accretion rates during the main accretion phase are an important discriminator for star formation models. The Shu model predicts a constant accretion rate,  $\dot{M} \sim a^3/G$ , while isothermal non-singular core density profiles generally result in rates that are initially high and decrease with time (e.g., Henriksen, Andre, & Bontemps, 1997). The logotropic core equation of state adopted by McLaughlin & Pudritz (1997), in contrast, produces accretion rates that increase with time as  $\dot{M} \propto t^3$ .

Directly measuring the accretion rates of newly formed protostars is nearly impossible due to their embedded nature (although  $\dot{M}$  has been measured for a few optically visible Class I sources (White et al., 2007)). We can constrain these rates, however, using evolutionary models, which have been developed to reproduce the observed spectrum of protostellar sources as a function of time by varying initial conditions, mass accretion rates, and final stellar mass. Some models apply analytic solutions to the problem of core collapse (e.g., Myers et al., 1998), while others utilize self-consistent radiative transfer codes to predict observable properties (e.g., Young & Evans, 2005; Whitney et al., 2003). Ideally, a comparison between models and observed source properties will differentiate between the input initial conditions and assumed star formation models, as well as provide estimates of the accretion rate, age, and final mass for individual sources.

Figure 1.5 shows the results of simple evolutionary models from Myers et al. (1998), plotted as tracks on a bolometric luminosity versus bolometric temperature ( $L_{bol} - T_{bol}$ ) diagram. The  $L_{bol} - T_{bol}$  diagram for protostellar sources is analogous to the Hertzsprung-Russell (H-R) diagram (Hertzsprung, 1905; Russell, 1914) for more evolved objects. Protostellar cores do not have a well-defined photosphere, and

thus do not have a well-defined effective temperature. Instead, the temperature is quantified by  $T_{bol}$ , defined as the temperature of a blackbody with the same mean frequency  $\langle\nu\rangle$  as the observed SED:

$$T_{bol} = \frac{\zeta(4)}{4\zeta(5)} \frac{h\langle\nu\rangle}{k} = 1.25 \times 10^{-11} \langle\nu\rangle \text{ K Hz}^{-1} \quad (1.9)$$

(Myers & Ladd, 1993). The mean frequency is the luminosity weighted mean,

$$\langle\nu\rangle = \frac{\int \nu S_\nu d\nu}{\int S_\nu d\nu}, \quad (1.10)$$

and  $\zeta(n)$  is the Riemann zeta function.

Myers et al. (1998) develop analytic expressions for  $T_{bol}$  and  $L_{bol}$  as a function of time, assuming an accretion rate that is initially the Shu value,  $dM/dt = c_s^3/G$ , and then falls off exponentially with time. The emergent bolometric luminosity is the sum of the infall (accretion) and stellar contraction luminosities. They also assume that a significant fraction of the original core mass is dissipated during the star formation process ( $M_{core}/M_* = 6$ ). This simple model was a good match to the properties of Class 0 and Class I sources known at the time, suggesting that accretion rates decrease with time after protostar formation. It must be reevaluated based on more complete samples and more sensitive data, however. More detailed models using accretion rates that are constant (Young & Evans, 2005), or derived from turbulent simulations (Froeblich et al., 2006), can also be tested against observations.

Mass accretion rates are directly linked to the length of time sources spend in any given evolutionary stage. The relative number of sources in sequential stages of evolution can be used as a simple measure of the relative lifetimes of those stages:  $t_1/t_2 = N_1/N_2$ . This kind of analysis relies on a number of assumptions, including that (1) star formation is steady in time, i.e. we are not observing sources at a special time in their evolution, (2) we have correctly categorized sources into a true evolutionary sequence, and (3) there are no significant variations of the lifetime with source mass. Observations of protostars in  $\rho$  Ophiuchi originally led to an extremely short estimate

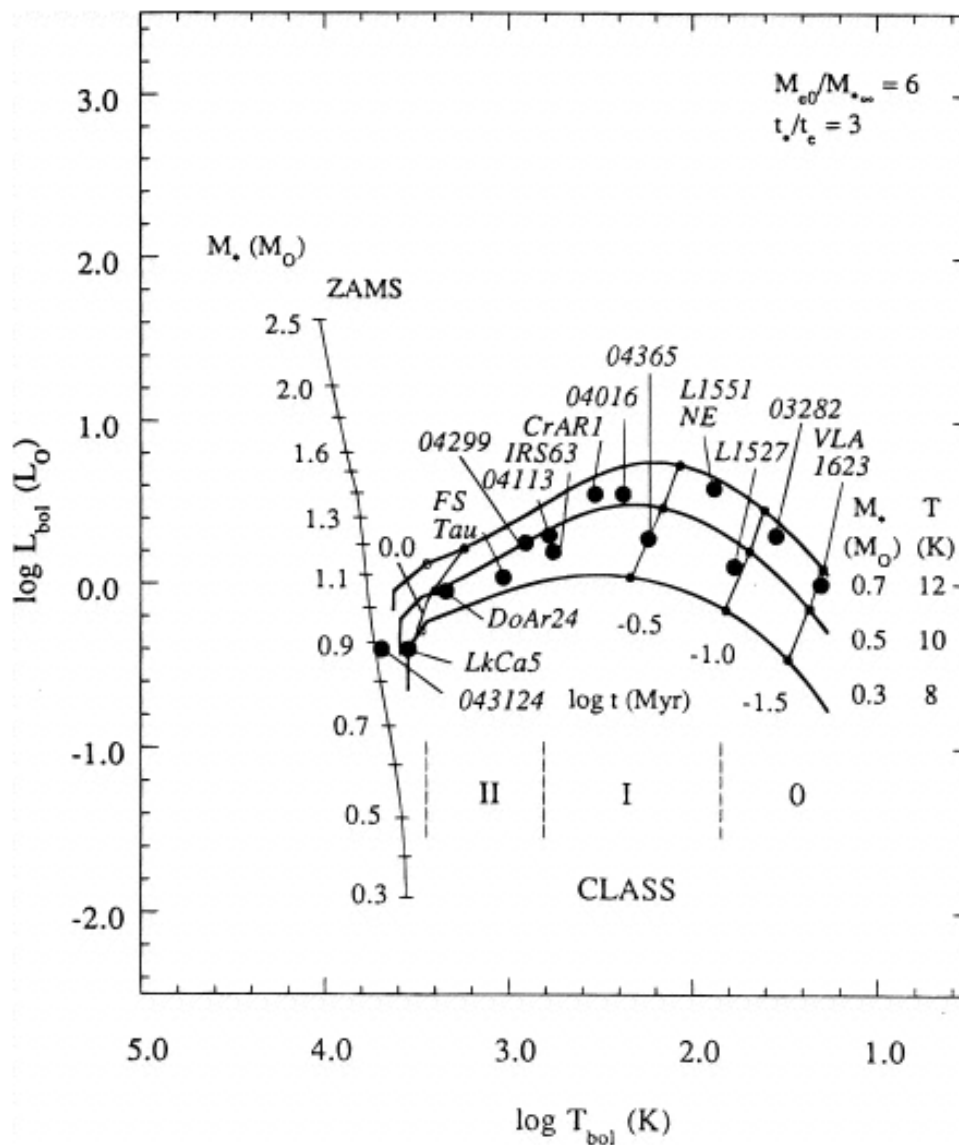


Figure 1.5 Simple models of the evolution of protostars from Myers et al. (1998), plotted on the bolometric luminosity-temperature diagram, and compared to data for young protostars available at the time. Myers et al. (1998) assume an exponentially decreasing accretion rate and derive analytic expressions for  $T_{bol}$  and  $L_{bol}$  as a function of time.

for the Class 0 phase,  $t_{Class0} \sim 10^4$  yr, based on the relative number of Class 0 and Class I objects (André & Montmerle, 1994). Such a short Class 0 lifetime would require very high accretion rates immediately after protostellar formation. More recent studies of a sample of Lynds dark clouds (Visser et al., 2002) and protostars in Perseus (Hatchell et al., 2007) have concluded that the Class 0 lifetime is similar

to the Class I lifetime, approximately  $2 - 4 \times 10^5$  yr.

The Class 0 lifetime can be used as a further test of protostellar evolutionary models, which predict varying lengths of time spent in the Class 0 phase. In the exponentially declining accretion rate models of Myers et al. (1998), a source with final stellar mass  $0.3 M_{\odot}$  reaches the end of the Class 0 phase (when  $M_* = M_{env}$ ) at  $t \sim 10^5$  yr. Young & Evans (2005) assume a constant Shu accretion rate, finding that  $M_* = M_{env}$  at a much earlier time,  $t \sim 3.5 \times 10^4$  yr. Froebrich et al. (2006) compare accretion rates predicted by numerical simulations of gravo-turbulent fragmentation models (Schmeja & Klessen, 2004) to a sample of observed protostars, finding a lifetime for Class 0 sources of  $2 - 6 \times 10^4$  yr.

A complete census of young protostars is important for comparing to evolutionary models, and for calculating a statistically significant lifetime for the Class 0 phase. In contrast to less embedded sources, the highly obscuring envelopes of Class 0 sources make them invisible at short wavelengths, so sensitive mid- to far-infrared measurements are necessary to obtain a more complete picture of how protostars evolve through this early stage. Larger samples will provide more robust statistics, and help to differentiate the sometimes degenerate effects of environment, viewing geometry, and age.

### 1.1.6 Effects of Environment

Cloud environmental factors such as turbulence and average cloud density may have strong effects on the outcome of star formation. Nearly all of the observational measures discussed above may vary with large-scale cloud conditions, including the CMD, initial conditions of cores, protostellar accretion rates, and the efficiency of star formation. For example, starless cores in regions of clustered star formation are observed to have smaller radii and higher column density, by as much as an order of magnitude, than isolated cores. Even the dominant physical processes controlling core formation and evolution (e.g., quasi-static versus dynamic) may depend on environment (Ward-Thompson et al., 2007). Vázquez-Semadeni et al. (2005) suggest that the strength of

magnetic fields in turbulent clouds has a significant impact on the efficiency of star formation.

Differences with environment are important to quantify if we are to understand the implications of observations. In addition, it is important to know which observed properties do *not* seem to change with environment; e.g., if the IMF is truly universal but the CMD varies from cloud to cloud, any successful theory of star formation would be required to explain the discrepancy. Ideally, theories and simulations of star formation can make predictions based on varying environmental factors, enabling observations in different environments to place strong constraints on star formation models.

Several authors have been able to reproduce the slope of the IMF directly from turbulent fragmentation into cores (e.g., Padoan & Nordlund, 2002; Li et al., 2004), but special assumptions are often required. Ballesteros-Paredes et al. (2006) test the dependence on Mach number of the CMD resulting from smoothed particle hydrodynamics (SPH) simulations of turbulent fragmentation, finding that the emergent mass spectrum of dense cores depends strongly on the turbulent Mach number in the cloud (figure 1.6). The Mach number is a measure of the strength of turbulence:  $\mathcal{M} = \sigma_v/c_s$ , where  $\sigma_v$  is the rms velocity dispersion,  $c_s = \sqrt{kT/\mu m_H}$  is the isothermal sound speed, and  $\mu$  is the mean molecular weight per particle.

As demonstrated in figure 1.6, Ballesteros-Paredes et al. (2006) find that models with stronger turbulence (i.e. higher Mach numbers) result in a larger number of low mass cores and relatively few high mass cores (solid curve). Strong turbulence creates more sub-structure on smaller scales, thus favoring many cores of low mass. Conversely, weaker turbulence (lower Mach numbers) results in cores with higher masses in general, and significantly fewer low mass cores (dotted curve). Furthermore, the slope of the CMD for  $M \gtrsim 0.3 M_\odot$  is noticeably flatter for the low Mach number models. These important differences make it possible to test predictions of simulations such as this one by measuring the core mass distribution in clouds with varying turbulent properties.

For the most part, previous samples of prestellar cores and very young protostars

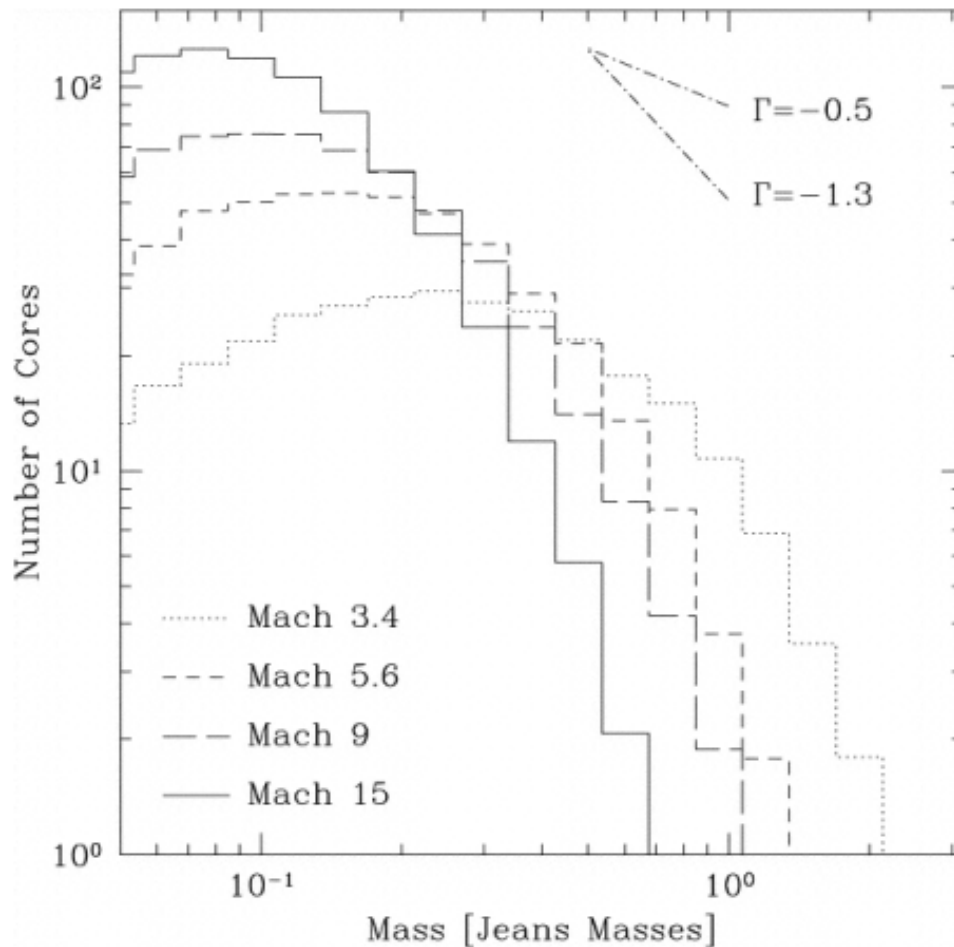


Figure 1.6 Core mass distributions resulting from the SPH turbulent fragmentation simulations of Ballesteros-Paredes et al. (2006), for a range of turbulent Mach numbers. Larger Mach numbers result in a higher fraction of low mass cores, and a steeper slope at the high mass end of the CMD.

have not been large enough to disentangle the effects of environment from systematic uncertainties and small number statistics. Many studies have combined data from different instruments or resulting from different reduction and analysis techniques, complicating the picture further. Large, unbiased, complete samples in a range of environments are necessary to test the effect of environment on the core mass distribution, the initial conditions and spatial distributions of cores, the star formation efficiency, and protostellar evolution.

## 1.2 Observations

In order to make significant progress on the problems described above, a complete census of starless cores and young protostars in molecular clouds is required. Thus large-scale observations of entire molecular clouds are necessary, particularly at far-infrared to millimeter wavelengths, where the emission from starless cores and deeply embedded protostars peaks. Sensitive mid-infrared data are also essential for the reliable identification of prestellar cores and characterization of young protostars. In addition, surveys of many different regions and in clouds with diverse properties are needed to address the possible environmental dependencies of the star formation process.

### 1.2.1 Millimeter Surveys

Large-scale millimeter-wavelength continuum surveys are essential for addressing the outstanding questions outlined in §1.1.2. Millimeter emission from molecular clouds traces the total mass of prestellar cores and protostellar envelopes, and is one of the best ways to detect prestellar cores, which are only visible at far-infrared to millimeter wavelengths. Furthermore, millimeter surveys provide a large-scale picture of the ongoing star formation in molecular clouds by detecting the current, and even future, populations of star-forming cores.

Historically, most studies at submillimeter and millimeter wavelengths have focused on individual objects or small regions of less than  $1 \text{ deg}^2$ , due to instrumental limitations. Recently, however, the development of large-format bolometer arrays on 10 m class telescopes has made it possible to complete large-scale maps of nearby molecular clouds, covering many square degrees on the sky. Examples of currently operating bolometer arrays, and their characteristics, are given in table 1.1.

In the last few years, wide-field mapping of several nearby molecular clouds has been completed. Approximately  $0.2 \text{ deg}^2$  of the Ophiuchus molecular cloud was mapped by Johnstone et al. (2000) at  $850 \mu\text{m}$  with SCUBA, while a larger  $4 \text{ deg}^2$  map is referred to by Johnstone et al. (2004) and available from the COMPLETE

Table 1.1. Millimeter and submillimeter bolometer arrays

Telescope	Instrument	Wavelength(s)	Pixels	Field of view	Resolution	Reference
CSO	Bolocam	1.1, 1.4, 2.1 mm	144	7'5 <sup>a</sup>	30'' <sup>a</sup>	(1)
CSO	SHARC II	350, 450, 850 $\mu\text{m}$	384	2'6 $\times$ 1'	9''	(2)
JCMT	SCUBA	450, 850 $\mu\text{m}$	37 <sup>b</sup>	2'3 <sup>b</sup>	14'' <sup>b</sup>	(3)
IRAM 30 m	MAMBO2	1.2 mm	117	4'	11''	(4)
SEST	SIMBA	1.2 mm	37	5'	24''	(5)

Note. — References: (1) Glenn et al. 1998; (2) Dowell et al. 2003; (3) Holland et al. 1999; (4) Kreysa et al. 1998; (5) Nyman et al. 2001. CSO: Caltech Submillimeter Observatory, JCMT: James Clerk Maxwell Telescope, SEST: Swedish-ESO Submillimetre Telescope.

<sup>a</sup>at  $\lambda = 1.1$  mm

<sup>b</sup>at  $\lambda = 850$   $\mu\text{m}$

website.<sup>1</sup> Most recently, Stanke et al. (2006) mapped 1.3 deg<sup>2</sup> in Ophiuchus at 1.2 mm with SIMBA. In the Perseus molecular cloud, Hatchell et al. (2005) mapped 3 deg<sup>2</sup> with SCUBA at 850 and 450  $\mu\text{m}$ . Combining SCUBA archive data with new observations of an additional 1.3 deg<sup>2</sup>, Kirk et al. (2006) analyzed a total area of 3.5 deg<sup>2</sup>. The Bolocam 1.1 mm surveys presented in this thesis cover significantly larger areas in Perseus (7.5 deg<sup>2</sup>) and Ophiuchus (10.8 deg<sup>2</sup>), and include a 1.5 deg<sup>2</sup> map of the Serpens molecular cloud.

### 1.2.1.1 Prestellar Cores

As is evident from the SED in figure 1.1, prestellar cores are only visible at wavelengths longer than about 50  $\mu\text{m}$ , and their SEDs peak at 200–400  $\mu\text{m}$ . Consequently, submillimeter ( $\lambda \sim 350 - 850 \mu\text{m}$ ) and millimeter ( $\lambda \sim 1 - 3$  mm) continuum observations are ideal for studying these cold objects. In contrast to FIR observations, which must be completed above the earth's atmosphere, (sub)mm observations can utilize large ground-based telescopes. Continuum surveys for prestellar cores also have advantages over spectral line and dust extinction studies. Even spectral line surveys

<sup>1</sup><http://cfa-www.harvard.edu/COMPLETE>

using molecules with relatively high critical densities (e.g.,  $\text{NH}_3$ , which is sensitive to  $n_{\text{H}_2} \gtrsim 3 \times 10^3 \text{ cm}^{-3}$ ), are generally sensitive to lower density material than millimeter observations, and can be subject to chemistry effects such as depletion, freeze-out, and evaporation (e.g., Lee, Bergin, & Evans, 2004). Dust extinction maps are sensitive to all material along the line of sight, not just that in dense cores, and are more likely than millimeter surveys to detect diffuse structures that will never form stars.

Observationally, it is difficult to separate true prestellar cores, which are gravitationally bound and will eventually collapse to form stars, from stable or unbound cores that will eventually disperse back into the general cloud medium. Throughout this thesis I follow Di Francesco et al. (2007) in defining “starless” cores as low mass dense cores without a compact internal luminosity source, “prestellar” cores, at least conceptually, as starless cores that are gravitationally bound, and “protostellar” cores as dense cores that already harbor a compact internal source. A practical method of distinguishing prestellar cores is required as well; our operational definition of a prestellar core is a starless core that is detected at submillimeter or millimeter wavelengths. Such sources have mean densities  $\gtrsim 2 - 3 \times 10^4 \text{ cm}^{-3}$  (see Ward-Thompson et al. 1994 and chapter 5), and are more likely to show evidence for infall motions than lower density starless cores (Gregersen & Evans, 2000).

### 1.2.1.2 Masses

Dust grains in cold ( $5 - 30 \text{ K}$ ), dense ( $n \gtrsim 10^4 \text{ cm}^{-3}$ ) prestellar and protostellar cores produce thermal emission at far-infrared (FIR) to millimeter wavelengths. The relationship between the observed flux from an individual source of millimeter continuum emission and the mass of dust in that source can be easily derived. Radiative transfer gives us the flux density from a spherical source of dust emission at a frequency  $\nu$ :

$$F_\nu = \int I_\nu \cos \theta d\Omega, \quad (1.11)$$

where

$$I_\nu = \int \rho \kappa_\nu S_\nu ds \quad (1.12)$$

is the specific intensity,  $S_\nu = B_\nu(T_D)$  is the source function,  $\rho$  is the mass density of dust,  $T_D$  is the dust temperature, and  $\kappa_\nu$  is the dust opacity at frequency  $\nu$ . Integrations are over source solid angle in equation (1.11), and line-of-sight distance in equation (1.12).

Assuming that the emission is optically thin at the observed frequency. and that  $\kappa_\nu$  and  $\rho$  do not vary with position, the integral in equation (1.12) simplifies to:

$$I_\nu = \rho\kappa_\nu B_\nu(T_D) \int_{-R}^R ds = 2R\rho\kappa_\nu B_\nu(T_D), \quad (1.13)$$

where  $R$  is the radial extent of the source. Combining equations (1.11) and (1.13) produces

$$F_\nu = \rho\kappa_\nu B_\nu(T_D) \int_0^{2\pi} d\phi \int_0^{\theta_c} 2R \sin^2\theta \cos\theta d\theta = \rho\kappa_\nu B_\nu(T_D) 2\pi d \frac{\sin^3\theta_c}{3}, \quad (1.14)$$

where  $\sin\theta_c = R/d$  and  $d$  is the distance to the source. Finally,

$$F_\nu = \frac{4\pi R^3}{3} \frac{\rho\kappa_\nu B_\nu(T_D)}{d^2} = M_D \frac{\kappa_\nu B_\nu(T_D)}{d^2}, \quad (1.15)$$

where we have assumed a spherical source and substituted the total mass of dust:  $M_D = \frac{4}{3}\pi R^3 \rho$ .

Thus for optically thin emission the observed flux density of a core is proportional to the total mass of dust, and equation (1.15) can be inverted to give us the mass:

$$M_D = \frac{d^2 S_\nu}{B_\nu(T_D) \kappa_\nu}. \quad (1.16)$$

Although the millimeter emission arises only from the dust and not the gas that provides the majority of mass in a core, we can infer the total mass of gas *and* dust by assuming a gas to dust mass ratio of 100, which is generally included in the value of  $\kappa_\nu$ . As long as the bulk of a given core remains optically thin at millimeter wavelengths, this equation provides a straightforward method for measuring the total mass in starless cores and protostellar envelopes, assuming  $\kappa_\nu$  is known.

Directly measuring the (sub)mm emissivity, or equivalently the opacity  $\kappa_\nu$ , of dust in molecular clouds and dense cores is extremely difficult, as it requires independent knowledge of the amount of dust present (e.g., Alton et al., 2000). Although the wavelength dependence of dust extinction in the interstellar medium is well known, and has been successfully characterized by models of grain composition and size distributions together with synthesized dielectric functions of grain components (Mathis, Rumpl, & Nordsieck, 1977; Draine & Lee, 1984), dust grains in dense cores differ from those in the general interstellar medium due to grain coagulation and the formation of molecular ice mantles. The optical properties of such particles are a sensitive function of the assumed structure and chemical composition of the grains; detailed modeling of the accretion and coagulation of dust grains are necessary to calculate the opacity as a function of wavelength (Ossenkopf & Henning, 1994).

Resulting opacities still vary by at least a factor of two ( $\kappa_{1mm} \sim 0.008 - 0.017 \text{ cm}^2 \text{ g}^{-1}$ ; Ossenkopf & Henning 1994), depending on gas density and coagulation time, and must be constrained using high-resolution observations of individual cores, together with radiative transfer modeling (e.g., Shirley, Evans, & Rawlings, 2002; Young et al., 2003) or comparison to extinction from deep near-infrared maps (e.g., Bianchi et al., 2003). Here I adopt  $\kappa_{1mm} = 0.0114 \text{ cm}^2 \text{ g}^{-1}$ , with the caveat that all masses retain an uncertainty of at least a factor of two. This value is interpolated from Ossenkopf & Henning (1994) table 1 column 5, for dust grains with thin ice mantles, coagulated for  $10^5$  years at a gas density of  $10^6 \text{ cm}^{-3}$ .

### 1.2.2 Infrared Surveys

When millimeter surveys are combined with *Spitzer* infrared data they provide an even more powerful probe of star formation. Detecting and characterizing the compact, accreting objects embedded within protostellar cores requires information at mid- to far-infrared wavelengths to complete the story. Sensitive infrared data, especially from  $\lambda \sim 10\mu\text{m}$  to a few  $\times 100\mu\text{m}$ , are necessary for calculating source spectral energy distributions, as well as properties such as  $L_{bol}$  and  $T_{bol}$ , which are essential

for comparisons to evolutionary models. Furthermore, infrared data are required to identify starless cores, and to make the accurate classifications of protostellar sources needed to estimate the lifetimes of evolutionary stages.

The Bolocam 1.1 mm maps of Serpens, Perseus, and Ophiuchus presented in this thesis are coordinated to cover the same regions as *Spitzer* Space Telescope Infrared Array Camera (IRAC) and Multiband Imaging Photometer for *Spitzer* (MIPS) maps from the “Cores to Disks” *Spitzer* Legacy program. IRAC consists of four arrays simultaneously viewing the sky at  $\lambda = 3.6, 4.5, 5.8,$  and  $8.0 \mu\text{m}$ , while MIPS images at  $\lambda = 24, 70,$  and  $160 \mu\text{m}$  simultaneously. Thus *Spitzer* maps provide complete wavelength coverage from 3.6 to  $1100 \mu\text{m}$  when combined with the Bolocam data.

### 1.2.2.1 “Cores to Disks” Legacy Program

As part of the *Spitzer* Legacy program “From Molecular Cores to Planet-forming Disks” (“Cores to Disks” or c2d; Evans et al. 2003), the five nearest large molecular clouds, including Perseus, Serpens, and Ophiuchus, were mapped with IRAC and MIPS on the *Spitzer* Space Telescope. The c2d IRAC and MIPS maps cover 3.9 and  $10.6 \text{ deg}^2$ , respectively, in Perseus, 0.9 and  $1.5 \text{ deg}^2$  in Serpens, and 6.6 and  $13.7 \text{ deg}^2$  in Ophiuchus. *Spitzer* observations were designed to cover down to  $A_V \sim 2$  mag in the Perseus cloud based on the  $^{13}\text{CO}$  map of Padoan et al. (1999), and  $A_V \sim 3$  mag in Ophiuchus and  $A_V \sim 6$  mag in Serpens based on the visual extinction maps of Cambr esy (1999). Goals of the c2d project include determining how the youngest stars and protostars are distributed in position and mass, and using unbiased determinations of cloud populations to measure statistical lifetimes for various evolutionary stages (Evans et al., 2003).

All data from the c2d project, including post-pipeline improved images and catalogs containing IRAC and MIPS ( $24, 70 \mu\text{m}$ ) fluxes of all detected sources in each cloud, are publicly available (Evans et al., 2007). Near-infrared data are also included in the c2d catalogs for sources that appear in the Two Micron All Sky Survey (2MASS) catalogs. Photometry at  $160 \mu\text{m}$  has been calculated by the c2d team for point-like sources in the MIPS  $160 \mu\text{m}$  maps, but is not included in the public cat-

alogs. Data reduction, mapping, and source extraction are described in detail in a series of “basic data papers” (e.g., Jørgensen et al., 2006; Harvey et al., 2006; Rebull et al., 2007), in which cloud maps are also presented. Harvey et al. (2007) discuss the method for identifying young stellar object (YSO) candidates, which cover the range from infrared-excess stars to deeply embedded protostars. A careful accounting for extragalactic contamination is also included in Harvey et al. (2007).

### 1.3 Thesis Goals and Outline

As already indicated, there are a number of outstanding questions that remain regarding the formation of low mass stars in molecular clouds. The nature of the dominant physical processes controlling the formation and support of prestellar cores, and their subsequent collapse into protostars, is still a matter of debate. Initial conditions of the prestellar core populations of molecular clouds are important probes of the star formation process, including cloud support, core formation, and core collapse physics. In particular, the prestellar core mass distribution and the lifetime of prestellar cores provide important tests of star formation theories. The evolution of protostars from initial core collapse through the main accretion phase, including mass accretion rates and timescales, have remained difficult to characterize due to the highly embedded nature of such sources. A combination of millimeter and far-infrared observations are necessary to understand these deeply embedded sources. Finally, relatively little is understood about how the star formation process depends on environmental factors such as average cloud density or the strength of large-scale turbulence. Addressing this question requires large-scale surveys in many different star-forming environments.

The goal of this thesis is to address each of these important issues. To that end, I utilize large-scale,  $\lambda = 1.1$  mm dust continuum surveys in combination with deep *Spitzer* IRAC and MIPS maps, to build a complete sample of the youngest star-forming objects in three nearby molecular clouds. Chapters 2, 3, and 4 present the basic results of Bolocam 1.1 mm continuum surveys of the Perseus, Ophiuchus, and Serpens molecular clouds, respectively. Also in chapter 2, I introduce the 1.1 mm

survey techniques and basic data reduction procedures, and describe an iterative mapping routine that I developed for the Bolocam reduction pipeline, which is essential for analysis of the molecular cloud data. Results from the Perseus survey include source identifications and fundamental source properties such as fluxes, sizes, shapes, masses. The relationship between dense cores and other column density tracers such as visual extinction and  $^{13}\text{CO}$  molecular line mapping is also discussed, as is the spatial clustering properties of cores. This chapter has already been published (Enoch et al., 2006).

Results from the Ophiuchus and Serpens surveys are presented in a similar way in chapters 3 and 4. They are accompanied by relatively little analysis, and are intended to provide the basic source properties, as well as background information about the clouds and observations. The Ophiuchus survey was led by graduate student Kaisa Young at the University of Texas, Austin (Young et al., 2006). Reduction and analysis of that cloud followed the pipeline I established, however. I also contributed significantly to the interpretation and writing of the published paper.

In chapter 5, I compare the properties of the millimeter core populations in the three molecular clouds, to better understand the environmental dependencies of low mass star formation. The physical implications of core sizes and shapes are discussed, and the relative shapes of the cloud core mass distributions are compared to simulations. I look at the cloud-to-cloud similarities and differences in spatial clustering properties, core formation efficiency, and in the relationship between dense cores and cloud column density. This analysis, together with the Serpens results, are included in a paper accepted to ApJ, and currently in press.

Bolocam maps of each cloud are combined with *Spitzer* data from the c2d Legacy project in chapter 6, enabling a separation of starless and protostellar cores. I measure the initial conditions of the starless core populations in each cloud, including masses, sizes, shapes, and mean densities, and compare the starless and protostellar populations to infer how the formation of a central protostar alters core properties. The prestellar core mass distribution is constructed from the combined starless core samples, and compared to the initial mass function of stars. Complete SEDs of cold

protostellar candidates, from  $\lambda = 1.25 - 1100\mu\text{m}$ , are used to calculate source properties such as bolometric luminosities, bolometric temperatures, and envelope masses, and to classify sources into an evolutionary sequence. I compare protostellar sources in each cloud to evolutionary models in order to draw conclusions about mass accretion rates, and place constraints on models. Finally, the relative number of sources in different evolutionary stages are used to estimate lifetimes for the prestellar and Class 0 phases.

A brief summary of this thesis, and discussion of future projects that can build upon this work to more fully understand the formation of low mass stars in molecular clouds, is presented in chapter 7.

## Bibliography

- Adams, F. C., Lada, C. J., & Shu, F. H. 1987, ApJ, 312, 788
- Adams, F. C., & Shu, F. H. 1986, ApJ, 308, 836
- Alton, P. B., Xilouris, E. M., Bianci, S., Davies, J., Kylafis, N. 2000, A&A, 356, 795
- Alves, J., Lombardi, M., & Lada, C. J. 2007, A&A, 462L, 17
- André, P. 1994, in *The Cold Universe*, Editors T. Montmerle, C. J. Lada, I. F. Mirabel, & J. Tran Thanh Van, p. 179
- André, P. 1996, in *Memorie della Societa Astronomia Italiana*, vol. 67, p. 901
- André, P. & Montmerle, T. 1994, ApJ, 420, 837
- André, P., Ward-Thompson, D., & Barsony, M. 1993, ApJ, 406, 122
- Bachiller, R. 1996, ARA&A, 34, 111
- Ballesteros-Paredes, J., Gazol, A., Kim, J., Klessen, R. S., Jappsen, A-K., & Tejero, E., 2006, ApJ, 637, 384
- Ballesteros-Paredes, J., Klessen, R. S., & Vázquez-Semadeni, E. 2003, ApJ, 592, 188
- Bianchi, S., Gonalves, J., Albrecht, M., Caselli, P., Chini, R., Galli, D., Walmsley, M. 2003, A&A, 399, L43
- Bonnell, I. A., Bate, M. R., Clarke, C. J., & Pringle, J. E. 2001, 323, 785
- Bonnor, W. B. 1956, MNRAS, 116, 351
- Bourke, T. L., Hyland, A. R., Robinson, G., James, S. D., & Wright, C. M. 1995, MNRAS, 276, 1067
- Cambrésy, L. 1999, A&A, 345, 965
- Chabrier, G. 2005 in *The Stellar Initial Mass Function Fifty Years Later*, editors E. Corbelli, F. Palla, and H. Zinnecker, p. 41

- Di Francesco, J., Evans, N. J., II, Caselli, P., Myers, P. C., Shirley, Y., Aikawa, Y., & Tafalla, M. 2007, in *Protostars and Planets V*, editors B. Reipurth, D. Jewitt, and K. Keil, p. 17
- Dowell, C. D., Allen, C. A., Babu, R. S., Freund, M. M., Gardner, M., Groseth, J., Jhabvala, M. D., et al. 2003, *SPIE*, 4855, 73
- Draine, B. T., & Lee, H. M. 1984, *ApJ*, 285, 89
- Ebert, R. 1955, *Zeitschrift Astrophysics*, 37, 217
- Enoch, M. L., Young, K. E., Glenn, J., Evans, N. J., II, Golwala, S., Sargent, A. I., Harvey, P., et al. 2006, *ApJ*, 638, 293
- Evans, N. J., II 1999, *ARA&A*, 37, 311
- Evans, N. J., II, Allen, L. E., Blake, G. A., Boogert, A. C. A., Bourke, T., Harvey, P. M., Kessler, J. E., et al. 2003, *PASP*, 115, 965
- Evans, N. J., II, et al. 2007, *Final Delivery of Data from the c2d Legacy Project: IRAC and MIPS*
- Froebrich, D., Schmeja, S., Smith, M. D., & Klessen, R. S. 2006, *MNRAS*, 368, 435
- Glenn, J., Bock, J. J., Chattopadhyay, G., Edgington, S. F., Lange, A. E., Zmuidzinas, J., Mauskopf, P. D., Rownd, B., Yuen, L., & Ade, P. A. 1998, *SPIE*, 3357,326
- Gregersen, E. M. & Evans, N. J., II 2000, *ApJ*, 538, 260
- Harvey, P. M., Chapman, N., Lai, S.-P., Evans, N. J., II, Allen, L. E., Jørgensen, J. K., Mundy, L. G., et al. 2006, *ApJ*, 644, 307
- Harvey, P. M., Merin, B., Huard, T. L., Rebull, L. M., Chapman, N., Evans, N. J., II, & Myers, P. C. 2007, *ApJ*, in press (preprint: arXiv:0704.0009 [astro-ph])
- Hatchell, J., Fuller, G. A., Richer, J. S., Harries, T. J., & Ladd, E. F. 2007, *A&A*, accepted (preprint:astro-ph/0612601)

- Hatchell, J., Richer, J. S., Fuller, G. A., Qualtrough, C. J., Ladd, E. F., & Chandler, C. J. 2005, *A&A*, 440, 151
- Henriksen, R., Andre, P., & Bontemps, S. 1997, *A&A*, 323, 549
- Hertzsprung, E. 1905, *Sur Strahlung der Sterne* (Z. Wiss Photog., 3)
- Holland, W. S., Robson, E. I., Gear, W. K., Cunningham, C. R., Lightfoot, J. F., Jenness, T., Ivison, R. J., et al. 1999, *MNRAS*, 303, 659
- Hoyle, F. 1953, *ApJ*, 118, 513
- Jayawardhana, R., Hartmann, L., Calvet, N. 2001, *ApJ*, 548, 310
- Jeans, J. H. 1928, *Astronomy and Cosmogony*, p. 340
- Jessop, N. E., & Ward-Thompson, D. 2000, *MNRAS*, 311, 63
- Johnstone, D., DiFrancesco, J., & Kirk, H. 2004, *ApJ*, 45, 611L
- Johnstone, D., Wilson, C. D., Moriarty-Schieven, G., Joncas, G., Smith, G., Gregersen, E., & Fich, M. 2000, *ApJ*, 545, 327
- Jørgensen, J. K., Johnstone, D., Kirk, H., & Myers, P. C. 2007, *ApJ*, 656, 293
- Jørgensen, J. K., Harvey, P. M., Evans, N. J., II, Huard, T. L., Allen, L. E., Porras, A., Blake, G. A., et al. 2006, *ApJ*, 645, 1246
- Kirk, H., Johnstone, D., & DiFrancesco, J. 2006, *ApJ*, 646, 1009
- Kreysa, E., Gemuend, H.-P., Gromke, J., Haslam, C. G., Reichertz, L., Haller, E. E., Beeman, J. W., Hansen, V., Sievers, A., & Zylka, R. 1998 *SPIE*, 3357, 319
- Kroupa, P. 2002, *Science*, 295, 82
- Lada, C. J. 1987, In *Star Forming Regions*, IAU Symp. 115, editors M. Peimbert, J. Jugaku, p. 1
- Lada, C. J., & Lada, E. A. 2003, *ARA&A*, 41, 57

- Lada, C. J. & Wilking, B. A. 1984, *ApJ* 287, 610
- Lee, J.-E., Bergin, E. A., & Evans, N. J., II 2004, *ApJ*, 617, 360
- Lee, W. C., & Myers, P. C. 1999, *ApJS*, 123, 233
- Li, P. S., Norman, M. L., Mac Low, M., & Heitsch, F. 2004, *ApJ*, 605, 800
- Luhman, K. L., Stauffer, J. R., Muench, A. A., Reike, G. H., Lada, E. A., Bouvier, J., & Lada, C. J. 2003, *ApJ*, 593, 1115
- Mac Low, M.-M., & Klessen, R. S. 2004, *RevPhys*, 76, 125
- Mathis, J. S., Rumpl, W., & Nordsieck, K. H. 1977, *ApJ*, 217, 425
- McKee, C. F. 1989, *ApJ*, 345, 782
- McKee, C. F., & Zweibel, E. G. 1992, *ApJ*, 399, 551
- McLaughlin, D. E. & Pudritz, R. E. 1997, *ApJ*, 476, 750
- Meyer, M. R., Adams, F. C., Hillenbrand, L. A., Carpenter, J. M., & Larson, R. B. 2000, in *Protostars and Planets IV*, editors V. Mannings, A. P. Boss, & S. S. Russell, p. 121
- Motte, F., André, P., & Neri, R. 1998, *A&A*, 336, 150
- Muench, A. A., Lada, E. A., Lada, C. J., & Alves, J. 2002, *ApJ*, 573, 366
- Myers, P. C. 1998, *ApJ*, 496, L109
- Myers, P. C., Adams, F. C., Chen, H., & Schaff, E. 1998, *ApJ*, 492, 703
- Myers, P. C. & Benson, P. J. 1983, *ApJ*, 266, 309
- Myers, P. C. & Ladd, E. F. 1993, *ApJ*, 413, L47
- Nakano, T. 1998, *ApJ*, 494, 587
- Nyman, L.-Å., Lerner, M., Nielbock, M., et al. 2001, *The Messenger*, 106, 40

- Onishi, T., Kawamura, A., Tachihara, K., & Fukui, Y. 2002, *ApJ*, 575, 950
- Ossenkopf, V., & Henning, Th. 1994, *A&A*, 291, 943
- Padoan, P., Bally, J., Billawala, Y., Juvela, M., & Nordlund, Å. 1999, *ApJ*, 525, 318
- Padoan, P., & Nordlund, Å. 2002, *ApJ*, 576, 870
- Palla, F., & Stahler, S. W. 2002, *ApJ*, 581, 1194
- Rebull, L. M., Stapelfeldt, K. R., Evans, N. J., II, Joergensen, J. K., Harvey, P. M., Brooke, T. Y., Bourke, T. L., et al. 2007, *ApJ*, in press (preprint:astro-ph/0701711)
- Reid, I. N., Gizis, J. E., & Hawley, S. L. 2002, *AJ*, 124, 2721
- Russell, H. N. 1914, *Pop. Astron.*, 22, 275, 321
- Salpeter, E. E. 1955, *ApJ*, 121, 161
- Scalo, J. M. 1986, *Fundam. Cosmic Phys.*, 11, 1
- Scalo, J. M. 2005 in *The Stellar Initial Mass Function Fifty Years Later*, editors E. Corbelli, F. Palla, and H. Zinnecker, p. 23
- Schmeja, S. & Klessen, R. S. 2004 *A&A*, 419, 405
- Schröder, K.-P., & Pagel, B. E. J. 2003, *MNRAS*, 343, 1231
- Shirley, Y. L., Evans, N. J., II, & Rawlings, J. M. C. 2002, *ApJ*, 575, 337
- Shu, F. H. 1977, *ApJ*, 214, 488
- Shu, F. H., Adams, F. C., & Lizano, S. 1987, *ARA&A*, 25, 23
- Shu, F. H., Najita, J., Galli, D., Ostriker, E., & Lizano, S. 1993 In: *Protostars and planets III* p. 3
- Spitzer, L. Jr. 1968, *Diffuse Matter in Space*
- Spitzer, L. Jr. 1978, *Physical Processes in the Interstellar Medium*, p. 282

- Stanke, T., Smith, M. D., Gredel, R., & Khanzadyan, T. 2006, *A&A*447, 609
- Testi, L., & Sargent, A. I. 1998, *ApJ*, 508, L91
- Vázquez-Semadeni, E., Kim, J., Shadmehri, M., & Ballesteros-Paredes, J. 2005, *ApJ*, 618, 344
- Visser, A. E., Richer, J. S., & Chandler, C. J. 2002, *AJ*, 124, 2756
- Ward-Thompson, D., André, P., Crutcher, R., Johnstone, D., Onishi, T., & Wilson, C. 2007, in *Protostars and Planets V*, editors B. Reipurth, D. Jewitt, and K. Keil, p. 33
- Ward-Thompson, D., Scott, P. F., Hills, R. E., & Andre, P. 1994, *MNRAS*, 268, 276
- White, R. J., Greene, T. P., Doppmann, G. W., Covey, K. R., Hillenbrand, L. A. 2007, in *Protostars and Planets V*, editors B. Reipurth, D. Jewitt, and K. Keil, p. 117
- Whitney, B. A., Wood, K., Bjorkman, J. E., & Cohen, M. 2003, *ApJ*, 598, 1079
- Wiling, B. A., 1989, *PASP*, 101, 229
- Young, C. & Evans, N. J., II 2005, *ApJ*, 627, 293
- Young, C. H., Shirley, Y. L., Evans, N. J., II, & Rawlings, J. M. C. 2003, *ApJS*, 145, 111
- Young, K. E., Enoch, M. L., Evans, N. J., II, Glenn, J., Sargent, A., Huard, T. L., Aguirre, J., et al. 2006, *ApJ*, 644, 326
- Zuckerman, B. & Palmer, P. 1974, *ARA&A*, 12, 279

## Chapter 2

# Bolocam Survey for 1.1 mm Dust Continuum Emission in the Perseus Molecular Cloud

### Abstract

We have completed a  $\lambda = 1.1$  mm continuum survey of  $7.5 \text{ deg}^2$  of the Perseus Molecular Cloud using Bolocam at the Caltech Submillimeter Observatory. This represents the largest millimeter or submillimeter continuum map of Perseus to date. Our map covers more than 30,000  $31''$  (FWHM) resolution elements to a  $1\sigma$  rms of  $15 \text{ mJy beam}^{-1}$ . We detect a total of 122 cores above a  $5\sigma$  point source mass detection limit of  $0.18 M_{\odot}$ , assuming a dust temperature of  $T_D = 10 \text{ K}$ , 60 of which are new millimeter or submillimeter detections. The 1.1 mm mass function is consistent with a broken power law of slope  $\alpha_1 = 1.3$  ( $0.5 M_{\odot} < M < 2.5 M_{\odot}$ ) and  $\alpha_2 = 2.6$  ( $M > 2.5 M_{\odot}$ ), similar to the local initial mass function slope ( $\alpha_1 = 1.6$   $M < 1 M_{\odot}$ ,  $\alpha_2 = 2.7$   $M > 1 M_{\odot}$ ). No more than 5% of the total cloud mass is contained in discrete 1.1 mm cores, which account for a total mass of  $285 M_{\odot}$ . We suggest an extinction threshold for millimeter cores of  $A_V \sim 5 \text{ mag}$ , based on our calculation of the probability of finding a 1.1 mm core as a function of  $A_V$ . Much of the cloud is devoid of compact millimeter emission; despite the significantly greater area covered compared to previous surveys, only 5 – 10 of the newly identified sources lie outside

---

This chapter has been published previously as Enoch et al. 2006, ApJ, 638, 293.

previously observed areas. The two-point correlation function confirms that dense cores in the cloud are highly structured, with significant clustering on scales as large as  $2 \times 10^5$  AU. Our 1.1 mm emission survey reveals considerably denser, more compact material than maps in other column density tracers such as  $^{13}\text{CO}$  and  $A_V$ , although the general morphologies are roughly consistent. These 1.1 mm results, especially when combined with recently acquired c2d Spitzer Legacy data, will provide a census of dense cores and protostars in Perseus and improve our understanding of the earliest stages of star formation in molecular clouds.

## 2.1 Introduction

Observations of the earliest stages of molecular core collapse and protostellar formation are extremely important pieces in the puzzle of low mass star formation, not only illuminating the transition from dense cloud cores to later protostellar phases, but also providing clues about initial conditions and a crucial link between theoretical and empirical scenarios. Prestellar cores have no internal luminosity source and are therefore very cold (5 – 20 K), with spectral energy distributions (SEDs) that peak at submillimeter or millimeter wavelengths. At very early times in an embryonic protostar’s life, generally referred to as the Class 0 phase (André, Ward-Thompson, & Barsony, 1993), it is deeply embedded in an obscuring envelope of gas and dust. Most of the continuum emission from the hot young star is absorbed and reradiated by the cool (10 – 30 K) dust envelope at far-infrared (far-IR) to millimeter wavelengths.

We follow Gregersen & Evans (2000) and distinguish prestellar cores, which are expected to eventually form a star or stellar system, from starless cores, which are dense cores without IRAS sources that may or may not collapse in the future, by the presence of submillimeter or millimeter emission. Gregersen & Evans (2000) found that strong submillimeter emission correlates well with collapse signatures and the presence of  $\text{NH}_3$ , making these sources likely to be prestellar. In this chapter, we refer to a  $\lambda = 1.1$  mm (hereafter 1.1 mm) core as any discrete source of 1.1 mm emission, a prestellar core as any 1.1 mm core not detected at wavelengths shorter

than  $70 \mu\text{m}$  (e.g. with IRAS or *Spitzer*), and a protostar as any protostellar object with a substantial envelope (Class 0/I; see Lada (1987); André et al. (1993) for a description of classifications).

The millimeter wavelength range is an ideal region in which to study such objects for several reasons. At these long wavelengths thermal emission from dust becomes optically thin, and the observed flux density traces the total mass of dust in cores and envelopes. Because they lack an internal luminosity source, prestellar cores are generally invisible at shorter wavelengths. Additionally, flux density measurements in the millimeter contribute important information to the SED, helping to clarify the evolutionary state of a given object. Although deeply embedded objects have remained relatively elusive due to the difficulty of observing at submillimeter and millimeter wavelengths, continually improving technology and instrumentation are now making sensitive observations in this regime possible.

Large format bolometer arrays like SCUBA (Holland et al., 1999), SHARC II (Dowell et al., 2003) and MAMBO (Kreysa et al., 1998) have made it feasible to scan relatively large fields at continuum submillimeter and millimeter wavelengths, while interferometers such as OVRO (Woody, Serabyn, & Schinckel, 1998), BIMA (Welch et al., 1996), PdBI (Guilloteau et al., 1992) and the SMA (Ho, Moran, & Lo, 2004) begin to resolve the details of individual sources. Nevertheless, time constraints have, for the most part, prohibited coverage of entire molecular clouds with current millimeter continuum instruments. Large, complete, high resolution surveys of entire star forming regions are necessary to minimize bias and systematic effects, improve statistics, and develop a clear framework within which to interpret the many observations of individual objects that are now available. Bolocam, a 144-element bolometer array designed for mapping large fields at millimeter wavelengths (Glenn et al., 2003), is well suited to the kind of large scale surveys now needed.

Nearby molecular clouds such as Perseus, Ophiuchus and Serpens, where there is considerable evidence of ongoing star formation (e.g., Evans, 1999), provide the best opportunity to observe stars in the earliest stages of their formation. Perseus is located in the larger Taurus-Auriga-Perseus dark cloud complex at about  $3^{\text{h}}30^{\text{m}}$ ,

+31°, and extending approximately 7° in right ascension (RA) and 3° in declination (Dec). The Perseus cloud is often cited as an intermediate case between the low-mass, quiescent Taurus and turbulent, high-mass Orion star formation regions (e.g., Ladd, Lada, & Myers, 1993; Ladd, Myers, & Goodman, 1994), making it perhaps an ideal environment for studying “typical” low mass star formation. Two young clusters lie in Perseus: IC 348 is a young infrared cluster of age about 2Myr containing several hundred members of total mass about 160  $M_{\odot}$  (Luhman et al., 2003). NGC 1333 is a very young (< 1Myr) highly obscured cluster with about 150 stars totaling  $\sim 79 M_{\odot}$  (Lada, Alves, & Lada, 1996; Wilking et al., 2004), and evidence of ongoing star formation. Perseus contains several Lynds and Barnard dark clouds, including B5 at the eastern end, B1, and L1455 and L1448 at the western end. A number of dense ammonia ( $\text{NH}_3$ ) cores have also been identified by Ladd et al. (1994).

Recent estimates of the distance to Perseus range from 220 pc to 350 pc (e.g. Černis, 1990; Herbig & Jones, 1983). Larger values (300 – 350 pc) are often adopted based on the Perseus OB2 association, which has a fairly well established distance of  $\sim 330$  pc from Hipparcos parallax and reddening measurements of its members (e.g., Borgman & Blaauw, 1964; de Zeeuw, Hoogerwerf, & deBruijne, 1999). There is evidence, however, that Per OB2 may lie well behind the complex of dark clouds in which we are interested, and are probably at a distance closer to 250 pc (Černis, 1993; Belikov et al., 2002). On the other hand, a single distance for the whole cloud might not be appropriate. Early CO observations (Sargent, 1979) indicated a smoothly varying LSR velocity gradient across the cloud from  $v = +3\text{km s}^{-1}$  at the western end to  $v = +10\text{km s}^{-1}$  at the eastern end. Given this gradient in velocity, there may also be a distance gradient across the cloud. Extinction studies of several different regions point to an increase in distance from 220 pc to 260 pc moving from west to east (Černis, 1990, 1993; Černis & Straizys, 2003).

Another possibility is the superposition of two or more clouds. Based on star counts, Cernicharo, Bachiller, & Duvert (1985) suggest two dust layers at  $d \sim 200$  pc and  $d \sim 300$  pc. New data compiled by the COMPLETE team also indicate that Perseus may actually be composed of several separate clouds at different distances,

projected together on the sky (Ridge et al., 2005). We acknowledge that the structure and dynamics of the Perseus cloud are complicated; it is possible, perhaps likely, that it will ultimately be shown that Perseus is, in fact, a superposition of a number of smaller clouds. For the purpose of this work, however, we adopt a distance of 250 pc for the entire area surveyed, based on the most recent extinction studies and parallax measurements of IC 348 members (Černis, 1993; Černis & Straizys, 2003; Belikov et al., 2002).

Perseus has been fully mapped in CO isotopes tracing densities up to a few thousand particles per cubic centimeter (Padoan et al., 1999; Ridge et al., 2005). Most previous submillimeter and millimeter continuum and molecular line mapping of higher-density gas tracers, however, has been confined to the dense cluster region of NGC 1333 (e.g., Sandell & Knee, 2001), or focused on bright IRAS sources (e.g., Ladd et al., 1994) or energetic outflow sources (e.g., Froebrich et al., 2003; Mathews & Wilson, 2002; Barsony et al., 1998), with the notable exception of the recent SCUBA survey by Hatchell et al. (2005). Conclusions about the cloud based on such existing observations may be problematic. The gas traced by CO observations has relatively low density and therefore is not necessarily representative of current star formation activity, while isolated small-scale studies may be providing a biased picture of the cloud.

The observations presented here have the distinct advantage that they overlap entirely with the Perseus fields observed with IRAC and MIPS as part of the Spitzer Legacy Project, “From Molecular Cloud Cores to Planet Forming Disks” (“Cores to Disks” or c2d; Evans et al., 2003). The c2d project has mapped five large star forming clouds with the IRAC ( $\lambda = 3.6 - 8.0 \mu\text{m}$ ) and MIPS ( $\lambda = 24 - 160 \mu\text{m}$ ) instruments on Spitzer. While millimeter observations are essential to trace core and envelope mass and directly observe prestellar cores, IR observations are necessary to characterize embedded protostars. Additionally, IR measurements are more sensitive to temperature than to total mass, making them an excellent complement to millimeter observations.

We have completed millimeter continuum observations of the entire Perseus cloud

with Bolocam at the Caltech Submillimeter Observatory (CSO). This map, observed at  $\lambda = 1.1\text{mm}$  during 2003, January–February, is the first unbiased, flux-limited survey of cores and protostars in Perseus at millimeter wavelengths. As part of the same project, the remaining two large c2d clouds accessible from Mauna Kea, Ophiuchus and Serpens, also have coordinated large scale Bolocam 1.1 mm and Spitzer observations (Young et al., 2006; Enoch et al., 2007). When joined with the Perseus data, this combined sample will provide a unique basis for comparing star forming properties in varying environments, without the systematic difficulties introduced by observations from different instruments or variable coverage. Detailed SEDs for this complete sample of objects will be made possible through the combination of Spitzer IR and Bolocam 1.1 mm fluxes, as well as  $850\ \mu\text{m}$  fluxes when available, allowing the construction of a more quantitative evolutionary sequence than currently available, and calculation of statistical lifetimes.

Here we present the results of our Bolocam survey of Perseus. In §2.2 we describe the observations, and in §2.3 we describe in detail the reduction techniques used for the Perseus Bolocam data, including an iterative mapping scheme we have developed to restore source brightness lost during sky subtraction. Results are presented in §2.4, including source flux, size, and mass statistics and a comparison of the cloud appearance at 1.1 mm to other column density tracers. In §2.5 we discuss the completeness limits of the survey and the mass versus size distribution, the 1.1 mm Perseus mass function, and the clustering characteristics of the cloud. We end with a summary and plans for future work in §2.6.

## 2.2 Observations

Continuum observations at 1.1 mm were made with Bolocam<sup>1</sup> at the Caltech Submillimeter Observatory (CSO) on Mauna Kea, Hawaii during 2003, January 28–February 15. Bolocam is a 144-element bolometer array that operates at  $\lambda = 1.1, 1.4,$  and 2.1 mm. The instrument consists of a monolithic wafer of silicon nitride micromesh

---

<sup>1</sup><http://www.cso.caltech.edu/bolocam>

AC-biased bolometers, cooled to 260 mK. During the Perseus observations 81 of 144 bolometers were operational. The field of view (FOV) is  $7'.5$  and the beams are well approximated by a Gaussian with a FWHM of  $31''$  at  $\lambda = 1.1\text{mm}$ . The focal plane is flat over the FOV due to a cold field lens coupling the telescope to the array (Glenn et al., 1998, 2003; Haig et al., 2004). All observations of Perseus were completed in the 1.1 mm mode, which has a bandwidth of 45 GHz and band center at 268 GHz.

The integrated intensity  $^{13}\text{CO}$  map of Padoan et al. (1999) was used to define the area of the Bolocam observations, as shown in figure 2.1. The chosen boundaries correspond to an approximate extinction limit of  $A_V \sim 2$  mag (Evans et al., 2003), and were designed to overlap entirely with the area to be observed with Spitzer as part of the c2d Legacy project. Maps were made in raster scan mode in sets of three scans offset by  $-11''$ ,  $0''$ ,  $+11''$ , with a scan speed of  $60'' \text{ s}^{-1}$  and a subscan spacing of  $162''$ . A subscan is defined as one pass of the array across the field, and a scan as a set of consecutive subscans that cover the field entirely. Offset scans are necessary to obtain a fully sampled map because the array elements are separated on the sky by  $1.5f\lambda$ , whereas  $0.5f\lambda$  corresponds to Nyquist sampling. Simulations indicated that  $11''$  offsets were optimal for obtaining the best coverage perpendicular to the scan direction.

The total area was divided into three large rectangles for the most efficient scanning. On each of 19 nights Perseus was observed for approximately two hours before and after transit, with a total of 12 scans of each section completed. A number of subscans have been omitted from the final map due to bad weather, manifested as very large sky noise, or temporarily poor bolometer performance. The total observing time was about 40 hours for the  $7.5$  square degree region, with 31 hours actually spent integrating on-source, or an observing efficiency of 75%. This corresponds to a mapping speed for Perseus of  $3 \text{ arcmin}^2 \text{ mJy}^{-2} \text{ hr}^{-1}$ . No chopping was done for any of the observations, thereby retaining, in principle, sensitivity to large-scale structure up to the angular size of the array ( $7'.5$ ). Chopping is not required because the bolometers are AC-biased, which elevates the signal band above the atmospheric and instrumental  $1/f$  noise. Demodulation brings the signal down to near-DC, with the

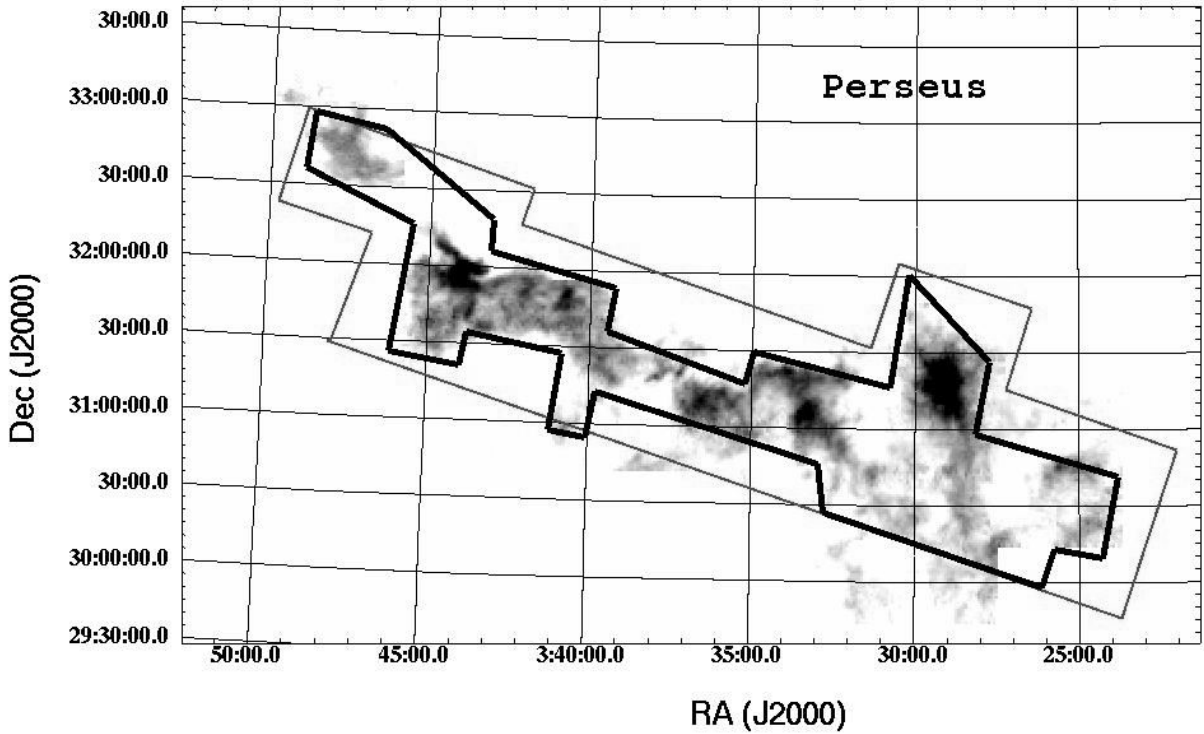


Figure 2.1 Bolocam 1.1 mm (thin line) and Spitzer c2d IRAC (thick line) coverage of Perseus overlaid on a  $^{13}\text{CO}$  integrated intensity map from Padoan et al. (1999). The area observed by IRAC was chosen based on the  $^{13}\text{CO}$  intensity, and corresponds approximately to  $A_V \geq 2$  mag (Evans et al., 2003). The Bolocam observations were designed to cover the same region. The MIPS data cover a somewhat larger area.

signal band determined by the scan speed and beam size.

One night at the beginning of the run was devoted to pointing and calibration observations only, in order to set the focus and pointing constants for the run. Each night secondary calibrators, including the bright Class 0 object NGC 1333-IRAS4A, were observed approximately every two hours, with calibrator sources from many areas of the sky used to derive a calibration curve for the entire run (see §2.3.3). All calibrator observations were taken at the same scanning speed as science fields ( $60'' \text{ s}^{-1}$ ), and most were small  $4' \times 4'$  scan maps. At least one primary calibrator, usually Mars, was observed nightly, and six large  $10' \times 10'$  beam maps made over the 3 week run. These beam maps are used to define the distortion corrections and the beam shape, which is found to be very Gaussian. Nightly sky dips were used to measure the sky and telescope optical loading (the quiescent optical power received

by the bolometers from the sky, telescope, and dewar). Weather was mostly clear for the run, with an average zenith 225 GHz tau of  $\tau \sim 0.07$ , ranging between 0.05 and 0.09.

## 2.3 Data Reduction

Given that these observations utilize a new instrument, we describe the data reduction process for Bolocam data in general, as well as reduction techniques specific to the Perseus data, in some detail. Preliminary data reduction was accomplished using a reduction pipeline written by the Bolocam instrument team, as described below and in Laurent et al. (2005). A number of problems specific to the bright sources and very long subscans of more than a few degrees observed for this project required the development of additional reduction techniques, in particular the iterative mapping routine described in §2.3.4.

Initial steps in the pipeline include calculating the pointing model as a function of azimuth and elevation, and calculating the RA/Dec of each bolometer for every time sample. The bulk of the data reduction effort goes into removing the (considerable) sky noise. Subsequently, bright pixel spikes from cosmic rays are flagged, and the power spectral density (PSD) of each subscan is calculated. The  $N_{bolo}$  bolometer timestreams are converted into a 2D pixel map using pixel offsets, subscan PSDs, and calibration constants. Finally, an iterative mapping scheme developed for this purpose is used to recover flux density lost in the sky subtraction process.

### 2.3.1 Pointing

All pointing observations made during the 2003, January observing run, including secondary calibrators as well as additional variable sources such as quasars, are used to calculate precise pointing corrections. The resulting pointing model serves to refine the recorded telescope pointing position. The rms of the global pointing model for 2003, January as determined from the positions of known galaxies in the Lockman Hole is 9.1" (Laurent et al., 2005). The pointing model is somewhat better in Perseus,

likely due at least in part to the proximity of many pointing sources to the Galactic plane.

We compared our positions for 11 known sources to the literature, using sub-millimeter, millimeter, or radio positions when possible, and otherwise IRAS positions. There was a small systematic offset in RA ( $\delta\text{RA} = -3''.2 \pm 1''.3$ ), but not large enough to warrant a correction to positions, and no systematic offset in Dec ( $\delta\text{Dec} = -0''.5 \pm 1''.5$ ). We find a  $1\sigma$  rms compared to previous positions of  $7''$ , independent of azimuth or elevation. Given that this dispersion includes potentially large uncertainties in the literature positions, as well as possible physical offsets between IR and 1.1 mm sources, we conservatively estimate the overall accuracy for point source positions in Perseus to be  $7''$ . In addition to uncertainties in source positions, pointing errors increase the effective beam size, causing sources to be blurred in the coadded map and affecting the measured size and peak flux density, but not the total flux density.

Position offsets of the various bolometers in the array from the telescope pointing center, as well as optical distortions – collectively termed pixel offsets – are measured using fully sampled observations of planets. Distortion corrections account for distortion in the optics, due primarily to an off-axis ellipsoidal mirror, and secondarily to imperfect optical alignments. Corrections are typically of order  $2'' - 3''$ . Pixel offsets of each bolometer are used to compute the RA and Dec value of every time sample in a subscan, and later used to convert bolometer timestreams into a 2D pixel map.

### 2.3.2 Removal of Sky Noise

The sensitivity of a given Bolocam observation is determined by the intrinsic sensitivity of and optical loading on the bolometers, the integration time, and the success of sky noise subtraction. The most important reduction step is the removal of sky noise, or cleaning. On scales comparable to or larger than the beam, the instrument is limited by  $1/f$  noise, which is primarily atmospheric but also instrumental in nature. Sky noise originates as fluctuations in the brightness temperature, or column

density, of the atmosphere and dominates most astronomical sources at  $\lambda = 1.1\text{mm}$ . Because chopping is not done, this noise is present in the bolometer timestreams before cleaning.

The bolometer beams overlap almost completely in the near-field where the sky noise originates, but do not overlap in the far-field where astronomical signals originate. Therefore, to first order the sky noise is identical for each bolometer and a sky template can be constructed quite simply by taking an average or median across the bolometer array at each point in time. This average cleaning method is appealingly simple, but does not deal well with multiple correlated  $1/f$  noises with different correlation coefficients, or with  $1/f$  noises that are correlated on spatial scales smaller than the array. The latter might arise if the beams do not overlap completely at the height of the sky noise.

In principle, the correlated noise can be removed because it is correlated in time, whereas the astronomical signal is correlated in space across the array. A more sophisticated approach that addresses this issue is Principal Component Analysis (PCA) cleaning (see Laurent et al. (2005) and references therein for a discussion of PCA cleaning). In a PCA analysis the raw timestreams are projected along eigenvectors, bringing out common modes, or principal components, in the data. Patterns common to all bolometers correspond to sky noise, so subtracting such common modes from the data is an efficient sky subtraction technique. Removing the first principal component is nearly equivalent to performing average subtraction.

Any number of components can be subtracted from the data, each removing progressively less correlated  $1/f$  noise. The actual reduction in the rms noise depends on the initial sky noise present, but typically removing 3 PCA components reduces the overall noise by 10% – 30% compared to average cleaning. Although removing more components will reduce the noise further, the disadvantage of PCA cleaning is that higher components tend to remove source flux density (most of which can be recovered, see §2.3.4). Tests performed on observations of Serpens with both compact and extended sources indicate that removing between 1 and 5 components is most effective at eliminating stripes from  $1/f$  noise while retaining source flux density and

structure.

### 2.3.3 Mapping and Calibration

To make a 2D pixel map from the bolometer timestreams, the pointing model and empirically derived pixel offsets are used to project each bolometer time sample onto an RA/Dec grid of pixel values. Timestreams are coadded using a weighted (by the inverse of the PSD) average. We bin the map at a resolution equal to 1/3 of the true instrumental resolution, or  $10'' \text{ pixel}^{-1}$ , which gives sufficient hits per pixel for significant statistics without degrading the resolution. Given the nature of the instrument and observations, a single pixel in the map will contain data from many bolometers and many scans. We refer to the coverage map as an image of the number of hits per pixel, or seconds per pixel, in the map. The coverage is dependent on pixel size, scan strategy, the number of bolometers, and the number of scans in the map. The average coverage for Perseus is about  $500 \text{ hits pix}^{-1}$  (or  $10 \text{ s pix}^{-1}$ ), varying by 30% across the map and leading to  $\sim 15\%$  variation in the rms noise.

To maximize the signal to noise of, and thus our chance of detecting, point sources, we optimally filter the map. Because the signal from a point source lies in a limited frequency band, we can use an optimal (Wiener) filter to attenuate  $1/f$  noise at low frequencies, as well as high frequency noise above the signal band. Attenuating the  $1/f$  noise reduces the overall rms *per pixel* by  $\sim \sqrt{3}$  (making the rms  $\text{pixel}^{-1} \sim \text{rms beam}^{-1}$ ), maximizing the probability of detection for faint point-like sources. The optimal filter  $g(q)$  is given by:

$$g(q) = \frac{s^*(q)/J(q)}{\int |s(q)|^2 / J(q) d^2q}, \quad (2.1)$$

where  $q$  is the spatial wavenumber,  $J(q)$  is the azimuthally averaged PSD,  $s(q)$  is the Fourier transform of the beam, and  $g(q)$  is normalized so that the peak brightness of point sources and the resolution of the map are preserved. Note that the optimally filtered map is used for source detection only; all maps shown are unfiltered.

The flux calibration factor at any given time depends on the bolometer DC re-

sistance, which changes with atmospheric attenuation and bolometer optical loading. Therefore, the calibration cannot be applied as a single factor to the final map, but must be calculated as a function of time for each subscan based on the average DC resistance of that subscan. This is a powerful calibration method because it makes real-time corrections for the atmospheric attenuation and bolometer operating point using the bolometer optical loading, effectively providing flux calibration on the timescale of minutes.

In practice, the calibration (in mV/Jy) as a function of the DC voltage is determined using a second-order polynomial fit to observations of Mars, Saturn, and a number of secondary calibrator sources (see Laurent et al. (2005) for an expanded discussion). All calibrators with reliable known flux densities (one observed every 1–2 hours per night throughout the run) are used to define the calibration curve, not only those observed during a given science observation. This enables a comprehensive calibration curve over a range of atmospheric optical depths. Reference flux densities are from the JCMT planetary flux website<sup>2</sup> and Sandell (1994), corrected for the Bolocam bandpass. The effects of non-linearity due to optical loading from the sky and the finite beam size are also accounted for, using large beam maps of Mars and assuming a uniform disk model. Measured flux densities are from a Gaussian fit after application of a point-source filter.

The resulting peak-normalized map can be divided by the beam area to obtain a surface brightness-normalized map. The integral of a point source in the surface brightness map returns the total flux of the point source, thus this map is suitable for photometry. The absolute calibration uncertainty, derived from the deviation of measured calibrator values from the quadratic fit, is 9.7% ( $1\sigma$ ; Laurent et al. 2005).

---

<sup>2</sup><http://jach/hawaii.edu/JACpublic/JCMT/software/bin/fluxes.pl>

## 2.3.4 Iterative Mapping

### 2.3.4.1 Method

Although they utilize different methods, both average and PCA cleaning contain a step that essentially removes the mean of each bolometer subscan (see §2.3.2). This step is necessary to eliminate sky noise, but when there is a bright source in a subscan it biases the mean. Consequently, sky subtraction introduces negative lobes around bright sources, which are asymmetric in the scan direction. Furthermore, subsamples containing sources tend to be underweighted in the coadded map because the source brightness contaminates the integrated PSD, causing a decrease in the weighting factor. Both effects tend to suppress source flux density and are mildly dependent on the brightness and structure of the source. There is an additional effect due to PCA cleaning that non-linearly removes the flux density of bright sources as more PCA components are removed. To correct for diminished source brightness and negative artifacts introduced by the above effects, we have developed an iterative mapping code that robustly restores lost flux density and structure to the map.

The iterative mapping algorithm we have implemented iteratively subtracts a source model from the real data (somewhat similar to CLEAN (Högbom, 1974; Schwarz, 1978), but working in the image plane). The following is a more robust method than using, for example, a source model comprised of the sum of many Gaussians, because many of our sources are likely to be extended and non-Gaussian. For the following,  $j$  refers to bolometer number ( $j = 1 - 81$ ), and  $i$  refers to the iteration number ( $i = 0 - N$ , where the zeroth iteration  $i = 0$  indicates raw or cleaned data before any source model has been subtracted). We begin with the raw timestream data,  $t_{j,i=0}$ . These data are sent through the cleaning and mapping process to produce the zeroth iteration map,  $M_{i=0}$ , which contains negative artifacts and is missing some fraction of the flux density of each source. Next, a cut is applied at  $+N_\sigma$  to  $M_{i=0}$ , removing any negative pixels as well as most of the noise (pixels with values  $\leq +N_\sigma$  times the rms noise are set to zero). We now have a source model map,  $M'_i$ , our current best guess of the true source flux density.

From the source model  $M'_i$  a model timestream  $t'_{j,i}$  is generated for each bolometer and subtracted from the raw timestreams,  $dt_{j,i} = t_{j,0} - t'_{j,i}$ . The difference timestreams  $dt_{j,i}$  contain residual source flux density that was missing from the original map. When the difference timestreams are subsequently cleaned and mapped to produce a residual map  $dM_i$ , there is much less contamination of the sky template by source brightness, so the negative artifacts are greatly reduced. A threshold cut at  $+N_\sigma$  is again applied to  $dM_i$  producing a residual source model  $dM'_i$ , which is added to the original source model to create a new source model for the next iteration ( $M'_{i+1} = M'_i + dM'_i$ ). This process is iterated until there is no remaining residual source flux density in the difference timestream. After  $N$  iterations, the final residual map  $dM_N$ , containing only noise and any source flux below the threshold cutoff, is added to the last source map to create the final map ( $M_N = M'_{N-1} + dM_N$ ).

#### 2.3.4.2 Performance

The performance of iterative mapping depends on two parameters: the number of PCA components removed during cleaning ( $N_{PCA}$ ), and the rms threshold cut ( $N_\sigma$ ) used to make the source model. While iterative mapping greatly improves the appearance and photometric reliability of the map, our chosen values of  $N_{PCA}$  and  $N_\sigma$  will introduce some systematic uncertainties into the final photometry. Using Monte Carlo simulations, which consisted of inserting simulated sources into the real map before the iterative mapping process, we found that  $N_{PCA} = 3$  and  $N_\sigma = 2$  produce the best combination of accurate final photometry (recovery of lost source flux density) and reduced noise compared to average cleaning (by  $\sim 20\% - 30\%$ ). Using a value of  $N_\sigma < 2$  tends to introduce noise into the source model, increasing the rms noise and raising the background level of the map; increasing  $N_\sigma$  leaves source flux density out of the source model, leaving some negative artifacts and making it difficult to recover extended source features. Decreasing  $N_{PCA}$  leaves significantly more  $1/f$  noise in the map and increases the overall rms noise; if we increase  $N_{PCA}$  much above 3 it again becomes difficult to fully correct for the loss of source brightness, which is severe and non-linear for  $N_{PCA} > 5$ .

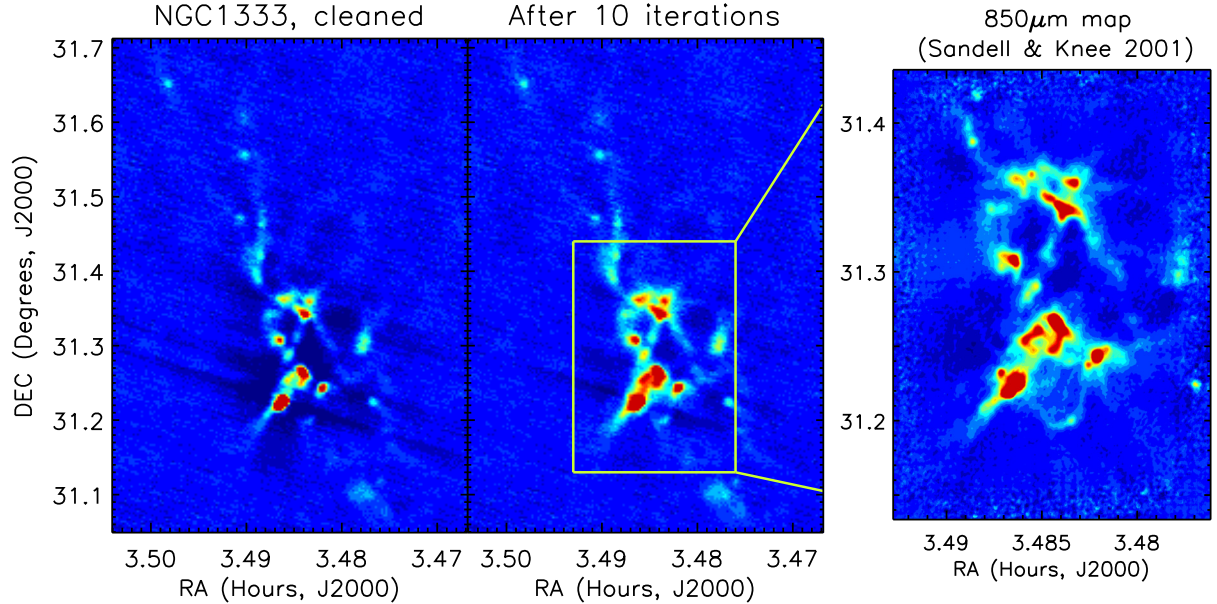


Figure 2.2 NGC 1333, before (left) and after (center) iterative mapping, shown on the same intensity scale. Dark blue regions are negative lobes introduced by cleaning. These images illustrate the effectiveness of iterative mapping in reducing such negative artifacts and restoring source flux density lost during PCA cleaning. After 10 iterations, the brightest source has increased in peak brightness by 14%. Although some negative artifacts remain, they are greatly reduced both in extent and intensity (the most negative pixel has decreased in amplitude from  $-238 \text{ mJy beam}^{-1}$  to  $-88 \text{ mJy beam}^{-1}$ ). No fine-scale structure is lost, and all recovered extended structure is real; for comparison we show the  $850 \mu\text{m}$  map of Sandell & Knee (2001), with a resolution of  $14''$ , on approximately the same intensity scale.

Figure 2.2 demonstrates the results of iterative mapping on a portion of the Bolocam map containing the crowded region NGC 1333. The left panel shows NGC 1333 after PCA cleaning only with  $N_{PCA} = 3$ , where the dark blue areas are negative bowls caused by cleaning. The same region after 10 iterations is shown on the same intensity scale in the center panel. All sources have increased considerably in brightness (the brightest peak by 14%), and most of the negative features have been corrected. Although some negative artifacts remain, their extent and intensity is greatly re-

duced; the worst remaining negative pixel in the iterated map is  $-88 \text{ mJy beam}^{-1}$ , compared to  $-238 \text{ mJy beam}^{-1}$  in the cleaned map. For comparison, the  $850 \mu\text{m}$  map of the central portion of NGC 1333 from Sandell & Knee (2001) is also shown on approximately the same intensity scale. Clearly, the extended structure in the higher resolution ( $14''$ )  $850 \mu\text{m}$  map is recovered in the 10 iteration Bolocam map. The recovered structure is almost certainly real, therefore, and we are not missing any structure at  $1.1 \text{ mm}$  that is present at  $850 \mu\text{m}$  (although Sandell & Knee (2001) note that flux densities for extended emission in their map are unreliable due to similar residual artifacts).

Monte Carlo tests were done to quantify the effectiveness of the iterative mapping and characterize any systematic errors introduced throughout the cleaning and iterative mapping process, using  $N_{PCA} = 3$  and  $N_{\sigma} = 2$ . Simulated Gaussian sources of varying amplitudes ( $3\sigma - 300\sigma$ ) and sizes ( $30'' - 250''$  FWHM) were inserted into an empty region of the map, then cleaned and iterated. Finally, the resulting peak amplitude, flux density and FWHM were measured. The fractional missing peak flux density after 10 iterations for a range of test sources is shown as a function of the input peak amplitude in figure 2.3. Sources of FWHM  $30''$ ,  $50''$ ,  $80''$ , and  $120''$  are indicated. The  $1\sigma$  rms noise per beam is also plotted as a percentage of the input amplitude. The fact that most points lie beneath this line indicates that the residual bias in measured flux densities after iterative mapping are consistent with the rms noise. Only for the largest sources ( $120''$  FWHM, few of which are found in the real map), is there a residual systematic reduction in flux density that is larger than the rms. The measured FWHM, axis ratio, and position angle are not significantly affected by either cleaning or iterative mapping.

Figure 2.4 shows the fractional lost flux density in a  $40''$  aperture as a function of iteration number for four representative FWHM sizes. A range of input amplitudes from  $S/N = 5$  (detection limit) to  $S/N = 175$  are plotted as different line styles. Large, bright sources (bottom right panel) are the most affected by cleaning – more than 50% of the flux density is removed during PCA cleaning – but are almost entirely corrected by iterative mapping, with only  $\sim 2\%$  residual missing flux density after 5

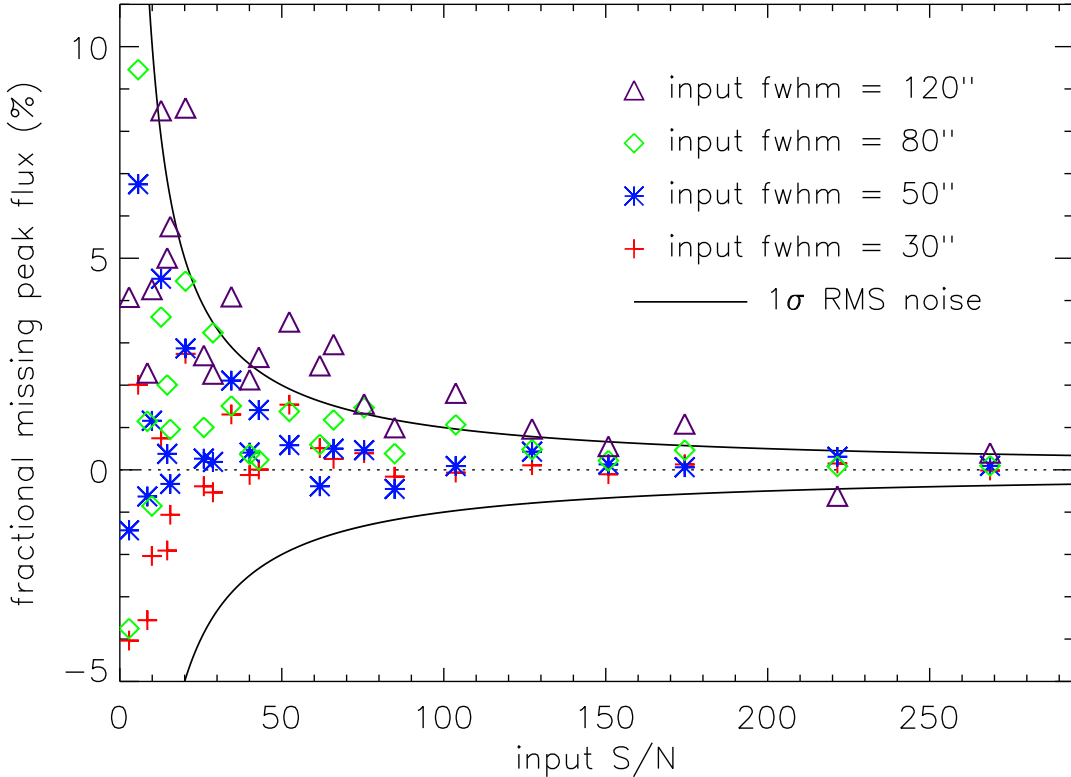


Figure 2.3 Fractional lost peak flux density of simulated sources after 10 iterations, as a function of the input signal to noise (S/N) and FWHM. Solid lines are the  $1\sigma$  rms noise as a fraction of the input amplitude, indicating the spread in recovered peak that might be expected from noise alone. Except for the largest ( $120''$  FWHM) sources, most points lie within the rms noise, so residual systematic effects from cleaning are not important for measured peak flux densities.

iterations. For large faint sources  $\lesssim 20\sigma$  (e.g., the dotted line, bottom right), iterative mapping is unable to recover all the flux density to better than 5%–10%, but note that the  $1\sigma$  rms in a  $40''$  aperture is  $\geq 10\%$  for sources  $\leq 18\sigma$ . Sources larger than  $\sim 200''$  FWHM (not shown) are not fully recovered even after 20 iterations, making this the effective maximum source size detectable. No sources larger than  $150''$  FWHM are measured in the real map.

We conservatively assign a systematic uncertainty of 5% to all integrated flux densities. In almost all cases the measured flux density is lower than the true value, making the uncertainty a bias in that measured values underestimate the true flux

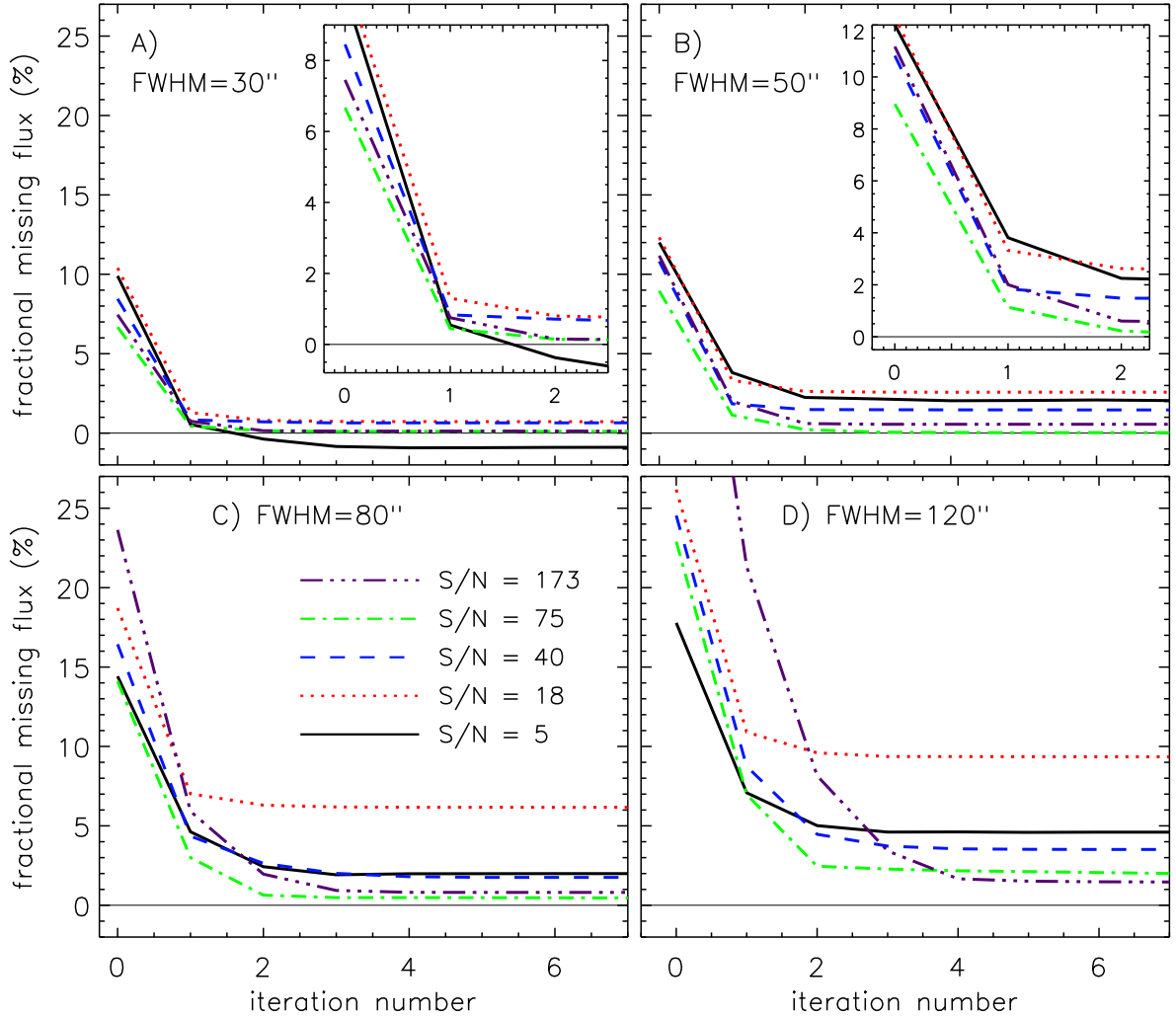


Figure 2.4 Fractional lost integrated flux density in a  $40''$  aperture for simulated sources, as a function of input signal to noise (S/N), FWHM, and iteration number. Representative source FWHM of  $30''$ ,  $50''$ ,  $80''$ ,  $120''$  are shown, with insets to magnify confused regions. Larger sources require more iterations to recover the input flux density, and tend to have the most remaining fractional missing flux density after 10 iterations. Except for sources with  $\text{FWHM} \gtrsim 100''$  the flux has converged by  $\sim 5$  iterations. The integrated flux density is usually recovered to within 5%, and to within 10% even for large ( $\text{FWHM} \geq 80''$ ), faint ( $\text{S/N} \leq 20$ ) sources. Note that the  $1\sigma$  rms in a  $40''$  aperture is  $\geq 10\%$  for sources with  $\text{S/N} \leq 18$ .

densities. We do not attempt to correct for this residual bias, instead including the 5% iterative mapping uncertainty in the overall systematic uncertainty of 15%.

## 2.4 Results

The final coadded  $10''$  pixel<sup>-1</sup> Perseus map is shown in figure 2.5. The map has a beam size of  $31''$  and a total area of 7.5 square degrees, covering a total of  $3.4 \times 10^4$  resolution elements. The mean rms is  $15$  mJy beam<sup>-1</sup>. Well known regions are marked, including the conspicuous bright cluster NGC 1333. Note that the infrared cluster IC 348 actually lies slightly to the northeast of the group of 1.1 mm sources indicated as IC 348 here.

While nearly all previously known sources are seen, with the exception of some crowded regions where blending occurs (e.g., in NGC 1333 and L1448), perhaps the most striking feature of the map is its relative emptiness. In fact, few new sources are detected far from known cluster regions, and those that are tend to be faint objects near the detection limit. There does not appear to be any symmetric extended emission larger than approximately  $3'$  in the map. Although it should in principle be possible to recover symmetric structures up to the array size ( $7.5'$ ), our simulations show that sources larger than  $4'$  are severely affected by cleaning and difficult to fully recover with iterative mapping.

### 2.4.1 Source Identification

Discrete sources of 1.1 mm emission, or cores, are identified within the optimally filtered, iterated map using a simple peak finding algorithm. An optimal filter (as described in §2.3.3) is applied to the iterated map to facilitate the detection of point sources. This decreases the noise in the map, as well as increasing the peak brightness (and therefore the probability of detection) of sources larger than the beam. After optimal filtering the noisy edges of the map are removed using a cutoff based on the coverage map. A cutoff at 20% of the peak coverage is chosen empirically based on the number of false edge sources detected. All peaks  $5\sigma$  above the map-average rms are flagged as possible sources.

To make the final cut, candidate sources must also be  $5\sigma$  above the local rms, and have a well-defined centroid. The centroid is a weighted average position based on

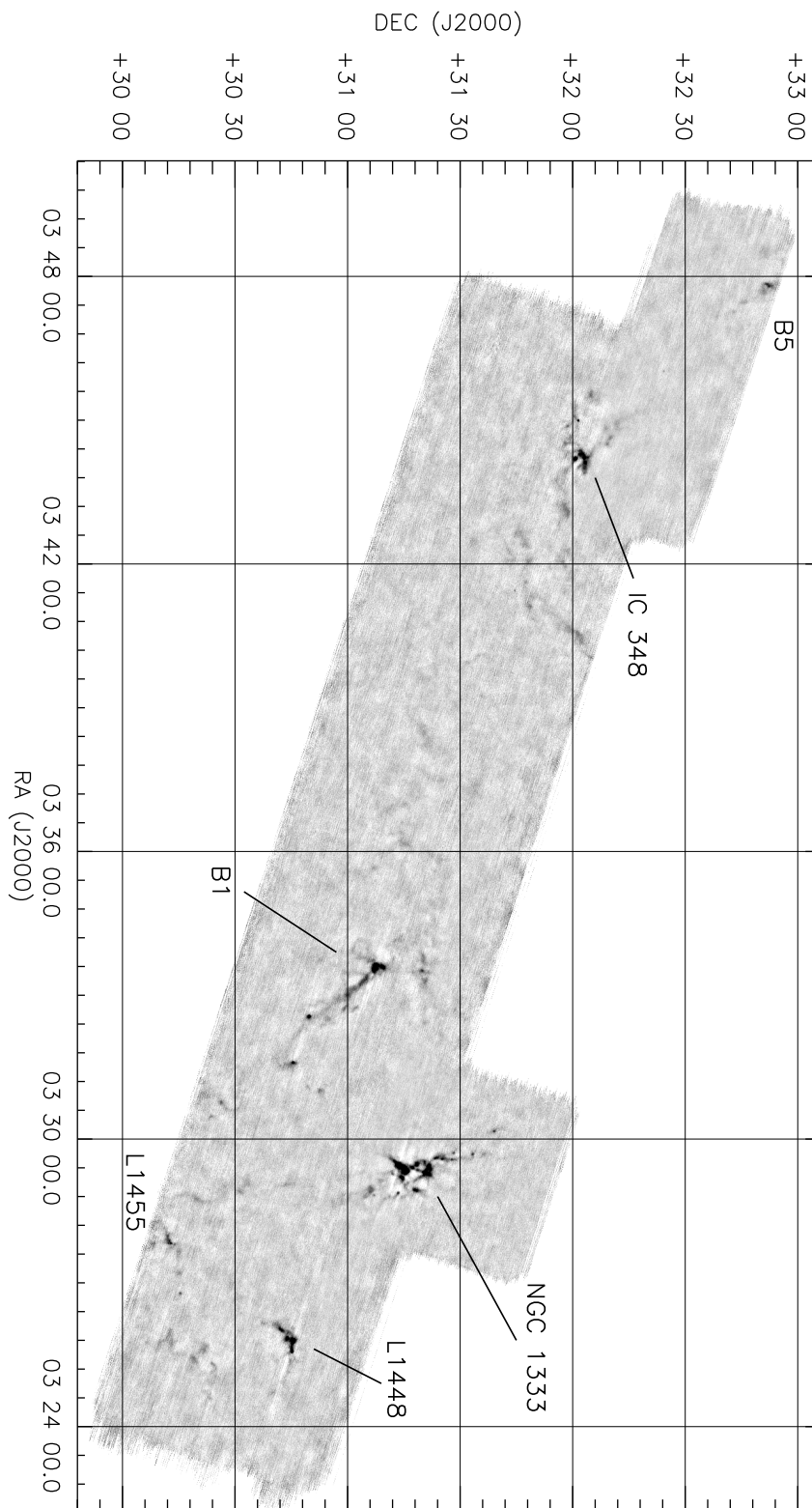


Figure 2.5 Bolocam 1.1 mm map of the Perseus molecular cloud ( $10''$  pixel $^{-1}$ ). The  $31''$  resolution map covers  $7.5 \text{ deg}^2$  ( $143 \text{ pc}^2$  at  $d = 250 \text{ pc}$ ), or  $3.4 \times 10^4$  resolution elements. The average  $1\sigma$  rms is  $15 \text{ mJy beam}^{-1}$ , varying by 15% across the map due to variable coverage. In this and other figures all maps shown are unfiltered.

the surface brightness within a specified aperture, and is computed as the position at which the derivatives of the partial sums of the input image over  $(y,x)$  with respect to  $(x,y)$  equal zero. A given centroid is considered “well-defined” as long as the computed derivatives are decreasing.

The local rms noise per beam is calculated in small ( $\sim 45$  arcmin<sup>2</sup>) boxes in a noise map, from which sources have been removed using the source model generated during iterative mapping (see §2.3.4). The average rms is 15 mJy beam<sup>-1</sup>, varying across the map by 15%. Most of the variation in rms is due to 30% variations in observational coverage rather than to a change in the calibration, which is very stable. Peaks separated by more than one beam size from a previously identified source centroid are considered to be distinct sources. A few false sources at the edge of the map were not automatically cut and had to be removed by visual inspection.

A total of 122 confirmed sources are identified in the optimally filtered map, the locations of which are indicated by small circles on the unfiltered map in figure 2.6. This figure also includes insets of the densest source regions. Because the rms varies very little across the map, the lack of sources over large regions of the image is real. Many of the sources seen in the 1.1 mm Bolocam map were very recently identified at 850  $\mu$ m in the SCUBA survey by Hatchell et al. (2005). The number of new sources not previously identified at submillimeter or millimeter continuum wavelengths is  $\sim 60/122$ , most of which are within the region covered by Hatchell et al. (2005) but not detected in that survey due to their somewhat higher mass detection limit (0.4  $M_{\odot}$  (12K) versus 0.2  $M_{\odot}$  (10 K) for the present survey). A number of these new sources lie within dense NH<sub>3</sub> cores (Per3-Per9; Ladd et al., 1994), or coincide with IRAS sources. Most are faint, and in the vicinity of known groups, although there are a few more isolated sources. A selection of new sources chosen to demonstrate the wide range in source properties is shown in figure 2.7.

We additionally identify cores using the 2D Clumpfind routine of Williams, deGeus, & Blitz (1994). Clumpfind is useful for separating sources in crowded regions, where it may be more effective than aperture photometry in defining total flux densities. It assigns pixels to each source by first contouring the map with a small contour inter-

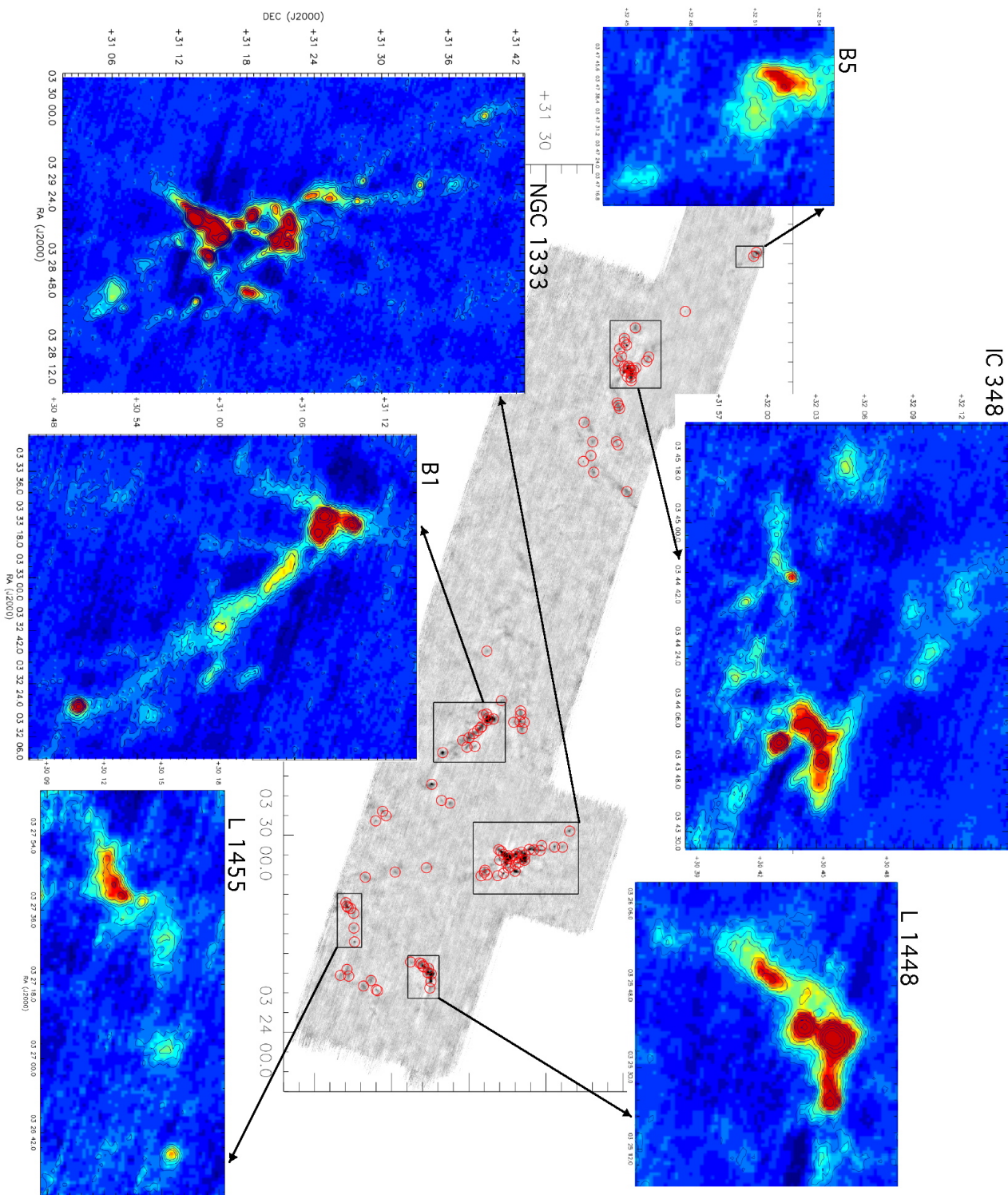


Figure 2.6 Bolocam 1.1 mm map of Perseus, with the 122 1.1 mm sources detected above  $5\sigma$  indicated by small circles. The rms varies very little across the map (15%), so the apparent lack of sources over large regions of the image is real. Despite the greater area surveyed compared to previous work, few new sources are found; much of the cloud is devoid of 1.1 mm emission at this sensitivity. Regions of high source density are magnified for clarity.

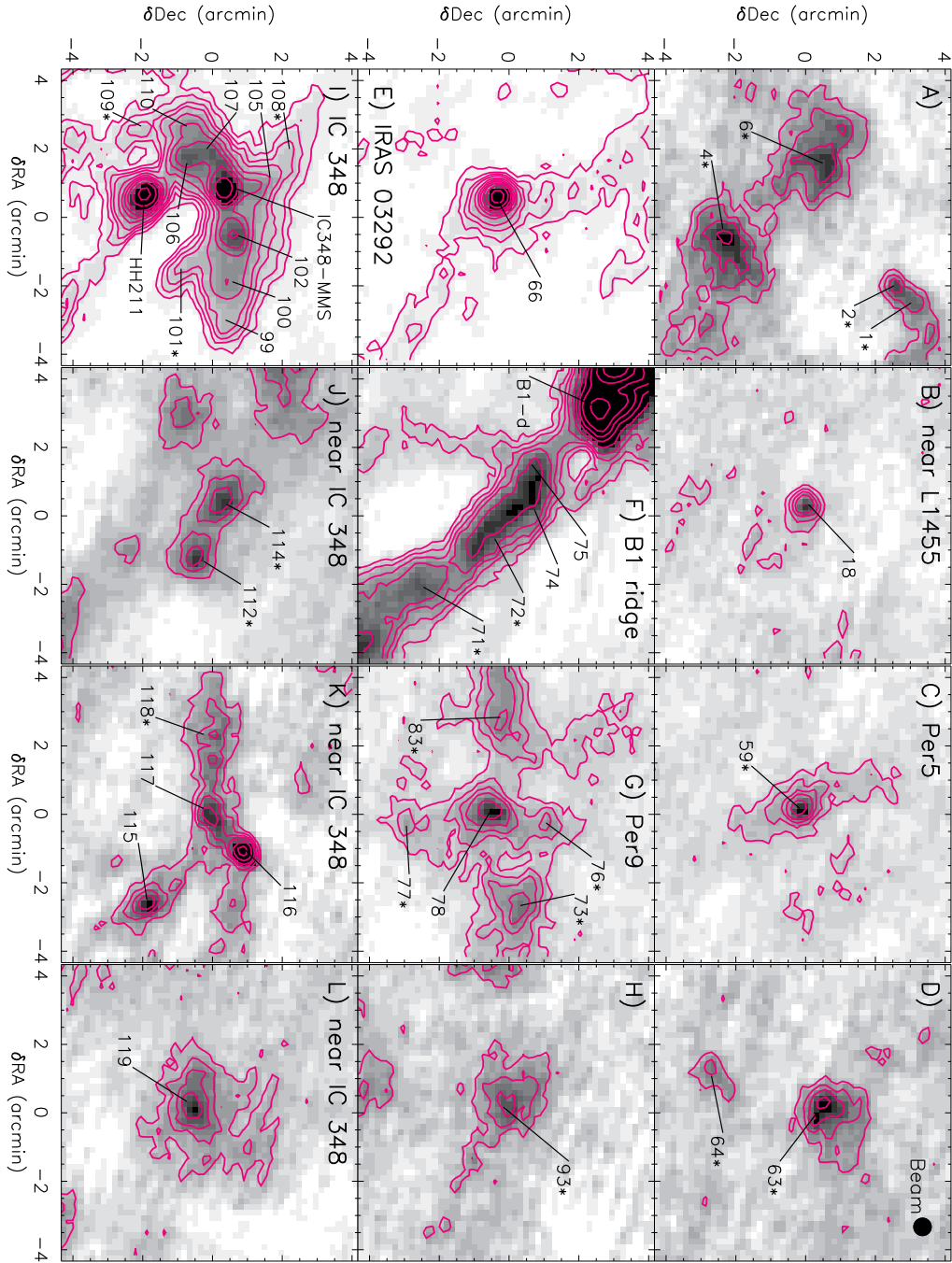


Figure 2.7 Examples of new millimeter detections. Each image is  $8.5' \times 8.5'$ , and has been smoothed to an effective resolution of  $35''$ . Contours are  $(2, 4, 6, 8, 12, 16, 20, 25, 35, 50, 75)\sigma$  on the grayscale 1.1 mm map. Any well-know sources are labeled with their common names. Numbers give the “Bolo#” identification from this paper (table 2.1); those sources with a “\*” next to the ID were either not covered by or not detected in the  $850 \mu\text{m}$  SCUBA survey of Hatchell et al. (2005). Sources range from compact (B) to extended (L) and crowded (I) to isolated (C).

val ( $2\sigma$ ). For each peak, contours are followed using a “friends-of-friends” algorithm down to one contour below the  $5\sigma$  detection limit, or until they run into another source at the same contour level. Clumpfind makes no assumptions about the clump profile, so the sources need not be Gaussian.

Clumpfind identifies 119 cores in the unfiltered map. Hereafter we refer to the sample of cores detected using peak finding in the optimally filtered map as “Peak-find sources”, and the sample identified with Clumpfind as “Clumpfind sources”. The total number of Clumpfind and Peak-find sources is very similar, but there is not a one-to-one correlation between the two sets. Fewer faint sources are found with Clumpfind because sources are detected above  $5\sigma$  using the rms *per pixel* of the unfiltered map, which is  $\sim \sqrt{3}$  times the rms *per beam* used to detect sources in the optimally filtered map. On the other hand, Clumpfind breaks up many of the brighter Peak-find sources into multiple sources. Faint extended sources that one would consider single if examining by eye are often partitioned into multiple sources by Clumpfind, and for this reason we favor the Peak-find source identification and photometry. We keep Clumpfind calculations for comparison to previous work, as well as to illustrate differences between the two methods.

## 2.4.2 Comparison to Molecular and $A_V$ Maps

Large-scale CO and extinction maps of Perseus are available for public use as part of “The COMPLETE Survey of Star-Forming Regions”<sup>3</sup> (COMPLETE; Goodman et al., 2004). These observations have been coordinated to cover the Spitzer c2d area of Perseus, therefore they also overlap with the Bolocam observations presented here. For the following we make use of the COMPLETE  $^{13}\text{CO}$  map, and calculate our own NIR extinction ( $A_V$ ) map. It is most instructive to compare the 1.1 mm,  $A_V$ , and  $^{13}\text{CO}$  maps if they are all converted to the same resolution and column density scale. The three maps are shown as  $A_V$  contours overlaid on the grayscale 1.1 mm emission in figures 2.8–2.10. Contours in all plots are  $A_V = 2, 3, 4, 6, 8$  mag except for the

---

<sup>3</sup><http://cfa-www.harvard.edu/COMPLETE/>

1.1 mm data (figure 2.10), where  $A_V = 2, 5, 10, 15, 20$  mag to avoid confusion, and smoothed to an effective resolution of  $5'$ .

The extinction contours in figure 2.8 were calculated from the H-K<sub>s</sub> color excesses of 2MASS sources using the *NICE* method (e.g., Lada, Alves, & Lada, 1999; Huard et al., 2006) and convolving with a Gaussian beam with FWHM of  $5'$ . This method depends on background stars to probe the column density through the cloud. In constructing the extinction map, we eliminate from the 2MASS catalog most foreground and embedded sources that would yield unreliable extinction estimates. Foreground sources were identified by color excesses representing a small line-of-sight visual extinction,  $A_{V,LOS} \leq 3$  mag, within a  $5' \times 5'$  region exhibiting a large mean extinction of  $A_V \geq 8$  mag. Embedded sources were identified as those sources positioned at least  $1\sigma$  redward of the reddened main-sequence region on a (J-H, H-K) color-color diagram. We use only those sources with reasonably good photometry at J, H, and K<sub>s</sub> (photometric errors less than 0.5, 0.2, and 0.2 mag, respectively) to construct the extinction map. The color excesses were computed assuming that the intrinsic color of non-extincted stars in off-cloud fields are representative of the background star population. These two off-cloud regions, having a total of more than 5700 stars, were  $1.5 \times 0.4$  fields centered on RA =  $03^h56^m48.0^s$ , Dec =  $35^\circ06'00''$  and RA =  $03^h49^m12.0^s$ , Dec =  $27^\circ54'00''$  (J2000.0).

The NIR-derived extinction contours in figure 2.8 verify that the Bolocam 1.1 mm map covers most of the  $A_V \geq 2$  mag area. All bright 1.1 mm sources occur in regions of high extinction, but the reverse is not necessarily true; high extinction does not guarantee the presence either of young protostars or dense millimeter cores with strong 1.1 mm emission. Note that the extinction map saturates around  $A_V \gtrsim 10$  mag.

Where  $^{13}\text{CO}$  is optically thin it provides another measure of column density. This may only be true for a small range of densities, however, as  $^{13}\text{CO}$  can be underexcited at small densities and becomes optically thick at  $A_V \sim 6$  mag for a typical line width of  $\Delta v \sim 1$  km s<sup>-1</sup>. To convert  $^{13}\text{CO}$  integrated intensity to H<sub>2</sub> column density, we assume LTE,  $\tau \ll 1$ , and an excitation temperature  $T_x = 10$  K, following Dickman (1978).  $A_V$  contours are calculated taking  $N_{LTE}(^{13}\text{CO}) = 2.5 \times 10^{15} (A_V - 0.8)$  cm<sup>-2</sup> in

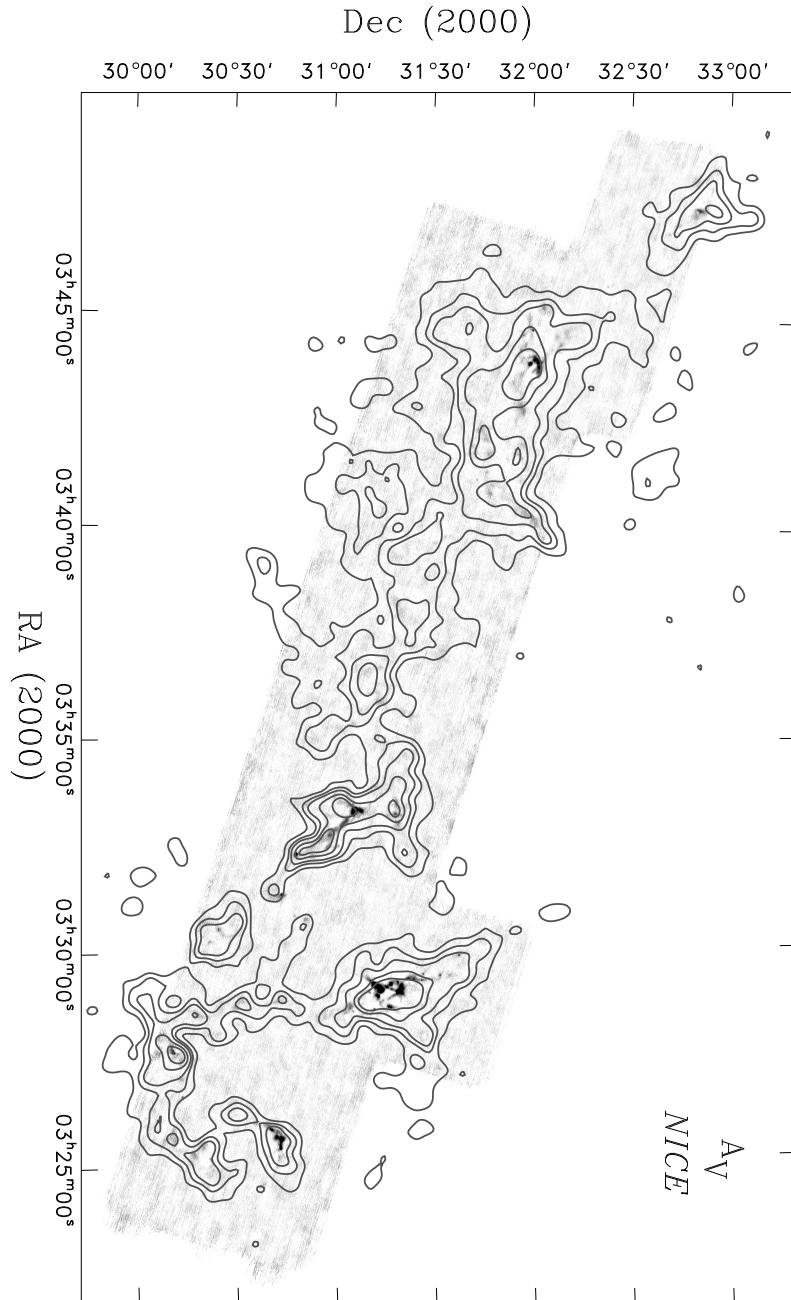


Figure 2.8 Visual extinction ( $A_V$ ) contours calculated from 2MASS data using the *NICE* method (see §2.4.2), overlaid on the grayscale 1.1 mm map. Contours in the following plots are  $A_V = 2, 3, 4, 6, 8$  mag with an effective resolution of  $5'$  unless otherwise noted. Most 1.1 mm sources lie within relatively high extinction ( $A_V \gtrsim 5$ ) peaks.



Figure 2.9  $A_V$  contours calculated from the COMPLETE  $^{13}\text{CO}$  map, smoothed to  $5'$  to match the resolution of the *NICE* extinction map, overlaid on the Bolocam 1.1 mm map. Thick black lines indicate the observational boundaries of the COMPLETE map. As a tracer of column density,  $^{13}\text{CO}$  is only accurate where it is optically thin.  $A_V(^{13}\text{CO})$  becomes more compact compared to extinction  $A_V$ , especially around 1.1 mm sources.

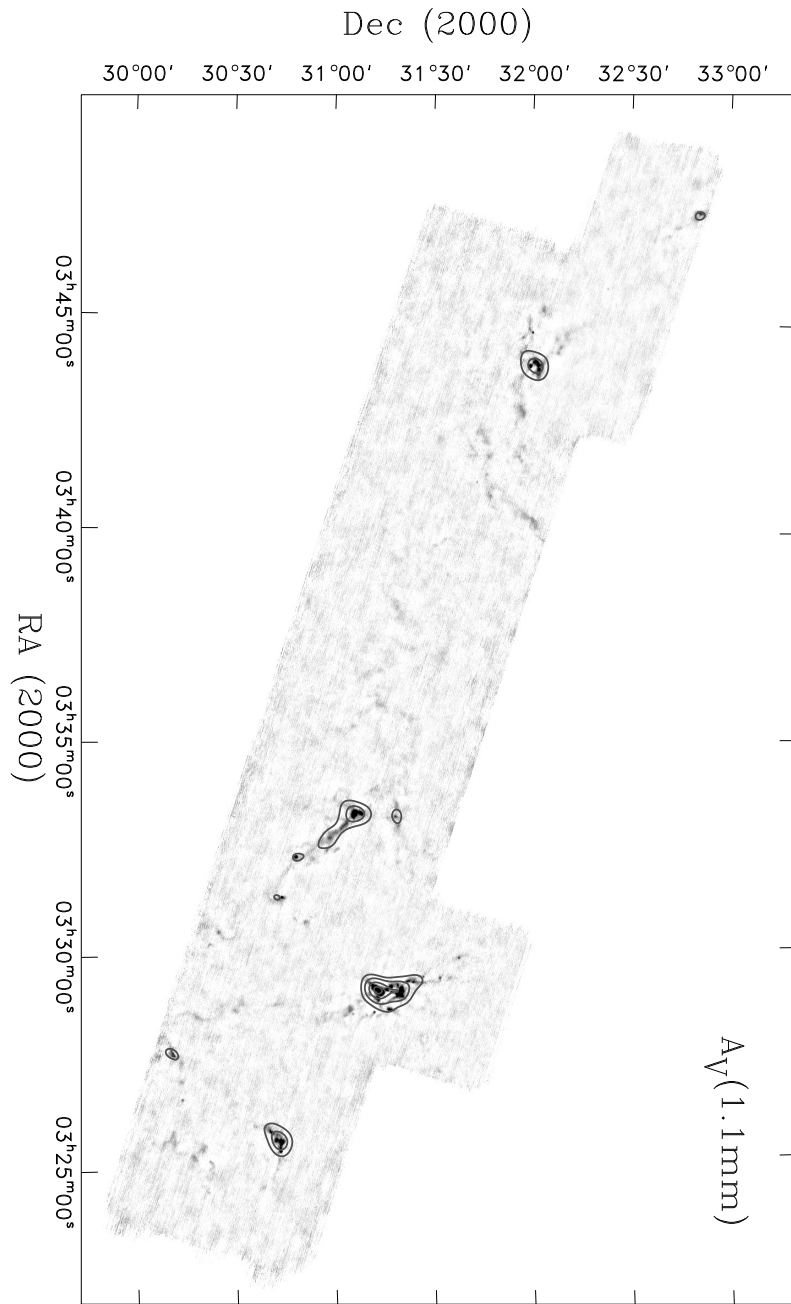


Figure 2.10  $A_V$  contours calculated from the 1.1 mm map, smoothed to 5' resolution. Contours are  $A_V = 2, 5, 10, 15, 20$  mag. The 1.1 mm contours are much more compact and extend to higher column density than the other column density tracers, likely because 1.1 mm emission traces only the densest regions of the cloud.

Perseus for  $1 < A_V < 5$  mag (Bachiller & Cernicharo, 1986), and shown in figure 2.9. The  $A_V(^{13}\text{CO})$  and *NICE* extinction maps display the same general morphology. Although the  $^{13}\text{CO}$  contours do not reach peak densities as high as those in the *NICE*  $A_V$  map, they do become more compact compared to the NIR extinction derived  $A_V$ , especially around 1.1 mm sources.

$\text{H}_2$  column density is calculated from the 1.1 mm map using a conversion from 1.1 mm flux density per beam ( $S_{1.1\text{mm}}^{\text{beam}}$ ) of

$$N(\text{H}_2) = \frac{S_{\nu}^{\text{beam}}}{\Omega_{\text{beam}} \mu_{\text{H}_2} m_H \kappa_{\nu} B_{\nu}(T_D)}. \quad (2.2)$$

Here  $\Omega_{\text{beam}}$  is the beam solid angle,  $m_H$  is the mass of hydrogen,  $\kappa_{1.1\text{mm}} = 0.0114 \text{ cm}^2 \text{ g}^{-1}$  is the dust opacity per gram of gas,  $B_{\nu}$  is the Planck function,  $T_D = 10 \text{ K}$  is the dust temperature, and  $\mu_{\text{H}_2} = 2.8$  is the mean molecular weight per  $\text{H}_2$  molecule, which is the relevant quality for conversion to extinction. We interpolate  $\kappa_{1.1\text{mm}}$  from Ossenkopf & Henning (1994, table 1 column 5, hereafter OH5) for dust grains with thin ice mantles, coagulated for  $10^5$  years at a gas density of  $10^6 \text{ cm}^{-3}$ . A gas to dust ratio of 100 is assumed. OH5 dust has found to be the best choice for star-forming cores by several authors using radiative transfer modeling (Evans et al., 2001; Shirley, Evans, & Rawlings, 2002; Young et al., 2003). Column densities calculated from thermal emission depend on  $T_D$ , which varies with position. Thus there may be local discrepancies with other tracers when  $T_D$  is not independently known, but agreement should be good overall.

We assume a conversion from column density to  $A_V$  of  $N(\text{H}_2)/A_V = 0.94 \times 10^{21} \text{ cm}^2 \text{ mag}^{-1}$  (Frerking, Langer, & Wilson, 1982). Note that this relation uses  $R_V = 3.1$ , determined in the diffuse interstellar medium, and may not be correct for the highly extinguished lines of sight we are probing. The resulting  $A_V(1.1 \text{ mm})$  contours in figure 2.10 clearly demonstrate that the 1.1 mm emission is considerably more compact compared to the other column density tracers. It appears that only the densest material is traced by the 1.1 mm emission, as manifested in both the compact nature of the  $A_V(1.1 \text{ mm})$  contours and the high  $A_V$  reached in the bright cores

( $A_{V,max} \sim 17$  at  $5'$  resolution). The  $5\sigma$  detection limit per  $31''$  beam corresponds to a minimum  $A_V \sim 5$  mag, so it is not surprising that there is not 1.1 mm emission seen in the lower  $A_V$  regions of the  $A_V$  and  $^{13}\text{CO}$  maps. We note, however, that our simulations indicate that the Bolocam map may not be sensitive to more extended emission ( $\gtrsim 4'$ ) even if it is present in the cloud.

### 2.4.3 Source Statistics

Source identifications, positions, peak flux densities ( $S_{peak}$ ), and signal to noise (S/N) for the 122 1.1 mm sources identified in the Bolocam map are listed in table 2.1. The S/N is measured in the optimally filtered map, because this is the S/N that determines detection. Photometry and all other source properties are measured in the unfiltered, surface brightness-normalized map.  $S_{peak}$  is the peak pixel value in  $\text{mJy beam}^{-1}$  as measured in the  $10''$   $\text{pixel}^{-1}$  map. The uncertainty in  $S_{peak}$  is the local rms  $\text{beam}^{-1}$ , calculated as described in §2.4.1. There is an additional systematic error of  $\sim 15\%$  associated with all flux densities, from the absolute calibration uncertainty (10%) and the systematic bias remaining after iterative mapping ( $\sim 5\%$ , see §2.3.4). Table 2.1 also lists the most commonly used name from the literature for known sources, and indicates if the 1.1 mm source is coincident (within  $40''$ ) with a MIPS  $24 \mu\text{m}$  source from the c2d database (Rebull et al., 2007). The c2d MIPS data for some regions of Perseus are not yet available, in which case “N/A” is listed in the table. For these sources, the presence of an IRAS source (within  $1'$ ) is indicated if appropriate.

Table 2.2 lists photometry in fixed apertures of diameter  $40''$ ,  $80''$ , and  $120''$ , the total integrated flux density ( $S_\nu$ ), total mass, peak  $A_V$ , full-width at half maximum (FWHM) sizes along the major and minor axes, position angle (PA, measured east of north), mean particle density  $\langle n \rangle$ , and morphology descriptions for each source. Integrated flux densities are measured assuming a sky value of zero, and corrected for the Gaussian beam so that a point source has the same integrated flux density in all apertures with diameter greater than the beam. No integrated flux density is given if the distance to the nearest neighboring source is smaller than the aperture diameter.

To calculate the total flux density, we compute integrated flux densities in apertures of  $30'' - 160''$  in intervals of  $10''$ , and use the largest aperture diameter that is smaller than the distance to the nearest neighbor. An aperture of  $120''$  is generally sufficient unless the source FWHM is  $> 100''$ , in which case apertures up to  $160''$  are used. If the flux density decreases in larger apertures (due to residual negative artifacts), then the aperture giving the largest flux density is used. Uncertainties in all integrated flux densities are  $\sigma_{ap} = \sigma_{beam} \sqrt{A_{ap}/A_{beam}}$ , where  $\sigma_{beam}$  is the local rms beam $^{-1}$  and  $(A_{ap}, A_{beam})$  are the aperture and beam areas respectively, and do not include an additional 15% systematic uncertainty. The FWHM and PA are from the best fit elliptical Gaussian after masking out nearby sources using a mask radius equal to half the distance to the nearest neighbor. The errors given are the formal fitting errors and do not include uncertainties due to noise or residual cleaning effects, which are of order 10% – 15% for the FWHM and  $\sim 5^\circ$  for the PA.

Table 2.1. Identified sources in Perseus

ID	RA (2000) (h m s)	Dec (2000) (° ' ")	Peak (mJy/beam)	S/N	Other Names	MIPS 24 $\mu$ m Source?
Bolo 1	03 25 07.8	+30 24 21.6	109 (16)	6.1		N
Bolo 2	03 25 09.5	+30 23 51.3	121 (16)	8.7		N
Bolo 3	03 25 10.2	+30 44 43.4	125 (17)	6.6		N
Bolo 4	03 25 17.0	+30 18 53.2	149 (17)	7.2		N
Bolo 5	03 25 22.2	+30 45 09.3	727 (18)	42.0	L 1448-IRS2 (1)	Y
Bolo 6	03 25 26.5	+30 21 50.0	143 (19)	5.9		N
Bolo 7	03 25 35.4	+30 13 06.2	126 (17)	6.0		N
Bolo 8	03 25 35.9	+30 45 17.2	2241 (19)	128	L 1448-N (2)	Y
Bolo 9	03 25 37.2	+30 09 55.4	113 (16)	5.7		N
Bolo 10	03 25 38.4	+30 43 58.0	980 (20)	45.2	L 1448-C (2)	Y
Bolo 11	03 25 46.0	+30 44 10.3	240 (20)	8.4		Y
Bolo 12	03 25 47.5	+30 12 25.9	118 (18)	5.1		N
Bolo 13	03 25 48.8	+30 42 24.1	407 (19)	19.0	H32 (3)	N
Bolo 14	03 25 50.6	+30 42 01.4	342 (19)	17.9	H33 (3)	N
Bolo 15	03 25 55.1	+30 41 25.8	188 (17)	6.4		N
Bolo 16	03 25 56.2	+30 40 41.1	154 (17)	6.3		N
Bolo 17	03 25 58.4	+30 37 13.4	122 (15)	6.7		N
Bolo 18	03 26 36.9	+30 15 23.0	225 (15)	14.9	IRAS 03235+3004; H80 (3)	Y
Bolo 19	03 27 02.0	+30 15 07.9	115 (14)	7.3		N
Bolo 20	03 27 28.8	+30 15 02.1	114 (16)	5.9		N
Bolo 21	03 27 37.5	+30 13 53.4	164 (17)	9.0	H39 (3)	Y
Bolo 22	03 27 39.3	+30 12 52.9	317 (18)	16.3	RNO 15-FIR (4)	Y
Bolo 23	03 27 41.7	+30 12 24.1	283 (18)	12.8	H36 (3)	Y
Bolo 24	03 27 47.9	+30 12 02.1	220 (19)	11.2	L 1455-IRS2 (5); H37 (3)	Y
Bolo 25	03 28 32.1	+31 11 08.8	106 (16)	6.7	H74 (3)	N/A
Bolo 26	03 28 32.4	+31 04 42.9	117 (14)	7.6		N/A
Bolo 27	03 28 33.3	+30 19 35.0	155 (16)	6.4		Y
Bolo 28	03 28 34.0	+31 07 01.2	137 (14)	9.7	H69 (3)	N/A
Bolo 29	03 28 36.2	+31 13 26.4	267 (19)	17.1	NGC 1333-IRAS 1 (6); SK6 (7)	N/A (IRAS)
Bolo 30	03 28 39.0	+31 05 59.2	189 (15)	11.3	in Per3 (8); H71 (4)	N/A
Bolo 31	03 28 39.9	+31 17 56.7	385 (19)	20.1	NGC 1333-IRAS 5 (6)	N/A (IRAS)
Bolo 32	03 28 41.7	+30 31 13.0	144 (15)	6.4	RNO 17	Y
Bolo 33	03 28 42.6	+31 06 12.2	173 (14)	9.6	in Per 3 (8); H75 (3)	N/A
Bolo 34	03 28 45.9	+31 15 19.8	150 (20)	6.2		N/A
Bolo 35	03 28 48.4	+31 16 01.9	130 (20)	5.9		N/A
Bolo 36	03 28 48.7	+30 43 24.6	127 (14)	6.3		Y

Table 2.1 (cont'd)

ID	RA (2000) (h m s)	Dec (2000) (° ' ")	Peak (mJy/beam)	S/N	Other Names	MIPS 24 $\mu$ m Source?
Bolo 37	03 28 52.1	+31 18 07.9	160 (20)	7.4	ASR 40	N/A
Bolo 38	03 28 55.3	+31 14 32.2	1220 (20)	59.4	NGC 1333-IRAS 2 (6,9)	N/A (IRAS)
Bolo 39	03 28 55.3	+31 19 17.7	210 (20)	9.7	ASR 64; H68 (3)	N/A
Bolo 40	03 29 00.0	+31 21 37.8	685 (17)	34.2	SK31 (7)	N/A
Bolo 41	03 29 00.6	+31 11 58.9	190 (19)	10.7	SK1 (7)	N/A
Bolo 42	03 29 01.3	+31 20 33.0	1079 (18)	58.8	NGC 1333-IRAS 6 (6); SK24 (7)	N/A (IRAS)
Bolo 43	03 29 02.6	+31 15 56.8	2160 (20)	103	SVS 13 (9)	N/A
Bolo 44	03 29 04.5	+31 18 42.1	270 (20)	13.7		N/A
Bolo 45	03 29 07.7	+31 17 16.8	460 (20)	21.8	Cor 1 (9); SK17/18 (7)	N/A
Bolo 46	03 29 08.3	+31 15 11.1	740 (20)	28.6	SK16 (7)	N/A
Bolo 47	03 29 08.9	+31 21 43.5	612 (18)	30.9	SK28 (7)	N/A (IRAS)
Bolo 48	03 29 10.9	+31 13 26.4	5180 (20)	264	NGC 1333-IRAS 4 (6,10)	N/A (IRAS)
Bolo 49	03 29 11.3	+31 18 24.8	840 (20)	40.6	NGC 1333-IRAS 7 (6,9)	N/A (IRAS)
Bolo 50	03 29 14.5	+31 20 30.1	310 (20)	14.2	SK22 (7)	N/A
Bolo 51	03 29 17.0	+31 12 25.9	423 (19)	16.4	H59 (3)	N/A
Bolo 52	03 29 17.1	+31 27 38.8	269 (18)	13.7	in Per 4 (8); H61 (3)	N/A
Bolo 53	03 29 18.2	+31 25 17.0	336 (19)	16.7	SK33 (7)	N/A (IRAS)
Bolo 54	03 29 19.1	+31 23 26.5	330 (19)	16.7	SK32 (7)	N/A
Bolo 55	03 29 19.4	+31 11 36.6	184 (17)	9.8	ASR 129; H72 (3)	N/A
Bolo 56	03 29 22.4	+31 36 24.4	102 (14)	6.8	H91 (3)	N/A
Bolo 57	03 29 22.9	+31 33 16.5	224 (16)	16.2	in Per 4 (8); H58 (3)	N/A (IRAS)
Bolo 58	03 29 25.7	+31 28 16.3	273 (17)	14.0	H64 (3)	N/A
Bolo 59	03 29 51.5	+31 39 12.9	249 (14)	19.3	Per 5 (8)	N/A (IRAS)
Bolo 60	03 30 14.9	+30 23 36.9	125 (15)	8.3	IRAS 03271 (11); H15 (3); Per 6 (8)	Y
Bolo 61	03 30 24.0	+30 27 38.5	106 (17)	5.1		N
Bolo 62	03 30 32.0	+30 26 18.6	199 (17)	11.1		Y
Bolo 63	03 30 45.5	+30 52 34.3	141 (14)	10.2		N/A (IRAS)
Bolo 64	03 30 50.4	+30 49 17.4	86 (14)	6.4		N/A
Bolo 65	03 31 20.0	+30 45 30.2	522 (17)	31.7	IRAS 03282+3035 (11); H77 (3)	N/A (IRAS)
Bolo 66	03 32 17.3	+30 49 44.0	1068 (15)	73.5	IRAS 03292+3039; H76 (3)	Y
Bolo 67	03 32 26.9	+30 59 11.0	165 (19)	8.8	H89 (3)	N
Bolo 68	03 32 28.1	+31 02 17.5	110 (18)	6.6		Y
Bolo 69	03 32 39.3	+30 57 28.8	155 (16)	5.7		N
Bolo 70	03 32 44.0	+31 00 00.0	238 (17)	11.1	in Per 7 (8)	N
Bolo 71	03 32 51.2	+31 01 47.6	180 (20)	7.3		N
Bolo 72	03 32 57.0	+31 03 20.8	240 (20)	9.4		N

Table 2.1 (cont'd)

ID	RA (2000) ( <i>h m s</i> )	Dec (2000) ( $^{\circ}$ $'$ $''$ )	Peak (mJy/beam)	S/N	Other Names	MIPS 24 $\mu$ m Source?
Bolo 73	03 33 00.0	+31 20 43.8	178 (16)	8.8	in Per 9 (8)	N
Bolo 74	03 33 01.9	+31 04 31.8	260 (20)	9.3	H5 (3)	N
Bolo 75	03 33 04.4	+31 04 58.8	260 (20)	9.7	H8 (3)	N
Bolo 76	03 33 11.4	+31 21 30.9	116 (16)	6.5	in Per 9 (8)	N
Bolo 77	03 33 11.4	+31 17 24.0	110 (19)	5.0		N
Bolo 78	03 33 13.2	+31 19 50.1	262 (16)	16.3	in Per 9 (8); H82 (3)	Y
Bolo 79	03 33 15.0	+31 07 01.9	605 (19)	30.0	B1-d (12)	Y
Bolo 80	03 33 17.8	+31 09 29.8	1080 (20)	53.2	B1-c (12)	Y
Bolo 81	03 33 20.5	+31 07 37.2	1220 (20)	59.9	B1-b (12)	Y
Bolo 82	03 33 25.1	+31 05 34.8	147 (17)	7.1		N
Bolo 83	03 33 25.4	+31 20 07.4	165 (17)	7.2	in Per 9 (8)	N
Bolo 84	03 33 26.8	+31 06 49.6	190 (20)	7.0	H10 (3)	Y
Bolo 85	03 33 32.1	+31 20 03.8	155 (17)	6.9	in Per 9 (8)	N
Bolo 86	03 33 51.1	+31 12 36.7	131 (18)	5.2		Y
Bolo 87	03 35 21.6	+31 06 55.4	99 (14)	5.9		N
Bolo 88	03 40 14.5	+32 01 29.6	162 (17)	6.7		N
Bolo 89	03 40 49.3	+31 48 34.5	151 (16)	8.1		Y
Bolo 90	03 41 09.0	+31 44 33.0	139 (15)	8.0		Y
Bolo 91	03 41 19.7	+31 47 28.3	106 (15)	6.5		N
Bolo 92	03 41 40.0	+31 58 04.8	94 (14)	6.4		N
Bolo 93	03 41 45.1	+31 48 09.7	118 (16)	6.3		N
Bolo 94	03 41 45.8	+31 57 21.6	132 (14)	7.3		N
Bolo 95	03 42 20.6	+31 44 49.2	108 (14)	6.2		Y
Bolo 96	03 42 47.1	+31 58 40.8	148 (16)	7.1		N
Bolo 97	03 42 52.3	+31 58 12.3	149 (17)	6.0		Y
Bolo 98	03 42 57.3	+31 57 49.3	134 (18)	6.0		Y
Bolo 99	03 43 38.3	+32 03 08.6	164 (13)	12.0	H23 (3)	N/A
Bolo 100	03 43 44.0	+32 03 10.0	250 (14)	15.3	H26 (3)	N/A
Bolo 101	03 43 45.6	+32 01 45.1	139 (19)	7.5		N/A
Bolo 102	03 43 50.5	+32 03 17.2	432 (16)	23.5	H81 (3)	N/A
Bolo 103	03 43 55.9	+32 00 46.4	994 (19)	56.5	HH 211 (13)	N/A (IRAS)
Bolo 104	03 43 57.3	+32 03 03.9	777 (17)	44.2	IC 348-MMS (14)	N/A
Bolo 105	03 43 57.8	+32 04 06.2	283 (16)	12.5	H17 (3)	N/A
Bolo 106	03 44 01.6	+32 02 02.0	426 (18)	18.1	H16 (3)	N/A
Bolo 107	03 44 02.1	+32 02 33.7	388 (18)	16.5	H18 (3)	N/A
Bolo 108	03 44 02.3	+32 04 57.3	139 (16)	6.1		N/A

Table 2.1 (cont'd)

ID	RA (2000) ( <i>h m s</i> )	Dec (2000) ( $^{\circ}$ $'$ $''$ )	Peak (mJy/beam)	S/N	Other Names	MIPS $24\mu\text{m}$ Source?
Bolo 109	03 44 05.0	+32 00 27.7	127 (17)	6.3		N/A
Bolo 110	03 44 05.2	+32 02 05.6	257 (19)	11.8	H20 (3)	N/A
Bolo 111	03 44 14.5	+31 58 00.1	170 (17)	8.9		N/A
Bolo 112	03 44 14.8	+32 09 12.6	127 (15)	8.2		N/A
Bolo 113	03 44 22.6	+31 59 23.2	122 (18)	6.2		N/A
Bolo 114	03 44 22.7	+32 10 01.2	140 (15)	8.0		N/A
Bolo 115	03 44 36.4	+31 58 39.3	167 (17)	10.4	H19 (3)	N/A
Bolo 116	03 44 43.9	+32 01 24.6	289 (18)	18.8	H14 (3)	N/A (IRAS)
Bolo 117	03 44 48.8	+32 00 29.5	150 (18)	8.7	H25 (3)	N/A
Bolo 118	03 44 56.0	+32 00 31.3	109 (17)	5.7		N/A
Bolo 119	03 45 15.9	+32 04 48.3	181 (16)	9.3	H90 (3)	N/A
Bolo 120	03 45 48.1	+32 24 15.1	83 (10)	8.8	LkHA 330	Y
Bolo 121	03 47 33.5	+32 50 54.9	136 (15)	6.3		N
Bolo 122	03 47 40.8	+32 51 57.2	262 (17)	14.3	B5-IRS1 (15)	Y

Note. — Numbers in parentheses are  $1\sigma$  uncertainties, and do not include an additional systematic uncertainty of 15% in the peak flux density. Other names listed are the most common identifications from the literature, and are not meant to be a complete list. Presence of MIPS source is from the c2d database (Rebull et al., 2007). References – (1) O’Linger et al. 1999; (2) Barsony et al. 1998; (3) Hatchell et al. 2005; (4) Froebrich et al. 2003; (5) Juan et al. 1993; (6) Jennings et al. 1987; (7) Sandell & Knee 2001; (8) Ladd et al. 1994; (9) Lefloch et al. 1998; (10) Sandell et al. 1991; (11) Bachiller, Martín-Pintado, & Planesas 1991; (12) Mathews & Wilson 2002; (13) McCaughrean et al. 1994; (14) Eisloffel et al. 2003; (15) Motte & André 2001.

Table 2.2. Photometry, masses, sizes, and morphology for sources in Perseus

ID	Flux(40'')	Flux(80'')	Flux(120'')	Total Flux	Mass (10K)	Peak $A_V$	FWHM	FWHM	PA	$\langle n \rangle$	Morphology <sup>1</sup>
	(Jy)	(Jy)	(Jy)	(Jy)	( $M_\odot$ )	(mag)	(minor, '')	(major, '')	( $^\circ$ )	( $\text{cm}^{-3}$ )	
Bolo 1	...	...	...	0.114 (0.016)	0.27 (0.04)	8	38 (1.1)	57 (1.7)	-52 (6)	$1 \times 10^5$	multiple, round, weak
Bolo 2	...	...	...	0.148 (0.016)	0.36 (0.04)	9	33 (1.0)	54 (1.6)	48 (6)	$3 \times 10^5$	multiple, round, weak
Bolo 3	0.15 (0.02)	0.30 (0.05)	0.38 (0.07)	0.38 (0.07)	0.9 (0.2)	9	65 (1.3)	134 (3)	-68 (2)	$3 \times 10^4$	extended, round, weak
Bolo 4	0.21 (0.02)	0.48 (0.05)	0.87 (0.07)	1.24 (0.09)	3.0 (0.2)	11	99 (1.2)	122 (1.4)	74 (4)	$5 \times 10^4$	extended, round
Bolo 5	0.93 (0.02)	1.48 (0.05)	2.05 (0.07)	2.05 (0.07)	4.9 (0.2)	51	45 (0.2)	79 (0.4)	88 (1)	$7 \times 10^5$	multiple, extended, elongated
Bolo 6	0.19 (0.03)	0.43 (0.05)	0.79 (0.08)	1.18 (0.10)	2.9 (0.2)	10	93 (1.3)	132 (1.8)	-54 (3)	$4 \times 10^4$	extended, round, weak
Bolo 7	0.16 (0.02)	0.36 (0.04)	0.67 (0.07)	0.96 (0.09)	2.3 (0.2)	9	88 (1.4)	122 (1.9)	4 (4)	$4 \times 10^4$	multiple, extended, round, weak
Bolo 8	2.95 (0.03)	4.70 (0.05)	...	4.70 (0.05)	11.3 (0.12)	160	45 (0.1)	54 (0.1)	-47 (1)	$4 \times 10^6$	multiple, extended, round
Bolo 9	0.15 (0.02)	0.31 (0.04)	0.52 (0.07)	0.70 (0.09)	1.7 (0.2)	8	76 (1.3)	144 (3)	-52 (2)	$3 \times 10^4$	extended, round, weak
Bolo 10	1.22 (0.03)	2.04 (0.06)	...	2.04 (0.06)	4.9 (0.14)	69	53 (0.2)	55 (0.2)	-10 (10)	$1 \times 10^6$	multiple, extended, round
Bolo 11	0.31 (0.03)	0.75 (0.05)	...	0.90 (0.06)	2.2 (0.15)	17	78 (0.8)	81 (0.8)	30 (20)	$1 \times 10^5$	multiple, extended, round
Bolo 12	0.16 (0.02)	0.37 (0.05)	0.69 (0.07)	0.97 (0.10)	2.3 (0.2)	8	77 (1.2)	135 (2)	-72 (2)	$5 \times 10^4$	multiple, extended, round, weak
Bolo 13	...	...	...	0.47 (0.02)	1.14 (0.05)	29	44 (0.4)	59 (0.5)	33 (2)	$3 \times 10^5$	multiple, extended, elongated
Bolo 14	...	...	...	0.41 (0.02)	1.00 (0.04)	24	44 (0.4)	60 (0.5)	-43 (2)	$3 \times 10^5$	multiple, extended, elongated
Bolo 15	0.25 (0.02)	...	...	0.25 (0.02)	0.60 (0.06)	13	54 (0.8)	60 (0.9)	52 (13)	$1 \times 10^5$	multiple, extended, round
Bolo 16	0.21 (0.02)	...	...	0.21 (0.02)	0.51 (0.06)	11	53 (1.0)	58 (1.0)	-76 (16)	$9 \times 10^4$	multiple, extended, round
Bolo 17	0.13 (0.02)	...	...	0.36 (0.06)	0.9 (0.14)	9	67 (1.6)	81 (1.9)	29 (10)	$6 \times 10^4$	extended, round, weak
Bolo 18	0.25 (0.02)	0.24 (0.04)	0.36 (0.06)	0.40 (0.06)	1.0 (0.15)	16	39 (0.7)	45 (0.8)	-64 (11)	$8 \times 10^5$	extended, round, weak
Bolo 19	0.16 (0.02)	0.35 (0.04)	0.40 (0.06)	0.40 (0.06)	1.4 (0.14)	8	86 (1.4)	93 (1.5)	58 (16)	$4 \times 10^4$	multiple, extended, round, weak
Bolo 20	0.16 (0.02)	0.37 (0.04)	0.59 (0.06)	0.59 (0.06)	1.4 (0.14)	8	86 (1.4)	93 (1.5)	-82 (4)	$6 \times 10^4$	multiple, extended, elongated
Bolo 21	0.22 (0.02)	...	...	0.69 (0.07)	1.7 (0.16)	8	75 (1.2)	102 (1.7)	88 (5)	$2 \times 10^5$	multiple, extended, elongated
Bolo 22	0.41 (0.02)	...	...	0.27 (0.03)	0.65 (0.08)	12	44 (0.9)	61 (1.2)	-66 (4)	$3 \times 10^5$	multiple, extended, elongated
Bolo 23	0.40 (0.02)	...	...	0.41 (0.02)	0.99 (0.06)	22	44 (0.5)	54 (0.6)	75 (5)	$2 \times 10^5$	multiple, extended, elongated
				0.40 (0.02)	0.96 (0.06)	20	52 (0.5)	60 (0.6)			

Table 2.2 (cont'd)

ID	Flux(40'') (Jy)	Flux(80'') (Jy)	Flux(120'') (Jy)	Total Flux (Jy)	Mass (10K) ( $M_{\odot}$ )	Peak $A_V$ (mag)	FWHM (minor,'')	FWHM (major,'')	PA ( $^{\circ}$ )	$\langle n \rangle$ ( $\text{cm}^{-3}$ )	Morphology <sup>1</sup>
Bolo 24	0.32 (0.03)	0.66 (0.05)	...	0.66 (0.05)	1.6 (0.12)	16	53 (0.6)	79 (0.9)	-1 (2)	$2 \times 10^5$	multiple, extended, elongated
Bolo 25	0.12 (0.02)	0.18 (0.04)	0.21 (0.07)	0.23 (0.08)	0.6 (0.18)	8	51 (1.7)	132 (4)	-7 (2)	$2 \times 10^4$	multiple, extended, round, weak
Bolo 26	0.17 (0.02)	0.37 (0.04)	...	0.53 (0.05)	1.3 (0.12)	8	60 (0.9)	91 (1.4)	-31 (3)	$8 \times 10^4$	multiple, extended, round, weak
Bolo 27	0.17 (0.02)	0.41 (0.04)	0.71 (0.06)	1.03 (0.09)	2.5 (0.2)	11	87 (1.2)	136 (1.8)	37 (2)	$4 \times 10^4$	extended, round
Bolo 28	0.15 (0.02)	...	...	0.19 (0.03)	0.47 (0.08)	10	36 (0.9)	46 (1.2)	-66 (8)	$5 \times 10^5$	multiple, round
Bolo 29	0.35 (0.03)	...	...	0.42 (0.04)	1.00 (0.09)	19	33 (0.5)	47 (0.7)	-53 (4)	$1 \times 10^6$	multiple, extended, elongated
Bolo 30	0.29 (0.02)	...	...	0.29 (0.02)	0.69 (0.05)	13	51 (0.6)	56 (0.7)	-3 (11)	$2 \times 10^5$	multiple, extended, elongated
Bolo 31	0.59 (0.03)	1.24 (0.05)	1.92 (0.08)	1.92 (0.08)	4.6 (0.2)	27	59 (0.4)	90 (0.6)	-75 (1)	$3 \times 10^5$	multiple, extended, elongated
Bolo 32	0.16 (0.02)	0.37 (0.04)	0.63 (0.06)	0.76 (0.07)	1.8 (0.17)	10	94 (1.4)	107 (1.6)	-68 (9)	$4 \times 10^4$	extended, round
Bolo 33	0.27 (0.02)	...	...	0.27 (0.02)	0.65 (0.05)	12	55 (0.6)	58 (0.6)	90 (20)	$1 \times 10^5$	multiple, extended, round
Bolo 34	0.19 (0.03)	...	...	0.23 (0.04)	0.55 (0.08)	10	40 (1.1)	57 (1.6)	4 (6)	$2 \times 10^5$	multiple, extended, round, weak
Bolo 35	0.17 (0.03)	...	...	0.20 (0.04)	0.48 (0.08)	9	38 (1.2)	56 (1.8)	-46 (6)	$2 \times 10^5$	multiple, round, weak
Bolo 36	0.13 (0.02)	0.28 (0.04)	0.44 (0.06)	0.61 (0.08)	1.5 (0.18)	9	65 (1.2)	121 (2)	72 (2)	$5 \times 10^4$	extended, round
Bolo 37	0.21 (0.03)	0.38 (0.06)	...	0.38 (0.06)	0.9 (0.14)	11	36 (0.8)	75 (1.8)	49 (2)	$2 \times 10^5$	multiple, extended, round, weak
Bolo 38	1.54 (0.03)	2.39 (0.06)	3.33 (0.08)	3.33 (0.08)	8.0 (0.2)	87	47 (0.2)	63 (0.2)	56 (1)	$2 \times 10^6$	multiple, extended, elongated
Bolo 39	0.29 (0.03)	0.59 (0.06)	...	0.59 (0.06)	1.4 (0.14)	15	42 (0.7)	76 (1.2)	-32 (2)	$2 \times 10^5$	multiple, extended, round
Bolo 40	0.96 (0.02)	...	...	1.40 (0.03)	3.39 (0.08)	48	54 (0.2)	63 (0.3)	-75 (2)	$5 \times 10^5$	multiple, extended, round
Bolo 41	0.24 (0.03)	0.37 (0.05)	...	0.37 (0.05)	0.9 (0.12)	13	44 (0.8)	63 (1.2)	57 (4)	$2 \times 10^5$	multiple, extended, elongated
Bolo 42	1.54 (0.03)	...	...	2.54 (0.04)	6.1 (0.10)	76	49 (0.1)	56 (0.2)	28 (2)	$2 \times 10^6$	multiple, extended, round
Bolo 43	2.76 (0.03)	4.46 (0.06)	...	4.46 (0.06)	10.8 (0.14)	150	47 (0.1)	62 (0.1)	59 (1)	$2 \times 10^6$	multiple, extended, elongated
Bolo 44	0.39 (0.03)	0.72 (0.06)	...	0.72 (0.06)	1.7 (0.14)	19	45 (0.5)	78 (0.9)	-67 (2)	$3 \times 10^5$	multiple, extended, elongated
Bolo 45	0.68 (0.03)	1.35 (0.06)	...	1.35 (0.06)	3.3 (0.14)	32	55 (0.4)	71 (0.5)	2 (2)	$4 \times 10^5$	multiple, extended, elongated
Bolo 46	1.12 (0.03)	2.62 (0.06)	...	2.62 (0.06)	6.3 (0.14)	52	68 (0.2)	77 (0.3)	41 (2)	$4 \times 10^5$	multiple, extended, elongated

Table 2.2 (cont'd)

ID	Flux(40'') (Jy)	Flux(80'') (Jy)	Flux(120'') (Jy)	Total Flux (Jy)	Mass (10K) ( $M_{\odot}$ )	Peak $A_V$ (mag)	FWHM (minor, '')	FWHM (major, '')	PA ( $^{\circ}$ )	$\langle n \rangle$ ( $\text{cm}^{-3}$ )	Morphology <sup>1</sup>
Bolo 47	0.93 (0.02)	2.08 (0.05)	...	2.81 (0.06)	6.8 (0.15)	43	72 (0.3)	85 (0.3)	12 (2)	$3 \times 10^5$	multiple, extended, elongated
Bolo 48	6.06 (0.03)	9.83 (0.06)	...	10.59 (0.06)	25.6 (0.15)	370	39 (0.0)	56 (0.0)	-48 (1)	$1 \times 10^7$	multiple, extended, round
Bolo 49	1.13 (0.03)	1.98 (0.06)	...	1.98 (0.06)	4.8 (0.13)	59	52 (0.2)	58 (0.2)	-49 (3)	$1 \times 10^6$	multiple, extended, elongated
Bolo 50	0.45 (0.03)	0.96 (0.05)	...	1.31 (0.07)	3.2 (0.16)	22	68 (0.5)	84 (0.6)	-39 (3)	$2 \times 10^5$	multiple, extended, elongated
Bolo 51	0.52 (0.03)	...	...	0.62 (0.03)	1.49 (0.08)	30	41 (0.3)	58 (0.5)	-51 (2)	$5 \times 10^5$	multiple, extended, round
Bolo 52	0.31 (0.02)	0.55 (0.05)	...	0.79 (0.07)	1.9 (0.16)	19	44 (0.5)	103 (1.3)	89 (1)	$2 \times 10^5$	multiple, extended, elongated
Bolo 53	0.46 (0.03)	0.92 (0.05)	...	1.37 (0.07)	3.3 (0.17)	24	61 (0.5)	94 (0.7)	13 (1)	$2 \times 10^5$	multiple, extended, elongated
Bolo 54	0.45 (0.03)	0.90 (0.05)	...	1.24 (0.07)	3.0 (0.17)	23	47 (0.4)	81 (0.7)	72 (1)	$4 \times 10^5$	multiple, extended, elongated
Bolo 55	0.29 (0.02)	...	...	0.37 (0.03)	0.89 (0.07)	13	46 (0.6)	59 (0.8)	39 (4)	$2 \times 10^5$	multiple, extended, elongated
Bolo 56	0.15 (0.02)	0.32 (0.04)	0.50 (0.06)	0.59 (0.07)	1.4 (0.16)	7	78 (1.4)	104 (1.9)	76 (5)	$4 \times 10^4$	extended, round, weak
Bolo 57	0.30 (0.02)	0.51 (0.04)	...	0.51 (0.04)	1.2 (0.10)	16	42 (0.6)	56 (0.7)	-80 (4)	$4 \times 10^5$	multiple, extended, round
Bolo 58	0.26 (0.02)	...	...	0.33 (0.03)	0.78 (0.08)	19	39 (0.7)	45 (0.8)	-47 (10)	$6 \times 10^5$	multiple, extended, elongated
Bolo 59	0.30 (0.02)	0.52 (0.04)	...	0.52 (0.04)	1.24 (0.09)	18	46 (0.5)	56 (0.6)	50 (5)	$3 \times 10^5$	multiple, extended, elongated
Bolo 60	0.16 (0.02)	0.28 (0.04)	0.37 (0.06)	0.37 (0.06)	0.9 (0.14)	9	44 (1.0)	76 (1.7)	-37 (3)	$1 \times 10^5$	extended, round, weak
Bolo 61	0.12 (0.02)	0.22 (0.05)	0.37 (0.07)	0.37 (0.07)	0.9 (0.17)	8	58 (1.7)	104 (3)	50 (4)	$5 \times 10^4$	multiple, round, weak
Bolo 62	0.27 (0.02)	0.53 (0.05)	0.80 (0.07)	0.80 (0.07)	1.9 (0.17)	14	65 (0.9)	80 (1.1)	-38 (6)	$1 \times 10^5$	multiple, extended, elongated
Bolo 63	0.21 (0.02)	0.44 (0.04)	0.67 (0.06)	0.67 (0.06)	1.6 (0.13)	10	82 (1.0)	89 (1.1)	-12 (12)	$6 \times 10^4$	extended, elongated
Bolo 64	0.11 (0.02)	0.17 (0.04)	...	0.20 (0.05)	0.5 (0.12)	6	37 (1.2)	82 (3)	53 (3)	$1 \times 10^5$	extended, round, weak
Bolo 65	0.67 (0.02)	...	...	0.76 (0.03)	1.84 (0.07)	37	41 (0.3)	48 (0.3)	4 (4)	$1 \times 10^6$	multiple, extended, elongated
Bolo 66	1.32 (0.02)	1.83 (0.04)	2.31 (0.06)	2.31 (0.06)	5.6 (0.15)	76	41 (0.1)	44 (0.1)	-32 (4)	$4 \times 10^6$	extended, round
Bolo 67	0.23 (0.03)	0.45 (0.05)	0.70 (0.07)	0.86 (0.10)	2.1 (0.2)	12	47 (0.7)	125 (1.8)	37 (1)	$1 \times 10^5$	extended, round
Bolo 68	0.15 (0.02)	0.29 (0.05)	...	0.36 (0.07)	0.9 (0.16)	8	43 (1.0)	95 (2)	56 (2)	$9 \times 10^4$	extended, round, weak
Bolo 69	0.17 (0.02)	0.42 (0.04)	0.82 (0.07)	1.28 (0.09)	3.1 (0.2)	11	109 (1.3)	128 (1.6)	59 (6)	$4 \times 10^4$	multiple, extended, round

Table 2.2 (cont'd)

ID	Flux(40'')	Flux(80'')	Flux(120'')	Total Flux	Mass (10K)	Peak $A_V$	FWHM	FWHM	PA	$\langle n \rangle$	Morphology <sup>1</sup>
	(Jy)	(Jy)	(Jy)	(Jy)	( $M_\odot$ )	(mag)	(minor, '')	(major, '')	( $^\circ$ )	( $\text{cm}^{-3}$ )	
Bolo 70	0.35 (0.02)	0.85 (0.05)	1.59 (0.07)	1.96 (0.08)	4.7 (0.2)	17	94 (0.7)	112 (0.8)	-63 (4)	$9 \times 10^4$	multiple, extended, elongated
Bolo 71	0.28 (0.03)	0.69 (0.05)	...	1.15 (0.07)	2.8 (0.18)	13	79 (0.8)	102 (1.1)	61 (3)	$9 \times 10^4$	multiple, extended, elongated
Bolo 72	0.34 (0.03)	0.78 (0.06)	...	0.93 (0.06)	2.2 (0.15)	17	59 (0.7)	84 (1.0)	38 (3)	$2 \times 10^5$	multiple, extended, elongated
Bolo 73	0.23 (0.02)	0.53 (0.04)	0.93 (0.07)	1.11 (0.08)	2.7 (0.18)	13	87 (1.0)	114 (1.3)	-79 (3)	$6 \times 10^4$	multiple, extended, elongated
Bolo 74	0.38 (0.03)	...	...	0.38 (0.03)	0.91 (0.07)	18	51 (0.6)	60 (0.7)	52 (6)	$2 \times 10^5$	multiple, extended, elongated
Bolo 75	0.38 (0.03)	...	...	0.38 (0.03)	0.91 (0.07)	18	51 (0.6)	61 (0.7)	-54 (6)	$2 \times 10^5$	multiple, extended, elongated
Bolo 76	0.16 (0.02)	0.32 (0.04)	...	0.43 (0.05)	1.0 (0.13)	8	64 (1.2)	89 (1.7)	89 (5)	$6 \times 10^4$	multiple, extended, round, weak
Bolo 77	0.13 (0.03)	0.24 (0.05)	0.38 (0.08)	0.38 (0.08)	0.9 (0.18)	8	72 (2)	97 (3)	-62 (8)	$4 \times 10^4$	multiple, round, weak
Bolo 78	0.36 (0.02)	0.72 (0.04)	...	0.93 (0.05)	2.3 (0.13)	19	65 (0.6)	77 (0.7)	-78 (4)	$2 \times 10^5$	multiple, extended, round
Bolo 79	0.98 (0.03)	...	...	1.84 (0.04)	4.4 (0.11)	43	59 (0.2)	64 (0.3)	4 (4)	$6 \times 10^5$	multiple, extended, round
Bolo 80	1.36 (0.03)	2.26 (0.06)	...	3.08 (0.08)	7.4 (0.18)	77	57 (0.2)	76 (0.3)	-62 (1)	$7 \times 10^5$	multiple, extended, elongated
Bolo 81	1.62 (0.03)	...	...	2.61 (0.05)	6.3 (0.12)	86	53 (0.2)	59 (0.2)	-26 (2)	$1 \times 10^6$	multiple, extended, round
Bolo 82	0.20 (0.02)	...	...	0.36 (0.04)	0.88 (0.09)	10	54 (1.0)	62 (1.2)	-4 (11)	$1 \times 10^5$	multiple, extended, round
Bolo 83	0.21 (0.02)	0.47 (0.05)	...	0.47 (0.05)	1.1 (0.11)	12	60 (1.0)	74 (1.2)	75 (6)	$1 \times 10^5$	multiple, extended, round
Bolo 84	0.25 (0.03)	...	...	0.47 (0.05)	1.1 (0.12)	13	61 (0.9)	68 (1.0)	21 (11)	$1 \times 10^5$	multiple, extended, round
Bolo 85	0.19 (0.02)	0.40 (0.05)	...	0.40 (0.05)	1.0 (0.11)	11	54 (1.0)	77 (1.4)	72 (4)	$1 \times 10^5$	multiple, extended, round
Bolo 86	0.13 (0.02)	0.27 (0.05)	0.43 (0.07)	0.64 (0.10)	1.5 (0.2)	9	80 (1.7)	132 (3)	-39 (3)	$3 \times 10^4$	extended, round, weak
Bolo 87	0.13 (0.02)	0.25 (0.04)	0.41 (0.06)	0.45 (0.07)	1.1 (0.16)	7	68 (1.5)	101 (2)	70 (4)	$4 \times 10^4$	extended, round, weak
Bolo 88	0.21 (0.02)	0.52 (0.04)	0.97 (0.07)	1.43 (0.09)	3.4 (0.2)	11	94 (1.0)	152 (1.6)	-39 (2)	$4 \times 10^4$	extended, elongated
Bolo 89	0.19 (0.02)	0.44 (0.04)	0.74 (0.06)	0.99 (0.08)	2.4 (0.2)	11	81 (1.0)	126 (1.6)	-17 (2)	$5 \times 10^4$	extended, round
Bolo 90	...	...	...	0.126 (0.015)	0.31 (0.04)	10	22 (0.9)	33 (1.2)	-90 (8)	...	extended, round
Bolo 91	0.14 (0.02)	0.24 (0.04)	0.35 (0.06)	0.37 (0.07)	0.9 (0.17)	8	58 (1.5)	105 (3)	-79 (3)	$4 \times 10^4$	extended, round, weak
Bolo 92	0.13 (0.02)	0.24 (0.04)	...	0.24 (0.04)	0.57 (0.09)	7	54 (1.4)	67 (1.7)	56 (10)	$8 \times 10^4$	multiple, extended, round, weak

Table 2.2 (cont'd)

ID	Flux(40'') (Jy)	Flux(80'') (Jy)	Flux(120'') (Jy)	Total Flux (Jy)	Mass (10K) ( $M_{\odot}$ )	Peak Av (mag)	FWHM (minor, '')	FWHM (major, '')	PA ( $^{\circ}$ )	( $n$ ) ( $\text{cm}^{-3}$ )	Morphology <sup>1</sup>
Bolo 93	0.17 (0.02)	0.38 (0.04)	0.66 (0.06)	0.89 (0.08)	2.2 (0.2)	8	92 (1.4)	111 (1.7)	33 (6)	$4 \times 10^4$	extended, round, weak
Bolo 94	0.16 (0.02)	0.32 (0.04)	...	0.32 (0.04)	0.77 (0.09)	9	57 (1.2)	67 (1.3)	66 (10)	$9 \times 10^4$	multiple, extended, round
Bolo 95	0.14 (0.02)	0.28 (0.04)	0.51 (0.06)	0.77 (0.08)	1.9 (0.18)	8	93 (1.4)	116 (1.8)	27 (6)	$3 \times 10^4$	extended, round, weak
Bolo 96	0.22 (0.02)	...	...	0.46 (0.04)	1.1 (0.09)	10	59 (0.8)	70 (1.0)	8 (6)	$1 \times 10^5$	multiple, extended, round
Bolo 97	0.22 (0.02)	...	...	0.35 (0.03)	0.85 (0.08)	11	60 (0.9)	66 (1.0)	-40 (15)	$1 \times 10^5$	multiple, extended, round, weak
Bolo 98	0.20 (0.02)	...	...	0.32 (0.04)	0.77 (0.09)	9	59 (1.0)	64 (1.1)	89 (16)	$9 \times 10^4$	multiple, extended, round, weak
Bolo 99	0.24 (0.02)	...	...	0.43 (0.03)	1.04 (0.07)	12	53 (0.6)	61 (0.7)	75 (6)	$2 \times 10^5$	multiple, extended, round
Bolo 100	0.41 (0.02)	...	...	0.81 (0.03)	1.95 (0.08)	18	59 (0.4)	67 (0.5)	-7 (5)	$2 \times 10^5$	multiple, extended, round
Bolo 101	0.21 (0.03)	...	...	0.35 (0.04)	0.8 (0.10)	10	48 (0.9)	66 (1.3)	49 (5)	$1 \times 10^5$	multiple, extended, round, weak
Bolo 102	0.63 (0.02)	1.41 (0.04)	...	1.41 (0.04)	3.4 (0.11)	31	62 (0.3)	76 (0.4)	7 (2)	$3 \times 10^5$	multiple, extended, round
Bolo 103	1.28 (0.03)	2.07 (0.05)	...	2.42 (0.06)	5.8 (0.15)	70	46 (0.2)	57 (0.2)	49 (1)	$2 \times 10^6$	multiple, extended, elongated
Bolo 104	1.05 (0.02)	...	...	1.42 (0.03)	3.43 (0.08)	55	46 (0.2)	55 (0.2)	77 (2)	$1 \times 10^6$	multiple, extended, round
Bolo 105	0.40 (0.02)	...	...	0.61 (0.03)	1.47 (0.08)	20	51 (0.4)	64 (0.5)	-7 (3)	$2 \times 10^5$	multiple, extended, elongated
Bolo 106	...	...	...	0.50 (0.02)	1.21 (0.04)	30	52 (0.4)	55 (0.4)	-87 (10)	$3 \times 10^5$	multiple, extended, round
Bolo 107	...	...	...	0.48 (0.02)	1.17 (0.04)	27	53 (0.3)	60 (0.4)	-76 (4)	$2 \times 10^5$	multiple, extended, round
Bolo 108	0.18 (0.02)	...	...	0.32 (0.04)	0.78 (0.09)	10	53 (0.9)	72 (1.2)	-59 (5)	$9 \times 10^4$	multiple, extended, round, weak
Bolo 109	0.16 (0.02)	0.33 (0.05)	...	0.39 (0.05)	0.9 (0.13)	9	50 (1.1)	80 (1.8)	61 (4)	$1 \times 10^5$	multiple, extended, round, weak
Bolo 110	0.44 (0.03)	...	...	0.44 (0.03)	1.05 (0.06)	18	53 (0.5)	59 (0.5)	89 (7)	$2 \times 10^5$	multiple, extended, elongated
Bolo 111	0.22 (0.02)	0.47 (0.04)	0.71 (0.07)	0.83 (0.08)	2.0 (0.19)	12	71 (1.0)	101 (1.5)	-45 (3)	$8 \times 10^4$	multiple, extended, round
Bolo 112	0.17 (0.02)	0.33 (0.04)	...	0.45 (0.06)	1.1 (0.14)	9	60 (1.3)	65 (1.3)	-70 (20)	$1 \times 10^5$	multiple, extended, round, weak
Bolo 113	0.18 (0.02)	0.35 (0.05)	0.56 (0.07)	0.74 (0.09)	1.8 (0.2)	9	75 (1.3)	112 (2)	9 (3)	$5 \times 10^4$	multiple, extended, round, weak
Bolo 114	0.18 (0.02)	0.38 (0.04)	...	0.55 (0.05)	1.3 (0.13)	10	59 (1.0)	88 (1.4)	-53 (3)	$9 \times 10^4$	multiple, extended, elongated
Bolo 115	0.22 (0.02)	0.37 (0.05)	0.53 (0.07)	0.54 (0.08)	1.3 (0.19)	12	45 (0.8)	96 (1.8)	-39 (2)	$1 \times 10^5$	extended, elongated

Table 2.2 (cont'd)

ID	Flux(40'') (Jy)	Flux(80'') (Jy)	Flux(120'') (Jy)	Total Flux (Jy)	Mass (10K) ( $M_{\odot}$ )	Peak $A_V$ (mag)	FWHM (minor, '')	FWHM (major, '')	PA ( $^{\circ}$ )	$\langle n \rangle$ ( $\text{cm}^{-3}$ )	Morphology <sup>1</sup>
Bolo 116	0.39 (0.02)	0.51 (0.05)	...	0.51 (0.05)	1.2 (0.12)	20	35 (0.5)	47 (0.6)	46 (4)	$1 \times 10^6$	multiple, extended, round
Bolo 117	0.22 (0.02)	0.40 (0.05)	...	0.40 (0.05)	1.0 (0.11)	11	44 (0.8)	70 (1.3)	76 (3)	$2 \times 10^5$	multiple, extended, round, weak
Bolo 118	0.14 (0.02)	0.29 (0.05)	...	0.34 (0.05)	0.8 (0.12)	8	47 (1.1)	88 (2)	4 (3)	$9 \times 10^4$	multiple, extended, round, weak
Bolo 119	0.24 (0.02)	0.53 (0.04)	0.91 (0.06)	1.29 (0.09)	3.1 (0.2)	13	92 (1.0)	123 (1.4)	-89 (3)	$5 \times 10^4$	extended, elongated
Bolo 120	...	...	...	0.08 (0.01)	0.19 (0.02)	6	24 (0.9)	25 (1.0)	-3 (90)	...	multiple, extended, round, weak
Bolo 121	0.18 (0.02)	0.44 (0.04)	...	0.65 (0.05)	1.6 (0.12)	10	85 (1.1)	94 (1.2)	-86 (11)	$5 \times 10^4$	multiple, extended, elongated
Bolo 122	0.38 (0.02)	0.88 (0.04)	...	1.34 (0.06)	3.2 (0.15)	19	63 (0.5)	91 (0.7)	-63 (2)	$2 \times 10^5$	multiple, extended, elongated

Note. — No integrated flux density is given if the distance to the nearest neighboring source is smaller than the aperture diameter. Masses are calculated according to equation (2.3) from the total flux density assuming a single dust temperature of  $T_D = 10\text{K}$  and a dust opacity at  $1.1\text{mm}$  of  $\kappa_{1.1\text{mm}} = 0.0114 \text{ cm}^2 \text{ g}^{-1}$ . Peak  $A_V$  is calculated from the peak flux density as in §2.4.2. FWHM and PAs are from a Gaussian fit; the PA is measured in degrees east of north of the major axis.  $\langle n \rangle$  is the mean particle density as calculated from the total mass and the deconvolved average FWHM size. Numbers in parentheses are  $1\sigma$  uncertainties. Uncertainties for masses are from photometry only, and do not include uncertainties from  $\kappa$ ,  $T_D$ , or  $d$ , which can be up to a factor of a few or more. Uncertainties for the FWHM and PA are formal fitting errors from the elliptical Gaussian fit; additional uncertainties of 10% – 15% apply to the FWHM, and  $\sim 5^{\circ}$  to the PA (determined from simulations).

<sup>1</sup>The morphology keyword(s) given indicates whether the source is multiple (within  $3'$  of another source), extended (major axis FW at  $2\sigma > 1'$ ), elongated (axis ratio at  $4\sigma > 1.2$ ), round (axis ratio at  $4\sigma < 1.2$ ), or weak (peak flux densities less than 5 times the RMS/pixel in the unfiltered map).

The distribution of source flux densities is shown in figure 2.11. In addition to peak flux densities ( $\text{Jy beam}^{-1}$ ) and total flux densities ( $\text{Jy}$ ) from aperture photometry of Peak-find sources, Clumpfind  $3\sigma$  flux densities ( $\text{Jy}$ ) are also shown. Clumpfind flux densities are calculated from the source map generated by Clumpfind as the sum over all pixels (above  $3\sigma$ ) assigned to a given source, divided by the beam area. We find empirically that Clumpfind is good at separating, and calculating a reasonable flux density for, bright, crowded sources. It is not, however, very effective at determining the total flux density of isolated faint or extended sources. For example, faint sources will have a smaller total flux density than for aperture photometry because Clumpfind only includes pixels above  $3\sigma$ .

The large average size of sources accounts for the fact that the mean total flux density ( $0.96 \pm 1.21 \text{ Jy}$ ; hereafter, numbers quoted are mean  $\pm$  dispersion in the sample, *not* mean  $\pm$  error in the mean) is significantly larger than the mean peak flux density ( $0.35 \pm 0.56 \text{ Jy beam}^{-1}$ ). Clumpfind sources tend to have slightly larger  $3\sigma$  flux densities ( $1.13 \pm 1.80 \text{ Jy}$ ), in part because bright, crowded sources may be integrated over a larger area than with aperture photometry, and in part because one Clumpfind source sometimes encompasses more than one Peak-find source.

Figure 2.12 gives the distribution of major and minor FWHM sizes, as well as the full-width at  $3\sigma$  (FW $3\sigma$ ) sizes of Clumpfind sources, defined as  $\text{FW}3\sigma = 2\sqrt{N_{pix}A_{pix}/\pi}$ , where  $N_{pix}$  is the total number of pixels assigned to a source and  $A_{pix}$  is the pixel area. The average minor axis FWHM is  $58'' \pm 17''$ , the average major axis FWHM is  $80'' \pm 27''$ , and the average mean FWHM is  $68'' \pm 20''$ . Clumpfind sources have a large average FW $3\sigma$  of  $77'' \pm 30''$ , as expected given that the size is measured at  $3\sigma$  rather than at half-max. There are very few sources near the resolution limit of  $31''$ . Most sources are somewhat elongated as well as extended; the average axis ratio is 1.4, and the distribution (figure 2.13) extends to large axis ratios  $> 2$ . Note, however, that measured axis ratios  $< 1.2$  are found to be unreliable based on simulations, and should be considered indistinguishable from an axis ratio of unity.

The total mass  $M$  of gas and dust in a core is proportional to the total flux density  $S_\nu$ , assuming the dust emission at 1.1 mm is optically thin and both the dust

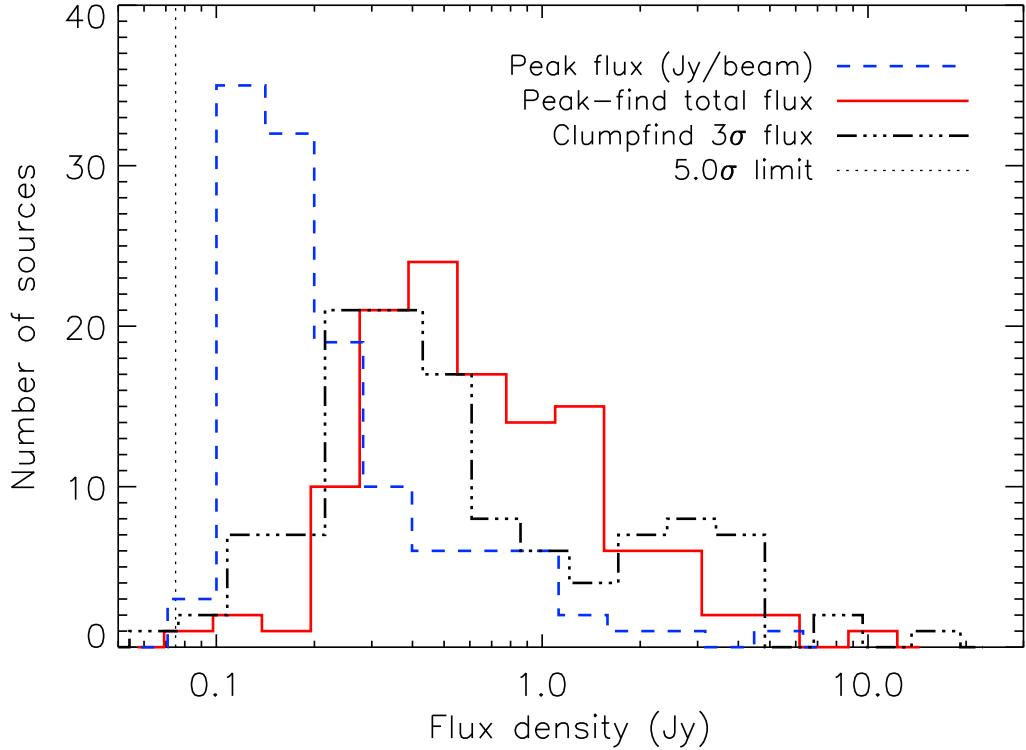


Figure 2.11 Distribution of source peak flux densities (dashed line,  $\text{mJy beam}^{-1}$ ) and total flux densities (solid line, Jy) from aperture photometry. Clumpfind  $3\sigma$  flux densities are also shown for comparison (dash-dot line, Jy). The vertical dotted line is the  $5\sigma$  peak detection limit. The peak flux density distribution has a mean of  $0.35 \text{ Jy beam}^{-1}$  and dispersion of  $0.56 \text{ Jy beam}^{-1}$  ( $0.35 \pm 0.56$ ), and the total flux density distribution a mean of  $0.96 \pm 1.21 \text{ Jy}$ . The mean flux from Clumpfind ( $1.13 \pm 1.80 \text{ Jy}$ ) is somewhat larger than that from aperture photometry.

temperature and opacity are independent of position within a core:

$$M = \frac{d^2 S_\nu}{B_\nu(T_D) \kappa_\nu}, \quad (2.3)$$

where  $\kappa_{1.1\text{mm}} = 0.0114 \text{ cm}^2 \text{ g}^{-1}$  is the dust opacity,  $d = 250 \text{ pc}$  is the distance, and  $T_D$  is the dust temperature. Although the millimeter emission arises only from the dust, we can infer the total mass of gas and dust by assuming a gas to dust mass ratio of 100, which is included in  $\kappa_{1.1\text{mm}}$ . For the masses in table 2.2, we assume a single dust temperature  $T_D = 10 \text{ K}$  for all sources. The uncertainties given are from

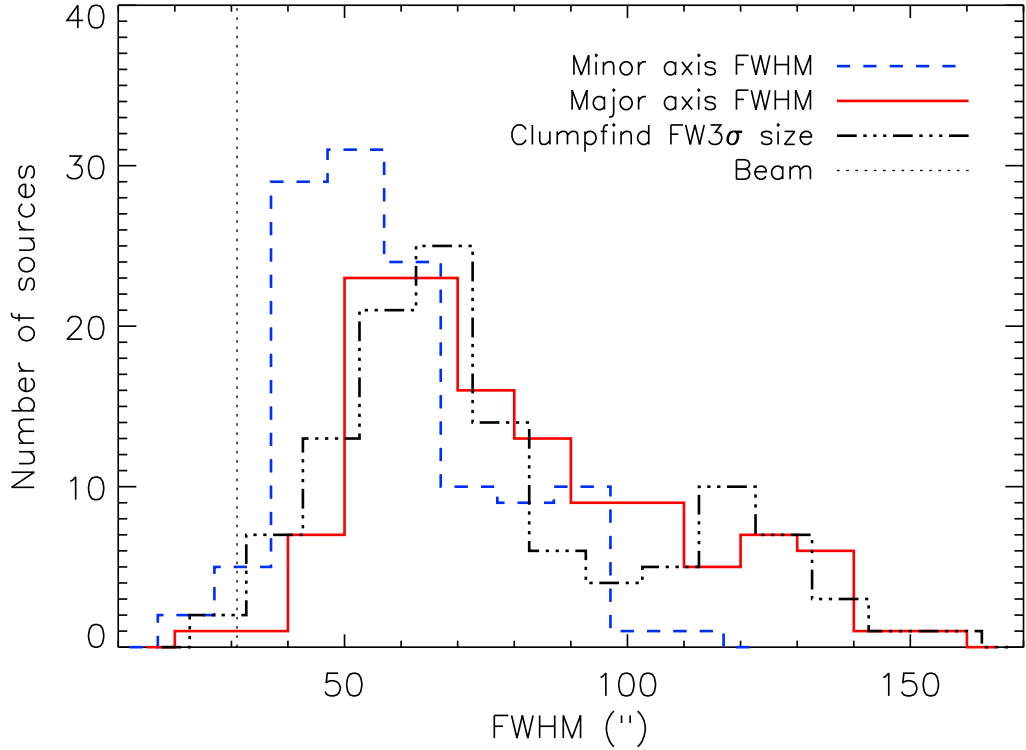


Figure 2.12 Distribution of minor axis (dashed line) and major axis (solid line) FWHM sizes, as determined from an elliptical Gaussian fit. The beam size is indicated by the dotted line. The mean minor axis FWHM is  $58'' \pm 17''$ , and the mean major axis FWHM is  $80'' \pm 27''$ . Full-width at  $3\sigma$  sizes for Clumpfind sources are also shown (dash-dot line), where  $(FW3\sigma = 2\sqrt{N_{pix}A_{pix}/\pi})$ . The mean size from Clumpfind ( $77'' \pm 30''$ ) is larger than the mean FWHM ( $68'' \pm 20''$ ), as expected because the Clumpfind size is measured at the  $3\sigma$  contour rather than at the half-max.

the uncertainty in the total flux density only. Other sources of error from  $\kappa$ ,  $T_D$ , and  $d$  (up to a factor of 4 or more) are discussed in §2.5.2.

For dense regions without internal heating, the mean temperature is about 10 K, warmer on the outside and colder on the inside (Evans et al., 2001). Centrally heated cores will be warmer on the inside, but much of the mass is located at low temperatures. Shirley et al. (2002) and (Young et al., 2003) found good agreement with masses of Class 0 and Class I sources determined from detailed models using  $T_D \sim 15$  K. Taking 10 K is a reasonable compromise to cover both prestellar and protostellar sources, but keep in mind that it will overestimate the masses of the latter by a factor

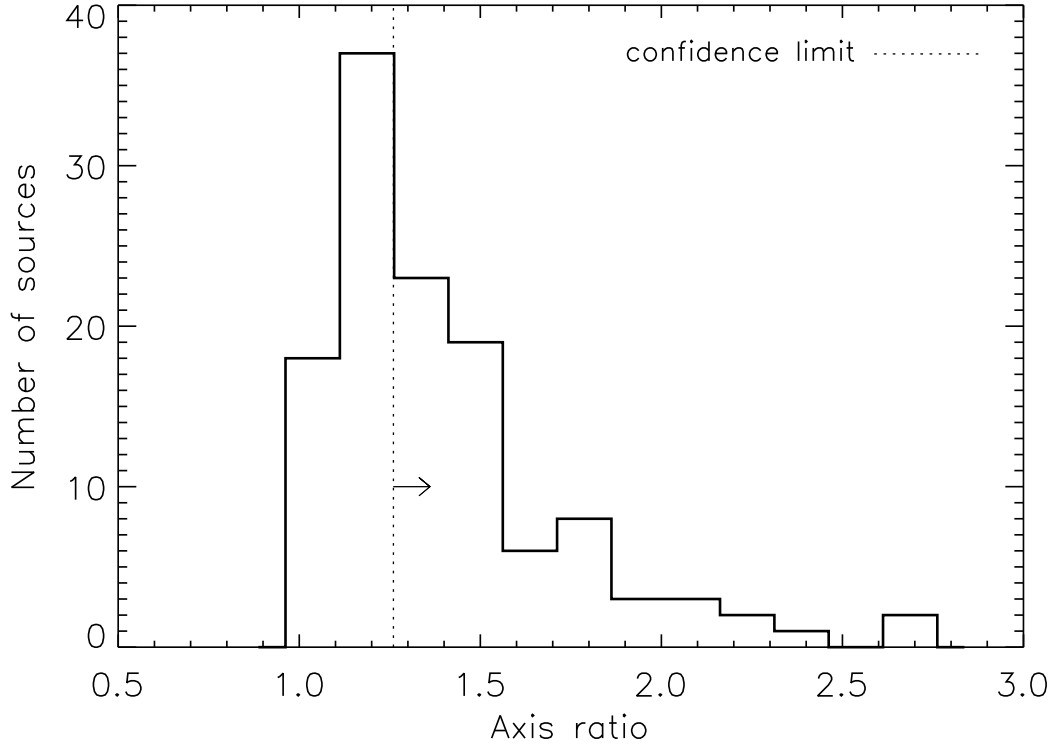


Figure 2.13 Distribution of source axis ratios. The mean axis ratio is 1.4, and the sample contains some very elongated sources with axis ratios  $\geq 2$ . We find that measured axis ratios  $< 1.2$  are unreliable based on Monte Carlo tests.

of 2 – 3.

The peak  $A_V$  in table 2.2 is calculated from the peak 1.1 mm flux density  $S_{peak}$  as in equation (2.2). The average peak  $A_V$  of the sample is 24.7 mag. The mean particle density for each source is estimated as  $\langle n \rangle = M/(4/3\pi R^3 \mu)$ , where  $M$  is the total mass,  $R$  is the mean deconvolved HWHM size, and  $\mu_p = 2.33$  is the mean molecular weight per particle. The average  $\langle n \rangle$  of the sample is  $4.3 \times 10^5 \text{ cm}^{-3}$ . The morphology keywords listed indicate if the source is multiple (within  $3'$  of another source), extended (major axis FW at  $2\sigma > 1'$ ), elongated (axis ratio at  $4\sigma > 1.2$ ), round (axis ratio at  $4\sigma < 1.2$ ), or weak (peak flux densities less than 5 times the rms per pixel in the unfiltered map). Monte Carlo simulations (§2.3.4) indicate that we cannot recover structures larger than  $\sim 200''$ , and we do not find any sources larger than  $\sim 120''$  in the real map. We do not resolve any source pairs closer than  $32''$ ,

close to the minimum separation of  $30''$  required by the peak finding algorithm.

## 2.5 Discussion

### 2.5.1 Completeness and the Mass versus Size Distribution

The distribution of total mass versus FWHM size is shown in figure 2.14. The solid line shows the expected mass detection limit for Gaussian sources assuming a simple scaling with source area. The Gaussian mass limit varies with source size ( $M_{lim} \propto \text{size}^2$ ) because our ability to detect sources is based on the peak flux density above the noise ( $5\sigma$ ), whereas the mass is calculated from the total flux density ( $S_\nu \propto \text{size}^2$ ). The real mass completeness limit is more complicated, even for Gaussian sources, due to our reduction and detection techniques. We also show, therefore, empirical mass detection limits as a function of size for 10%, 50%, and 90% completeness.

Completeness is determined by Monte-Carlo simulations, taking into account effects from cleaning, iterative mapping, and optimal filtering. Simulated sources of varying total mass and size are inserted into an empty region of the real map before cleaning and iterative mapping. The 10% completeness limit is the mass at which 10% of the simulated sources are detected in the optimally filtered map. Nearly all detected sources lie above the 10% completeness limit, as expected. Note that the completeness curve represent the true, not measured, mass and size of input simulated sources.

Typical measurement error bars in  $M$  and FWHM are shown for  $50''$  and  $100''$  FWHM sources near the detection limit. For these,  $\sigma_M$  are from the uncertainty in the integrated flux, and  $\sigma_{\text{FWHM}}$  are estimated from simulations. The maximum size of the pointing-smear beam is indicated by a shaded band. Using the optimally filtered map to detect sources tends to lower the mass limit for sources with  $\text{FWHM} > 30''$  because the peak is enhanced by the filter. Conversely, very large sources ( $> 100''$ ) tend to have a higher mass limit because they are not fully recovered by iterative mapping. Both effects are illustrated by the empirical 50% completeness curve, which

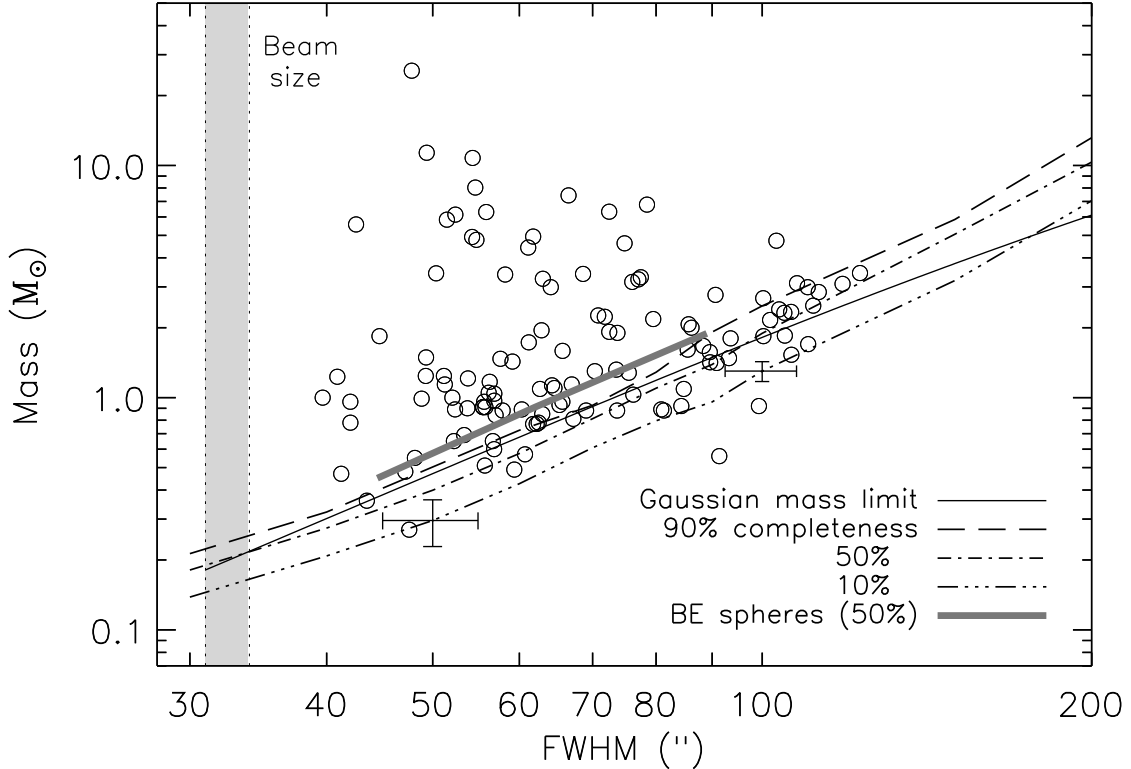


Figure 2.14 Total mass versus FWHM size for Peak-find sources. The solid line denotes the analytic mass detection limit as a function of size ( $M \propto R^2$ ) for Gaussian sources. Empirical 10%, 50%, and 90% completeness curves are also shown, derived using Monte Carlo with simulated sources and taking into account the effects of cleaning, iterative mapping, and optimal filtering. 50% completeness for Bonnor-Ebert spheres (thick shaded line) were similarly determined using BE models with  $n_c = (8 \times 10^4, 8 \times 10^4, 9.5 \times 10^4) \text{ cm}^{-3}$  and  $r_o = (8 \times 10^3, 1.5 \times 10^4, 3 \times 10^4) \text{ AU}$ . Representative error bars for 50'' and 100'' FWHM sources near the detection limit are shown, as estimated from the results of Monte Carlo simulations. Note the lack of sources near the resolution limit, which cannot be entirely be accounted for by pointing errors of  $\lesssim 7''$ , although the pointing-smear beam could be as large as 34'' (shaded region).

falls below the Gaussian 50% completeness line for  $\text{FWHM} \sim 40'' - 60''$ , and above for  $\text{FWHM} \gtrsim 100''$ .

There is an additional complication due to the fact that the sources may not be Gaussian in shape. Without knowing the true source structure this effect is difficult to quantify. We explore the effects of different source structures by running completeness

tests for sources with a Bonnor-Ebert (BE) sphere profile (Ebert, 1955; Bonnor, 1956), which has been found by several authors to be a good representation of the structure of some prestellar cores (Schnee & Goodman, 2005; Kirk, Ward-Thompson, & André, 2005; Evans et al., 2001; Ward-Thompson et al., 1994). The 50% completeness limits for BE spheres are indicated in figure 2.14 by a thick shaded line. FWHM sizes of BE spheres, measured with a Gaussian fit for consistency with other limits, are set by the chosen outer radius ( $r_o$ ) in the BE model. The total mass is determined by a combination of  $r_o$  and the central density  $n_c$ , and detection primarily by  $n_c$ . The BE sphere models used to calculate completeness have  $n_c = (8 \times 10^4, 8 \times 10^4, 9.5 \times 10^4) \text{ cm}^{-3}$ ,  $r_o = (8 \times 10^3, 1.5 \times 10^4, 3 \times 10^4) \text{ AU}$ , and  $M_{tot} = (0.45, 0.91, 1.89) M_{\odot}$ .

Figure 2.15 is similar to figure 2.14 except that the mass versus FW3 $\sigma$  size is plotted for both Peak-find and Clumpfind sources. For Peak-find sources, FW3 $\sigma$  is scaled from the FWHM assuming a Gaussian profile ( $\text{FW3}\sigma = \text{FWHM} \times \sqrt{\ln(S_{peak}/3\sigma)/\ln 2}$ ). Masses for the two are calculated slightly differently: the Peak-find mass is the total mass from aperture photometry, whereas the Clumpfind 3 $\sigma$  mass is from the integrated flux density within the 3 $\sigma$  contour. The total mass for Peak-find sources (circles) has not changed from figure 2.14, but the distribution of mass versus size looks very different because the FW3 $\sigma$  size tends to be larger than the FWHM for bright sources (by about a factor of 2, because the 3 $\sigma$  contour is well below the half-max), but smaller than the FWHM for faint sources. The apparent decrease in scatter is not real, but simply an effect of the size definition used. For faint sources the Clumpfind 3 $\sigma$  mass is smaller than the Peak-find aperture photometry mass, because Clumpfind only integrates down to 3 $\sigma$ , which corresponds to a small aperture for faint sources near the 5 $\sigma$  detection limit.

The appearance of the mass versus size distribution depends very strongly on the definitions of both size and total mass, as illustrated by figures 2.14 and 2.15, making comparisons between plots calculated in different ways quite deceptive. For example, the 3 $\sigma$  mass versus 3 $\sigma$  size distribution for Clumpfind sources in figure 2.15 (crosses) is very similar to that in Ophiuchus from Johnstone et al. (2000), but comparing the Ophiuchus plot to the Peak-find total mass versus FWHM size would make the two

distributions seem very different.

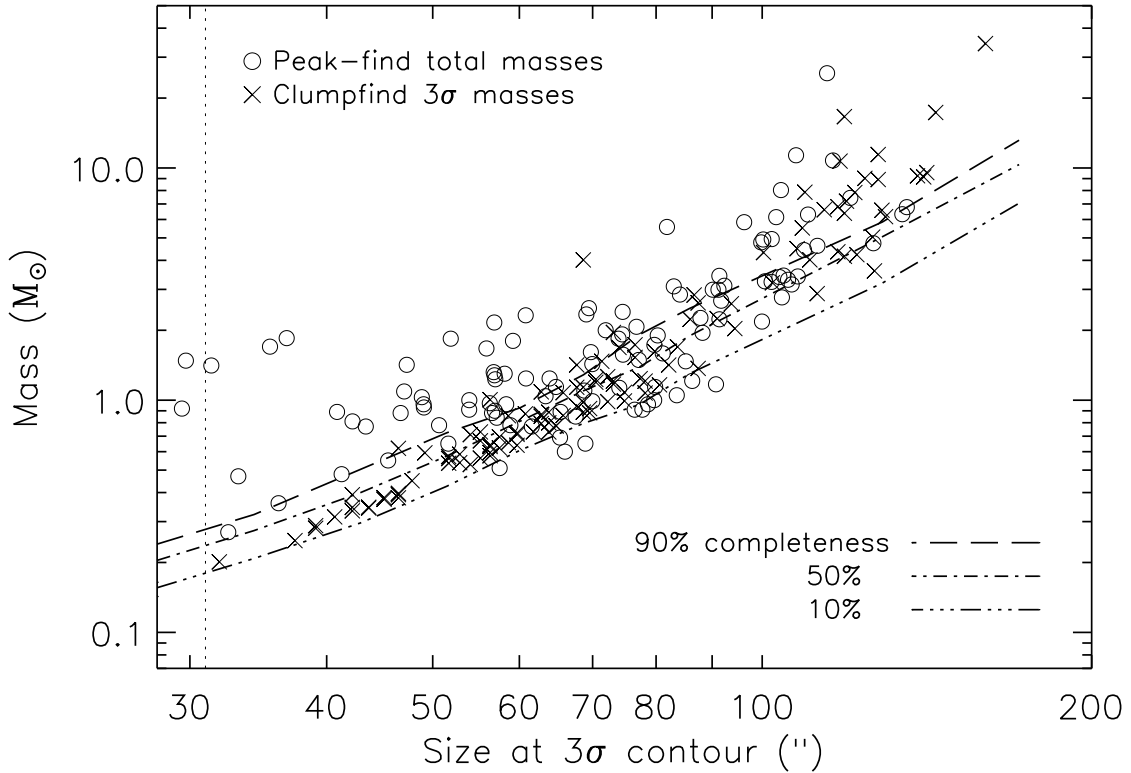


Figure 2.15 Total mass versus FW $3\sigma$  size for Peak-find and Clumpfind sources. The difference in the two distributions lies in the total flux calculation: aperture photometry for Peak-find, and integrating over the  $> 3\sigma$  pixels for Clumpfind. Sizes for Peak-find sources are computed by scaling the FWHM to the  $3\sigma$  contour ( $\text{FW}3\sigma = \text{FWHM} \times \sqrt{\ln(S_{\nu, \text{peak}}/3\sigma)/\ln 2}$ ), assuming the source is Gaussian. The Clumpfind size is based on the total pixel area above the  $3\sigma$  contour ( $\text{FW}3\sigma = 2\sqrt{N_{\text{pix}}A_{\text{pix}}/\pi}$ ). Completeness curves are as in figure 2.14, scaled to the  $3\sigma$  size. The smaller apparent scatter compared to figure 2.14 is not real, but rather a consequence of the different size definitions used.

We find it significant that there seem to be very few point sources in Perseus at 1.1 mm. This is most clearly illustrated in figure 2.14, which demonstrates an obvious paucity of both faint and bright sources between  $\text{FWHM} \sim 30''$  and  $50''$  (although there are low mass, compact sources in figure 2.15, these are artificially created by the  $3\sigma$  cutoff). Given that the pointing-smear beam is no larger than  $34''$  (for pointing errors  $\lesssim 7''$ ) and the average FWHM is more than twice the beam

size (68'' versus 31''), the majority of sources are significantly extended. In fact, the average deconvolved size is  $61'' = 1.5 \times 10^4$  AU. This mean size is inconsistent with descriptions of cores as truncated spheres, which have been used to model very low mass cores. A truncated power law model for an  $0.3 M_{\odot}$  core requires an outer radius of  $2 \times 10^3$  AU (Young & Evans, 2005), which would be a point source at the resolution of Bolocam. Our mass limit is  $0.18 M_{\odot}$  for a point source at  $T_D = 10$  K, so we should be sensitive to such compact, low mass cores if they are present in Perseus.

## 2.5.2 The 1.1 mm Mass Function

The differential mass function  $dN/dM$  for all 122 1.1 mm sources is shown in figure 2.16. The average mass of the sample is  $\langle M \rangle = 2.3 M_{\odot}$ , with individual masses ranging from 0.2 to  $26 M_{\odot}$ . A dust opacity of  $\kappa_{1.1mm} = 0.0114 \text{ cm}^2 \text{ g}^{-1}$  (OH5), temperature of  $T_D = 10$  K, and distance of  $d = 250$  pc are assumed for all masses. Error bars are  $\sqrt{N}$  statistical errors, and are meant to demonstrate the typical uncertainties from photometry, but do not include errors due to uncertainties in the distance or dust properties. Completeness becomes important around  $0.2 M_{\odot}$  (50% completeness) for point sources, and around  $0.8 M_{\odot}$  for sources with a FWHM of  $\sim 70''$ , the average FWHM of the sample. The mass distribution is not corrected for incompleteness, therefore the turnover below  $\sim 0.8 M_{\odot}$  may not be real.

The best fit to the mass function is a broken power law

$$\frac{dN}{dM} \propto M^{-\alpha}, \quad (2.4)$$

with  $\alpha_1 = 1.3 \pm 0.3$  ( $0.8 M_{\odot} < M < 2.5 M_{\odot}$ ) and  $\alpha_2 = 2.6 \pm 0.3$  ( $M > 2.5 M_{\odot}$ ). This result has a reduced chi-squared of  $\tilde{\chi}^2 = 0.4$  and is true for any break mass between  $2 M_{\odot}$  and  $3 M_{\odot}$ . The best fit broken power law is shown in figure 2.16. The best fit single power law ( $\alpha = 2.1 \pm 0.1$ ,  $M > 0.8 M_{\odot}$ ) is also shown ( $\tilde{\chi}^2 = 0.8$ ).

Johnstone et al. (2000) report  $\alpha_1 = 1.5$  ( $M \lesssim 1 M_{\odot}$ ) and  $\alpha_2 = 2.5$  ( $M \gtrsim 1 M_{\odot}$ ) for 850  $\mu\text{m}$  sources in the central 700 arcmin<sup>2</sup> of Ophiuchus assuming a single dust temperature of 20 K and using Clumpfind photometry. The Ophiuchus slopes are very

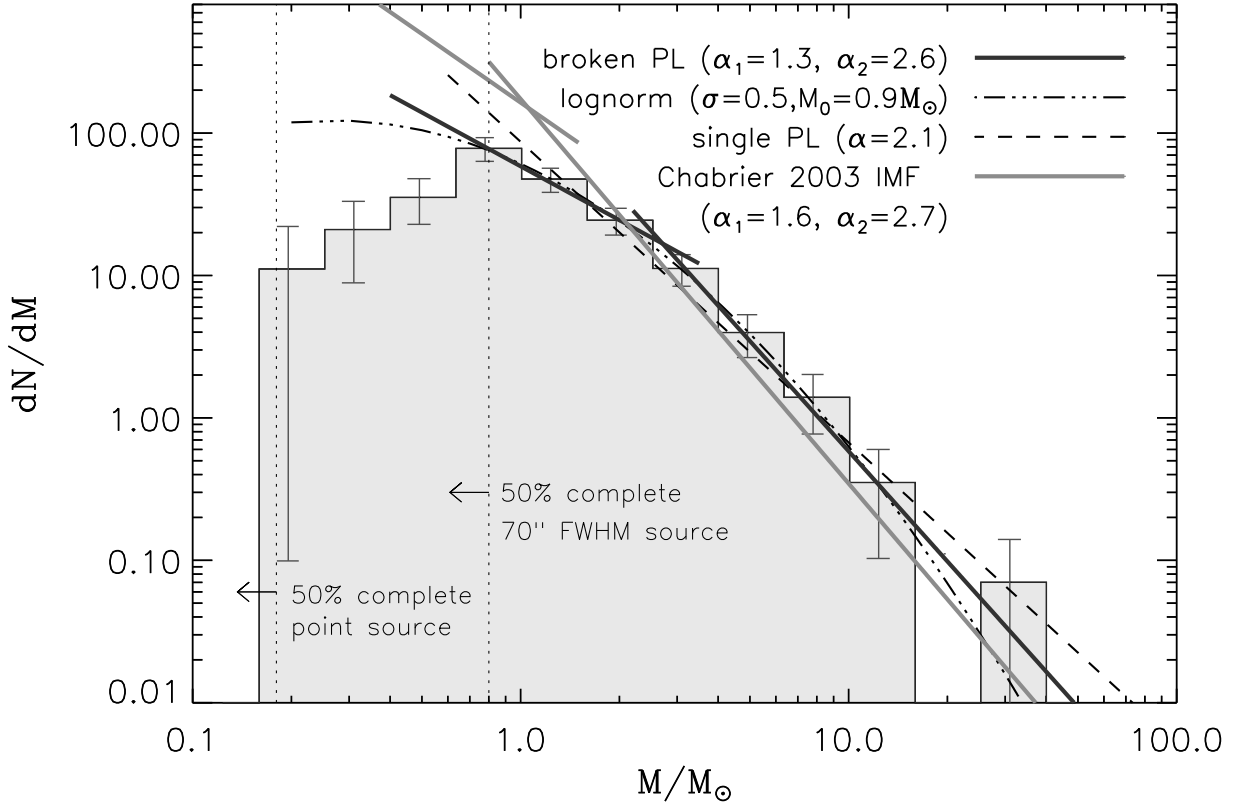


Figure 2.16 Differential mass distribution  $dN/dM$  for masses calculated from aperture photometry and a single dust temperature  $T_D = 10$  K. The 50% completeness limit is  $0.18 M_\odot$  ( $T_D = 10$  K) for a point source, and  $0.8 M_\odot$  for a  $70''$  FWHM source, the average size of the sample. Assuming a broken power law of the form  $N(M) \propto M^{-\alpha}$ , the best fit slopes are  $\alpha_1 = 1.3 \pm 0.3$  ( $0.5 M_\odot < M < 2.5 M_\odot$ ) and  $\alpha_2 = 2.6 \pm 0.3$  ( $M > 2.5 M_\odot$ ). The slope, but not the break mass, is very similar to the local IMF:  $\alpha_1 = 1.6$  ( $M < 1 M_\odot$ ),  $\alpha_2 = 2.7$  ( $M > 1 M_\odot$ ) (Chabrier, 2003). The data for  $M > 0.8 M_\odot$ , where the distribution is not affected by completeness, are also well fitted by a lognormal with  $\sigma = 0.5 \pm 0.1$ ,  $M_0 = 0.9 \pm 0.4 M_\odot$ . The best fit single power law is  $\alpha = 2.1 \pm 0.1$  for  $M > 0.5 M_\odot$ . For comparison,  $850 \mu\text{m}$  sources in Ophiuchus were found to have  $\alpha_1 \sim 1.5$  below  $1 M_\odot$  and  $\alpha_2 \sim 2.5$  above  $1 M_\odot$  (Johnstone et al., 2000).

close to those for the Perseus sample, and if we assume the same dust temperature as Johnstone et al. (2000) ( $T = 20$  K), the break mass of  $\sim 2.5 M_\odot$  becomes  $\sim 1 M_\odot$  (the shape of the mass function does not change with  $T_D$  as long as a single temperature is assumed). Thus the submillimeter/millimeter mass distributions in Perseus and Ophiuchus are quite similar despite different environments, distances ( $d = 160$  pc for

Ophiuchus,  $d = 250$  pc for Perseus), and resolutions ( $14''$  versus  $31''$ ). Comparisons are complicated, however, by blending, differing analysis and assumptions, and dust property uncertainties.

We also fit a lognormal distribution to the  $M > 0.8 M_{\odot}$  region where the mass function is reasonably complete:

$$\frac{dN}{d\log M} = A \exp \left[ \frac{-(\log M - \log M_0)^2}{2\sigma^2} \right], \quad (2.5)$$

where

$$\frac{dN}{dM} = \frac{1}{(\ln 10)M} \frac{dN}{d\log M}. \quad (2.6)$$

Here  $A$  is a normalization factor,  $\sigma$  is the width of the distribution, and  $M_0$  is the characteristic mass. The best-fitting lognormal for  $M > 0.8 M_{\odot}$  has  $\sigma = 0.5 \pm 0.1$  and  $M_0 = 0.9 \pm 0.4 M_{\odot}$ . A lognormal is a somewhat better fit than a broken power law ( $\tilde{\chi}^2 = 0.2$ ). For  $T_D = 20$  K, the best fit parameters are  $\sigma = 0.5$  and  $M_0 = 0.3 M_{\odot}$  (note again that only the characteristic mass, and not the shape, changes with  $T_D$ ).

Uncertainties in the dust temperature  $T_D$  should have only a linear effect on the estimated mass as long as we are in the Rayleigh-Jeans (RJ) regime of the SED, where  $B_{\nu}$  scales linearly with  $T_D$ . At low temperatures, however, the departure of RJ from a true blackbody can cause large errors in the estimated mass. If, for example, the true dust temperature of a source is  $T_D = 10$  K, assuming a temperature of  $T_D = 5$  K would cause a miscalculation of the mass by a factor of 4.7, and assuming a temperature of  $T_D = 20$  K would result in a factor of 3 error.

Figure 2.17 demonstrates the effect on the differential mass function of varying the dust temperature. For each curve the mass function is calculated for a single value for  $T_D$ . Note that the shape of  $dN/dM$  does not change with the assumed value of  $T_D$ , the distribution simply shifts to higher masses (lower  $T_D$ ) or lower masses (higher  $T_D$ ). The shape *will* change, however, if there is a range of dust temperatures in the real cores. Ideally we could determine  $T_D$  independently using observations at two different wavelengths. For our purposes  $T_D = 10$  K is a good compromise for prestellar and protostellar sources, but will overestimate by a factor of 3 the mass of

sources with a true dust temperature of 20 K.

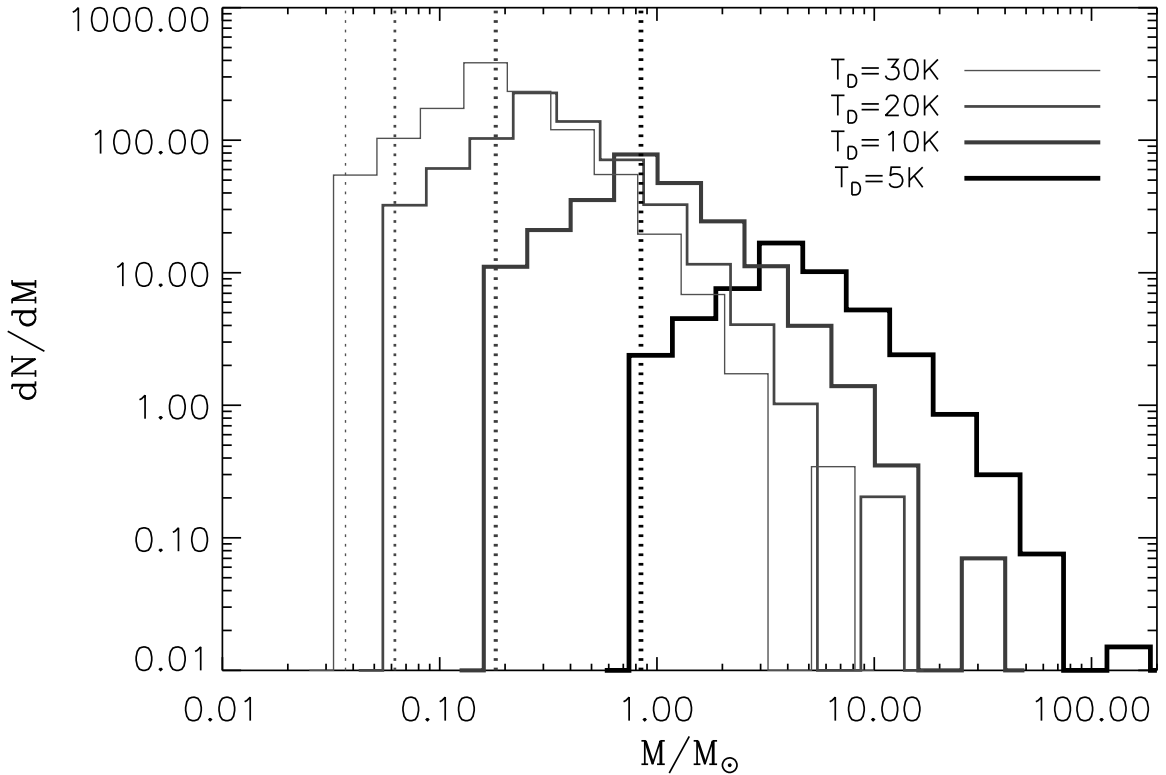


Figure 2.17 The differential mass function, shown for different values of the assumed dust temperature  $T_D$ . The dashed lines correspond to the mass limit for a point source at each  $T_D$ . Changing the temperature shifts the distribution to higher (for lower  $T_D$ ) or lower (for higher  $T_D$ ) masses, but does not change its shape. A dust opacity of  $\kappa_{1.1mm} = 0.0114 \text{ cm}^2\text{g}^{-1}$  and a distance of  $d = 250 \text{ pc}$  are assumed for all masses. Increasing  $\kappa_{1.1mm}$  shifts the distribution to lower masses, while increasing  $d$  shifts it to higher masses. Given the range of plausible values ( $\kappa_{1.1mm} = 0.005 - 0.02 \text{ cm}^2/\text{g}$ ,  $d = 200 - 300 \text{ pc}$ ), the effects of varying  $\kappa_{1.1mm}$  and  $d$  are smaller than the effect of varying the temperature ( $T_D = 5 - 30 \text{ K}$ ).

Variations in  $\kappa_{1.1mm}$  and  $d$  have similar effects. The dust opacity is uncertain by up to a factor of two or more (Ossenkopf & Henning, 1994), owing to large uncertainties in the assumed dust properties as well as the possibility that  $\kappa_\nu$  varies with position within a core. Increasing the opacity shifts the mass distribution to lower masses, while increasing the distance shifts it to higher masses. Both are smaller effects than changing the dust temperature for the range of plausible values ( $\kappa_{1.1mm} = 0.005 -$

$0.02 \text{ cm}^2 \text{ g}^{-1}$ ;  $d = 200 - 300 \text{ pc}$ ;  $T_D = 5 - 30 \text{ K}$ ). As for variable dust properties within the sample, blending of close sources will also distort the shape of the mass function, biasing it toward higher masses. We know from previous observations that some sources are blends, but do not attempt to distinguish blends from single sources here. The total uncertainties in all masses are at least a factor of 4 or more (e.g., Shirley et al., 2002; Young et al., 2003).

A comparison of the prestellar clump mass function to the stellar initial mass function (IMF) may reveal the origin of the IMF shape. If stellar masses are determined by competitive accretion or by the protostars themselves through feedback mechanisms (e.g., outflows and winds), we would not expect the emergent IMF to reflect the original clump mass function (Adams & Fatuzzo, 1996). If, on the other hand, stellar masses are determined by the initial fragmentation into cores, as might be expected in crowded regions where the mass reservoir is limited to a protostar's nascent core, the IMF should closely trace the clump MF (Myers, 1998). In Serpens (Testi & Sargent, 1998) and  $\rho$  Oph (Motte, André, & Neri, 1998) the clump MF has been found to be quite similar to the stellar IMF, suggesting that fragmentation is responsible for determining final masses. In reality, of course, it may well be a combination of these effects and turbulence that shapes the IMF (e.g., Clark & Bonnell, 2005), but we consider the simplest cases here.

The local IMF follows a broken power law with  $\alpha_1 = 1.6$  ( $M < 1 M_\odot$ ) and  $\alpha_2 = 2.7$  ( $M > 1 M_\odot$ ), flattening around  $0.3 M_\odot$  (Chabrier, 2001). Chabrier (2003) also find that the IMF is well fit by a lognormal with  $\sigma = 0.6$  and  $M_0 = 0.2 M_\odot$ . Thus the slope of the IMF, but not the break mass, is very similar to the Perseus mass function. Even the characteristic masses are quite similar if we assume  $T_D = 20 \text{ K}$  for the Perseus sample. Currently, a direct connection between the mass distribution in Perseus and the IMF is difficult to make because our sample contains sources at a range of ages, with varying amounts of the envelope already accreted onto the protostar or ejected in an outflow, and varying envelope temperatures. After combining these data with Spitzer c2d data it will be possible to determine the evolutionary state of each source, separating prestellar cores from more evolved objects. Even for a sample

containing only prestellar cores, however, the association with final stellar masses may be problematic (see Johnstone et al., 2000).

### 2.5.3 Clustering

Visually, the 1.1 mm sources in Perseus appear very clustered: 89/122 or 73%, have a neighboring source within  $3'$ , with most isolated sources being faint objects near the detection limit. In their 850  $\mu\text{m}$  SCUBA survey Hatchell et al. (2005) find that 80% of the 850  $\mu\text{m}$  sources are in groups of three or more sources (within 0.5 pc), and 40% – 60% of the sources are in the massive clusters of NGC 1333 and IC 348 (HH 211 in their paper). Using similar criteria, we also find  $\sim 80\%$  of the total number of sources lie in groups of  $> 3$  within 0.5 pc, and  $\sim 45\% - 50\%$  in the massive clusters. Despite the fact that our 1.1 mm map covers more than twice as much area as the 850  $\mu\text{m}$  map of Hatchell et al. (2005) ( $7.5 \text{ deg}^2$  compared to  $\sim 3 \text{ deg}^2$ ), the clustering properties of sources in the two surveys are quite similar. This result is perhaps not surprising considering that we only detect about 5 – 10 sources in the additional  $\sim 4.5 \text{ deg}^2$  covered by the Bolocam map.

For a more quantitative understanding of the clustering properties in Perseus, we calculate the two-point correlation function:

$$w(r) = \frac{H_s(r)}{H_r(r)} - 1, \quad (2.7)$$

where  $H_s(r)$  is the number of core pairs with separation between  $\log(r)$  and  $\log(r) + d\log(r)$ . The definition of  $H_r(r)$  is similar to  $H_s(r)$ , but for a random distribution. The random sample is constructed by generating a uniform random distribution of sources with the same RA and Dec limits as the real sample (i.e. there are no sources in the random sample outside the actual area observed). The two-point correlation function is often used in cosmological studies of the clustering of galaxies (e.g Maddox et al., 1990), but may also be a good way to compare the properties of different molecular clouds.

Plots of  $H_s(r)$  and  $w(r)$  for the entire observed region of Perseus are shown in

figure 2.18, with the random distribution ( $H_r(r)$ , dashed line) included for comparison. If the sources were randomly distributed in the cloud, we would expect the two curves to be similar. The resolution limit ( $31'' = 8 \times 10^3$  AU), and average deconvolved source FWHM size ( $1.5 \times 10^4$  AU) are also indicated, the latter a being representation of the effective resolution limit. It is clear that the source pair function  $H_s(r)$  shows an excess over the random distribution  $H_r(r)$  at small scales (the differences at large scales is not significant). This is confirmed by the correlation function  $w(r)$  (middle panel), which is  $> 3\sigma$  on scales  $2 \times 10^4$  AU  $< r < 2.5 \times 10^5$  AU. Note that the random distribution shows no correlation ( $w_r \sim 0$ ), as expected.

If we characterize the correlation function as a power law,  $w(r) \propto r^{-\gamma}$ , then a good fit ( $\tilde{\chi}^2 = 0.7$ ) is obtained for  $\gamma = 1.25 \pm 0.06$  in the range  $2 \times 10^4$  AU  $< r < 2 \times 10^5$  AU. Since the average deconvolved source size corresponds to  $\sim 1.5 \times 10^4$  AU, Perseus essentially shows clustering from the average source size up to  $r_{max} = 2 \times 10^5$  AU = 1.2 pc. In Ophiuchus Johnstone et al. (2000) find  $\gamma = 0.75$  for separations  $r < 3 \times 10^4$  AU and negligible clustering for  $r > 3 \times 10^4$  AU, for a distance of 160 pc and a beam size of  $2 \times 10^3$  AU. Those authors associate  $r_{max} = 3 \times 10^4$  AU with the Jeans length in Ophiuchus, and note that  $\gamma = 0.7$  for galaxy clustering (Maddox et al., 1990), where gravity is the dominant process. It is possible that different slopes could be associated with different processes dominating fragmentation, but given the considerable uncertainties involved we choose not to speculate further.

While the correlation function provides a good comparison of clustering between the clouds, we note that the range over which  $w(r)$  can be computed ( $8 \times 10^3 - 5 \times 10^6$  AU for Perseus and  $4 \times 10^3 - 10^5$  AU for Oph) differs due to the different resolution limits, spatial coverages, and distances of the two clouds. Even so, it seems that clustering occurs on larger scales in Perseus than in Oph ( $r_{max,Per} > r_{max,Oph}$ ), but drops off more quickly as a function of separation ( $\gamma_{Per} > \gamma_{Oph}$ ). It is important to note that the measured correlation function depends on the area observed; if we break the Perseus map into smaller pieces the derived slope does vary, but it remains between  $1 < \gamma < 1.5$  for a range of chosen areas.

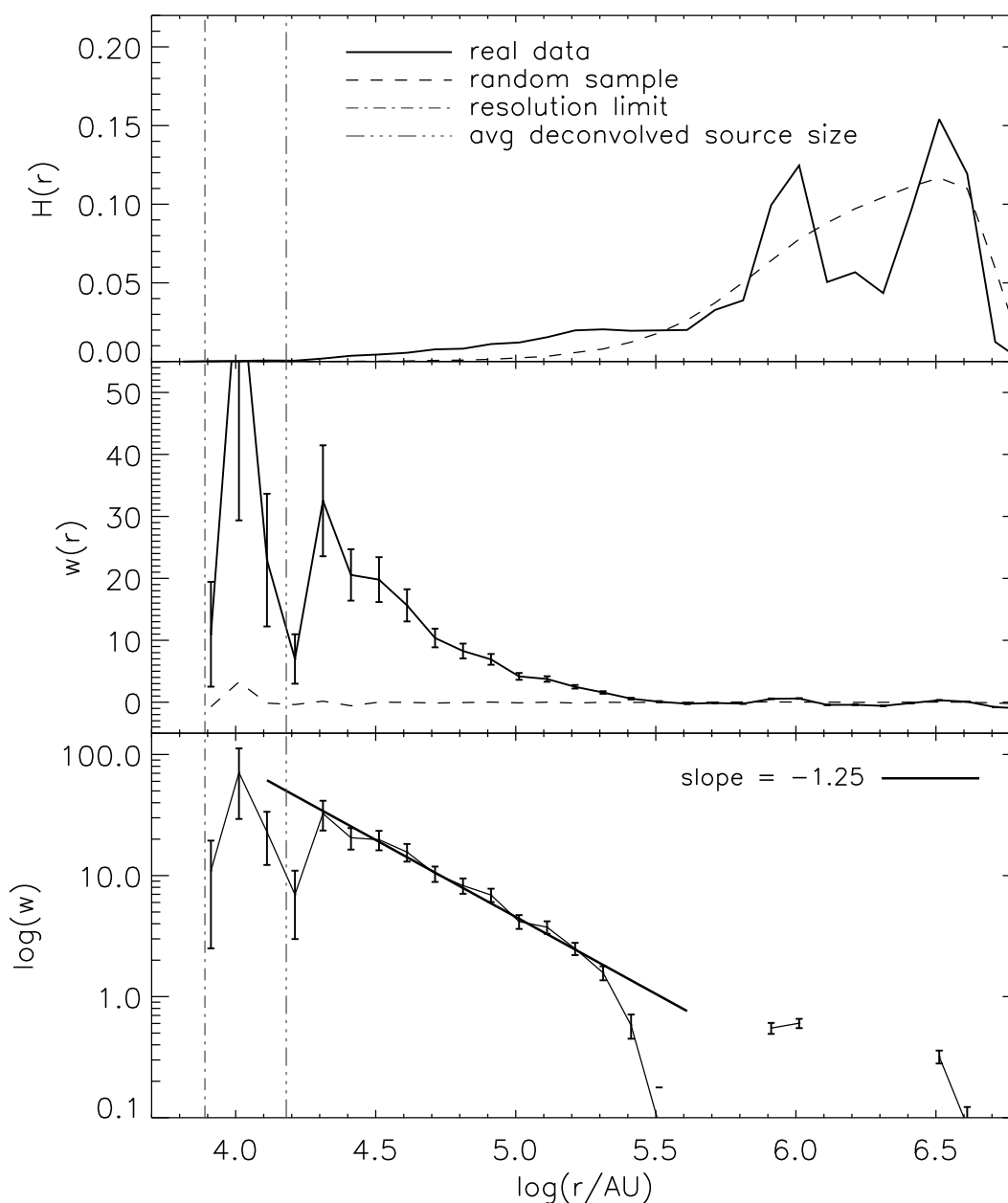


Figure 2.18 The two-point correlation function, illustrating the degree of clustering in the cloud. Top:  $H(r)$  is the number of source pairs between  $\log(r)$  and  $d\log(r)$  as a function of  $\log(r/AU)$ . The solid line indicates the real data, and the dashed line is for a uniform random distribution of sources with the same RA/Dec limits as the real sample. In all plots the dotted line denotes the resolution limit, and the dot-dash line the mean deconvolved source FWHM. Center: The two point correlation function  $w(r)$  as defined in the text, with  $\sqrt{N}$  errors. Where  $w(r) > 0$  there is a correlation between sources at that separation, thus  $w(r)$  indicates clustering on scales  $\log(r/AU) < 5.5$  for the Perseus sample. When calculated using two randomly distributed samples (dashed line)  $w(r)$  shows no correlation, as expected. Bottom:  $w(r)$  is well fitted by a power law,  $w(r) \propto r^{-1.25}$ , for  $2.5 \times 10^4 \text{ AU} < r < 2 \times 10^5 \text{ AU}$ .

### 2.5.4 An Extinction Threshold for 1.1 mm Cores

The total mass contained in the 122 detected 1.1 mm cores is  $285 M_{\odot}$ , assuming  $\kappa_{1.1mm} = 0.0114 \text{ cm}^2 \text{ g}^{-1}$ ,  $T_D = 10 \text{ K}$ , and a gas to dust ratio of 100. The total cloud mass based on CO observations is  $1 - 2 \times 10^4 M_{\odot}$  for  $d = 250 \text{ pc}$  (Sargent, 1979; Cernicharo et al., 1985; Ungerechts & Thaddeus, 1987; Carpenter, 2000). Based on the *NICE* extinction map, we calculated a total mass for  $A_V \geq 2$  of  $5900 M_{\odot}$  in the area observed by Bolocam. Thus only a very small fraction, between 1% and 5%, of the cloud mass is contained in dense cores at  $\lambda = 1.1 \text{ mm}$ . This small fraction is consistent with the evidence from comparisons of molecular cloud masses to total stellar masses that molecular cloud material is relatively sterile (Evans, 1999). Hatchell et al. (2005) find a significantly larger fraction of mass (20%) in  $850 \mu\text{m}$  emission. Their large total mass at  $850 \mu\text{m}$  of  $\sim 2600 M_{\odot}$  is due in part to differences in the assumed distance and opacity, and in part to the fact that those authors integrate over all pixels in the map above  $5\sigma$  to get the total mass, whereas we only include only the mass in discrete cores. The total mass in the 1.1 mm maps, calculated from the sum of all pixels  $> 5\sigma$ , is  $376 M_{\odot}$ , or 2% to 6% of the total cloud mass.

The low efficiency of 1.1 mm cores may be related to the conditions required for a dense core to form. Johnstone, DiFrancesco, & Kirk (2004) have recently suggested that there is an extinction threshold for forming  $850 \mu\text{m}$  cores in Ophiuchus. The derived threshold for the presence of stable cores in Ophiuchus ( $A_{V,lim}^{Oph} \sim 15 \text{ mag}$ ) is greater than the maximum extinction in Perseus as traced by our *NICE* extinction map ( $A_{V,max}^{Per} \sim 16 \text{ mag}$ ), suggesting that if conditions in the two regions were similar there should be very few millimeter cores in Perseus, which is clearly not the case. In fact, the mean extinction from our *NICE* map toward all cores in Perseus is  $\langle A_V \rangle = 7.1 \pm 3.1 \text{ mag}$ , similar to the minimum  $A_V$  at which any  $850 \mu\text{m}$  core is found in Ophiuchus ( $A_{V,min}^{Oph} = 7 \text{ mag}$ ; Johnstone et al. 2004). Bear in mind, however, if the cloud material is very clumpy, beam effects will be important given that the distance to Perseus is twice that of Ophiuchus. For comparison, the mean  $A_V$  for the entire area observed by Bolocam is  $\langle A_V \rangle \sim 2 \text{ mag}$ , and the mean  $A_V$  for the area observed

by Johnstone et al. (2004) in Ophiuchus was  $\langle A_V \rangle \sim 4$  mag.

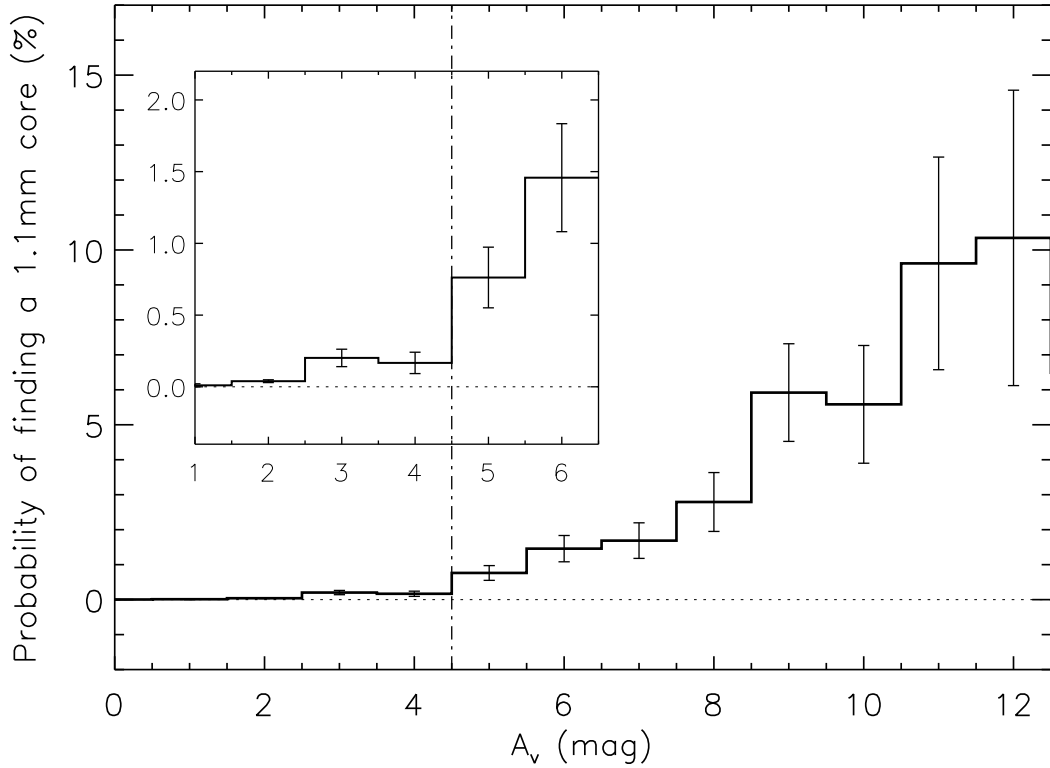


Figure 2.19 Probability of finding a 1.1 mm core as a function of  $A_V$ , computed using the *NICE* extinction map. The probability is the number of  $50''$  pixels at a given  $A_V$  containing one or more 1.1 mm cores, divided by the total number of pixels at that  $A_V$ . Error bars are Poisson statistical errors, and become large where the  $A_V$  map saturates at  $A_V \sim 10$  mag. The low  $A_V$  region is magnified for clarity. It appears that there is an approximate extinction limit at  $A_V \sim 5$  mag, below which it becomes very unlikely that a 1.1 mm core will be found. The extinction limit of  $A_V \sim 5$  mag is considerably lower than the  $A_V \sim 15$  mag limit for forming  $850 \mu\text{m}$  cores found by Johnstone et al. (2004) in Ophiuchus, although beam effects could be important. Our  $A_V \sim 5$  mag limit is consistent with the fact that few sources are found outside previously surveyed regions.

All dense groups of 1.1 mm sources in Perseus lie in regions of high  $A_V \gtrsim 5$  mag, but not all regions of high  $A_V$  correspond to 1.1 mm sources, suggesting that relatively high extinction may be necessary, but not sufficient, for star formation. The probability of finding a 1.1 mm core as a function of  $A_V$  is shown in figure 2.19. The probability for a given  $A_V$  is calculated from the extinction map as the number of

50'' pixels containing a 1.1 mm core divided by the total number of pixels at that  $A_V$  ( $p/100 = N_{src}/N_{A_V}$ ). Error bars are Poisson statistical errors ( $\sigma_p/100 = \sqrt{N_{src}}/N_{A_V}$ ). It appears that there is an approximate extinction limit of  $A_V \sim 5$  mag below which it becomes very unlikely that a 1.1 mm core will be found. Above  $A_V \sim 5$  mag, the probability of finding a 1.1 mm core rises with  $A_V$ . Error bars are large for high  $A_V$  because our *NICE*  $A_V$  map is not sensitive to  $A_V \gtrsim 10$  mag, so there are few pixels at high extinctions.

Hatchell et al. (2005) take a more sophisticated approach to the probability of finding 850  $\mu\text{m}$  cores as a function of column density, concluding that there is no column density (or  $A_V$ ) limit for submillimeter cores in Perseus. This result is consistent with our extinction limit of  $A_V \sim 5$  mag given that the Hatchell et al. (2005) survey covers only the  $A_V \gtrsim 4$  mag regions in Perseus. An extinction threshold around  $A_V \sim 5$  mag in Perseus would also explain why very few (5 – 10) sources are found in the Bolocam 1.1 mm map outside of the region covered by the Hatchell et al. (2005) survey, despite the much greater area imaged. The additional area covered is primarily low column density  $A_V \sim 2 - 4$  mag material, and therefore would not be expected to contain many millimeter cores.

### 2.5.5 Comparison to c2d Observations: B1 Ridge

As an example of the analysis of the complementary c2d Spitzer IR and Bolocam 1.1 mm observations, we compare the Spitzer 24  $\mu\text{m}$  and 1.1 mm images for a small area of Perseus around B1. The B1 Ridge is a narrow ridge of extended 1.1 mm emission below the group of protostars B1a–d. Figure 2.20 shows the B1 Ridge region of the Bolocam map (left), with the position of all detected MIPS 24  $\mu\text{m}$  sources, as well as MIPS sources with  $S_{24} > 5$  mJy, indicated. The c2d MIPS 24  $\mu\text{m}$  image is also shown (right) with Bolocam 1.1 mm contours overlaid. The B1(a–d) protostellar sources are bright at both 24  $\mu\text{m}$  and 1.1 mm, with  $(S_{24}, S_{1.1\text{mm}}) = (0.2, 1.2)$  Jy beam $^{-1}$  (B1-b),  $(0.8, 1.1)$  Jy beam $^{-1}$  (B1-c) and  $(0.13, 0.6)$  Jy beam $^{-1}$  (B1-d). The little-known protostar IRAS 03292+3039 is relatively faint at 24  $\mu\text{m}$

( $0.08 \text{ Jy beam}^{-1}$ ), but very bright at  $1.1 \text{ mm}$  ( $1.1 \text{ Jy beam}^{-1}$ ), suggesting a young evolutionary state.

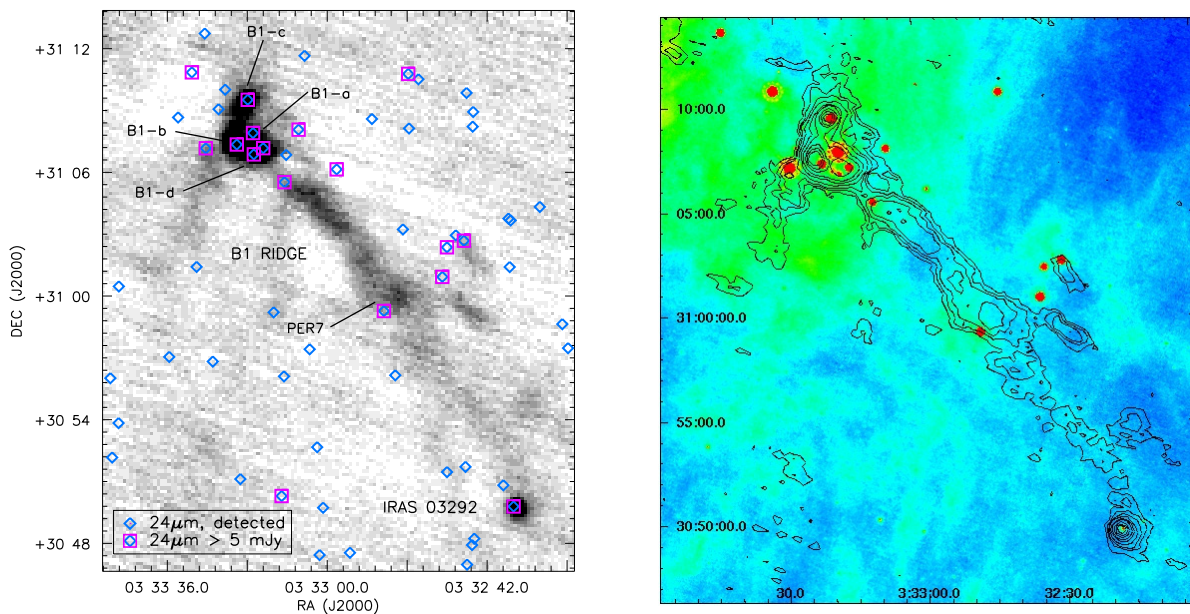


Figure 2.20 Spitzer sources in the B1 Ridge region overlaid on the Bolocam 1.1 mm map (left). Blue diamonds show the positions of all detected  $24 \mu\text{m}$  sources in the MIPS c2d image (Rebull et al., 2007), and pink boxes indicate sources with  $S_{24} > 5 \text{ mJy}$ . The MIPS  $24 \mu\text{m}$  image is also shown (right) with Bolocam 1.1 mm contours overlaid ( $2, 4, \dots, 20\sigma$ ). There are no  $24 \mu\text{m}$  sources in the main part of the B1 Ridge, suggesting that the ridge may be made up of a number of prestellar cores.

There are a few bright  $24\mu\text{m}$  protostellar sources nearby and in the lower part of the extended B1 ridge (e.g., near the  $\text{NH}_3$  core Per 7 (Ladd et al., 1994)), but in the main part of the ridge there are no  $24 \mu\text{m}$  sources. Given the lack of mid-IR sources in the main B1 ridge, we suggest that it is made up of a number of prestellar cores. High resolution submillimeter and millimeter follow-up observations of both the ridge and nearby protostars have already been completed with OVRO ( $\lambda = 3\text{mm}$ ) and SHARC II ( $\lambda = 350 \mu\text{m}$ ). Detailed analysis of this region combining IRAC and MIPS data with high resolution millimeter data to study the precise nature of the prestellar cores and embedded protostars, including envelope structure and outflow dynamics, is underway.

## 2.6 Summary

We present a  $7.5 \text{ deg}^2$  ( $143 \text{ pc}^2$  for  $d = 250 \text{ pc}$ ) survey for 1.1 mm dust continuum emission in the Perseus molecular cloud using Bolocam at the CSO. This map is the largest millimeter or submillimeter continuum image of the region to date. Given that Bolocam has a beam of  $31''$  (FWHM), the Perseus map covers a remarkable total number of resolution elements ( $3.4 \times 10^4$ ) down to a  $5\sigma$  point source mass detection limit of  $0.18 M_\odot$  ( $T_D = 10 \text{ K}$ ).

We detect 122 1.1 mm cores above the  $5\sigma = 75 \text{ mJy beam}^{-1}$  detection limit. Nearly half (60/122) of the detected sources are new millimeter or submillimeter detections, including previously unknown sources as well as known objects not previously observed at these wavelengths. Our 1.1 mm map covers more than twice the area of the recent  $850 \mu\text{m}$  SCUBA survey by Hatchell et al. (2005) but, despite the significantly greater area imaged, only  $\sim 5 - 10$  of our new detections lie outside their map. Thus, much of the Perseus cloud is devoid of compact millimeter emission and, by implication, active star formation.

In order to compare the general morphology of our 1.1 mm map to the COMPLETE  $^{13}\text{CO}$  map and our *NICE* extinction map, we convert all three images to a column density scale. Our 1.1 mm map reveals significantly higher column density features than the other tracers and exhibits much more compact structure, even when degraded to the  $5'$  resolution of the *NICE* extinction map. The general appearance of the 1.1 mm emission is roughly consistent with the molecular and extinction data, however, in that most 1.1 mm sources lie within  $^{13}\text{CO}$  and  $A_V$  peaks.

The total mass in discrete 1.1 mm cores is  $285 M_\odot$  ( $T_D = 10 \text{ K}$ ), accounting for no more than 5% of the total mass of the cloud. The small fraction of mass in dense cores, which are usually associated with star formation, supports the idea that most of the mass in molecular clouds is relatively sterile (Evans, 1999). Calculating the probability of finding a 1.1 mm core as a function of  $A_V$  leads us to conclude that there is an extinction threshold in Perseus at  $A_V \sim 5 \text{ mag}$ , above which 1.1 mm cores are likely to be observed. Such an extinction limit is consistent with the fact that

very few new sources are found outside of the area covered by the  $A_V \gtrsim 4$  mag map of Hatchell et al. (2005).

The average mass of the sample, based on the total flux density from aperture photometry, is  $2.3 M_\odot$  ( $T_D = 10$  K). The differential mass function  $dN/dM$  is well fitted by a broken power law with  $\alpha \sim 1.3$  ( $0.5 M_\odot < M < 2.5 M_\odot$ ) and  $\alpha \sim 2.6$  ( $M > 2.5 M_\odot$ ). The derived values are similar to those found in Ophiuchus ( $\alpha = 2.5$   $M > 1 M_\odot$ ,  $\alpha = 1.5$   $M < 1 M_\odot$  Johnstone et al. 2000), and to the local IMF ( $\alpha = 2.7$   $M > 1 M_\odot$ ,  $\alpha = 1.6$   $M < 1 M_\odot$ , Chabrier 2003). We compute the two-point correlation function, confirming that compact millimeter emission in the cloud is highly structured. Significant clustering of sources from the average source size up to scales of  $2 \times 10^5$  AU is seen. Within this range, the correlation function exhibits a power law shape with index  $\gamma = -1.25$ , steeper than the correlation in Ophiuchus (Johnstone et al., 2000).

The Bolocam 1.1 mm data presented here were designed to cover the same region as the Spitzer c2d legacy program IRAC ( $\lambda = 3.6 - 8.0 \mu\text{m}$ ) and MIPS ( $\lambda = 24 - 160 \mu\text{m}$ ) maps of Perseus. Combining the 1.1 mm data with the c2d IRAC and MIPS data will enable a complete census of the properties and distribution of the protostars and dense cores in Perseus (see chapter 6), especially when complemented by the publicly available 2MASS catalogs and COMPLETE molecular and continuum maps. Follow-up observations have already been completed with SHARC II (CSO,  $\lambda = \mu\text{m}$ ) and the OVRO interferometer ( $\lambda = 3$  mm) for several of the most interesting sources identified in the Bolocam map, including the B1 ridge.

## Acknowledgments

We gratefully thank the referee, Alyssa Goodman, as well as Karl Stapelfeldt and Philip Myers, for their helpful comments. Support for this work, part of the Spitzer Legacy Science Program, was provided by NASA through contracts 1224608 and 1230782 issued by the Jet Propulsion Laboratory, California Institute of Technology, under NASA contract 1407. Additional support was obtained from NASA Origins

Grant NNG04GG24G to the University of Texas at Austin. Support for the development of Bolocam was provided by NSF grants AST-9980846 and AST-0206158. MLE acknowledges support of an NSF Graduate Research Fellowship.

## Bibliography

- Adams, F. C., & Fatuzzo, M. 1996, *ApJ*, 464, 256
- André, P., Ward-Thompson, D., & Barsony, M. 1993, *ApJ*, 406, 122
- Bachiller, R., & Cernicharo, J. 1986, *A&A*, 168, 262
- Bachiller R., Martín-Pintado, J., & Planesas, P. 1991, *A&A*, 251, 639
- Barsony, M., Ward-Thompson, D., André, P., & O’Linger, J. 1998, *ApJ*, 509, 733
- Belikov, A. N., Kharchenko, N. V., Piskunov, A. E., Shilbach, E., & Scholz, R.-D. 2002, *A&A*, 387, 117
- Bonnor, W. B. 1956, *MNRAS*, 116, 351
- Borgman, J., & Blaauw, A. 1964, *B.A.N.*, 17, 358
- Carpenter, J. M. 2000, *AJ*, 120, 3139
- Cernicharo, J., Bachiller, R., & Duvert, G. 1985, *A&A*, 149, 273
- Černis, K. 1990, *Ap&SS*, 166, 315
- Černis, K. 1993, *Baltic Astronomy*, 2, 214
- Černis, K., & Straizys 2003, *Baltic Astronomy*, 12, 301
- Chabrier, G. 2001, *ApJ*, 554, 1274
- Chabrier, G. 2003, *PASP*, 115, 763
- Clark, P. C. & Bonnell, I. A. 2005, *MNRAS*, 361, 2
- Dickman, R. L. 1978, *ApJS*, 37, 407
- Dowell, C. D., Allen, C. A., Babu, R. S., Freund, M. M., Gardner, M., Groseth, J., Jhabvala, M. D., et al. 2003, *SPIE*, 4855, 73

- de Zeeuw, P. T., Hoogerwerf, R., & deBruijne, J. H. J. 1999, *AJ*, 117, 354
- Ebert, R. 1955, *Zeitschrift Astrophysics*, 37, 217
- Eislöffel, J., Froebrich, D., Stanke, T., & McCaughrean, M. J. 2003, *ApJ*, 595, 259
- Enoch, M. L., Glenn, J., Evans, N. J., II, Sargent, A. I., Young, K. E., & Huard, T. L. 2007, *ApJ*, in press
- Evans, N. J., II 1999, *ARA&A*, 37, 311
- Evans, N. J., II, Allen, L. E., Blake, G. A., Boogert, A. C. A., Bourke, T., Harvey, P. M., Kessler, J. E., et al. 2003, *PASP*, 115, 965
- Evans, N. J., II, Rawlings, J. M. C., Shirley, Y. L., & Mundy, L. G. 2001, *ApJ*, 557, 193
- Frerking, M. A., Langer, W. D., & Wilson, R. W. 1982, *ApJ*, 262, 590
- Froebrich, D., Smith, M. D., Hodapp, K.-W., & Eislöffel, J. 2003, *MNRAS*, 346, 163
- Glenn, J., Ade, P. A. R., Amarie, M., Bock, J. J., Edgington, S. F., Goldin, A., Golwala, S., et al. 2003, *SPIE*, 4855, 30
- Glenn, J., Bock, J. J., Chattopadhyay, G., Edgington, S. F., Lange, A. E., Zmuidzinas, J., Mauskopf, P. D., Rownd, B., Yuen, L., & Ade, P. A. 1998, *SPIE*, 3357, 326
- Goodman, A. A., & the COMPLETE Team, 2004, in *Star Formation in the Interstellar Medium* (San Francisco: ASP), in press.
- Gregersen, E. M. & Evans, N. J., II 2000, *ApJ*, 538, 260
- Guilloteau, S., Delannoy, J., Downes, D., Greve, A., Guelin, M., Lucas, R., Morris, D., et al. 1992, *A&A*, 262, 624
- Haig, D., Ade, P. A. R., Aguirre, J. E., Bock, J. J., Edgington, S. F., Enoch, M. L., Glenn, J., et al. 2004, *SPIE*, 5498, 78

- Hatchell, J., Richer, J. S., Fuller, G. A., Qualtrough, C. J., Ladd, E. F., & Chandler, C. J. 2005, *A&A*, 440, 151
- Herbig, G. H., & Jones, B. F. 1983, *AJ*, 88, 1040
- Ho, P. T. P, Moran, J. M., & Lo, K. Y. 2004, *ApJ*, 616, L1
- Högbom, J. A. 1974, *A&A*, 15, 417
- Holland, W. S., Robson, E. I., Gear, W. K., Cunningham, C. R., Lightfoot, J. F., Jenness, T., Ivison, R. J., et al. 1999, *MNRAS*, 303, 659
- Huard, T. L., Myers, P. C., Murphy, D. C., Crews, L. J., Lada, C. J., Bourke, T. L., Crapsi, A., Evans, N. J., II, McCarthy, D. W., Jr., & Kulesa, C. 2006, *ApJ*, 640, 391
- Jennings, R. E., Cameron, D. H. M., Cudlip, W., & Hirst, C. J. 1987, *MNRAS*, 226, 461
- Johnstone, D., DiFrancesco, J., & Kirk, H. 2004, *ApJ*, 45, 611L
- Johnstone, D., Wilson, C. D., Moriarty-Schieven, G., Joncas, G., Smith, G., Gregersen, E., & Fich, M. 2000, *ApJ*, 545, 327
- Juan, J., Bachiller, R., Kömpe, C., & Martín, J. 1993, *A&A*, 270, 432
- Kirk, J. M., Ward-Thompson, D., & André, P. 2005, *MNRAS*, 360, 1506
- Kreysa, E., Gemuend, H.-P., Gromke, J., Haslam, C. G., Reichertz, L., Haller, E. E., Beeman, J. W., Hansen, V., Sievers, A., & Zylka, R. 1998 *SPIE*, 3357, 319
- Lada, C. J. 1987, *IAUS*, 115
- Lada, C. J., Alves, J., & Lada, E. A. 1996, *AJ*, 111, 1964
- Lada, C. J., Alves, J., & Lada, E. A. 1999, in *The Physics and Chemistry of the Interstellar Medium*, editors V. Ossenkopf, J. Stutzki, G. Winnewisser, 161

- Ladd, E. F., Lada, E. A., & Myers, P. C. 1993, ApJ, 410, 168
- Ladd, E. F., Myers, P.C., & Goodman, A. A. 1994, ApJ, 433, 117
- Laurent, G., Aguirre, J. E., Glenn, J., Ade, P. A. R., Bock, J. J., Edgington, S. F., Goldin, A., et al. 2005, ApJ, 623, 742
- Lefloch, B., Castets, A., Cernicharo, J., Langer, W. D., & Zylka, R. 1998, A&A, 334, 269
- Luhman, K. L., Stauffer, J. R., Muench, A. A., Rieke, G. H., Lada, E. A., Bouvier, J., & Lada, C. J. 2003, ApJ, 593, 1093
- Maddox, S. J., Efstathiou, G., Southerland, W. J., & Loveday, J. 1990, MNRAS, 242, 43
- Mathews, B. C., & Wilson, C. D. 2002, ApJ, 547, 822
- McCaughrean, M. J., Rayner, J. T., & Zinnecker, H. 1994, ApJ, 436, L189
- Motte, F., & André, P. 2001, A&A, 365, 440
- Motte, F., André, P., & Neri, R. 1998, A&A, 336, 150
- Myers, P. C. 1998, ApJ, 496, L109
- O'Linger, J., Wolfe-Chase, G., Barsony, M., & Ward-Thompson, D. 1999, ApJ, 515, 696
- Ossenkopf, V., & Henning, Th. 1994, A&A, 291, 943
- Padoan, P., Bally, J., Billawala, Y., Juvela, M., & Nordlund, A. 1999, ApJ, 525, 318
- Rebull, L. M., Stapelfeldt, K. R., Evans, N. J., II, Joergensen, J. K., Harvey, P. M., Brooke, T. Y., Bourke, T. L., et al. 2007, ApJ, in press (preprint:stro-ph/0701711)
- Ridge, N. A., Schnee, S. L, Goodman, A. A., Li, J. G., & Foster, J. B. 2006, ApJ, 643, 942

- Sandell, G., 1994, MNRAS, 271, 75
- Sandell, G., Aspin, C., Williams, D. D., Russel, A. P. G., & Robson, E. I. 1991, ApJ, 367, L17
- Sandell, G. & Knee, L. B. G. 2001, ApJ, 546, L49
- Sargent, A. I. 1979, ApJ, 233, 163
- Schnee, S. & Goodman, A. 2005, ApJ, 624, 254
- Schwarz, U. J. 1978, A&A, 65, 345
- Shirley, Y. L., Evans, N. J., II, & Rawlings, J. M. C. 2002, ApJ, 575, 337
- Testi, L., & Sargent, A. I. 1998, ApJ, 508, L91
- Ungerechts, H., & Thaddeus, P. 1987, ApJS, 63, 645
- Ward-Thompson, D., Scott, P. F., Hills, R. E., & Andre, P. 1994, MNRAS, 268, 276
- Welch, W. J., Thornton, D. D., Plambeck, R. L., Wright, M. C. H., Lugten, J., Urry, L., Fleming, M., et al. 1996, PASP, 108, 93
- Wiling, B. A., Meyer, M. R., Greene, T. P, Mikhail, A., & Carlson, G. 2004, AJ, 127, 1131
- Williams, J. P., deGeus, E. J., & Blitz, L. 1994, ApJ, 428, 693
- Woody, D. P., Serabyn, E., & Schinckel, A. 1998, SPIE, 3357, 474
- Young, C. H., & Evans, N. J., II 2005, ApJ, 627, 293
- Young, C. H., Shirley, Y. L., Evans, N. J., II, & Rawlings, J. M. C. 2003, ApJS, 145, 111
- Young, K. E., Enoch, M. L., Evans, N. J., II, Glenn, J., Sargent, A., Huard, T. L., Aguirre, J., et al. 2006, ApJ, 644, 326

## Chapter 3

# Bolocam Survey for 1.1 mm Dust Continuum Emission in the Ophiuchus Molecular Cloud

### Abstract

We present a large-scale millimeter continuum map of the Ophiuchus molecular cloud. Nearly 11 square degrees, including all of the area in the cloud with  $A_V \geq 3$  magnitudes, was mapped at 1.1 mm with Bolocam on the Caltech Submillimeter Observatory (CSO). By design, the map also covers the region mapped in the infrared with the *Spitzer Space Telescope*. We detect 44 definite sources, and a few likely sources are also seen along a filament in the eastern streamer. The map indicates that dense cores in Ophiuchus are very clustered and often found in filaments within the cloud. Most sources are round, as measured at the half power point, but elongated when measured at lower contour levels, suggesting spherical sources lying within filaments. The masses, for an assumed dust temperature of 10 K, range from 0.24 to 3.9  $M_\odot$ , with a mean value of 0.96  $M_\odot$ . The total mass in distinct cores is 42  $M_\odot$ , 0.5% to 2% of the total cloud mass, and the 1.1 mm mass above  $4\sigma$  is about 80  $M_\odot$ . The mean densities of the cores are quite high, with an average of  $1.6 \times 10^6 \text{ cm}^{-3}$ , suggesting short free-fall times. The core mass distribution can be fitted with a power law with slope  $\alpha = 2.1 \pm 0.3$  for  $M > 0.5 M_\odot$ , similar to that found in other regions, but

---

Portions of this chapter were previously published in Young, Enoch, Evans, et al. 2006, ApJ, 644, 326.

slightly shallower than that of some determinations of the local IMF. In agreement with previous studies, our survey shows that dense cores account for a very small fraction of the cloud volume and total mass. They are nearly all confined to regions with  $A_V \geq 11$  mag, a lower threshold than found previously.

### 3.1 Introduction

The Ophiuchus molecular cloud is a well-known birthplace of stars. Located at a distance of  $125 \pm 25$  pc (de Geus, de Zeeuw, & Lub, 1989), Ophiuchus contains the L1688 dark cloud region, which contains the Ophiuchus cluster ( $16^h 27^m, -24^\circ 30'$  (J2000)) of young stars and embedded objects. The cluster region has been studied in great detail at a variety of wavelengths from millimeter molecular lines (Loren 1989; Ridge et al. 2006) to near-infrared (e.g., Wilking, Lada, & Young 1989; Allen et al. 2002) to X-ray (Imanishi, Koyama, & Tsuboi, 2001). It has also been mapped in dust continuum emission (Johnstone et al. 2000; Motte, André, & Neri 1998). The embedded cluster is itself surrounded by a somewhat older population of stars extending over  $1.3 \text{ deg}^2$  (Wilking et al., 2005). The cloud is home to two other known regions of star formation, the Lynds dark clouds L1689 ( $16^h 32^m, -24^\circ 29'$ ) and L1709 ( $16^h 31^m, -24^\circ 03'$ ). However, little is known about star formation outside of these three regions.

In this chapter we present the first large-scale millimeter continuum map of the entire Ophiuchus molecular cloud. This survey represents the second in the series of millimeter surveys of three nearby molecular clouds: Perseus (Enoch et al. 2006; chapter 2), Ophiuchus, and Serpens (Enoch et al. 2007; chapter 4). Maps at millimeter wavelengths of the dust continuum emission find regions of dense gas and dust, both those with embedded protostars and those that are starless. Previously published maps of the Ophiuchus cloud covered only small regions: Motte et al. (1998) mapped about  $0.13 \text{ deg}^2$  at 1.3 mm and Johnstone et al. (2000) mapped about  $0.19 \text{ deg}^2$  at  $850 \mu\text{m}$ . A larger ( $4 \text{ deg}^2$ ) map at  $850 \mu\text{m}$  is referred to but not published by Johnstone, Di

Francesco, & Kirk (2004); it is available from the COMPLETE website<sup>1</sup> and discussed in Ridge et al. (2006). Most recently, Stanke et al. (2006) have mapped a 1.3 deg<sup>2</sup> area of L1688 at 1.2 mm. Our map covers 10.8 deg<sup>2</sup>, providing a total picture of the dense gas in Ophiuchus.

Our survey complements the *Spitzer* c2d Legacy project “From Molecular Cores to Planet-forming Disks” (Evans et al., 2003). All of the area in the cloud with  $A_V \geq 3$  magnitudes (according to the map of Cambr esy (1999)) was observed with Bolocam and the InfraRed Array Camera (IRAC) on *Spitzer* (figure 3.1). A somewhat larger area was also mapped at 24, 70, and 160  $\mu\text{m}$  with the Multiband Imaging Photometer for *Spitzer* (MIPS). Maps of millimeter molecular line emission for this same area have been made by the COMPLETE team<sup>2</sup> (Goodman 2004; Ridge et al. 2006). Previously, the largest maps of molecular lines were those of Loren (1989) and Tachihara, Mizuno, & Fukui (2000).

This chapter applies the analysis methods described in chapter 2. Observations with Bolocam (§3.2), data reduction (§3.3), and source identification (§3.3.3) are described to the extent that they differ from those detailed in chapter 2 for Perseus. Basic results including cloud morphology and source properties are presented in §3.4. Completeness is discussed in §3.5.1, the core mass distribution in §3.5.2, clustering of cores in §3.5.3, and an extinction threshold for finding cores in §3.5.4

## 3.2 Observations

We mapped the Ophiuchus molecular cloud at 1.12 mm (hereafter 1.1 mm for brevity) with Bolocam on the Caltech Submillimeter Observatory (CSO)<sup>3</sup> during two observing runs: 21 May – 09 June 2003 and 06 – 11 May 2004. See chapter 2 for information about the instrument. In May 2003, there were 95 channels; in May 2004, the observations were taken with 114 channels. The cloud was observed in three large sections,

---

<sup>1</sup><http://cfa-www.harvard.edu/COMPLETE>

<sup>2</sup><http://cfa-www.harvard.edu/COMPLETE>

<sup>3</sup>The CSO is operated by the California Institute of Technology under funding from the National Science Foundation, contract AST-0229008.

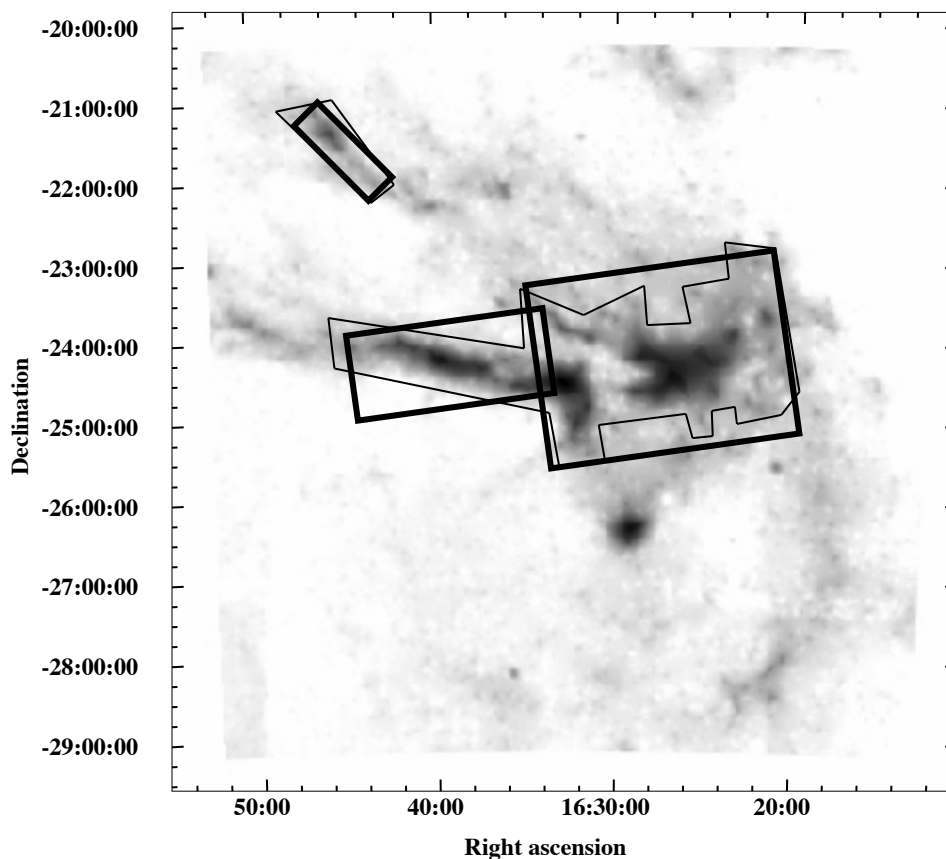


Figure 3.1 Extinction map of Ophiuchus from Cambr esy (1999) with the outline of the Bolocam observation area (thick lines) and the *Spitzer* IRAC observation area (thin lines). The area observed with IRAC was chosen to cover the cloud down to  $A_V \geq 3$ . The Bolocam observations were designed to cover approximately the same region observed with IRAC.

as indicated in figure 3.1: the main L1688 cluster region, the large eastern streamer that extends to the east of L1689, and a smaller northeastern streamer that is not contiguous with the other regions.

Each section was observed with a scan rate of  $60''$  per second, with subsequent subscans offset from the previous one by  $162''$ , perpendicular to the scan direction. With this scan pattern,  $1 \text{ deg}^2$  was observed with 23 subscans in approximately half an hour of telescope time, including 20-second turn-around times at the edges of the maps. Map sections were scanned in two orthogonal directions, rotated slightly from

right ascension (RA) and declination (Dec) by small angles. This technique allows for good cross-linking of the final map with sub-Nyquist sampling and minimal striping from  $1/f$  noise. The northeastern streamer is a little more than  $0.5 \text{ deg}^2$ , the eastern streamer section is about  $2.7 \text{ deg}^2$ , and the large L1688/main cloud section covers a total of  $7.4 \text{ deg}^2$ , which was observed in four sections of approximately  $4 \text{ deg}^2$  each.

The best-weather observations from both runs for each of the three sections were averaged and combined into a single large map: for the northeastern streamer, three scans in RA and three in Dec, were combined for a total observation time of 4.4 hours. The eastern streamer sections consists of three scans in RA and two in Dec, contributing 6 hours of observation time. The main cloud region was observed in four pieces, with two RA and two Dec scans each, requiring 13 hours of integration time. The resulting coverage varies by  $\sim 25\%$ .

In addition to the Ophiuchus maps, small maps of secondary calibrators and pointing sources were made every 2 hours throughout the run. All observed calibration sources used to derive the flux calibration factor for that run. Planets provided beam maps and primary flux calibration sources. Uranus and Mars were observed during both runs, and Neptune was also observed on the May 2004 run.

## 3.3 Data Reduction

### 3.3.1 Pointing and Flux Calibration

A pointing model was generated from beam maps of planets, Galactic HII regions, and the protostellar source IRAS 16293–2422, which lies within the Ophiuchus cloud complex. For May 2003, the root-mean-square (rms) pointing uncertainty was  $6''$ , based on the dispersion of the centroid of IRAS 16293–2422 after the pointing model was applied. For May 2004, the rms pointing uncertainty was  $2''$  to  $3''$ ; however, the number of IRAS 16293–2422 observations is small (seven), so the rms is not well characterized.

A flux density calibration curve was generated for each run from observations of

planets and secondary calibrators (Sandell, 1994) throughout each night and over a range of elevations, thereby sampling a large range in atmospheric optical depths.

### 3.3.2 Iterative Mapping

The iterative mapping procedure described in §2.3.4 was run for each section of Ophiuchus and for each observing run. The May/June 2003 data and May 2004 were iteratively mapped separately because they required different calibration and pointing corrections. The final map is a weighted average of the maps from each run.

### 3.3.3 Source Identification

After the final calibrated maps were created, sources were identified as in §2.4.1. The average coverage in the map varies from 40 hits per pixel, or 20 sec of integration time, in most of the L1688 region, to 60 hits pixel<sup>-1</sup> (30 sec of integration) in the northeastern streamer. Only parts of the map with coverage greater than 0.22 times the maximum coverage (corresponding to a range in the local rms over the map of a factor of  $\sim 2$ ), were used for source finding. Finally, a peak-finding routine was used to detect sources in the Wiener-filtered map above 4 times the local rms noise.

A detection limit as low as  $4\sigma$  was necessary to detect some previously known sources from earlier SCUBA 850  $\mu\text{m}$  surveys (Johnstone et al., 2000). This limit was not strict enough to avoid all false detections, however, and some artifacts were incorrectly identified as sources. Therefore, each source was also inspected by eye. Most of the artifacts were unambiguous because they were found close to the edges of the map or were caused by striping: one pixel wide and extended in one of the scan directions. Single-pixel peaks were also discarded, which might have excluded some faint sources. Although in principle it should be possible to recover structure up to the array size of  $7.5'$ , it was found in chapter 2 that structures larger than approximately  $4'$  are severely affected by cleaning, and not well recovered by iterative mapping.

## 3.4 Results

### 3.4.1 General Cloud Morphology

The map of the cloud is shown in figure 3.2, with known regions identified. Our map covers  $10.8 \text{ deg}^2$  ( $51.4 \text{ pc}^2$  at a distance of 125 pc), which is equivalent to  $1.4 \times 10^5$  resolution elements given the beam size of  $31''$ . Most of the compact emission is confined to the L1688 cluster region. Several sources are also detected in L1709, L1689, and around the extensively studied Class 0 protostar IRAS 16293–2422. No emission that is extended  $\gtrsim 2'$  is seen in the map.

The noise in the final map varied from section to section because of differences in the number of good observations and changes in sky noise. A map of the noise (figure 3.3) shows the variations in noise in the different map areas, ranging from 11 to 30 mJy beam $^{-1}$ . The average rms in the regions of the map where most sources were detected was about 27 mJy beam $^{-1}$ . High noise regions are apparent in figure 3.3 as a strip above L1709 and in the regions around strong sources, especially in the L1688 cluster.

We detected 44 sources with signal-to-noise greater than  $4\sigma$  that were confirmed as real by inspection. Sources are listed in table 3.1 and identified as Bolo 1, etc. All sources were identified in the main cloud and eastern streamer sections. Figure 3.4 plots the positions of the sources as red circles on the grayscale 1.1 mm map, with insets showing magnifications of the densest source regions. We did not detect any sources in the northeastern streamer, where the noise is lowest. Most of the sources are concentrated in the previously well-studied regions in Ophiuchus, suggesting that dense cores are highly clustered in the Ophiuchus cloud. Figure 3.4 contains blowups of the main regions of emission, including the well known Ophiuchus cluster in L1688, L1689, IRAS 16293–2422, and L1709.

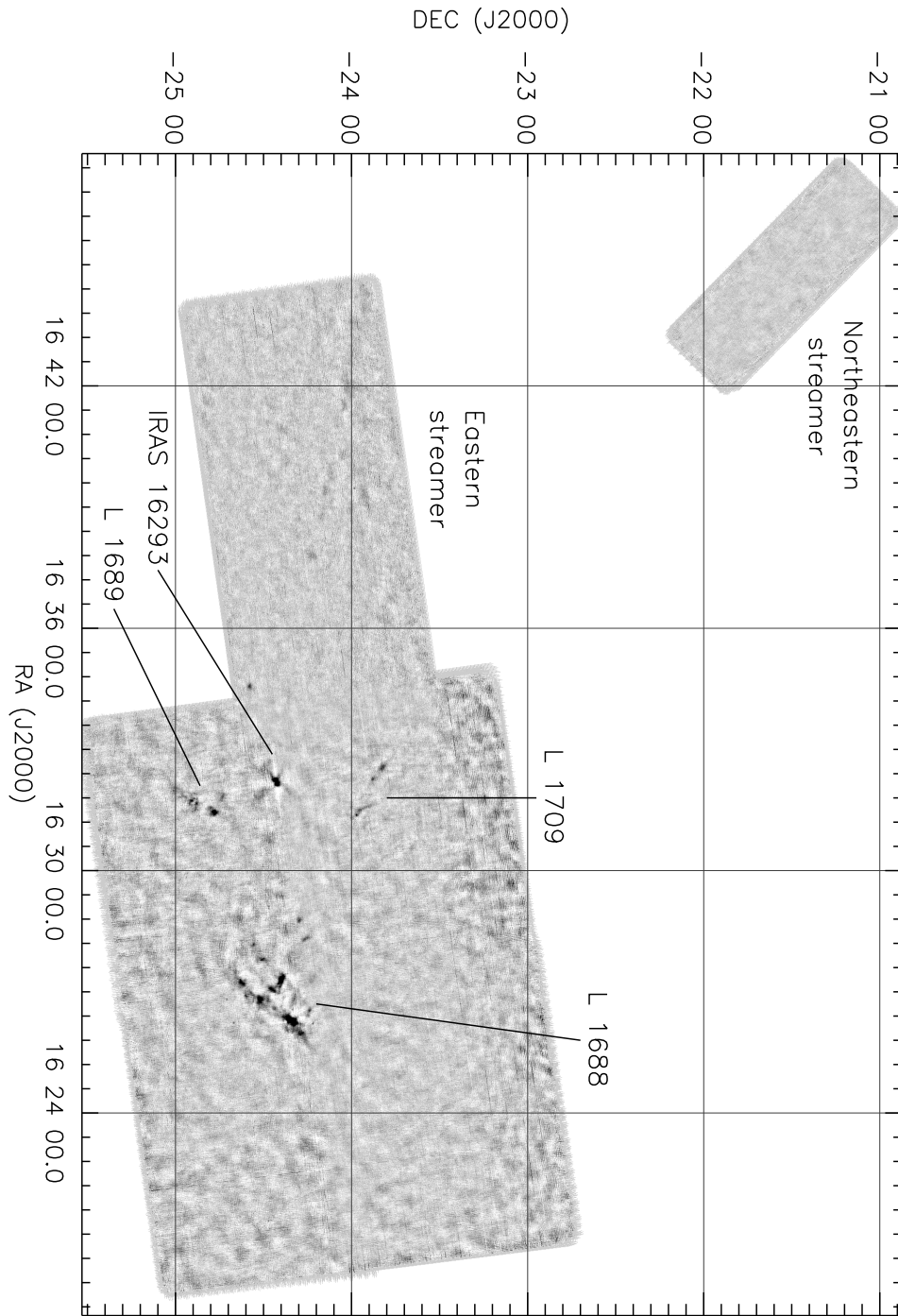


Figure 3.2 1.1 mm Bolocam map of  $10.8 \text{ deg}^2$  ( $51.4 \text{ pc}^2$  at  $d = 125 \text{ pc}$ ) in the Ophiuchus molecular cloud, with  $10''$  pixels and a beam size of  $31''$ . The gray scale is proportional to intensity weighted by the coverage to avoid confusion by noise in regions with low coverage. Well-known regions and those discussed by name in the text are indicated.

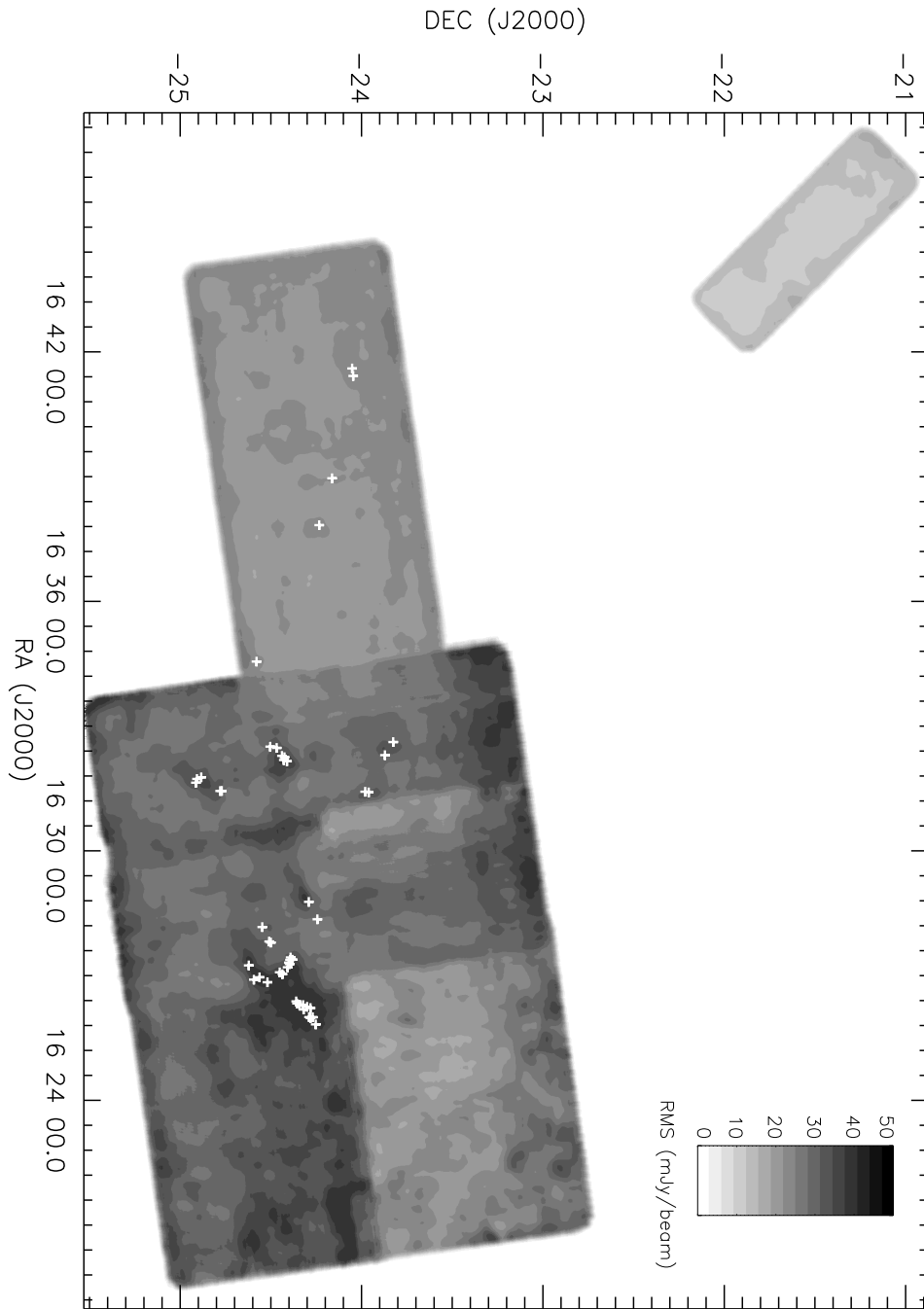


Figure 3.3 A map of the noise in gray scale with sources indicated by white plus signs. The gray scale runs from 11 mJy beam<sup>-1</sup> to 30 mJy beam<sup>-1</sup>. High noise regions are apparent in a strip above L1709, and in the area containing L1688. Note the increased noise near bright sources caused by residual systematics from sky subtraction.

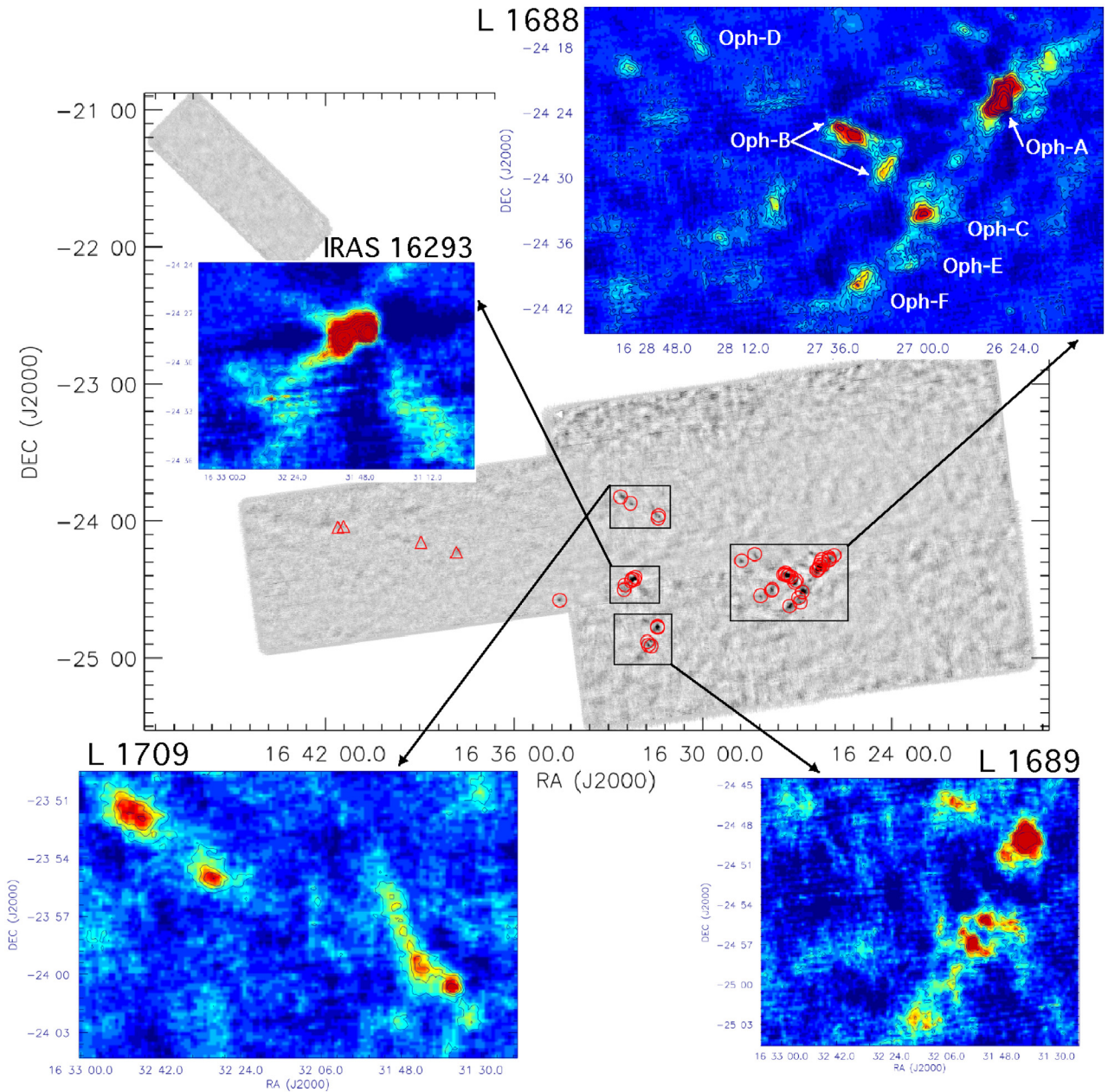


Figure 3.4 1.1 mm Bolocam map of the Ophiuchus molecular cloud, with the positions of the 44 sources detected above  $4\sigma$  marked as circles. The gray scale shows the intensity *not* weighted by the coverage. The inset maps show particular regions on an expanded scale. The conversion from intensity to color differs among the insets to cover the large range of intensity. Sources marked by triangles in the eastern streamer are below the  $4\sigma$  detection limit so are tentative detections (but see figure 3.5).

Visual comparison to previous maps of dust continuum emission in the L1688 cluster indicates reasonable agreement on the overall shape of the emission, considering differences in resolution (Motte et al., 1998) and wavelength (Johnstone et al., 2000). However, detailed comparison of source positions in table 3.1 and those in Johnstone et al. (2000) shows that a substantial number of our sources are separated into multiple sources by Johnstone et al. (2000), who used the the Clumpfind algorithm on data with better resolution by a factor of two; in the same area, they list 48 sources compared to our 23. The list of 48 includes some small, weak, but unconfused sources that we do not see. Assuming that  $S_\nu \propto \nu^3$ , as expected for emission in the Rayleigh-Jeans limit with an opacity proportional to  $\nu$ , some of these sources should still lie above our detection limit, but not far above.

The Stanke et al. (2006) map covers  $1.3 \text{ deg}^2$  of L1688 (slightly less than one of the boxes defined by the grid lines in figure 3.2), with lower noise ( $\sim 10 \text{ mJy}$ ) and a slightly smaller beam ( $24''$ ) at nearly the same wavelength (1.2 mm). Their images are qualitatively very similar to the L1688 inset image in figure 3.4. However, they find 143 sources in this region, using wavelet analysis and Clumpfind, and by essentially cleaning down to the noise. They include sources that are less than  $3\sigma$  but extended. These differences make it difficult to compare sources in detail, but it appears that many of our sources would be split into multiple sources by Stanke et al. (2006).

Another useful comparison is with the work of Visser, Richer, & Chandler (2002) in a less crowded area of Ophiuchus. They found 5 sources along a filament in L1709; we find three sources in reasonable agreement in position, while L1709-SMM3 and L1709-SMM5 from their paper are blended into Bolo 30 in table 3.1. We see additional structure below the  $4\sigma$  limit extending to the northeast of that group of sources that is not seen in the Visser et al. (2002) map. The most diffuse source in their map, L1709-SMM4, shows up strongly in our map, but shifted about  $25''$  east, an example of position shifts caused by different sensitivity to large scale structure and source finding algorithms. Visser et al. (2002) also found a weak source in L1704 that we do not see, consistent with our detection limit. These points should be borne in mind when we compare source statistics to those of previous work in later sections.

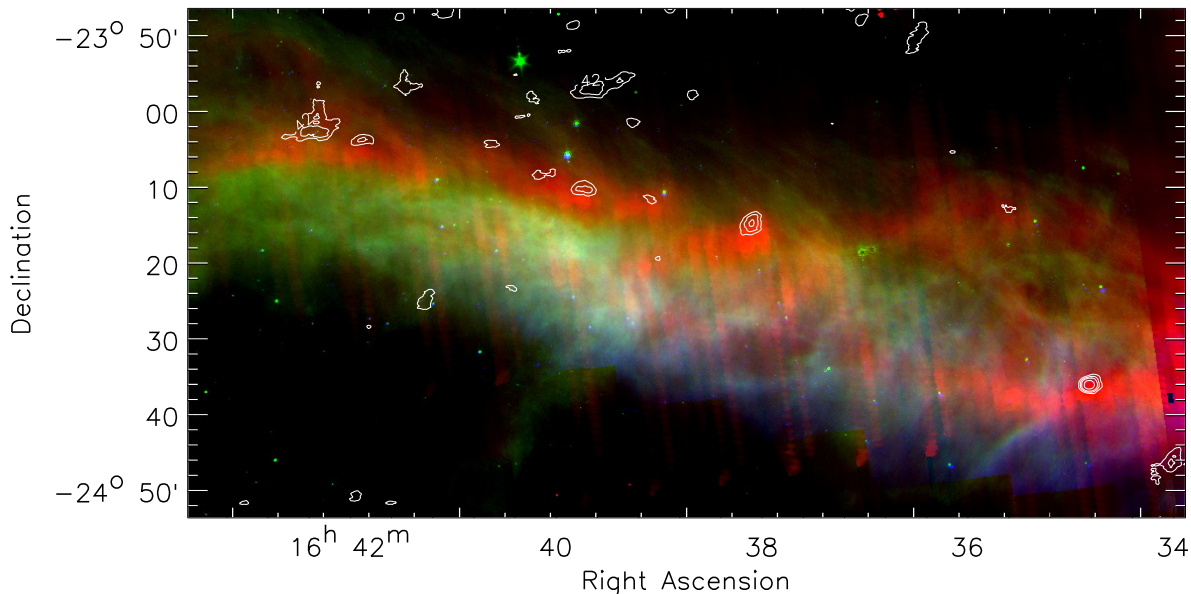


Figure 3.5 Emission at 1.1 mm seen with Bolocam in the eastern streamer (2, 3, 4, 6, 8  $\sigma$  contours) is overlaid on a three color image from *Spitzer*, with IRAC band 4 (8  $\mu\text{m}$ ) in blue, MIPS band 1 (24  $\mu\text{m}$ ) in green, and MIPS band 3 (160  $\mu\text{m}$ ) in red. The 160  $\mu\text{m}$  map is incompletely sampled and saturated emission produces stripes. The 160  $\mu\text{m}$  map has been smoothed, but artifacts remain. The 1.1 mm emission does line up with the relatively opaque part of the streamer, as indicated by weak emission at 8  $\mu\text{m}$  and strong emission at 160  $\mu\text{m}$ .

Several diffuse emission peaks were observed in the eastern streamer, an area that includes L1712 ( $16^{\text{h}} 38^{\text{m}}, -24^{\circ} 26'$ ) and L1729 ( $16^{\text{h}} 43^{\text{m}}, -24^{\circ} 06'$ ). However, these cores, though visible by eye in the map, are only  $3\sigma$  detections; they are listed separately as tentative detections in table 3.1, and are not included in our source statistics. These sources are in a long filament of extinction that extends east from the main cloud (Cambr sy 1999; Ridge et al. 2006). We believe at least some of these sources are real, based on inspection by eye and comparison to *Spitzer* maps of the region. In figure 3.5, the tentative 1.1 mm sources align with an elongated structure that is dark at 8  $\mu\text{m}$ , but bright at 160  $\mu\text{m}$ , suggestive of a cold, dense filament. This filament was previously observed in  $^{13}\text{CO}$  (Loren, 1989) and  $\text{C}^{18}\text{O}$  (Tachihara et al., 2000), but it has not been mapped in the millimeter continuum until now. While the overall morphology is similar to that seen in  $\text{C}^{18}\text{O}$  (Tachihara et al., 2000), only

Bolo 45 has an obvious counterpart,  $\rho$ -Oph 10, in the table of Tachihara et al. (2000).

The most striking feature of the Bolocam map of Ophiuchus is the lack of 1.1 mm emission in regions outside of known regions of star formation, even in areas with significant extinction ( $A_V > 3$  mag). Figure 3.6 shows the Bolocam map of Ophiuchus overlaid with extinction contours constructed using the *NICE* method (e.g., Lada, Alves, & Lada 1999; Huard et al. 2006), making use of 2MASS sources, and convolving the line-of-sight extinctions with a Gaussian beam with FWHM of  $5'$ . This method depends on background stars to probe the column densities through the cloud (see also §2.4.2) In order to calibrate the extinction map, we identified two “off-cloud” regions, which were free of structure and assumed to be non-extincted regions near the Ophiuchus cloud. These off-cloud regions contained a total of more than 13,000 stars and were  $0.6 \times 0.6$  and  $1.5 \times 0.2$  fields centered on  $\alpha = 16^h 44^m 00^s$ ,  $\delta = -22^\circ 54' 00''$  and  $\alpha = 16^h 39^m 12^s$ ,  $\delta = -25^\circ 24' 00''$  (J2000.0), respectively. The mean intrinsic H–K color of the stars in these off-cloud fields was found to be  $0.190 \pm 0.003$  magnitudes. We assume  $A_V = 15.9 E(H-K)$  to convert to  $A_V$  (Rieke & Lebofsky, 1985).

The 1.1 mm sources are all in regions of high extinction, but not all regions of substantial extinction have Bolocam sources. For example, we found no 1.1 mm sources in the small northeastern streamer of Ophiuchus that could be confirmed as real by eye despite having much lower noise in this region than for the rest of the map. The beam-averaged extinctions in the northeastern streamer are  $A_V \approx 3$  to 8 magnitudes. The  $4\sigma$  detection limit in this region corresponds to objects with masses as small as  $0.06 M_\odot$  (see §3.4.2). Thus even in relatively high extinction regions, much of the Ophiuchus cloud appears devoid of dense cores down to a very low mass limit.

## 3.4.2 Source Properties

### 3.4.2.1 Positions and Photometry

Table 3.1 lists the position, peak flux density, and signal-to-noise ratio (S/N) of the 44  $4\sigma$  sources, with the four  $3\sigma$  detections in the eastern streamer are listed separately.

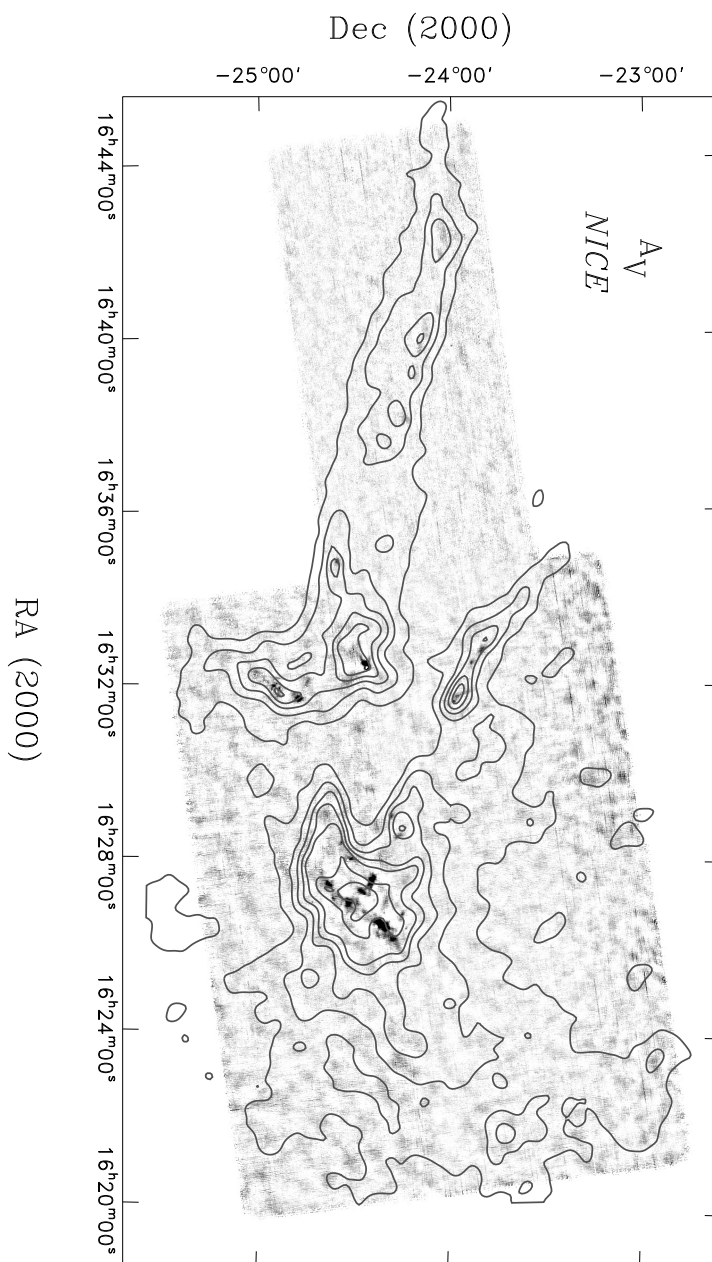


Figure 3.6 Visual extinction ( $A_V$ ) contours calculated from 2MASS data using the *NICE* method, overlaid on the grayscale 1.1 mm map. Contours are  $A_V = 2, 4, 6, 8, 10, 15,$  and  $20$  mag with an effective resolution of  $5'$ .

All statistical analysis is based on the 44 secure detections only. For known sources the most common names from the literature are also given. Some are known to host protostars while others may be starless. The uncertainty in the peak flux density is the local rms beam $^{-1}$  and does not include an additional 15% systematic uncertainty.

Table 3.1. Identified sources in Ophiuchus

ID	RA (2000) (h m s)	Dec (2000) (° ' ")	Peak (Jy/beam)	S/N	other names
Bolo 1	16 25 59.1	-24 18 16.2	0.26 (0.03)	4.5	
Bolo 2	16 26 08.1	-24 20 00.6	0.39 (0.03)	4.7	CRBR 2305.4-1241?
Bolo 3	16 26 09.6	-24 19 15.6	0.31 (0.03)	4.1	SMM J16261-2419 (1)
Bolo 4	16 26 09.9	-24 20 28.6	0.40 (0.03)	6.2	GSS26?
Bolo 5	16 26 20.7	-24 22 17.0	0.37 (0.04)	4.3	GSS30-IRS3 (2); SMM J16263-2422 (1); LFAM1 (3)
Bolo 6	16 26 22.9	-24 20 00.9	0.27 (0.03)	4.5	SMM J16263-2419 (1)
Bolo 7	16 26 24.7	-24 21 07.5	0.41 (0.04)	4.9	A-MM4? (5)
Bolo 8	16 26 27.2	-24 22 26.7	1.38 (0.04)	16.0	SM1 FIR1 (4); A-MM5/6? (5); SMM J16264-2422 (1)
Bolo 9	16 26 27.6	-24 23 36.6	2.70 (0.04)	45.2	SM1 FIR2 (4); SM1N
Bolo 10	16 26 29.7	-24 24 28.8	2.66 (0.04)	47.5	SM2
Bolo 11	16 26 32.6	-24 24 45.3	1.25 (0.04)	14.8	A-MM8 (5)
Bolo 12	16 27 00.7	-24 34 17.0	0.54 (0.03)	8.4	SMM J16269-2434 (1); C-MM3 (5)
Bolo 13	16 27 04.3	-24 38 47.4	0.23 (0.03)	4.8	E-MM2d (5); SMM J16270-2439 (1)
Bolo 14	16 27 07.9	-24 36 54.3	0.26 (0.03)	4.4	SMM J16271-2437a/b (1); Elias29?
Bolo 15	16 27 12.2	-24 29 18.9	0.44 (0.04)	6.1	B1-MM2/3 (5); IRAS 16242-2422; SMM J16272-2429 (1)
Bolo 16	16 27 15.1	-24 30 12.6	0.45 (0.04)	7.1	SMM J16272-2430 (1); B1-MM4 (5)
Bolo 17	16 27 22.3	-24 27 36.3	0.40 (0.04)	4.4	B2-MM4 (5)
Bolo 18	16 27 25.2	-24 40 28.9	0.47 (0.03)	9.7	F-MM2 (5); IRS43? (5)
Bolo 19	16 27 27.0	-24 26 57.1	0.62 (0.04)	7.4	SMM J16274-2427s (1)
Bolo 20	16 27 29.1	-24 27 11.1	0.69 (0.04)	9.4	B2-MM8 (5); SMM J16274-2427b (1)
Bolo 21	16 27 33.1	-24 26 48.8	0.53 (0.04)	6.8	B2-MM15 (5); SMM J16275-2426 (1)
Bolo 22	16 27 33.4	-24 25 57.3	0.50 (0.03)	9.4	B2-MM13 (5); SMM J16275-2426 (1)
Bolo 23	16 27 36.7	-24 26 36.2	0.40 (0.03)	5.1	B2-MM17 (5)
Bolo 24	16 27 58.3	-24 33 09.7	0.29 (0.03)	6.0	
Bolo 25	16 28 00.1	-24 33 42.8	0.33 (0.03)	6.0	H-MM1 (8)
Bolo 26	16 28 21.0	-24 36 00.0	0.23 (0.03)	5.5	
Bolo 27	16 28 32.1	-24 17 43.4	0.17 (0.03)	4.1	D-MM3/4 (5)
Bolo 28	16 28 57.7	-24 20 33.7	0.28 (0.03)	5.8	I-MM1 (8)
Bolo 29	16 31 36.4	-24 00 41.7	0.28 (0.03)	7.0	L1709-SMM1 (6); IRS63
Bolo 30	16 31 37.2	-24 01 51.9	0.29 (0.03)	6.3	L1709-SMM3,5 (6)
Bolo 31	16 31 40.0	-24 49 58.0	0.45 (0.03)	6.8	
Bolo 32	16 31 40.4	-24 49 26.4	0.45 (0.03)	7.4	
Bolo 33	16 31 52.6	-24 58 00.8	0.20 (0.03)	4.5	
Bolo 34	16 31 58.0	-24 57 38.8	0.26 (0.03)	5.2	
Bolo 35	16 32 00.6	-24 56 13.9	0.19 (0.03)	4.5	IRAS 16289-2450; L1689S; IRS67
Bolo 36	16 32 22.5	-24 27 47.5	1.65 (0.03)	17.9	

Source photometry is presented in table 3.2, which gives flux densities within set apertures of 40", 80", and 120", as well as the best-estimate total flux density. Only apertures smaller than the distance to the nearest neighboring source are used, to avoid contamination from neighboring sources. The total flux density is calculated in the largest aperture (up to 160") that does not include flux from nearby sources. Uncertainties in table 3.2 do not include an additional 15% systematic uncertainty.

Table 3.1 (cont'd)

ID	RA (2000) (h m s)	Dec (2000) (° ' ")	Peak (Jy/beam)	S/N	other names
Bolo 37	16 32 24.7	-24 28 51.2	3.03 (0.03)	80.7	IRAS 16293-2422
Bolo 38	16 32 28.6	-24 28 37.5	1.07 (0.03)	17.0	
Bolo 39	16 32 30.1	-23 55 18.4	0.25 (0.03)	4.8	L1709-SMM2 (6)
Bolo 40	16 32 30.8	-24 29 28.3	0.74 (0.03)	14.7	
Bolo 41	16 32 42.3	-24 31 13.0	0.15 (0.02)	4.5	
Bolo 42	16 32 44.1	-24 33 21.6	0.20 (0.03)	4.3	
Bolo 43	16 32 49.2	-23 52 33.9	0.28 (0.03)	4.1	L1709-SMM4? (6); LM182
Bolo 44	16 34 48.3	-24 37 24.6	0.21 (0.02)	5.6	L1689B-3
Tentative detections in the eastern streamer					
Bolo 45	16 38 07.8	-24 16 36.4	0.15 (0.02)	3.6	$\rho$ -Oph 10 (7)
Bolo 46	16 39 15.8	-24 12 20.8	0.10 (0.02)	3.2	
Bolo 47	16 41 44.5	-24 05 20.4	0.14 (0.02)	3.0	
Bolo 48	16 41 55.6	-24 05 41.6	0.12 (0.02)	3.0	

Note. — Numbers in parentheses are  $1\sigma$  errors. The peak flux density is the peak pixel value in the  $10''$  pixel $^{-1}$  unfiltered map (without the Wiener filter applied). The uncertainty in the peak flux density is the local (calculated within a  $400''$  box) rms beam $^{-1}$ , calculated from the noise map, and does not include an additional 15% systematic uncertainty from calibration uncertainties and residual errors after iterative mapping. Other names listed are the most common identifications from the literature, and are not meant to be a complete list. References – (1) Johnstone et al. 2000; (2) Castelaz et al. 1985; Weintraub et al. 1993; (3) Leous et al. 1991; (4) Mezger et al. 1992; (5) Motte et al. 1998; (6) Visser et al. 2002; (7) Tachihara et al. 2000; (8) Johnstone et al. 2004

Table 3.2. Photometry, masses, sizes, and morphology for sources in Ophiuchus

ID	Flux(40'') (Jy)	Flux(80'') (Jy)	Flux(120'') (Jy)	Total Flux (Jy)	Mass (10K) ( $M_{\odot}$ )	Peak $A_V$ (mag)	FWHM (minor, '')	FWHM (major, '')	PA ( $^{\circ}$ )	$\langle n \rangle$ $\text{cm}^{-3}$	Morphology <sup>1</sup>
Bolo1	0.34 (0.03)	0.82 (0.07)	1.55 (0.1)	2.13 (0.13)	1.29 (0.08)	18	88 (0.9)	133 (1.4)	-24 (2)	$2 \times 10^5$	multiple, extended, round
Bolo2	...	...	...	0.46 (0.03)	0.28 (0.02)	27	55 (0.6)	58 (0.6)	29 (17)	$4 \times 10^5$	multiple, round
Bolo3	0.46 (0.04)	...	...	0.58 (0.05)	0.35 (0.03)	22	53 (0.7)	58 (0.8)	88 (10)	$5 \times 10^5$	multiple, extended, round
Bolo4	...	...	...	0.49 (0.03)	0.3 (0.02)	28	52 (0.6)	56 (0.7)	-10 (11)	$5 \times 10^5$	multiple, elongated
Bolo5	0.55 (0.05)	1.32 (0.1)	...	1.61 (0.11)	0.97 (0.07)	26	64 (0.8)	70 (0.8)	26 (11)	$7 \times 10^5$	multiple, extended, elongated
Bolo6	0.32 (0.05)	...	...	0.58 (0.08)	0.35 (0.05)	19	59 (1.3)	67 (1.5)	-61 (14)	$3 \times 10^5$	multiple, extended, weak
Bolo7	0.56 (0.05)	...	...	1.08 (0.08)	0.65 (0.05)	29	56 (0.6)	66 (0.8)	-50 (6)	$7 \times 10^5$	multiple, extended, elongated
Bolo8	1.86 (0.05)	...	...	3.93 (0.09)	2.37 (0.05)	98	55 (0.2)	63 (0.2)	81 (2)	$3 \times 10^6$	multiple, extended, round
Bolo9	4.2 (0.05)	...	...	6.49 (0.08)	3.92 (0.05)	191	46 (0.1)	56 (0.1)	-68 (1)	$9 \times 10^6$	multiple, extended, round
Bolo10	3.42 (0.05)	...	...	3.42 (0.05)	2.07 (0.03)	189	44 (0.1)	56 (0.1)	22 (1)	$5 \times 10^6$	multiple, extended, round
Bolo11	1.72 (0.05)	...	...	1.72 (0.05)	1.04 (0.03)	88	49 (0.2)	54 (0.2)	50 (3)	$2 \times 10^6$	multiple, extended, round
Bolo12	0.86 (0.04)	2.11 (0.09)	3.91 (0.13)	5.56 (0.17)	3.36 (0.1)	38	105 (0.5)	125 (0.6)	-45 (2)	$4 \times 10^5$	extended, elongated
Bolo13	0.35 (0.04)	0.75 (0.08)	1.35 (0.12)	1.35 (0.12)	0.82 (0.07)	16	76 (1.2)	96 (1.5)	44 (5)	$2 \times 10^5$	multiple, extended, elongated, weak
Bolo14	0.32 (0.05)	0.68 (0.09)	1.19 (0.14)	1.19 (0.14)	0.72 (0.08)	18	66 (1.2)	108 (2.)	41 (3)	$2 \times 10^5$	multiple, extended, weak
Bolo15	0.61 (0.05)	...	...	0.92 (0.07)	0.56 (0.04)	31	50 (0.7)	64 (0.8)	19 (4)	$8 \times 10^5$	multiple, extended, elongated
Bolo16	0.7 (0.05)	...	...	1.08 (0.07)	0.65 (0.04)	32	51 (0.6)	62 (0.7)	-58 (5)	$9 \times 10^5$	multiple, extended, elongated
Bolo17	0.54 (0.05)	...	...	1.03 (0.09)	0.62 (0.06)	29	56 (0.8)	68 (1.)	-62 (6)	$6 \times 10^5$	multiple, extended, elongated
Bolo18	0.65 (0.04)	1.49 (0.08)	2.64 (0.11)	3.76 (0.15)	2.27 (0.09)	33	96 (0.6)	149 (1.)	41 (1)	$2 \times 10^5$	extended, elongated
Bolo19	...	...	...	0.8 (0.04)	0.48 (0.02)	44	54 (0.4)	58 (0.4)	-8 (9)	$7 \times 10^5$	multiple, round
Bolo20	...	...	...	0.87 (0.04)	0.53 (0.02)	49	51 (0.4)	57 (0.4)	80 (6)	$9 \times 10^5$	multiple, extended, round
Bolo21	0.82 (0.04)	...	...	1.01 (0.06)	0.61 (0.03)	37	53 (0.5)	60 (0.5)	40 (5)	$9 \times 10^5$	multiple, extended, round
Bolo22	0.77 (0.04)	...	...	0.96 (0.06)	0.58 (0.03)	35	54 (0.5)	55 (0.5)	-75 (61)	$10 \times 10^5$	multiple, extended, elongated
Bolo23	0.55 (0.04)	...	...	0.68 (0.05)	0.41 (0.03)	28	53 (0.6)	56 (0.7)	-88 (20)	$7 \times 10^5$	multiple, extended, round

Table 3.2 (cont'd)

ID	Flux(40'') (Jy)	Flux(80'') (Jy)	Flux(120'') (Jy)	Total Flux (Jy)	Mass (10K) ( $M_{\odot}$ )	Peak $A_V$ (mag)	FWHM (minor, '')	FWHM (major, '')	PA ( $^{\circ}$ )	$\langle n \rangle$ $\text{cm}^{-3}$	Morphology <sup>1</sup>
Bolo24	0.39 (0.04)	...	...	0.39 (0.04)	0.24 (0.02)	21	48 (0.8)	57 (0.9)	14 (7)	$5 \times 10^5$	multiple, extended, elongated
Bolo25	0.39 (0.04)	...	...	0.39 (0.04)	0.24 (0.02)	23	47 (0.8)	56 (0.9)	-66 (7)	$5 \times 10^5$	multiple, elongated
Bolo26	0.3 (0.03)	0.63 (0.07)	1.14 (0.1)	1.62 (0.14)	0.98 (0.08)	16	108 (1.4)	132 (1.8)	84 (5)	$9 \times 10^4$	extended, elongated
Bolo27	0.23 (0.03)	0.52 (0.07)	0.97 (0.1)	1.48 (0.13)	0.9 (0.08)	12	89 (1.1)	157 (2.)	58 (2)	$2 \times 10^4$	extended, elongated, weak
Bolo28	0.37 (0.03)	0.86 (0.07)	1.55 (0.1)	2.17 (0.13)	1.31 (0.08)	20	102 (1.)	113 (1.1)	74 (8)	$2 \times 10^5$	extended, elongated
Bolo29	0.28 (0.04)	...	...	0.5 (0.07)	0.3 (0.04)	20	54 (1.)	57 (1.1)	11 (29)	$5 \times 10^5$	multiple, extended, elongated
Bolo30	0.28 (0.04)	...	...	0.46 (0.06)	0.28 (0.04)	20	46 (1.1)	57 (1.3)	66 (9)	$6 \times 10^5$	multiple, extended, elongated
Bolo31	...	...	...	0.55 (0.03)	0.33 (0.02)	32	54 (0.5)	57 (0.5)	-61 (15)	$5 \times 10^5$	multiple, round
Bolo32	...	...	...	0.53 (0.03)	0.32 (0.02)	31	56 (0.5)	58 (0.5)	74 (20)	$4 \times 10^5$	multiple, round
Bolo33	0.26 (0.04)	0.57 (0.07)	...	0.57 (0.07)	0.35 (0.04)	14	54 (1.2)	65 (1.5)	-33 (10)	$4 \times 10^5$	multiple, extended, elongated, weak
Bolo34	0.38 (0.04)	0.87 (0.08)	...	0.87 (0.08)	0.52 (0.05)	19	59 (0.9)	68 (1.1)	-73 (9)	$4 \times 10^5$	multiple, extended, elongated
Bolo35	0.22 (0.04)	0.39 (0.08)	...	0.46 (0.09)	0.28 (0.06)	13	66 (1.7)	77 (2.1)	40 (14)	$2 \times 10^5$	multiple, extended, elongated, weak
Bolo36	1.35 (0.04)	...	...	2.49 (0.07)	1.51 (0.04)	117	53 (0.2)	57 (0.2)	-17 (5)	$2 \times 10^6$	multiple, extended, round
Bolo37	3.63 (0.04)	...	...	4.47 (0.06)	2.7 (0.04)	214	35 (0.1)	45 (0.1)	49 (1)	$3 \times 10^7$	multiple, round
Bolo38	1.52 (0.04)	...	...	2.33 (0.06)	1.41 (0.04)	76	54 (0.2)	54 (0.2)	-15 (38)	$2 \times 10^6$	multiple, extended, round
Bolo39	0.26 (0.04)	0.55 (0.07)	0.94 (0.11)	1.29 (0.14)	0.78 (0.08)	17	101 (1.7)	128 (2.2)	-51 (6)	$9 \times 10^4$	extended
Bolo40	1.11 (0.04)	...	...	1.67 (0.06)	1.01 (0.04)	52	49 (0.3)	58 (0.3)	55 (3)	$2 \times 10^6$	multiple, extended, round
Bolo41	0.2 (0.03)	0.39 (0.06)	0.73 (0.09)	0.85 (0.1)	0.51 (0.06)	11	40 (1.2)	53 (1.6)	-27 (9)	$2 \times 10^6$	multiple, extended, elongated, weak
Bolo42	0.19 (0.03)	0.39 (0.07)	0.72 (0.1)	0.83 (0.11)	0.5 (0.07)	14	53 (1.6)	66 (1.9)	80 (11)	$6 \times 10^5$	multiple, extended, elongated, weak
Bolo43	0.33 (0.04)	0.84 (0.07)	1.63 (0.11)	2.45 (0.15)	1.48 (0.09)	20	98 (0.9)	143 (1.3)	47 (2)	$1 \times 10^5$	extended, elongated
Bolo44	0.3 (0.03)	0.72 (0.06)	1.21 (0.09)	1.71 (0.12)	1.03 (0.08)	15	96 (1.1)	119 (1.4)	55 (4)	$1 \times 10^5$	extended, round
Tentative detections in the eastern streamer											
Bolo45	0.20 (0.03)	0.47 (0.06)	0.94 (0.09)	1.36 (0.11)	0.82 (0.06)	11	123 (1.5)	157 (1.9)	-51 (4)	$5 \times 10^4$	extended, elongated, weak

Table 3.2 (cont'd)

ID	Flux(40'')	Flux(80'')	Flux(120'')	Total Flux (Jy)	Mass (10K) ( $M_{\odot}$ )	Peak $A_V$ (mag)	FWHM (minor, '')	FWHM (major, '')	PA ( $^{\circ}$ )	$\langle n \rangle$ $\text{cm}^{-3}$	Morphology <sup>1</sup>
Bolo46	...	...	...	0.08 (0.02)	0.05 (0.01)	7	64 (3)	153 (6)	7 (3)	$9 \times 10^3$	extended, round, weak
Bolo47	0.13 (0.03)	...	...	0.15 (0.04)	0.09 (0.02)	10	87 (2)	112 (3)	-42 (9)	$2 \times 10^4$	multiple, extended, round, weak
Bolo48	...	...	...	0.86 (0.13)	0.52 (0.08)	8	84 (2)	111 (3)	-8 (7)	$1 \times 10^5$	multiple, extended, round, weak

Note. — Masses are calculated according to equation (2.3) from the total flux density assuming a single dust temperature of  $T_D = 10K$  and a dust opacity at 1.1mm of  $\kappa_{1.1mm} = 0.0114 \text{ cm}^2 \text{ g}^{-1}$ . Peak  $A_V$  is calculated from the peak flux density as in equation (2.2). FWHM and PAs are from a Gaussian fit; the PA is measured in degrees east of north of the major axis.  $\langle n \rangle$  is the mean particle density as calculated from the total mass and the deconvolved average FWHM size. Numbers in parentheses are  $1\sigma$  uncertainties. Uncertainties for masses are from photometry only, and do not include uncertainties from  $\kappa$ ,  $T_D$ , or  $d$ , which can be up to a factor of a few or more. Uncertainties for the FWHM and PA are formal fitting errors from the elliptical Gaussian fit; additional uncertainties of 10% – 15% apply to the FWHM, and  $\sim 5^{\circ}$  to the PA (determined from simulations).

<sup>1</sup>The morphology keyword(s) given indicates whether the source is multiple (within  $3'$  of another source), extended (major axis FW at  $2\sigma > 1'$ ), elongated (axis ratio at  $4\sigma > 1.2$ ), round (axis ratio at  $4\sigma < 1.2$ ), or weak (peak flux densities less than 8.7 times the rms beam  $^{-1}$ ).

The distribution of flux densities for the 44 detected sources is shown in figure 3.7. This figure compares the distribution of peak flux densities to the total flux densities. The peak flux density distribution has a mean of  $\sim 0.6 \text{ Jy beam}^{-1}$ . The total flux density distribution has a mean of about  $1.6 \text{ Jy}$ . The shaded region in figure 3.7 indicates the  $4\sigma$  detection limit, which varies throughout the map from  $\sim 0.06 - 0.12 \text{ Jy beam}^{-1}$ . The flux density distributions shown in figure 3.7 are similar to the distributions of peak and total flux densities of Bolocam sources in Perseus (chapter 2) in that the total flux density distribution is shifted from the peak distribution because most sources are larger than the beam.

### 3.4.2.2 Sizes and Shapes

Sizes and position angles (PA) in table 3.2 were found by fitting a 2D elliptical Gaussian to each source. The size of any given source is limited by the distance to its nearest neighbor, because emission at radii greater than half the distance to the nearest source is masked out for the Gaussian fit. This method also ensures that the size and the total flux density of a source are measured in approximately the same aperture. The sources in the L1688 cluster are quite crowded and source sizes and fluxes may be affected by nearby sources.

Figure 3.8 shows the distributions of source major and minor axis FWHMs. Both distributions peak between  $50''$  and  $60''$ , and the average axis ratio is 1.2. Only a few sources have large FWHM sizes larger than  $100''$ . Many of the sources in the map are part of more extended structures. Large clumps of emission can be broken into several smaller sources by our source-finding routine if the clumps contain several local peaks. Our method of finding cores and the filamentary nature of the dense gas in Ophiuchus could result in a slight elongation of the sources. However, the majority (61%) of sources in the entire sample are not elongated at the half-max contour (axis ratio  $< 1.2$ ).

Morphology keywords for each source are also listed in table 3.2. Of the 44 sources, 18 are classified as round, with axis ratio at the  $4\sigma$  level less than 1.2. The difference between this result and the fact that 61% had axis ratios from the Gaussian fits  $< 1.2$

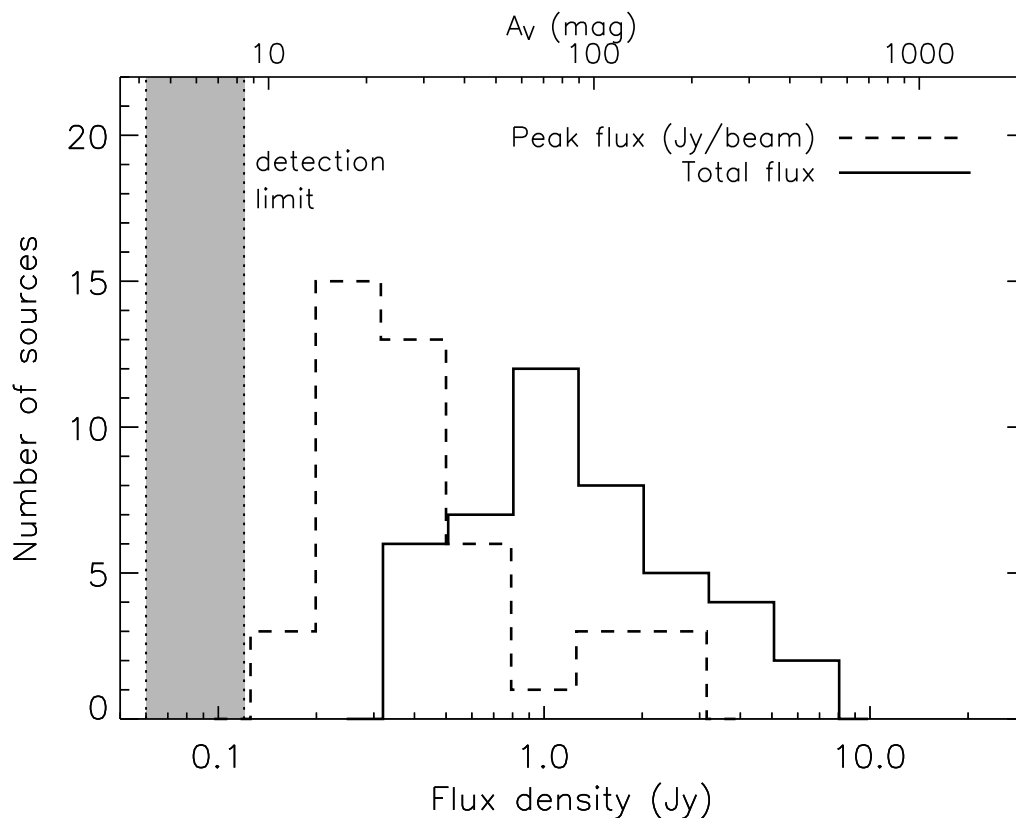


Figure 3.7 The distribution of the peak flux densities (dashed line) and total flux densities (solid line) of the  $4\sigma$  sources. The peak flux density is the peak pixel value in the map, in  $\text{Jy beam}^{-1}$ . The top axis shows the value of  $A_V$  inferred from the emission, using equation (2.2). The mean peak flux density of the sample is  $0.6 \text{ Jy/beam}$  and the mean total flux is  $1.6 \text{ Jy}$ . The  $4\sigma$  detection limit varies from  $0.06$  to  $0.12 \text{ Jy/beam}$  across the map due to variations in the local noise, although most sources are detected in the higher noise regions. The range in noise is indicated by the shaded region.

suggests spherical sources embedded along more elongated filamentary structures. Visual inspection indicates that at lower contours sources are usually elongated along the local filamentary structure, as seen both in the still lower contours and in the extinction map (figure 3.6). Future polarimetric observations could determine the role of magnetic fields in the filamentary structures.

Of the 44 sources, 36 are multiple, reflecting the strongly clustered nature of the sources (see §3.5.3). Also 36 sources are extended. Only two sources are neither multiple nor extended. We see no evidence for a population of isolated, small, dense

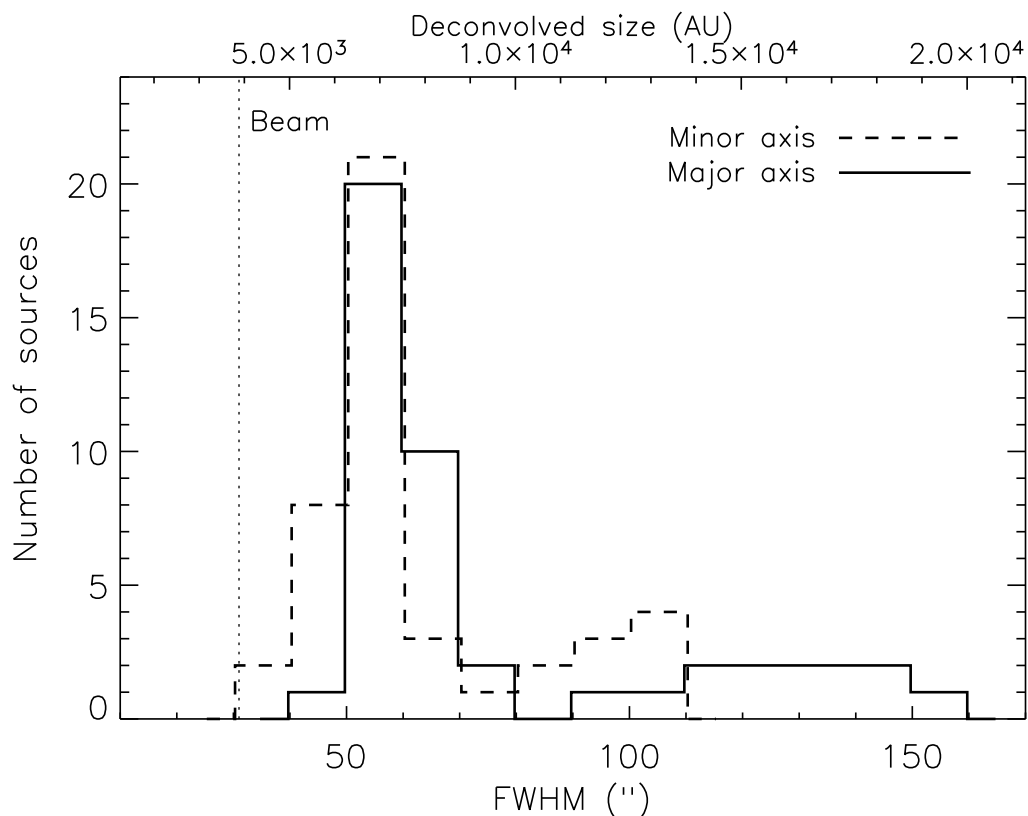


Figure 3.8 The distribution of source FWHM minor axis (dashed line) and major axis (solid line), as determined from an elliptical Gaussian fit. The beam size is indicated by the dotted line. The mean FWHM sizes of the sample are  $62''$  (minor) and  $77''$  (major). The top axis gives deconvolved sizes in AU, assuming a  $31''$  beam and  $d = 125$  pc.

cores.

### 3.4.2.3 Masses, Densities, and Extinctions

Isothermal masses were calculated as in chapter 2 (equation (2.3)), and are listed in table 3.2. Uncertainties in the masses are from the uncertainty in the total flux density only and do not include uncertainties in distance, opacity, and  $T_D$ , which combined can be at least a factor of 4. The total mass of the 44  $4\sigma$  sources is  $42 M_\odot$ , with a mean of  $0.96 M_\odot$ , and a range from  $0.24$  to  $3.9 M_\odot$ . The Johnstone et al. (2004) survey of Ophiuchus found a larger total mass ( $50 M_\odot$ ) in a smaller area than we covered. Those authors assumed a larger distance (160 pc), a value for  $\kappa_\nu$

at 850  $\mu\text{m}$  that is 1.1 times higher than OH5 dust, and  $T_D = 15$  K. If we used the assumptions of Johnstone et al. (2004) for our data, we would derive a total mass of 32  $M_\odot$  from our data. The source of the difference between our result for total mass in cores and that of Johnstone et al. (2004) does not seem to be explained by the assumptions used to obtain mass. More likely, it arises from differences in methods of defining sources. If we integrate all the areas of the map above  $4\sigma$ , we get 131 Jy, which translates to 79  $M_\odot$ , using our usual assumptions, or 60  $M_\odot$ , using the assumptions of Johnstone et al. (2004). Thus about half the mass traced by 1.1 mm emission cannot be assigned to a particular core, primarily because it is in confused regions.

de Geus et al. (1989) estimate a mass for the whole Ophiuchus cloud of  $10^4 M_\odot$  while we find 2300  $M_\odot$  above  $A_V = 2$ . We calculate the cloud mass using the 2MASS extinction map and a conversion from  $A_V$  to column density of  $N(\text{H}_2)/A_V = 0.94 \times 10^{21} \text{ mag cm}^{-2}$  (Bohlin, Savage, & Drake, 1978). Thus the percentage of cloud mass in dense cores is between 0.4% and 1.8%. This fraction is even lower than that found in chapter 2 for Perseus (between 1% and 3%).

Mean densities (calculated as in §2.4.3) are quite high compared to the surrounding cloud, ranging from  $\langle n \rangle = 9 \times 10^4 \text{ cm}^{-3}$  to  $3 \times 10^7 \text{ cm}^{-3}$ , with an average value of  $1.6 \times 10^6 \text{ cm}^{-3}$ . The free-fall timescale estimated from this mean density is only  $2.7 \times 10^4$  yr. Peak extinctions calculated from the peak 1.1 mm flux density (table 3.2 and figure 3.7) range from  $A_V = 11$  to 214 mag for the  $4\sigma$  sources, with a mean value of 43 mag. Values for the tentative detections in the eastern streamer range from  $A_V = 7$  to 11 mag.

Peak extinctions within the cores should be distinguished from the surrounding cloud extinction as traced by the 2MASS extinction map. While reddened 2MASS sources probe low-to-moderate extinctions within the Ophiuchus cloud, the sensitivity of the 2MASS observations is not sufficient to probe reliably the high extinction regions traced by the millimeter emission. By considering both tracers of extinction, the morphology of the cloud can be inferred over a large range of column densities, from the diffuse and vast regions of the cloud (containing most of the mass) to the

densest cores. A quantitative comparison between 1.1 mm cores and cloud extinction will be made in §3.5.4.

## 3.5 Discussion

### 3.5.1 Completeness

Figure 3.9 shows the distribution of source mass versus size, where the size is the geometric average of the major and minor FWHM for each source. The minimum detectable mass and source size are related because we detect sources from their peak flux density, but calculate the mass from the total flux density. Therefore, we are biased against detecting large, faint, low-mass sources. For Gaussian sources, the mass detection limit as a function of size is simply related to the point source detection limit:

$$M_{lim}(\theta_s) = M_{lim}^{ps} (\theta_s/\theta_b)^2 [1 - \exp(-4 \ln 2 (120/\theta_s)^2)], \quad (3.1)$$

where  $M_{lim}^{ps}$  is the detection limit for a point source, and  $\theta_s$  and  $\theta_b$  are the FWHM of source and beam, respectively. The last factor corrects for flux from sources larger than our largest aperture, but has very little effect except at the largest sizes. This Gaussian completeness curve (which is essentially a line with  $M \propto R^2$ , where  $R$  is the radius) is plotted in the middle panel of figure 3.9 (solid lines). The two lines represent the range in rms over the map.

The real mass completeness limit is more complicated, even for Gaussian sources, as a result of the reduction and detection processes applied to the data. Empirical 10%, 50%, and 90% completeness limits are also plotted in figure 3.9 (bottom, middle, and top panels, respectively). These limits were determined by introducing simulated sources with a range of masses and sizes (from 30'' to 100'') into a portion of the Ophiuchus data with no real, then processing the map identically to the real data, as described in §2.5.1. The resulting completeness limits indicate what percentage of simulated sources with a particular size and mass were detected above  $4\sigma$  in the

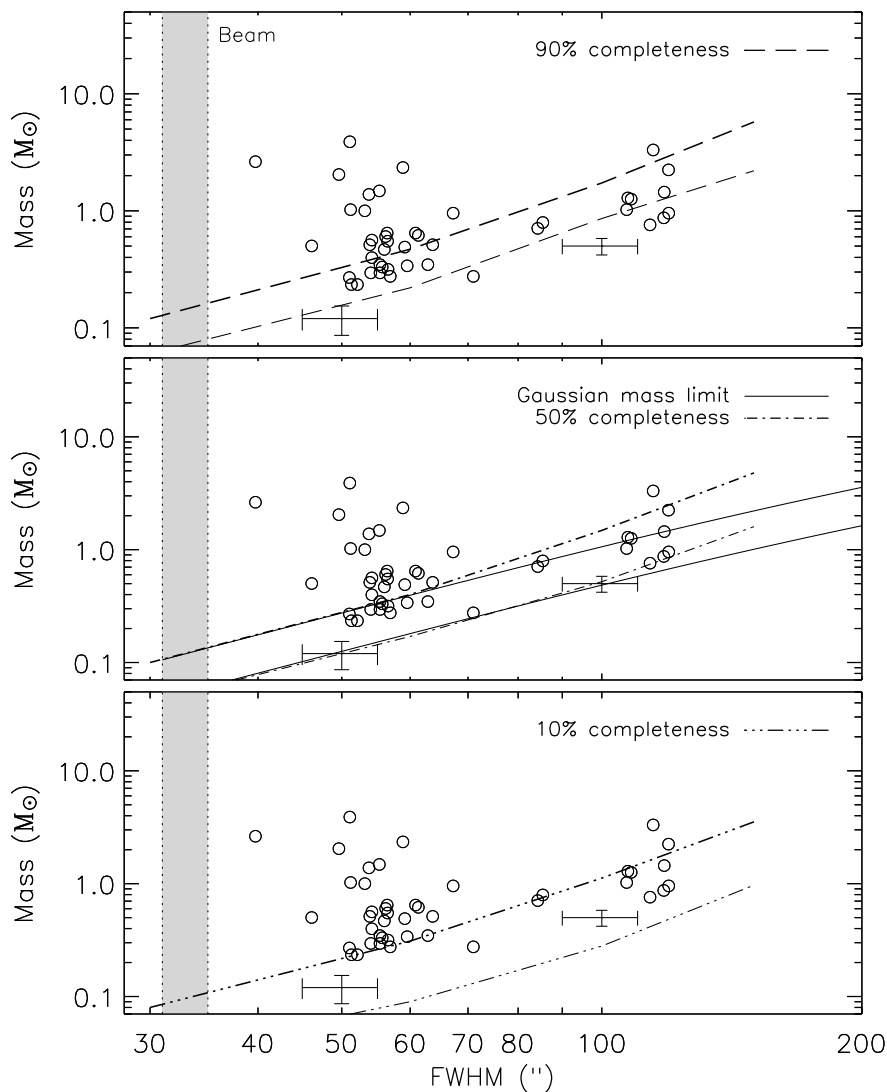


Figure 3.9 Distribution of source mass versus FWHM size. The size is the geometric average of the FWHM of the major and minor axes as given in table 3.1. The maximum size of the pointing-smear beam is represented by the shaded regions. Solid lines are the 50% analytic mass detection limit as a function of size for Gaussian sources (equation (3.1)). Empirical 90% (top panel), 50% (middle panel), and 10% (bottom panel) completeness limits are indicated, derived using Monte Carlo methods with simulated sources and taking into account the effects of cleaning, iterative mapping, and optimal filtering. Each completeness limit is calculated both in a low rms region (lower line) and a high rms region (upper line). Most real sources are found in the higher rms regions. Representative error bars for 50'' and 100'' FWHM sources near the detection limit are shown, as estimated from Monte Carlo simulations.

Wiener-convolved map. Because the local rms varies substantially across the map, completeness limits have been calculated both in low rms (20 mJy beam<sup>-1</sup>, lower line in each panel) and high rms (25 to 30 mJy beam<sup>-1</sup>, upper line) regions.

Most of the 44 sources are found in the higher rms regions of the map, corresponding to the upper curves in figure 3.9. Some of this noise is caused by mapping artifacts near strong sources (figure 3.3). Very large sources (FWHM > 100'') are not fully recovered by the iterative mapping routine (see chapter 2), and therefore tend to have a higher mass limit than expected for a simple scaling with source size. This is illustrated in the middle panel of figure 3.9, where the empirical completeness limit (dash-dot line) rises above the Gaussian limit (solid line) for large sources. Typical 1 $\sigma$  error bars in  $M$  and FWHM are shown for 50'' and 100'' FWHM sources near the detection limit. The uncertainty in mass is from the uncertainty in the integrated flux (including the 5% uncertainty from the cleaning process, but not the absolute calibration uncertainty), and the uncertainty in size is estimated from simulations.

The distribution of source mass versus size values in figure 3.9 does not look like a distribution of constant density cores of varying sizes ( $M \propto R^3$ ), nor like a collection of cores with constant column density ( $M \propto R^2$ ). Rather, it looks as if there are two populations, with different sizes but, given the completeness limitations, similar masses.

### 3.5.2 The Core Mass Distribution

Figure 3.10 shows the differential ( $dN/dM$ ) core mass distribution (CMD) for the 44 secure detections. These include both starless cores and cores with protostars. The masses are taken from table 3.2, and error bars are  $\sqrt{N}$  statistical errors only. The shaded regions on the figure represent the range in detection limit for a point source (left), and the 50% completeness limit for sources with a FWHM of 70'' (right), which is approximately the average FWHM of the sample. We do not attempt to correct for incompleteness in the mass function. Most sources are found in the higher noise regions of the map; therefore the mass function is likely to be incomplete below 0.5

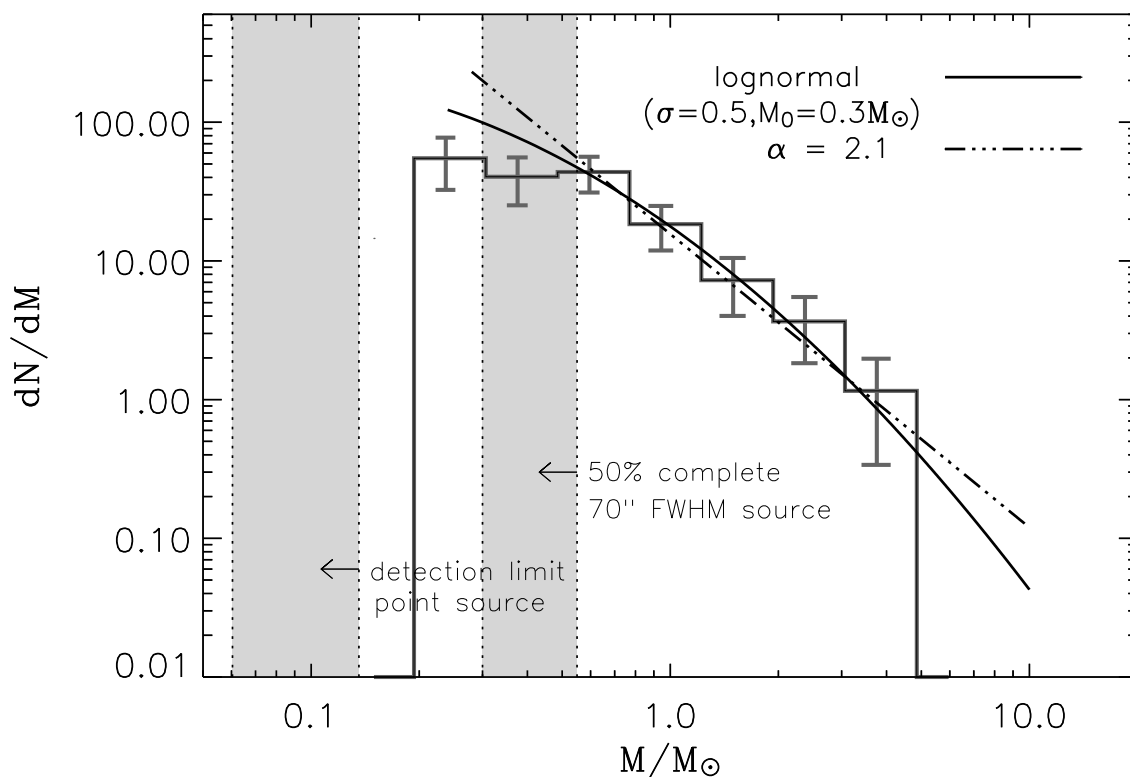
$M_{\odot}$ .

Figure 3.10 Differential mass distribution of all detected sources for masses calculated with  $T_D = 10$  K. The range in completeness, due to the range in local rms, is indicated by the shaded regions. To the left is the range in detection limit for a point source, and to the right is the range in 50% completeness limit for  $70''$  FWHM sources, which is similar to the average source size of the sample. The best fitting power law ( $\alpha = 2.1$ ) is shown, as well as the best-fitting lognormal function.

The CMD above  $0.5 M_{\odot}$  can be fitted with either a power law ( $N(M) \propto M^{-\alpha}$ ), for which the best fit is  $\alpha = 2.1 \pm 0.3$ , or with a lognormal function (equation (2.5)), for which we find  $\sigma_M = 0.5 \pm 0.4$  and  $M_0 = 0.3 \pm 0.7 M_{\odot}$  (where  $\sigma_M$  is the width of the distribution, and  $M_0$  is the characteristic mass). The power law fit has a reduced chi-squared of  $\chi_r^2 = 0.4$ , and the lognormal fit  $\chi_r^2 = 0.3$ . The slightly better  $\chi_r^2$  value for the lognormal function reflects the tendency of the distribution to flatten at lower masses, but incompleteness prevents us from distinguishing between these two functions.

The CMD depends on assumptions about distance, opacity, and dust temperature. Experiments in which cores in the main cluster were given higher temperatures, or small cores were given higher temperatures, produced little change in the mass distribution. If cores in the L1688 cluster are assigned  $T_D = 20$  K and other cores assigned  $T_D = 10$  K, the best-fit value becomes  $\alpha = 2.2$  for  $M > 0.5 M_\odot$ , insignificantly different. However, the evidence for a turnover at low masses became even less significant. Such effects should be considered before inferring turnovers in CMDs.

Johnstone et al. (2000) (see their figure 7) fit the cumulative mass distribution for 850  $\mu\text{m}$  cores within the L1688 region, assuming  $T_D = 20$  K, with a broken power law. They found  $\alpha_1 = 1.5$  for masses less than about  $0.6 M_\odot$  and  $\alpha_2 = 2.5$  for  $M > 0.6 M_\odot$ . The Johnstone et al. (2000) sample is complete down to about  $M \sim 0.4 M_\odot$ . If we assume  $T_D = 20$  K, the best-fit power law slope remains  $\alpha = 2.1$ , but our completeness limit becomes  $0.2 M_\odot$ . Thus, our mass function declines less rapidly than that of Johnstone et al. (2000), but the difference is not very significant. Since Johnstone et al. (2000) split some of our sources into multiple, smaller sources, it is not unexpected that they would find a larger value of  $\alpha$ . Stanke et al. (2006) do not give a table of masses, but their CMD extends up to roughly  $3 M_\odot$ , similar to our result, despite differences in source identification and mass calculation. They argue for breaks in their CMD around  $0.2$  and  $0.7 M_\odot$ , with  $\alpha \sim 2.6$  for large masses. Similarly, Motte et al. (1998) found  $\alpha = 2.5$  above  $0.5 M_\odot$  for a broken power-law fit to cores in the Ophiuchus cluster. Broken power-law fits tend to produce steeper slopes at higher masses, and the slopes are steeper if a higher break mass is assumed, suggesting that lognormal fits may be appropriate.

The CMD is naturally compared to predictions from models of turbulent fragmentation in molecular clouds. Padoan & Nordlund (2002) argue that turbulent fragmentation naturally produces a power law with  $\alpha = 2.3$  (for the differential CMD that we plot). However, Ballesteros-Paredes et al. (2006) question this result, showing that the shape of the CMD depends strongly on Mach number in the turbulence. As the numerical simulations develop further, the observed CMD will provide a powerful observational constraint, with appropriate care in turning the simulations into

observables.

The shape of the CMD may also be related to the process that determines final stellar masses. Assuming the simplest case in which a single process dominates the shape of the stellar initial mass function (IMF), the IMF should closely resemble the original CMD if stellar masses are determined by the initial fragmentation into cores (Adams & Fatuzzo, 1996). Alternatively, if stellar masses are determined by other processes, such as further fragmentation within cores, merging of cores, competitive accretion, or feedback, the IMF need not be related simply to the CMD (e.g., Ballesteros-Paredes et al. 2006).

The IMF itself is still uncertain (Scalo, 2005). For example, the Salpeter IMF would have  $\alpha = 2.35$  (Salpeter, 1955) using our conventions, but more recent work on the local IMF finds evidence for a break in the slope around  $1 M_{\odot}$ . The slope above the break depends on the choice of break mass. For example, Reid, Gizis, & Hawley (2002) find  $\alpha = 2.5$  above  $0.6 M_{\odot}$ , and  $\alpha = 2.8$  above  $1 M_{\odot}$ . Chabrier (2003) suggests  $\alpha = 2.7$  ( $M > 1 M_{\odot}$ ), while Schröder & Pagel (2003) finds  $\alpha = 2.7$  for  $1.1 < M_{\star} < 1.6 M_{\odot}$  and  $\alpha = 3.1$  for  $1.6 < M_{\star} < 4 M_{\odot}$ . Given the uncertainties and the differences between fitting single and broken power laws, all these values for  $\alpha$  are probably consistent with each other and with determinations of the CMD.

Currently, we cannot separate prestellar cores from more evolved objects in Ophiuchus, so a direct connection to the IMF is difficult to make. After combining these data with *Spitzer* data it will be possible to determine the evolutionary state of each source and compare the mass function of prestellar cores only (chapter 6).

### 3.5.3 Clustering

The majority of the sources detected with Bolocam in Ophiuchus are very clustered. Of the 44 sources, 36 are multiple (table 3.2) with a neighboring source within  $3'$ , corresponding to 22500 AU at a distance of 125 pc. The average separation for the entire sample is  $153''$ , or 19,000 AU. If we consider only sources in the L1688 region for comparison to previous studies, the mean separation is  $116''$ , or 14,500 AU. The

*median* separation in L1688 is substantially smaller ( $69'' = 8600$  AU). The median separation in L1688 is very similar to the mean size of the sources in the sample,  $68''$ . This indicates that many source pairs are barely resolved. It also means that the measured size of many sources is limited to something like the mean separation, since the Gaussian fitting routine takes into account the distance to the nearest neighbor when determining source size.

The median separation of 8600 AU for the L1688 cluster is only slightly larger than the fragmentation scale of 6000 AU suggested by Motte et al. (1998) in their study of the main Ophiuchus cluster by examining the mean separation between cores in their data. Resolution effects likely play a role here, as our resolution (3900 AU) is approximately twice that of Motte et al. (1998). Stanke et al. (2006) find two peaks in the distribution of source separations of neighboring cores ( $\sim 5000$  AU and  $\sim 13,000$  AU), suggesting that they also distinguish the cores in the Ophiuchus cluster from those in the more extended cloud. The median core separation is still smaller than the median separation of T Tauri stars in Taurus of 50,000 AU (Gomez et al., 1993) as pointed out by Motte et al. (1998).

Another description of source clustering is provided by the two-point correlation function, as was used in chapter 2 and in Johnstone et al. (2000). Figure 3.11 plots  $H(r)$ ,  $w(r)$ , and  $\log(w(r))$  versus the log of the distance between sources,  $r$ .  $H(r)$  is the fractional number of source pairs with a separation between  $\log(r)$  and  $\log(r) + d\log(r)$ , and is plotted in figure 3.11 (upper panel) for the Ophiuchus sample (solid line), and for a uniform random distribution of sources (dashed lines). Because it is discontinuous from the rest of the map, the northeastern streamer is not included in this analysis.

The top panel of figure 3.11 shows an excess in  $H_s(r)$  over the random sample  $H_r(r)$  for small separations. The excess indicates that the sources in Ophiuchus are not randomly distributed within the cloud, but clustered on small scales. The middle panel shows that the two-point correlation function for the Ophiuchus data exceeds zero by  $2.5 \sigma$  for  $r < 4 \times 10^4$  AU, while the random distribution shows no correlation ( $w(r) = 0$ ). The correlation function can be fit with a power law, ( $w(r) \propto r^{-\gamma}$ ,

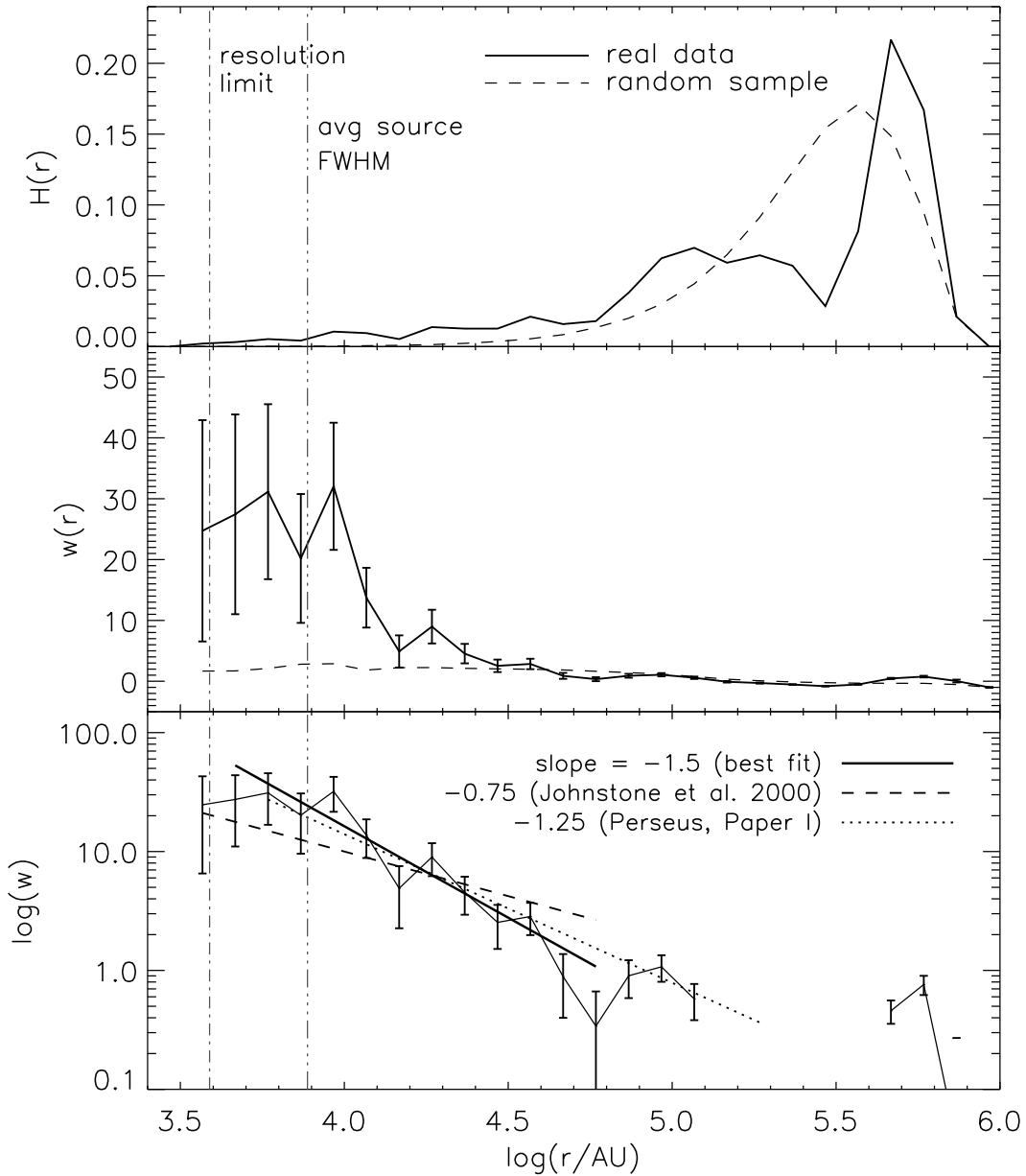


Figure 3.11 Top:  $H(r)$ , the fractional number of source pairs between  $\log(r)$  and  $d\log(r)$ , versus  $\log(r)$ . The solid line indicates the real data, and the dashed line is for a uniform random distribution of sources with the same RA/Dec limits as the real sample. In all plots, the resolution limit and the average source FWHM are shown. Middle: Two-point correlation function  $w(r)$ , with  $\sqrt{N}$  errors. Bottom: Log of  $w(r)$ , with power-law fits. The best fit slope is  $-1.5 \pm 0.3$ . The slope found by Johnstone et al. (2000) in Ophiuchus is shallower ( $-0.75$ ), while the slope found in Perseus in chapter 2 was similar ( $-1.25 \pm 0.06$ ).

bottom panel); the best fit gives  $\gamma = 1.5 \pm 0.3$  for  $1 \times 10^4 \text{ AU} < r < 4 \times 10^4 \text{ AU}$ , with  $\chi_r^2 = 1.2$ . The correlation function for Perseus (chapter 2) was characterized by  $\gamma = 1.25 \pm 0.06$  ( $\chi_r^2 = 0.7$ ) for  $2 \times 10^4 \text{ AU} < r < 2 \times 10^5 \text{ AU}$ .

Stanke et al. (2006) found  $\gamma = 0.63$  out to  $r \sim 1 \times 10^5 \text{ AU}$ . Johnstone et al. (2000) also fitted the correlation for the Ophiuchus cluster with a shallower power law,  $\gamma = 0.75$  for  $r < 3 \times 10^4$  in the L1688 cluster region of Ophiuchus. This power law is also shown in figure 3.11, but it clearly does not fit our data. Johnstone et al. (2000) were able to measure the correlation function to smaller scales,  $r = 4.5 \times 10^3 \text{ AU}$ , than this study, which may result in some discrepancy in the best-fit power law between the two data sets. The correlation function does appear flatter at smaller separations, but the slope there may be complicated by blending. If the correlation function is restricted to sources in the L1688 cluster, the slope becomes more consistent with those found by Johnstone et al. (2000) and Stanke et al. (2006).

We conclude from this analysis that the sources in Ophiuchus are clearly clustered. Determining the parameters of the correlation function is complicated by effects of map size and resolution.

### 3.5.4 Extinction threshold

Johnstone et al. (2004) suggested that there is a threshold at  $A_V = 15 \text{ mag}$  in Ophiuchus for the formation of cores, with 94% of the mass in cores found at or above that extinction level. They did see cores below that level, but they were faint (low peak flux) and low in mass. Johnstone et al. (2004) mapped  $4 \text{ deg}^2$  of Ophiuchus at  $850 \mu\text{m}$  and compared their data to an extinction map of Ophiuchus created from 2MASS and R-band data as part of the COMPLETE project. Comparison of our own extinction map (figure 3.6) with the COMPLETE extinction map shows reasonable agreement, so we use our extinction map.

We use a simple analysis (see §2.5.4) to study the extinction threshold. Figure 3.12 plots the probability of finding a 1.1 mm core in Ophiuchus as a function of  $A_V$ , where the probability is calculated from the extinction map as the number of  $50''$

pixels containing a 1.1 mm core divided by the total number of pixels at a given  $A_V$ . Error bars are Poisson statistical errors.

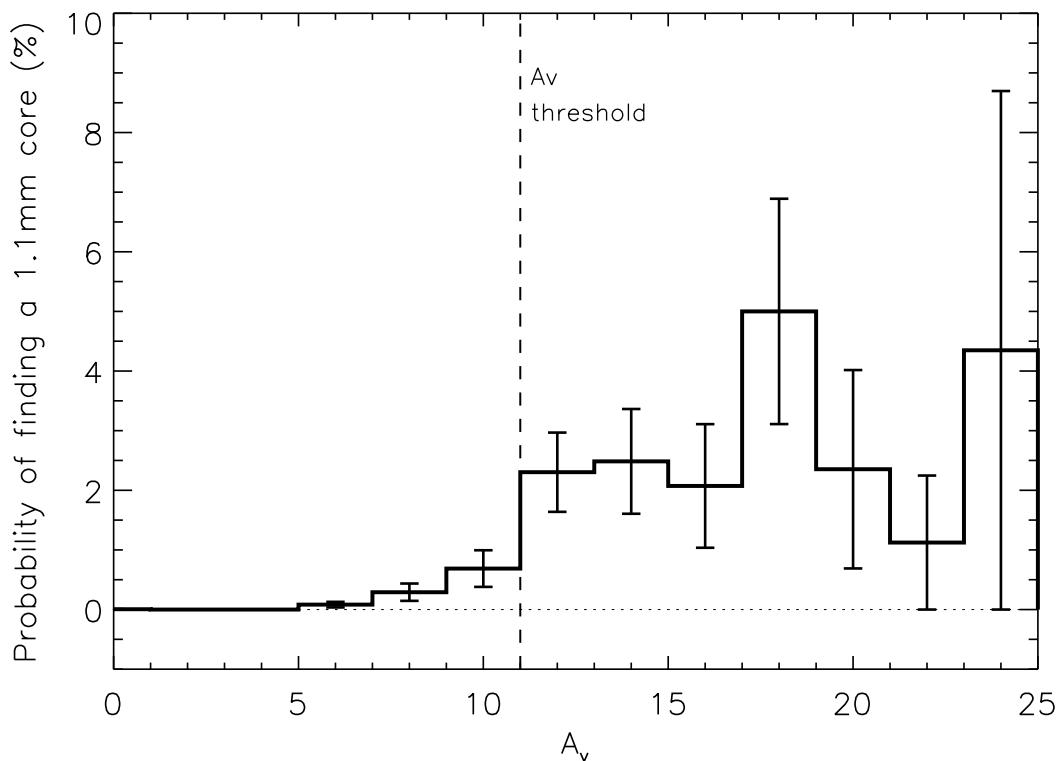


Figure 3.12 Probability of finding a 1.1 mm core as a function of  $A_V$ . The probability is the number of  $50''$  pixels at a given  $A_V$  containing one or more 1.1 mm cores, divided by the total number of pixels at that  $A_V$ . Error bars are Poisson statistical errors. The dashed vertical line shows our proposed threshold at  $A_V = 11$  mag.

Very few sources are found below  $A_V = 11$  mag, and 88% of the mass in cores is found above  $A_V = 10$  mag (see table 3.3). We suggest, therefore, that  $A_V = 11$  mag is the extinction limit for finding 1.1 mm cores in Ophiuchus. The probability of finding a core increases with  $A_V$  beyond this point, although the uncertainties are large at high  $A_V$  because there are few pixels in the extinction map at very high extinctions. This extinction limit is much higher than that found for Perseus in chapter 2 ( $A_V = 5$  mag).

To explore this issue further, we plot in figure 3.13 source total flux density, peak flux density, FWHM, and mass versus  $A_V$ . All bright (peak  $> 0.5$  Jy) and massive

( $M > 1.5M_{\odot}$ ) cores are found above the extinction threshold of  $A_V = 11$  mag. Note, however, that the tentative detections listed in table 3.1 are in regions with  $A_V < 10$  mag. In contrast to the Johnstone et al. (2004) study, we find many (12 out of the total core sample of 44) bright (total flux density  $> 3$  Jy) and massive ( $M > 2M_{\odot}$ ) sources at  $A_V < 15$  mag. Thus conclusions about thresholds likely depend on sensitivity to large structures, slight differences in extinction contours, and differing resolution.

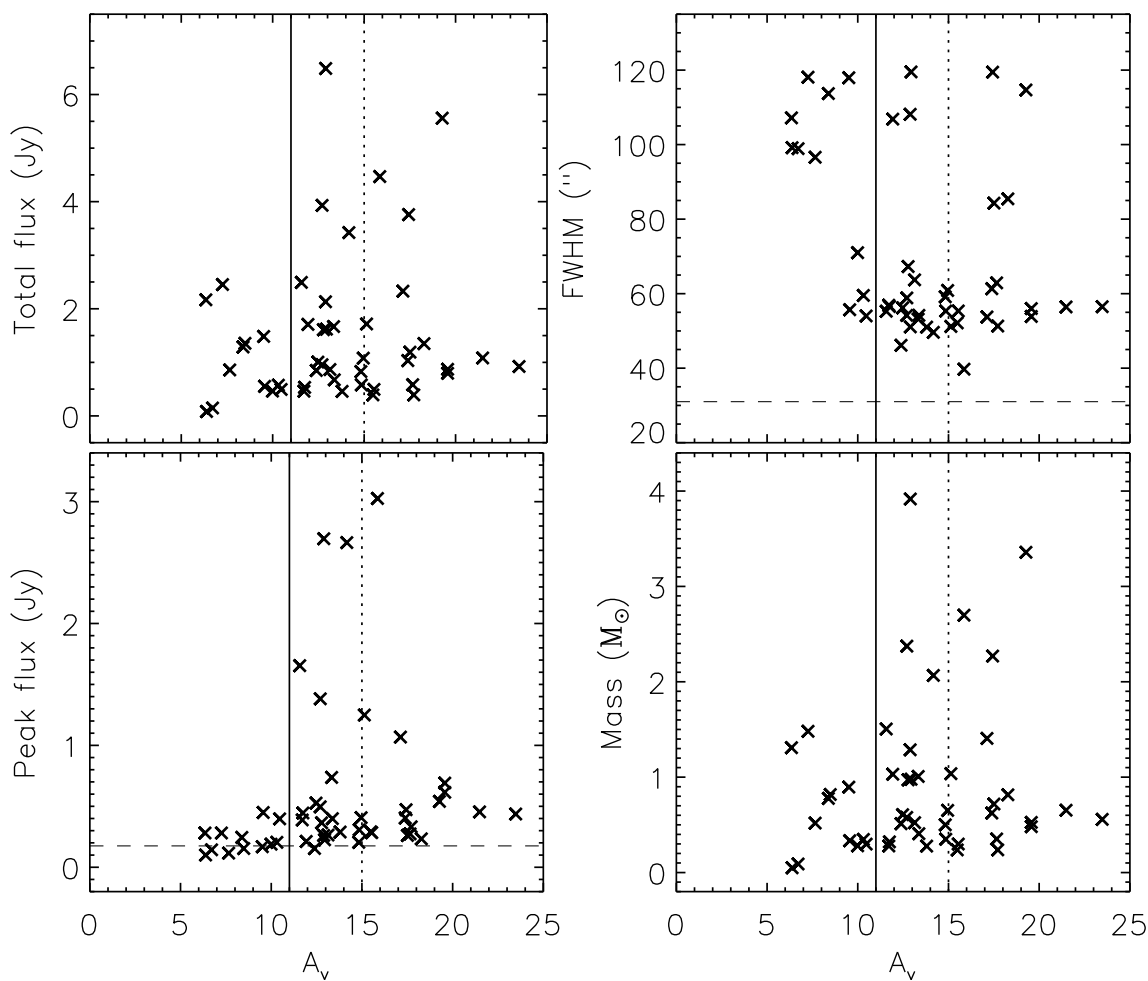


Figure 3.13 1.1 mm source properties versus  $A_V$ . The dotted vertical lines are the  $A_V = 15$  mag threshold proposed by Johnstone et al. (2004). The solid vertical line is the  $A_V = 11$  mag extinction threshold derived from figure 3.12. The dashed horizontal lines are the beam size in the upper right panel and the average  $4\sigma$  detection limit in the lower left panel.

Table 3.3. Cumulative mass as a function of extinction for sources in Ophiuchus

Min. $A_V$ mag	Area (%)	Cloud Mass ( $M_\odot$ )	Percent (%)	Core Mass ( $M_\odot$ )	Percent (%)	Mass Ratio <sup>1</sup> (%)
2	100	2300	100	42	100	1.8
4	39	1500	65	42	100	2.8
6	17	920	40	42	100	4.6
8	8.8	640	28	39	93	6.1
10	5.5	470	20	37	88	7.9
12	3.8	350	15	33	79	9.4
14	2.3	240	10	20	47	8.3
16	1.4	170	7.4	12	29	7.1
18	0.9	120	5.2	6.4	15	5.3
20	0.5	73	3.1	1.2	2.9	1.6

Note. — Cloud areas and masses are calculated from the extinction and conversions from §3.4.2.3. Core masses are taken from table 3.2.

<sup>1</sup>The Mass Ratio is computed from the ratio of core mass to cloud mass within the same contour of  $A_V$ .

Cloud areas and masses within a given  $A_V$  contour, measured from the extinction map, are listed in table 3.3 along with total core masses within the same  $A_V$  contour. The percentages of the total cloud and core masses are also given. Finally, the mass ratio, or fraction of the cloud mass that is contained in dense cores is listed in the last column. This is similar to table 2 of Johnstone et al. (2004), except that our cloud and core masses are cumulative and we use bins of  $A_V = 2$  mag. Even with our lower threshold, nearly half the total core mass lies above the  $A_V = 14$  mag contour, which occupies only 2.3% of the cloud area and 10% of the cloud mass. Dense cores are clearly concentrated in the regions of high extinction; the ratio of core to cloud mass increases from about 2% at the lowest contour ( $A_V = 2$ ) to an average of 7.4% for contours between 8 and 18 mag. (The contour above 20 mag has such little area that the core mass fraction is not very reliable.)

### 3.6 Summary

We present a 1.1 mm dust continuum emission map of 10.8 deg<sup>2</sup> of the Ophiuchus molecular cloud. We detected 44 sources at  $4\sigma$  or greater, almost all concentrated around well known clusters (near the dark clouds L1688, L1689, and L1709). A few weaker sources ( $3\sigma$ ) were seen along the eastern streamer of the cloud, coincident with a filament seen in both extinction (figure 3.6) and emission at 160  $\mu\text{m}$  (figure 3.5). These cores have been previously seen in maps of CO, but ours are the first millimeter dust continuum observations of the eastern streamer. We did not detect any emission in the northeastern streamer, and in fact most of the cloud area has no detectable sources.

Visually, the  $4\sigma$  sources appear highly clustered, and this impression is confirmed by the two-point correlation function, the fraction of multiple sources, and the median separation. Fully 82% of the sources are classified as multiple (i.e., another source lies within  $3'$ ).

Most sources are round as measured at the FWHM, but many are elongated when measured at lower contour levels. We suggest that this difference is reflective of the fact that many cores are relatively spherical condensations within more elongated filaments. Filamentary structure with embedded condensations is the dominant morphological theme.

The total mass of the 1.1 mm sources is only  $42 M_{\odot}$ , approximately 0.4% to 1.8% of the total cloud mass and lower than in Perseus (chapter 2), while the total mass in 1.1 mm emission above  $4\sigma$  is  $79 M_{\odot}$ . The differential core mass distribution (CMD) can be fitted with a power law with slope  $\alpha = -2.1 \pm 0.3$  or with a lognormal function ( $\sigma_M = 0.5 \pm 0.4$ ,  $M_0 = 0.3 \pm 0.7 M_{\odot}$ ). The CMD is similar to that in Perseus, but does not extend as high in mass, with the most massive core containing only  $3.9 M_{\odot}$ . Core mean densities are quite high, averaging  $1.6 \times 10^6 \text{ cm}^{-3}$ , implying a short free-fall time.

We suggest an extinction threshold for finding millimeter continuum sources at  $A_V = 11$  mag, higher than in Perseus but lower than found in previous studies of

Ophiuchus by Johnstone et al. (2004). Approximately half the total mass of dense cores are in contours of extinction below  $A_V = 14$  mag, which was the threshold seen by Johnstone et al. (2004). Still, the cores are clearly concentrated in a small fraction of the cloud area and mass, and in regions of relatively high extinction.

Analysis of these data in combination with the c2d *Spitzer* maps of Ophiuchus will give a more complete picture of star formation in the cloud (see chapter 6).

## Acknowledgments

We would like to thank A. Urban for assistance observing at the CSO, and other members of the larger Bolocam team for instrumental support, including A. Goldin, A. Lange, P. Maloney, and P. Rossinot. We thank the Lorentz Center in Leiden for hosting several meetings that contributed to this work. Support for this work, part of the *Spitzer* Legacy Science Program, was provided by NASA through contracts 1224608 and 1230782 issued by the Jet Propulsion Laboratory, California Institute of Technology, under NASA contract 1407. Bolocam was built and commissioned under grants NSF/AST-9618798 and NSF/AST-0098737. KEY and GL were supported by NASA under Grants NGT5-50401 and NGT5-50384, respectively, issued through the Office of Space Science. Additional support came from NASA Origins grant NNG04GG24G to NJE and NSF grant AST 02-06158 to JG. MLE acknowledges support of an NSF Graduate Research Fellowship. SG was supported in part by a Millikan fellowship at Caltech and CSO grant NSF/AST-9980846.

## Bibliography

- Adams, F. C., & Fatuzzo, M. 1996, *ApJ*, 464, 256
- Allen, L. E., Myers, P. C., DiFrancesco, J., Matheiu, R., Chen, H., & Young, E. 2002, *ApJ*, 566, 993
- Ballesteros-Paredes, J., Gazol, A., Kim, J., Klessen, R. S., Jappsen, A.-K., & Tejero, E. 2006, *ApJ*, 637, 384
- Bohlin, R. C., Savage, B. D., & Drake, J. F. 1978, *ApJ*, 224, 132
- Cambr esy, L. 1999, *A&A*, 345, 965
- Castelaz, M. W., Gehrz, R. D., Grasdalen, G. L., & Hackwell, J. A. 1985, *PASP*, 97, 924
- Chabrier, G. 2003, *PASP*, 115, 763
- de Geus, E. J., de Zeeuw, P. T., Lub, J. 1989, *A&A*, 216, 44
- Enoch, M. L., Glenn, J., Evans, N. J., II, Sargent, A. I., Young, K. E., & Huard, T. L. 2007, *ApJ*, in press
- Enoch, M. L., Young, K. E., Glenn, J., Evans, N. J., II, Golwala, S., Sargent, A. I., Harvey, P., et al. 2006, *ApJ*, 638, 293 (Paper I)
- Evans, N. J., II, Allen, L. E., Blake, G. A., Boogert, A. C. A., Bourke, T., Harvey, P. M., Kessler, J. E., et al. 2003, *PASP*, 115, 965
- Gomez, M., Hartmann, L., Kenyon, S. J., & Hewett, R. 1993, *AJ*, 105, 1927
- Goodman, A. A., 2004, in *Star Formation in the Interstellar Medium*, ASPC, 323, 171 (<http://cfa-www.harvard.edu/COMPLETE>)
- Huard, T. L., Myers, P. C., Murphy, D. C., Crews, L. J., Lada, C. J., Bourke, T. L., Crapsi, A., Evans, N. J., II, McCarthy, D. W., Jr., & Kulesa, C. 2006, *ApJ*, 640, 391

- Imanishi, K., Koyama, K., & Tsuboi, Y. 2001, *ApJ*, 557, 747
- Johnstone, D., Di Francesco, J., & Kirk, H. 2004, *ApJ*, 611, L45
- Johnstone, D., Wilson, C. D., Moriarty-Schieven, G., Joncas, G., Smith, G., Gregersen, E., & Fich, M. 2000, *ApJ*, 545, 327
- Lada, C. J., Alves, J., & Lada, E. A. 1999, in *The Physics and Chemistry of the Interstellar Medium*, editors V. Ossenkopf, J. Stutzki, G. Winnewisser, 161
- Leous, J. A., Feigelson, E. D., Andre, P., & Montmerle, T. 1991, *ApJ*, 379, 683
- Loren, R. B. 1989, *ApJ*, 338, 902
- Mezger, P. G., Sievers, A., Zylka, R., Haslam, C. G. T., Kreysa, E., & Lemke, R. 1992, *A&A*, 265, 743
- Motte, F., André, P., & Neri, R. 1998, *A&A*, 336, 150
- Padoan, P., & Nordlund, Å. 2002, *ApJ*, 576, 870
- Reid, I. N., Gizis, J. E., & Hawley, S. L. 2002, *AJ*, 124, 2721
- Ridge, N. A., Di Francesco, J., Kirk, H., Li, D., Goodman, A. A., Alves, J. F., Arce, H. G., et al. 2006, *ApJ*, 131, 2921
- Rieke, G. H., & Lebofsky, M. J. 1985, *ApJ*, 288, 618
- Salpeter, E. E. 1955, *ApJ*, 121, 161
- Sandell, G. 1994, *MNRAS*, 271, 75
- Scalo, J., 2005 in *The Stellar Initial Mass Function Fifty Years Later*, Kluwer Academic Publishers, editors E. Corbelli, F. Palla, and H. Zinnecker, p. 23
- Schröder, K.-P., & Pagel, B. E. J. 2003, *MNRAS*, 343, 1231
- Stanke, T., Smith, M. D., Gredel, R., & Khanzadyan, T. 2006, *A&A*447, 609

Tachihara, K., Mizuno, A., & Fukui, Y. 2000, ApJ, 528, 817

Visser, A. E., Richer, J. S., & Chandler, C. J. 2002, AJ, 124, 2756

Weintraub, D. A., Kastner, J. H., Griffith, L. L., & Campins, H. 1993, AJ, 105, 271

Wilking, B. A., Lada, C. J., & Young, E. T. 1989, ApJ, 340, 823

Wilking, B. A., Meyer, M. R., Robinson, J. G., & Greene, T. P. 2005, AJ, 130, 1733

## Chapter 4

# Bolocam Survey for 1.1 mm Dust Continuum Emission in the Serpens Molecular Cloud

### Abstract

We present the results from a 1.1 mm survey for dust continuum emission of the Serpens molecular cloud, using Bolocam at the CSO. This represents the final survey in a three-cloud study of nearby star-forming molecular clouds. We identify 35 1.1 mm sources a point source detection limit of  $0.13 M_{\odot}$ . Sources are slightly elongated on average, and have a narrow distribution of sizes with a mean of  $55''$ . The average mass of the sample is  $2.6 M_{\odot}$ , and the total mass in 1.1 mm cores is  $92 M_{\odot}$ , accounting for 2.7% of the total cloud mass. The differential mass distribution can be fit by a power law with slope  $\alpha = 1.6 \pm 0.2$  above  $0.35 M_{\odot}$ . These basic results will be utilized in the next chapter to compare the properties of the core populations of Perseus, Ophiuchus, and Serpens.

### 4.1 Introduction

We have recently completed 1.1 mm surveys of the Perseus (Enoch et al. 2006; chapter 2) and Ophiuchus molecular clouds (Young et al. 2006; chapter 3) with Bolocam

---

This chapter is adapted from the first half of Enoch et al. 2007, ApJ, in press.

at the Caltech Submillimeter Observatory (CSO). In this chapter we present a similar 1.1 mm survey of  $1.5 \text{ deg}^2$  of the Serpens cloud, completing our three-cloud study of dust continuum emission in nearby northern star-forming molecular clouds. Millimeter maps trace ongoing star formation on large scales by detecting dust emission from dense protostellar envelopes and starless cores. These observations are coordinated to cover the area mapped with *Spitzer* Space Telescope IRAC and MIPS observations of Serpens from the “Cores to Disks” (hereafter c2d; Evans et al., 2003) legacy project.

The Serpens molecular cloud is an active star formation region at a distance of  $d = 260 \pm 10 \text{ pc}$  (Straizys, Cernis, & Bartasiute, 1996). Although the cloud extends more than  $10 \text{ deg}^2$  as mapped by optical extinction (Cambr esy, 1999), most observations of the region have been focused near the main Serpens cluster at a Right Ascension (RA) of  $18^h30^m$  and declination (Dec) of  $1^\circ15'$  (J2000).

The Serpens cluster is a highly extincted region with a high density of young stellar objects (YSOs), including a number of Class 0 protostars. It has been studied extensively at near-infrared, far-infrared, submillimeter, and millimeter wavelengths (e.g., Eiroa & Casali, 1992; Hurt & Barsony, 1996; Larsson et al., 2000; Davis et al., 1999; Casali, Eiroa, Duncan, 1993; Testi & Sargent, 1998). Some recent work has also drawn attention to a less well known cluster to the south, sometimes referred to as Serpens/G3-G6 (Djupvik et al., 2006; Harvey et al., 2006). Beyond these two clusters no continuum millimeter or submillimeter continuum surveys have been done that could shed light on large-scale star formation processes.

In this chapter we briefly present the basic results from the Serpens survey. In the next chapter (chapter 5), we will compare the results from the three clouds to gain a more complete understanding of star formation in molecular clouds. The Bolocam observations and data reduction (§4.2) are described, to the extent that they differ from the detailed information in chapter 2. We then discuss general results such as cloud morphology (§4.3) and source properties (§4.3.2), including the 1.1 mm core mass distribution. We end with a summary in (§4.4).

## 4.2 Observations and Data Reduction

Observations and data reduction for Serpens follow the same methodology as for Perseus and Ophiuchus. The data reduction techniques we have developed for the Bolocam molecular cloud data are described in detail in chapter 2, including removal of sky noise, construction of pointing and calibration models, application of iterative mapping, and source extraction. Given these previous descriptions, only details specific to Serpens will be presented here. Further information about the Bolocam instrument and reduction pipeline is also available in Laurent et al. (2005).

### 4.2.1 Observations

As for Perseus and Ophiuchus, millimeter continuum observations of Serpens were made with Bolocam<sup>1</sup> at the CSO on Mauna Kea, Hawaii. The 1.1 mm observations were designed to cover a region with  $A_V \geq 6$  mag in the visual extinction map of Cambr esy (1999), shown in figure 4.1. As demonstrated in figure 4.1, this ensures that the Bolocam observations overlap as closely as possible with the region of Serpens observed with *Spitzer* IRAC and MIPS as part of the c2d Legacy project. In practice, the Bolocam survey covers a region slightly larger than the IRAC map, and slightly smaller than the MIPS map.

Serpens was observed during two separate runs in 2003 May 21–June 9 and 2005 June 26–30. During the 2003 run, 94 of the 144 channels were operational, compared to 109 during the 2005 run. Scans of Serpens were made at a rate of  $60'' \text{ sec}^{-1}$  with no chopping of the secondary. The final map consists of 13 scans from 2003 in good weather, and 17 scans from 2005 in somewhat poorer conditions. Each scan covered the entire  $1.5 \text{ deg}^2$  area and took 35 – 40 minutes to complete depending on the scan direction. Scans were made in two orthogonal directions, approximately half in RA and half in Dec. This strategy allows for good cross-linking in the final map, sub-Nyquist sampling, and minimal striping from  $1/f$  noise. Scans were observed in sets of three offset by  $-43''$ ,  $0''$ ,  $+43''$  to optimize coverage.

---

<sup>1</sup><http://www.cso.caltech.edu/bolocam>

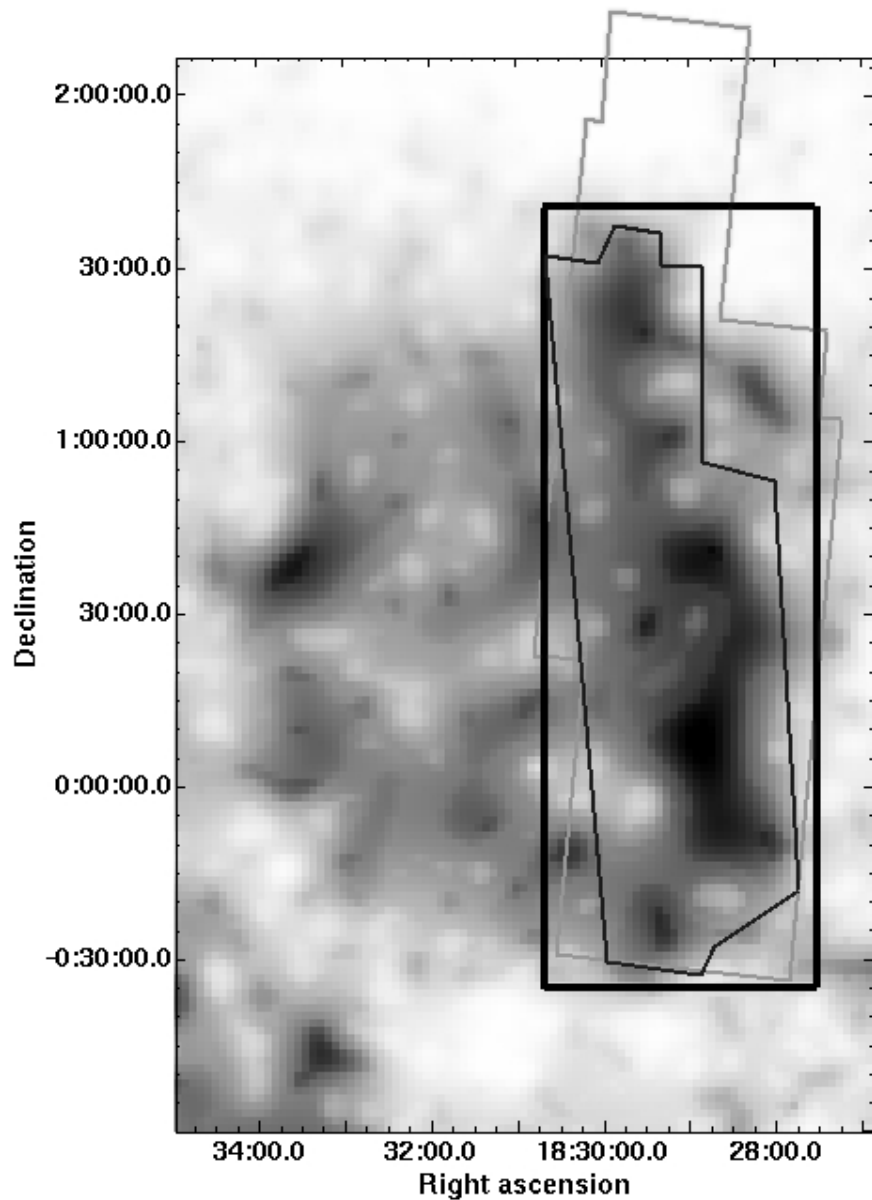


Figure 4.1 Bolocam 1.1 mm (thick line) and Spitzer c2d IRAC (thin line) and MIPS (gray line) coverage of Serpens overlaid on the Cambr esy (1999) visual extinction map. The area observed with IRAC was chosen to cover  $A_V \geq 6$  mag in this portion of the cloud. Our Bolocam survey covers the same area as the IRAC and a slightly smaller area than the MIPS observations.

In addition, small maps of pointing sources were observed approximately every 2 hours, and at least one primary flux calibration source, including Neptune, Uranus, and Mars, was observed each night. Several larger beam maps of planets were also made during each run, to characterize the Bolocam beam at 1.1 mm.

### 4.2.2 Pointing and Flux Calibration

A pointing model for Serpens was generated using two nearby pointing sources, G 34.3 and the quasar 1749+096. After application of the pointing model, a comparison to the literature SCUBA 850  $\mu\text{m}$  positions of four bright known sources (Davis et al., 1999) in the main Serpens cluster indicated a constant positional offset of  $(\delta\text{RA}, \delta\text{Dec}) = (5'', -10'')$ . We corrected for the positional offset, but estimate an uncertainty in the absolute pointing of  $10''$ , still small compared to the beam size of  $31''$ . The relative pointing errors, which cause blurring of sources and an increase in the effective beam size, should be much smaller, approximately  $5''$ . Relative pointing errors are characterized by the rms pointing uncertainty, derived from the deviations of G 34.3 from the pointing model.

Calibrator maps of Neptune, Uranus, and G 34.3, observed at least once per night, were used to construct a calibration curve for each run. A systematic uncertainty of approximately 10% is associated with the absolute flux calibration, but relative fluxes should be much more accurate.

### 4.2.3 Cleaning and Mapping

Aggressive sky subtraction techniques are required for Bolocam data to remove sky noise, which dominates over the astronomical signal before cleaning. As in chapter 2, we remove sky noise from the Serpens scans using Principal Component Analysis (PCA) cleaning (Laurent et al. (2005) and references therein), subtracting 3 PCA components. Iterative mapping is necessary to restore source flux lost in the sky subtraction process. Data from the 2003 and 2005 observing runs were iteratively mapped separately because they required different pointing and flux calibration models. After

iterative mapping the two epochs were averaged, weighting by the square root of the observational coverage.

The final  $10''$  pixel<sup>-1</sup> Serpens map is shown in figure 4.2, with the well known northern Serpens cluster, Cluster A (Harvey et al., 2006), indicated, as well as the southern cluster, Cluster B (Serpens/G3-G6). Covering a total area of  $1.5 \text{ deg}^2$ , or  $30.9 \text{ pc}^2$  at a distance of 260 pc, the map has a linear resolution of  $7.3 \times 10^3 \text{ AU}$ .

#### 4.2.4 Source Identification

Observational coverage, which depends on the scan strategy, number of scans, and number of bolometer channels, was very uniform for Serpens; trimming regions where the coverage was less than 30% of the peak coverage was equivalent to cutting off the noisy outer edges of the map. The average coverage in the Serpens map is 1600 hits per pixel, where a hit means a bolometer passed over this position, with variations across the map of 18%. The average coverage corresponds to an integration time of 13 minutes per pixel, although individual pixels are not independent because the map is oversampled.

Sources are identified in the optimally filtered map, using the peak-finding routine described in §2.4.1 and a detection limit of 5 times the local rms noise. We identify 35 sources above the  $5\sigma$  detection limit, which is typically  $50 \text{ mJy beam}^{-1}$ . The local rms noise per beam is calculated in small ( $\sim 45 \text{ arcmin}^2$ ) boxes in the noise map of Serpens, shown in figure 4.3 with the positions of identified sources overlaid. The mean rms noise is  $9.5 \text{ mJy beam}^{-1}$ , but is higher near bright sources. Most of the 18% variations in the local rms noise occur in the main cluster region, where calculation of the noise is confused by residual artifacts from bright sources. Such artifacts must contribute significantly to noise fluctuations; coverage variations alone would predict rms noise variations of only  $\sqrt{18} = 4\%$ . This means that faint sources near bright regions have a slightly lower chance of being detected than those in isolation.

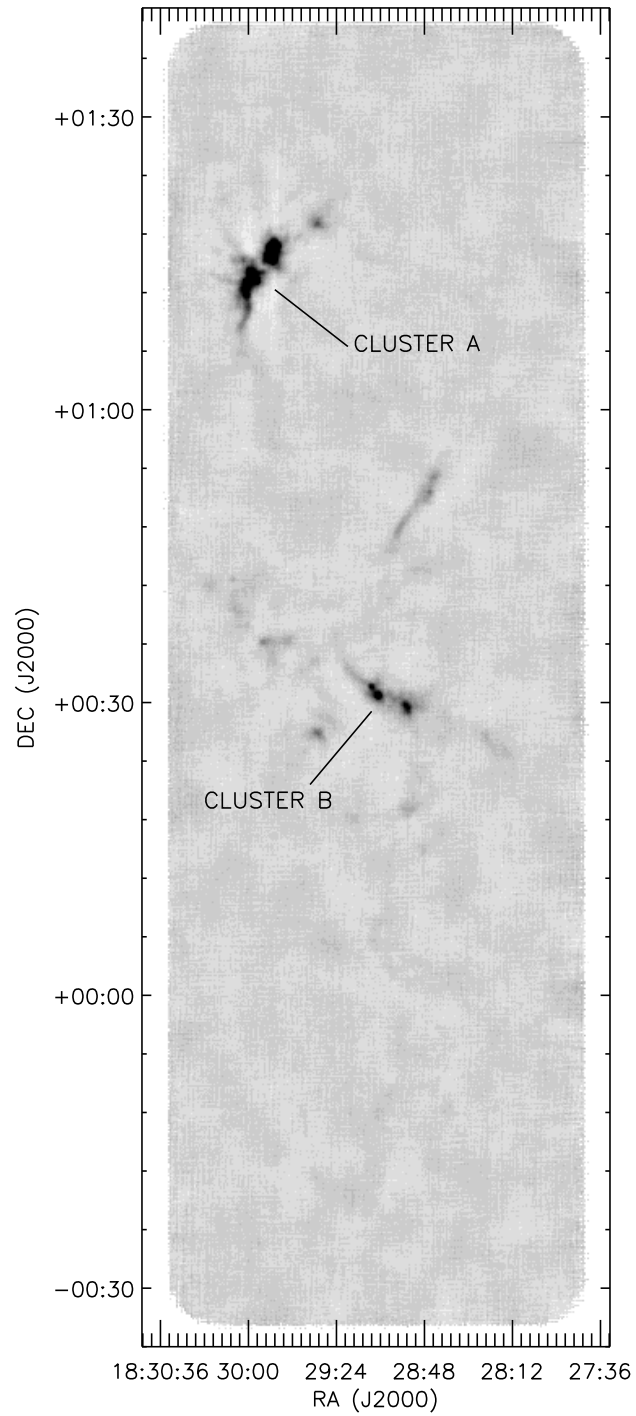


Figure 4.2 Bolocam 1.1 mm map of 1.5 deg<sup>2</sup> (31 pc<sup>2</sup> at  $d = 260$  pc) in the Serpens molecular cloud. Bolocam has a resolution of 31", and the map is binned to 10" pixel<sup>-1</sup>.

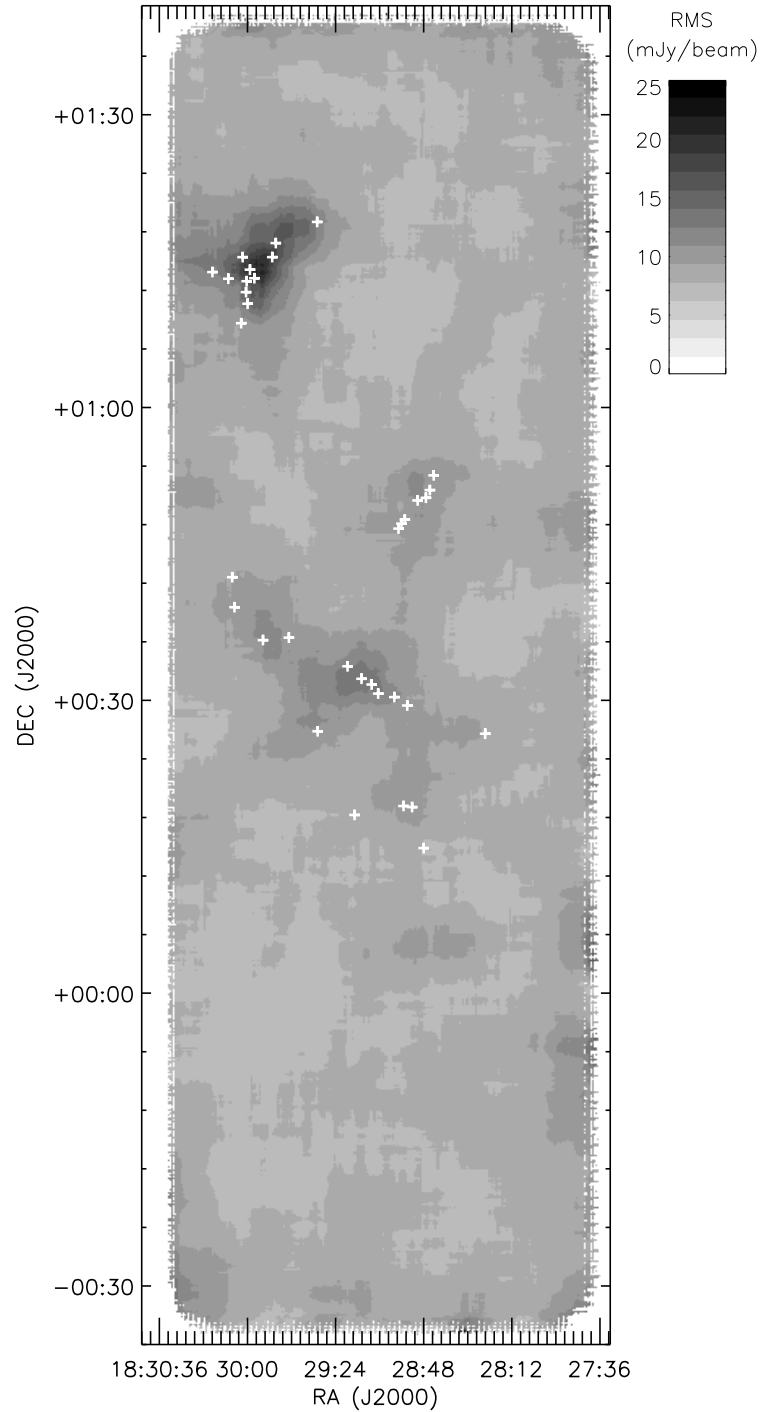


Figure 4.3 Map of the local  $1\sigma$  rms noise per beam in the Serpens map. Positions of the 35 sources are indicated by white plus symbols. The average rms noise is 9.5 mJy beam<sup>-1</sup>, varying by 18% across the map. The noise is higher near bright sources due to sky subtraction residuals.

### 4.3 Results

Positions of the 35 detected sources are listed in table 4.1, and identified by red circles in figure 4.4. Figure 4.4 also shows magnifications of the more densely populated source regions, including Cluster A and Cluster B. We do not see any circularly symmetric extended emission on scales  $\gtrsim 3'$  in the map. It should, in principle, be possible to recover symmetric structures up to the array size of  $7'.5$ , but our simulations show that sources  $\gtrsim 4'$  in size are severely affected by cleaning and therefore difficult to fully recover with iterative mapping. The map does contain larger filamentary structures up to  $8'$  long. In particular, the long filament between Cluster A and Cluster B is reminiscent of the elongated ridge near B1 in Perseus (chapter 2). The Serpens filament does not contain the bright compact sources at either end that are seen in the B1 ridge, however.

Previous millimeter-wavelength maps of Cluster A, such as the 1.1 mm UKT14 map of Casali, Eiroa, & Duncan (1993) and the  $850 \mu\text{m}$  SCUBA map of Davis et al. (1999), generally agree with our results in terms of morphology and source structure. Not all of the individual  $850 \mu\text{m}$  sources are detected by our peak-finding routine, presumably due to the poorer resolution of Bolocam ( $30''$ ) compared to SCUBA ( $14''$ ), but most can, in fact, be identified by eye in the Bolocam map. An IRAM 1.3 mm continuum map of Cluster B with  $11''$  resolution (Djupvik et al., 2006) is visually quite similar to our Bolocam map of the region. We detect each of the four 1.3 mm sources identified (MMS1-4), although the 1.3 mm triplet MMS1 is seen as a single extended source in our map.

Most of the brightest cores, in particular those in Cluster A, are associated with known YSOs including a number of Class 0 objects (Hurt & Barsony, 1996; Harvey et al., 2006). All bright 1.1 mm sources are aligned with bright  $160 \mu\text{m}$  emission in the *Spitzer* MIPS map of Serpens observed by the c2d legacy project (Harvey et al., 2007). Fainter millimeter sources are usually associated with extended  $160 \mu\text{m}$  filaments, but do not necessarily correspond to point sources in the MIPS map. Conversely, one bright extended region of  $160 \mu\text{m}$  emission just south of Cluster A contains no 1.1 mm

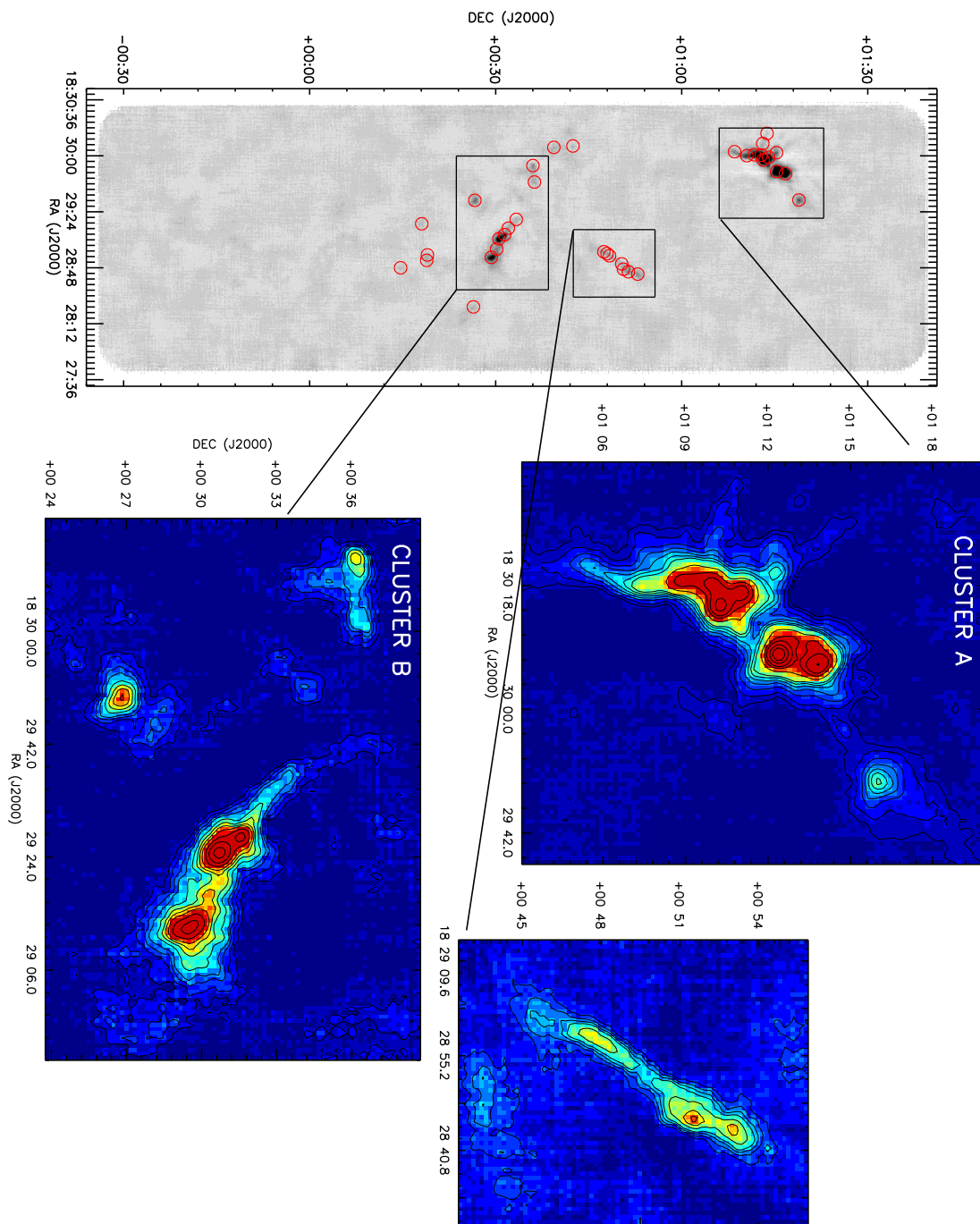


Figure 4.4 Bolocam 1.1 mm map of Serpens with the positions of the 35 sources detected above  $5\sigma$  indicated by red circles. Inset maps magnify the most densely populated source regions, including the well known northern Cluster A, Cluster B to the south, and an elongated filament reminiscent of the B1 ridge in Perseus (chapter 2). Despite the low rms noise level reached ( $9.5 \text{ mJy beam}^{-1}$ ), few sources are seen outside the cluster regions. Many bright 1.1 mm sources are associated with YSOs (Harvey et al., 2006), and all are coincident with  $160 \mu\text{m}$  emission.

sources. This area also exhibits extended emission at 70 and 24  $\mu\text{m}$ , which may be indicative of warmer, more diffuse material than that of the dense cores detected at 1.1 mm.

### 4.3.1 Comparison to Visual Extinction

Despite the low rms noise level achieved in Serpens, very few sources are seen outside the main clusters; most of the area that we mapped appears devoid of 1.1 mm emission, despite being in a region of high extinction. Figure 4.5 shows a comparison between the Bolocam millimeter map (gray-scale) and visual extinction (contours) derived from c2d near- and mid-infrared Spitzer data.

The majority of sources (90%–95%) detected by IRAC and MIPS in the c2d clouds have spectral energy distributions characteristic of reddened stars. Thus we have measures of the visual extinction for many lines of sight through the molecular clouds imaged by c2d, including Perseus, Ophiuchus, and Serpens. Here we describe the derivation of extinction ( $A_V$ ) maps that will be used in this and the following chapters.

Line-of-sight extinction values are derived by fitting the  $R_V=5.5$  dust model of Weingartner & Draine (2001) to the near-infrared through mid-infrared SED (Evans et al., 2006). For each of the three clouds, the derived line-of-sight extinctions were convolved with uniformly spaced  $90''$  Gaussian beams to construct an extinction map. The c2d extinction maps accurately trace column densities up to  $A_V \sim 40$  mag, but are relatively insensitive to small regions of high volume density, because they rely on the detection of background stars. Thus the extinction maps are complementary to the 1.1 mm observations, which trace high volume density structures (see §5.3). In figure 4.5, the  $A_V$  map for Serpens is smoothed to an effective resolution of  $2'.5$ .

As can be seen in figure 4.5, nearly all Serpens millimeter sources lie within regions of high visual extinction ( $A_V \geq 10$  mag) and, in particular, all bright Bolocam sources are associated with areas of  $A_V \geq 15$  mag. Nevertheless, there are a number of high extinction areas ( $A_V \geq 12$  mag) with no detectable 1.1 mm sources. A similar

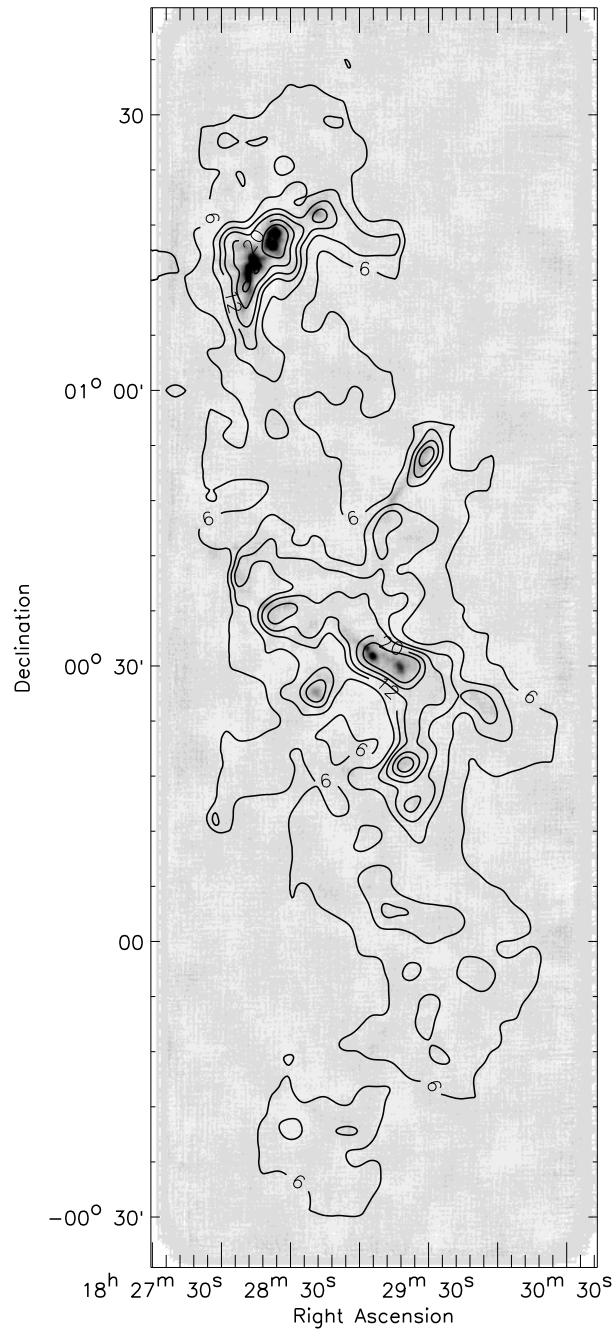


Figure 4.5 Visual extinction ( $A_V$ ) contours calculated from c2d Spitzer maps, as described in §4.3.2.3, overlaid on the gray-scale 1.1 mm map. Contours are  $A_V = 6, 9, 12, 15, 20, 25$  mag and are smoothed to an effective resolution of  $2''.5$ . All bright 1.1 mm cores are found in regions of high ( $> 15$  mag) extinction, but not all high  $A_V$  areas are associated with strong millimeter sources.

general trend was noted in both Perseus (chapter 2) and Ophiuchus (chapter 3), with relatively few sources found outside the major groups and clusters associated with the highest extinction. In chapter 5 (§5.5.5) we examine the relationship between  $A_V$  and 1.1 mm sources in more detail.

## 4.3.2 Source Properties

### 4.3.2.1 Positions and Photometry

Positions, peak flux densities, and signal-to-noise ratio (S/N) for the 35 1.1 mm sources identified in the Bolocam map of Serpens are listed in table 4.1. Table 4.1 also lists the most commonly used name from the literature for known sources, and indicates if the 1.1 mm source is coincident (within  $60''$ ) with a MIPS  $24\ \mu\text{m}$  source from the c2d database (Harvey et al., 2007). The uncertainty in the peak flux density is the local rms  $\text{beam}^{-1}$  and does not include an additional 15% systematic uncertainty.

Table 4.2 lists photometry in fixed apertures of diameter  $40''$ ,  $80''$ , and  $120''$ , the total integrated flux density. Aperture sizes for the total flux density are limited by the distance to the nearest neighboring source, or  $120''$ , whichever is larger. Uncertainties are based on the local rms noise and the aperture size, and do not include an additional 15% systematic uncertainty.

Table 4.1. Identified sources in Serpens

ID	RA (2000) ( <i>h m s</i> )	Dec (2000) ( $^{\circ}$ <i>' "</i> )	Peak (mJy/beam)	S/N	other names	MIPS source?
Bolo1	18 28 23.1	+00 26 34.6	95 (12)	5.0		N
Bolo2	18 28 44.0	+00 53 02.8	198 (12)	9.9		N
Bolo3	18 28 45.8	+00 51 32.4	227 (12)	13.7	IRAS 18262+0050	Y
Bolo4	18 28 47.2	+00 50 45.1	145 (10)	7.1		N
Bolo5	18 28 48.3	+00 14 51.5	73 (9)	5.8		N
Bolo6	18 28 50.8	+00 50 28.6	115 (10)	7.3		N
Bolo7	18 28 53.0	+00 19 03.6	119 (11)	5.4		Y
Bolo8	18 28 55.2	+00 29 28.0	617 (13)	30.8	IRAS 18263+0027; MMS1 (1)	Y
Bolo9	18 28 55.9	+00 48 30.3	141 (10)	9.1		N
Bolo10	18 28 56.6	+00 19 10.4	107 (11)	5.7		N
Bolo11	18 28 57.3	+00 48 06.5	162 (11)	10.9		N
Bolo12	18 28 58.4	+00 47 35.7	172 (11)	12.0		N
Bolo13	18 29 00.2	+00 30 19.8	239 (15)	5.5		Y
Bolo14	18 29 07.0	+00 30 41.5	1016 (14)	59.2	IRAS 18265+0028; MMS2 (1)	Y
Bolo15	18 29 09.6	+00 31 36.9	626 (14)	33.0	MMS3 (1)	Y
Bolo16	18 29 13.5	+00 32 12.6	175 (13)	5.8		N
Bolo17	18 29 16.4	+00 18 15.4	82 (8)	6.7	IRAS 18267+0016	Y
Bolo18	18 29 19.3	+00 33 29.1	104 (12)	6.0		N
Bolo19	18 29 31.5	+00 26 49.3	279 (14)	14.8	MMS4 (1)	N
Bolo20	18 29 31.9	+01 19 00.9	337 (13)	18.3		Y
Bolo21	18 29 43.4	+00 36 25.2	129 (11)	7.7		N
Bolo22	18 29 48.8	+01 16 50.6	1694 (16)	80.7	SMM 9 (2); S68N	Y
Bolo23	18 29 50.2	+01 15 24.6	3010 (20)	138	SMM 1 (2); FIRS 1	Y
Bolo24	18 29 53.8	+00 36 10.1	202 (10)	17.2	IRAS 18273+0034	Y
Bolo25	18 29 57.4	+01 13 14.9	1980 (23)	62.7	SMM 4 (2)	Y
Bolo26	18 29 59.2	+01 14 07.4	1331 (19)	43.0	SMM 3 (2)	Y
Bolo27	18 30 00.3	+01 10 37.8	425 (19)	14.5		Y
Bolo28	18 30 00.7	+01 12 56.5	1266 (19)	34.3	SMM 2 (2)	Y
Bolo29	18 30 01.0	+01 11 49.1	979 (19)	33.5	SMM 11 (2)	Y
Bolo30	18 30 02.5	+01 15 24.5	319 (16)	11.3	SMM 8 (2)	Y
Bolo31	18 30 02.8	+01 08 38.3	214 (16)	10.0		Y
Bolo32	18 30 05.7	+00 39 32.2	105 (12)	5.0		Y
Bolo33	18 30 06.4	+00 42 37.0	126 (11)	8.3		Y
Bolo34	18 30 08.2	+01 13 11.5	153 (11)	7.8		N
Bolo35	18 30 14.7	+01 13 52.6	85 (11)	5.6		N

Note. — Numbers in parentheses are  $1\sigma$  errors. The peak flux density is the peak value per beam in the  $10''$  pixel $^{-1}$  unfiltered map (without the optimal filter applied). The uncertainty in the peak flux density is the local rms beam $^{-1}$  and does not include an additional 15% systematic uncertainty from calibration uncertainties and residual errors after iterative mapping. Other names listed are the most common identifications from the literature, and are not meant to be a complete list. A 1.1 mm source is considered coincident with a MIPS source if the position is within  $60''$  of a  $24\ \mu\text{m}$  source from the c2d catalog (Harvey et al., 2007). References – (1) Djupvik et al. 2006; (2) Casali, Eiroa, & Duncan 1993

Table 4.2. Photometry, masses, sizes, and morphology for sources in Serpens

ID	Flux(40'')	Flux(80'')	Flux(120'')	Total Flux (Jy)	Mass (10K) ( $M_{\odot}$ )	Peak $A_V$ (mag)	FWHM (minor, '')	FWHM (major, '')	PA ( $^{\circ}$ )	$\langle n \rangle$ $\text{cm}^{-3}$	Morphology <sup>1</sup>
Bolo1	0.137 (0.016)	...	...	0.25 (0.03)	0.65 (0.07)	8	52 (1.0)	62 (1.2)	55 (8)	$1.0 \times 10^5$	extended, elongated, weak
Bolo2	0.282 (0.017)	...	...	0.51 (0.03)	1.34 (0.08)	17	51 (0.5)	63 (0.6)	-57 (4)	$2.1 \times 10^5$	multiple, extended, elongated
Bolo3	0.324 (0.015)	...	...	0.382 (0.019)	1.00 (0.05)	19	43 (0.4)	55 (0.5)	-77 (3)	$3.2 \times 10^5$	multiple, extended, round
Bolo4	0.226 (0.013)	...	...	0.28 (0.017)	0.73 (0.04)	12	43 (0.5)	55 (0.6)	49 (4)	$2.2 \times 10^5$	multiple, extended, elongated
Bolo5	0.094 (0.013)	...	...	0.16 (0.02)	0.41 (0.06)	6	50 (1.2)	63 (1.4)	-68 (8)	$7 \times 10^4$	extended, round, weak
Bolo6	0.172 (0.013)	...	...	0.210 (0.016)	0.55 (0.04)	10	46 (0.6)	62 (0.8)	-40 (3)	$1.1 \times 10^5$	multiple, extended, elongated
Bolo7	0.162 (0.015)	...	...	0.162 (0.015)	0.42 (0.04)	10	46 (0.8)	57 (0.9)	-30 (7)	$1.0 \times 10^5$	multiple, extended, elongated
Bolo8	0.933 (0.018)	1.99 (0.04)	...	2.63 (0.04)	6.87 (0.12)	52	62 (0.2)	74 (0.2)	68 (1)	$5.2 \times 10^5$	multiple, extended, elongated
Bolo9	...	...	...	0.169 (0.010)	0.44 (0.03)	12	38 (0.5)	61 (0.7)	-58 (2)	$1.5 \times 10^5$	multiple, extended, elongated
Bolo10	0.146 (0.015)	...	...	0.146 (0.015)	0.38 (0.04)	9	51 (0.8)	54 (0.9)	11 (25)	$8 \times 10^4$	multiple, round,
Bolo11	...	...	...	0.199 (0.011)	0.52 (0.03)	14	37 (0.4)	61 (0.7)	-59 (2)	$1.8 \times 10^5$	multiple, extended, elongated
Bolo12	0.246 (0.014)	...	...	0.246 (0.014)	0.64 (0.04)	15	39 (0.4)	58 (0.6)	-65 (2)	$2.2 \times 10^5$	multiple, extended, round
Bolo13	0.36 (0.02)	...	...	0.36 (0.02)	0.94 (0.05)	20	52 (0.5)	59 (0.5)	-78 (6)	$1.7 \times 10^5$	multiple, extended, elongated
Bolo14	1.381 (0.019)	...	...	2.16 (0.03)	5.65 (0.09)	86	47 (0.1)	54 (0.1)	-44 (2)	$1.5 \times 10^6$	multiple, extended, round
Bolo15	0.856 (0.018)	...	...	0.856 (0.018)	2.24 (0.05)	53	44 (0.2)	56 (0.2)	-27 (1)	$6.5 \times 10^5$	multiple, extended, elongated
Bolo16	0.222 (0.018)	...	...	0.27 (0.02)	0.71 (0.06)	15	42 (0.5)	62 (0.8)	32 (3)	$1.8 \times 10^5$	multiple, extended, elongated
Bolo17	0.118 (0.011)	0.24 (0.02)	0.4 (0.03)	0.40 (0.03)	1.05 (0.09)	7	80 (1.1)	97 (1.3)	-66 (5)	$3 \times 10^4$	extended, elongated
Bolo18	0.144 (0.016)	...	...	0.25 (0.03)	0.65 (0.08)	9	48 (0.8)	71 (1.2)	-41 (3)	$9 \times 10^4$	multiple, extended, elongated, weak
Bolo19	0.41 (0.018)	0.85 (0.04)	1.28 (0.06)	1.28 (0.06)	3.34 (0.14)	24	74 (0.5)	89 (0.6)	-74 (3)	$1.3 \times 10^5$	extended, elongated
Bolo20	0.494 (0.018)	1.01 (0.04)	1.57 (0.05)	1.57 (0.05)	4.11 (0.14)	29	87 (0.5)	90 (0.5)	9 (11)	$1.2 \times 10^5$	extended, elongated
Bolo21	0.177 (0.014)	0.38 (0.03)	...	0.38 (0.03)	0.98 (0.07)	11	53 (0.7)	64 (0.8)	47 (6)	$1.3 \times 10^5$	multiple, extended, elongated
Bolo22	2.32 (0.02)	...	...	3.78 (0.04)	9.86 (0.10)	144	47 (0.1)	57 (0.1)	73 (1)	$2.3 \times 10^6$	multiple, extended, round
Bolo23	3.8 (0.03)	5.91 (0.05)	...	5.91 (0.05)	15.44 (0.14)	256	46 (0.1)	47 (0.1)	39 (4)	$6.1 \times 10^6$	multiple, extended, round

Table 4.2 (cont'd)

ID	Flux(40'') (Jy)	Flux(80'') (Jy)	Flux(120'') (Jy)	Total Flux (Jy)	Mass (10K) ( $M_{\odot}$ )	Peak $A_V$ (mag)	FWHM (minor, '')	FWHM (major, '')	PA ( $^{\circ}$ )	$\langle n \rangle$ $\text{cm}^{-3}$	Morphology <sup>1</sup>
Bolo24	0.291 (0.014)	...	...	0.40 (0.02)	1.04 (0.05)	17	46 (0.4)	55 (0.5)	-12 (4)	$2.9 \times 10^5$	multiple, extended, elongated
Bolo25	2.75 (0.03)	...	...	3.19 (0.04)	8.33 (0.10)	168	44 (0.1)	51 (0.1)	79 (1)	$2.9 \times 10^6$	multiple, extended, round
Bolo26	1.9 (0.03)	...	...	1.90 (0.03)	4.95 (0.07)	113	48 (0.1)	59 (0.1)	-21 (1)	$1.0 \times 10^6$	multiple, extended, round
Bolo27	0.65 (0.03)	...	...	1.18 (0.05)	3.09 (0.12)	36	47 (0.3)	69 (0.4)	89 (1)	$4.6 \times 10^5$	multiple, extended, elongated
Bolo28	1.9 (0.03)	...	...	1.90 (0.03)	4.96 (0.06)	108	48 (0.1)	59 (0.1)	-47 (1)	$1.0 \times 10^6$	multiple, extended, round
Bolo29	1.41 (0.03)	...	...	2.44 (0.05)	6.37 (0.12)	83	47 (0.1)	59 (0.2)	-86 (1)	$1.4 \times 10^6$	multiple, extended, round
Bolo30	0.43 (0.02)	...	...	0.43 (0.02)	1.13 (0.06)	27	48 (0.4)	55 (0.5)	33 (5)	$2.6 \times 10^5$	multiple, extended, elongated
Bolo31	0.32 (0.02)	0.65 (0.04)	...	0.65 (0.04)	1.70 (0.11)	18	45 (0.5)	74 (0.8)	-65 (2)	$2.4 \times 10^5$	multiple, extended, elongated
Bolo32	0.151 (0.016)	0.34 (0.03)	...	0.34 (0.03)	0.88 (0.08)	9	57 (0.9)	74 (1.2)	50 (5)	$8 \times 10^4$	extended, elongated
Bolo33	0.12 (0.015)	...	...	0.128 (0.019)	0.34 (0.05)	11	35 (0.9)	39 (1.1)	25 (17)	$6.9 \times 10^6$	round
Bolo34	0.181 (0.015)	...	...	0.216 (0.019)	0.56 (0.05)	13	40 (0.6)	60 (0.9)	-70 (3)	$1.7 \times 10^5$	multiple, extended, elongated
Bolo35	...	...	...	0.06 (0.011)	0.16 (0.03)	7	24 (1.1)	61 (2.9)	-69 (4)	$2.4 \times 10^5$	multiple, weak

Note. — Masses are calculated according to equation (2.3) from the total flux density assuming a single dust temperature of  $T_D = 10$  K and a dust opacity at 1.1mm of  $\kappa_{1.1\text{mm}} = 0.0114 \text{ cm}^2 \text{g}^{-1}$ . Peak  $A_V$  is calculated from the peak flux density as in equation (2.2). FWHM and PAs are from an elliptical Gaussian fit; the PA of the major axis is measured in degrees east of north.  $\langle n \rangle$  is the mean particle density as calculated from the total mass and the deconvolved average FWHM size. Numbers in parentheses are  $1\sigma$  uncertainties. Uncertainties for masses are from photometry only, and do not include uncertainties from  $\kappa$ ,  $T_D$ , or  $d$ , which can be up to a factor of a few or more. Uncertainties for the FWHM and PA are formal fitting errors from the elliptical gaussian fit; additional uncertainties of 10% – 15% apply to the FWHM, and  $\sim 5^{\circ}$  to the PA (determined from simulations).

<sup>1</sup>The morphology keywords given indicates whether the source is multiple (within  $3'$  of another source), extended (major axis FW at  $2\sigma > 1'$ ), elongated (axis ratio at  $4\sigma > 1.2$ ), round (axis ratio at  $4\sigma < 1.2$ ), or weak (peak flux density less than 5 times the rms pixel<sup>-1</sup> in the unfiltered map).

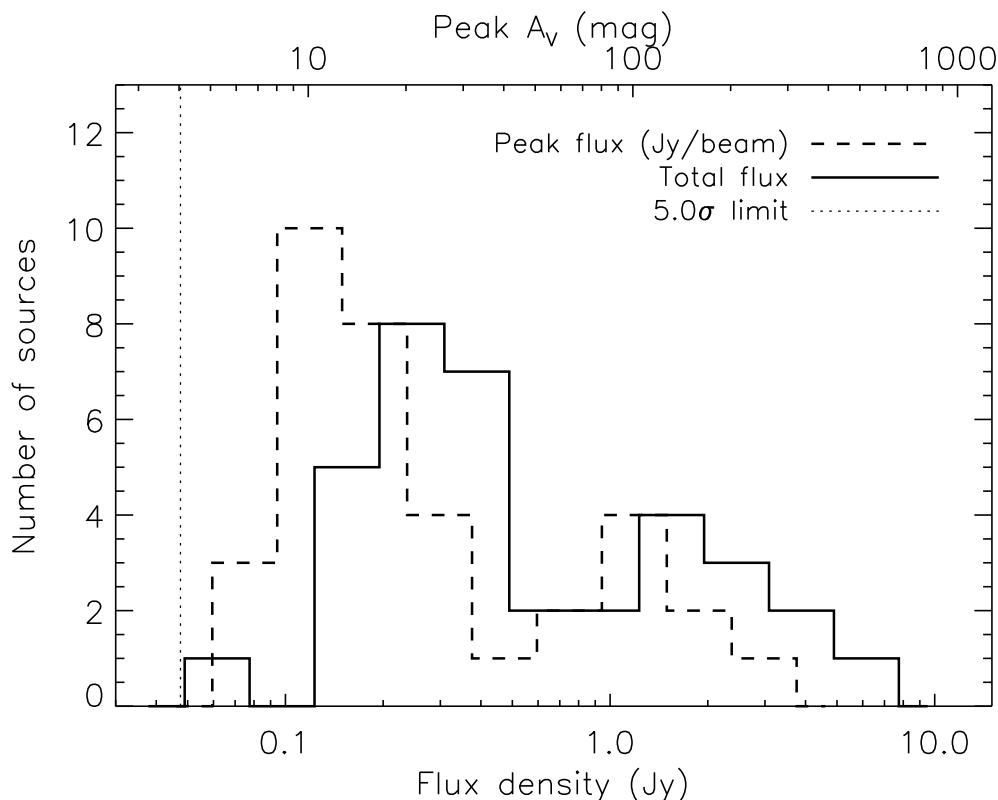


Figure 4.6 Distribution of peak (dashed line) and total (solid line) flux densities of the 35 1.1 mm sources in Serpens. Peak  $A_V$  values derived from the 1.1 mm peak flux densities using equation (2.2) are shown on the upper axis. The mean peak flux density of the sample is  $0.5 \text{ Jy beam}^{-1}$ , the mean peak  $A_V$  is 40 mag, and the mean total flux density is 1.0 Jy. The  $5\sigma$  detection limit of 0.05 Jy (dotted line) is relatively uniform across the cloud.

Peak and total flux density distributions for the 35 1.1 mm sources in Serpens are shown in figure 4.6, with the  $5\sigma$  detection limit indicated. In general, source total flux densities are larger than peak flux densities because most sources in the map are extended, with sizes larger than the beam. Both distributions look bimodal; all of the sources in the brighter peak are in either Cluster A or Cluster B. The mean peak flux density of the sample is  $0.5 \text{ Jy beam}^{-1}$ , and the mean total flux density is 1.0 Jy, both with large standard deviations of order the mean value. Peak  $A_V$  values of the cores, calculated from the peak flux density as in equation (2.2), are indicated on the upper axis.

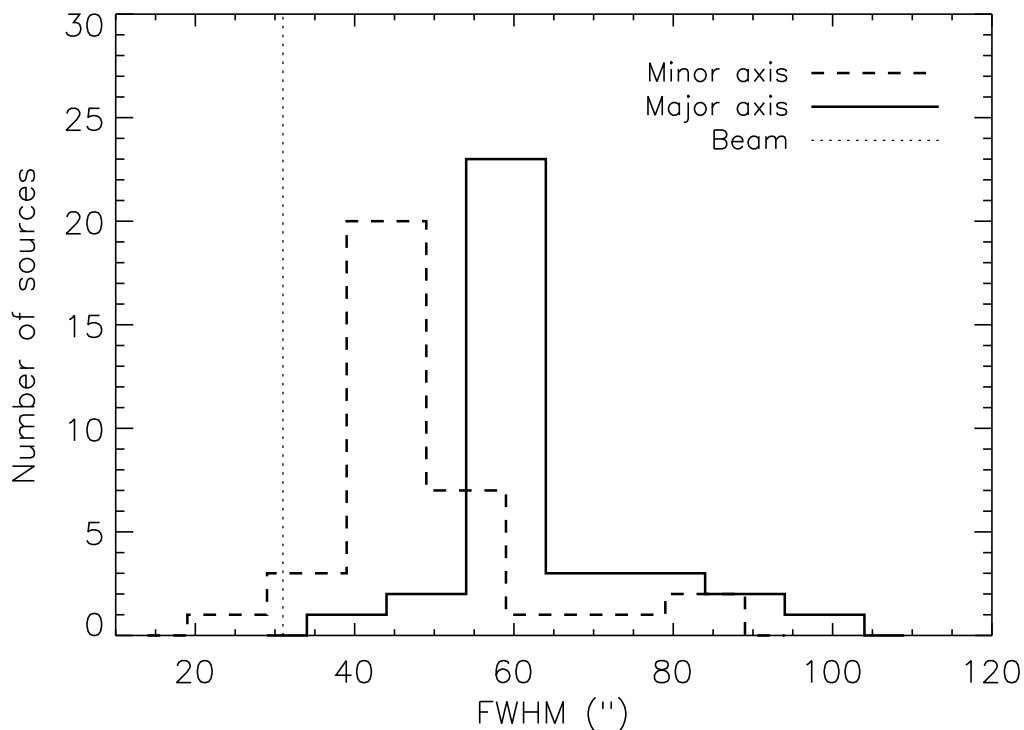


Figure 4.7 Distribution of source FWHM minor axis (dashed line) and major axis (solid line) sizes, determined by an elliptical Gaussian fit. The mean FWHM sizes are  $49''$  (minor axis) and  $63''$  (major axis), and the mean axis ratio (major/minor) is 1.3.

#### 4.3.2.2 Sizes and Shapes

Source FWHM sizes and position angles (PA, measured east of north) are measured by fitting an elliptical Gaussian after masking out nearby sources. The best fit major and minor axis sizes and PAs are listed in table 4.2. As can be seen in figure 4.7, the minor axis FWHM values are fairly narrowly distributed around the sample mean of  $49''$ , with a standard deviation of  $12''$ . The major axis FWHM have a similarly narrow distribution with a mean of  $63''$  and a scatter of  $12''$ . On average sources are slightly elongated, with a mean axis ratio at the half-max contour (major axis FWHM / minor axis FWHM) of 1.3.

A morphology keyword for each source is also given in table 4.2, to describe the general source shape and environment. The majority (28/35) of sources are multiple

(within  $3'$  of another source), and nearly all (32/35) are extended at the  $2\sigma$  contour (major axis  $> 1'$ ).

### 4.3.2.3 Masses, Densities, and Extinctions

Masses listed in table 4.2 calculated as described in §2.5.2 are listed in table 4.2 for the 35 detected sources. A dust temperature of  $T_D = 10$  K is assumed for all sources, and a dust opacity of  $\kappa_{1.1mm} = 0.0114 \text{ cm}^2 \text{ g}^{-1}$ , which has been found to be the best fit in a number of radiative transfer models (Evans et al., 2001; Shirley et al., 2002; Young et al., 2003). Uncertainties listed are from the uncertainty in the total flux density only; additional uncertainties from  $\kappa$ ,  $T_D$ , and  $d$  together introduce a total uncertainty in the mass of up to a factor of 4 or more. The total mass in 1.1 mm cores is  $92 M_\odot$ , which is only 2.7% of the total cloud mass ( $3470 M_\odot$ ). The cloud mass is estimated from the c2d visual extinction map using  $N(\text{H}_2)/A_V = 0.94 \times 10^{21} \text{ mag cm}^{-2}$  (Bohlin, Savage, & Drake, 1978) (see also chapter 5).

Figure 4.8 shows the differential mass function of all 1.1 mm sources in Serpens. The point source detection limit of  $0.13 M_\odot$  is indicated, as well as the 50% completeness limit for sources of FWHM  $55''$  ( $0.35 M_\odot$ ), which is the average size of the sample. Completeness is determined from Monte Carlo simulations of simulated sources inserted into the raw data and run through the reduction pipeline, as described in chapter 2. The best fit power law slope to  $dN/dM \propto M^{-\alpha}$  is shown ( $\alpha = 1.6$ ), as well as the best fit lognormal slope ( $\sigma = 0.7$ ,  $M_0 = 1.1 M_\odot$ ).

Our mass distribution has a flatter slope than that found by Testi & Sargent (1998) from higher resolution ( $5''$ ) OVRO observations ( $\alpha = -2.1$  for  $M > 0.35 M_\odot$ ). This may be due in part to the fact that most of our detections, at least 25/35, lie outside the  $5.5 \times 5.5$  area observed by Testi & Sargent (1998). The resolution differences of the observations may also contribute significantly; for example, a number of our bright sources break down into multiple objects in the  $5''$  resolution map.

We calculate peak extinction values for each source from the peak flux density per beam; these peak  $A_V$  values are listed in table 4.2, and are also shown on the upper axis of figure 4.6. The average peak  $A_V$  of the sample is 41 mag with a

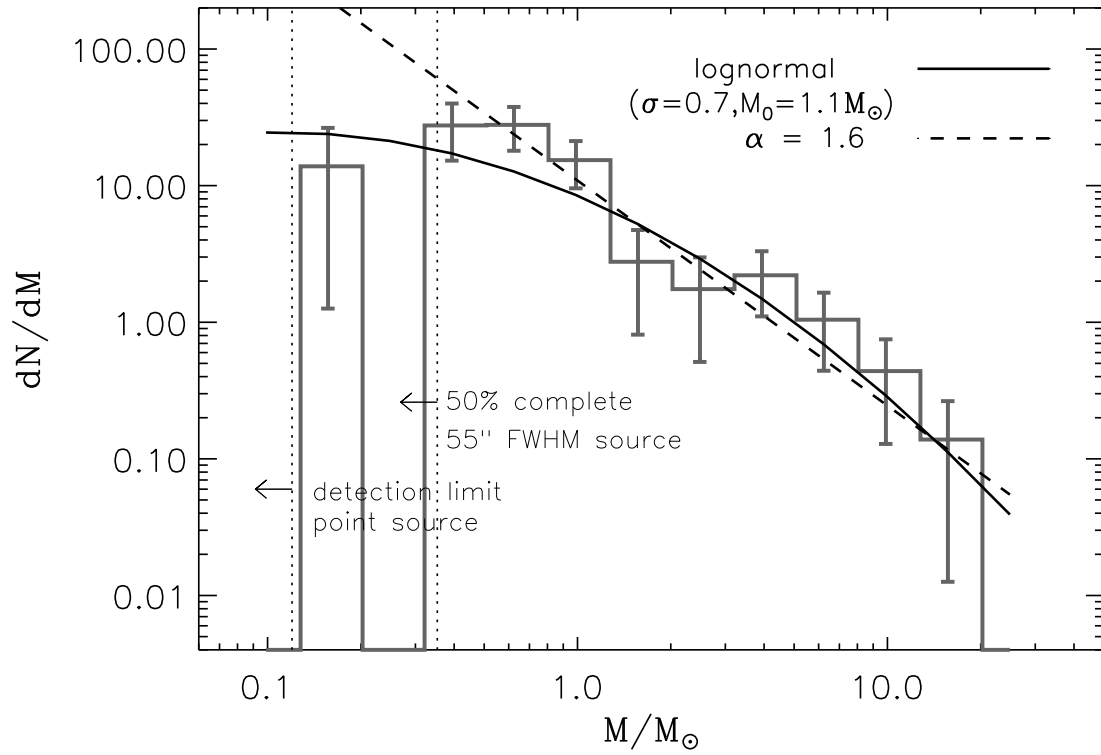


Figure 4.8 Differential mass distribution of the 35 detected 1.1 mm sources in Serpens for masses calculated with  $T_D = 10$  K. Dotted lines indicate the point source detection limit and the empirically derived 50% completeness limit for sources with the average FWHM size of 55". The best fit power law ( $\alpha = 1.6 \pm 0.2$ ) is shown, as well as the best fit lognormal function.

large standard deviation of 55 mag and a maximum  $A_V$  of 256 mag. Extinctions calculated from the millimeter emission are generally higher than those from the c2d visual extinction map by approximately a factor of 7, likely a combination of both the higher resolution of the Bolocam map (30" compared with 90") and the fact that the extinction map cannot trace the highest volume densities because it relies on the detection of background sources. Grain growth in dense cores beyond that included in the dust opacity from Ossenkopf & Henning (1994) could also lead to an overestimate of the  $A_V$  from our 1.1 mm data.

Also listed in table 4.2 is the mean particle density:  $\langle n \rangle = 3M/(4\pi R^3 m_H \mu_p)$ , where  $M$  is the total mass,  $R$  is the linear deconvolved radius at half-max, and  $\mu_p = 2.33$  is the mean molecular weight per particle. The median of the source mean densities is  $2.3 \times 10^5 \text{ cm}^{-3}$ , with values ranging from  $3.1 \times 10^4$  to  $6.1 \times 10^6 \text{ cm}^{-3}$ .

## 4.4 Summary

We have completed a 1.1 mm dust continuum survey of Serpens, covering  $1.5 \text{ deg}^2$ , with Bolocam at the CSO. We identify 35 1.1 mm sources in Serpens above the  $5\sigma$  detection limit, which is  $50 \text{ mJy beam}^{-1}$ , or  $0.13 M_\odot$ , on average. The sample has an average mass of  $2.6 M_\odot$ , and an average source FWHM size of  $55''$ . On average, sources are slightly elongated with a mean axis ratio at half-max of 1.3. The differential mass distribution of all 35 cores is consistent with a power law of slope  $\alpha = 1.6 \pm 0.2$  above  $0.35 M_\odot$ . The total mass in dense 1.1 mm cores in Serpens is  $92 M_\odot$ , accounting for 2.7% of the total cloud mass, as estimated from our c2d visual extinction map.

This work represents the third in a series of three surveys for millimeter continuum emission in nearby star-forming molecular clouds. In chapters 2–4 we have presented the basic results from large-scale mapping of Perseus, Ophiuchus, and Serpens. In the next chapter, we will compare the 1.1 mm source populations in each cloud to infer the effects of environment on dense star-forming cores, and implications for physical conditions in molecular clouds.

## Acknowledgments

The authors thank members of the Bolocam team for instrumental and software support, including James Aguirre, Jack Sayers, Glenn Laurent, and Sunil Golwala. Support for this work, part of the Spitzer Legacy Science Program, was provided by NASA through contracts 1224608 and 1230782 issued by the Jet Propulsion Laboratory, California Institute of Technology, under NASA contract 1407. Bolocam was built and commissioned under grants NSF/AST-9618798 and NSF/AST-0098737. KEY was supported by NASA under Grant NGT5-50401, issued through the Office of Space Science. Additional support came from NASA Origins grant NNG04GG24G to NJE and NSF grant AST 02-06158 to JG. MLE acknowledges support of a Moore Fellowship and an NSF Graduate Research Fellowship.

## Bibliography

- Bohlin, R. C., Savage, B. D., & Drake, J. F. 1978, *ApJ*, 224, 132
- Cambrésy, L. 1999, *A&A*, 345, 965
- Casali, M. M., Eiroa, C., & Duncan, W. D. 1993, *A&A*, 275, 195
- Davis, C. J., Matthews, H. E., Ray, T. P., Dent, W. R. F., & Richer, J. S. 1999, *MNRAS*, 309, 141
- Djupvik, A. A., André, Ph., Bontemps, S., Motte, F., Olofsson, G., Gålfalk, M., & Florén, H.-G. 2006, *A&A*, 485, 789
- Eiroa, C. & Casali, M. M.. 1992, *A&A*, 262, 468
- Enoch, M. L., Young, K. E., Glenn, J., Evans, N. J., II, Golwala, S., Sargent, A. I., Harvey, P., et al. 2006, *ApJ*, 638, 293
- Evans, N. J., II, Allen, L. E., Blake, G. A., Boogert, A. C. A., Bourke, T., Harvey, P. M., Kessler, J. E., et al. 2003, *PASP*, 115, 965
- Evans, N. J., II, Rawlings, J. M. C., Shirley, Y. L., & Mundy, L. G. 2001, *ApJ*, 557, 193
- Evans, N. J., II, et al. 2006, Final Delivery of Data from the c2d Legacy Project: IRAC and MIPS (Pasadena: Caltech), <http://data.spitzer.caltech.edu>
- Harvey, P. M., Chapman, N., Lai, S.-P., Evans, N. J., II, Allen, L. E., Jørgensen, J. K., Mundy, L. G., et al. 2006, *ApJ*, 644, 307
- Harvey, P. M., Rebull, L. M., Brooke, T., Spiesman, W. J., Chapman, N., Huard, T. L., Evans, N. J., II, et al. 2007, *ApJ*, in press (preprint: arXiv:0704.0253 [astro-ph])
- Hurt, R. L., & Barsony, M. 1996, *ApJ*, 460, L45
- Larsson, B., Liseau, R., Men'shchikov, A. B., Olofsson, G., Caux, E., Ceccarelli, C., Lorenzetti, D., et al. 2000 *A&A*, 363, 253

- Laurent, G., Aguirre, J. E., Glenn, J., Ade, P. A. R., Bock, J. J., Edgington, S. F., Goldin, A., et al. 2005, *ApJ*, 623, 742
- Ossenkopf, V., & Henning, Th. 1994, *A&A*, 291, 943
- Shirley, Y. L., Evans, N. J., II, & Rawlings, J. M. C. 2002, *ApJ*, 575, 337
- Straizys, V., Cernis, K., & Bartasiute, S. 1996, *Baltic Astronomy*, 5, 125
- Testi, L. & Sargent, A. I. 1998, *ApJ*, 508, L91
- Weingartner, J. C. & Draine, B. T. 2001, *ApJ*, 548, 296
- Young, C. H., Shirley, Y. L., Evans, N. J., II, & Rawlings, J. M. C. 2003, *ApJS*, 145, 111
- Young, K. E., Enoch, M. L., Evans, N. J., II, Glenn, J., Sargent, A., Huard, T. L., Aguirre, J., et al. 2006, *ApJ*, 644, 326

## Chapter 5

# Comparing Star Formation on Large Scales in the c2d Legacy Clouds: Bolocam Surveys of Serpens, Perseus, and Ophiuchus

### Abstract

We have undertaken an unprecedentedly large 1.1 millimeter continuum survey of three nearby star forming clouds using Bolocam at the Caltech Submillimeter Observatory. We mapped the largest areas in each cloud at millimeter or submillimeter wavelengths to date: 7.5 deg<sup>2</sup> in Perseus (chapter 2), 10.8 deg<sup>2</sup> in Ophiuchus (chapter 3), and 1.5 deg<sup>2</sup> in Serpens with a resolution of 31", detecting 122, 44, and 35 cores, respectively. Here we report on results of the Serpens survey and compare the three clouds. Average measured angular core sizes and their dependence on resolution suggest that many of the observed sources are consistent with power law density profiles. Tests of the effects of cloud distance reveal that linear resolution strongly affects measured source sizes and densities, but not the shape of the mass distribution. Core mass distribution slopes in Perseus and Ophiuchus ( $\alpha = 2.1 \pm 0.1$  and  $\alpha = 2.1 \pm 0.3$ ) are consistent with recent measurements of the stellar IMF, whereas the Serpens distribution is flatter ( $\alpha = 1.6 \pm 0.2$ ). We also compare the relative mass distribution shapes to predictions from turbulent fragmentation simulations. Dense

---

This chapter is adapted from Enoch et al. 2007, ApJ, in press.

cores constitute less than 10% of the total cloud mass in all three clouds, consistent with other measurements of low star-formation efficiencies. Furthermore, most cores are found at high column densities; more than 75% of 1.1 mm cores are associated with  $A_V \gtrsim 8$  mag in Perseus, 15 mag in Serpens, and 20 – 23 mag in Ophiuchus.

## 5.1 Introduction

Large-scale physical conditions in molecular clouds influence the outcome of local star formation, including the stellar initial mass function, star-formation efficiency, and the spatial distribution of stars within clouds (e.g., Evans, 1999). The physical processes that provide support of molecular clouds and control the fragmentation of cloud material into star-forming cores has been a source of recent debate. In the classical picture magnetic fields provide support and collapse occurs via ambipolar diffusion (e.g., Shu, Adams, & Lizano, 1987), but many simulations now suggest that turbulence dominates both support and fragmentation (for a review see Mac Low & Klessen, 2004).

Dense prestellar and protostellar condensations, or cores (for definitions and an overview see Di Francesco et al., 2007), provide a crucial link between the global processes that control star formation on large scales and the properties of young stars. The mass and spatial distributions of such cores retain imprints of the fragmentation process, prior to significant influence from later protostellar stages such as mass ejection in outflows, core dissipation, and dynamical interactions. These cold (10 K), dense ( $n > 10^4 \text{ cm}^{-3}$ ) cores are most easily observed at millimeter and submillimeter wavelengths where continuum emission from cold dust becomes optically thin and traces the total mass. Thus, complete maps of molecular clouds at millimeter wavelengths are important for addressing some of the outstanding questions in star formation.

Recent advances in millimeter and submillimeter wavelength continuum detectors have enabled a number of large-scale surveys of nearby molecular clouds (e.g., Johnstone, Di Francesco, & Kirk, 2004; Kirk, Ward-Thompson, & André, 2005; Hatchell

et al., 2005; Enoch et al., 2006; Stanke et al., 2006; Young et al., 2006). In addition to tracing the current and future star-forming activity of the clouds on large scales, millimeter and submillimeter observations are essential to understanding the properties of starless cores and the envelopes of the most deeply embedded protostars (for more on the utility of millimeter observations, see Enoch et al., 2006).

We have recently completed 1.1 mm surveys of Perseus (Enoch et al., 2006, and chapter 2), Ophiuchus (Young et al., 2006, and chapter 3), and Serpens (Enoch et al., 2007, and chapter 4) with Bolocam at the Caltech Submillimeter Observatory (CSO). Unlike previous work, our surveys not only cover the largest area in each cloud to date, but the uniform instrumental properties allow a comprehensive comparison of the cloud environments in these three regions. A comparison of the results for all three clouds provides insights into global cloud conditions and highlights the influence that cloud environment has on properties of star forming cores.

The Bolocam observations of each cloud are coordinated to cover the area mapped with *Spitzer* Space Telescope IRAC and MIPS observations of Serpens, Perseus, and Ophiuchus from the “Cores to Disks” (c2d Evans et al., 2003) Legacy project. While millimeter and submillimeter observations are essential to understanding the properties of dense prestellar cores and protostellar envelopes, infrared observations are necessary to characterize the protostars embedded within those envelopes. In chapter 6 we will take advantage of the overlap between our 1.1 mm maps and the c2d *Spitzer* Legacy maps to characterize the deeply embedded and prestellar populations in the northern c2d clouds.

Our large-scale millimeter surveys of Perseus, Ophiuchus, and Serpens, completed with the same instrument and reduction techniques, provide us with a unique basis for comparing the properties of 1.1 mm emission in a variety of star-forming environments. In chapters 2–4 we presented the basic results from the three surveys. In this chapter, we examine similarities and differences in the star-forming core samples and discuss implications for physical properties of cores, global cloud conditions, and the effects of environment.

We first outline our operational definition of a millimeter core including instru-

mental effects in §5.3, and discuss the observational biases introduced by different cloud distances in §5.4. Physical implications of source sizes and shapes, and differences between the clouds, are discussed in §5.5.1. We examine source densities and compare the cloud mass versus size distributions in §5.5.2. We analyze the core mass distributions and their relation to cloud turbulence in §5.5.3, and the spatial distributions of the core samples and clustering in §5.5.4. Extinction thresholds for finding 1.1 mm cores and the efficiency of forming such cores are discussed in §5.5.5 and §5.5.6. We end with a summary in §5.6.

## 5.2 Three-Cloud Sample

The millimeter continuum observation of Perseus, Ophiuchus, and Serpens were described in detail in chapters 2–4. All observations were completed at  $\lambda = 1.1$  mm with Bolocam<sup>1</sup> at the CSO. Bolocam is a large-format bolometer array that has a resolution of  $31''$  at 1.1 mm and a field of view of  $7'5$ , and was designed for mapping large fields quickly. Our surveys cover the largest areas in each cloud at millimeter or submillimeter wavelengths to date; we mapped  $7.5 \text{ deg}^2$  in Perseus (chapter 2),  $10.8 \text{ deg}^2$  in Ophiuchus (chapter 3), and  $1.5 \text{ deg}^2$  in Serpens, detecting 122, 44, and 35 cores, respectively. For each cloud, the same reduction and peak-finding algorithms were applied, creating a uniform sample that is ideally suited for examining similarities and differences in the current star formation activity of these three clouds.

## 5.3 What is a Core?

Before comparing results from the three clouds, we first describe our operational definition of a millimeter core. The response of Bolocam to extended emission, together with observed sensitivity limits determine the type of structure that is detectable in our 1.1 mm maps. The Bolocam 1.1 mm observations presented here are sensitive to sub-structures in molecular clouds with volume density  $n \gtrsim 2 \times 10^4 \text{ cm}^{-3}$ . One way

---

<sup>1</sup><http://www.cso.caltech.edu/bolocam>

to see this is to calculate the mean density along the curve defined by the detection as a function of size in each cloud.

Figure 5.1 demonstrates how the completeness in each cloud varies as a function of source size. Plotted symbols give the total mass versus linear deconvolved size for all sources detected in each cloud, and lines indicate the empirically derived 50% completeness limits. For Ophiuchus the average completeness curve is plotted; as the rms noise varies considerably in Ophiuchus, some regions have higher or lower completeness limits than the curve shown here. Completeness is determined from Monte Carlo simulations by adding simulated sources to the raw data, processing them in the same way as the real data, and attempting to detect them using our peak-finding algorithm (see chapter 2). We are biased against detecting large diffuse sources because we detect sources based on their peak flux density, whereas the mass is calculated from the total flux, which scales approximately as the size squared.

Calculating mean densities along the 50% completeness curve in each cloud yields  $n_{lim} \sim 3 - 7 \times 10^4 \text{ cm}^{-3}$  in Serpens,  $n_{lim} \sim 2 - 4 \times 10^4 \text{ cm}^{-3}$  in Perseus, and  $n_{lim} \sim 10 - 30 \times 10^4 \text{ cm}^{-3}$  in Ophiuchus. By comparison, the mean cloud density as probed by the extinction map is approximately  $1000 \text{ cm}^{-3}$  in Serpens,  $220 \text{ cm}^{-3}$  in Perseus, and  $390 \text{ cm}^{-3}$  in Ophiuchus. To be identified as a core, therefore, individual structures must have a mean density  $n \gtrsim 2 \times 10^4 \text{ cm}^{-3}$ , and a contrast compared to the average background density of at least 30–100. The mean cloud density is estimated from the total cloud mass (§5.5.6) and assumes a cloud volume of  $V = A^{1.5}$ , where  $A$  is the area of the extinction map within the  $A_V = 2$  contour.

Although we are primarily sensitive to cores with high density contrast compared to the background, it is clear that there is structure in the 1.1 mm map at lower contrasts as well, and that many cores are embedded within lower density filaments. The total mass in each of the 1.1 mm maps, calculated from the sum of all pixels  $> 5\sigma$ , is approximately twice the mass in dense cores:  $176 M_\odot$  versus  $92 M_\odot$  in Serpens,  $376 M_\odot$  versus  $278 M_\odot$  in Perseus, and  $83 M_\odot$  versus  $44 M_\odot$  in Ophiuchus, for ratios of total 1.1 mm mass to total core mass of 1.9, 1.4, and 1.9 respectively. Thus about half the mass detectable at 1.1 mm is not contained in dense cores, but is rather

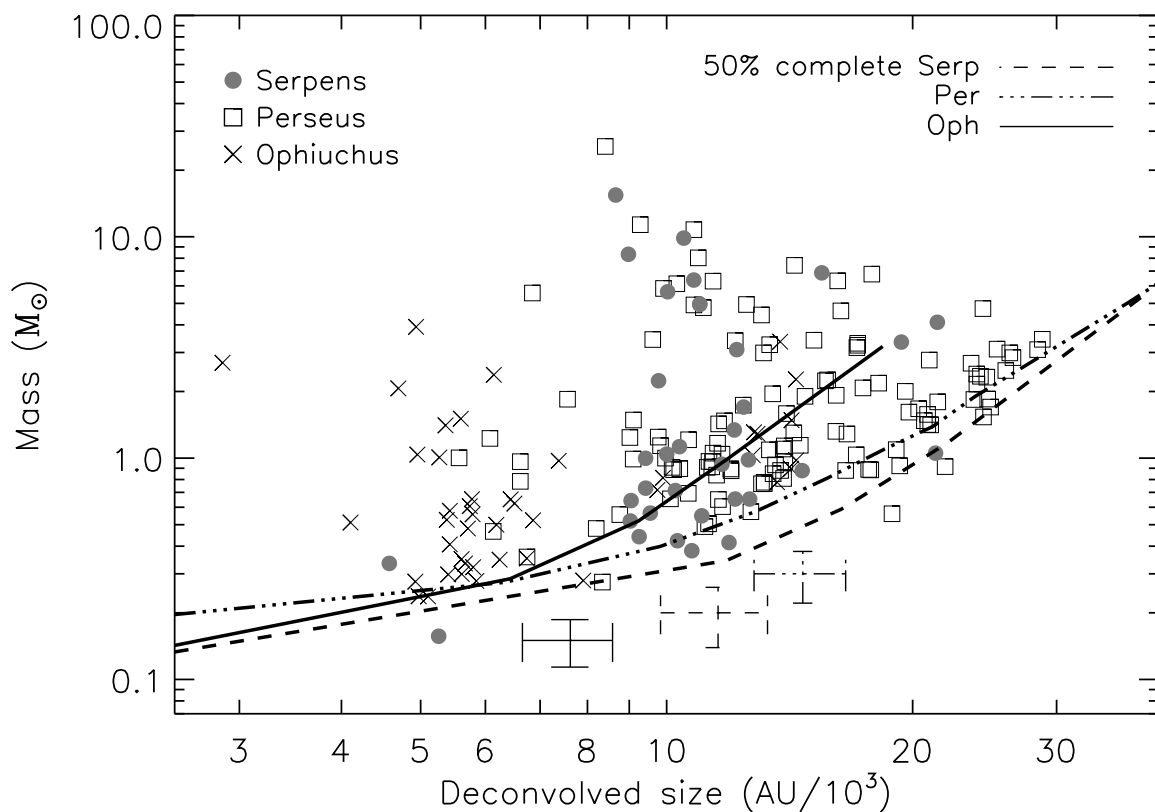


Figure 5.1 Completeness as a function of linear deconvolved source size in Serpens, Perseus, and Ophiuchus. Symbols show the distribution of source mass versus deconvolved size in each of the three clouds, where the size is the linear deconvolved average FWHM. Curves are empirical 50% completeness limits determined from Monte Carlo simulations, and demonstrate the dependence of completeness on source size and cloud distance. The beam FWHM of  $31''$  corresponds to approximately  $8 \times 10^3$  AU in Serpens and Perseus, and  $4 \times 10^3$  AU in Ophiuchus. Error bars for average sized sources near the detection limit in each cloud are also shown, as estimated from the results of Monte Carlo simulations and pointing uncertainties of approximately  $10''$ .

in the “foothills” between high density cores and the lower density cloud medium.

Structures that meet the above sensitivity criteria and are identified by our peak-finding routine are considered cores. Our peak-finding method will cause extended filaments to be broken up into several separate “cores” if there are local maxima in the filament separated by more than one beam size, and if each has a well-defined centroid (see §4.2.4). There is some question as to whether these objects should be considered separate sources or a single extended structure, but we believe that our

method is more reliable for these data than alternative methods such as Clumpfind (Williams, de Geus, & Blitz, 1994). In chapter 2 we found that faint extended sources in our maps, which one would consider single if examining by eye, are often partitioned into multiple sources by Clumpfind. Using our method, one filamentary structure in Serpens is broken up into several sources, as are two filaments in Perseus.

Monte Carlo tests were done to quantify biases and systematic errors introduced by the cleaning and iterative mapping process, which affect the kind of structure we can detect. Measured FWHM, axis ratios, and position angles are not significantly affected by either cleaning or iterative mapping for sources with  $\text{FWHM} \lesssim 120''$ ; likewise, any loss of flux for such sources has an amplitude less than that of the rms noise. Sources with  $\text{FWHM} \gtrsim 200''$  are detected, but with reduced flux density (by up to 50%), and large errors in the measured FWHM sizes of up to a factor of two.

The limitation on measurable core sizes of approximately  $120''$  corresponds to  $3 \times 10^4$  AU in Perseus and Serpens, and  $1.5 \times 10^4$  AU in Ophiuchus. Note that these sizes are of order the median core separation in each cloud (see §5.5.4), meaning that we are just as likely to be limited by the crowding of cores as by our sensitivity limits in the measurement of large cores. The dependence of measurable core size on cloud distance can be seen in figure 5.1, where the completeness rises steeply at smaller linear deconvolved sizes for Ophiuchus than for Perseus or Serpens. Thus we are biased against measuring large cores in Ophiuchus compared to the other two clouds. Although there are cores in our sample with sizes up to  $3 \times 10^4$  AU (figure 5.1), most cores have sizes substantially smaller than the largest measurable value, again indicating that we are not limited by systematics.

To summarize, the Bolocam 1.1 mm observations presented here naturally pick out sub-structures in molecular clouds with high volume density ( $n \gtrsim 2 \times 10^4 \text{ cm}^{-3}$ ). These millimeter cores have a contrast of at least 30 – 100 compared to the average cloud density as measured by the visual extinction map ( $2 - 10 \times 10^3 \text{ cm}^{-3}$ ). Many cores are embedded in lower density extended structures, which contribute approximately half the mass measurable in the Bolocam 1.1 mm maps. Finally, Monte Carlo tests indicate that we can detect cores with intrinsic sizes up to approximately  $120''$ .

## 5.4 Distance Effects

To test the effects of instrumental resolution and its dependence on distance, we convolve the Ophiuchus map with a larger beam to simulate putting it at approximately the same distance as Perseus and Serpens. After convolving the unfiltered Ophiuchus map to  $62''$  resolution, we apply the optimal filter and re-compute the local rms noise, as described for Serpens (§4.2.4). The pixel scale in the convolved map is still  $10''$   $\text{pixel}^{-1}$ , but the resolution is now  $62''$  and the rms is lower than in the original map, with a median value of  $17 \text{ mJy beam}^{-1}$  in the main L 1688 region. Source detection and photometry is carried out in the same way as for the original map, with the exception that a  $62''$  beam is assumed.

We detect 26 sources in the degraded-resolution map, or 40% fewer than the 44 sources in the original map. Therefore a number of sources do become confused at lower resolution. The basic source properties for the original and degraded-resolution samples, including angular deconvolved sizes, axis ratios, mass distribution, and mean densities, are compared in figure 5.2. Here the angular deconvolved size is defined as  $\theta_{dec} = \sqrt{\theta_{meas}^2 - B^2}$ , where  $\theta_{meas}$  is the geometric mean of the measured minor and major axis FWHM sizes and  $B$  is the pointing-smear beam FWHM ( $32.5''$ ).

We note that the average source size in the degraded-resolution map is nearly twice that in the original Ophiuchus map (average angular deconvolved size of  $61''$  versus  $98''$ ). Such a large size difference cannot be fully accounted for by blending of sources, as even isolated sources show the same effect. This behavior provides clues to the intrinsic intensity profile of the sources. For example, a Gaussian intensity profile or a solid disk of constant intensity will both have measured deconvolved sizes that are similar in maps with  $31''$  and  $62''$  beams. Conversely, a power law intensity profile will have a larger measured size in the  $62''$  resolution map.

The ratio of angular deconvolved size to beam size ( $\theta_{dec}/\theta_{mb}$ ; figure 5.3) are similar for the degraded-resolution (median  $\theta_{dec}/\theta_{mb} = 1.7$ ) and original (median  $\theta_{dec}/\theta_{mb} = 1.5$ ) samples, further evidence for power law intensity profiles. An intrinsic Gaussian or solid disk intensity profile will result in  $\theta_{dec}/\theta_{mb}$  values in the degraded-resolution

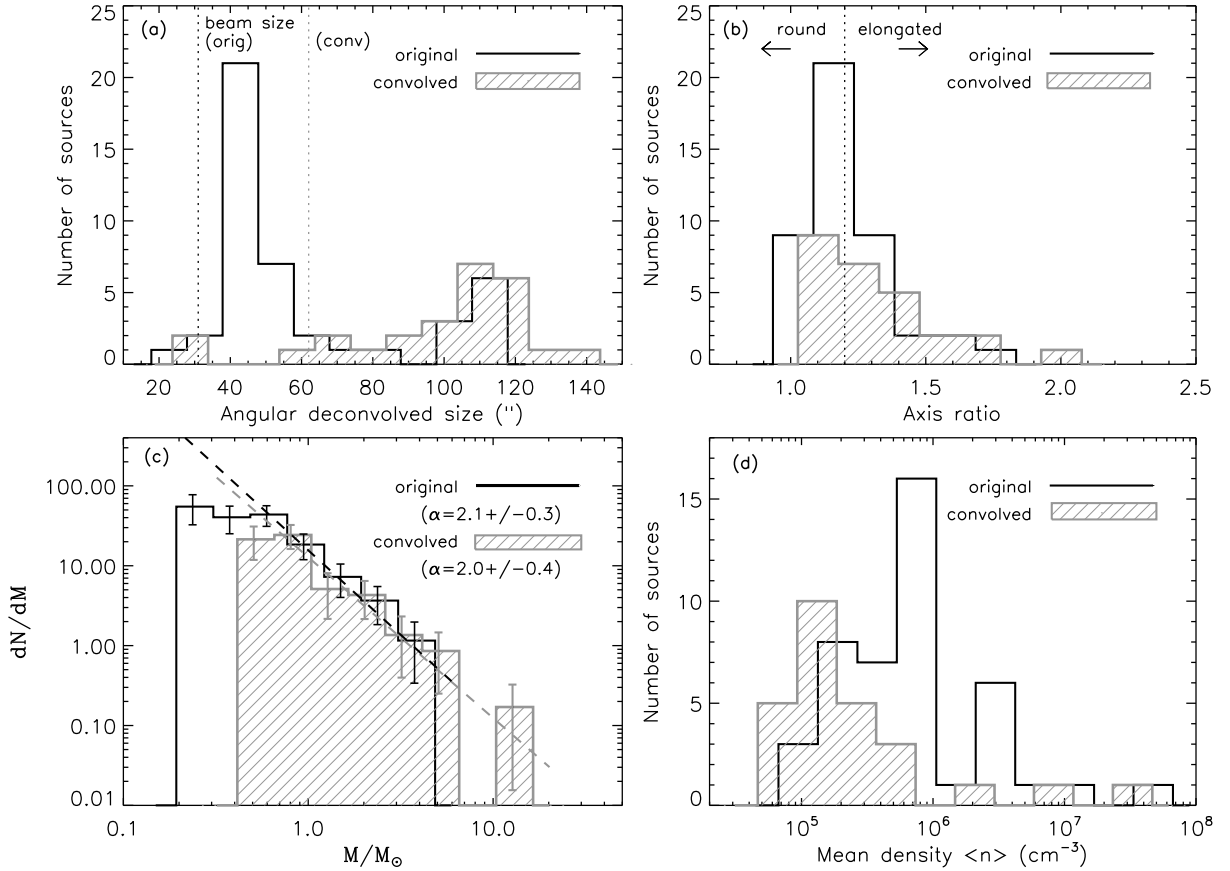


Figure 5.2 Comparison of the basic source properties for the original (black curve) and degraded-resolution, or convolved, (gray hatched curve) Ophiuchus source samples, which contain 44 and 26 cores respectively. (a) Measured angular deconvolved sizes are larger in the degraded-resolution map than in the original map by approximately a factor of two (respective mean values of  $98''$  and  $61''$ ). (b) Sources tend to be slightly more elongated in the degraded-resolution map, with an average axis ratio of  $1.3 \pm 0.2$  compared to  $1.2 \pm 0.2$  in the original map. (c) The slope of the CMD is not significantly changed for the degraded-resolution sample, but a number of low mass cores are blended into a few higher mass sources. (d) Larger deconvolved sizes lead to lower mean densities for the degraded-resolution sample (median values of  $1.6 \times 10^5 \text{ cm}^{-3}$  and  $5.8 \times 10^5 \text{ cm}^{-3}$ ).

map that are approximately half those in the original map, while a  $1/r^2$  intensity profile results in similar values in the degraded-resolution and original map (0.9 versus 1.3). We discuss source profiles further in Section 5.5.1 below.

Sources in the degraded-resolution map appear slightly more elongated, with an average axis ratio at the half-maximum contour of  $1.3 \pm 0.2$  compared to  $1.2 \pm 0.2$

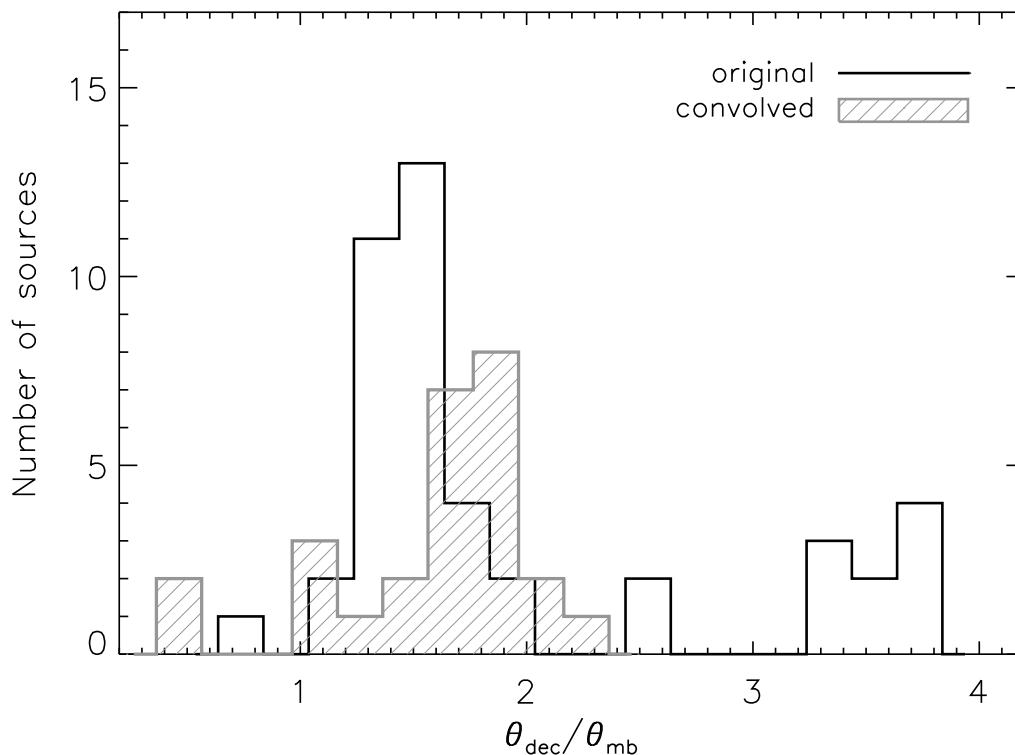


Figure 5.3 Ratio of angular deconvolved size to beam size ( $\theta_{dec}/\theta_{mb}$ ) for the original and degraded-resolution, or convolved, Ophiuchus maps. Note that  $\theta_{mb}$  is  $31''$  for the original map and  $62''$  for the degraded-resolution map. Measured  $\theta_{dec}/\theta_{mb}$  values are similar for the degraded-resolution (median  $\theta_{dec}/\theta_{mb} = 1.7$ ) and original (median  $\theta_{dec}/\theta_{mb} = 1.5$ ) samples, providing evidence for power law intensity profiles. An intrinsic Gaussian or solid disk intensity profile will result in  $\theta_{dec}/\theta_{mb}$  values in the degraded-resolution map that are nearly half those in the original map, while a  $1/r^2$  intensity profile results in similar values in the degraded-resolution and original map (0.9 versus 1.3).

for the original map. Larger axis ratios are expected for blended sources in a lower-resolution map. The slope of the mass distribution is not significantly changed:  $2.0 \pm 0.4$  for the degraded-resolution sample compared to  $2.1 \pm 0.3$  for the original sample. The factor of two increase in deconvolved sizes do create lower mean densities in the degraded-resolution sample, however (median density of  $1.6 \times 10^5 \text{ cm}^{-3}$  compared to  $5.8 \times 10^5 \text{ cm}^{-3}$  for the original sample). The effect of resolution on mean densities will be discussed further in §5.5.2.

Given the small number of sources in the degraded-resolution map, we carry out

the three-cloud comparison below using the original Ophiuchus map to mitigate uncertainties from small number statistics. Any notable differences between the original and degraded-resolution Ophiuchus results will be discussed where appropriate.

## 5.5 Discussion

In the following sections we discuss the results of the three-cloud comparison and implications for the physical properties of cores, global cloud conditions, and the effects of environment on star formation in nearby molecular clouds.

### 5.5.1 Physical Implications of Source Sizes and Shapes

To compare sources in clouds at different distances, we first look at the linear deconvolved size:  $D_{dec} = d\sqrt{\theta_{meas}^2 - B^2}$ , where  $d$  is the cloud distance,  $\theta_{meas}$  is measured angular size, and  $B$  is the beam size. The distributions of linear deconvolved source sizes for the three clouds are shown in figure 5.4, left. Sources in Ophiuchus have smaller deconvolved sizes than those in Perseus or Serpens by almost a factor of two, with mean values of  $7.5 \times 10^3$  AU in Ophiuchus compared to  $1.2 \times 10^4$  AU in Serpens and  $1.5 \times 10^4$  AU in Perseus. There is a systematic uncertainty in the deconvolved size associated with the uncertainty in the effective beam size, which becomes larger with larger pointing errors. The effective beam in any of the three clouds may be as large as  $35''$ , which would decrease deconvolved sizes negligibly, by up to  $10^3$  AU depending on the distance and measured size.

While there are possible physical explanations for intrinsic size differences, for instance a denser medium with a shorter Jeans length should produce smaller cores on average, we are more likely seeing a consequence of the higher linear resolution in Ophiuchus, as discussed in §5.4. Thus cores in Serpens and Perseus would likely appear smaller if observed at higher resolution, and measured linear deconvolved sizes should be regarded as upper limits. To reduce the effects of distance, we examine the ratio of angular deconvolved size to beam size ( $\theta_{dec}/\theta_{mb}$ ; figure 5.4, right). We

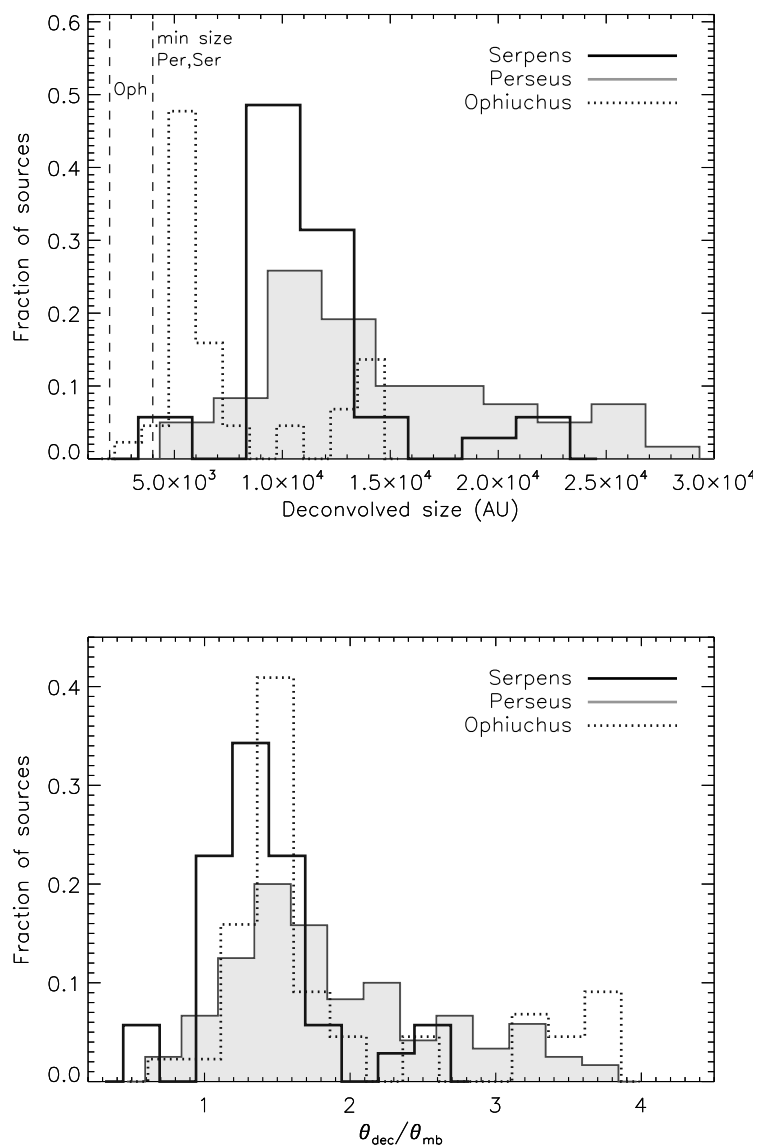


Figure 5.4 *Top*: Comparison of the distribution of deconvolved linear source sizes in Serpens (solid line), Perseus (shaded), and Ophiuchus (dotted line). Histograms are plotted as the fraction of total sources in the cloud as a function of deconvolved size in AU. Estimates of the minimum resolvable source size (dashed lines) are based on smearing of the beam by pointing errors. Although measured angular source sizes in Ophiuchus are similar to those in Perseus and Serpens, the deconvolved sizes are much smaller due to the different cloud distances. *Bottom*: Similar, but sizes are measured as the angular deconvolved size in units of the beam FWHM. For isolated sources with power law density profiles,  $\theta_{dec}/\theta_{mb}$  is inversely proportional to the power law index and is independent of cloud distance (Young et al., 2003).

found in §5.4 that  $\theta_{dec}/\theta_{mb}$  does not depend strongly on the linear resolution, but does depend on the intrinsic source intensity profile.

If the millimeter sources follow power law density distributions, which do not have a well defined size, then Young et al. (2003, hereafter Y03) show that  $\theta_{dec}/\theta_{mb}$  depends on the index of the power law, and not on the distance of the source. So, for example, if sources in Perseus and Ophiuchus have the same intrinsic power law profile, the mean  $\theta_{dec}/\theta_{mb}$  should be similar in the two clouds, and the mean linear deconvolved size should be twice as small in Ophiuchus because it lies at half the distance. This is precisely the behavior we observe, suggesting that many of the detected 1.1 mm sources have power law density profiles.

Considering that a number of the 1.1 mm sources have internal luminosity sources (see chapter 6), and that protostellar envelopes are often well described by power law profiles (Shirley, Evans, & Rawlings 2002; Y03), this is certainly a plausible scenario. According to the correlation between  $\theta_{dec}$  and density power law exponent  $p$  found by Y03, median  $\theta_{dec}/\theta_{mb}$  values of 1.7 in Perseus, 1.5 in Ophiuchus and 1.3 in Serpens would imply average indices of  $p = 1.4$ , 1.5, and 1.6 respectively. These numbers are consistent with mean  $p$  values found from radiative transfer modeling of Class 0 and Class I envelopes ( $p \sim 1.6$ , Shirley et al. (2002); Y03), although the median for those samples is somewhat higher ( $p \sim 1.8$ ). Note that source profiles could deviate from a power law on scales much smaller than the beam size, or on scales larger than our size sensitivity ( $200''$ ) without affecting our conclusions.

Perseus displays the widest dispersion of angular sizes, ranging continuously from  $1 - 4\theta_{mb}$ . By contrast, more than half the sources in Serpens and Ophiuchus are within  $0.5\theta_{mb}$  of their respective mean values. Although there is a group of Ophiuchus sources at large sizes in figure 5.4, note that the degraded-resolution Ophiuchus sample displays a very narrow range of sizes (figure 5.3), similar to Serpens. The observed size range in Perseus would correspond to a wide range of power law indices, from very shallow ( $p \sim 1$ ) to that of a singular isothermal sphere ( $p = 2$ ). A more likely possibility, however, is that sources with large  $\theta_{dec}/\theta_{mb}$  do not follow power law density profiles.

The axis ratio at the half-maximum contour is a simple measure of source shape. Figure 5.5 shows the distribution of 1.1 mm source axis ratios in the three clouds. Our simulations suggest that axis ratios of up to 1.2 can be introduced by the data reduction (chapter 2), so we consider sources with an axis ratio  $< 1.2$  to be round, and those with a ratio  $> 1.2$  to be elongated. Sources in Ophiuchus tend to be round, with a mean axis ratio of 1.2, but note that the mean axis ratio in the degraded-resolution Ophiuchus sample is 1.3. The average axis ratio in Serpens is 1.3, and Perseus sources exhibit the largest axis ratios with a mean of 1.4 and a tail out to 2.7.

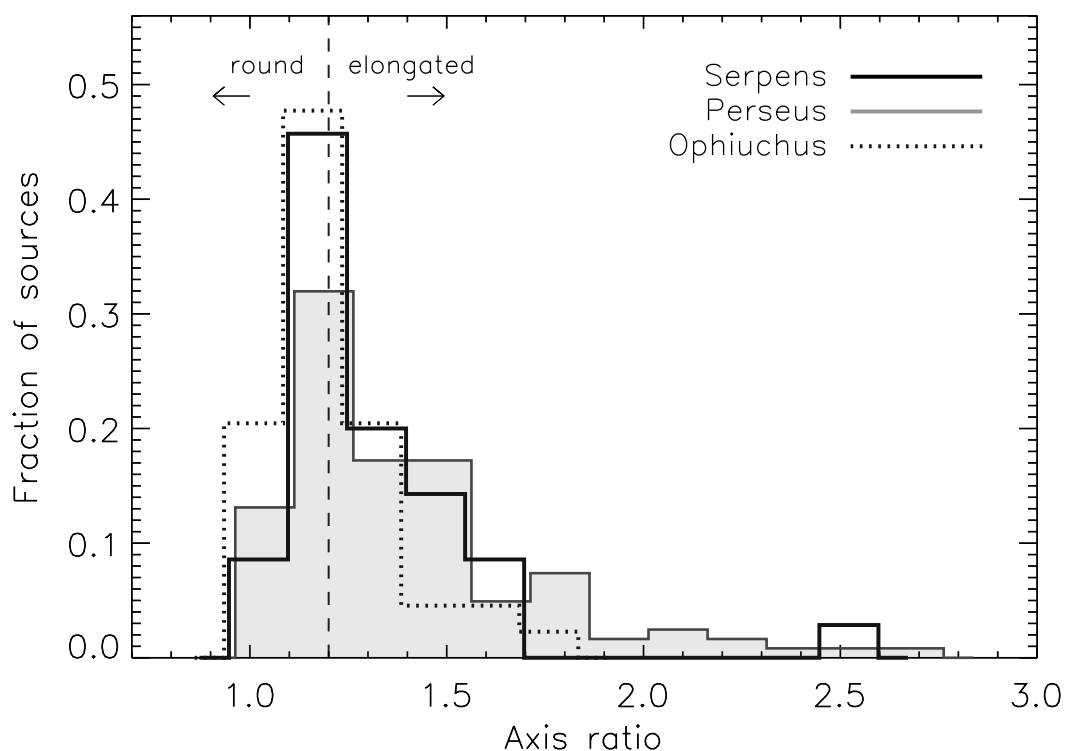


Figure 5.5 Comparison of the distribution of axis ratios, where the ratio is calculated at the half-max contour. Axis ratios  $< 1.2$  are considered round, and  $> 1.2$  elongated, based on Monte Carlo simulations. Sources are primarily round in Ophiuchus and Serpens, with mean axis ratio of 1.2 and 1.3, respectively. Perseus exhibits the most elongated sources, with a mean axis ratio of 1.4 and a distribution tail extending up to 2.7.

We found in chapter 3 that Ophiuchus sources were more elongated at the  $4\sigma$

contour than at the half-max contour, as would be the case for round cores embedded in more elongated filaments. A similar situation is seen in Serpens; the average axis ratio at the  $4\sigma$  contour is 1.4 in all three clouds. Thus cores in Perseus are somewhat elongated on average, while objects in Serpens and Ophiuchus appear more round at the half-max contour but elongated at the  $4\sigma$  contour, suggesting round cores embedded in filamentary structures.

In addition to angular sizes, Y03 also note a relationship between axis ratio and density power law exponent, finding that aspherical sources are best modeled with shallower density profiles. The inverse proportionality between  $p$  and axis ratio demonstrated in figure 25 of Y03 suggests power law indices in all three clouds between 1.5 and 1.7. These values are consistent with those inferred from the average angular deconvolved source sizes, and the wider variation of axis ratios in Perseus again points to a larger range in  $p$  for that cloud.

### 5.5.2 Densities and the Mass versus Size Distribution

Mean densities calculated using linear deconvolved FWHM sizes appear to be significantly higher in Ophiuchus, where the median of the mean densities of the sample is  $5.4 \times 10^5 \text{ cm}^{-3}$ , than in Serpens (median density  $2.2 \times 10^5 \text{ cm}^{-3}$ ) or Perseus (median density  $1.6 \times 10^5 \text{ cm}^{-3}$ ), as seen in figure 5.6, left. There is a large scatter with standard deviation of order twice the mean value in all three clouds. Sources in Ophiuchus tend to be less massive than in the other two clouds, so the larger mean densities can be entirely attributed to smaller deconvolved sizes in the Ophiuchus sample, which are sensitive to the shape of the intrinsic density distribution (Y03). As noted in §5.4, linear resolution has a strong systematic effect on deconvolved sizes, and consequently on mean densities. The median density of the degraded-resolution Ophiuchus sample is  $1.6 \times 10^5 \text{ cm}^{-3}$ , similar to both Perseus and Serpens.

We additionally calculate mean densities using the full-width at  $4\sigma$  size rather than the FWHM size (figure 5.6, right) to test the hypothesis that mean density differences are largely an effect of how source sizes are measured. Using this definition, differences

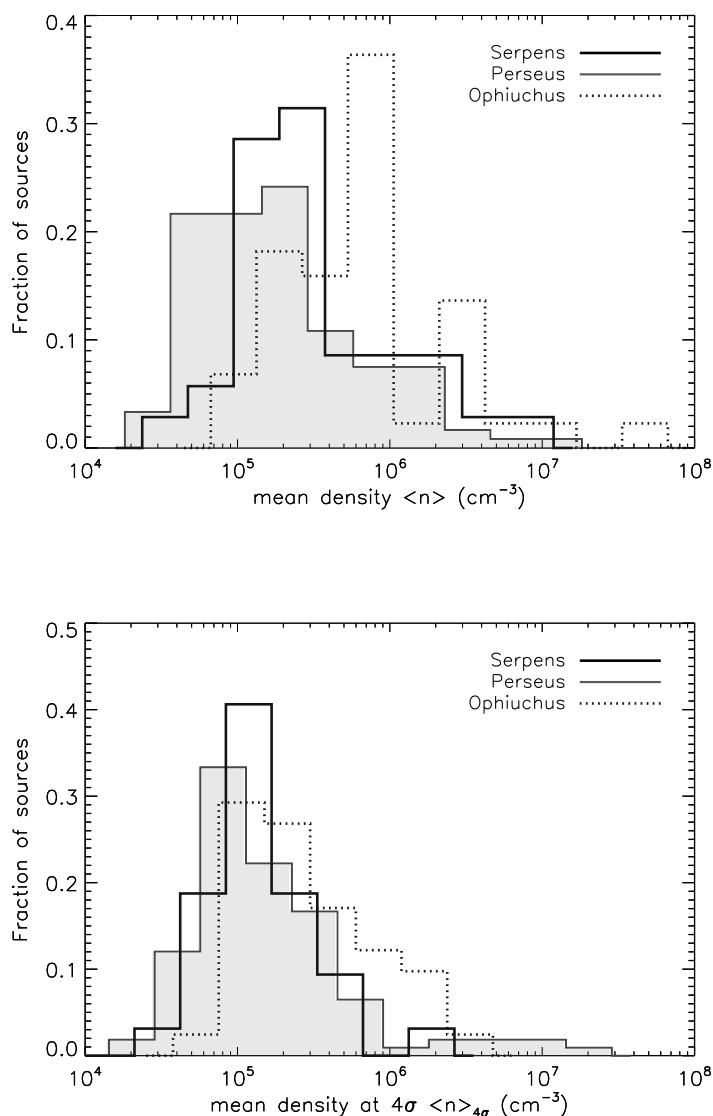


Figure 5.6 Comparison of the distributions of core mean densities. *Top:* The mean density is calculated from the total mass and the linear deconvolved source size, assuming spherical cores. Despite the lower masses of cores in Ophiuchus compared to Serpens and Perseus, mean densities in Ophiuchus are higher on average due to small linear deconvolved sizes (see figure 5.4). The mean densities in the degraded-resolution Ophiuchus sample are more consistent with Perseus and Serpens, suggesting cloud distance has a strong effect. *Bottom:* Similar, except that the mean density is calculated using the full-width at  $4\sigma$  size rather than of FWHM size. Differences between the clouds are diminished; thus the mean density is less dependent on cloud distance when the source size is measured at the radius where the source merges into the background, rather than at the half-max.

between the clouds are less pronounced, with median densities of  $1.2 \times 10^5 \text{ cm}^{-3}$  in Perseus,  $1.3 \times 10^5 \text{ cm}^{-3}$  in Serpens, and  $2.0 \times 10^5 \text{ cm}^{-3}$  in Ophiuchus. These numbers suggest that source mean densities are less dependent on cloud distance when measured at the radius where the source merges into the background, rather than at the half-max.

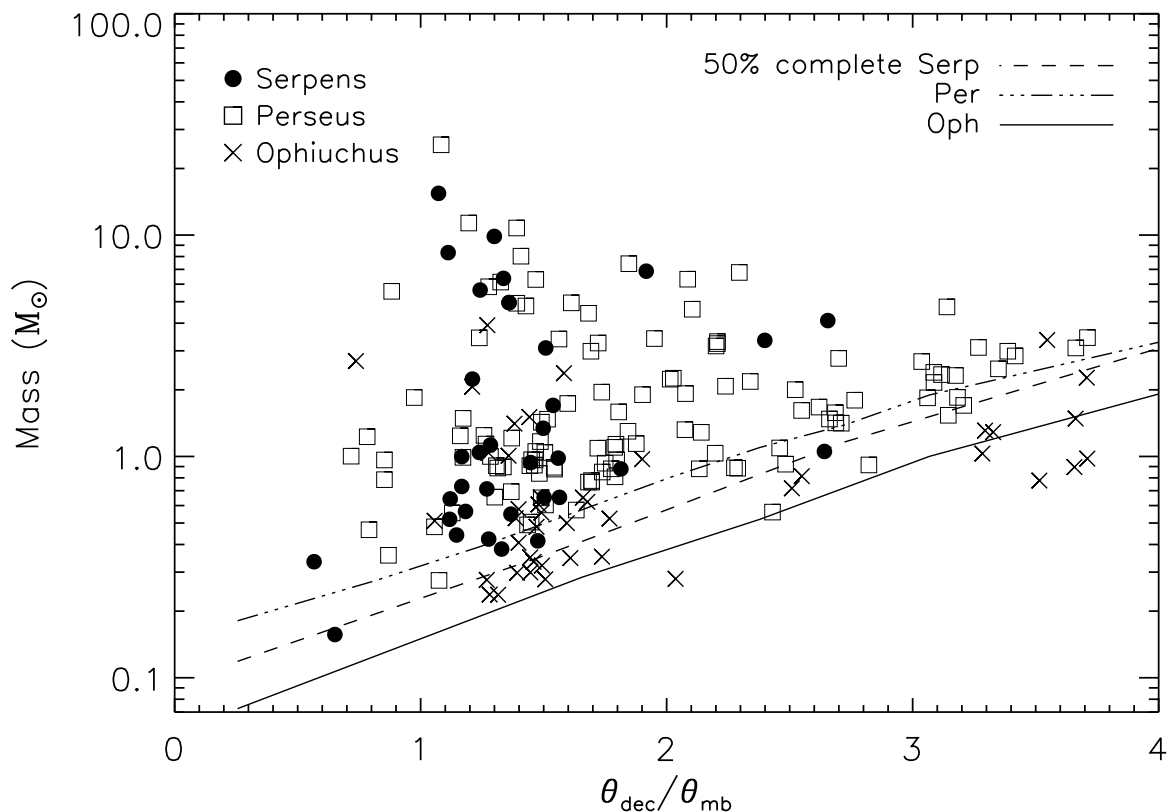


Figure 5.7 Source total mass versus angular deconvolved size (in units of the beam FWHM) for Serpens, Perseus, and Ophiuchus. The angular size is less dependent on cloud distance than the linear deconvolved source size (§5.4). Sources in Perseus fill more of the parameter space than those in Serpens or Ophiuchus, suggesting a wider range of physical conditions in that cloud. Empirically derived 50% completeness limits are also shown (lines).

Figure 5.7 again displays the source total mass versus size distribution, using the angular deconvolved size ( $\theta_{\text{dec}}$ , in units of the beam size) rather than the linear deconvolved size. With the exception of two low mass compact sources, 1.1 mm sources in Serpens exhibit a wide range of masses and a narrow range of sizes. Sources in

Perseus, in contrast, demonstrate a wide range in both mass and size. This difference likely reflects a wider variety of physical conditions in the Perseus cloud, including the existence of more sources outside the main cluster regions. In such lower density regions, sources may be more extended than in densely populated groups. This idea is supported by our observations: Perseus sources within the NGC 1333 region are smaller on average (mean size of  $59 \pm 13''$ ) than those in the rest of the cloud (mean size of  $71 \pm 21''$ ). Sources in Ophiuchus have a more bimodal distribution, with the majority occupying a narrow range of sizes, and a smaller group with  $\theta_{dec} > 3\theta_{mb}$ .

### 5.5.3 Fragmentation and the Core Mass Distribution

Differential ( $dN/dM$ ) core mass distributions (CMDs) of 1.1 mm sources in Serpens, Perseus, and Ophiuchus are shown in figure 5.8, with those of Perseus and Ophiuchus scaled down for clarity. Error bars reflect  $1\sigma \sqrt{N}$  statistical uncertainties. Dashed lines indicate empirical 50% completeness limits for average sized sources in each cloud, which are determined as described in §5.3 and in chapter 2. Mass distributions include all 1.1 mm cores in each cloud, including those that may be associated with embedded protostellar sources.

The shape of the Ophiuchus and Perseus mass distributions are quite similar above their respective completeness limits ( $M \gtrsim 0.5 M_{\odot}$  in Ophiuchus and  $M \gtrsim 0.8 M_{\odot}$  in Perseus). Fitting a power law ( $dN/dM \propto M^{-\alpha}$ ) to the CMDs, we find that both Perseus and Ophiuchus have a best fit slope of  $\alpha = 2.1$ , although the error is larger on the slope for Ophiuchus ( $\sigma_{\alpha} = 0.3$ ) than for Perseus ( $\sigma_{\alpha} = 0.1$ ). The slope of the Serpens CMD is marginally different ( $\alpha = 1.6 \pm 0.2$ ), being flatter than in the other two clouds by approximately  $2\sigma$ .

The two-sided Kolmogorov-Smirnov test, performed on the samples of discrete masses, indicates a high probability (46%) that the Perseus and Ophiuchus mass distributions are representative of the same parent population. Conversely, the probabilities that the Serpens core masses are sampled from the same population as the Perseus (probability = 12%) or Ophiuchus (probability = 5%) masses are much lower.

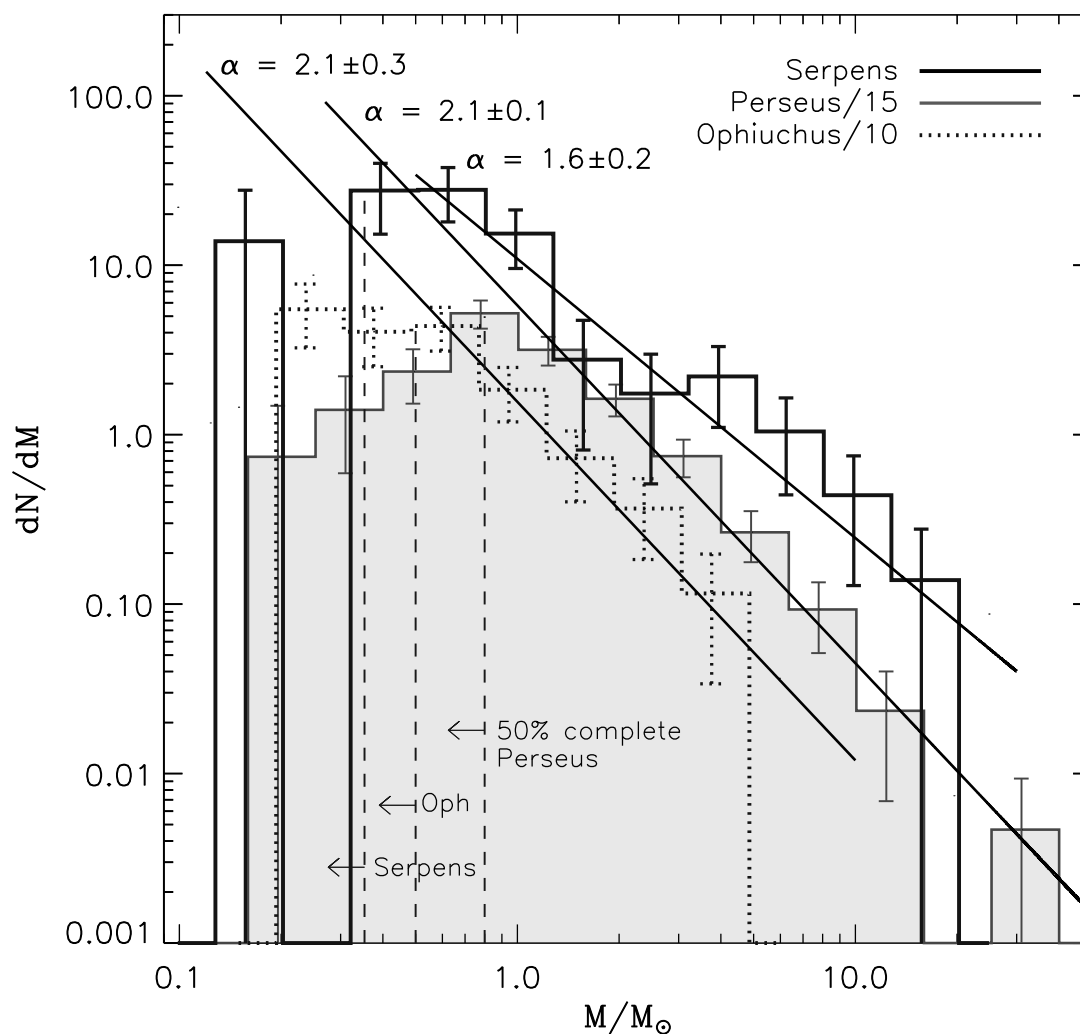


Figure 5.8 Comparison of the differential core mass distributions (CMDs) of sources in Serpens, Perseus, and Ophiuchus. The Ophiuchus curve has been scaled by 1/10, and the Perseus curve by 1/15 for clarity. Uncertainties reflect  $\sqrt{N}$  counting statistics only. Vertical dotted lines show the 50% completeness limits for average sized sources in each cloud (55" FWHM in Serpens, 68" in Perseus and 69" in Ophiuchus). The shape of the Perseus and Ophiuchus distributions are quite similar ( $\alpha = 2.1$ ) in the region where both CMDs are complete. The shape of the Serpens CMD is marginally different ( $\alpha = 1.6$ ) from the other two clouds.

Although it is possible that the lower linear resolution in Perseus and Serpens has led to larger masses via blending, the test we conducted to increase the effective beam size in the Ophiuchus map did not appreciably change the shape of the Ophiuchus mass distribution (see figure 5.2).

If the shape of the CMD is a result of the fragmentation process, then the slope of the CMD can be compared to models, e.g., of turbulent fragmentation. Padoan & Nordlund (2002) argue that turbulent fragmentation naturally produces a power law with  $\alpha = 2.3$ , consistent with the slopes we measure in Perseus and Ophiuchus ( $\alpha = 2.1$ ), but not with Serpens ( $\alpha = 1.6$ ). Recently Ballesteros-Paredes et al. (2006, hereafter BP06) have questioned that result, finding that the shape of the CMD depends strongly on the Mach number of the turbulence in their simulations. The BP06 SPH simulations show that higher Mach numbers result in a larger number of sources with lower mass and a steep slope at the high mass end (their figure 5; see also figure 1.6). Conversely, lower Mach numbers favor sources with higher mass, resulting in a smaller number of low mass sources, more high mass cores, and a shallower slope at the high mass end.

Using an analytic argument, Padoan & Nordlund (2002) also note a relationship between core masses and Mach numbers, predicting that the mass of the largest core formed by turbulent fragmentation should be inversely proportional to the square of the Alfvénic Mach number on the largest turbulent scale  $\mathcal{M}_A^2$ . Given that our ability to accurately measure the maximum core mass is limited by resolution, small number statistics, and cloud distance differences, we focus here on the overall CMD shapes.

To compare our observational results to the simulations of BP06, we estimate the sonic Mach number  $\mathcal{M} = \sigma_v/c_s$  in each cloud. Here  $\sigma_v$  is the observed rms velocity dispersion,  $c_s = \sqrt{kT/\mu m_H}$  is the isothermal sound speed, and  $\mu = 2.33$  is the mean molecular weight per particle. Large  $^{13}\text{CO}$  maps of Perseus and Ophiuchus observed with FCRAO at a resolution of  $44''$  are publicly available as part of “The COMPLETE Survey of Star Forming Regions”<sup>2</sup> (COMPLETE; Goodman, 2004; Ridge et al., 2006). Average observed rms velocity dispersions kindly provided by the COMPLETE team are  $\sigma_v = 0.68 \text{ km s}^{-1}$  in Perseus,  $\sigma_v = 0.44 \text{ km s}^{-1}$  in Ophiuchus, and  $\sigma_v = 0.92 \text{ km s}^{-1}$  in Serpens (J. Pineda, personal communication). These were measured by masking out all positions in the map that have peak temperatures with a S/N less than 10, fitting a Gaussian profile to each, and taking an average of the standard deviations.

---

<sup>2</sup><http://cfa-www.harvard.edu/COMPLETE/>

We note that the value of  $\sigma_v = 0.68 \text{ km s}^{-1}$  for Perseus is smaller than a previous measurement of  $\sigma_v = 2.0 \text{ km s}^{-1}$  based on AT&T Bell Laboratory 7 m observations of a similar area of the cloud (Padoan, Goodman, & Juvela, 2003). The smaller value derived by the COMPLETE team is most likely a consequence of the method used: a line width is calculated at every position and then an average of these values is taken. In contrast to calculating the width of the averaged spectrum this method removes the effects of velocity gradients across the cloud. The different resolutions of the surveys ( $44''$  and  $0.07 \text{ km s}^{-1}$  for the COMPLETE observations,  $100''$  and  $0.27 \text{ km s}^{-1}$  for the Padoan et al. observations) may also play a role. Sources of uncertainty in the line width measurement are not insignificant, and include the possibility that  $^{13}\text{CO}$  is optically thick to an unknown degree, and the fact that line profiles are not necessarily well fit by a Gaussian, especially in Perseus where the lines sometimes appear double peaked.

Assuming that the sound speed is similar in all three clouds, the relative velocity dispersions suggest that turbulence is more important in Serpens than in Perseus or Ophiuchus, by factors of approximately 1.5 and 2, respectively. Mach numbers calculated using the observed  $\sigma_v$  and assuming a gas kinetic temperature of 10 K are  $\mathcal{M} = 4.9$  (Serpens),  $\mathcal{M} = 3.6$  (Perseus), and  $\mathcal{M} = 2.3$  (Ophiuchus). We focus on Serpens and Ophiuchus, as they are the most different. Serpens is observed to have a higher Mach number than Ophiuchus, but the CMD indicates a larger number of high mass cores, a shallower slope at the high mass end, and a dearth of low mass cores compared to Ophiuchus. This result is contrary to the trends found by BP06, which would predict a steeper slope and more low mass cores in Serpens.

One core of relatively high mass is measured in the degraded-resolution map of Ophiuchus, as is expected for blending at lower resolution (figure 5.2), making the difference between the Serpens and Ophiuchus CMDs less dramatic. The degraded-resolution CMD for Ophiuchus still has a steeper slope ( $\alpha = 2.0 \pm 0.4$ ) than the Serpens CMD, however, and a larger fraction of low mass sources: 81% of sources in the degraded-resolution Ophiuchus sample have  $M < 2M_\odot$  compared to 49% in the Serpens sample.

More accurate measurements of the Mach number and higher resolution studies of the relative CMD shapes will be necessary to fully test the BP06 prediction, given that uncertainties are currently too large to draw firm conclusions. As both numerical simulations and observations improve, however, the observed CMD and measurements of the Mach number will provide a powerful constraint on turbulent star formation simulations.

Comparing the shape of the CMD to the stellar initial mass function (IMF) may give insight into what determines final stellar masses: the initial fragmentation into cores, competitive accretion, or feedback processes. The shape of the local IMF is still uncertain (Scalo, 2005), but recent work has found evidence for a slope of  $\alpha = 2.5\text{--}2.8$  for stellar masses  $M \gtrsim 1 M_\odot$ , somewhat steeper than the slopes we observe in all three clouds. For example, Reid, Gizis, & Hawley (2002) find  $\alpha = 2.5$  above  $0.6 M_\odot$ , and  $\alpha = 2.8$  above  $1 M_\odot$ . Chabrier (2003) suggests  $\alpha = 2.7$  ( $M > 1 M_\odot$ ), while Schröder & Pagel (2003) finds  $\alpha = 2.7$  for  $1.1 < M < 1.6 M_\odot$  and  $\alpha = 3.1$  for  $1.6 < M < 4 M_\odot$ . For reference, the Salpeter IMF has a slope of  $\alpha = 2.35$  (Salpeter, 1955).

For comparison to the IMF, we would ideally like to construct a CMD that includes starless cores only, so that it is a measure of the mass initially available to form a star. Although we cannot separate prestellar cores from more evolved objects with millimeter maps alone, a comparison of the Bolocam data with c2d *Spitzer* Legacy maps of the same regions will allow us to distinguish prestellar cores from those with internal luminosity sources (chapter 6).

#### 5.5.4 Clustering

We use the two-point correlation function,

$$w(r) = \frac{H_s(r)}{H_r(r)} - 1, \quad (5.1)$$

as a quantitative measure of the clustering of cores. Here  $H_s(r)$  is the number of core pairs with separation between  $\log(r)$  and  $\log(r) + d\log(r)$ , and  $H_r(r)$  is similar but

for a random distribution (see chapter 2). Thus  $w(r)$  is a measure of excess clustering over a random distribution, as a function of separation.

Figure 5.9 plots the cloud two-point correlation functions, with the best fit power laws,  $w(r) \propto r^n$ , shown. The average linear source FWHM size is indicated, as well as the minimum possible separation (the beam size), and the linear map size. The best fit slopes to  $w(r)$  for Serpens ( $n = -1.5 \pm 0.2$ ), Perseus ( $n = -1.18 \pm 0.06$ ), and Ophiuchus ( $n = -1.5 \pm 0.1$ ) are consistent within  $2\sigma$ , but there is an indication both from the slopes and a visual examination of the plot that  $w(r)$  falls off more steeply in Serpens and Ophiuchus than in Perseus. A shallower slope suggests that clustering remains strong out to larger scales in Perseus than in the other two clouds.

We do find that a broken power law with slopes of  $n = -0.75$  ( $1.3 \times 10^4 < r < 6.3 \times 10^4 \text{AU}$ ) and  $n = -3.3$  ( $r > 6.3 \times 10^4 \text{AU}$ ) is a better fit to the Serpens correlation function than a single power law, indicating that clustering remains strong to intermediate scales, as in Perseus, but then drops off quickly. Also shown in figure 5.9 is  $w(r)$  for the degraded-resolution Ophiuchus sample (gray hatched curve). The degraded-resolution sample is fit by a shallower slope ( $n = -1.2 \pm 0.3$ ) because there are fewer sources at small separations, but it is broadly consistent with the original Ophiuchus sample.

Our general conclusion that clustering of 1.1 mm sources remains strong over larger scales in Perseus than in Serpens and Ophiuchus can also be reached by visually examining each map. Perseus has highly clustered regions spread over a larger area as well as a number of more distributed sources, whereas Serpens and Ophiuchus have a single main cluster with fewer small groups spread throughout the cloud.

A few caveats should be noted here. First, the fact that clustering seems to extend over larger scales in Perseus could simply be due to the fact that Perseus has more widely separated regions of star formation, and the physical association of all these regions has not been firmly established. Second, the map of Serpens covers a much smaller linear area than that of Perseus ( $30 \text{ pc}^2$  versus  $140 \text{ pc}^2$ ); we need to be sure that the steepening of the slope in Serpens is not caused by the map size. This was confirmed by taking a piece of the Perseus map equal in size to the Serpens map and

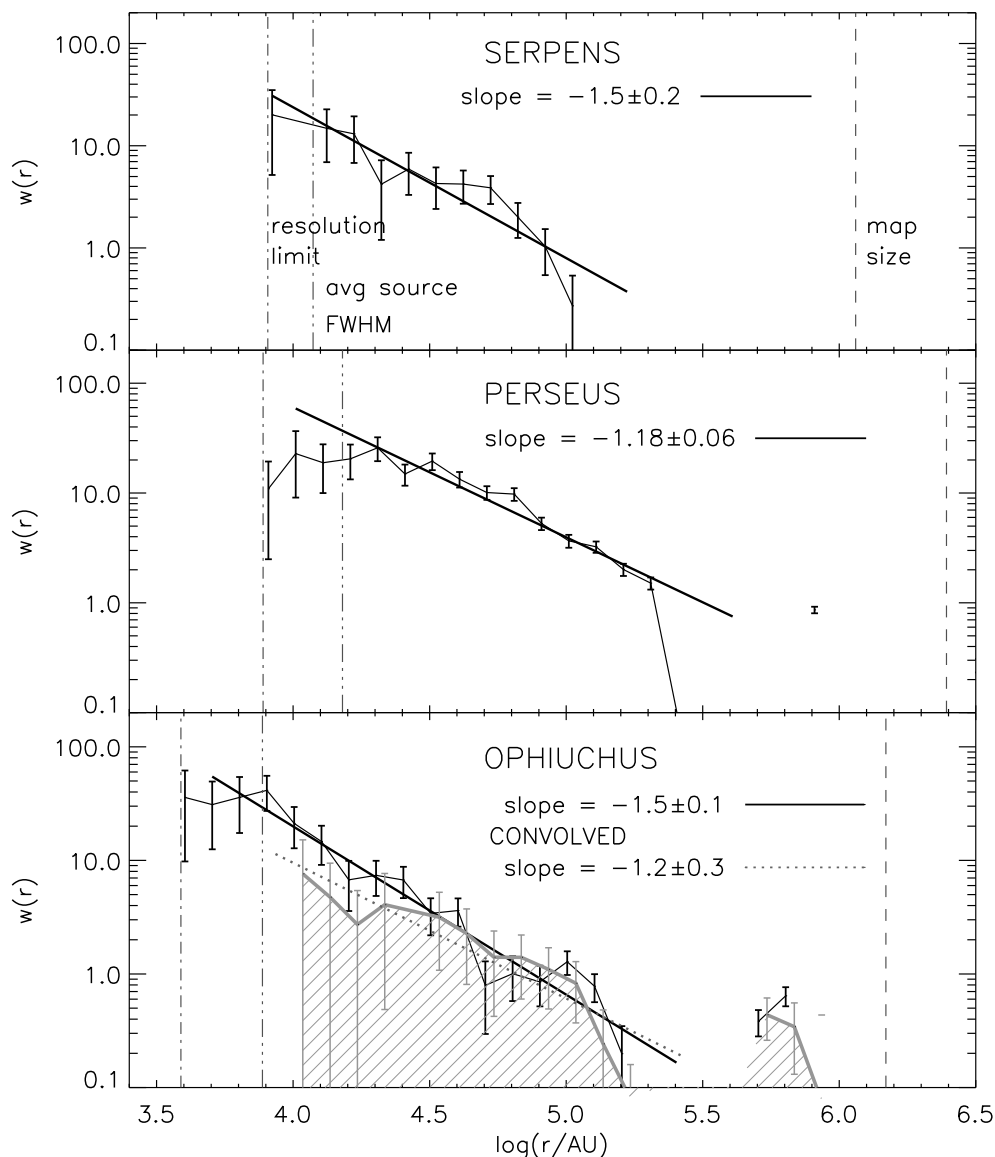


Figure 5.9 Comparison of the correlation function  $w(r)$  for the three clouds, with power law fits. For each cloud the average source FWHM size, resolution limit, and linear map size in AU are indicated. The best fit slope to  $w(r) \propto r^n$  is  $n = -1.5 \pm 0.2$  in Serpens,  $n = -1.18 \pm 0.06$  in Perseus, and  $n = -1.5 \pm 0.1$  in Ophiuchus. The slope found by Johnstone et al. (2000) for a smaller map of Ophiuchus is shallower ( $-0.75$ ). The slope of  $w(r)$  derived for the degraded-resolution Ophiuchus sample (hatched gray curve) is also shallower ( $-1.2 \pm 0.3$ ), but the curve appears consistent with the original sample. Differences in the slope of the correlation function likely trace differences in clustering properties of millimeter cores in the clouds.

recalculating  $w(r)$ . Although the value of the slope changed slightly, the smaller map size did not cause the slope to steepen at large separations. A more serious issue is that the overall amplitude, but not the slope, of  $w(r)$  depends on how large an area the random distribution  $H_r(r)$  covers. We choose each random distribution such that the largest pair separation is similar to the largest pair separation in the real data. For Serpens and Ophiuchus this means that the random distribution does not cover the entire observed area.

Finally, we look at two other measures of clustering: the peak number of cores per square parsec, and the median separation of cores. Although the median separation of cores is much smaller in Ophiuchus ( $6.2 \times 10^3$  AU) than in Perseus ( $2.6 \times 10^4$  AU) or Serpens ( $2.3 \times 10^4$  AU), the median separation in the degraded-resolution Ophiuchus map ( $2.6 \times 10^4$  AU) is consistent with the other two clouds. Imposing a uniform flux limit of  $75 \text{ mJy} \times (\frac{250 \text{ pc}}{d})^2$  across all three clouds, equivalent to the  $5\sigma$  limit in the shallowest map (Perseus), does not significantly change these results. The expected Jeans length in a moderately dense (mean particle density approximately  $2 \times 10^4 \text{ cm}^{-3}$ ), cool ( $T \sim 10$  K) medium is  $\lambda_J \sim 2.5 \times 10^4$  AU. Gravitationally-driven fragmentation can account, therefore, for the median separation of dense cores in all three clouds.

We calculate the number of cores within one square parsec at each point in the map, and take the peak value to be the peak number of cores per square parsec. The peak values are  $12 \text{ pc}^{-2}$  in Serpens,  $22 \text{ pc}^{-2}$  in Perseus, and  $24 \text{ pc}^{-2}$  in the original Ophiuchus map. Differences in linear resolution and completeness both have an effect in this case; the peak number in Ophiuchus falls to  $20 \text{ pc}^{-2}$  when using a uniform flux limit, and to  $12 \text{ pc}^{-2}$  in the degraded-resolution map. The peak number of cores per parsec provides further evidence that clustering is stronger in Perseus than in the other two clouds.

### 5.5.5 Relationship to Cloud Column Density

In contrast to the extinction map, which is a measure of the general cloud (line-of-sight averaged) column density, the 1.1 mm map is sensitive only to regions of high volume density (see §5.3). A comparison of the two tells us, therefore, about the relationship between dense star-forming structures and the column density of the larger-scale cloud. A visual comparison of the 1.1 mm maps of each cloud with visual extinction maps derived from the reddening of background stars (e.g., figure 4.5) suggests that 1.1 mm cores are generally found in regions of the cloud with high  $A_V$ .

Figure 5.10 quantifies the relationship between dense cores and the surrounding cloud column density by plotting the cumulative fraction of 1.1 mm cores in each cloud as a function of cloud  $A_V$ . In all three clouds the majority of cores are found at high cloud column density ( $A_V > 7^m$ ). The  $A_V$  levels above which 75% of cores are found in each cloud are indicated by thin lines in figure 5.10: 75% of 1.1 mm cores in Perseus, Serpens, and Ophiuchus are found at visual extinctions of  $A_V \gtrsim 8^m$ ,  $A_V \gtrsim 15^m$ , and  $A_V \gtrsim 23^m$ , respectively. Although there is not, in general, a strict extinction threshold for finding cores, below these  $A_V$  levels the likelihood of finding a 1.1 mm core is very low. Only in Ophiuchus does there appear to be a true  $A_V$  threshold; only two cores are found at  $A_V < 17^m$  in this cloud.

The cumulative distribution for the degraded resolution Ophiuchus sample is nearly identical to the original Ophiuchus sample, but shifted to lower  $A_V$  by 1–2 mag. For the degraded resolution map, 75% of cores are found at  $A_V \gtrsim 20^m$ . Based on this result and the value for the original Ophiuchus sample, we adopt  $A_V \sim 20 - 23^m$  for the 75% level in Ophiuchus. Requiring that all cores in the Perseus and Serpens sample meet the detection threshold for Ophiuchus (approximately 110 mJy) changes the distributions negligibly. Only for Serpens is the 75% level increased slightly, from  $A_V \sim 15^m$  to  $16^m$ .

Cloud to cloud differences could indicate variations in the core formation process with environment, differing degrees of sub-structure in the clouds, or varying amounts of foreground extinction. Note that in chapters 2 and 3 we found extinction

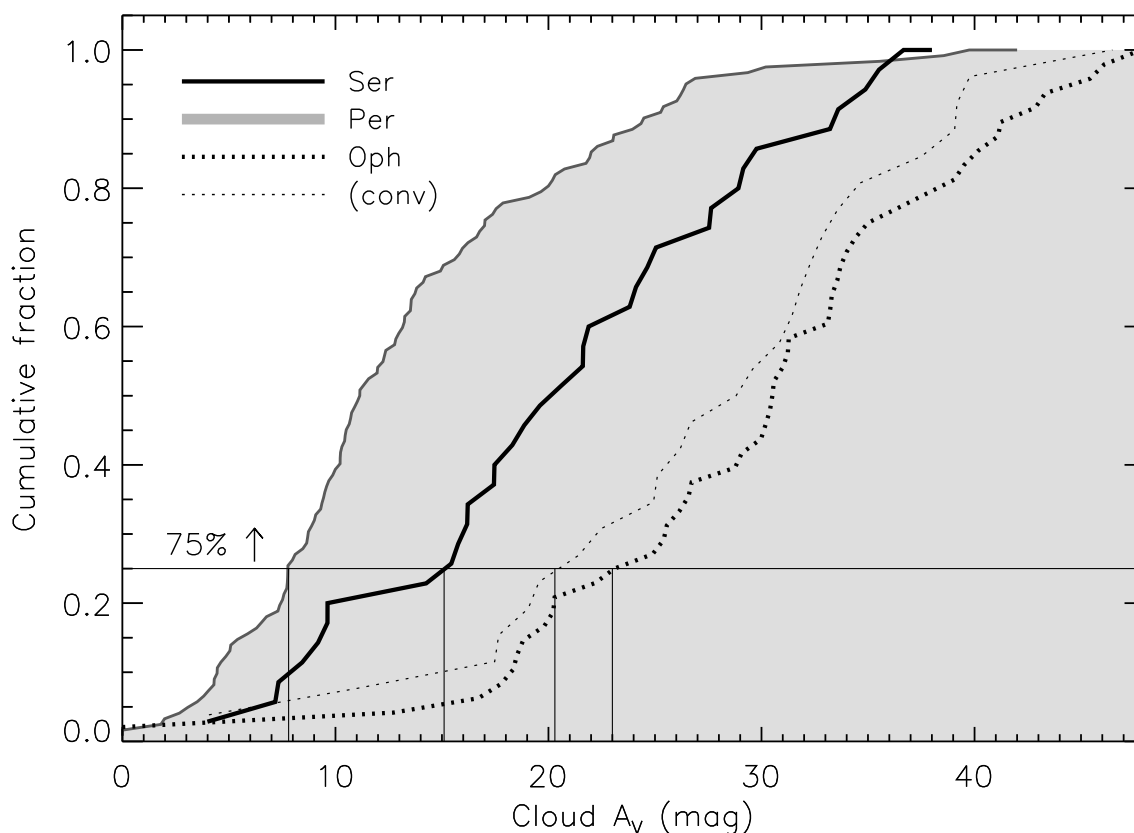


Figure 5.10 Cumulative fraction of 1.1 mm cores as a function of cloud  $A_V$  for sources in Perseus, Serpens, and Ophiuchus. The cloud  $A_V$  is derived from the reddening of background stars using 2MASS and IRAC data as described in §4.3.1. Thin solid lines denote the  $A_V$  levels above which 75% of dense cores are found in each cloud. More than 75% of 1.1 mm cores lie above  $A_V \sim 8^m$  in Perseus,  $A_V \sim 15^m$  in Serpens, and  $A_V \sim 23^m$  in Ophiuchus. Results for the degraded resolution Ophiuchus map are shown as well (thin dotted line), but do not vary substantially from the original Ophiuchus sample, with 75% of cores above  $A_V \sim 20^m$ .

“thresholds” for Perseus and Ophiuchus, using a different analysis that looked at the probability of finding a 1.1 mm core as a function of  $A_V$ , of  $A_V \sim 5^m$  and  $A_V \sim 9^m$ , respectively. Those values were derived using 2MASS-only  $A_V$  maps, rather than the c2d extinction maps used here.

Johnstone et al. (2004) have suggested an extinction threshold for forming dense cores in Ophiuchus at  $A_V \sim 15^m$ , based on the lowest  $A_V$  at which SCUBA cores were observed to have sizes and fluxes consistent with those of stable Bonnor-Ebert

spheres. We find that most Bolocam cores in Ophiuchus are found at even higher extinctions (75% at  $A_V > 20 - 23^m$ ); the discrepancy likely arises from differences in the extinction maps used. Johnstone et al. (2004) used a 2MASS-derived extinction map, while the c2d extinction map used here includes IRAC data as well and probes somewhat higher  $A_V$  values. Hatchell et al. (2005) find no evidence for an extinction threshold in Perseus using 850  $\mu\text{m}$  SCUBA data, but Kirk et al. (2006), also using SCUBA data, find a threshold of  $A_V \sim 5^m$ . Despite differences in detail, the relative 75%  $A_V$  levels found here (highest in Ophiuchus and lowest in Perseus) are consistent with the relative values of previous extinction threshold measurements in Perseus and Ophiuchus.

An extinction threshold has been predicted by McKee (1989) for photoionization-regulated star formation in magnetically supported clouds. In this model star formation is governed by ambipolar diffusion, which depends on ionization levels in the cloud. Core collapse and star formation will occur only in shielded regions of a molecular cloud where  $A_V \gtrsim 4 - 8^m$ . Johnstone et al. (2004) note that it is not clear how turbulent models of star formation would produce an extinction threshold for star-forming objects, and interpret such a threshold as evidence for magnetic support.

### 5.5.6 Efficiency of Forming Cores

Another interesting measure of global cloud conditions is the fraction of cloud mass contained in dense cores. Table 5.1 lists the cloud area and cloud mass within increasing  $A_V$  contours, calculated from the c2d visual extinction maps, as well as the total mass in cores within the same extinction contour. Cloud masses are calculated from the c2d  $A_V$  maps using  $N(\text{H}_2)/A_V = 0.94 \times 10^{21} \text{ mag cm}^{-2}$  (Bohlin, Savage, & Drake, 1978) and

$$M(\text{cloud}) = d^2 m_H \mu_{\text{H}_2} \Omega \sum N(\text{H}_2), \quad (5.2)$$

where  $d$  is the distance,  $\Omega$  is the solid angle,  $\sum$  indicates summation over all  $A_V > 2$  mag pixels in the extinction map, and  $\mu_{\text{H}_2} = 2.8$  is the mean molecular weight per  $\text{H}_2$  molecule. The total cloud mass within  $A_V > 2$  mag is 3470  $M_\odot$  for Serpens,

Table 5.1. Cumulative mass as a function of extinction for sources in Serpens, Perseus, and Ophiuchus

Min. $A_V$ mag	Area (%)	Cloud Mass ( $M_\odot$ )	Percent (%)	Core Mass ( $M_\odot$ )	Percent (%)	Mass Ratio <sup>1</sup> (%)
Serpens						
2	100	3470	100	92	100	2.7
4	97	3420	99	92	100	2.7
6	60	2560	74	92	100	3.6
8	28	1530	44	91	98	5.9
10	15	1010	29	91	98	9.0
12	9.4	740	21	89	96	12
14	6.0	540	15	89	96	16
16	3.9	390	11	86	93	22
18	2.6	290	8.3	83	90	29
20	2.0	230	6.7	79	85	34
25	1.0	130	3.7	61	66	47
30	0.4	60	1.7	39	42	65
Perseus						
2	100	7340	100	278	97	3.8
4	55	5460	74	273	96	5.0
6	27	3620	49	258	91	7.1
8	14	2370	32	244	86	10
10	8.0	1620	22	205	72	13
12	4.8	1140	15	161	57	14
14	3.2	840	12	127	45	15
16	2.0	610	8.3	112	39	18
18	1.3	440	6.0	96	34	22
20	0.9	340	4.6	88	31	26
25	0.4	180	2.5	53	19	29
30	0.2	100	1.4	6.1	2.2	6.1
Ophiuchus						
2	100	3570	100	44	100	1.2
4	55	2710	76	44	100	1.6
6	25	1830	51	40	92	2.2
8	14	1330	37	40	92	3.0
10	9.0	1070	30	40	92	3.7
12	7.0	940	26	40	92	4.3
14	5.6	820	23	40	92	4.9
16	4.6	730	20	40	92	5.5
18	3.8	640	18	39	90	6.1

7340  $M_\odot$  for Perseus, and 3570  $M_\odot$  for Ophiuchus.

Table 5.1 (cont'd)

Min. $A_V$ mag	Area (%)	Cloud Mass ( $M_\odot$ )	Percent (%)	Core Mass ( $M_\odot$ )	Percent (%)	Mass Ratio <sup>1</sup> (%)
20	3.1	560	16	37	84	6.6
25	2.0	400	11	32	73	8.0
30	1.2	260	7.3	23	52	8.8

Note. — Cloud areas and masses are calculated using the c2d extinction maps of each cloud and equation (5.2) (see §5.5.6). Core masses are taken from chapter 1 table 2.2 for Perseus, chapter 2 table 3.2 for Ophiuchus, and chapter 3 table 4.2 for Serpens.

<sup>1</sup>The Mass Ratio is computed from the ratio of total core mass to cloud mass within the same contour of  $A_V$ .

Within a given  $A_V$  contour, the mass ratio is defined as the ratio of total core mass to total cloud mass, and is a measure of the efficiency of core formation at that  $A_V$  level. For example, the mass ratio at the  $A_V = 2$  mag contour is equivalent to the fraction of total cloud mass that is contained in dense cores. In each cloud 1.1 mm cores account for less than 5% of the total cloud mass. The mass ratios at  $A_V = 2$  mag are similar in all three clouds: 3.8% in Perseus, 2.7% in Serpens, and 1.2% in Ophiuchus. If we restrict ourselves to  $A_V > 6$  mag in each cloud, which is reasonable given that the Serpens map was only designed to cover  $A_V > 6$  mag, the mass ratio is still low in all three clouds ( $< 10\%$ ), and remains higher in Perseus (7%) than in Serpens (4%) or Ophiuchus (2%). Low mass ratios are consistent with measurements of the overall star-formation efficiency of 1 – 2%, which suggests that molecular cloud material is relatively sterile (e.g., Evans, 1999; Leisawitz, Bash, & Thaddeus, 1989).

Johnstone et al. (2004) find a mass ratio of 2.5% in a survey of approximately 4 deg<sup>2</sup> of Ophiuchus, quite similar to our result. Note, however, that the Johnstone et al. (2004) core masses (and mass ratio) should be multiplied by a factor of 1.5 to compare to our values, due to differences in assumed values of  $T_D$ ,  $\kappa_\nu$ , and  $d$ . In a similar analysis of 3.5 deg<sup>2</sup> in Perseus, also using SCUBA 850  $\mu\text{m}$  data, Kirk et al. (2006) found a mass ratio for  $A_V > 0$  of only 1%. The difference between this result and our value arises primarily from the smaller core masses of those authors, which

should be multiplied by 2.5 to compare to ours.

In all three clouds the mass ratio rises with increasing  $A_V$  contour, indicating that in high extinction regions a greater percentage of cloud mass has been assembled into cores, consistent with the idea that star formation is more efficient in dense regions. Although this is an intuitively obvious result, it is not a necessary one. If, for example, a constant percentage of cloud mass were contained in dense cores at all column densities, there would be a large number of dense cores lying in a low  $A_V$  background. On the other hand, a molecular cloud might consist of large regions of uniformly high extinction in which we would find no 1.1 mm cores because there is no sub-structure, and millimeter cores require high density contrast (see §5.3).

At higher  $A_V$  levels, mass ratios vary considerably from cloud to cloud. The mass ratio remains fairly low in Ophiuchus, with a maximum value of 9% at  $A_V = 30$  mag. In contrast, the mass ratio rises rapidly in Serpens to 65% at  $A_V = 30$  mag, which may suggest that Serpens has formed cores more efficiently than Ophiuchus at high  $A_V$ .

## 5.6 Summary

This work completes a three-cloud study of the millimeter continuum emission in Perseus, Ophiuchus, and Serpens. We examine similarities and differences in the current star formation activity within the clouds using large-scale 1.1 mm continuum maps completed with Bolocam at the CSO. In total, our surveys cover nearly 20 deg<sup>2</sup> with a resolution of 31" (7.5 deg<sup>2</sup> in Perseus, 10.8 deg<sup>2</sup> in Ophiuchus, and 1.5 deg<sup>2</sup> in Serpens), and we have assembled a sample of 200 cores (122 in Perseus, 44 in Ophiuchus, and 35 in Serpens). Point mass detection limits vary from approximately 0.1 to 0.2  $M_\odot$  depending on the cloud. The results presented here provide an unprecedented global picture of star formation in three clouds spanning a range of diverse environments.

These Bolocam 1.1 mm observations naturally select dense cores with  $n \gtrsim 2 \times 10^4$  cm<sup>-3</sup> and density contrast compared to the background cloud of at least 30 –

100. We test instrumental biases and the effects of cloud distance by degrading the resolution of the Ophiuchus map to match the distance of Perseus and Serpens. We find that linear resolution strongly biases measured linear deconvolved source sizes and mean densities, but not the mass distribution slope. Angular deconvolved sizes are less strongly affected by cloud distance.

Rather than a true physical difference, the small mean linear deconvolved sizes in Ophiuchus ( $0.8 \times 10^4$  AU) compared to Perseus ( $1.5 \times 10^4$  AU) and Serpens ( $1.2 \times 10^4$  AU) are likely a result of observing sources with power law density profiles, which do not have a well defined size, at a distance of 125 pc in Ophiuchus versus 250 pc in Perseus and 260 pc in Serpens. The observed mean angular deconvolved sizes and axis ratios in each cloud suggest average power law indices ranging from  $p = 1.4$  to 1.7 (Y03).

Sources in Perseus exhibit the largest range in sizes, axis ratios, and densities, whereas sources in both Serpens and Ophiuchus display a fairly narrow range of sizes for a large range of masses. We suggest that this is indicative of a greater variety of physical conditions in Perseus, supported by the fact that Perseus contains both dense clusters of millimeter sources and more isolated distributed objects. A wide range in angular deconvolved sizes may also imply a range in the power law index of source profiles in Perseus (Y03).

The slope of the clump mass distribution for both Perseus and Ophiuchus is  $\alpha = 2.1$ , marginally different than the Serpens slope of  $\alpha = 1.6$ . Only Perseus and Ophiuchus are consistent within the substantial errors with the stellar initial mass function ( $\alpha \sim 2.5 - 2.8$ ) and with the slope predicted for turbulent fragmentation ( $\alpha = 2.3$ ) by Padoan & Nordlund (2002).

Turbulent fragmentation simulations by BP06 predict that higher cloud Mach numbers should result in a large number of low mass cores, and low Mach numbers in a smaller number of higher mass cores. Given the measured Mach numbers of  $\mathcal{M} = 4.9$  in Serpens, 3.6 in Perseus and 2.3 in Ophiuchus, our observed core mass distribution (CMD) shapes are inconsistent with the turbulent fragmentation prediction from BP06. We cannot rule out a turbulent fragmentation scenario, however,

due to uncertainties in the observations and in our assumptions.

We argue that clustering of 1.1 mm sources remains stronger out to larger scales in Perseus, based on the slope of the two-point correlation function ( $-1.5$  in Serpens and Ophiuchus, and  $-1.2$  in Perseus). This result is supported by the fact that the peak number of cores per square parsec is larger in Perseus ( $22 \text{ pc}^{-2}$ ) than in Serpens ( $12 \text{ pc}^{-2}$ ) or the degraded-resolution Ophiuchus map ( $12 \text{ pc}^{-2}$ ).

Finally, we examine relationship between dense cores and the local cloud column density, as measured by visual extinction ( $A_V$ ). Extinction thresholds for star formation have been suggested based on both theory and observation (McKee, 1989; Johnstone et al., 2004). Although in general we do not observe a strict  $A_V$  threshold, dense 1.1 mm cores do tend to be found at high  $A_V$ : 75% of cores in Perseus are found at  $A_V \gtrsim 8^m$ , in Serpens at  $A_V \gtrsim 15^m$ , and in Ophiuchus at  $A_V \gtrsim 20 - 23^m$ . Our results confirm that forming dense cores in molecular clouds is a very inefficient process, with 1.1 mm cores accounting for less than 10% of the total cloud mass in each cloud. This result is consistent with measurements of low star formation efficiencies of a few percent from studies of the stellar content of molecular clouds (e.g., Evans, 1999).

While millimeter-wavelength observations can provide a wealth of information about the detailed properties of star forming cores as well as insight into the large scale physical properties of molecular clouds, they do not tell a complete story. Detecting and understanding the youngest embedded protostars currently forming within those cores requires information at mid- to far-infrared wavelengths. The Bolocam maps for all three clouds presented here are coordinated to cover the same regions as the c2d *Spitzer* Legacy IRAC and MIPS maps of Serpens, Perseus, and Ophiuchus. Combining millimeter and *Spitzer* data for these clouds will allow us to separate starless cores from cores with embedded luminosity sources and to better understand the evolution of cores through the early Class 0 and Class I protostellar phases (chapter 6).

## Acknowledgments

The authors are grateful to Paul Harvey, Yancy Shirley, and an anonymous referee for comments that significantly improved this work. We thank members of the Bolocam team for instrumental and software support. We also thank the Lorentz Center in Leiden for hosting several meetings that contributed to this paper. Support for this work, part of the Spitzer Legacy Science Program, was provided by NASA through contracts 1224608 and 1230782 issued by the Jet Propulsion Laboratory, California Institute of Technology, under NASA contract 1407. Bolocam was built and commissioned under grants NSF/AST-9618798 and NSF/AST-0098737. KEY was supported by NASA under Grant NGT5-50401, issued through the Office of Space Science. Additional support came from NASA Origins grant NNG04GG24G to NJE and NSF grant AST 02-06158 to JG. MLE acknowledges support of a Moore Fellowship and an NSF Graduate Research Fellowship.

## Bibliography

- Ballesteros-Paredes, J., Gazol, A., Kim, J., Klessen, R. S., Jappsen, A-K., & Tejero, E., 2006, *ApJ*, 637, 384
- Bohlin, R. C., Savage, B. D., & Drake, J. F. 1978, *ApJ*, 224, 132
- Chabrier, G. 2003, *PASP*, 115, 763
- Di Francesco, J., Evans, N. J., II, Caselli, P., Myers, P. C., Shirley, Y., Aikawa, Y., & Tafalla, M. 2007, in *Protostars and Planets V*, editors B. Reipurth, D. Jewitt, and K. Keil, p. 17
- Enoch, M. L., Young, K. E., Glenn, J., Evans, N. J., II, Golwala, S., Sargent, A. I., Harvey, P., et al. 2006, *ApJ*, 638, 293
- Enoch, M. L., Glenn, J., Evans, N. J., II, Sargent, A. I., Young, K. E., & Huard, T. L. 2007, *ApJ*, in press
- Evans, N. J., II 1999, *ARA&A*, 37, 311
- Evans, N. J., II, Allen, L. E., Blake, G. A., Boogert, A. C. A., Bourke, T., Harvey, P. M., Kessler, J. E., et al. 2003, *PASP*, 115, 965
- Goodman, A. A., 2004, in *Star Formation in the Interstellar Medium*, ASPC, 323, 171
- Hatchell, J., Richer, J. S., Fuller, G. A., Qualtrough, C. J., Ladd, E. F., & Chandler, C. J. 2005, *A&A*, 440, 151
- Johnstone, D., Di Francesco, J., & Kirk, H. 2004, *ApJ*, 45, 611L
- Johnstone, D., Wilson, C. D., Moriarty-Schieven, G., Joncas, G., Smith, G., Gregersen, E., & Fich, M. 2000, *ApJ*, 545, 327
- Kirk, J. M., Ward-Thompson, D., & André, P. 2005, *MNRAS*, 360, 1506
- Kirk, H., Johnstone, D., & Di Francesco, J. 2006, *ApJ*, 646, 1009

- Leisawitz, D., Bash, F., & Thaddeus, P. 1989, ApJS, 70, 731
- Mac Low, M.-M. & Klessen, R. S. 2004, Reviews of Modern Physics, 76, 125
- McKee, C. F. 1989, ApJ, 345, 782
- Padoan, P., Goodman, A. A., & Juvela, M. 2003, ApJ, 588 881
- Padoan, P., & Nordlund, Å. 2002, ApJ, 576, 870
- Reid, I. N., Gizis, J. E., & Hawley, S. L. 2002, AJ, 124, 2721
- Ridge, N. A., et al. 2006, AJ, 131, 2921
- Salpeter, E. E. 1955, ApJ, 121, 161
- Scalo, J., 2005 in The Stellar Initial Mass Function Fifty Years Later, Kluwer Academic Publishers, editors E. Corbelli, F. Palla, and H. Zinnecker, p. 23
- Schröder, K.-P., & Pagel, B. E. J. 2003, MNRAS, 343, 1231
- Shirley, Y. L., Evans, N. J., II, & Rawlings, J. M. C. 2002, ApJ, 575, 337
- Shu, F. H., Adams, F. C., & Lizano, S. 1987, ARA&A, 25, 23
- Stanke, T., Smith, M. D., Gredel, R., Khanzadyan, T. 2006, A&A, 447, 609
- Williams, J. P., de Geus, E. J., & Blitz, L. 1994, ApJ, 428, 693
- Young, C. H., Shirley, Y. L., Evans, N. J., II, & Rawlings, J. M. C. 2003, ApJS, 145, 111
- Young, K. E., Enoch, M. L., Evans, N. J., II, Glenn, J., Sargent, A., Huard, T. L., Aguirre, J., et al. 2006, ApJ, 644, 326

## Chapter 6

# Prestellar Cores and Deeply Embedded Protostars with Spitzer and Bolocam: Properties of the Youngest Objects in Perseus, Serpens, and Ophiuchus

### Abstract

We present an unbiased census of prestellar cores and deeply embedded protostars in Perseus, Serpens, and Ophiuchus, assembled by combining large-scale 1.1 mm surveys and *Spitzer* c2d maps of these clouds. First, we identify protostellar candidates based on *Spitzer* data, and use them to separate starless from protostellar cores in each cloud. A comparison of the properties of the starless and protostellar populations reveals both initial conditions of the starless cores and how formation of a central protostar alters core properties. Starless cores in Perseus have similar masses but larger sizes and lower densities on average than protostellar cores, by factors of 1.5 and 3, respectively, and the sizes suggest density profiles similar to Bonnor-Ebert spheres, or substantially flatter than  $\rho \propto r^{-2}$ . By contrast, starless cores in Serpens are compact and have lower masses than protostellar cores, while in Ophiuchus there is very little difference between the starless and protostellar populations. The combined

---

Enoch et al., in preparation; to be submitted to ApJ.

starless core mass distribution includes 108 cores and has a slope of  $\alpha = -2.5 \pm 0.2$  for  $M > 0.8 M_{\odot}$ , consistent with recent measurements of the stellar initial mass function. This result provides support for the idea that stellar masses are directly linked to the core formation process.

We construct well-sampled SEDs for cold protostar candidate using the extensive wavelength coverage ( $\lambda = 1.25 - 1100 \mu\text{m}$ ). Examining different protostellar classification methods, we conclude that bolometric temperature is a better measure of evolutionary state than the spectral index  $\alpha_{IR}$  for deeply embedded sources. Source classification yields a total of 43 Class 0 and 94 Class I sources in the three cloud sample. Compared to protostellar evolutionary models using the bolometric temperature-luminosity diagram, we find a population of low luminosity Class I sources that are inconsistent with constant or monotonically decreasing mass accretion rates. This result argues strongly for episodic accretion during the Class I phase, with 25% of sources in a quiescent state. Finally, the relative number of starless, Class 0, and Class I sources are used to estimate lifetimes for the starless and Class 0 phases; we find a Class 0 timescale in Perseus and Serpens of  $1 - 2 \times 10^5$  yr. In Ophiuchus, by contrast, we find very few Class 0 sources ( $N_{Class0}/N_{ClassI} \sim 0.1$ ), consistent with previous observations in that cloud. The dense prestellar core phase lasts for approximately as long as the entire embedded protostellar phase,  $2 - 5 \times 10^5$  yr, or only a few free-fall timescales, and is much shorter than the timescale predicted from ambipolar diffusion.

## 6.1 Introduction

The problem of how low mass stars like the sun form has been studied extensively over the last few decades. Much of this work has naturally focused on isolated objects, where interactions with the local environment or with other objects is limited, and observations are somewhat easier to interpret. It is well established, however, that most of the star formation in our Galaxy occurs in clusters and groups within large molecular clouds (e.g., Lada & Lada, 2003, and references therein). Molecular clouds

are known to be turbulent, with supersonic linewidths (e.g., McKee & Zweibel, 1992), and to have complex magnetic fields that are likely important to the cloud physics (e.g., Crutcher, 1999). To understand the formation of typical stars we must focus our studies on this complicated environment.

As discussed in chapter 1, a number of open questions remain regarding the formation of stars in molecular clouds, including: (1) What are the physical processes controlling core formation, support, and collapse? (2) What are the initial conditions of star formation, as traced by prestellar cores? (3) How do protostars evolve through the earliest phases, from protostellar formation through Class I? Compared to more evolved protostars and pre-main sequence objects, the earliest stages of the star formation process, from the formation of dense cores through the main mass accretion phase, are relatively poorly understood. This lack of information is due in large part to the difficulty of observing young, deeply embedded sources, which are shrouded within dense protostellar envelopes and only observable via reprocessed emission at mid-infrared to millimeter wavelengths. Large surveys at these wavelengths are essential for addressing the above questions, as is a complete sample of young objects. Large samples are also important for characterizing variations in the star formation process with environment, and to account for biases of such differences in the interpretation of results.

With a few notable, recent exceptions (Jørgensen et al., 2007; Hatchell et al., 2007), previous samples of very young sources have typically been compiled from many different surveys, and suffered from systematics, unquantified environmental effects, and small number uncertainties. The Bolocam surveys of Perseus, Serpens, and Ophiuchus described in chapters 2–4 complement large *Spitzer* Space Telescope IRAC and MIPS maps of the same clouds from the “From Molecular Cores to Planet-forming Disks” *Spitzer* Legacy program (“Cores to Disks” or c2d; Evans et al. 2003). Combining these data sets enables us to assemble a mass limited, unbiased census of the youngest star-forming objects, including prestellar cores, Class 0, and Class I protostars, in three different environments.

The 1.1 mm surveys of Perseus, Serpens, and Ophiuchus were completed with

Bolocam at the Caltech Submillimeter Observatory (CSO). We mapped  $7.5 \text{ deg}^2$  ( $140 \text{ pc}^2$  at our adopted cloud distance of  $d = 250 \text{ pc}$ ) in Perseus,  $1.5 \text{ deg}^2$  ( $30 \text{ pc}^2$  at  $d = 260 \text{ pc}$ ) in Serpens, and  $10.8 \text{ deg}^2$  ( $50 \text{ pc}^2$  at  $d = 125 \text{ pc}$ ) in Ophiuchus (Enoch et al., 2006; Young et al., 2006; Enoch et al., 2007), with a resolution of  $31''$ . Both Bolocam and *Spitzer* maps were designed to cover down to a visual extinction of  $A_V \gtrsim 2 \text{ mag}$  in Perseus,  $A_V \gtrsim 3 \text{ mag}$  in Ophiuchus, and  $A_V \gtrsim 6 \text{ mag}$  in Serpens (Evans et al., 2003). Millimeter emission traces the properties of starless cores and protostellar envelopes, including sizes, masses, and spatial distribution. The *Spitzer* data are complementary in that they provide information about the properties of young protostars embedded within dense cores. The *Spitzer* c2d IRAC and MIPS surveys of each cloud are described in detail in Jørgensen et al. (2006); Harvey et al. (2006); Rebull et al. (2007); Harvey et al. (2007b). The young stellar object (YSO) population in Serpens is discussed in detail by Harvey et al. (2007a). The c2d *Spitzer* surveys are complete at the 50% level to young objects with luminosities as low as  $0.01L_\odot$  (based on the Serpens survey; Harvey et al. 2007a).

In chapter 5, we looked at how the global cloud environment influences the properties of star-forming cores, by comparing the 1.1 mm core populations in Perseus, Serpens, and Ophiuchus. In this chapter we use the combination of the Bolocam 1.1 mm surveys with *Spitzer* c2d MIPS and IRAC maps to study initial conditions and early protostellar evolution. We separate starless cores from protostellar cores in each cloud to probe the initial conditions of star formation on large scales as traced by the starless core samples. Given that we are sensitive to both starless cores and the envelopes around protostars of variable evolutionary state, we can also infer how the formation of a protostar alters the core properties. Extensive wavelength coverage from  $\lambda = 1.25 - 1100 \mu\text{m}$  allows us to construct well-sampled spectral energy distributions (SEDs) for protostellar sources in their main mass accretion phase, in order to trace their evolution.

We follow Di Francesco et al. (2007) in defining starless cores as low mass dense cores without a compact internal luminosity source, and prestellar cores, at least conceptually, as starless cores that are gravitationally bound. A practical method

of distinguishing prestellar cores is required as well; our operational definition of a prestellar core is a starless core that is detected at submillimeter or millimeter wavelengths. Such sources have mean densities  $\gtrsim 2 - 3 \times 10^4 \text{ cm}^{-3}$  (see Ward-Thompson et al. 1994 and §5.3), and are more likely to show evidence for infall motions than lower density starless cores (Gregersen & Evans, 2000). For millimeter cores containing a compact luminous internal source (i.e., an embedded protostar) we follow Di Francesco et al. (2007) in terming these “protostellar cores”, regardless of whether the final object will be stellar or sub-stellar in nature. Unlike protostellar cores, which are internally heated by the embedded source, starless cores are externally heated by the interstellar radiation field, with decreasing temperatures toward the core center. In general, we will use the terms Class 0 and Class I to refer to an evolutionary sequence of embedded protostars with  $M_* < M_{env}$  and  $M_* > M_{env}$ , respectively, following André (1994), although the validity of these physical associations is not firmly established (see chapter 1). Our observational definition of Class 0 and Class I, and classification of sources will be discussed in §6.7.

The organization of this chapter is as follows: In §6.2 we describe the combination of the 1.1 mm and *Spitzer* infrared (IR) data. Cold protostar candidates are identified based on their mid- and far-infrared properties in §6.3. Criteria for source selection are discussed, as well as basis on which we determine association with a 1.1 mm core, and the method for distinguishing starless from protostellar cores. The resulting starless and protostellar 1.1 mm core populations for each cloud are compared in §6.4, including core sizes and shapes (§6.4.1), peak and mean particle densities (§6.4.2), distribution in mass versus size (§6.4.3), differential mass distributions (§6.4.4), relationship to cloud column density (§6.4.5), and spatial clustering (§6.4.6). We combine the starless core populations to produce the prestellar core mass distribution (CMD), which is discussed in relation to the stellar initial mass function and combined protostellar CMD in §6.5.

In the second half of this chapter we use our extensive wavelength coverage to study the properties of the embedded protostar populations in each cloud (§6.6), beginning with the calculation of bolometric luminosities and temperatures in §6.6.1

and a discussion of selected individual sources in §6.6.4. We compare protostellar classification methods in §6.7, and discuss alternative classification schemes made possible by our large, unbiased sample in §6.7.1. Sources are placed on a bolometric temperature-luminosity diagram (§6.8) in order to compare to protostellar evolutionary models. Finally, in §6.9 we calculate timescales for the Class 0 and prestellar evolutionary phases.

## 6.2 Combining Bolocam and Spitzer c2d Data

Our Bolocam 1.1 mm maps of Perseus, Serpens, and Ophiuchus cover nearly the same area as *Spitzer* c2d maps of the sample clouds. The actual overlap in area between Bolocam and IRAC maps is shown in figure 2.1 of chapter 2 for Perseus, figure 3.1 of chapter 3 for Ophiuchus, and figure 4.1 of chapter 4 for Serpens. Catalogs listing c2d measured *Spitzer* fluxes of all sources in each of the three clouds, as well as near-infrared fluxes for sources in the 2MASS catalogs, are available through the *Spitzer* database (Evans et al., 2007). Thus, we have wavelength coverage from  $\lambda = 1.25$  to 1100  $\mu\text{m}$ , using 2MASS (1.25, 1.65, 2.17  $\mu\text{m}$ ), IRAC (3.6, 4.5, 5.8, 8.0  $\mu\text{m}$ ), MIPS (24, 70, 160  $\mu\text{m}$ ), and Bolocam (1.1 mm) data. Note that 160  $\mu\text{m}$  flux measurements are internal c2d products only, and not included in the public catalogs.

Basic data papers describe the processing and analysis of the *Spitzer* IRAC and MIPS maps of Perseus, Serpens, and Ophiuchus, as well as presenting general properties of the sources in each cloud, such as color-color and color-magnitude diagrams (Jørgensen et al., 2006; Harvey et al., 2006; Rebull et al., 2007; Harvey et al., 2007b). Here we are most interested in cold protostellar sources that are most likely to be embedded in the millimeter cores detected with Bolocam. For the following we will use the term “cold protostar” in general to encompass candidate Class I and younger objects. Although it will become apparent in §6.3 that our criteria also pick up a number of Class II sources, in general we focus on sources with evidence for a protostellar envelope (Class 0 and Class I).

In figures 6.1–6.4 we show the result of combining *Spitzer* and Bolocam data for a

few examples from each cloud. Representative starless cores from Perseus (top row), Serpens (middle row), and Ophiuchus (bottom row) are displayed in figure 6.1 as three-color (8, 24, 160  $\mu\text{m}$ ) *Spitzer* images with 1.1 mm Bolocam contours overlaid. Note that the determination of whether or not a core is starless is done in §6.3.1. Symbols (“x”) mark the position of all identified 1.1 mm cores, and the Bolocam identification (ID) of the central sources, from table 1 of chapters 2–4, is given at the top of each image. Red 160  $\mu\text{m}$  images are often affected by saturation, pixel artifacts (bright pixels), and incomplete coverage. Saturation by bright sources affects many pixels in a given scan; this and incomplete sampling accounts for the striped appearance of the red images, especially in Ophiuchus. In some cases (e.g., Oph-Bolo 14), large regions are saturated at 160  $\mu\text{m}$ .

Figure 6.1 demonstrates the range of starless cores that we see in each of the clouds. Starless cores may be isolated single sources (Pers-Bolo 62), associated with filaments or groups of other starless cores (Pers-Bolo 73, Oph-Bolo 26), or found near bright protostars (Pers-Bolo 57, Oph-Bolo 14). Although most of the starless cores are extended (e.g., Oph-Bolo 43), some are quite compact (e.g., Pers-Bolo 57), barely resolved by the 31" Bolocam beam. Some starless cores are distinguished in the *Spitzer* bands by their bright 160  $\mu\text{m}$  emission. For example, Pers-Bolo 62 is not detectable at 24 or 70  $\mu\text{m}$ , but emerges as a relatively bright, diffuse source at 160  $\mu\text{m}$ , indicating a cold, extended core. The 1.1 mm source is also extended and closely mirrors the 160  $\mu\text{m}$  emission. Other starless cores are less identifiable at 160  $\mu\text{m}$ , but rather stand out as dark “shadows” in the shorter wavelength bands. Serp-Bolo 18 and Oph-Bolo 26 are two examples of such cores; the dark shadows against bright 8 and 24  $\mu\text{m}$  emission are suggestive of dense cores obscuring background nebular emission. These objects generally exhibit 160  $\mu\text{m}$  emission as well, but it is not necessarily well distinguished from local extended 160  $\mu\text{m}$  emission. Again, contours at 1.1 mm closely trace the *Spitzer* short-wavelength shadows.

Figures 6.2–6.4 show examples of embedded protostellar sources in each cloud. Images are now three-color *Spitzer* maps at (8, 24, 70  $\mu\text{m}$ ), and do not include 160  $\mu\text{m}$  data. As before, 1.1 mm contours are overlaid. Sources were chosen both to

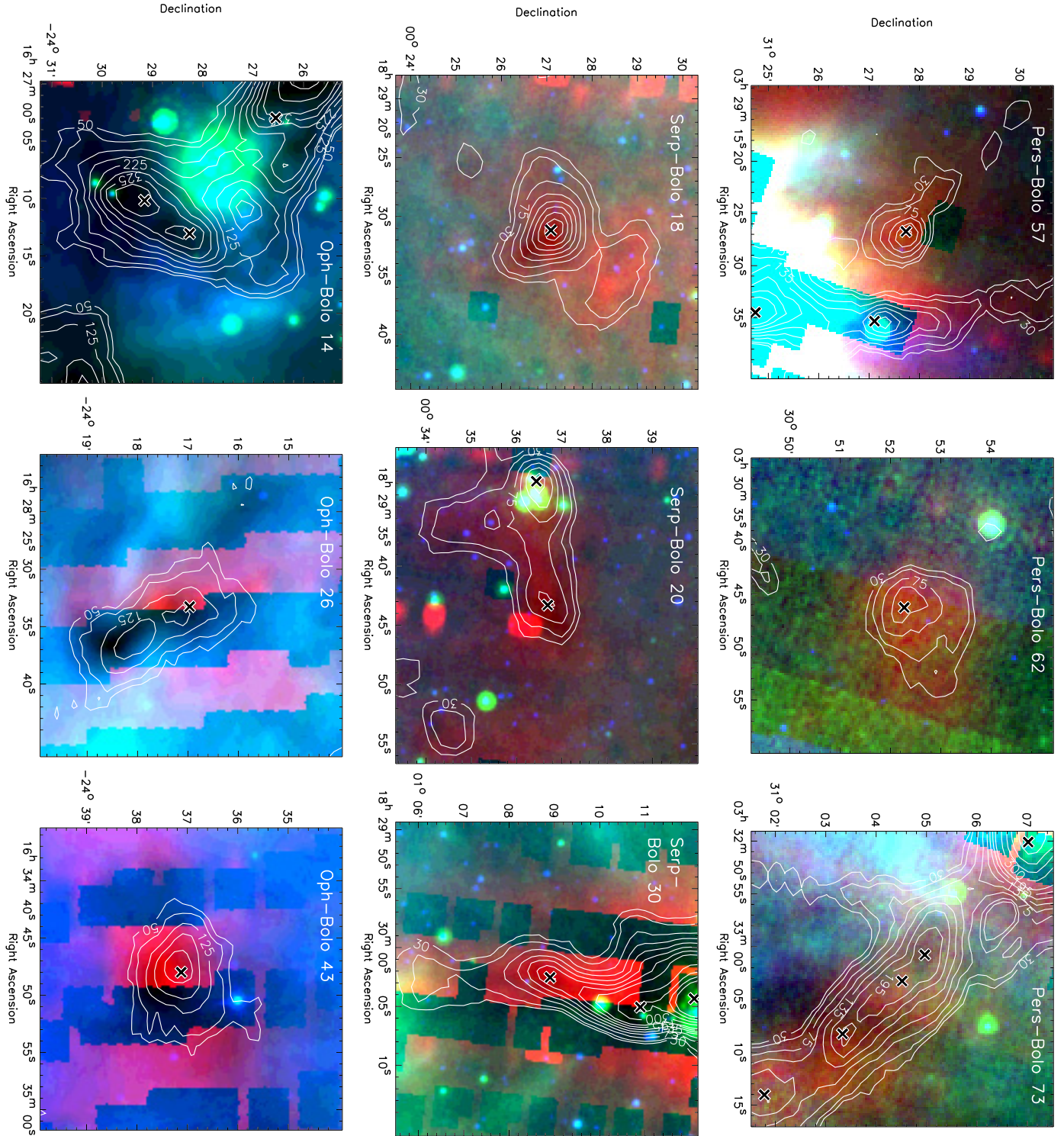


Figure 6.1 Three color Spitzer images (8.0, 24, 160  $\mu\text{m}$ ) of selected starless cores in Perseus, Serpens, and Ophiuchus, with 1.1 mm contours. Contour intervals are 2, 3, 5, 7, 9, 11, 13, 15, 20, 25, 30, 35 $\sigma$ , where 1 $\sigma$  is the mean rms noise in each cloud (15 mJy in Perseus, 10 mJy in Serpens, and 25 mJy in Ophiuchus). Positions of identified Bolocam 1.1 mm cores are indicated by an “x”, and the Bolocam ID of the centered core is given. Saturation, image artifacts, and incomplete sampling causes the striped appearance of some of the red 160  $\mu\text{m}$  images.

highlight newly identified highly embedded objects, as well as to illustrate the wide variety of sources that we are able to characterize by combining these data. As for figure 6.1, the Bolocam ID of the centered 1.1 mm core is given. We use the 2MASS, IRAC, MIPS, and Bolocam data to construct complete spectral energy distributions (SEDs) from 2 to 1100  $\mu\text{m}$  for each protostellar source associated with the central Bolocam core in figures 6.2–6.4. The SEDs are also shown in these figures in the lower panels, and will be discussed further in §6.6. Additional SHARC II 350  $\mu\text{m}$  fluxes (Wu et al., in preparation) and SCUBA 850  $\mu\text{m}$  fluxes (Kirk et al., 2006, open circles) are included when available.

Protostellar sources in our sample may be isolated (e.g., Pers-Bolo 57) or lie in crowded regions (e.g., Pers-Bolo 49), similar to starless cores. Approximately 5%–20% of the time, depending on cloud, more than one protostellar source lies within a single 1.1 mm core. This is almost certainly due to the fact that the Bolocam beam (31'') is larger than the *Spitzer* beam at 24  $\mu\text{m}$  (7''), and multiple *Spitzer* sources will be blended in the 1.1 mm map. Sometimes the SEDs of such multiple sources look similar to each other (Pers-Cold 19 and 24 in the lower-left panel of figure 6.2), and sometimes quite different (Pers-Cold 50 of the same panel).

Although the coverage of the IRAC, MIPS and Bolocam maps overlaps nearly perfectly for our purposes, there are a few cases in which cold protostar candidates are outside the boundaries of the MIPS 70  $\mu\text{m}$  map (three sources in Serpens) or 1.1 mm map (one source in Perseus). In addition, the 160  $\mu\text{m}$  maps are often saturated near bright sources and in regions of bright extended emission, such as near bright clusters of sources. Reliable 160  $\mu\text{m}$  fluxes are especially difficult to determine in crowded regions, due both to the large beam size (40'') and saturation issues. The lack of 160  $\mu\text{m}$  data is most problematic in Ophiuchus, where the 160  $\mu\text{m}$  maps are saturated in all of the dense source regions. Even for isolated sources, the measured 160  $\mu\text{m}$  flux density, determined from a point spread function (PSF) fit, may be underestimated if the source is extended. The effects of these issues on our analysis are discussed in more detail in the appendix Section 6.11

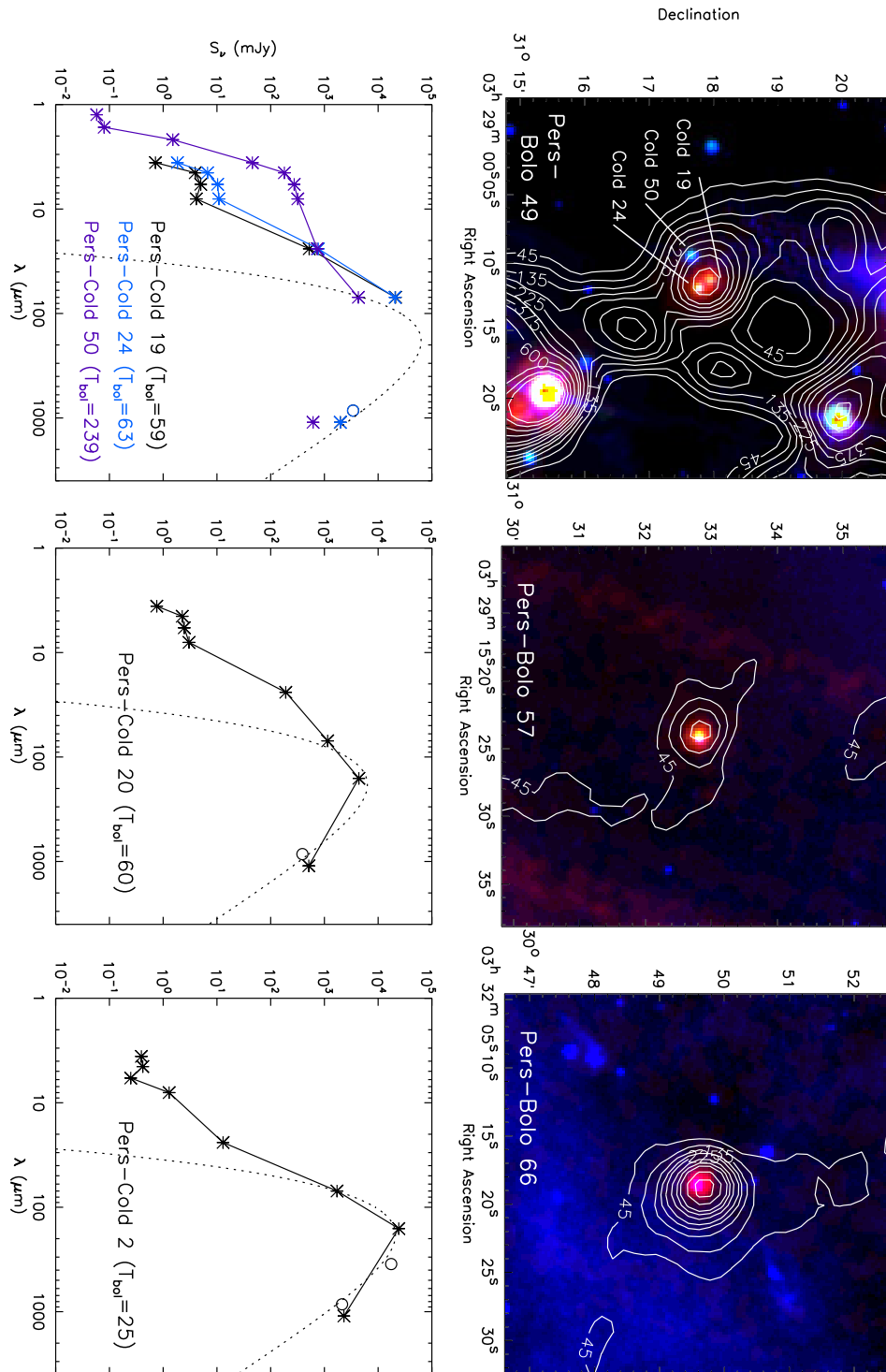


Figure 6.2 three-color Spitzer images (8.0, 24, 70  $\mu\text{m}$ ) of selected protostellar cores in Perseus, with 1.1 mm contours. Spectral energy distributions (SEDs) of protostellar sources associated with each core are plotted in the lower panels. SEDs include 2MASS, IRAC, and MIPS photometry from the c2d database and 1.1 mm fluxes (asterisks), as well as published 350  $\mu\text{m}$  and 850  $\mu\text{m}$  points if available (open circles). The Bolocam ID of the centered core is also given. Contour intervals for the 1.1 mm emission are 3, 6, 9, 12, 15, 20, 25, ...,  $\sigma$ .

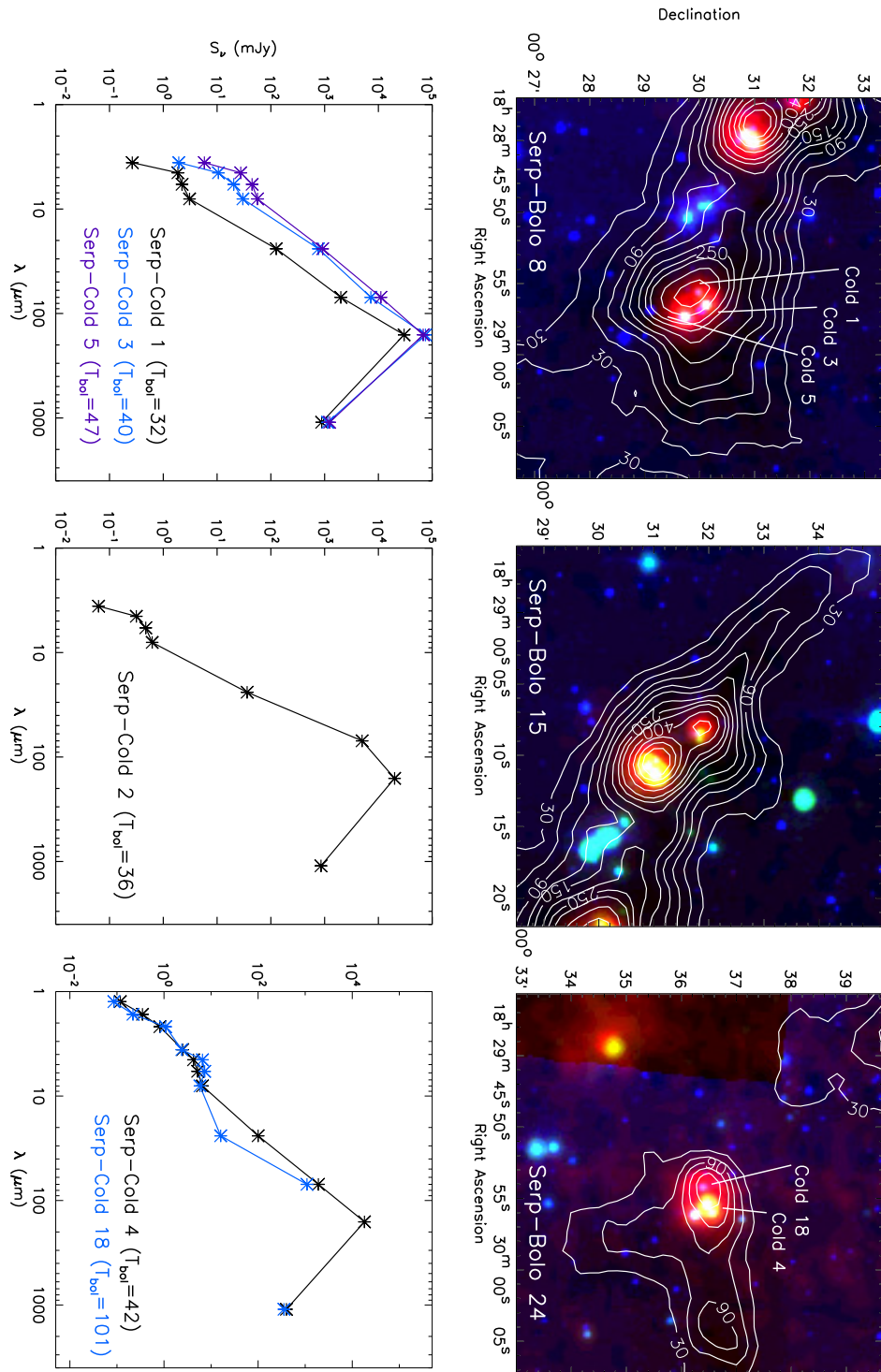


Figure 6.3 three-color Spitzer images (8.0, 24, 70  $\mu\text{m}$ ) of selected protostellar cores in Serpens, with 1.1 mm contours. Spectral energy distributions of protostellar sources associated with each core are plotted in the lower panels. Contours, photometry, and identifications are as in figure 6.2.

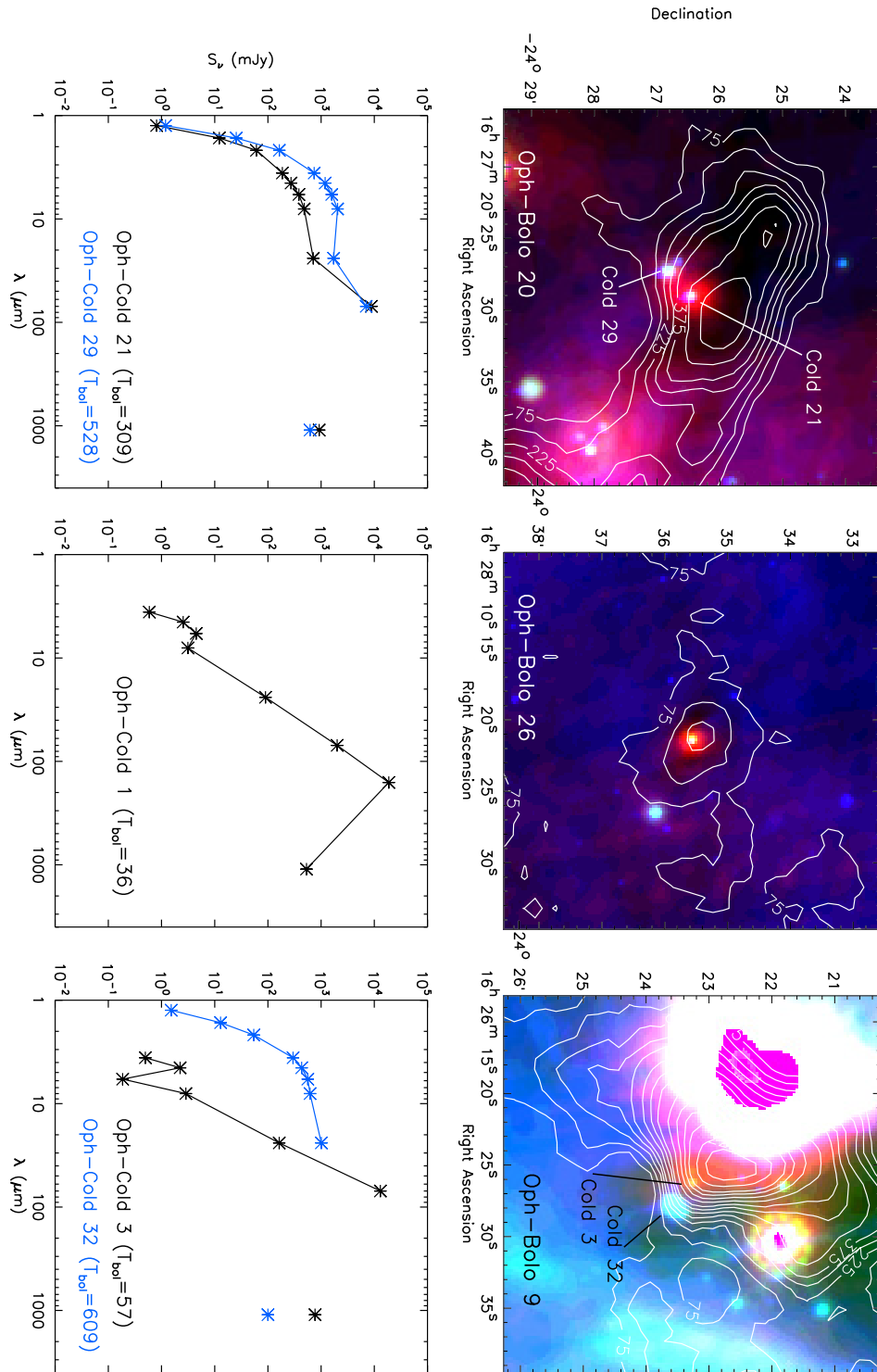


Figure 6.4 three-color Spitzer images (8.0, 24, 70  $\mu\text{m}$ ) of selected protostellar cores in Ophiuchus, with 1.1 mm contours. Spectral energy distributions of protostellar sources associated with each core are plotted in the lower panels. Contours, photometry, and identifications are as in figure 6.2.

### 6.3 Identifying Cold Protostars

We form a sample of candidate cold protostars from the c2d catalogs; the first cut is based on the source “class.” All sources in the c2d catalogs are assigned a class parameter based on colors, magnitudes, and stellar SED fits, as discussed in the c2d Delivery Document (Evans et al., 2007) and Harvey et al. (2007a). Class parameters include “star”, “star+disk”, “YSOc” (young stellar object candidate), “red”, “rising”, “Galc” (galaxy candidate), etc. Serpens is used as an example and to test our method, because the list of YSO candidates in Serpens, which includes embedded protostars as well as more evolved star-plus-disk sources, has also been carefully checked by Harvey et al. (2007a). Cold protostars will generally be a subset of YSOc sources, but some of the most embedded may also be assigned to the “red” class if they are not detected in all four IRAC bands. Thus, we begin by selecting all sources from the c2d database that are classified as “YSOc” or “red.” From this list, we keep only sources that meet *all* of the following criteria:

- (a) flux density at 24  $\mu\text{m}$  ( $S_{24\mu\text{m}}$ )  $\geq 3$  mJy
- (b)  $S_{24\mu\text{m}} \geq 5\alpha_{IR} + 8$  mJy, where  $\alpha_{IR}$  is the near- to mid-infrared spectral index, determined by a least-squares fit to all fluxes shortward of 24  $\mu\text{m}$ .
- (c)  $S_{24\mu\text{m}}$  and  $S_{8\mu\text{m}}$  must be of high quality, i.e., both measured flux densities have signal to noise (S/N) higher than 7.
- (d) if  $S_{24\mu\text{m}} < 50$  mJy, then it is not a “band-filled” flux. For sources not originally detected in all *Spitzer* bands, a flux or upper limit is measured at the source position (band-filling, Harvey et al. 2007a). Because the resolution is lower at 24  $\mu\text{m}$  than at the shorter wavelengths, some IRAC-only sources have unreliable band-filled fluxes at 24  $\mu\text{m}$  (e.g., sources are confused with the PSF wings of a nearby source).

In addition, we include in our sample any 70  $\mu\text{m}$  point sources that are not classified as galaxy candidates (“Galc”). In each cloud, a few deeply embedded sources that have strong 70  $\mu\text{m}$  emission but very weak 24  $\mu\text{m}$  emission (e.g., HH211 in Perseus) are recovered by this last criteria, as are a few very bright sources that are saturated at 8  $\mu\text{m}$  or 24  $\mu\text{m}$  (these are often classified as “rising”).

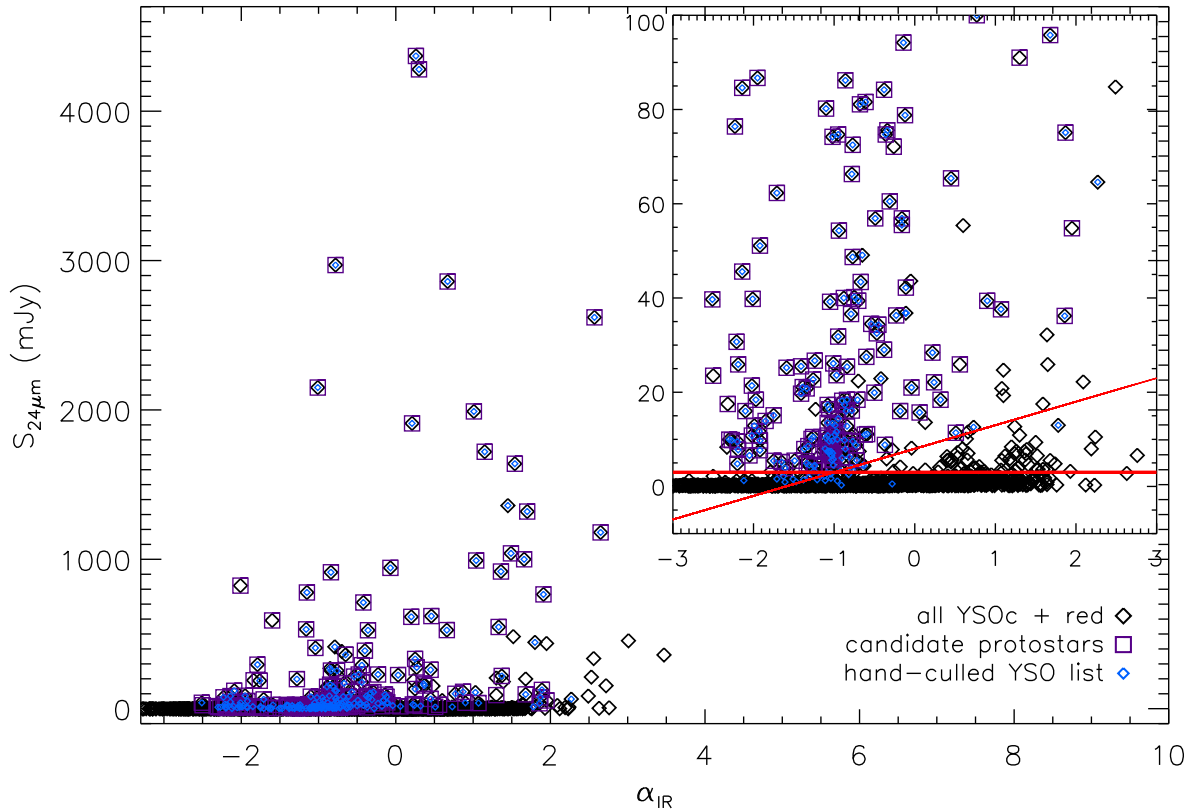


Figure 6.5 Plot of  $S_{24\mu\text{m}}$  versus spectral index  $\alpha_{IR}$  for sources in Serpens, to demonstrate selection criteria for the cold protostar samples. Black diamonds represent all catalog sources labeled as “YSOc” or “red.” Smaller blue diamonds show the carefully vetted YSO sample from Harvey et al. (2006). Red lines (inset) show 24  $\mu\text{m}$  flux cuts imposed by criteria (a) and (b), which remove most sources not in the hand-culled sample. Boxes indicate the final cold protostar sample, after applying criteria (a)-(d). The hand-culled and final candidate protostar samples match well, with the exception of a few sources that require examination by eye (see text).

The sample formed using the above criteria (a–d) is quite similar to the carefully vetted list of YSO candidates from Harvey et al. (2007a), as shown in figure 6.5. In this figure, which plots  $S_{24\mu\text{m}}$  versus  $\alpha_{IR}$ , black diamonds are the original “YSOc” + “red” sample for Perseus, blue diamonds are the “hand-culled” YSOs from Harvey et al. (2007a), and our cold protostar candidates after applying criteria (a)-(d) are indicated by purple boxes. The majority of the black-only points, which were rejected as true YSOs by Harvey et al. (2007a), are removed by criteria (a) and (b) (shown as red lines). The 14 sources in the hand-culled list but not in our sample (blue diamonds,

no box) are classified as “star+dust” and were examined by hand and found to have Class II-like SEDs, with no nearby 1.1 mm emission. There are also a few sources in our sample that are not in the hand-culled sample (black diamond plus box). Most of these were fairly easily identified as non-protostellar when examining by eye. We do identify three additional cold protostar candidates based on their  $70\ \mu\text{m}$  fluxes, which are not in the hand-culled sample but seem to be associated with 1.1 mm emission (see §6.3.1): one “red”, one “rising”, and one “cup-up.”

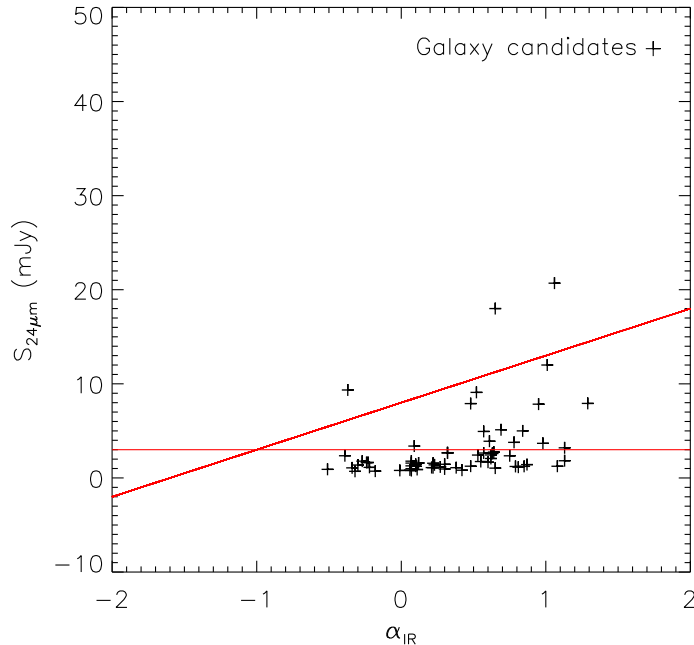


Figure 6.6 Plot of  $S_{24\mu\text{m}}$  versus spectral index  $\alpha_{IR}$  for galaxy candidates (“Galc”) in Serpens. Selection criteria (a) and (b) are plotted, as in figure 6.5. The selection criteria eliminate most of the parameter space inhabited by extragalactic sources.

In addition to weeding out false “YSOc” sources, our cold protostar criteria are efficient at removing objects with the properties of extragalactic sources, as shown in figure 6.6. In this figure,  $S_{24\mu\text{m}}$  is plotted versus  $\alpha_{IR}$  for all “Galc” galaxy candidates in Serpens. As in figure 6.5, red lines show criteria (a) and (b), which effectively eliminate most galaxy candidates. Therefore, if any extragalactic sources are mistakenly classified as “YSOc”, the majority would be removed from our sample by these criteria. After having checked our criteria using the Serpens sample, we apply them to the other clouds to produce candidate cold protostar samples for Perseus

and Ophiuchus. Finally, the images and SEDs of each source are examined by eye to remove any galaxies that are extended in the near-infrared, and other obviously non-embedded sources.

In some cases, there is no available point-source flux at 70 or 160  $\mu\text{m}$  even if there is emission at the position of the source, generally because the source is extended at these wavelengths. In these cases a flux density is measured by hand, if possible, using aperture photometry. A few bright sources were saturated at 8 or 24  $\mu\text{m}$ ; the flux for these was estimated using aperture photometry and interpolating over bad pixels. Large uncertainties for these saturated or band-filled flux measurements (50% or more) are reflected in the errors on these flux points.

### 6.3.1 Association with a 1.1 mm Core

Once we have a sample of candidate cold protostars, we next determine which of these objects are associated with 1.1 mm emission. Rather than use a single distance criteria, we examine the distance from the protostar to the nearest 1.1 mm peak, and assign a protostellar source to a given millimeter core if it is within  $1.0 \times \theta_{1mm}$  of the 1.1 mm core centroid position, where  $\theta_{1mm}$  is the angular full-width at half-maximum (FWHM) size of the core. To justify this choice, we plot in figure 6.7 (left) the distribution of cold protostar candidates in Perseus, including all “YSOc”, “red” and 70  $\mu\text{m}$  sources, around each core position. This is inspired by a similar analysis done by Jørgensen et al. (2007) (their figure 2). The distance from each protostar candidate to the nearest 1.1 mm core is shown in units of the core FWHM size; large circles enclose sources within  $0.5 \times \theta_{1mm}$  and  $1.0 \times \theta_{1mm}$  of a core position. Sources with  $T_{bol} < 70$  K and  $70 < T_{bol} < 650$  K (as determined in Section 6.7) are color coded red and blue, respectively. In general we find that the coldest protostars are all within  $1.0 \times \theta_{1mm}$  of a millimeter core position, as expected if they are deeply embedded.

Figure 6.7 (right) is similar, but for a spatially random distribution of *Spitzer* sources over the Bolocam map area. This is equivalent to taking the candidate pro-

tostars that appear in the left panel and spreading them randomly across the cloud. There are approximately the same number of sources in the random distribution as in the candidate protostar sample, but only a small number of the randomly distributed sources fall within a few core FWHM of a 1.1 mm core position. There are two sources from the random distribution within  $1.0 \times \theta_{1mm}$  of a core position; thus we can expect up to two false associations with 1.1 mm cores in each cloud using this criteria. Using  $0.5 \times \theta_{1mm}$  would be a more restrictive choice, but might miss some cold protostars or mis-identify protostellar cores as starless.

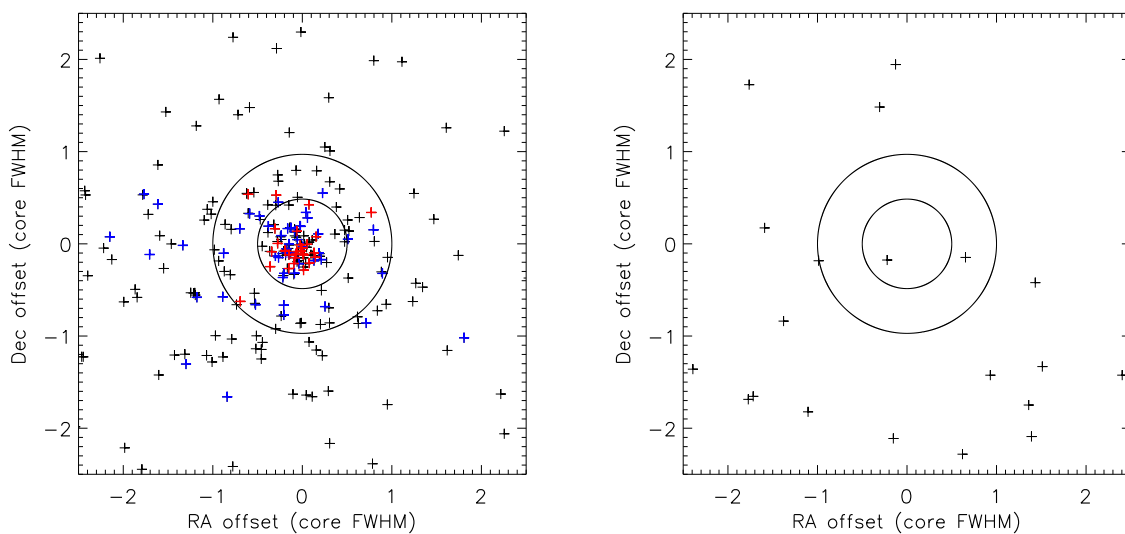


Figure 6.7 *Left*: Distribution of the distance from cold protostar candidates in Perseus to the nearest core position, including all “YSOc”, “red” and  $70 \mu\text{m}$  sources. Distances are in units of the core FWHM size  $\theta_{1mm}$ . Sources with  $T_{bol} < 70 \text{ K}$  and  $70 < T_{bol} < 650 \text{ K}$  are color coded red and blue, respectively. *Right*: Similar, but for a spatially random distribution of *Spitzer* sources over the Bolocam map area. There are approximately the same number of *Spitzer* sources in the random distribution as in the candidate protostar sample at left, but only a small number fall within a few FWHM of a 1.1 mm core position. Circles enclose sources within 0.5 and 1.0  $\theta_{1mm}$  of a core position. Our definition that candidate protostars within 1.0  $\theta_{1mm}$  are associated with a given core may result in approximately two false identifications in each cloud.

If a cold protostar candidate is found to be associated with a millimeter core by the above criteria, the 1.1 mm flux is included in the protostellar SED, and is used to calculate an envelope mass ( $M_{env}$ ) for that protostellar source (see §6.6.2). If a given

cold protostar candidate is not within  $1.0 \times \theta_{1mm}$  of a millimeter core, we calculate an upper limit from the original 1.1 mm map. In a number of cases (12 in Perseus, 4 in Serpens, and 15 in Ophiuchus) there is clearly 1.1 mm flux at the protostar position, that was not identified as a core in the original 1.1 mm source extraction because it is below  $5\sigma$  or is in a confused region of the map. If this emission exceeds a threshold of approximately 3 times the local rms noise, we measure a 1.1 mm flux using a small aperture ( $30''$ – $40''$ ). In regions of blended 1.1 mm emission, we also re-compute the 1.1 mm flux density in small apertures, rather than simply adopting the total core flux. When more than one protostar candidate is associated with a single compact millimeter core, we divide the 1.1 mm flux equally between the protostellar sources.

Approximately 20% of the cold protostar candidates in each cloud (40% in Oph) are lacking 1.1 mm emission, even after re-examining the 1.1 mm maps at each source position. Most of these sources appear to be late Class I or early Class II sources, with little or no remaining envelope. Any 1.1 mm emission from these objects, therefore, is likely below our detection limit of  $\sim 0.1M_{\odot}$ . A few of these may actually be low luminosity sources that are truly embedded in a low mass envelope below our detection limit. For this reason, we only claim completeness to protostars with  $M_{env} > 0.1 M_{\odot}$ , as discussed further in §6.9.

### 6.3.2 Separating Starless and Protostellar Cores

To study the initial conditions of star formation, as traced by prestellar cores, as well as how the formation of a central protostar alters core properties, we first must differentiate cores with internal luminosity sources (protostellar cores) from those without an embedded self-luminous source (starless cores). Protostellar cores will have lost some mass due to accretion onto the embedded protostar, and may be otherwise altered so that they are no longer representative of core initial conditions. Any core that has a cold protostar candidate within  $1.0 \times \theta_{1mm}$  of the core center is considered protostellar, based on the discussion in §6.3.1. In addition, we examine the remaining 1.1 mm cores, searching for any “YSOc” source that has  $S_{24\mu m} > 3$  mJy

and is within  $1.0 \times \theta_{1mm}$  of the core center, even those that do not meet the criteria of §6.3.1. A flux limit at  $S_{24\mu m}$  of 3 mJy is chosen because that is the flux of the most embedded known protostar at  $24 \mu m$  (HH211), and it is high enough to eliminate sources with SEDs that are clearly inconsistent with an embedded nature (e.g., sources with  $S_{24\mu m} < S_{8\mu m}$ ).

An additional 2 cores in Perseus, 2 in Serpens, and 5 in Ophiuchus are determined to be protostellar cores by this latter method. Note, however, that the “YSOc” sources assumed to be associated with these cores are not added to the cold protostar sample; in general they do not meet our criteria because they are very faint at  $24 \mu m$  and are not detected at  $70 \mu m$ . It is not at all clear that these YSOc sources are truly associated with the 1.1 mm cores with which they are spatially coincident, especially as the 1.1 mm core flux density is generally much higher than what would be expected from the *Spitzer*  $24 \mu m$  flux, and none are detected at 70 or  $160 \mu m$ . In fact, some associations are probably just an effect of projection on the sky. Figure 6.7 demonstrates that at least a few non-embedded sources will be projected within  $1.0 \times \theta_{1mm}$  of a core position. As we do not want to mistakenly contaminate our starless core sample with more evolved sources, however, we adopt this very conservative criteria for starless cores. Therefore the number of starless cores in each cloud is likely a lower limit to the true value.

Table 6.1 gives the number of starless ( $N_{SL}$ ) and protostellar ( $N_{PS}$ ) cores in each cloud, as well as the ratio  $N_{SL}/N_{PS}$ . Note that the number of starless and protostellar cores are approximately equal in each cloud ( $N_{SL}/N_{PS} = 1.2$  in Perseus, 0.8 in Serpens, and 1.4 in Ophiuchus), a fact that will be important for our discussion of the starless core lifetime in §6.9. Differences between the clouds are not significant, as the mis-identification of only a few starless cores as protostellar in Serpens would make the ratio closer to 1.1, similar to the other clouds. The number of cold protostar candidates from §6.3.1 that are associated with 1.1 mm emission is given in column six of table 6.1. Notice that this number is larger than the number of protostellar cores in each cloud. Part of the difference is explained by sources that have been “band-filled” at 1.1 mm, while the remaining excess is accounted for by individual

Table 6.1. Statistics of 1.1 mm cores in the three clouds

Cloud	$N_{\text{total}}^1$	$N_{\text{SL}}^2$	$N_{\text{PS}}^3$	$N_{\text{SL}}/N_{\text{PS}}$	$N_{\text{Cold}}^4(\text{w}/1\text{mm})$	$N_{\text{PS}}(\text{mult})^5$
Perseus	122	67	55	1.2	68	13
Serpens	35	15	20	0.8	37	11
Ophiuchus	44	26	18	1.4	32	3

<sup>1</sup>Total number of identified 1.1 mm cores.

<sup>2</sup>Number of starless 1.1 mm cores, i.e., cores that do not have a YSO candidate (with  $S_{24\mu\text{m}} > 3$  mJy) within  $1.0 \times \theta_{1\text{mm}}$  of the core center.

<sup>3</sup>Number of protostellar cores.

<sup>4</sup>Number of cold protostar candidates that are associated with 1.1 mm emission, as determined in §6.3.1.

<sup>5</sup>Number of protostellar cores that are associated with more than one candidate cold protostar (within  $1.0 \times \theta_{1\text{mm}}$  of the core center).

cores that are associated with more than one cold protostar candidate. There are 13 such multiple protostellar sources in Perseus (24% of the protostellar core sample), 11 in Serpens (55%), and 3 in Ophiuchus (17%), as noted in the last column of table 6.1.

## 6.4 Comparing the Starless and Protostellar 1.1 mm Core Populations

Having separated the starless and protostellar core populations in each cloud, we now compare their physical properties, with two primary goals. First, isolating a starless core sample allows us to probe the initial conditions of star formation in each cloud, as reflected in the properties of the starless cores. Second, differences between the starless and protostellar core samples are indicative of how the formation of a central protostar alters core properties. In the next several sections we follow the methodology of chapter 5, examining the sizes and shapes of cores, their peak and mean densities, the distribution of core mass versus size, their spatial clustering properties, and their relationship to the surrounding cloud column density.

### 6.4.1 Sizes and Shapes

Figure 6.8 shows the distribution of the angular deconvolved sizes of protostellar and starless cores in Perseus, Serpens, and Ophiuchus. The angular deconvolved size is calculated as  $\theta_{dec} = \sqrt{\theta_{meas}^2 - \theta_{mb}^2}$ , where  $\theta_{meas}$  is the geometric mean of the measured minor and major axis FWHM sizes and  $\theta_{mb}$  is the beam FWHM (31"). Recall from chapter 5 that the measured size does not necessarily represent a physical boundary, but rather is a characteristic scale that depends on the linear resolution and intrinsic source density profile. Starless cores are larger on average in Perseus than protostellar cores (figure 6.8, left panel), with average  $\theta_{dec}$  values of  $67'' \pm 23''$  and  $50'' \pm 17''$ , respectively. Note that the standard deviation quoted here and in the rest of §6.4 is the dispersion in the sample, *not* the error in the mean.

As discussed in chapter 5, for sources with power law density profiles, which do not have a well defined size,  $\theta_{dec}/\theta_{mb}$  is independent of distance and simply related to the index of the power law (Young et al., 2003). According to the correlation between  $\theta_{dec}/\theta_{mb}$  and density power law exponent  $p$  found by Young et al. (2003), a mean  $\theta_{dec}/\theta_{mb}$  value of  $(50''/31'' = 1.6)$  for protostellar cores in Perseus implies an average power law index of  $p \sim 1.4$  to  $1.5$ . Many well-known protostellar sources have been found to have envelopes consistent with power law density profiles, as determined by high-resolution imaging combined with radiative transfer modeling. Our inferred average index for Perseus protostellar cores ( $p = 1.4 - 1.5$ ) is consistent with, but slightly smaller than, the mean  $p \sim 1.6$  from radiative transfer modeling of Class 0 and Class I envelopes (Shirley et al., 2002; Young et al., 2003). For reference, a singular isothermal sphere has  $p = 2$ , and the profile expected for a free-falling envelope is  $p = 1.5$  (Shu, 1977).

In contrast, the distribution of  $\theta_{dec}$  for starless cores in Perseus is relatively flat, with a few barely resolved cores, and several larger than  $3 \theta_{mb}$ . It is difficult to reconcile such large values of  $\theta_{dec}$  with power law density profiles. The mean  $\theta_{dec}/\theta_{mb}$  value of 2.2 for starless cores in Perseus would imply an extremely shallow mean power law index of  $p \sim 1.1$ , and the maximum value ( $\theta_{dec}/\theta_{mb} \sim 3.5$ ) would correspond to

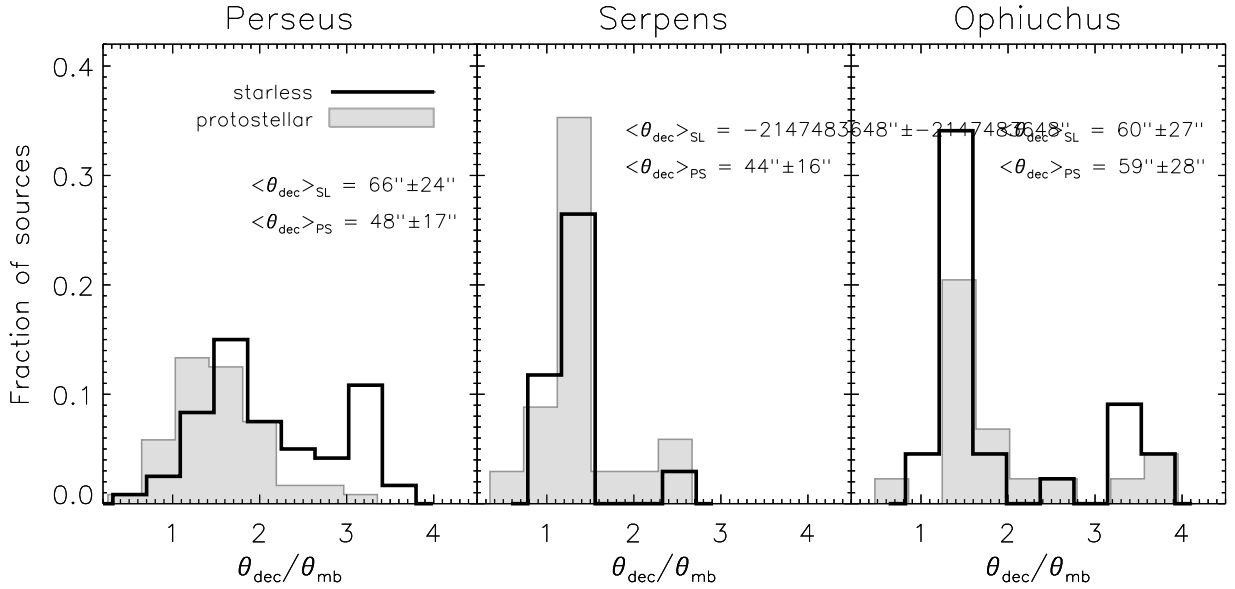


Figure 6.8 Distributions of the angular deconvolved sizes of starless and protostellar cores in the three clouds. The size is given in units of the beam FWHM ( $\theta_{mb}$ ), and the mean of each distribution  $\pm$  the dispersion in the sample is listed. Starless cores are larger on average than protostellar cores in Perseus, with a flattened distribution out to  $3.5 \theta_{mb}$ . In Serpens and Ophiuchus, however, there is very little difference between the starless and protostellar distributions, with a few very large cores.

$p < 0.8$ . On the other hand, a Bonnor-Ebert sphere (Ebert, 1955; Bonnor, 1956) with a central density of  $10^5 \text{ cm}^{-3}$  and an outer radius of  $6 \times 10^4 \text{ AU}$  would correspond to  $\theta_{dec}/\theta_{mb} = 2.0$  at the distance of Perseus. Thus, very large starless cores are more consistent with BE spheres or other flattened profiles than with a power law density profile. Although the classical pre-collapse singular isothermal sphere (SIS) follows a power law with  $p = 2$ , there is significant evidence that many starless cores do indeed look like BE spheres (e.g., Johnstone et al. 2000; Shirley et al. 2000; Alves et al. 2001). Note, however, that a sufficiently centrally condensed BE sphere will be indistinguishable from a power law on the scales to which we are sensitive.

Despite the size difference between starless and protostellar cores in Perseus, there is no difference between the two axis ratio distributions (figure 6.9, left panel). Here the axis ratio is defined at the half-max contour: major axis FWHM/minor axis

FWHM. Both starless and protostellar cores have a mean axis ratio of 1.4, with a dispersion of 0.3. Monte Carlo tests indicate that cores with axis ratios less than 1.2 should be considered round. Thus both starless and protostellar cores are slightly elongated on average in Perseus.

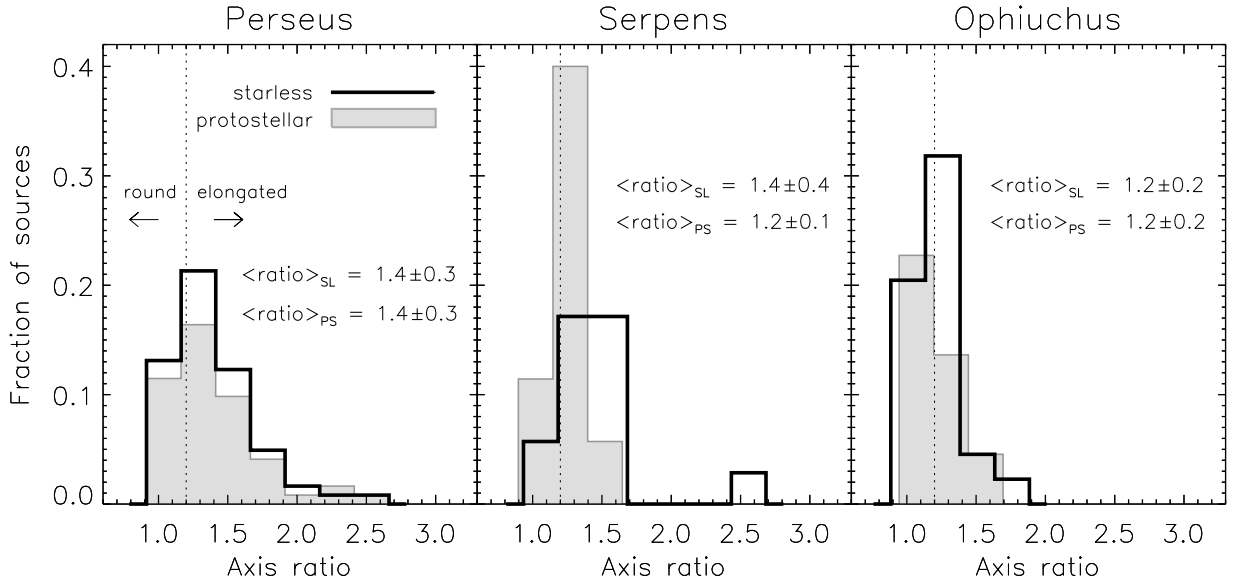


Figure 6.9 Distributions of the axis ratios of starless and protostellar cores in the three clouds. Cores with axis ratios  $< 1.2$  are considered round, and those with axis ratios  $> 1.2$  elongated. Only in Serpens, where starless cores tend to be slightly more elongated (mean axis ratio =  $1.4 \pm 0.4$ ) than protostellar cores (mean axis ratio =  $1.2 \pm 0.1$ ), is there a measurable difference between the starless and protostellar populations.

The relative properties of starless and protostellar cores are quite different in Serpens than in Perseus (figures 6.8 and 6.9, middle panels). Starless cores in Serpens have sizes ( $\langle \theta_{dec} \rangle = 42'' \pm 12''$ ) similar to protostellar cores ( $\langle \theta_{dec} \rangle = 45'' \pm 15''$ ). The mean value for protostellar cores ( $\theta_{dec}/\theta_{mb} = 1.5$ ) corresponds to an average power law index of  $p = 1.5$ , similar to that found for Perseus. In contrast to Perseus, starless cores do not appear to have flatter density profiles than protostellar cores. Starless cores in Serpens do tend to be slightly more elongated (mean axis ratio =  $1.4 \pm 0.4$ ) than protostellar cores (mean axis ratio =  $1.2 \pm 0.1$ ).

In Ophiuchus, there is no measurable difference between the starless and protostellar populations (figures 6.8 and 6.9, right panels). The starless and protostellar samples have similar mean sizes ( $\langle\theta_{dec}\rangle = 60'' \pm 27''$  and  $59'' \pm 28''$ , respectively), and both populations display a bimodal behavior. The lower peak is similar to the single peak seen in Serpens at  $\theta_{dec} = 1 - 2 \theta_{mb}$ , while the smaller upper peak is at sizes of  $\theta_{dec} = 3 - 4 \theta_{mb}$ , comparable to the largest starless cores in Perseus. The mean  $\theta_{dec}/\theta_{mb}$  for protostellar cores in Ophiuchus (1.9) corresponds to an average power law index of  $p = 1.3$ , and the median value (1.6) to  $p = 1.4$ . Both starless and protostellar cores in Ophiuchus appear quite round; the mean axis ratio is  $1.2 \pm 0.2$  for both populations. As discussed in chapter 5, the fact that cores in Ophiuchus are observed to be more round than in the other two clouds is likely a result of the higher linear resolution in that cloud, rather than a physical distinction.

To summarize, starless cores are larger on average than protostellar cores in Perseus. The protostellar distribution in Perseus is consistent with power law density sources with an average index  $p = 1.4 - 1.5$ , while the starless distribution is suggestive of Bonnor-Ebert spheres or very flattened profiles. Both starless and protostellar cores are compact in Serpens, with starless cores being somewhat more elongated on average. There is no difference in the sizes or axis ratio distributions of starless and protostellar cores in Ophiuchus; both populations have a bimodal distribution of sizes, with a few cores at very large sizes. The smaller sizes of both starless and protostellar cores in Serpens and Ophiuchus compared to Perseus may be related to the general lack of isolated sources in those clouds. The measured size of a core is limited by the distance to the nearest neighboring source, meaning that in crowded regions the measured size will tend to be smaller than for isolated sources.

### 6.4.2 Core Densities

Figures 6.10 and 6.11 compare the peak and mean densities of starless and protostellar cores in each cloud. We use the peak column density  $N_{H_2}$ , calculated from the peak 1.1 mm flux density (§2.4.2 and equation (2.2)), as a measure of the peak density.

Note that the peak density is an average over the 31'' beam. As discussed in §5.3, the 1.1 mm emission traces significantly higher column densities than other tracers such as the reddening of background stars. Mean particle densities are calculated at the half-max contour:  $\langle n \rangle = 3M/(4\pi R^3 \mu m_H)$ , where  $M$  is the core total mass,  $R$  is the linear deconvolved half-width at half-max size, and  $\mu = 2.33$  is the mean molecular weight per particle.

Core masses are calculated from the total 1.1 mm flux assuming the dust emission at  $\lambda = 1.1$  mm is optically thin, and that both the dust temperature and opacity are independent of position within a core:

$$M = \frac{d^2 S_\nu}{B_\nu(T_D) \kappa_\nu}, \quad (6.1)$$

where  $\kappa_\nu$  is the dust opacity,  $d$  is the cloud distance, and  $T_D$  is the dust temperature. We assume a dust opacity at 1.1 mm of  $\kappa_{1.1mm} = 0.0114 \text{ cm}^2 \text{ g}^{-1}$ , interpolated from table 1 column 5 of Ossenkopf & Henning (1994) for dust grains with thin ice mantles (see chapter 1). A gas to dust mass ratio of 100 is included in  $\kappa_{1.1mm}$ .

The dust temperature  $T_D$  should depend on whether a core is starless or has an internal source of luminosity, and we assume a slightly higher temperature for protostellar cores ( $T_D = 15$  K) than for starless cores ( $T_D = 10$  K). For dense regions without internal heating, the mean temperature is about 10 K, warmer on the outside and colder on the inside (Evans et al., 2001). Our assumed value of 15 K for protostellar cores is the average isothermal dust temperature found from radiative transfer models of a sample of Class 0 and Class I protostars (Shirley et al., 2002; Young et al., 2003). The isothermal dust temperature is the temperature that, when used in an isothermal mass equation (e.g., equation (6.1), above) yields the same mass as does a detailed model including temperature gradients. The difference in mass between assuming  $T_D = 10$  K and 15 K is a factor of 1.9, as can be easily seen from the difference between the starless and protostellar completeness curves in figure 6.12 (§6.4.3).

Both peak  $N_{H_2}$  values and mean densities are significantly lower on average for

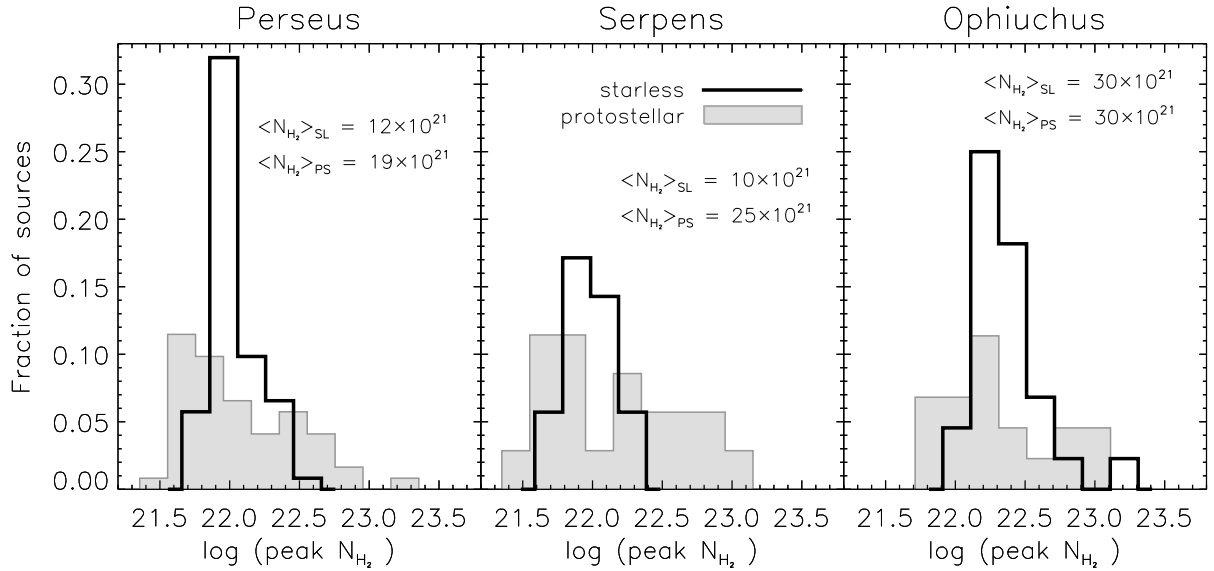


Figure 6.10 Distributions of the peak column density  $N_{H_2}$  of starless and protostellar cores in the three clouds. The peak  $N_{H_2}$  values of starless cores are considerably lower than those of protostellar cores in both Perseus ( $\langle N_{H_2} \rangle = 12 \times 10^{21} \text{ cm}^{-2}$  and  $19 \times 10^{21} \text{ cm}^{-2}$ , respectively) and Serpens ( $\langle N_{H_2} \rangle = 10 \times 10^{21} \text{ cm}^{-2}$  and  $25 \times 10^{21} \text{ cm}^{-2}$ ). In Ophiuchus there is no difference in the mean values ( $\langle N_{H_2} \rangle = 30 \times 10^{21} \text{ cm}^{-2}$ ), but in all three clouds the starless distribution is more peaked and the protostellar distribution is relatively flat.

starless cores than for protostellar cores in Perseus (figures 6.10 and 6.11, left panels), and the starless core distributions are much narrower. The average peak  $N_{H_2}$  for starless cores in Perseus is  $12 \times 10^{21} \text{ cm}^{-2}$ , while the average peak  $N_{H_2}$  for protostellar cores is 50% higher,  $19 \times 10^{21} \text{ cm}^{-2}$ , with a much wider dispersion. Similarly, the typical mean density of starless cores ( $1.3 \times 10^5 \text{ cm}^{-3}$ ) is more than a factor of three smaller than that of protostellar cores ( $4.8 \times 10^5 \text{ cm}^{-3}$ ). The large difference in mean densities in Perseus is due primarily to the significantly smaller sizes of protostellar cores. Recently, Jørgensen et al. (2007) found a similar result for Perseus, comparing SCUBA 850  $\mu\text{m}$  cores with and without internal luminosity sources, as determined using *Spitzer* c2d data. Those authors concluded that cores with embedded YSOs (within 15'' of the core position) have higher ‘‘concentrations’’ on average.

Unlike the large differences seen between Perseus and Serpens when looking at core sizes, the distributions of peak and mean densities for starless and protostellar cores

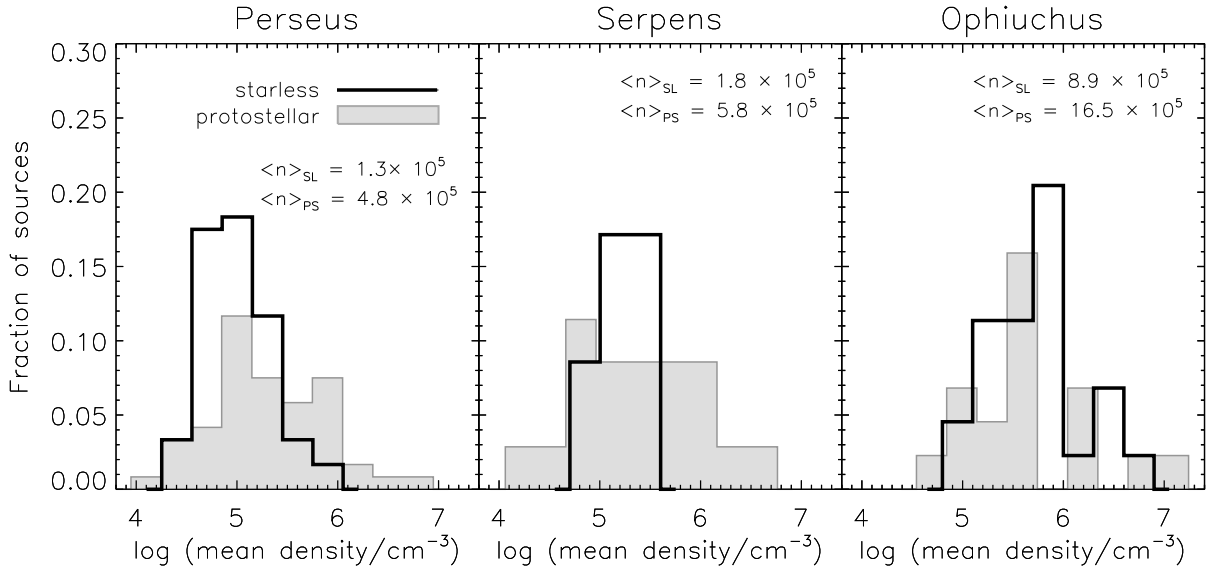


Figure 6.11 Distributions of the mean densities  $\langle n \rangle$  of starless and protostellar cores. As for the peak  $N_{H_2}$  distribution (figure 6.10), starless cores tend to have lower mean densities than protostellar cores in Perseus and Serpens, by approximately a factor of three. In Ophiuchus, by contrast, there is almost no difference between the two distributions. Higher mean densities on average in Ophiuchus are a result of the higher linear resolution in that cloud (see text and §5.4).

in Serpens (figures 6.10 and 6.11, middle panels) are quite similar to those in Perseus. Average peak densities are substantially smaller for starless ( $\langle N_{H_2} \rangle = 10 \times 10^{21} \text{ cm}^{-2}$ ) than for protostellar ( $\langle N_{H_2} \rangle = 25 \times 10^{21} \text{ cm}^{-2}$ ) cores, and form a much narrower distribution. Likewise, the typical mean density of starless cores ( $1.8 \times 10^5 \text{ cm}^{-3}$ ) is more than three times smaller than that of protostellar cores ( $5.8 \times 10^5 \text{ cm}^{-3}$ ). In contrast to Perseus, mean density differences in Serpens are entirely due to the significantly larger masses of protostellar cores in that cloud, as starless cores are slightly smaller on average than protostellar cores in Serpens.

As was also the case for core sizes and shapes, there is essentially no difference between the peak and mean densities of starless and protostellar cores in Ophiuchus (figures 6.10 and 6.11, right panels). Average peak densities are the same ( $\langle N_{H_2} \rangle = 30 \times 10^{21} \text{ cm}^{-2}$ ), and the two distributions have similar dispersions. The average mean density is slightly higher for protostellar than for starless cores ( $17 \times 10^5 \text{ cm}^{-3}$

versus  $9 \times 10^5 \text{ cm}^{-3}$ ), but the difference is primarily due to a few very high density protostellar cores. Larger mean densities in general in Ophiuchus compared to the other two clouds are likely not significant, but a consequence of the higher linear resolution in Ophiuchus, and resulting smaller linear deconvolved sizes (§5.4). This conjecture is confirmed using the “convolved” Ophiuchus sample, or the sample of sources extracted from the Ophiuchus map after having convolved it with a larger beam ( $62''$ ) to simulate putting it at the same distance as Perseus and Serpens. The median peak  $N_{H_2}$  values for starless and protostellar cores in the convolved sample are both  $10 \times 10^{21} \text{ cm}^{-2}$ , while the median mean densities are  $1.2 \times 10^5 \text{ cm}^{-3}$  and  $1.0 \times 10^5 \text{ cm}^{-3}$ , respectively, closer to those in Perseus and Serpens.

To summarize, the peak  $N_{H_2}$  and mean densities of starless cores in Perseus and Serpens are lower on average than for protostellar cores, whereas in Ophiuchus there is no difference between the starless and protostellar populations. Note that an error in the assumed dust temperature of approximately 30% for either protostellar or starless cores would bring the average peak  $N_{H_2}$  values of these two populations into agreement for Perseus and Serpens. The  $N_{H_2}$  distribution of starless cores does appear more peaked than that of protostellar cores in Ophiuchus, however, as in the other two clouds. Higher mean densities in Ophiuchus compared to the other clouds are found to be a result of the higher linear resolution, rather than a physical difference.

### 6.4.3 The Mass versus Size Distribution

Figure 6.12 shows the total core mass versus angular FWHM size for starless and protostellar cores in Perseus. There is a striking difference between the starless and protostellar distributions; in particular, starless cores seem to follow a constant surface density ( $M \propto R^2$ ) curve, consistent with the narrow distribution of peak densities. Protostellar cores, in contrast, have a narrower range of sizes for a similar range of masses. This is another way of visualizing the result found earlier, that protostellar cores are smaller and have higher densities than starless cores. Looking at this plot, it is easy to imagine how protostellar cores in Perseus might have evolved from the

current population of starless cores, by decreasing in size and increasing in density for a constant mass, until collapse and protostellar formation is triggered. Equivalently, the formation of a central protostar within a previously starless core is associated with a decrease in core size and an increase in core density.

Note that because the completeness limits as a function of size (dashed for starless cores and dash-dot for protostellar cores) are similar to  $M \propto R^2$ , the distribution of starless cores in mass and size only implies that the upper envelope of cores follows a constant surface density curve. For example, there could be a population of large, low mass cores that we are unable to detect. Nevertheless, the two populations clearly fill different regions of the mass versus size parameter space. Empirical 50% completeness

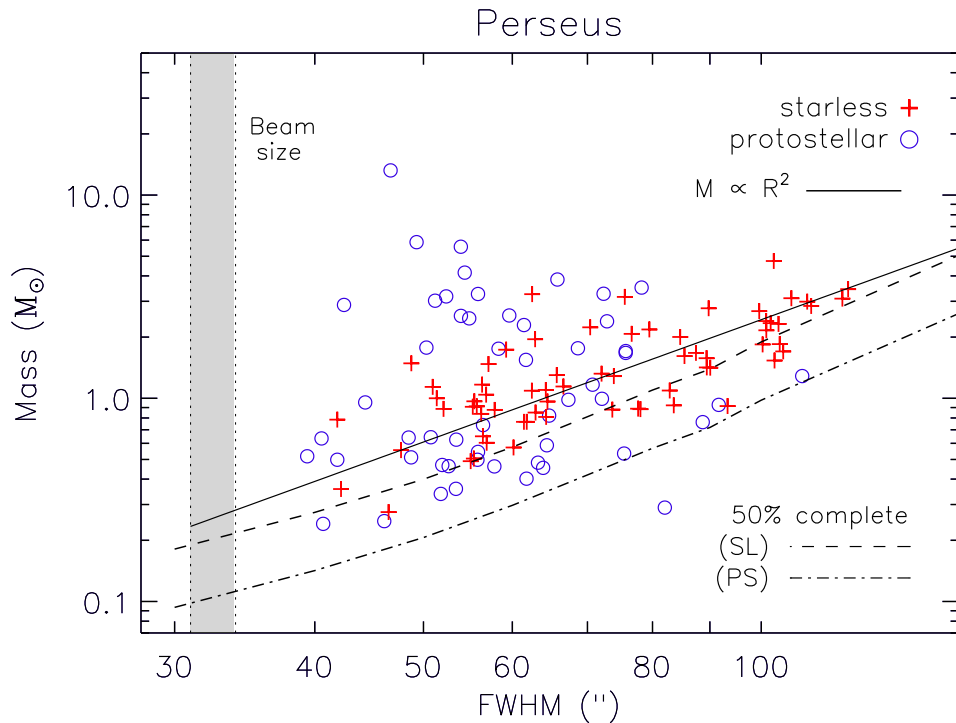


Figure 6.12 Total mass versus average angular FWHM size for starless and protostellar cores in Perseus. Starless cores tend to follow an  $M \propto R^2$  relationship (solid line), while protostellar cores have a wide range in masses for a relatively small range in sizes. Thus there is a relatively simple explanation for how protostellar cores might have evolved from starless cores, getting smaller and denser for the same mass until protostellar formation is triggered. Dashed and dash-dot lines indicate empirically derived 50% completeness limits for starless and protostellar cores, respectively.

limits are derived using Monte Carlo simulations, by inserting simulated sources of increasing sizes into the real maps.

Such a simple explanation of the relationship between the protostellar and starless populations is not consistent with the other clouds, however, as shown in figure 6.13. Although protostellar cores in Serpens have a similarly small range in sizes for a large range of masses, as seen in Perseus, there is no population of large starless cores in Serpens. In fact, it is unclear how the relatively high mass protostellar cores in Serpens could have evolved from the compact, low mass population of starless cores. This discrepancy raises the possibility that the Serpens cloud has used up its reserve of relatively massive prestellar cores, and any future star formation in the cloud

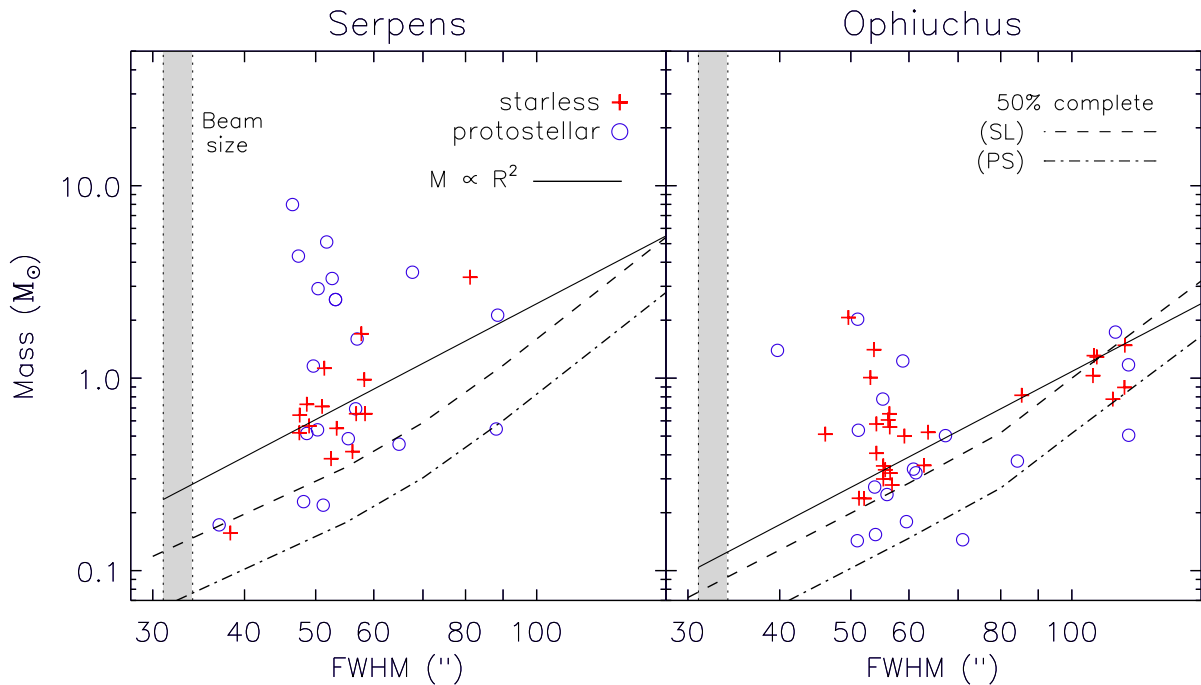


Figure 6.13 Total mass versus angular FWHM size for protostellar and starless cores in Serpens and Ophiuchus. Unlike in Perseus (figure 6.12), starless cores do not necessarily follow a constant surface density ( $M \propto R^2$ ) line. Strikingly, there is no population of large starless cores in Serpens that might be expected to eventually evolve to resemble the current protostellar population in that cloud. In contrast, the properties of starless and protostellar cores are indistinguishable in Ophiuchus. Dashed and dash-dot lines indicate empirically derived 50% completeness limits for starless and protostellar cores, respectively.

will result in stars of lower mass than those of the current protostellar population. In contrast to both Perseus and Serpens, there is essentially no difference between the starless and protostellar populations in Ophiuchus, suggesting that protostellar formation results in very little core evolution for sources in that cloud.

#### 6.4.4 Core Mass Distributions

Differential core mass distributions (CMDs) for the starless and protostellar core samples are shown for each cloud in figure 6.14. Note that the empirically derived 50% completeness limits for averaged size sources (dashed lines) occur at lower masses for protostellar cores, because a higher dust temperature is assumed ( $T_D = 15$  K) than for starless cores ( $T_D = 10$  K). For each distribution, we fit a single power law ( $dN/dM \propto M^\alpha$ ) above the 50% completeness limit.

In Perseus (upper left panel), the protostellar core mass distribution is considerably wider than the starless distribution and extends to higher masses, despite the fact that there are fewer sources in the protostellar sample. Furthermore, the best-fit power law slope is shallower for protostellar cores ( $\alpha = -1.7 \pm 0.1$ ) than for starless cores ( $\alpha = -2.8 \pm 0.3$ ). A widening of the mass distribution is expected if the protostellar CMD originally looked like the starless CMD, and individual cores gradually moved to smaller masses as core material was accreted or ejected by the protostar. Larger masses in the protostellar distribution at the high mass end of the CMDs are not expected in this scenario, however, unless the mass distribution from which the protostellar cores originated was shifted to higher masses than the current starless CMD. Another possibility, of course, is that we are underestimating the dust temperature  $T_D$  for protostellar cores, or overestimating  $T_D$  for starless cores.

In Serpens (upper right panel), the protostellar CMD is slightly wider than the starless distribution and has a shallow slope ( $\alpha = -1.3 \pm 0.3$ ), even shallower than in Perseus. Due to the small number of starless cores in Serpens (15), the starless mass distribution is very noisy, and we are unable to fit a power law slope with reasonable confidence. It is clear, however, that there are significantly more protostellar cores

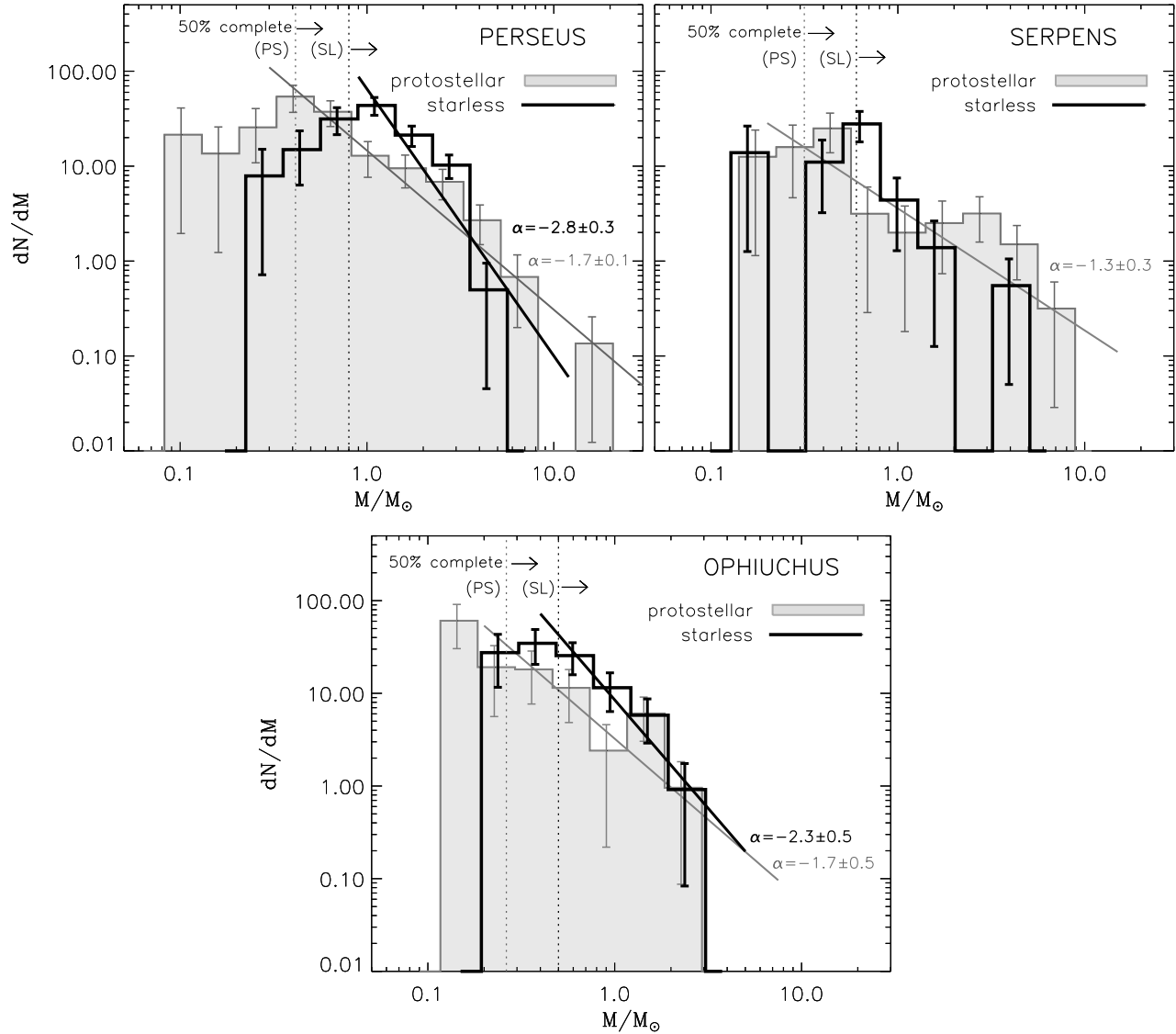


Figure 6.14 Differential core mass distributions (CMDs) of protostellar and starless cores in the three clouds. Empirical 50% completeness limits for average sized sources in each population are shown (dotted lines), and we fit power law slopes above those limits. The protostellar distributions appear to be wider and flatter in all three clouds, as expected if the protostellar CMDs have their origin in the starless CMDs and the distributions have shifted to lower masses as core material is accreted by the protostars within the protostellar cores. The starless CMD for Serpens is too noisy to fit a slope with any reasonable confidence.

than starless cores with high masses.

The slope of the protostellar distribution in Ophiuchus (lower panel) is again shallower ( $\alpha = -1.7 \pm 0.5$ ) than that of the starless CMD ( $\alpha = -2.3 \pm 0.5$ ). In

fact, the slope of the protostellar distribution is the same as was found for Perseus. In contrast to Perseus, however, the two distributions have quite similar widths, and the protostellar CMD extends to only slightly smaller masses. Unlike for the other two clouds, the Ophiuchus CMDs are completely consistent with the idea that the protostellar CMD was originally identical to the current starless CMD, and core evolution after protostellar formation moved some protostellar cores to lower masses. If this is indeed the case, the highest mass protostellar cores must contain quite young protostars, having evolved very little in mass since protostellar formation.

### 6.4.5 Relationship to Cloud Column Density

We use the cumulative fraction of starless and protostellar cores as a function of cloud  $A_V$ , shown in figure 6.15, to quantify the relationship between dense cores and the surrounding cloud material. The visual extinction ( $A_V$ ) is a measure of the cloud column density, and is derived based on the reddening of background 2MASS and IRAC sources, as described in §4.3.1. In chapter 5, we found that 75% of 1.1 mm cores in Perseus, Serpens, and Ophiuchus are found at visual extinctions of  $A_V \gtrsim 8$  mag,  $A_V \gtrsim 15$  mag, and  $A_V \gtrsim 20 - 23$  mag, respectively. Although these values do not define a strict threshold, below these  $A_V$  levels the likelihood of finding any 1.1 mm core is very low. Here we investigate if the relationship between dense cores and cloud column density is different for starless and protostellar cores.

Dotted lines in figure 6.15 identify the  $A_V$  level above which more than 75% of the 1.1 mm cores occur. In all three clouds the majority of cores are found at high cloud column density ( $A_V > 7$  mag): 75% of starless and protostellar cores in Perseus are located at  $A_V \gtrsim 7$  and 8.5 mag, respectively. The equivalent values are  $A_V \gtrsim 9.5$  and 16 mag in Serpens, and  $A_V \gtrsim 19.5$  and 23 mag in Ophiuchus. These values are quite similar to those found using the full core samples in chapter 5. Starless cores in Serpens tend to be found at somewhat lower  $A_V$  than protostellar cores, but this may be a consequence of small number statistics as there are only 15 starless and 20 protostellar cores in Serpens. In the other clouds, there is very little difference between

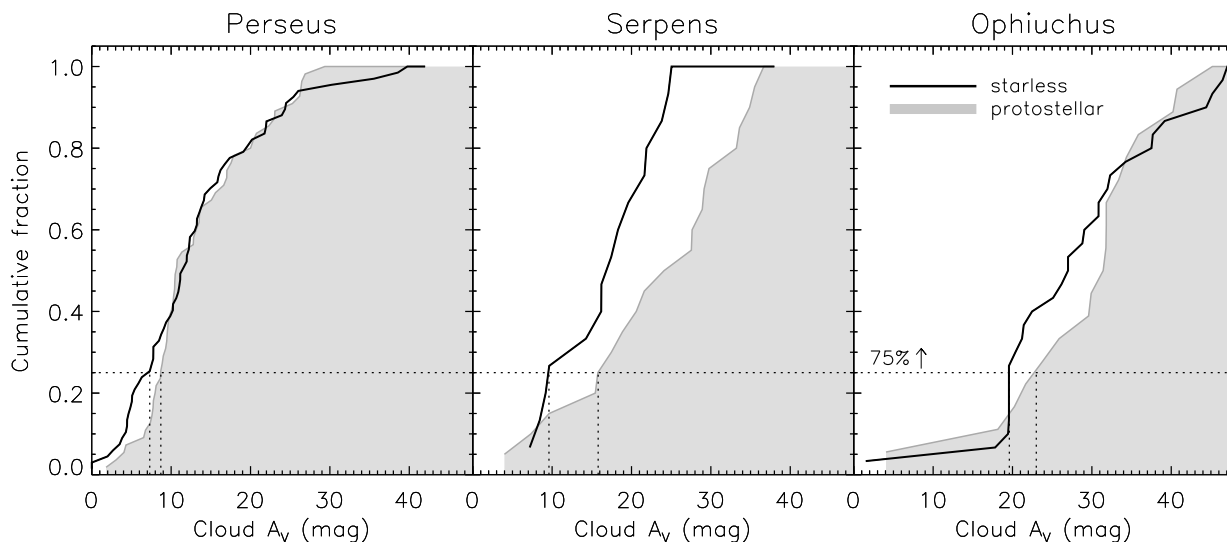


Figure 6.15 Cumulative fraction of starless and protostellar cores as a function of the cloud  $A_V$  in Perseus, Serpens, and Ophiuchus. In all three clouds, most cores are found at high cloud column density ( $A_V > 7$  mag): 75% of starless and protostellar cores in Perseus are located at  $A_V \gtrsim 7$  and 8.5 mag, respectively. The equivalent values are  $A_V \gtrsim 9.5$  and 16 mag in Serpens, and  $A_V \gtrsim 19.5$  and 23 mag in Ophiuchus. Except in Serpens, where starless cores are found at slightly lower  $A_V$  values, there is very little difference between the starless and protostellar core populations. Only Ophiuchus shows evidence for a strict extinction threshold, at  $A_V \sim 17$  mag.

the starless and protostellar populations. Only in Ophiuchus does there appear to be a true extinction threshold for finding 1.1 mm cores; only one protostellar and one starless core is found at  $A_V < 17$  mag in this cloud.

As discussed in chapter 5, an extinction threshold has been predicted by McKee (1989) for photoionization-regulated star formation in magnetically supported clouds. In this model, core collapse and star formation will occur only in shielded regions of a molecular cloud where  $A_V \gtrsim 4 - 8$  mag. The fact that 75% of both protostellar and starless cores are found above  $A_V = 7$  mag in each cloud is consistent with this model, and suggests that magnetic fields must be important, at least in the low column density regions of molecular clouds.

### 6.4.6 Clustering

Finally, we look at the spatial clustering of starless and protostellar cores, as measured by the two-point correlation function (figure 6.16), where  $H(r)$  and  $w(r)$  are defined as in chapter 2. In essence,  $w(r)$  is the excess clustering in the sample as compared to a random distribution of sources. The upper panels of figure 6.16 plot  $w(r)$  as a function of source separation  $r$ , with the linear beam size and average source size indicated. The lower panels plot  $\log(w)$ , with a power law fit ( $w(r) \propto r^p$ ) for  $r$  larger than the average source size. The amplitude of  $w(r)$  is a measure of the degree of clustering above a random distribution, while the slope is a measure of how quickly clustering falls off on increasing scales.

Although visually starless and protostellar cores tend to cluster in a similar way, the amplitude of  $w(r)$  is higher for the protostellar samples in all three clouds. This behavior suggests that clustering is stronger on all spatial scales for protostellar cores. In Serpens (middle panel), the slope of the starless and protostellar distributions are quite similar ( $p = -1.4 \pm 0.3$  and  $-1.3 \pm 0.6$ ). In Perseus and Ophiuchus, however, the slope of the starless distribution is shallower, by approximately  $4\sigma$  in Perseus and  $2\sigma$  in Ophiuchus ( $p = -1.14 \pm 0.13$  and  $-1.5 \pm 0.1$  for starless and protostellar cores in Perseus, and  $-1.3 \pm 0.3$  and  $-2.2 \pm 0.4$  in Ophiuchus). Shallower slopes for the starless samples suggest that although the amplitude of clustering is weaker for starless cores, it does not fall off as fast at larger spatial scales.

A lower degree of clustering for starless cores as compared to protostellar cores in Perseus and Serpens is confirmed by calculating the peak number of cores per square parsec (see §5.5.4). In Perseus, the peak number of starless cores is  $10 \text{ pc}^{-2}$ , compared to  $16 \text{ pc}^{-2}$  for protostellar cores. Likewise, in Serpens the peak number of starless cores is  $4 \text{ pc}^{-2}$ , and the peak number of protostellar cores  $8 \text{ pc}^{-2}$ , suggesting that clustering in the protostellar samples is a factor of 1.5–2 times stronger than in the starless samples for these clouds. In Ophiuchus, however, the values of the starless and protostellar populations are identical ( $12 \text{ pc}^{-2}$ ).

There are two plausible reasons that clustering might be stronger for protostellar

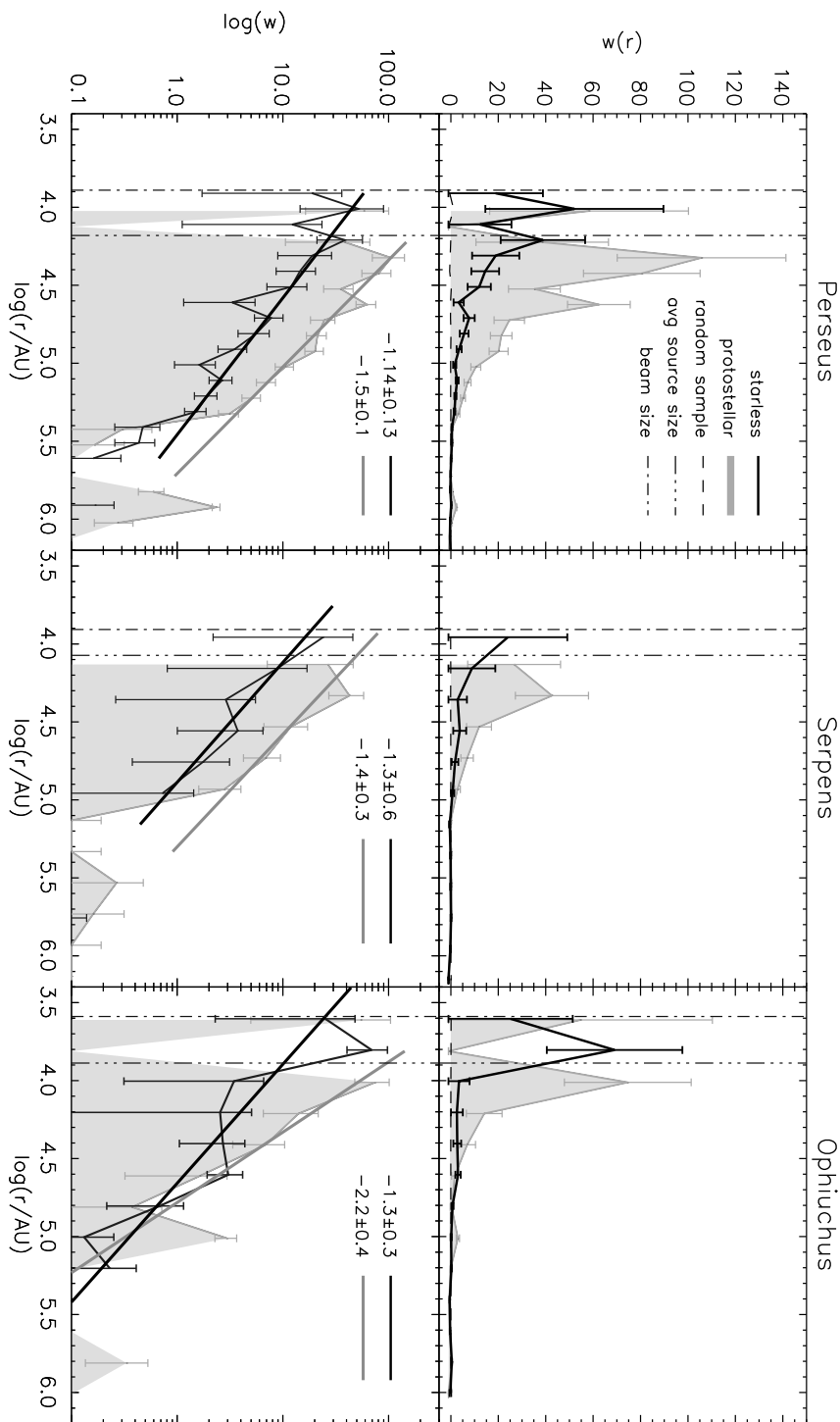


Figure 6.16 Two-point correlation function  $w(r)$ , as a function of source separation  $r$ , for protostellar and starless cores in Perseus, Serpens, and Ophiuchus (upper panels). The lower panel plots  $\log(w)$ , with the best fitting power law slope to each distribution, where slopes are fit above the average source size in each cloud. The amplitude of the protostellar  $w(r)$  is consistently higher than the starless  $w(r)$ , suggesting that clustering is stronger on all spatial scales for the protostellar samples. In Perseus, the slope of the starless distribution is shallower, indicating that clustering does not fall off as quickly on large scales.

cores, one environmental and one evolutionary. The difference may be an environmental effect if cores that are located in regions of the cloud with higher gas density are more likely to collapse to form protostars. In this case, more clustered sources would tend to be protostellar rather than starless. If evolution plays a more important role, however, the spatial distribution of cores might evolve after protostellar formation, for example as a result of dynamical effects.

## 6.5 The Prestellar Core Mass Distribution

One very important measure of the initial conditions of star formation is the prestellar core mass distribution (CMD). In particular, comparing the prestellar CMD to the stellar initial mass function (IMF) gives us insight into how the final masses of stars are determined. In the simplest case, there are two possible processes that might dictate what the final mass of forming star will be. If stellar masses are determined by the initial fragmentation into cores, i.e., the final star mass is always a fixed percentage of the original core mass, then the shape of the emergent stellar IMF should closely trace that of the starless CMD (e.g., Myers et al., 1998). This might be expected in crowded regions where the mass reservoir is limited to a protostar's nascent core. If, on the other hand, stellar masses are determined by competitive accretion (Bonnell et al., 2001) or by the protostars themselves through feedback mechanisms (e.g., outflows and winds, Shu et al. 1987), we would not expect the emergent IMF to reflect the original clump mass function (Adams & Fatuzzo, 1996).

We assume that all starless cores in our 1.1 mm samples will eventually form stars, and thus are true prestellar cores. While it is possible that some fraction of the starless cores are transient or stable structures that will never collapse to form a protostar, the cores detected by our Bolocam surveys have high mean densities ( $n > 2 - 3 \times 10^4 \text{ cm}^{-3}$ ; chapter 5), making them likely to be prestellar (Gregersen & Evans, 2000; Di Francesco et al., 2007). We attempt to estimate if cores are gravitationally bound by comparing the measured core masses to the Jeans mass for

material with the same mean density, where

$$M_J = \frac{a^3}{\rho^{0.5} G^{1.5}} = 1.6 M_\odot \left( \frac{n_{H_2}}{10^4 \text{cm}^{-3}} \right)^{-0.5}, \quad (6.2)$$

for a temperature of 10 K and internal support due to thermal motions only (Jeans, 1928). Using the mean particle density of each core to calculate the local Jeans mass, we find that nearly all sources have  $M > M_J$ , with median  $M/M_J$  ratios of 2.4 in Perseus, 1.5 in Serpens, and 2.4 in Ophiuchus. Thus the large majority of starless cores are likely to be bound or unstable, although there may be additional means of core support, such as turbulence or magnetic fields (e.g., Evans, 1999). Future comparison of our data to molecular line observations of the Bolocam cores in Perseus, recently acquired as part of the COMPLETE project, will provide a more robust method of determining if cores are in virial equilibrium, and for distinguishing prestellar from unbound starless cores.

Combining the starless core samples from all three clouds, and using  $T_D = 10$  K to calculate the mass, results in the prestellar CMD shown in figure 6.17. The highest empirical completeness limit is in the Perseus sample, where the 50% completeness for averaged size sources (70") is  $0.8 M_\odot$ . The completeness limit is lower in Serpens ( $0.6 M_\odot$ ) and Ophiuchus ( $0.5 M_\odot$ ), but as more than half of the total population of starless cores are in Perseus, we adopt  $0.8 M_\odot$  for the entire sample.

We fit a power law ( $dN/dM \propto M^\alpha$ ) to the CMD for  $M > 0.8 M_\odot$ , finding a slope of  $\alpha = -2.5 \pm 0.2$ , with a reduced chi-squared of  $\tilde{\chi}^2 = 3.1$ . We also fit a lognormal distribution (equation (1.7)) to  $M > 0.3 M_\odot$ , finding a best-fit width  $\sigma = 0.30 \pm 0.03$  and characteristic mass  $M_0 = 1.0 \pm 0.1 M_\odot$ . Although the lognormal function is quite a good fit ( $\tilde{\chi}^2 = 0.5$ ), the reliability of the turnover in the prestellar CMD is highly questionable, given that the completeness limit in Perseus coincides closely with the turnover mass. The prestellar CMD can also be fitted by a broken power law with  $\alpha = -4.3 \pm 1.1$  for  $M > 2.5 M_\odot$  and  $\alpha = -1.7 \pm 0.3$  for  $M < 2.5 M_\odot$ , although the uncertainties are large. Two recent estimates for the IMF shape are also shown in figure 6.17 for reference.

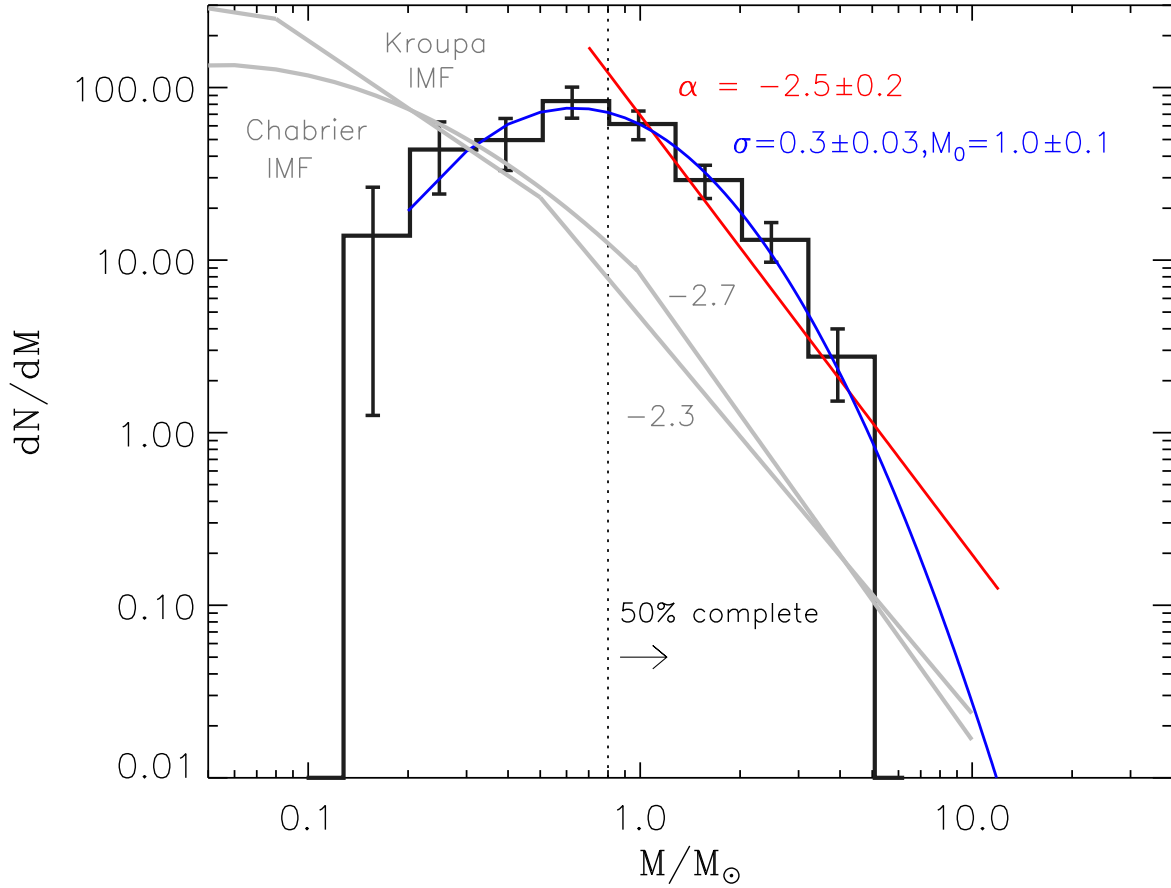


Figure 6.17 Combined prestellar core mass distribution, with power law (red curve) and lognormal (blue curve) fits. The prestellar sample is composed of all starless cores from Perseus, Serpens, and Ophiuchus, and the 50% mass completeness limit is defined by the completeness to average sized cores in Perseus, the least deep cloud. Recent measurements of the stellar IMF ( $\alpha = -2.3$  to  $-2.8$ ) are similar to the best fit power law slope ( $\alpha = -2.5$ ). Slopes of  $\alpha = 2.3$  and  $2.7$  are shown for reference (thick gray lines), as are IMF fits for low masses from Chabrier (2005) and Kroupa (2002).

For comparison, we show in figure 6.18 the CMD of the *protostellar* core sample combined from all three clouds, and assuming  $T_D = 15$  K. The protostellar CMD is considerably wider and flatter than the starless CMD. The best-fitting power law slope ( $\alpha = -1.9 \pm 0.2$ ;  $\tilde{\chi}^2 = 1.7$ ) is shallower than for the starless sample, and the best-fitting lognormal distribution ( $\sigma = 0.51 \pm 0.07$ ,  $M_0 = 0.8 \pm 0.2$ ;  $\tilde{\chi}^2 = 1.3$ ) is wider by nearly a factor of two. It is also possible to fit the protostellar distribution

with a broken power law:  $\alpha = -2.8 \pm 0.4$  ( $M > 2 M_{\odot}$ ) and  $\alpha = -1.3 \pm 0.2$  ( $0.3 M_{\odot} < M < 2 M_{\odot}$ ). A protostellar CMD that extends to lower masses than the starless CMD is expected, given that some fraction of mass has already been accreted on to the central source for protostellar cores. An extension to higher masses in the protostellar CMD as compared to the starless CMD, however, can only be explained if (a) we are underestimating the dust temperature of protostellar sources, (b) masses of protostellar cores are overestimated due to blending in clustered regions, or (c) the current populations of prestellar cores in these clouds have lower mass than the generation of cores that have already formed protostars.

The shape of the local IMF is still uncertain (Scalo, 2005), but recent work has found evidence for a slope of  $\alpha = -2.3$  to  $-2.8$  for stellar masses  $M \gtrsim 1 M_{\odot}$ , quite similar to the slope we measure for the combined prestellar CMD ( $\alpha = -2.5$ ). For example, Reid, Gizis, & Hawley (2002) find  $\alpha = -2.5$  above  $0.6 M_{\odot}$ , and  $\alpha = -2.8$  above  $1 M_{\odot}$ . Schröder & Pagel (2003) suggest  $\alpha = -2.7$  for  $1.1 < M < 1.6 M_{\odot}$  and  $\alpha = -3.1$  for  $1.6 < M < 4 M_{\odot}$ . For reference, the Salpeter IMF has a slope of  $\alpha = -2.35$  (Salpeter, 1955), and the Scalo (1986) slope for sources with mass  $M \gtrsim 1 M_{\odot}$  is  $\alpha \sim -2.7$ . At lower masses, the IMF flattens, and may be characterized by a lognormal function. Kroupa (2002) suggests a three-component power law for the average single-star IMF:  $\alpha = -2.3$  for  $0.5 < M < 1 M_{\odot}$ ,  $\alpha = -1.3$  for  $0.08 < M < 0.5 M_{\odot}$ , and  $\alpha = -0.3$  for  $0.01 < M < 0.08 M_{\odot}$ . Chabrier (2005) finds that a lognormal distribution with  $\sigma = 0.55$  and  $M_0 = 0.25 M_{\odot}$  is a good fit for  $M < 1 M_{\odot}$ . The system IMF, i.e., treating binaries and multiple systems as single rather than multiple objects, peaks at approximately  $0.2 - 0.3 M_{\odot}$  (e.g., Chabrier, 2005; Luhman et al, 2003). This system IMF is appropriate for comparison to our CMDs, which would not resolve these multiple systems even if they form from distinct cores.

The Kroupa (2002) three-component power law and the Chabrier (2005) lognormal IMF joined with  $\alpha = -2.7$  for  $M > 1 M_{\odot}$  are shown as thick gray lines in figure 6.17. The width of the Chabrier (2005) IMF lognormal is somewhat larger than the width of the prestellar CMD best-fit lognormal ( $\sigma = 0.3$ ), expected if we are incomplete

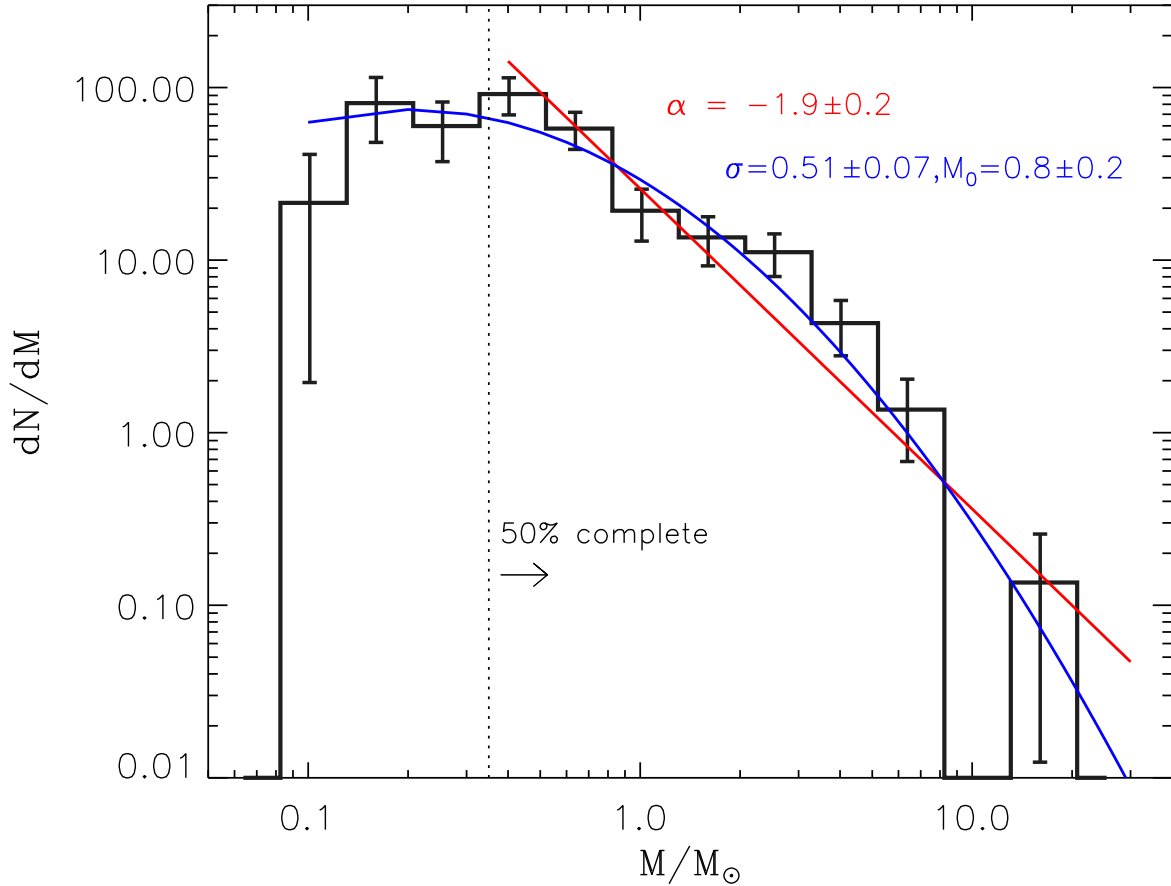


Figure 6.18 Combined protostellar mass distribution, with power law (red) and lognormal (blue) fits. The protostellar CMD includes all protostellar cores from Perseus, Serpens, and Ophiuchus, and the 50% mass completeness limit is defined by the completeness to average sized protostellar cores in Perseus. The best-fit power law ( $\alpha = -1.9$ ) is shallower, and the distribution as a whole wider, than the prestellar CMD (figure 6.17), as expected if the protostellar CMD evolved from the prestellar CMD. Higher masses than the prestellar CMD are more difficult to explain, however.

at lower masses, and the IMF characteristic mass ( $0.25 M_{\odot}$ ) is a factor of four lower than that of the CMD ( $1.0 M_{\odot}$ ). A lower characteristic mass for the IMF is expected if some fraction of the core mass is lost in the star-formation process. The power law slopes for  $M > 1 M_{\odot}$  appear to be quite similar for the CMD and IMF, however. While we cannot rule out the importance of feedback and other local processes, the fact that the prestellar CMD and the local IMF have similar shapes provides support

for the hypothesis that the final masses of stars are already determined during the core formation process.

If the prestellar CMD does have a one-to-one relationship with the stellar IMF, then the ratio of turnover masses ( $M_{\text{TO}}^{\text{IMF}}/M_{\text{TO}}^{\text{CMD}}$ ) is a measure of the core collapse efficiency  $f_{\text{eff}}$ , or the fraction of original core mass that ends up in the final star. Equivalently,  $M_{\text{TO}}^{\text{CMD}}/M_{\text{TO}}^{\text{IMF}} = 1 - f_{\text{eff}}$  is the fraction of core mass lost in the star formation process. Our limited completeness dictates that we can only measure a lower limit to  $f_{\text{eff}}$ . If there is a true turnover in the prestellar CMD, it occurs at  $M_{\text{TO}}^{\text{CMD}} \lesssim 0.8 M_{\odot}$ . For an IMF turnover mass of  $0.25 M_{\odot}$  (Chabrier, 2005), this value implies that least 30% of the initial core mass is accreted onto the final star. Characteristic masses associated with lognormal fits to both the IMF and CMD imply a similar ratio of at least  $f_{\text{eff}} \gtrsim M_0^{\text{IMF}}/M_0^{\text{CMD}} = 0.25/1.0 = 0.25$ . There is a suggestion of a break in the CMD at  $M \sim 2.5 M_{\odot}$ . Comparing to the three-component Kroupa (2002) IMF, which has a break at  $M = 0.5 M_{\odot}$ , again implies that the CMD is similar in shape to the IMF but shifted to higher masses by about a factor of four.

Evidence for a direct link between the CMD and the IMF has been found previously based on dust emission surveys of small regions (Testi & Sargent, 1998; Motte et al., 1998), as well as molecular line observations of dense cores (Onishi et al. 2002; see also chapter 1 for more discussion). Recently, Alves et al. (2007) found evidence for a break in the mass distribution of dense cores in the Pipe Nebula, as traced by dust extinction toward background stars. Those authors interpret the similarity between the Pipe Nebula CMD and the Trapezium cluster IMF (Muench et al., 2002) as evidence that the stellar IMF is a direct product of the CMD, with a uniform core-to-star efficiency of  $30\% \pm 10\%$ . Although the measured masses of Alves et al. (2007) are somewhat less uncertain than ours because they do not need to assume a dust opacity or temperature, the mean densities of cores traced by dust extinction,  $n \sim 5 \times 10^3 - 2 \times 10^4 \text{ cm}^{-3}$ , are considerably lower than the mean densities of cores traced by our Bolocam 1.1 mm surveys ( $n \sim 1 - 8 \times 10^5 \text{ cm}^{-3}$ ). Furthermore, extinction is sensitive to all material along the line of sight, and may be tracing diffuse structures that will never form stars. Despite these differences, however, the two

methods give similar results.

## 6.6 Properties of Cold Protostars

### 6.6.1 Bolometric Luminosity and Temperature

Our extensive wavelength coverage allows us to construct well-sampled SEDs for the cold protostar candidates in all three clouds, from which we calculate a bolometric luminosity ( $L_{bol}$ ) and bolometric temperature ( $T_{bol}$ ) for each source. The bolometric luminosity is calculated by integrating the SED  $S_\nu$  over frequency:

$$L_{bol} = 4\pi d^2 \int S_\nu d\nu. \quad (6.3)$$

The bolometric temperature is defined as the temperature of a blackbody with the same mean frequency as the source SED, and is given by  $T_{bol} = 1.35 \times 10^{-11} \langle \nu \rangle$  K (Myers & Ladd, 1993), where the mean frequency is

$$\langle \nu \rangle = \frac{\int \nu S_\nu d\nu}{\int S_\nu d\nu}. \quad (6.4)$$

Two methods for estimating the integrations over frequency for finitely sampled SEDs are discussed in the appendix (§6.11). We use the difference between the values calculated by the two methods to estimate overall uncertainties on measured  $L_{bol}$  and  $T_{bol}$  values of 20% – 50%, depending on whether or not a 160  $\mu\text{m}$  flux is available. Systematic errors introduced by missing 160  $\mu\text{m}$  flux points are also investigated in §6.11. Without a 160  $\mu\text{m}$  flux point,  $T_{bol}$  will almost certainly be an overestimate for very cold sources, which may affect our classification of protostellar candidates. Ophiuchus will be most affected, as only four sources in that cloud have reliable 160  $\mu\text{m}$  fluxes. We will revisit this issue in §6.9, when we look at the relative number of Class 0 and Class I protostars.

Tables 6.2–6.4 list the bolometric temperatures and luminosities derived for all candidate protostars in each cloud that are associated with 1.1 mm emission. Sources

are listed by increasing  $T_{bol}$ , and identified as, e.g., “Pers-Cold#”, as well as by their c2d name (SSTc2dJ...), which also gives the position. Note that the uncertainties given are formal errors from the midpoint integration only, and do not include our estimated systematic uncertainties of 20%–50%.

### 6.6.2 Envelope Mass

The envelope mass of candidate protostars,  $M_{env}$ , is calculated from the flux density at 1.1 mm using equation (6.1), by the same method used to derive the masses of protostellar cores. Of course, our protostellar “cores” and protostellar “envelopes” are often one and the same. We assume a dust temperature of  $T_D = 15$  K for all protostellar envelopes, as discussed in §6.4.4. The temperature will be higher close to the protostar, but the majority of the envelope mass is in the outer, cooler, regions of the envelope. Envelope masses are listed in tables 6.2–6.4; if the source is associated with a particular core the Bolocam identification from chapters 2–4 is given in the last column. If the source is not associated with a distinct core, but rather the flux has been “band-filled” at 1.1 mm, then no Bolocam ID is given. Furthermore, only sources with measured fluxes at 1.1 mm are listed in tables 6.2–6.4. We ignore sources with upper limits at 1.1 mm because we are interested primarily in young, embedded sources, and those without emission at 1.1 mm are unlikely to have substantial envelopes.

### 6.6.3 Completeness

Because we require a detection at 1.1 mm to be included in the final source lists, we are clearly incomplete to objects more evolved than Class I, which do not have a substantial envelope. A few Class II sources with massive disks do appear in our sample, and are discussed in §6.6.4.3. It is possible that we are missing low luminosity cold objects that are below our 1.1 mm detection threshold, as the 1.1 mm detection requirement is more restrictive than our 24  $\mu\text{m}$  flux criteria (e.g., Dunham et al., in preparation).

Taking the 1.1 mm detection limits for each cloud (75 mJy in Perseus, 50 mJy in Serpens, and 110 mJy in Ophiuchus), and assuming the spectrum of a modified blackbody,  $S_\nu = \nu^\beta B_\nu(T)$  with  $T = 15$  K, we can estimate the minimum detectable bolometric luminosity in each cloud. For  $\beta = 1$ , the minimum  $L_{bol}$  is  $0.02 L_\odot$  in Perseus,  $0.01 L_\odot$  in Serpens, and  $0.006 L_\odot$  in Ophiuchus. Assuming  $T = 20$  K raises these values by approximately a factor of 2, while taking  $\beta = 2$  causes an increase of a factor of 4. Although these are very rough estimates, they agree fairly well with the lowest observed bolometric luminosities for sources with 1.1 mm detections ( $0.04 L_\odot$  in Perseus,  $0.05 L_\odot$  in Serpens, and  $0.01 L_\odot$  in Ophiuchus). Harvey et al. (2007a) demonstrates that the c2d *Spitzer* surveys of Serpens are complete at the 50% level to young objects with luminosities as low as  $0.01 L_\odot$ , and at the 90% level to  $0.05 L_\odot$ .

Table 6.2. Bolometric temperatures, luminosities, and envelope masses of cold protostars in Perseus

ID	c2d name/position (SSTc2dJ...)	T <sub>bol</sub> (K)	L <sub>bol</sub> (L <sub>⊙</sub> )	M <sub>env</sub> <sup>1</sup> (M <sub>⊙</sub> )	Bolocam ID <sup>2</sup>
Class 0					
Pers-cold1	034356.74+320050.1	24 (3)	1.5 (0.14)	3.02 (0.08)	Bolo 103
Pers-cold2	033217.95+304947.4	25 (1)	1.3 (0.04)	2.88 (0.08)	Bolo 66
Pers-cold3	032900.70+311200.0	30 (11)	0.69 (0.2)	0.29 (0.03)	Bolo 41
Pers-cold4	032839.10+310601.7	31 (1)	0.22 (0.01)	0.36 (0.02)	Bolo 30
Pers-cold5	033120.96+304530.0	33 (2)	1.20 (0.04)	0.95 (0.04)	Bolo 65
Pers-cold6	033314.40+310710.8	36 (12)	0.64 (0.18)	1.04 (0.10)	Bolo 79
Pers-cold7	034443.94+320136.1	40 (10)	3.0 (0.66)	0.63 (0.06)	Bolo 116
Pers-cold8	032951.82+313906.0	41 (2)	0.46 (0.02)	0.64 (0.04)	Bolo 59
Pers-cold9	033316.56+310651.8	47 (1)	0.27 (0.01)	1.57 (0.16)	Bolo 79
Pers-cold10	034357.10+320304.2	49 (1)	0.45 (0.01)	1.78 (0.04)	Bolo 104
Pers-cold11	032910.50+311330.9	51 (5)	4.2 (0.28)	7.75 (0.78)	Bolo 48
Pers-cold12	032902.36+311533.9	53 (1)	2.40 (0.01)	1.87 (0.19)	Bolo 43
Pers-cold13	032912.04+311301.7	54 (26)	1.4 (0.49)	3.66 (0.37)	Bolo 48
Pers-cold14	032913.45+311355.5	54 (1)	0.49 (0.01)	0.5 (0.05)	Bolo 48
Pers-cold15	032911.11+312202.8	55 (1)	9.90 (0.03)	0.64 (0.06)	
Pers-cold16	032904.05+311446.5	56 (26)	0.53 (0.17)	1.16 (0.12)	
Pers-cold17	034350.95+320324.7	56 (25)	0.38 (0.12)	1.15 (0.11)	Bolo 102
Pers-cold18	032739.09+301303.1	59 (8)	4.2 (0.49)	0.51 (0.03)	Bolo 22
Pers-cold19	032911.25+311831.4	59 (27)	2.8 (0.94)	2.47 (0.07)	Bolo 49
Pers-cold20	032923.49+313329.5	60 (3)	0.36 (0.01)	0.64 (0.05)	Bolo 57
Pers-cold21	032743.23+301228.8	60 (3)	1.70 (0.06)	0.50 (0.03)	Bolo 23
Pers-cold22	032855.56+311436.8	61 (4)	18.0 (0.48)	2.81 (0.28)	Bolo 38
Pers-cold23	033313.78+312005.2	63 (17)	0.11 (0.03)	0.41 (0.04)	Bolo 78
Pers-cold24	032910.68+311820.6	63 (5)	2.8 (0.17)	2.47 (0.07)	Bolo 49
Pers-cold25	032522.33+304513.9	63 (5)	1.7 (0.11)	1.41 (0.14)	Bolo 5
Pers-cold26	032917.16+312746.4	66 (6)	0.29 (0.02)	0.5 (0.05)	Bolo 52
Pers-cold27	032845.30+310541.9	67 (3)	0.43 (0.02)	0.19 (0.02)	Bolo 33
Pers-cold28	032637.46+301528.0	68 (4)	0.95 (0.04)	0.5 (0.08)	Bolo 18
Pers-cold29	032538.82+304406.1	69 (5)	4.4 (0.26)	1.87 (0.19)	Bolo 10
Class I					
Pers-cold30	034351.02+320308.1	72 (6)	0.28 (0.02)	0.62 (0.06)	Bolo 102
Pers-cold31	032832.55+311105.1	74 (21)	0.18 (0.05)	0.19 (0.02)	Bolo 25
Pers-cold32	033317.85+310931.9	76 (6)	1.8 (0.11)	3.84 (0.09)	Bolo 80
Pers-cold33	033327.28+310710.2	78 (5)	1.7 (0.06)	0.59 (0.06)	Bolo 84
Pers-cold34	034402.40+320204.9	84 (6)	0.16 (0.01)	0.63 (0.02)	Bolo 106

Table 6.2 (cont'd)

ID	c2d name/position (SSTc2dJ...)	$T_{bol}$ (K)	$L_{bol}$ ( $L_{\odot}$ )	$M_{env}^1$ ( $M_{\odot}$ )	Bolocam ID <sup>2</sup>
Pers-cold35	032536.48+304522.1	90 (6)	4.3 (0.22)	4.47 (0.45)	Bolo 8
Pers-cold36	033015.12+302349.3	99 (6)	1.6 (0.06)	0.46 (0.07)	Bolo 60
Pers-cold37	032837.16+311331.6	103 (6)	9.1 (0.3)	0.44 (0.04)	Bolo 29
Pers-cold38	032857.36+311415.8	106 (7)	5.3 (0.27)	0.74 (0.07)	Bolo 38
Pers-cold39	032918.27+312319.8	106 (8)	0.07 (0.01)	0.44 (0.04)	Bolo 54
Pers-cold40	033229.18+310240.8	115 (3)	0.54 (0.01)	0.45 (0.08)	Bolo 68
Pers-cold41	033316.66+310755.1	132 (8)	1.5 (0.07)	1.12 (0.11)	
Pers-cold42	033320.30+310721.4	157 (8)	0.17 (0.01)	1.50 (0.15)	Bolo 81
Pers-cold43	032539.10+304358.1	163 (12)	0.68 (0.04)	1.82 (0.18)	Bolo 10
Pers-cold44	034202.16+314802.0	176 (12)	0.07 (0.01)	0.07 (0.02)	
Pers-cold45	033309.57+310531.1	197 (12)	0.05 (0.01)	0.21 (0.02)	
Pers-cold46	032903.76+311604.9	202 (16)	23.0 (1.4)	3.25 (0.32)	Bolo 43
Pers-cold47	032800.40+300801.2	221 (9)	0.3 (0.01)	0.17 (0.02)	
Pers-cold48	032834.50+310051.0	230 (9)	1.2 (0.04)	0.12 (0.02)	
Pers-cold49	032738.23+301358.6	238 (7)	0.87 (0.02)	0.34 (0.04)	Bolo 21
Pers-cold50	032912.94+311814.3	239 (10)	1.1 (0.04)	0.77 (0.08)	Bolo 49
Pers-cold51	032908.12+312157.8	254 (18)	10.0 (0.58)	1.62 (0.16)	Bolo 47
Pers-cold52	032834.53+310705.5	263 (11)	0.07 (0.01)	0.24 (0.04)	Bolo 28
Pers-cold53	032839.72+311731.9	278 (11)	0.16 (0.01)	0.49 (0.05)	Bolo 31
Pers-cold54	034741.56+325144.0	287 (10)	4.7 (0.13)	1.67 (0.08)	Bolo 122
Pers-cold55	034443.33+320131.5	302 (43)	1.9 (0.27)	0.32 (0.03)	Bolo 116
Pers-cold56	032901.46+312022.8	304 (23)	6.2 (0.39)	1.87 (0.19)	Bolo 42
Pers-cold57	034705.42+324308.5	312 (11)	0.54 (0.02)	0.14 (0.02)	
Pers-cold58	032903.33+312314.6	313 (15)	0.09 (0.01)	0.11 (0.02)	
Pers-cold59	032858.44+312217.5	322 (14)	0.63 (0.02)	0.71 (0.07)	Bolo 40
Pers-cold60	032835.04+302009.8	341 (18)	0.04 (0.01)	0.14 (0.02)	Bolo 27
Pers-cold61	032909.09+312128.7	354 (19)	0.34 (0.02)	0.74 (0.07)	Bolo 47
Pers-cold62	032920.07+312407.5	363 (16)	0.28 (0.01)	0.52 (0.05)	Bolo 54
Pers-cold63	034421.33+315932.5	371 (14)	0.24 (0.01)	0.17 (0.02)	Bolo 113
Pers-cold64	034412.98+320135.4	378 (14)	1.8 (0.06)	0.12 (0.02)	
Pers-cold65	032843.28+311732.9	436 (27)	1.9 (0.11)	0.25 (0.02)	Bolo 31
Pers-cold66	033312.85+312124.2	438 (16)	3.2 (0.1)	0.53 (0.07)	Bolo 76
Pers-cold67	032856.31+312227.8	440 (18)	0.16 (0.01)	0.25 (0.02)	
Pers-cold68	034345.15+320358.6	542 (19)	0.69 (0.02)	0.24 (0.02)	

<sup>1</sup>The envelope mass is calculated assuming a dust temperature  $T_D = 15$  K

<sup>2</sup>Bolocam IDs are from chapter 2-4, and indicate that the protostellar source is within 1.0 core FWHM of a given Bolocam core. If no ID is listed, the source was not originally identified as a distinct 1.1 mm core, but there is detectable ( $\gtrsim 3\sigma$ ) 1.1 mm emission at the position of the source (i.e., it has been “band-filled” at 1.1 mm).

Note. — Uncertainties for  $T_{bol}$ ,  $L_{bol}$ , and  $M_{env}$  are given in parentheses; uncertainties for  $T_{bol}$  and  $L_{bol}$  are formal fitting errors from the midpoint SED integration, and do not include systematic uncertainties of 20-30%. Uncertainties in  $M_{env}$  are from the photometry only. Absolute uncertainties in the mass may be a factor of 4 or more, from uncertainties in  $d$ ,  $\kappa_{1mm}$  and  $T_D$ , but relative values should be much more accurate.

Table 6.3. Bolometric temperatures, luminosities, and envelope masses of cold protostars in Serpens

ID	c2d name/position (SSTc2dJ...)	T <sub>bol</sub> (K)	L <sub>bol</sub> (L <sub>⊙</sub> )	M <sub>env</sub> (M <sub>⊙</sub> )	Bolocam ID
Class 0					
Serp-cold1	182855.92+002944.7	32 (12)	1.6 (0.47)	1.19 (0.12)	Bolo 8
Serp-cold2	182908.52+003130.5	36 (14)	1.4 (0.38)	1.16 (0.01)	Bolo 15
Serp-cold3	182854.84+002952.5	40 (12)	4.3 (1.1)	1.54 (0.15)	Bolo 8
Serp-cold4	182952.44+003611.7	42 (1)	1.0 (0.01)	0.54 (0.01)	Bolo 24
Serp-cold5	182854.12+002929.9	47 (12)	4.5 (1.)	1.67 (0.17)	Bolo 8
Serp-cold6	183000.72+011301.4	54 (1)	1.2 (0.01)	2.56 (0.01)	Bolo 28
Serp-cold7	182949.20+011654.7	55 (4)	0.58 (0.02)	2.42 (0.24)	Bolo 22
Serp-cold8	182854.84+001832.6	56 (16)	0.16 (0.04)	0.24 (0.02)	Bolo 7
Serp-cold9	182949.56+011521.9	57 (27)	11.0 (3.7)	7.98 (0.01)	Bolo 23
Serp-cold10	182948.12+011644.9	58 (1)	2.1 (0.02)	3.72 (0.37)	Bolo 22
Serp-cold11	182959.28+011401.7	59 (1)	1.7 (0.01)	2.56 (0.01)	Bolo 26
Class I					
Serp-cold12	182906.72+003034.3	77 (1)	1.9 (0.01)	1.39 (0.14)	Bolo 14
Serp-cold13	182948.84+011617.7	79 (1)	7.6 (0.01)	1.53 (0.15)	Bolo 22
Serp-cold14	182952.08+011547.8	85 (1)	2.6 (0.02)	1.23 (0.12)	Bolo 23
Serp-cold15	182902.04+003120.6	86 (1)	0.05 (0.01)	0.17 (0.02)	
Serp-cold16	182902.76+003009.5	95 (30)	1.0 (0.32)	0.22 (0.02)	Bolo 13
Serp-cold17	183005.40+004104.5	100 (1)	0.08 (0.01)	0.19 (0.02)	
Serp-cold18	182954.24+003601.3	101 (35)	0.17 (0.05)	0.48 (0.05)	Bolo 24
Serp-cold19	182844.76+005125.7	110 (6)	0.04 (0.01)	0.24 (0.02)	Bolo 3
Serp-cold20	182906.36+003043.2	117 (1)	1.5 (0.01)	1.38 (0.14)	Bolo 14
Serp-cold21	182952.80+011456.0	120 (1)	1.2 (0.01)	0.74 (0.07)	Bolo 23
Serp-cold22	183000.00+011311.6	129 (1)	2.0 (0.01)	2.56 (0.01)	Bolo 28
Serp-cold23	182951.00+011640.6	141 (1)	1.7 (0.01)	1.84 (0.18)	Bolo 22
Serp-cold24	182957.48+011300.4	157 (36)	2.6 (0.58)	2.35 (0.24)	Bolo 25
Serp-cold25	182957.84+011251.4	190 (40)	3.1 (0.63)	1.06 (0.11)	Bolo 25
Serp-cold26	182845.12+005203.5	204 (2)	0.24 (0.01)	0.29 (0.03)	Bolo 3
Serp-cold27	183000.00+011159.0	249 (36)	1.8 (0.25)	1.14 (0.11)	Bolo 29
Serp-cold28	182851.24+001927.3	250 (3)	0.06 (0.01)	0.16 (0.02)	Bolo 7
Serp-cold29	182949.56+011706.0	294 (9)	0.58 (0.02)	1.87 (0.19)	Bolo 22
Serp-cold30	182958.92+011426.2	303 (9)	0.62 (0.02)	2.0 (0.2)	Bolo 26
Serp-cold31	182956.76+011446.5	322 (1)	5.8 (0.02)	0.69 (0.07)	
Serp-cold32	182844.04+005337.9	360 (5)	0.19 (0.01)	0.26 (0.03)	Bolo 2
Serp-cold33	183002.88+011228.2	374 (2)	2.2 (0.01)	1.32 (0.13)	Bolo 28
Serp-cold34	182957.48+011404.5	426 (1)	19.0 (0.02)	1.9 (0.19)	Bolo 26

Table 6.3 (cont'd)

ID	c2d name/position (SSTc2dJ...)	$T_{bol}$ (K)	$L_{bol}$ ( $L_{\odot}$ )	$M_{env}$ ( $M_{\odot}$ )	Bolocam ID
Serp-cold35	182931.92+011842.9	430 (1)	5.3 (0.01)	2.12 (0.01)	Bolo 20
Serp-cold36	183005.76+003930.8	431 (6)	0.05 (0.01)	0.2 (0.02)	Bolo 32
Serp-cold37	182916.08+001822.7	437 (1)	1.7 (0.01)	0.54 (0.01)	Bolo 17

Note. — Columns are as in table 6.3, and uncertainties for  $T_{bol}$ ,  $L_{bol}$ , and  $M_{env}$  are given in parentheses.

## 6.6.4 Individual Sources

Here we briefly discuss a few examples of interesting or newly-identified cold protostellar sources.

### 6.6.4.1 IRAS 03292+3039

IRAS 03292+3039 (Pers-Cold 2) is a little-studied, Class 0 source associated with the 1.1 mm core Pers-Bolo 66, and was discussed briefly in chapter 2. An image of IRAS 03292+3039, together with the SED, is shown in figure 6.2. Jørgensen et al. (2006) identified this as an outflow source, noting on the large-scale outflow visible in the 4.5  $\mu\text{m}$  IRAC band (also seen in figure 6.2 as bright 8  $\mu\text{m}$  knots on either side of the protostellar source).

Bright 1.1 mm emission centered on this object indicates a fairly massive protostellar envelope ( $2.8 M_{\odot}$ ), while the powerful outflow and low bolometric temperature ( $T_{bol} = 25$  K) are evidence of an extremely young, energetic embedded protostar. The spectral energy distribution (figure 6.2) is similar to well-known Class 0 protostars in Perseus such as NGC 1333-IRAS 4, and the nearby source IRAS 03282+3035. The small fan-shaped nebulosity visible at 3.6 and 4.5  $\mu\text{m}$  (figure 6.19) is most easily explained by a cone-shaped cavity, carved out of the dense envelope by an energetic outflow. The orientation of the nebulosity corresponds well to the larger-scale outflow traced by IRAC emission, and the approximate orientation of the large-scale outflow is indicated by thick gray lines in figure 6.19. The one-sided nebulosity at 3.6  $\mu\text{m}$  is strikingly similar to the Whitney et al. (2003) model IRAC image of an early Class 0

Table 6.4. Bolometric temperatures, luminosities, and envelope masses of cold protostars in Ophiuchus

ID	c2d name/position (SSTc2dJ...)	$T_{\text{bol}}$ (K)	$L_{\text{bol}}$ ( $L_{\odot}$ )	$M_{\text{env}}$ ( $M_{\odot}$ )	Bolocam ID
Class 0					
Oph-cold1	162821.72–243623.4	36 (2)	0.25 (0.01)	0.17 (0.02)	Bolo 26
Oph-cold2	163222.56–242831.8	54 (5)	6.9 (0.48)	0.12 (0.02)	Bolo 37
Oph-cold3	162625.80–242428.8	57 (28)	0.41 (0.15)	0.24 (0.02)	Bolo 9
Class I					
Oph-cold4	163136.84–240419.7	77 (2)	0.18 (0.01)	0.03 (0.01)	
Oph-cold5	162718.36–242836.7	82 (14)	0.01 (0.01)	0.08 (0.01)	
Oph-cold6	162721.96–242727.5	87 (33)	0.08 (0.03)	0.12 (0.01)	Bolo 17
Oph-cold7	162715.84–243845.1	89 (35)	0.4 (0.13)	0.02 (0.01)	
Oph-cold8	162705.40–243629.5	106 (8)	0.15 (0.01)	0.09 (0.01)	Bolo 14
Oph-cold9	163151.96–245726.0	124 (12)	0.01 (0.01)	0.05 (0.01)	Bolo 33
Oph-cold10	162625.44–242301.3	135 (9)	0.1 (0.01)	0.53 (0.05)	Bolo 8
Oph-cold11	163200.96–245642.5	145 (14)	2.7 (0.2)	0.05 (0.01)	Bolo 35
Oph-cold12	162659.28–243458.6	177 (43)	2.0 (0.45)	0.21 (0.02)	Bolo 12
Oph-cold13	162717.64–242856.2	190 (11)	0.52 (0.03)	0.07 (0.01)	
Oph-cold14	162724.48–244103.0	191 (37)	0.33 (0.06)	0.12 (0.01)	Bolo 18
Oph-cold15	163152.32–245536.1	240 (13)	0.13 (0.01)	0.08 (0.01)	
Oph-cold16	162621.48–242305.4	254 (20)	4.4 (0.29)	0.22 (0.02)	Bolo 5
Oph-cold17	162727.00–244050.6	255 (34)	2.2 (0.25)	0.36 (0.04)	Bolo 18
Oph-cold18	162728.08–243932.5	264 (43)	2.7 (0.39)	0.11 (0.01)	
Oph-cold19	163135.76–240129.3	290 (8)	1.5 (0.03)	0.09 (0.01)	Bolo 30
Oph-cold20	162857.72–244054.8	304 (14)	0.03 (0.01)	0.04 (0.01)	
Oph-cold21	162728.44–242720.9	309 (14)	0.47 (0.02)	0.29 (0.03)	Bolo 20
Oph-cold22	162706.84–243814.8	310 (13)	0.6 (0.02)	0.05 (0.01)	Bolo 13
Oph-cold23	162640.56–242714.3	372 (17)	0.06 (0.01)	0.06 (0.01)	
Oph-cold24	162709.36–243718.6	383 (70)	4.8 (0.61)	0.07 (0.01)	Bolo 14
Oph-cold25	162702.16–243729.8	400 (45)	3.7 (0.39)	0.09 (0.01)	
Oph-cold26	162648.48–242838.6	428 (19)	0.12 (0.01)	0.03 (0.01)	
Oph-cold27	162737.08–244237.8	438 (16)	0.13 (0.01)	0.04 (0.01)	
Oph-cold28	163143.68–245524.6	496 (16)	0.28 (0.01)	0.04 (0.01)	
Oph-cold29	162730.24–242743.2	528 (16)	0.93 (0.02)	0.19 (0.02)	Bolo 20
Oph-cold30	162739.96–244314.9	551 (18)	0.74 (0.02)	0.04 (0.01)	
Oph-cold31	162721.60–244142.9	595 (17)	1.2 (0.03)	0.04 (0.01)	
Oph-cold32	162623.64–242439.4	609 (21)	0.3 (0.01)	0.03 (0.01)	

Note. — Columns are as in table 6.3, and uncertainties for  $T_{\text{bol}}$ ,  $L_{\text{bol}}$ , and  $M_{\text{env}}$  are given in parentheses.

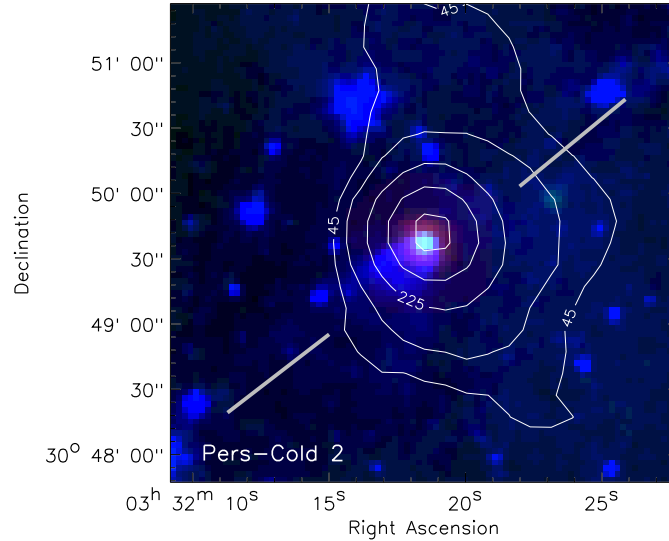


Figure 6.19 three-color *Spitzer* image (3.6, 24, 70  $\mu\text{m}$ ) of IRAS 03292+3039 (Pers-Cold 2), with 1.1 mm contours, showing the fan-shaped nebulosity that is visible at 3.6  $\mu\text{m}$ . The nebulosity is most likely scattered light from a narrow outflow cavity in this deeply embedded Class 0 source. Thick gray lines indicate the approximate orientation of the larger-scale outflow (Jørgensen et al., 2006).

sources viewed at an inclination angle of 30 deg (their figure 12a).

#### 6.6.4.2 Pers-Bolo 102

Pers-Bolo 102 is bright 1.1 mm source that was identified in Bolocam survey of Perseus (Enoch et al. 2006; chapter 2); it lies within the region of active star-formation near IC 348, which includes the famous outflow driving source HH 211 (McCaughrean et al., 1994). The *Spitzer* 24  $\mu\text{m}$  image resolves the luminous internal source into a double object (Pers-Cold 17 and Pers-Cold 30). Although they have very similar SEDs for  $\lambda \geq 8 \mu\text{m}$  (figure 6.20), variations at shorter wavelengths cause Pers-Cold 17 ( $T_{bol} = 56 \text{ K}$ ) to fall into Class 0, while Pers-Cold 30 ( $T_{bol} = 72 \text{ K}$ ) falls just outside the Class 0/Class I boundary at  $T_{bol} = 70 \text{ K}$ . These sources are good examples of why a more continuous evolutionary scheme is preferable to the standard classifications. Recently obtained CARMA interferometric observations at  $\lambda = 2.7 \text{ mm}$  resolve the millimeter core into two sources, coincident with the *Spitzer* source positions (Enoch

et al., in preparation). The 2.7 mm flux ratio of the northern (Pers-Cold 17) to southern (Pers-Cold 30) source is at least 2:1, further evidence that Pers-Cold 30 is slightly more evolved.

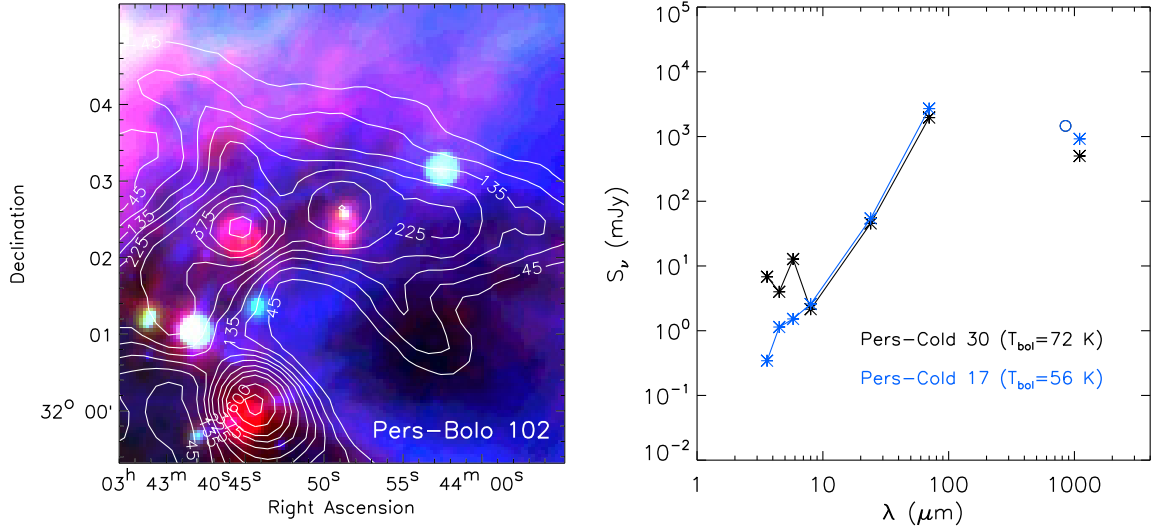


Figure 6.20 three-color *Spitzer* image (8, 24, 70  $\mu\text{m}$ ) of Pers-Bolo 102, a new candidate binary Class 0/I source, with 1.1 mm contours. SEDs of the two cold protostellar sources associated with the single 1.1 mm core are shown in the right panel. Although the SEDs look very similar at  $\lambda \geq 8 \mu\text{m}$ , the southern source is brighter at shorter wavelengths, and has a slightly higher bolometric temperature ( $T_{bol} = 72 \text{ K}$  versus  $T_{bol} = 56 \text{ K}$ ).

Although not as massive or cold as nearby HH 211 (Pers-Cold 1) and IC 348-mm (Pers-Cold 10), Pers-Bolo 102 is an interesting case study. It appears to be a separate-envelope binary system, with two late Class 0 or early Class I sources that are likely coeval. The separation of the sources is  $17''$ , or 4200 AU. Binary separations of this order are consistent with early fragmentation in a relatively dense cloud (“prompt initial fragmentation”, e.g., Pringle 1989; Looney et al. 2000), and the individual sources would most likely have distinct protostellar envelopes. If the binary formed via gravitational fragmentation, we would expect the separation to correspond to the local Jeans length:

$$\lambda_J = \left( \frac{\pi c_s^2}{G \mu_p m_H n} \right)^{1/2}, \quad (6.5)$$

where  $c_s$  is the local sound speed, and  $\mu_p = 2.33$  and  $n$  are the mean molecular weight and mean density per particle, respectively (Jeans, 1928). A Jeans length of 4200 AU would require a relatively high density of  $n \sim 6 \times 10^5 \text{ cm}^{-3}$  (assuming  $c_s = 0.2 \text{ km s}^{-1}$ ). The mean density of the Pers-Bolo 102 core, measured at the FWHM contour, is a factor of four lower than this required value, or  $1.4 \times 10^5 \text{ cm}^{-3}$ . The *peak* density measured within the beam size of  $30''$ , which corresponds to a linear size of approximately 4000 AU at the distance of Perseus, is considerably higher, however,  $16 \times 10^5 \text{ cm}^{-3}$ .

#### 6.6.4.3 Serp-Bolo 33 and Other Class II Objects

Given our sensitivity limit at 1.1 mm of approximately  $0.1 M_\odot$ , almost all sources detected at 1.1 mm will be dense cores or envelopes around relatively young protostars. In general, by the time a protostar has consumed or dispersed its massive envelope and enters the Class II (T Tauri) stage (e.g., Adams et al., 1987), the remnant disk of gas and dust has too little mass to be detected by our surveys. Typical measured masses of Class II disks are  $0.01 - 0.1 M_\odot$  (e.g., Beckwith & Sargent 1996), although values as large as  $1 M_\odot$  have been measured (Beckwith et al., 1990).

In a few a cases, however, we do detect 1.1 mm emission around sources with Class II-type SEDs. These objects have bolometric temperatures  $T_{bol} > 650 \text{ K}$ , which defines the Class I/Class II boundary, and a flux density at 1.1 mm that is lower than the flux densities from  $3.6$  to  $24 \mu\text{m}$ . With the exception of two “flat spectrum” objects ( $-0.3 < \alpha_{IR} < 0.3$ ; Greene et al. 1994), the near- to mid-infrared spectral index  $\alpha_{IR}$  is in the range  $-0.34$  to  $-1.04$ , confirming their Class II status. In some cases, the 1.1 mm emission is unresolved, consistent with a compact disk. Often, however, these Class II sources are in a region of confused millimeter emission; therefore the physical association of such objects with the 1.1 mm emission is not secure. Table 6.5 lists all of the sources with  $T_{bol} > 650 \text{ K}$  (Class II) in each cloud that are detected in our 1.1 mm surveys. Most of the sources lie in confused regions of 1.1 mm emission, indicated by a “\*” in the “Bolocam ID” column. The remaining objects have point-like 1.1 mm emission centered on the *Spitzer* position.

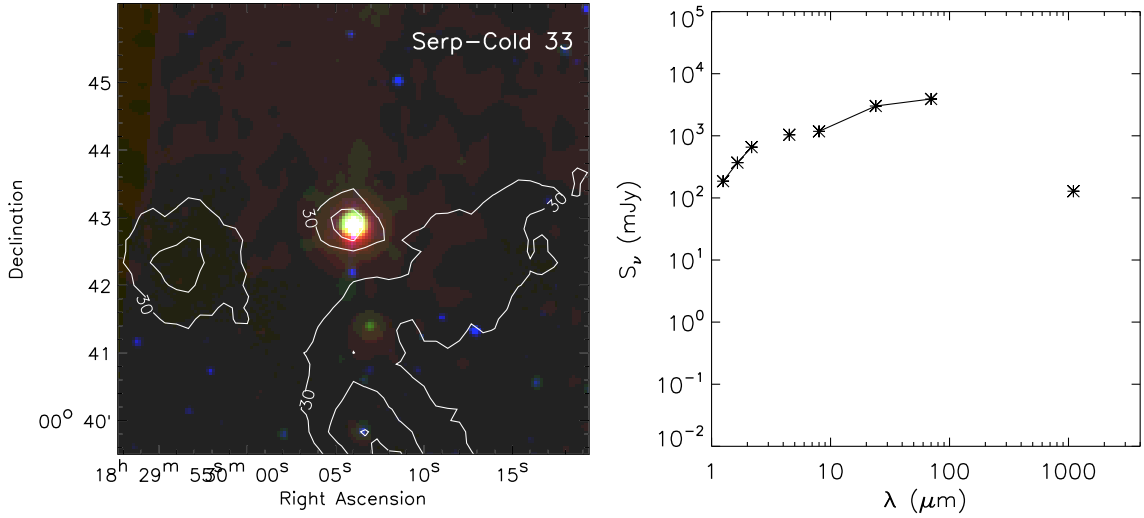


Figure 6.21 three-color *Spitzer* image (8, 24, 70  $\mu\text{m}$ ) of Serp-Cold 33, a bright Class II-type object with compact 1.1 mm emission. Contours of 1.1 mm emission at  $(3, 6, 9)\sigma$  are overlaid. The SED of Serp-Cold 33 is shown in the right panel; although this is clearly an evolved source, we are able to detect 1.1 mm emission, likely from a compact disk, due to the brightness of the source.

One noteworthy example is Serp-Bolo 33 in Serpens, a very bright *Spitzer* source with  $L_{bol} = 3.6 L_\odot$ ,  $T_{bol} = 871$  K, and compact 1.1 mm emission centered on the *Spitzer* position. It is also classified as Class II based on the spectral index  $\alpha_{IR} = -0.42$ . Vieira et al. (2003) included this source in a sample of Herbig Ae/Be candidates, believed to be the intermediate mass Class II counterparts of low-mass T Tauri objects, although the spectral type is F3. The 1.1 mm mass calculated assuming an optically thin disk is  $0.17 M_\odot$ , approximately 10% of the estimated stellar mass of  $M_* \sim 1.3 M_\odot$ , based on the measured effective temperature  $T_{eff} \sim 6300$  K (Vieira et al., 2003) and an empirical  $T_{eff} - M$  relation (Habets & Heintze, 1981).

Table 6.5. Class II sources detected at 1.1 mm in Perseus, Serpens, and Ophiuchus

c2d name/position (SSTc2dJ...)	$T_{\text{bol}}$ (K)	$L_{\text{bol}}$ ( $L_{\odot}$ )	$M_{1\text{mm}}^1$ ( $M_{\odot}$ )	Bolocam ID <sup>2</sup>	other names
Perseus					
032747.66+301204.5	662 (15)	2.80 (0.05)	0.82 (0.06)	Pers-Bolo 24	RNO 15 <sup>3</sup> (1)
034400.00+320154.1	700 (17)	1.60 (0.03)	0.40 (0.04)	Pers-Bolo 106*	
032900.00+312146.6	856 (26)	0.33 (0.01)	0.90 (0.09)	Pers-Bolo 40*	LkH $\alpha$ 353 (2)
034109.13+314437.8	873 (30)	1.70 (0.06)	0.16 (0.02)	Pers-Bolo 90	IRAS 03380+3135
032856.64+311835.5	993 (22)	0.42 (0.01)	0.10 (0.02)	Pers-Bolo 39*	ASR 120 (3)
034548.27+322412.0	1096 (23)	5.00 (0.09)	0.10 (0.02)	Pers-Bolo 120	LkH $\alpha$ 330 (2)
032917.66+312245.0	1297 (22)	1.50 (0.02)	0.19 (0.02)	Pers-Bolo 54*	LkH $\alpha$ 270 (2)
Serpens					
182900.00+003003.1	806 (5)	0.19 (0.01)	0.35 (0.03)	Serp-Bolo 13*	
183006.12+004233.8	871 (2)	3.60 (0.01)	0.17 (0.01)	Serp-Bolo 33	
182900.96+002931.6	892 (2)	1.20 (0.01)	0.23 (0.02)	Serp-Bolo 13*	
182901.32+002933.0	892 (6)	0.36 (0.01)	0.23 (0.02)	Serp-Bolo 13*	
182901.68+002954.6	1158 (3)	1.80 (0.01)	0.23 (0.02)	Serp-Bolo 13*	CoKu Ser G3 (4)
182901.68+002946.5	1212 (5)	0.70 (0.01)	0.25 (0.02)	Serp-Bolo 13*	CoKu Ser G4 (4)
Ophiuchus					
163151.96-245615.7	690 (18)	1.20 (0.03)	0.05 (0.01)		*
162610.32-242054.6	773 (20)	0.36 (0.01)	0.39 (0.03)	Oph-Bolo 4*	
162623.28-242100.8	1082 (28)	2.00 (0.04)	0.15 (0.01)	Oph-Bolo 7*	

<sup>1</sup>The 1.1 mm mass ( $M_{1\text{mm}}$ ) is calculated for an optically thin disk and a dust temperature of  $T_D = 15$  K. Our assumption for the dust opacity may be incorrect for typical Class II disks, however, where grain growth is a possibility (e.g., Natta et al., 2007).

<sup>2</sup>Bolocam IDs with "\*"s indicate that the source is in a confused region at 1.1 mm, and the association of the Spitzer object with the given 1.1 mm emission is not secure.

<sup>3</sup>Typically classified as a Class I source, RNO 15 has a bolometric temperature just above the Class I cutoff in our sample. The spectral index of RNO 15 is  $\alpha_{IR} = -0.09$ , placing it in the "flat spectrum" category, or close to the Class I boundary.

Note. — References: (2) Herbig & Kameswara 1972; (3) Aspin et al. 1994; (4) Cohen & Kuhl 1979.

## 6.7 Comparison of Classification Methods

Identifying the evolutionary states of sources in our sample is a necessary first step for studying the early evolution of protostars. The evolutionary status is typically estimated by classifying sources into groups based on SED characteristics. A number of different classification methods are employed in the literature; most often used are the near- to mid-infrared spectral index  $\alpha_{IR}$  ( $\alpha_{IR} = d \log(\lambda F_\lambda) / d \log(\lambda)$ ; Lada 1987), the bolometric temperature  $T_{bol}$  (Myers & Ladd 1993, see §6.6.1), and the ratio of submillimeter to bolometric luminosity  $L_{submm} / L_{bol}$  (André et al., 1993). Generally,  $L_{submm}$  is taken to be the integrated luminosity at wavelengths  $\lambda > 350 \mu\text{m}$ . We typically have only one flux measurement for  $\lambda > 160 \mu\text{m}$ , and a number of sources lack information even at  $160 \mu\text{m}$ , so an accurate determination of  $L_{submm}$  is not possible with these data. We will focus, therefore, on  $T_{bol}$  and the spectral index  $\alpha_{IR}$ .

In figure 6.22 we compare classifications based on  $\alpha_{IR}$  and  $T_{bol}$  for the cold protostar samples in Perseus, Serpens, and Ophiuchus. Thick colored symbols indicate sources associated with 1.1 mm emission, and thin black points represent sources with upper limits at 1.1 mm. The spectral index  $\alpha_{IR}$  is determined from a least squares fit to the SED from the shortest available wavelength (usually 2MASS 1.25  $\mu\text{m}$  or IRAC 3.6  $\mu\text{m}$ ) to  $\lambda = 24 \mu\text{m}$  (Evans et al., 2007). The calculation of  $T_{bol}$  is described in §6.11. We adopt class divisions for  $T_{bol}$  from Chen et al. (1995):  $T_{bol} < 70$  K (Class 0),  $70 < T_{bol} < 650$  K (Class I), and  $T_{bol} > 650$  K (Class II), and divisions for  $\alpha_{IR}$  from (André & Montmerle, 1994):  $\alpha_{IR} < 0$  (Class I) and  $\alpha_{IR} > 0$  (Class II). No well-defined  $\alpha_{IR}$  criteria exists for Class 0 sources; such deeply embedded objects were general not visible in the mid-IR prior to *Spitzer*, making the calculation of  $\alpha_{IR}$  impossible until recently.

The two classification methods agree fairly well for Class II and “warmer” Class I sources. Very cold ( $T_{bol} \lesssim 100$  K) sources, however, have a wide range of  $\alpha_{IR}$  values, a few even falling into Class II based on the spectral index. At least part of the reason for this large scatter in  $\alpha_{IR}$  values becomes apparent when examining the SEDs of some deeply embedded sources, which can have widely varying shapes at short wavelengths.

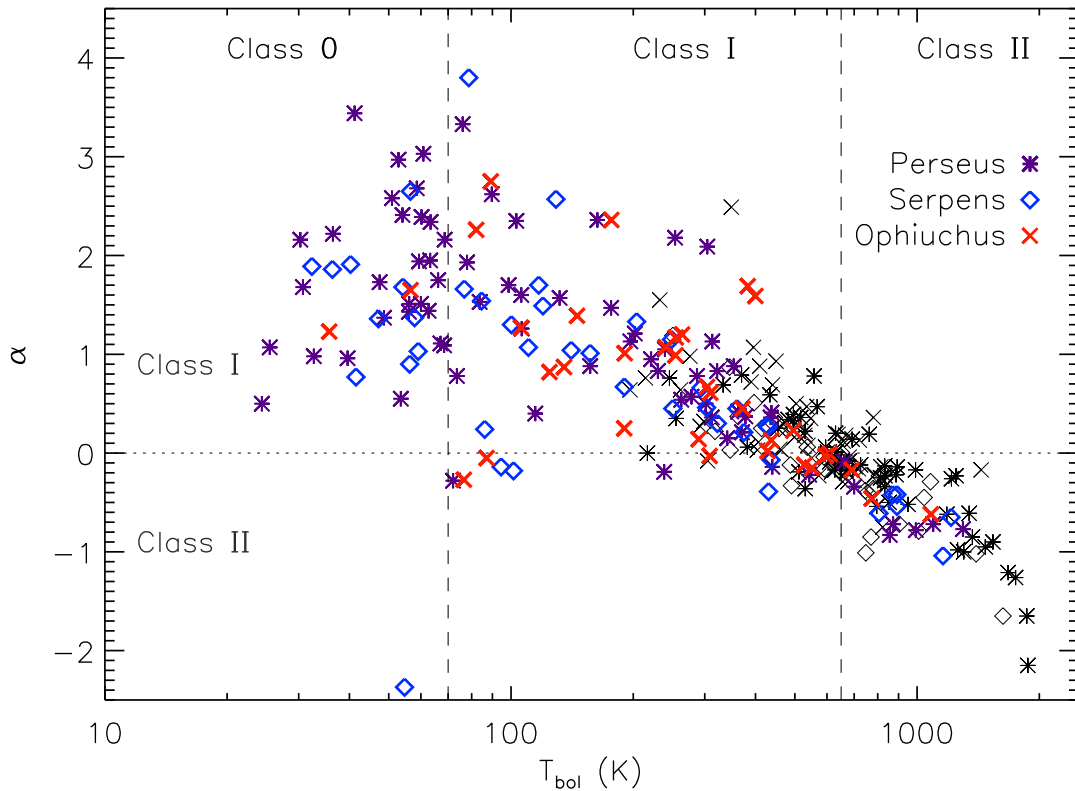


Figure 6.22 Bolometric temperature versus near- to mid-IR spectral index ( $\alpha_{IR}$ ), for the cold protostar samples in Perseus, Serpens, and Ophiuchus. Thick colored symbols indicate sources associated with 1.1 mm emission, and thin black points represent those with upper limits at 1.1 mm. Standard class divisions for both  $T_{bol}$  and  $\alpha_{IR}$  are shown. The two methods agree fairly well for Class II and “warmer” Class I sources, but very cold ( $T_{bol} \lesssim 100$  K) sources have a large range of  $\alpha_{IR}$  values.

Many protostellar SEDs are not monotonically increasing from 3.6 to 24  $\mu\text{m}$ , many falling from 5.8 to 8  $\mu\text{m}$ , and rising again at longer wavelengths, e.g., Pers-Cold 2, Pers-Cold 19, Pers-Cold 24 (figure 6.2), Oph-Cold 1 (figure 6.4). The most likely cause of these features are geometric effects such as scattered light from an outflow cavity, or dust and ice absorption features originating in the protostellar envelope. In any case, non-monotonic behavior at short wavelengths will clearly confuse the calculated slope  $\alpha_{IR}$ . Even using  $\alpha_{IR}$  calculated from a straight line fit to the two end-point wavelengths, however, still results in a large range of  $\alpha_{IR}$  values at low  $T_{bol}$ .

For further information about whether  $\alpha_{IR}$  or  $T_{bol}$  is a more accurate characteriza-

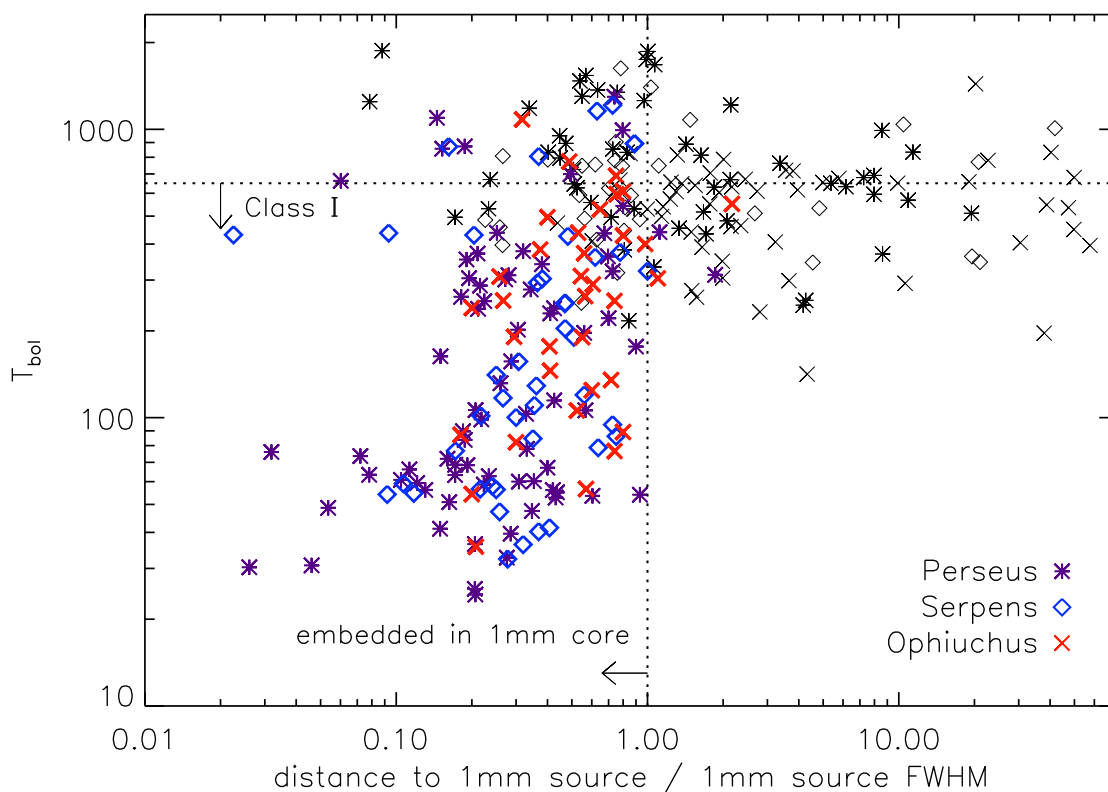


Figure 6.23 Distribution of bolometric temperature as a function of distance to the nearest 1.1 mm core for cold protostar candidates in all three clouds. Distances are in units of the 1.1 mm core FWHM size, and symbols are as in figure 6.22. Sources within 1.0 FWHM of a 1.1 mm core position are considered embedded within that core. There is a clear correlation between smaller distances, or more embedded sources, and lower  $T_{bol}$  values.

tion of the true evolutionary state, we look at the correlation between both measures and millimeter cores. Figure 6.23 shows the distribution of  $T_{bol}$  with respect to the distance to the nearest 1.1 mm core, in units of the core FWHM size. In all three clouds, essentially all sources with  $T_{bol} \lesssim 200$  K lie within one core FWHM of a 1.1 mm peak, and are likely associated with a millimeter core. Thus the majority of “cold” objects, as defined by low  $T_{bol}$ , appear to be embedded in dense envelopes, and likely at an early evolutionary stage. Furthermore, there is a clear correlation between smaller distance and lower  $T_{bol}$ , suggesting that sources with lower  $T_{bol}$  are more embedded than those with higher  $T_{bol}$ . If we affiliate the degree of embeddedness

with youth, then  $T_{bol}$  seems to correlate well with evolutionary state.

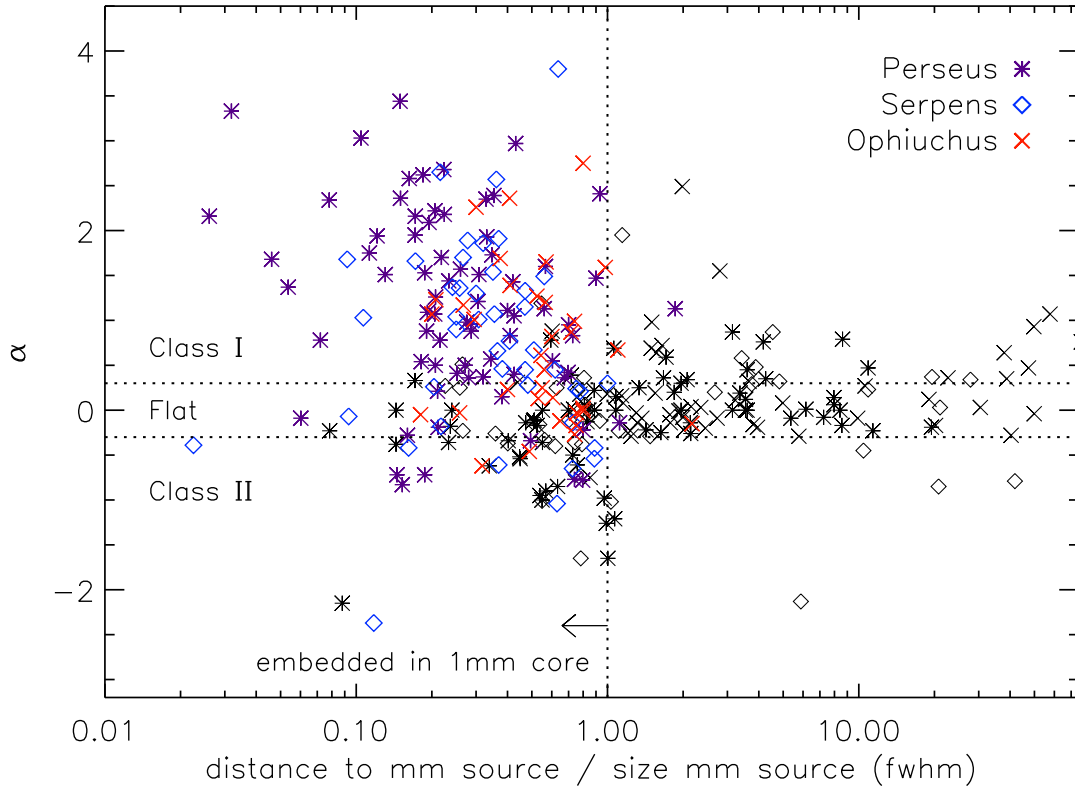


Figure 6.24 Distribution of the near- to mid-infrared spectral index  $\alpha_{IR}$  as a function of distance to the nearest 1.1 mm core, for cold protostar candidates in all three clouds. Distances are in units of the nearest 1.1 mm core FWHM size, and symbols are as in figure 6.22. While there is some correlation between higher  $\alpha_{IR}$  values and smaller distances, it is not as compelling as that observed for  $T_{bol}$  in figure 6.23.

A similar plot for  $\alpha_{IR}$  with respect to the distance to the nearest 1.1 mm core is shown in figure 6.24. While there is some correlation between higher  $\alpha_{IR}$  values and smaller distances, the relationship is not nearly as clear as it is for  $T_{bol}$  (figure 6.23). In particular, there are a number of sources with large  $\alpha_{IR}$  values for which the distance to the nearest core is much larger than one FWHM. Likewise, there are several deeply embedded sources with low  $\alpha_{IR}$  values.

Based on figures 6.22–6.24, and on an examination of sources with  $T_{bol} < 70$  K objects, a number of which are known Class 0 sources, we conclude that  $T_{bol}$  is more reliable than  $\alpha_{IR}$  for classifying the most embedded protostars. Hereafter,  $T_{bol}$  will

be used to characterize protostellar sources, and we use the divisions from Chen et al. (1995) noted above to place sources into Class 0, Class I, or Class II. Recall that we also require Class I sources to be detected at 1.1 mm in addition to the  $T_{bol}$  criteria. This is clearly a reasonable requirement, as our physical definition of Class I sources ( $M_{env} > M_*$ ) dictates that they should be detected at millimeter wavelengths. The point-source sensitivity of the Bolocam 1.1 mm surveys limit our completeness to Class I sources with  $M_{env} \gtrsim 0.09 M_\odot$  in Perseus,  $M_{env} \gtrsim 0.07 M_\odot$  in Serpens, and  $M_{env} \gtrsim 0.04 M_\odot$  in Ophiuchus.

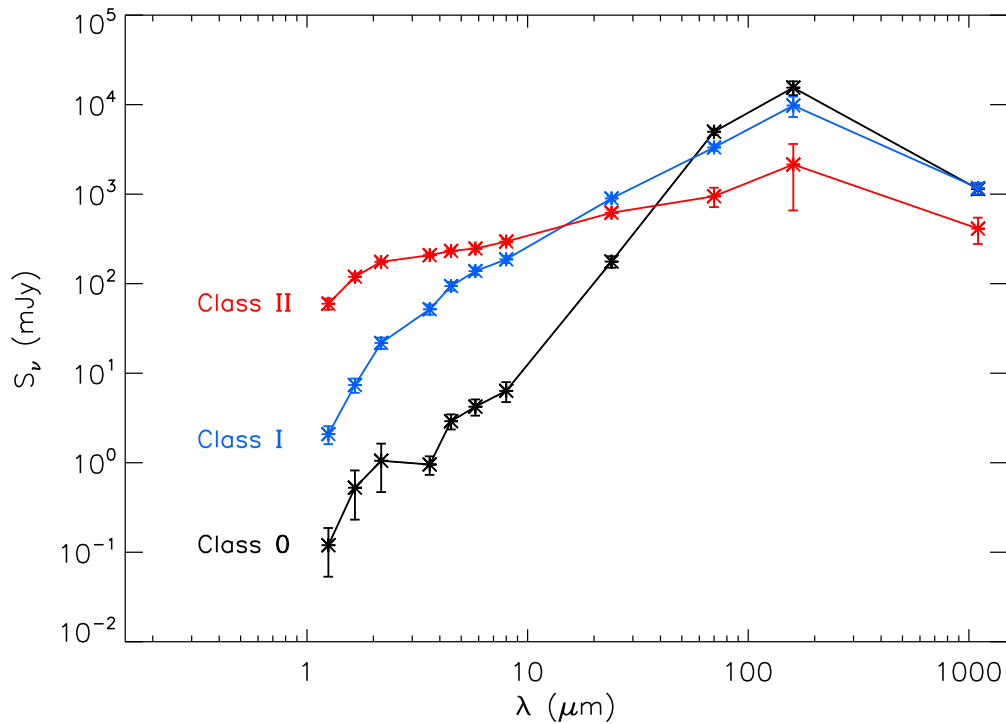


Figure 6.25 Average spectra for Class 0, Class I, and Class II sources, calculated using the SEDs of sources from Perseus and Serpens. Individual SEDs are weighted by the bolometric luminosity. Classifications are based on the source  $T_{bol}$ :  $T_{bol} < 70$  K (Class 0),  $70 < T_{bol} < 650$  K (Class I), and  $T_{bol} > 650$  K (Class II), with the additional requirement that Class I sources be detected at 1.1 mm. Error bars are the  $1\sigma$  error in mean, and not the sample dispersion, which is much larger. The Class II spectrum may not be representative of all Class II objects, as we are very incomplete to sources without protostellar envelopes.

The average spectra of all Class 0, Class I, and Class II sources, as defined by  $T_{bol}$

and the above criteria, are shown in figure 6.25. Average spectra for each class are calculated using sources from Perseus and Serpens, and individual SEDs are weighted by the bolometric luminosity. Flux density upper limits are ignored. Error bars in figure 6.25 represent the  $1\sigma$  error in the mean ( $\sigma_\lambda/\sqrt{N_\lambda}$ ), but the dispersion in the sample ( $\sigma_\lambda$ ) is much larger. Source SED shapes do not fall into discrete bins, but form a continuous distribution between the averages shown. Points with large error bars indicate either that a small number of flux points went into the average due to a number of sources with upper limits, or that there are significant differences between sources at that wavelength. We do not include Ophiuchus sources in the average because the lack of  $160\ \mu\text{m}$  fluxes for most of the Ophiuchus sample tends to bias  $T_{bol}$  to slightly higher values.

Note that the progression from Class 0 to Class I to Class II is as expected if this represents a sequence of physical evolution. In particular, the average Class 0 spectrum has the lowest flux densities from  $1.25$  to  $24\ \mu\text{m}$ , as expected for deeply embedded sources with massive, extinguishing envelopes, and the highest fluxes at  $70 - 1100\ \mu\text{m}$ , where reprocessed protostellar flux is emitted by the cold envelope. By contrast, the average Class II spectrum is relatively flat, with a much larger percentage of the protostar flux emerging at shorter wavelengths, as expected for older sources that do not have much circumstellar material. Between these two extremes is the average Class I spectrum, although the separation between the Class 0 and Class I spectra, as well as the variety of SED shapes, suggests that a more continuous means of estimating evolutionary status may be more appropriate. Large error bars for  $\lambda = 1 - 3\ \mu\text{m}$  for the average Class 0 spectrum are indicative of the wide range of behavior of Class 0 objects in the near-infrared, and the presence of non-monotonic behavior is apparent at  $\lambda = 3.6\ \mu\text{m}$ . It should be mentioned here that the average Class II spectrum is not necessarily representative of all Class II objects, as we are very incomplete to sources without protostellar envelopes. We only find 20 Class II objects in Serpens, while Harvey et al. (2007a) find 132 Class II sources.

When we include Ophiuchus in the average, the average spectra are shifted, have larger dispersion, and the similarity of SEDs within a bin is reduced. This behavior

seems to indicate that  $T_{bol}$  may be overestimated for many sources in Ophiuchus, likely due to the lack of information at  $160\ \mu\text{m}$ . To mitigate the biases caused by missing  $160\ \mu\text{m}$  points, we use the average spectra from figure 6.25 as templates, and assign each Ophiuchus source to Class 0, Class I, or Class II based on a least squares fit. The results of this analysis are shown for Class 0 and Class I in figure 6.26. The best-fitting average spectrum is determined by minimizing the reduced  $\chi^2$ , with the free parameter of each fit being the scaling factor between the template and source spectra.

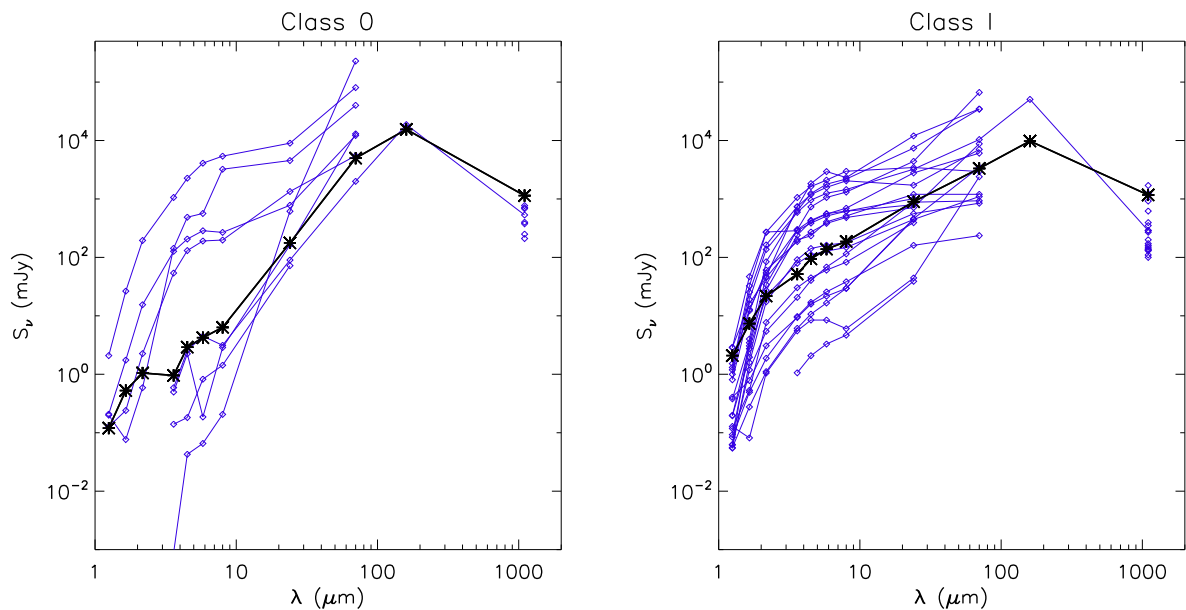


Figure 6.26 Results of using the average spectra from figure 6.25 as templates (thick black lines), to assign Ophiuchus sources (thin blue lines) to Class 0 and Class I. For each source in Ophiuchus, the best-fitting average spectrum (Class 0, Class I or Class III) is determined by a least squares fit, with the scaling factor between the template and source spectra left as a free parameter. An additional 5 sources fall into Class 0 by this method, but the spectra of 4 of those have shapes that may be indicative of high extinction.

In contrast to a simple  $T_{bol}$  cut, which results in only three sources designated as Class 0 and 29 as Class I, fitting to the average spectra results in 8 Class 0 and 20 Class I designations in Ophiuchus. Examining the spectra, however, half of those in the Class 0 group look quite different from the template spectrum. Neither do they look like the average Class I spectrum; there is a population of sources in Ophiuchus

with spectra that are steeply rising from 1.25 to 4.5  $\mu\text{m}$ , then relatively flat from 4.5 to 24  $\mu\text{m}$ . A few similar sources are seen in Serpens and Perseus, but not in the same numbers as observed for Ophiuchus. It is possible that the steep rise in the near-infrared for these sources is simply the result of a high degree of extinction. Although the average cloud extinction in Ophiuchus, as measured by the reddening of background stars, is similar to the other clouds,  $\langle A_V \rangle \sim 4 - 7$  mag, protostellar 1.1 mm cores do tend to be found at much higher extinctions in Ophiuchus (§6.4.5).

### 6.7.1 Alternative Classifications

One advantage of the large, complete sample provided by the combined Bolocam and *Spitzer* data is that we can explore alternative classification schemes; ideally, we could define a more continuous evolutionary sequence than the standard classes that were appropriate for the smaller samples previously available. Having well-sampled SEDs, we can use the overall SED shapes, rather than a single parameter, to characterize sources.

With this goal in mind, we first divide the protostellar sources in each cloud into smaller  $T_{bol}$  bins than those of the standard Class 0/I/II divisions. Average spectra for Perseus and Serpens, calculated in bins of  $T_{bol} < 50$  K (“early Class 0”),  $50 < T_{bol} < 100$  K (“late Class 0”),  $100 < T_{bol} < 300$  K (“early Class I”),  $300 < T_{bol} < 650$  K (“late Class I”), and  $T_{bol} > 650$  K (Class II), are shown in figure 6.27. Error bars represent the  $1\sigma$  error in the mean, and average spectra are calculated as described in the previous section. The largest errors are seen for the shortest wavelengths in the lowest  $T_{bol}$  bins, where NIR fluxes vary significantly from source to source, likely dependent on outflow opening angle and viewing geometry. Binning of  $T_{bol}$  is based on general agreement of SEDs in a given bin, as determined by eye, and should not be interpreted as suggestive of strict boundaries.

While there are significant similarities between the SEDs within each bin, individual source SEDs fill the continuum between the average spectra, as for figure 6.25. If we were to plot error bars representative of the dispersion in each bin rather than the

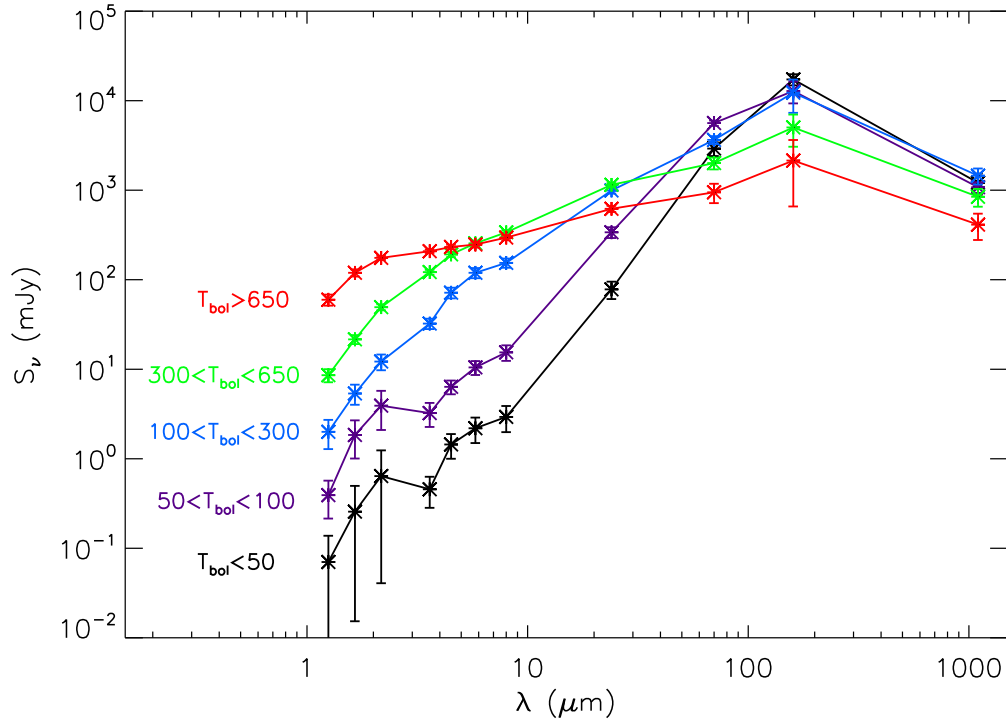


Figure 6.27 Average spectra in designated  $T_{bol}$  bins, using sources from Perseus and Serpens, where the average is calculated as described in figure 6.25 and the text. Error bars show the error in the mean. The progression in SED shape for increasing  $T_{bol}$  is as expected if this represents physical evolutionary sequence. The large difference at IRAC wavelengths between the “late Class 0” ( $50 < T_{bol} < 100$  K) and “early Class I” spectra ( $100 < T_{bol} < 300$  K) suggests that this transition occurs fairly rapidly.

error in the mean, each average spectra would be within  $1\sigma$  of the neighboring  $T_{bol}$  bins. The average spectra appear to evolve with  $T_{bol}$  as one would expect if  $T_{bol}$  is indeed an evolutionary indicator: increasing flux at short wavelengths, and decreasing flux at long wavelengths, with increasing  $T_{bol}$ . As discussed above, this kind of spectral evolution might be anticipated if the extinguishing envelope is continuously accreted or dispersed as the protostar becomes more visible. At all wavelengths except 24 and 70  $\mu\text{m}$ , the flux rises or falls monotonically with increasing  $T_{bol}$ . For these intermediate wavelengths, however, the observed flux rises initially as hotter dust close to the protostar is revealed, then falls as the mass of circumstellar material drops. Despite the relatively narrow bins, there is still a rather large change between “late Class 0” ( $50 < T_{bol} < 100$  K) and “early Class I” ( $100 < T_{bol} < 300$  K), particularly

at  $\lambda = 3.6 - 24 \mu\text{m}$ , suggesting that this transition occurs fairly rapidly.

We use the average spectra from figure 6.27 as templates to assign cold protostar candidates to one of the five categories defined above (“early Class 0”, “late Class 0”, etc.). The results are shown in figure 6.28. Source SEDs are color coded by cloud, and template spectra indicated by thick black lines. The number of sources in each category for each cloud is given in the lower right corner. Determination of the best-fitting template spectrum is accomplished as described in §6.7, above. As some SEDs have anomalous points at one wavelength, we redo the fit after removing the largest outlier if  $\tilde{\chi}_{best}^2/\tilde{\chi}_{worst}^2 < 2$ , where  $\tilde{\chi}_{best}^2$  is the reduced chi squared for the best-fitting template, and  $\tilde{\chi}_{worst}^2$  is that for the worst-fitting template. Source SEDs are not always well matched by any of the average spectra; the minimized  $\tilde{\chi}^2$  ranges from 1.2 to 50, with a median value of 13. Although the templates were originally defined based on  $T_{bol}$ , the sources assigned to each category do not necessarily have bolometric temperatures that falls within the original  $T_{bol}$  bins.

There are a number of caveats to this analysis. Even for infinitely well-sampled SEDs, spectrum shape is not necessarily directly correlated with age or degree of embeddedness. For example, viewing geometry can have a strong effect on SED shape. In the three dimensional radiative transfer models of Whitney et al. (2003), Class I and Class II sources can have quite similar SEDs when viewed at the right inclination angle (e.g., when the observer’s line-of-sight intersects the outflow opening angle of Class I sources). Even Class 0 sources can appear much warmer if we happen to be looking directly into the outflow cavity, although the probability of that occurring is small. In any case, the total mass of the envelope relative to the bolometric luminosity should be higher for more embedded sources, regardless of viewing angle.

## 6.8 Protostellar Evolution

We examine the evolution of cold protostars in more detail using the  $L_{bol} - T_{bol}$  diagram, which is the protostellar equivalent of the H-R diagram (Myers et al., 1998), where  $T_{bol}$  is used as a measure of temperature rather than  $T_{eff}$ , which is not well-

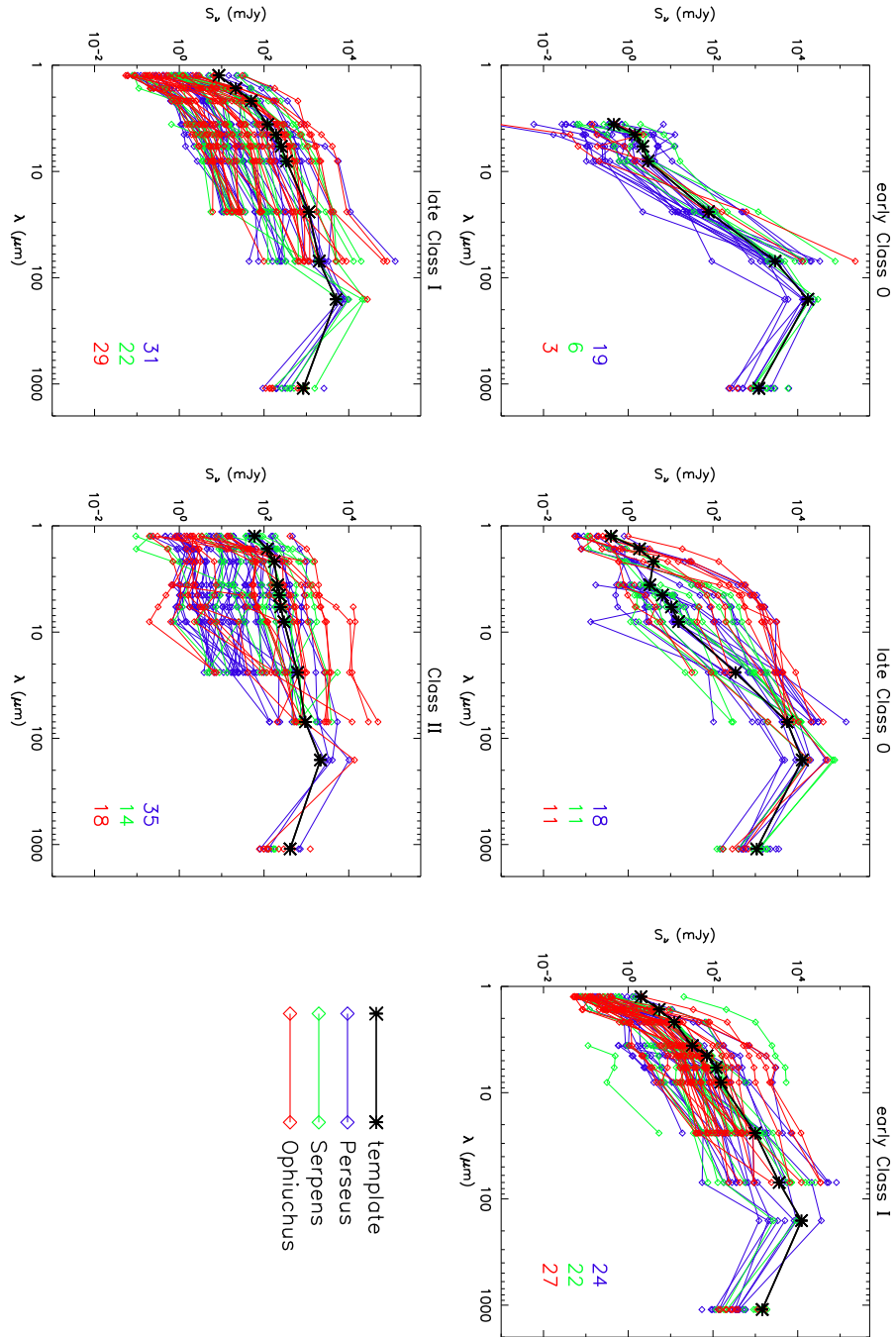


Figure 6.28 Results of fitting the SEDs of cold protostar candidates in Perseus, Serpens, and Ophiuchus to template spectra. Average spectra in  $T_{bol}$  bins of  $T_{bol} < 50$  K,  $50 < T_{bol} < 100$  K,  $100 < T_{bol} < 300$  K,  $300 < T_{bol} < 650$  K, and  $T_{bol} > 650$  K, calculated from all sources in Perseus and Serpens, are used as templates (thick black lines). Spectra are color coded by cloud, and the number of sources in each category for each cloud are given in the lower right corners.

characterized for embedded sources. As discussed in Myers et al. (1998), newly-formed protostars should begin at low  $L_{bol}$  and  $T_{bol}$ , increasing in both  $L_{bol}$  and  $T_{bol}$  as accretion proceeds. If accretion abates or is otherwise halted, then  $L_{bol}$  will decrease for steadily increasing  $T_{bol}$ . Eventually, sources will move onto the main sequence, at  $T_{bol} \gtrsim 3000$  K.

Figure 6.29 plots  $L_{bol}$  versus  $T_{bol}$  for the cold protostar samples in Perseus, Serpens, and Ophiuchus. Sources are color-coded according to whether they have reliable measured  $160 \mu\text{m}$  fluxes (red squares), are saturated at  $160 \mu\text{m}$  (blue circles), or are not detected at  $160 \mu\text{m}$  (purple triangles). Given the discussion in §6.11 regarding the effect of missing  $160 \mu\text{m}$  fluxes on the calculation of  $T_{bol}$ , blue circles would be expected to move up and to the right in this diagram for “cold” sources ( $T_{bol} \lesssim 100$  K), and down and to the left for “warm” sources ( $T_{bol} \gtrsim 100$  K), if  $160 \mu\text{m}$  fluxes were available. The “saturated” category also include all sources for which we are unable to measure a  $160 \mu\text{m}$  flux due to bad pixels or nearby saturated sources, but for which the inclusion of a  $160 \mu\text{m}$  point would likely result in a decrease of the estimated  $T_{bol}$ .

Filled symbols are used for sources that are associated with a 1.1 mm core, while “+” symbols indicate sources with upper limits at 1.1 mm. While upper limits may be expected for sources with large  $T_{bol}$ , colder sources with no 1.1 mm detection must either be misclassified, e.g., they are actually faint red galaxies or more evolved objects, or very low mass sources whose 1.1 mm flux is below our detection limit. Our physical definition of Class I ( $M_* \gtrsim M_{env}$ ) requires that any such objects have masses less than a few tenths of a solar mass, or have very little remaining envelope ( $M_* \gg M_{env}$ ), to be undetected at 1.1 mm. Note that although we plot sources with 1.1 mm upper limits here, our final Class I sample includes only sources with 1.1 mm detections.

Protostellar evolutionary tracks, which predict source properties as a function of age and mass, can be easily compared to our data using the  $L_{bol} - T_{bol}$  diagram. Model evolutionary tracks from Myers et al. (1998) (solid line) and Young & Evans (2005) (dotted lines) are shown in figure 6.29. From top to bottom, the Young & Evans (2005) models are for sources of mass 3.0, 1.0, and 0.3  $M_{\odot}$ , assuming a constant

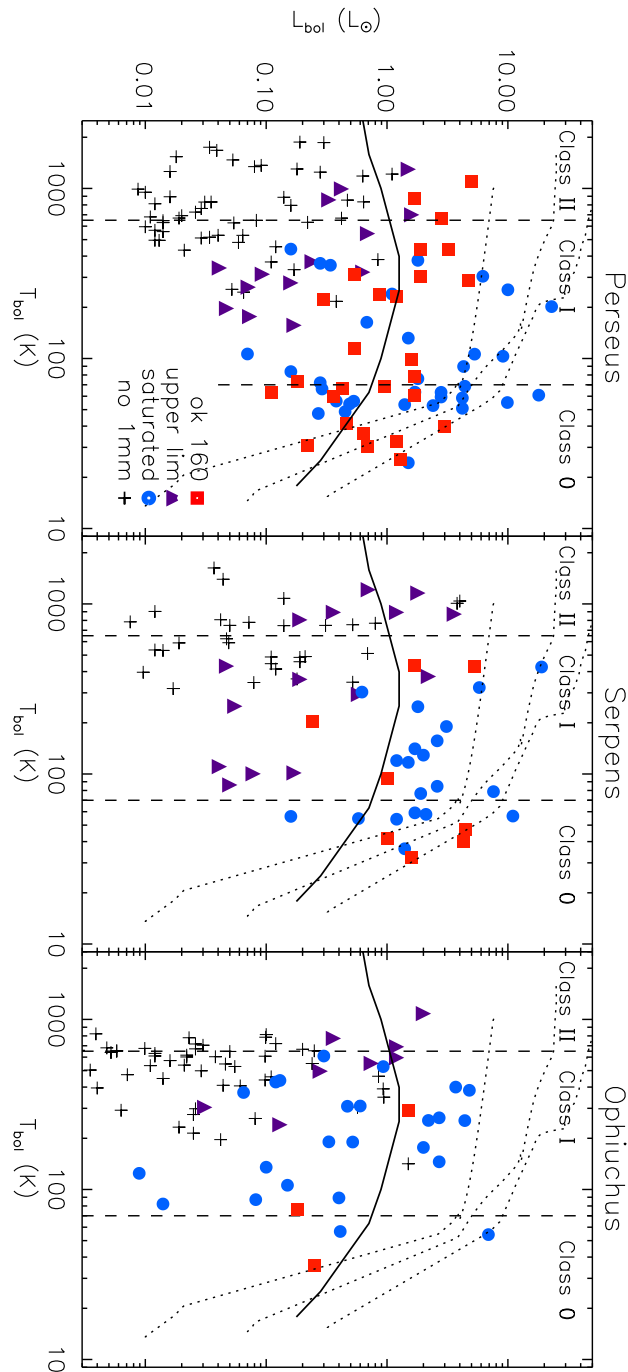


Figure 6.29 Bolometric luminosity plotted versus bolometric temperature ( $L_{bol} - T_{bol}$  diagram) for the cold protostar samples in Perseus, Serpens, and Ophiuchus. Filled symbols indicate that a given protostar is associated with 1.1 mm emission, while “+” symbols indicate upper limits at 1.1 mm. The significance of colored symbols is explained in the text. Model evolutionary tracks from Young & Evans (2005) for sources with 3.0, 1.0, 0.3  $M_{\odot}$  (dotted lines, from top to bottom) and from Myers et al. (1998) for a source with final mass 0.3  $M_{\odot}$  (solid line) are shown for comparison. The number that lie below the evolutionary models indicate that neither a constant or steadily decreasing accretion rate match the observations. In fact, the large population of the low-luminosity Class I objects argues strongly for episodic accretion.

accretion rate or “Shu accretion”:  $dM/dt = c_s^3/G$ , where  $c_s$  is the effective sound speed. These authors adopt the standard inside-out collapse model of Shu (1977), and assume that no mass is lost in the formation process. Finite masses are achieved by truncating the outer radius of the envelope. A one dimensional radiative transfer model (DUSTY) is used to calculate observational signatures ( $L_{bol}$ ,  $T_{bol}$ , etc.) from the accretion model.

Unlike Young & Evans (2005), Myers et al. (1998) do not assume that the entire mass of the original core ends up in the final star, but rather that a significant fraction of the core mass is lost in the star formation process. The Myers et al. (1998) model shown is for a source with initial core mass of  $1.8 M_\odot$  and final stellar mass of  $0.3 M_\odot$ . The luminosity is lower than the Young & Evans (2005) tracks at later times because Myers et al. (1998) assume an accretion rate that is initially  $dM/dt = c_s^3/G$ , but falls off exponentially with time, designed to match the observed luminosity of pre-main sequence stars. Both evolutionary models assume an accreting central protostar, a circumstellar accretion disk, and an extended envelope, and a contribution to the luminosity from gravitational contraction of the protostar. Young & Evans (2005) also include nuclear (D) burning.

If we ignore for the moment the population of Class I sources in each cloud with  $L_{bol}$  values well below both models, the Myers et al. (1998) model, for which a large fraction of the core mass is ejected or dispersed, is more consistent with the observed protostellar sources. We conclude, therefore, that if the accretion rate is constant, star formation models in which 100% of the original core material is accreted onto the final star are unable to match the observed data. On the other hand, the ratio of the final stellar mass to initial core mass for the Myers et al. (1998) model shown ( $f_{\text{eff}} = 0.3/1.8 = 0.17$ ) is smaller than the lower limit  $f_{\text{eff}} \gtrsim 0.25$  derived in §6.5 comparing the CMD and IMF shapes, and also smaller than the value found by Alves et al. (2007) ( $f_{\text{eff}} = 0.3 \pm 0.1$ ).

This may be a moot point, however, as the fact that many points lie below all four model tracks indicates that neither a constant nor a steadily decreasing accretion rate are entirely consistent with the observed protostellar populations in these clouds. In

particular, the large population of Class I sources with low  $L_{bol}$  in each cloud, together with the lack of low- $L_{bol}$  Class 0 sources, is difficult to understand in relation to most existing protostellar evolutionary models. A general feature of such models is that the bolometric luminosity peaks in the Class I stage, a result that is true for constant accretion rates (Young & Evans, 2005), decreasing rates (Myers et al., 1998), and gravo-turbulent models (Froebrich et al., 2006). Contrary to this prediction, we find that the mean luminosity of all Class I sources, is  $1.92 L_{\odot}$ , compared to  $2.4 L_{\odot}$  for all Class 0 sources.

Given the above discussion and the large observed spread in  $L_{bol}$  of 2–3 orders of magnitude for Class I sources, we suggest that mass accretion during the Class I stage is episodic. Class I sources with low  $L_{bol}$  can be explained by periods of relative quiescence when the bolometric luminosity, which is driven primarily by accretion luminosity at this point, drops by at least a factor of 10. Conversely, Class I sources with high  $L_{bol}$  values, e.g., those that form the upper envelope of the distribution and appear to be consistent with the Young & Evans (2005) models, would correspond to periods where the accretion rate is close to the “Shu accretion” value. Episodic accretion is not an unreasonable assumption; evidence for variable mass accretion and ejection is plentiful, including that based on modeling FU Orionis eruptions (e.g., Hartmann & Kenyon, 1985), and bow shocks in Herbig-Haro outflows (e.g., Reipurth & Bally, 2001). Given the number of Class I sources with  $L_{bol} < 0.1L_{\odot}$  (11/39 in Perseus, 7/26 in Serpens, and 10/29 in Ophiuchus), we estimate that any given source spends approximately 25% of its Class I lifetime in a quiescent accretion state.

Although the observed distribution of  $L_{bol}$  for Class I sources is a strong argument for episodic accretion, that is not the only possibility. One alternative is that the low- $L_{bol}$  Class I sources are simply very low mass objects, and we are somehow missing their low-mass Class 0 counterparts. We believe that this is unlikely, however. Based on our sensitivity limits at 70, 160  $\mu\text{m}$  and 1.1 mm, we should be able to detect Class 0 sources with  $L_{bol}$  at least as low as  $0.03L_{\odot}$ . In figure 6.30 we show the average spectrum of low-luminosity Class I sources ( $L_{bol} < 0.2L_{\odot}$ ,  $70 < T_{bol} < 650$  K) in

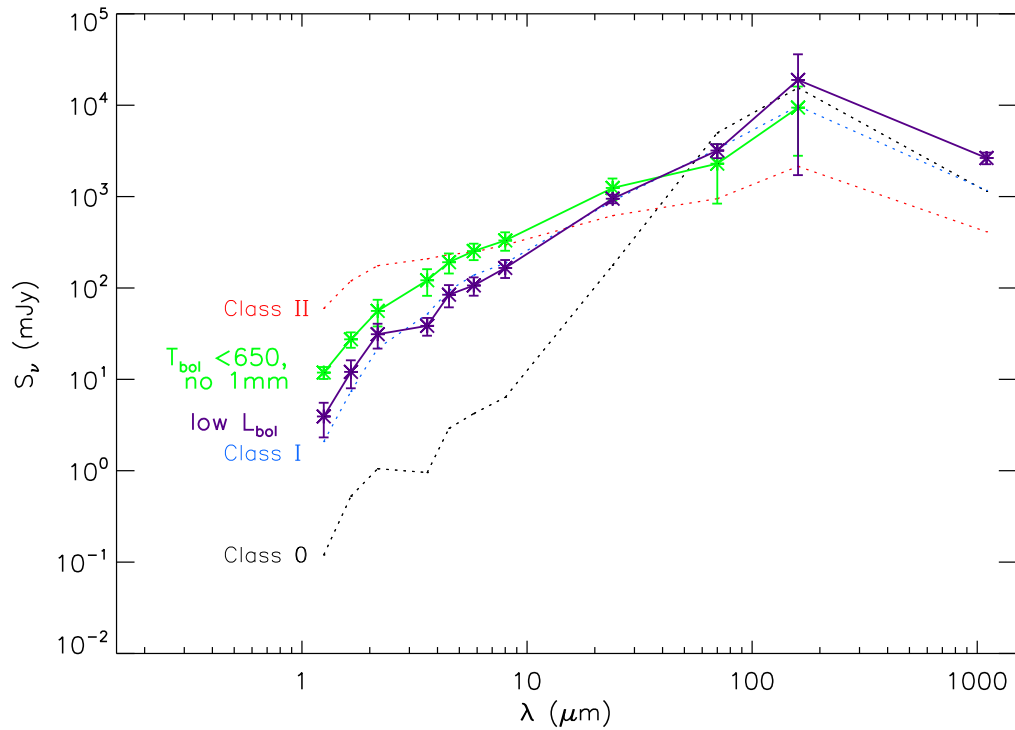


Figure 6.30 Average spectra of low-luminosity Class I sources (purple line), and sources that have  $T_{bol} < 650$  K but no 1.1 mm emission (“non-envelope Class I”). The low-luminosity Class I sources appear to have relatively higher 160  $\mu\text{m}$  and 1.1 mm fluxes compared to the shorter wavelength points, but are otherwise consistent with the average Class I spectrum (blue dotted line). The average non-envelope Class I spectrum is intermediate between the average Class I and Class II spectra, as expected if these represent an evolved stage in which there is little or no remaining envelope.

Perseus and Serpens that are detected at 1.1 mm (purple line). On average, these sources appear to have relatively higher 160  $\mu\text{m}$  and 1.1 mm fluxes compared to the shorter wavelength points, but are otherwise consistent in shape with the average Class I spectrum (blue dotted line). Most of these sources also lack 160  $\mu\text{m}$  fluxes which could cause an underestimate of  $L_{bol}$ .

The envelope mass  $M_{env}$  of protostellar sources in each cloud is plotted versus  $T_{bol}$  in figure 6.31. Symbols are the same as in figure 6.29, except that upper limits at 1.1 mm are now represented by arrows. Solid lines indicate the Young & Evans (2005) evolutionary tracks as before (top to bottom 3.0, 1.0, and 0.3  $M_{\odot}$ ). Sources

in all three clouds show a weak but consistent correlation of decreasing  $M_{env}$  with increasing  $T_{bol}$ , exactly the trend expected if the envelope is gradually depleted by accretion onto the protostar as sources evolve toward higher  $T_{bol}$ . This trend is not an effect of including the 1.1 mm flux, from which the envelope mass is derived, in the calculation of  $T_{bol}$ ; the same trend is apparent even if  $T_{bol}$  is calculated by excluding the 1.1 mm flux point. Some warmer sources have high 1.1 mm upper limits because they lie in regions of extended or confused emission. Our determination that these sources are not actually associated with the 1.1 mm emission is based on visual examination of the images and SEDs.

In contrast to the  $L_{bol} - T_{bol}$  diagram, the Young & Evans (2005) model tracks fit the  $M_{env} - T_{bol}$  distribution quite well. Thus a constant accretion rate reproduces the decrease in envelope mass with increasing  $T_{bol}$ , although it does not fit the evolution of  $L_{bol}$ . The distribution of  $M_{env}$  versus  $T_{bol}$  can also be understood in relation to an episodic accretion scenario, however. The rate of mass transfer from the envelope to the accretion disk likely remains constant even in an episodic scenario, with the accretion rate from the disk to the protostar being the variable quantity (e.g., Kenyon & Hartmann, 1995). Therefore the envelope mass will steadily decrease with increasing  $T_{bol}$  even for variable accretion. Note that accretion stops when the envelope mass, as defined by the outer radius, has been exhausted. In the context of the Young & Evans (2005) models, the spread of  $M_{env}$  as function of  $T_{bol}$  suggests stellar masses in the range  $M \sim 0.3 - 4 M_{\odot}$  in Perseus and Serpens, and  $M \sim 0.1 - 1.5 M_{\odot}$  in Ophiuchus.

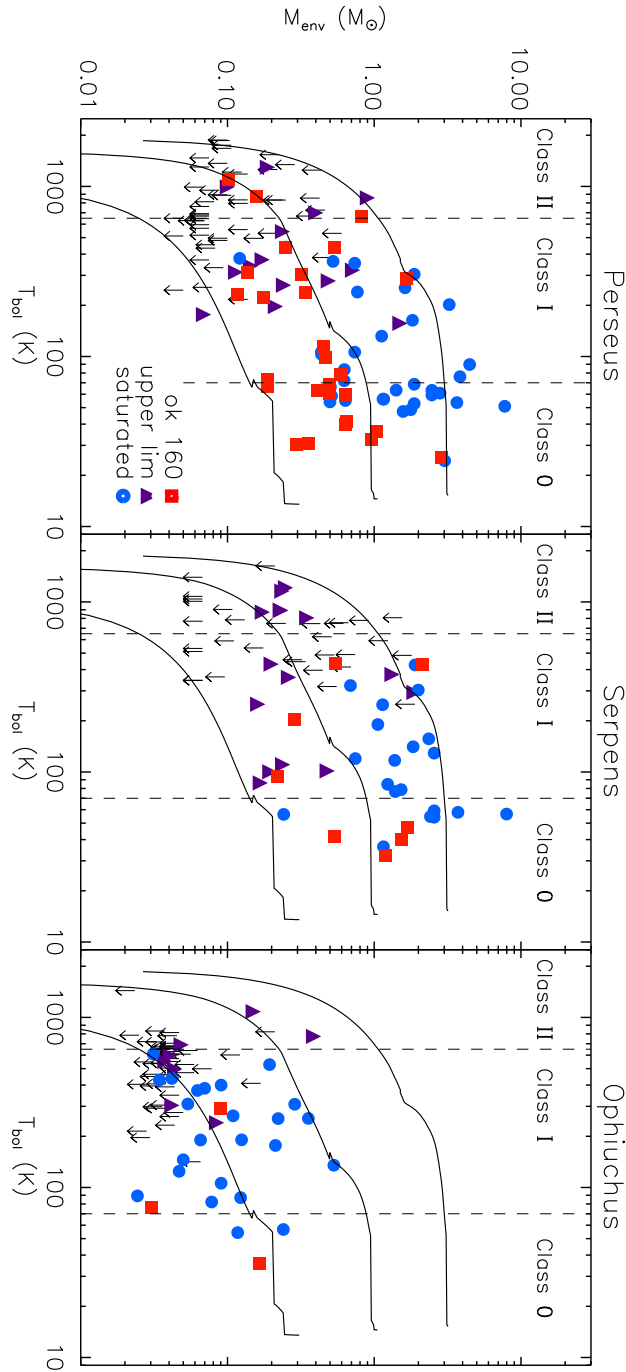


Figure 6.31 Envelope mass versus bolometric temperature for cold protostars in Perseus, Serpens, and Ophiuchus. Filled symbols indicate that a given protostar is associated with 1.1 mm emission, while sources with upper limits at 1.1 mm are plotted as arrows. Solid lines show the predictions of protostellar evolutionary models from Young & Evans (2005) for sources of mass (from top to bottom) 3.0, 1.0, 0.3  $M_{\odot}$ . The Young & Evans (2005) models describe the evolution of mass with  $T_{\text{bol}}$  quite well, in contrast to what was seen for the luminosity (figure 6.29).

## 6.9 Lifetimes

If we assume that star formation in these clouds is a steady-state process (i.e., not occurring in bursts), and that the starless–Class 0–Class I classifications represents a true evolutionary sequence, then we can use the number of objects in consecutive evolutionary phases to estimate the relative lifetimes of those phases. As we ultimately calibrate our timescales based on the lifetime of the Class II phase ( $\sim 10^6$  yr; Kenyon et al. 1990), star formation must have been steady in time for at least the last 1 Myr. In addition, we must assume that there are no significant dependence of the timescales on source mass. Despite a number of assumption that are required, this kind of analysis has the advantage of being quite straightforward to carry out, and it does not rely on an assumed accretion rate or star-formation model.

Table 6.6 list the total number of starless cores, Class 0, and Class I protostars in each cloud, as well as the ratios of the numbers of Class 0 to Class I sources, and starless cores to embedded protostars ( $N_{emb} = N_{Class0} + N_{ClassI}$ ) for all three clouds. The average mean density of the starless core samples  $\langle n \rangle_{SL}$ , and corresponding free-fall timescale  $t_{ff}$ , are also given for each cloud. The free-fall time is the timescale on which starless cores will collapse in the absence of internal support, and is calculated from the mean particle density (Spitzer, 1978):

$$t_{ff} = \sqrt{\frac{3\pi}{32G\rho}} = \sqrt{\frac{3\pi}{32G\langle n \rangle\mu_p m_H}}, \quad (6.6)$$

where  $m_H$  is the mass of hydrogen and  $\mu_p = 2.33$  is the mean molecular weight per particle.

### 6.9.1 Timescale of the Class 0 Phase

There are approximately half as many Class 0 as Class I sources in Perseus and Serpens ( $N_{Class0}/N_{ClassI} = 0.7$  and  $0.4$ , respectively), suggesting that the Class 0 phase lasts roughly half as long as the Class I phase. For a total embedded timescale of  $4 \times 10^5$  yr (Evans et al., in preparation), these ratios imply Class 0 timescales of

Table 6.6. Relative numbers of starless, Class 0, and Class I sources

Cloud	$N_{\text{SL}}$	$\langle n \rangle_{\text{SL}}$ ( $\text{cm}^{-3}$ )	$t_{\text{ff}}$ (yr)	$N_{\text{Class0}}$	$N_{\text{ClassI}}$	$N_{\text{Class0}}/N_{\text{ClassI}}$	$N_{\text{SL}}/N_{\text{emb}}^1$
Perseus	67	$1.3 \times 10^5$	$9 \times 10^4$	29	39	0.7	1.0
Serpens	15	$1.6 \times 10^5$	$8 \times 10^4$	11	26	0.4	0.4
Ophiuchus	26	$8.2 \times 10^5$	$4 \times 10^4$	3	29	0.1	0.8

Note. — The free-fall timescale  $t_{\text{ff}}$  of starless cores is calculated from the mean density  $\langle n \rangle_{\text{SL}}$  of the starless samples in each cloud using equation (6.6). The numbers of Class 0 and Class I sources are based on  $T_{\text{bol}}$  classifications:  $T_{\text{bol}} < 70$  K (Class 0) and  $70 < T_{\text{bol}} < 650$  K (Class I), with the additional requirement that Class I sources be detected at 1.1 mm.

<sup>1</sup> $N_{\text{emb}}$  refers to the total number of embedded protostars, i.e., those in the Class 0 and Class I phases:  $N_{\text{emb}} = N_{\text{Class0}} + N_{\text{ClassI}}$ .

$t_{\text{Class0}} \sim 1.7 \times 10^5$  yr in Perseus, and  $1.2 \times 10^5$  yr in Serpens. These lifetimes are significantly longer than a number of previous estimates of  $t_{\text{Class0}} \sim 10^4$  yr, based both on the number of Class 0 sources in Ophiuchus (André & Montmerle, 1994), and on comparison to evolutionary models ( $2 - 6 \times 10^4$  yr; Froebrich et al. 2006). A short Class 0 lifetime has been interpreted as evidence for a period of very rapid accretion early in the evolution of protostars (e.g., Visser, Richer, & Chandler, 2002). Our results in Perseus and Serpens argue against such a rapid accretion phase, however. Although accretion may decrease somewhat in Class I (or become episodic, see §6.8), it appears unlikely that the *average* accretion rate drops by more than a factor of two from Class 0 to Class I, based on the relative lifetimes of the two phases.

The derived Class 0 lifetimes for Perseus and Serpens are similar to the results of Visser et al. (2002) for a sample of Lynds dark clouds ( $t_{\text{Class0}} \sim 2 \times 10^5$  yr), and to the recent findings of Hatchell et al. (2007) that the Class 0 lifetime in Perseus is similar to the Class I timescale. Our large, unbiased sample provides a distinct advantage over many other previous studies, which have necessarily relied on small samples or accumulated sources from a number of different surveys, wavelengths, and

detection methods. For example, the Visser et al. (2002) Class 0 sample consists of 7 sources, and the André & Montmerle (1994) timescale for Ophiuchus is based on 1 Class 0 object. Froebrich et al. (2006) note that their 50 Class 0/I sources come from a variety of sources including NIR imaging of outflows, IRAS data, submillimeter and millimeter mapping, and radio continuum surveys, causing their source sample to be subject to strong selection effects. The recent work by Hatchell et al. (2007) comparing SCUBA 850  $\mu\text{m}$  maps and *Spitzer* c2d data of Perseus, with 34 Class 0 sources, is a notable exception. Within each cloud our surveys are very uniform, providing protostellar samples that are not biased by selection effects. For this reason, our estimated Class 0 lifetimes should be more robust than many previous measurements.

The results in Ophiuchus are strikingly different from Perseus and Serpens, with 10 times more Class I than Class 0 sources. In fact, our results for Ophiuchus are consistent with previously observed ratios of  $N_{\text{Class0}}/N_{\text{ClassI}} \sim 1/10$  in that cloud (André & Montmerle, 1994), and with the resulting estimates of a very short Class 0 lifetime ( $t_{\text{Class0}} \sim 10^4$  yr). More precisely, we find  $t_{\text{Class0}} \sim 4 \times 10^4$  yr. There are two obvious, but conflicting, explanations for the much smaller  $N_{\text{Class0}}/N_{\text{ClassI}}$  ratio in Ophiuchus. First, star formation may be highly temporally variable in Ophiuchus. Visser et al. (2002) suggest that a burst of star formation approximately  $10^5$  yr ago is responsible for the large ratio of Class I to Class 0 sources. Alternatively, the Class 0 phase may be much shorter in Ophiuchus than in the other two clouds due to higher accretion rates at early times. While a burst of star formation seems the more likely explanation, accretion rates, and thus lifetimes, could conceivably depend on cloud environment, particularly mean density.

Complicating both these scenarios is the fact that bolometric temperatures may be underestimated for sources without a 160  $\mu\text{m}$  flux measurement, as discussed in §6.11. The lack of 160  $\mu\text{m}$  fluxes is especially problematic in Ophiuchus, where the majority of sources are either saturated at 160  $\mu\text{m}$  or in regions of saturated pixels, and may be partially responsible for the small number of observed Class 0 sources in that cloud. When we fit the SEDs of Ophiuchus sources to the average Class 0 and Class I spectra (§6.7.1), we find as many as 8 sources are classified as Class 0. If these

are true Class 0 objects, the ratio of Class 0 to Class I sources becomes similar to the other clouds ( $\sim 0.4$ ). Note that the spectra of 4 of these vary considerably from the average Class 0 spectrum, however (figure 6.26), and their deeply embedded nature is suspect.

Recall that we only include sources in our Class I sample if they are detected at 1.1 mm. This criteria excludes 24 sources in Perseus with  $70 < T_{bol} < 650$  K, 18 sources in Serpens, and 36 in Ophiuchus (“+” symbols in figure 6.29). The average spectrum of these “non-envelope Class I” sources is shown in figure 6.30 (green line, Perseus and Serpens only). The average spectrum appears to be intermediate between the “envelope Class I” (blue dotted line) and Class II (red dotted line) averages. Furthermore, the mean  $T_{bol}$  values of these “non-envelope Class I” sources (570 K in Perseus, 520 K in Serpens, and 500 K in Ophiuchus) confirm that they fall at the warm end of the Class I distribution. While it is possible that we are simply not detecting the envelopes of these sources (e.g., if  $M_{env} \lesssim 0.1 M_{\odot}$  or they are very extended), it seems more likely that the transition from Class I (protostars that retain an envelope) to Class II (pre-main sequence stars with no envelope) occurs closer to  $T_{bol} = 500$  K than  $T_{bol} = 650$  K for these data.

When we include *all* sources with  $T_{bol} < 650$  K in our Class I sample, dropping the requirement that they be detected at 1.1 mm, the ratio of Class 0 to Class I sources becomes 0.5 in Perseus, 0.3 in Serpens, and 0.05 in Ophiuchus. This represents only a 25–30% change in the Class 0 lifetime for each cloud, but does bring Serpens ( $t_{Class0} \sim 0.6 - 1.2 \times 10^5$  yr), closer the “short Class 0” value.

## 6.9.2 Timescale of the Prestellar Phase

Assuming that all of the starless cores in our sample are in fact prestellar, and will eventually collapse to form stars or brown dwarfs (see §6.5), we can use the relative number of starless cores and embedded protostars to estimate the prestellar core lifetime. Knowing this prestellar timescale is essential for understanding the physical processes that govern the formation, support, and collapse of star-forming

cores. The ratio of the number of starless cores to the number of embedded protostars is  $N_{\text{SL}}/N_{\text{emb}} = 1.0$  in Perseus, 0.4 in Serpens, and 0.8 in Ophiuchus, where  $N_{\text{emb}} = N_{\text{Class0}} + N_{\text{ClassI}}$ . For an embedded protostar phase that lasts  $t_{\text{emb}} = 4 \times 10^5$  yr (Evans et al., in preparation), the observed ratios imply prestellar core lifetimes of  $4 \times 10^5$  yr in Perseus,  $2 \times 10^5$  yr in Serpens, and  $3 \times 10^5$  yr in Ophiuchus.

We also found approximately equal numbers of protostellar and starless cores in all three clouds (table 6.1), further confirmation that the timescale for starless cores is similar to that of the embedded protostellar phase. Thus, the dense starless cores we are sensitive to lasts  $2 - 4 \times 10^5$  yr in all three clouds. Approximately equal timescales for the prestellar and embedded protostellar phases were also found recently by Jørgensen et al. (2007) in Perseus using SCUBA maps and *Spitzer* c2d data. Furthermore, our values are only a factor of two shorter than the timescale derived by (Visser et al., 2002) for a sample of Lynds dark clouds.

The prestellar lifetime can be compared to the free-fall time for starless cores, calculated from the mean densities of the starless core samples in each cloud:  $t_{\text{ff}} \sim 9 \times 10^4$  yr in Perseus and  $8 \times 10^4$  yr in Serpens, based on mean densities of  $1.3 \times 10^5 \text{ cm}^{-3}$  and  $1.6 \times 10^5 \text{ cm}^{-3}$ , respectively. Thus prestellar cores last for only a few free-fall times in both Perseus and Serpens. Such a short core lifetime is inconsistent with the classical picture of magnetic support, in which the evolution of highly sub-critical cores is moderated by ambipolar diffusion (Shu et al., 1987). Specifically, in the magnetic paradigm prestellar cores should have lifetimes similar to the ambipolar diffusion timescale, or  $t_{\text{AD}} \sim 7 \times 10^6$  yr for typical ionization levels in low-mass star forming regions (e.g., Evans, 1999), which is more than an order of magnitude longer than our results. The calculated free-fall time is much shorter in Ophiuchus, however, due to higher mean densities, and a lifetime of  $\sim 8t_{\text{ff}}$  may be more consistent with ambipolar diffusion. Note that higher core densities were found to be a result of the higher linear resolution in Ophiuchus (§5.4), so it is possible that mean densities in the other clouds could be underestimated.

It is also important to emphasize here that our Bolocam surveys are sensitive to cores with relatively high mean density ( $n \gtrsim 2 - 3 \times 10^4 \text{ cm}^{-3}$ ). It is quite

possible, therefore, that we are sampling only the densest end stage in a longer core evolutionary picture, in which case a magnetic field dominated scenario might still be applicable at early times (e.g., Tassis & Mouschovias 2004). Ciolek & Basu (2001) also note that  $t_{AD}$  can be as short as a few free-fall times for marginally sub-critical cores.

## 6.10 Conclusions

Utilizing large-scale 1.1 mm surveys (Enoch et al., 2006; Young et al., 2006; Enoch et al., 2007) together with *Spitzer* IRAC and MIPS maps from the c2d Legacy program (Evans et al., 2003), we have constructed an unbiased census of prestellar cores and deeply embedded protostars in the Perseus, Serpens, and Ophiuchus molecular clouds. We first assembled a sample of candidate cold protostars in each cloud, and used them to distinguish starless cores from cores that have an internal luminosity source (protostellar cores).

Cloud environment appears to have a significant effect on the physical properties of starless cores, and how such properties are altered by the formation of a central protostar. Starless cores in Perseus are larger and have lower mean densities than protostellar cores, by factors of 1.3 and 3.7, respectively. Thus there is a relatively simple scenario by which protostellar cores might have evolved from starless cores in that cloud, becoming smaller and denser at a fixed mass. In Serpens, however, it is not clear how the relatively massive protostellar cores ( $\langle M \rangle = 2.1 M_{\odot}$ ) could have evolved from the current population of compact, low mass starless cores ( $\langle M \rangle = 0.9 M_{\odot}$ ), unless cores merge at later times. By contrast to both Serpens and Perseus, we see essentially no difference in Ophiuchus between cores that have formed stars and those that have not.

We also investigate the spatial clustering of cores, and relationship to the local cloud column density, as traced by visual extinction. Starless cores are observed to have a lower degree of spatial clustering in all three clouds, based on the amplitude of the two-point correlation function. For Perseus and Serpens this result is supported by

the peak surface density of cores, which is higher for protostellar cores by a factor of 1.5 to 2. In all three clouds both starless and protostellar cores are only found at relatively high cloud column densities: 75% of cores are associated with  $A_V \gtrsim 7 - 8.5$  mag in Perseus,  $A_V \gtrsim 9.5 - 16$  mag in Serpens, and  $A_V \gtrsim 19.5 - 23$  mag in Ophiuchus. An extinction threshold for forming dense cores at  $A_V = 4 - 8$  mag has been suggested for magnetically supported clouds (McKee, 1989). Our results are consistent with this prediction, but only in Ophiuchus is a true threshold observed; in that cloud only two cores are found at  $A_V < 17$  mag.

Assuming that all of our starless cores will eventually form stars, we construct the combined prestellar core mass distribution (CMD) with the 108 starless cores from all three clouds. The combined starless core mass distribution has a slope of  $\alpha = -2.5 \pm 0.2$ , consistent with recent measurements of the stellar initial mass function ( $\alpha = -2.4$  to  $-2.8$ ). Our result lends support to the idea that stellar masses are directly linked to the core formation process. The relationship of the prestellar CMD to the combined protostellar CMD, however, is more complex than anticipated if protostellar cores were originally drawn from the prestellar CMD. Although the protostellar CMD has a wider distribution to smaller masses as expected if core mass is lost to accretion, the high-mass tail of the protostellar CMD is difficult to understand unless any future star formation in these clouds will result in stars of lower mass than the current generation of protostars.

After examining the starless and protostellar core populations, we focus on the properties of the cold protostar samples. Bolometric luminosities, temperatures, and envelope masses are calculated for the candidate Class 0 and Class I sources in each cloud (tables 6.2–6.4). Our sample includes a total of 43 Class 0 sources and 94 Class I sources, with approximate detection limits of  $M_{env} > 0.2 M_\odot$  and  $M_{env} > 0.1 M_\odot$  for Class 0 and Class I sources, respectively. We compare different protostellar classification methods, concluding that the bolometric temperature is a better measure of evolutionary state than the near- to mid-infrared spectral index,  $\alpha_{IR}$ , for deeply embedded sources.

Observed source properties are compared to protostellar evolutionary models using

the bolometric temperature-luminosity ( $L_{bol} - T_{bol}$ ) diagram, the protostellar equivalent of the H-R diagram (Myers et al., 1998). Neither models with a constant mass accretion rate (Young & Evans, 2005), nor those with an exponentially decreasing rate (Myers et al., 1998) fit the observed sources. In particular, there is a large population of low luminosity Class I sources that cannot be explained by the general prediction that  $L_{bol}$  should peak during the Class I phase. We interpret this result as evidence for episodic accretion during the Class I stage; based on the number of sources with  $L_{bol} < 0.1L_{\odot}$ , protostars should spend approximately 25% of their Class I lifetime in a quiescent accretion state.

Finally, the relative number of starless, Class 0, and Class I sources are used to estimate timescales for the dense prestellar core and Class 0 phases. There are approximately half as many Class 0 as Class I sources in Perseus and Serpens, implying a Class 0 timescale of  $1 - 2 \times 10^5$  yr. In Ophiuchus the fraction of Class 0 sources is much smaller ( $N_{Class0}/N_{ClassI} \sim 0.1$ ). Part of this difference may be due to the lack of reliable 160  $\mu\text{m}$  flux measurements in Ophiuchus, but it seems likely that the Class 0 phase is either much shorter in that cloud or that a burst of star formation is responsible for the large population of Class I objects. In all three clouds the lifetime of dense prestellar cores is approximately equal to the timescale of the embedded protostellar phase, or  $2 - 5 \times 10^5$  yr. Such a short prestellar core lifetime, only a few free-fall timescales in Perseus and Serpens, is inconsistent with a scenario in which core support and evolution is dominated by magnetic fields, in which case the lifetime should be similar to the ambipolar diffusion timescale,  $t_{AD} \sim 10^7$  yr. These observations might still be consistent with ambipolar diffusion if we are only observing the densest stages of a longer-scale core evolution.

## Acknowledgments

Support for this work, part of the Spitzer Legacy Science Program, was provided by NASA through contracts 1224608 and 1230782 issued by the Jet Propulsion Laboratory, California Institute of Technology, under NASA contract 1407. Additional

support was obtained from NASA Origins Grant NNG04GG24G to the University of Texas at Austin. Support for the development of Bolocam was provided by NSF grants AST-9980846 and AST-0206158.

## 6.11 Appendix: Calculating the bolometric luminosity and temperature

We use two different methods to do the integrations over frequency in equations 6.3–6.4. The first (linear) method uses power law fit between flux points. For example, the fit between measured flux density points at  $\lambda_j$  and  $\lambda_{j+1}$  is given by  $S(\lambda) = 10^b \lambda^m$ , with

$$m = \frac{\log(S(\lambda_{j+1})/S(\lambda_j))}{\log(\lambda_{j+1}/\lambda_j)}, \text{ and } b = \log S(\lambda_j) - m \log \lambda_j. \quad (6.7)$$

The SED is extrapolated from the longest wavelength flux using  $S_\nu \propto \nu^2$ . The second (midpoint) method utilizes a simple midpoint interpolation. In both methods flux upper limits are treated as zero and removed from the fit (i.e., we interpolate over them). Uncertainties in flux density measurements are included in the midpoint calculation, and used to estimate formal fitting errors for  $T_{bol}$  and  $L_{bol}$ .

Figure 6.32 compares the results of using the linear and midpoint methods to calculate  $L_{bol}$  and  $T_{bol}$  for the cold protostar sample in Perseus. Except for the coldest sources, the midpoint  $T_{bol}$  is lower than the linear  $T_{bol}$ , by about 10%. Conversely,  $L_{bol}$  calculated by the midpoint method is nearly always higher than the linear  $L_{bol}$ . It is not unexpected that the linear estimate of  $L_{bol}$  would be too low, as a linear fit to a blackbody function will always be an underestimate to the true flux. The expected behavior for  $T_{bol}$  is not so clear, however.

To further test this behavior, we plot in figure 6.33 the fractional errors due solely to finite sampling, for  $L_{bol}$  and  $T_{bol}$  calculated from input blackbody spectra. Blackbody sources with input  $T_{bol}$  from 5–5000 K are sampled at the observed wavelengths ( $\lambda = 1.25, 1.65, 2.17, 3.6, 4.5, 5.8, 8, 24, 70, 160, 1100 \mu\text{m}$ ), and the bolometric temperature and luminosity calculated by the linear (left) and midpoint (right) methods. As anticipated, the linear  $L_{bol}$  is an underestimate of the true value, by more than 20% for input  $T_{bol} \lesssim 300$  K. The linear  $T_{bol}$  is often underestimated as well, but by less than 10%. In contrast, the midpoint  $L_{bol}$  is higher than the true values for input  $T_{bol} \lesssim 200$  K, by up to 20%. Although the amplitude of the fractional errors on  $T_{bol}$

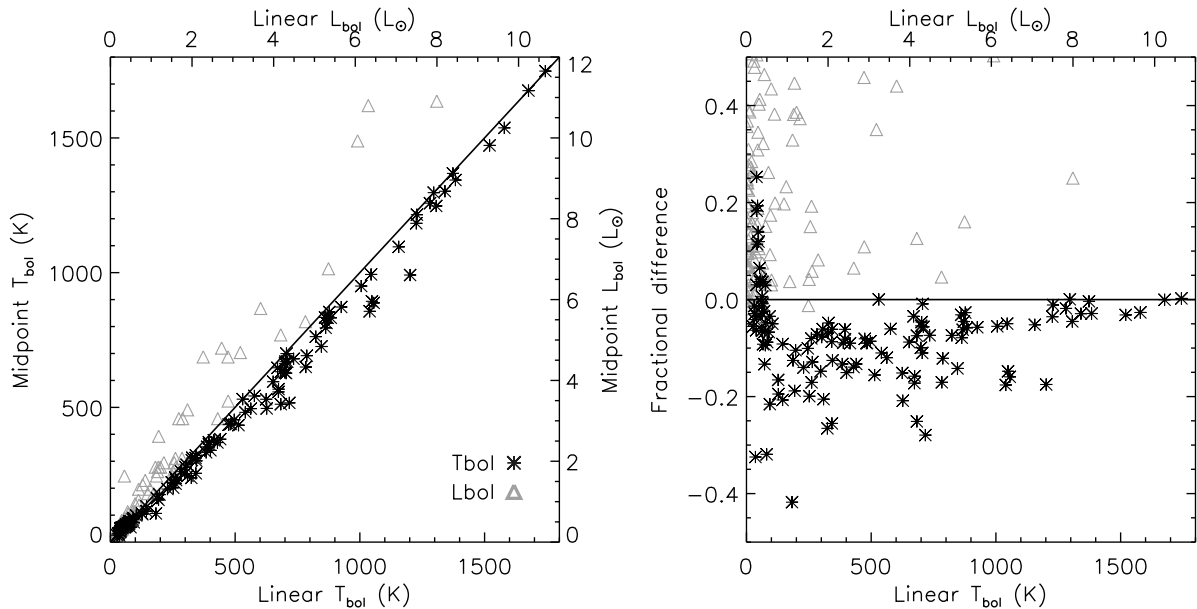


Figure 6.32 Comparison of the linear and midpoint methods for calculating  $L_{bol}$  and  $T_{bol}$ , for sources in Perseus. *Left*: Linear and midpoint  $T_{bol}$  (black asterisks) and  $L_{bol}$  (triangles) values are plotted for all cold protostar candidates in Perseus. *Right*: Fractional difference between the linear and midpoint methods, plotted as (midpoint-linear)/linear.  $L_{bol}$  calculated by the midpoint method is nearly always higher than the linear  $L_{bol}$ , and it is not unexpected that the linear value should be an underestimate. Except for the coldest sources, the midpoint  $T_{bol}$  is lower than the linear  $T_{bol}$  by 10–20%.

are larger for the midpoint method, they are centered on zero, and thus the midpoint method provides a more *accurate*, if not more *precise*, measurement of  $L_{bol}$  and  $T_{bol}$ . Based on figures 6.32–6.33, we use the midpoint method throughout this chapter, although it must be noted that the blackbody spectra tested here are not necessarily representative of the more complicated observed SEDs.

In general, measured  $160 \mu\text{m}$  fluxes are uncertain by up to a factor of 2, due to unquantified saturation effects and calibration uncertainties, and in many cases we are unable to measure a  $160 \mu\text{m}$  flux at all. In addition, the “point-source”  $160 \mu\text{m}$  fluxes of extended sources will likely be underestimated, because they are measured with a PSF fit rather than aperture photometry. Missing or severely underestimated fluxes at  $160 \mu\text{m}$  can significantly affect both  $L_{bol}$  and  $T_{bol}$  for cold sources that peak

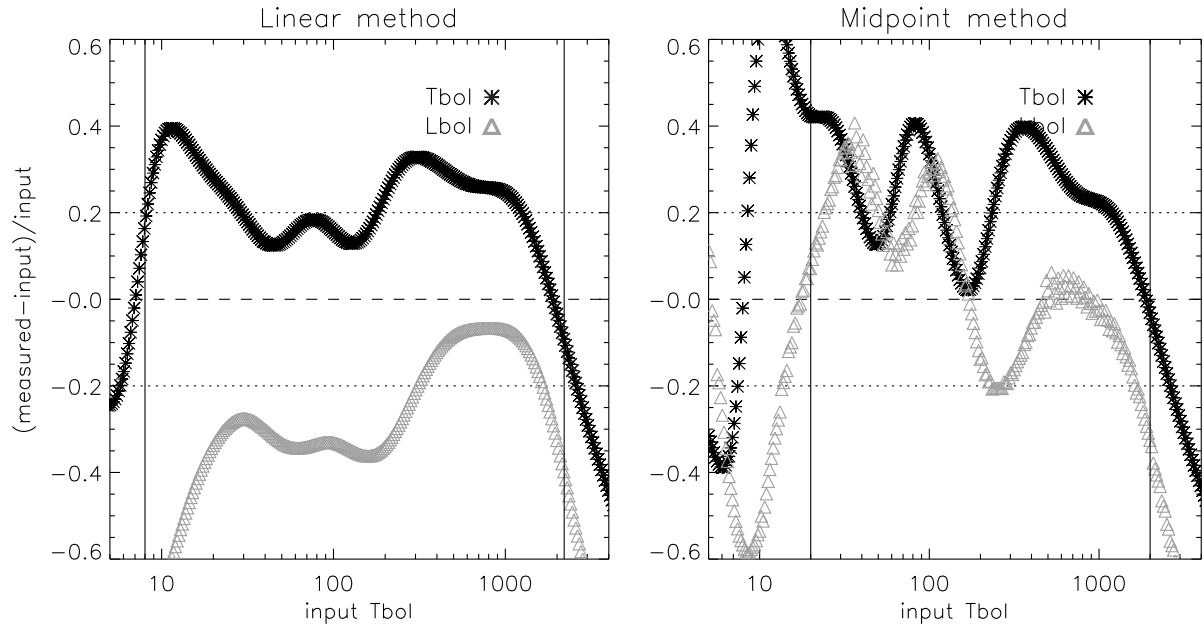


Figure 6.33 Characterization of sampling errors for  $T_{bol}$  and  $L_{bol}$  calculated using the linear (left) and midpoint (right) methods. The fractional difference between the input ( $T_{bol}, L_{bol}$ ) of blackbody spectra and the measured values when SEDs are sampled at the observed wavelengths is plotted as a function of input  $T_{bol}$ . The linear  $L_{bol}$  is underestimated, as expected. Although the absolute amplitude of the  $T_{bol}$  errors are smaller for the linear method, the midpoint method tends to be more accurate. Source SEDs, which are not pure blackbodies, may behave differently.

near  $100 \mu\text{m}$ . As we are primarily interested in the coldest sources, we attempt here to quantify the effects of missing or underestimated  $160 \mu\text{m}$  flux. One way of approaching this problem is to examine sources for which we have additional information near the peak of the SED, e.g., from IRAS or SHARC  $350 \mu\text{m}$  observations.

We first look at two example sources, one cold ( $T_{bol} \sim 33 \text{ K}$ ), and one warmer ( $T_{bol} \sim 163 \text{ K}$ ). The colder source (IRAS 03282+3039) is isolated, so we can use the IRAS fluxes without worrying about confusion due to the large IRAS beam. We calculate the “true”  $L_{bol}$  and  $T_{bol}$  by including the IRAS  $60$  and  $100 \mu\text{m}$  fluxes, a SHARC II  $350 \mu\text{m}$  flux (Wu et al., in preparation), and a MIPS  $160 \mu\text{m}$  flux measured in a large aperture, which is almost two times higher than the PSF-fit flux. Using the underestimated point source  $160 \mu\text{m}$  flux, and no longer including IRAS or SHARC II data, causes an *underestimate* of  $L_{bol}$  by 35% and an *overestimate* of  $T_{bol}$  by 15%

compared to the “true” values. Omitting the  $160\ \mu\text{m}$  point altogether, as would be appropriate for saturated sources, results in an underestimate of  $L_{bol}$  by 7% and an overestimate of  $T_{bol}$  by 9%.

Thus we conclude that while the  $160\ \mu\text{m}$  point is important for characterization of the SED of cold objects, our integration method can interpolate over a missing  $160\ \mu\text{m}$  flux to estimate  $L_{bol}$  and  $T_{bol}$  to within 20% for cold sources. Severely underestimated  $160\ \mu\text{m}$  flux densities will cause larger errors of up to 50%. Using a similar procedure for the warmer source ( $T_{bol} = 163\ \text{K}$ ), we find that omitting the  $160\ \mu\text{m}$  flux results in errors in the opposite sense compared to the colder source: an *overestimate* of  $L_{bol}$  by 28% and an *underestimate* of  $T_{bol}$  by 18%.

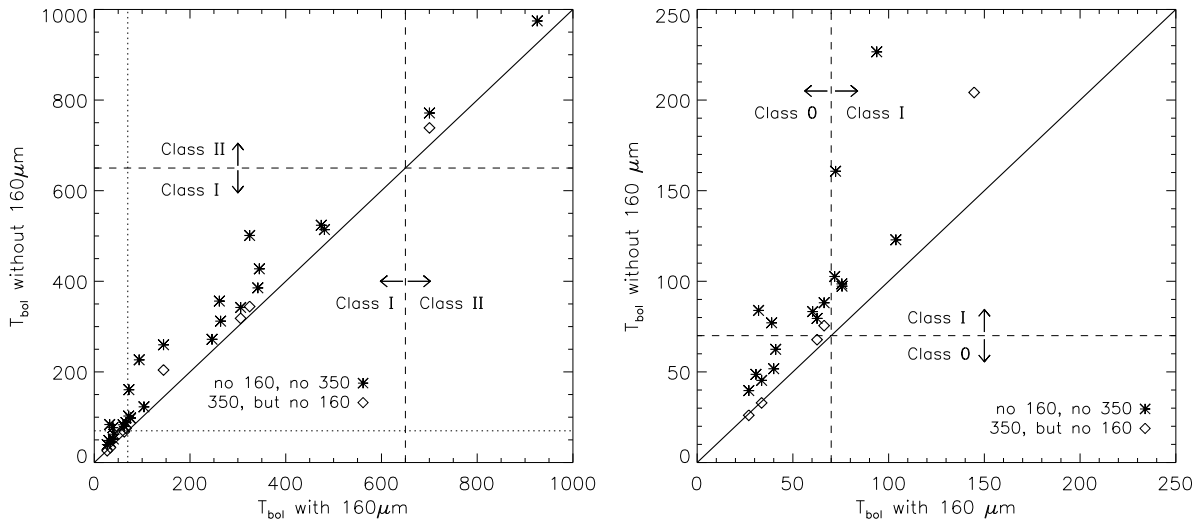


Figure 6.34 Characterization of the systematic errors introduced for  $T_{bol}$  when a  $160\ \mu\text{m}$  flux density is not available. *Left*: For all sources in Perseus with a reliable  $160\ \mu\text{m}$  flux, we calculate  $T_{bol}$  with and without the  $160\ \mu\text{m}$  point (asterisks).  $T_{bol}$  is always overestimated when the  $160\ \mu\text{m}$  flux is missing, but it does not change the classification of Class I sources for these data. *Right*: Similar, but with the scale adjusted to highlight lower  $T_{bol}$  sources. Not having a  $160\ \mu\text{m}$  point does change the classification of approximately half of the Class 0 ( $T_{bol} < 70\ \text{K}$ ) sources. Errors are substantially reduced when a flux at  $350\ \mu\text{m}$  is available (diamonds).

For a more general result, we compare  $T_{bol}$  calculated with the  $160\ \mu\text{m}$  flux included in the SED to the value found by omitting the  $160\ \mu\text{m}$  point, for all sources in Perseus

with a measured  $160\ \mu\text{m}$  flux (figure 6.34, left panel). For this plot, we have adopted Class 0/Class I/Class II divisions from Chen et al. (1995). Source classifications are discussed in §6.7. Although  $T_{bol}$  calculated without the  $160\ \mu\text{m}$  flux is always overestimated compared to  $T_{bol}$  calculated with the  $160\ \mu\text{m}$  flux, it is never a large enough effect to shift the source classification of objects with  $T_{bol} \gtrsim 100\ \text{K}$  (e.g., from Class I to Class II). This is not the case for Class 0 sources, however, as can be seen in the right panel of figure 6.34, where the scale has been adjusted to highlight the lowest  $T_{bol}$  values. Five sources that have  $T_{bol} < 70\ \text{K}$  (Class 0) when including the  $160\ \mu\text{m}$  flux are shifted to  $T_{bol} > 70\ \text{K}$  (Class I) when a  $160\ \mu\text{m}$  flux is not available. If a published  $350\ \mu\text{m}$  flux is available (diamonds), the errors in  $T_{bol}$  resulting from excluding the  $160\ \mu\text{m}$  flux are almost completely eliminated. Therefore we include  $350\ \mu\text{m}$  fluxes in the calculation of  $T_{bol}$  when available (nine sources in Perseus).

Based on figures 6.32–6.34 and the above examples, we estimate overall uncertainties for measured  $L_{bol}$  and  $T_{bol}$  values of  $20 - 50\%$ , depending on whether or not a  $160\ \mu\text{m}$  flux is available. If we are unable to measure a  $160\ \mu\text{m}$  flux,  $T_{bol}$  will almost certainly be an overestimate for very cold sources, which may affect our classification of protostellar candidates.

## Bibliography

- Adams, F. C., & Fatuzzo, M. 1996, ApJ, 464, 256
- Adams, F. C., Lada, C. J., & Shu, F. H. 1987, ApJ, 312, 788
- Alves, J., Lada, C. J., & Lada, E. A. 2001, Nature, 409, 159
- Alves, J., Lombardi, M., & Lada, C. J. 2007, A&A, 462L, 17
- André, P. 1994, *The Cold Universe*, editors Montmerle, T., Lada, C. J., Mirabel, I. F., & Tran Thanh Van, J. Gif-sur-Yvette, Editions Frontieres, p. 179
- André, P., & Montmerle, T. 1994, ApJ, 420, 837
- André, P., Ward-Thompson, D., & Barsony, M. 1993, ApJ, 406, 122
- Aspin, C., Sandell, G., & Russell, A. P. G. 1994, A&AS 106 165
- Beckwith, S. V. W. & Sargent, A. I. 1996, Nature, 383, 139
- Beckwith, S. V. W., Sargent, A. I., Chini, R. S., & Güsten, R. 1990, 99, 924
- Bonnell, I. A., Bate, M. R., Clarke, C. J., & Pringle, J. E. 2001, 323, 785
- Bonnor, W. B. 1956, MNRAS, 116, 351
- Chabrier, G. 2005 in *The Stellar Initial Mass Function Fifty Years Later*, editors E. Corbelli, F. Palla, and H. Zinnecker, p. 41
- Chen, H., Myers, P. C., Ladd, E. F., & Wood, D. O. S. 1995, ApJ, 445, 377
- Ciolek, G. E., & Basu, S. 2001, ApJ, 547, 272
- Cohen, M. & Kuhli, L. V. 1979, ApJS, 41, 743
- Crutcher, R. M. 1999, ApJ, 520, 706

- Di Francesco, J., Evans, N. J., II, Caselli, P., Myers, P. C., Shirley, Y., Aikawa, Y., & Tafalla, M. 2007, in *Protostars and Planets V*, editors B. Reipurth, D. Jewitt, and K. Keil, p. 17
- Ebert, R. 1955, *Zeitschrift Astrophysics*, 37, 217
- Enoch, M. L., Young, K. E., Glenn, J., Evans, N. J., II, Golwala, S., Sargent, A. I., Harvey, P., et al. 2006, *ApJ*, 638, 293
- Enoch, M. L., Glenn, J., Evans, N. J., II, Sargent, A. I., Young, K. E., & Huard, T. L., *ApJ*, in press
- Evans, N. J., II 1999, *ARA&A*, 37, 311
- Evans, N. J., II, Allen, L. E., Blake, G. A., Boogert, A. C. A., Bourke, T., Harvey, P. M., Kessler, J. E., et al. 2003, *PASP*, 115, 965
- Evans, N. J., II, Rawlings, J. M. C., Shirley, Y. L., & Mundy, L. G. 2001, *ApJ*, 557, 193
- Evans, N. J., II, et al. 2007, *Final Delivery of Data from the c2d Legacy Project: IRAC and MIPS*
- Froebrich, D., Schmeja, S., Smith, M. D., & Klessen, R. S. 2006, *MNRAS*, 368, 435
- Greene, T. P., Wilking, B. A., André, P., Young, E. T., & Lada, C. J. 1994, *ApJ*, 434, 614
- Gregersen, E. M. & Evans, N. J., II 2000, *ApJ*, 538, 260
- Habets, G. M. H. J., & Heintze, J. R. W. 1981, *A&A*, 46, 193
- Hartmann, L., & Kenyon, S. J. 1985, *ApJ*, 299, 462
- Harvey, P. M., Chapman, N., Lai, S.-P., Evans, N. J., II, Allen, L. E., Jørgensen, J. K., Mundy, L. G., et al. 2006, *ApJ*, 644, 307

- Harvey, P. M., Merin, B., Huard, T. L., Rebull, L. M., Chapman, N. Evans, N. J., II, & Myers, P. C. 2007a, ApJ, in press (preprint: arXiv:0704.0009 [astro-ph])
- Harvey, P. M., Rebull, L. M., Brooke, T., Spiesman, W. J., Chapman, N., Huard, T. L., Evans, N. J., II, et al. 2007b, ApJ, in press (preprint: arXiv:0704.0253 [astro-ph])
- Hatchell, J., Fuller, G. A., Richer, J. S., Harries, T. J., & Ladd, E. F. 2007, A&A, accepted (preprint:astro-ph/0612601)
- Herbig, G. H. & Kameswara, R. N. 1972, ApJ, 174, 401
- Jeans, J. H. 1928, *Astronomy and Cosmogony*, p. 340. Cambridge, U.K.: Cambridge University Press
- Johnstone, D., Wilson, C. D., Moriarty-Schieven, G., Joncas, G., Smith, G., Gregersen, E., & Fich, M. 2000, ApJ, 545, 327
- Jørgensen, J. K., Harvey, P. M., Evans, N. J., II, Huard, T. L., Allen, L. E., Porras, A., Blake, G. A., et al. 2006, ApJ, 645, 1246
- Jørgensen, J. K., Johnstone, D., Kirk, H., & Myers, P. C. 2007, ApJ, 656, 293
- Kenyon, S. J., & Hartmann, L. W. 1995, ApJS, 101, 117
- Kenyon, S. J., Hartmann, L. W., Strom, K. M., & Strom, S. E. 1990, AJ, 99, 869
- Kirk, H., Johnstone, D., & DiFrancesco, J. 2006, ApJ, 646, 1009
- Kroupa, P. 2002, Science, 295, 82
- Lada, C. J. 1987, in IAU Symp. 115, Star Forming Regions, editors M. Peimbert & J. Jugaku (Dordrecht: Reidel), p. 1
- Lada, C. J., & Lada, E. A. 2003, ARA&A, 41, 57
- Looney, L. W., Mundy, L. G., & Welch, W. J. 2000, ApJ, 529, 477

- Luhman, K. L., Stauffer, J. R., Muench, A. A., Reike, G. H., Lada, E. A., Bouvier, J., & Lada, C. J. 2003, *ApJ*, 593, 1115
- McCaughrean, M. J., Rayner, J. T., & Zinnecker, H. 1994, *ApJ*, 436, L189
- McKee, C. F. 1989, *ApJ*, 345, 782
- McKee, C. F., & Zweibel, E. G. 1992, *ApJ*, 399, 551
- Motte, F., André, P., & Neri, R. 1998, *A&A*, 336, 150
- Muench, A. A., Lada, E. A., Lada, C. J., & Alves, J. 2002, *ApJ*, 573, 366
- Myers, P. C., Adams, F. C., Chen, H., Schaff, E. 1998, *ApJ*, 492, 703
- Myers, P. C., & Ladd, E. F. 1993, *ApJ*, 413, 47
- Natta, A., Testi, L., Calvet, N., Henning, Th., Waters, R., & Wilner, D. 2007, in *Protostars and Planets V*, editors B. Reipurth, D. Jewitt, and K. Keil, p. 767
- Onishi, T., Kawamura, A., Tachihara, K., & Fukui, Y. 2002, *ApJ*, 575, 950
- Ossenkopf, V., & Henning, Th. 1994, *A&A*, 291, 943
- Pringle, J. E. 1989, *MNRAS*, 239, 361
- Rebull, L. M., et al. 2007, *ApJS*, in press (preprint: astro-ph/0701711)
- Reid, I. N., Gizis, J. E., & Hawley, S. L. 2002, *AJ*, 124, 2721
- Reipurth, B., & Bally, J. 2001, *ARA&A*, 39, 403
- Salpeter, E. E. 1955, *ApJ*, 121, 161
- Scalo, J. M. 1986, *Fundam. Cosmic Phys.*, 11, 1
- Scalo, J. M. 2005, in *The Stellar Initial Mass Function Fifty Years Later*, Kluwer Academic Publishers, editors E. Corbelli, F. Palla, and H. Zinnecker, p. 23
- Schröder, K.-P., & Pagel, B. E. J. 2003, *MNRAS*, 343, 1231

- Shirley, Y. L., Evans, N. J., II, & Rawlings, J. M. C. 2002, ApJ, 575, 337
- Shirley, Y. L., Evans, N. J., II, Rawlings, J. M. C., & Gregersen, E. M. 2000, ApJS, 131, 249
- Shu, F. H. 1977, ApJ, 214, 488
- Shu, F. H., Adams, F. C., & Lizano, S. 1987, ARA&A, 25, 23
- Spitzer, L. Jr. 1978, *Physical Processes in the Interstellar Medium*, New York: Wiley, p. 282
- Tassis, K. & Mouschovias, T. Ch. 2004, ApJ, 616, 283
- Testi, L., & Sargent, A. I. 1998, ApJ, 508, L91
- Vieira, S. L. A., Corradi, W. J. B., Alencar, S. H. P., Mendes, L. T. S., Torres, C. A. O., Quast, G. R., Guimarães, M. M., & da Silva, L. 2003, AJ, 126, 2971
- Visser, A. E., Richer, J. S., & Chandler, C. J. 2002, AJ, 124, 2756
- Ward-Thompson, D., Scott, P. F., Hills, R. E., & Andre, P. 1994, MNRAS, 268, 276
- Whitney, B. A., Wood, K., Bjorkman, J. E., & Cohen, M. 2003, ApJ, 598, 1079
- Young, C. H. & Evans, N. J., II 2005
- Young, C. H., Shirley, Y. L., Evans, N. J., II, & Rawlings, J. M. C. 2003, ApJS, 145, 111
- Young, K. E., Enoch, M. L., Evans, N. J., II, Glenn, J., Sargent, A., Huard, T. L., Aguirre, J., et al. 2006, ApJ, 644, 326

# Chapter 7

## Summary and Future work

### 7.1 Summary

In this thesis I have utilized large-scale millimeter and mid- to far-infrared surveys to address a number of outstanding questions regarding the formation of low mass stars in molecular clouds, including:

- (1) What are the global physical processes controlling the formation and support of prestellar cores, and their subsequent collapse into protostars?
- (2) What are the initial conditions of prestellar cores in molecular clouds, and how do their properties change after protostellar formation?
- (3) How do newly formed protostars evolve through the earliest phases; in particular, what are their mass accretion rates and timescales for evolution?
- (4) How do the properties of dense cores depend on environmental factors such as the strength of turbulence?

Using Bolocam, a recently implemented bolometer array at the Caltech Submillimeter Observatory, I have surveyed the Perseus, Serpens, and Ophiuchus molecular clouds at  $\lambda = 1.1$  mm, and developed methods to calibrate and analyze the resulting observations. These surveys have a resolution of  $31''$  and cover the largest areas observed at millimeter or submillimeter wavelengths to date in each cloud:  $7.5 \text{ deg}^2$  in Perseus, or  $140 \text{ pc}^2$  at the adopted cloud distance of  $d = 250 \text{ pc}$ ,  $10.8 \text{ deg}^2$  ( $50 \text{ pc}^2$  at  $d = 125 \text{ pc}$ ) in Ophiuchus, and  $1.5 \text{ deg}^2$  ( $30 \text{ pc}^2$  at  $d = 125 \text{ pc}$ ) in Serpens. They are sensitive to dense sub-structures with mean particle density  $\langle n \rangle \gtrsim 2 - 3 \times 10^4 \text{ cm}^{-3}$

and contrast with the average background density of at least a factor of 30 – 100. A total of 122 such 1.1 mm cores are detected in Perseus above a point source mass detection limit of  $0.18 M_{\odot}$ , 44 cores in Ophiuchus above a detection limit of  $0.1 M_{\odot}$ , and 35 cores in Serpens above a detection limit of  $0.13 M_{\odot}$ . The total mass contained in dense cores is  $285 M_{\odot}$  in Perseus,  $42 M_{\odot}$  in Ophiuchus, and  $92 M_{\odot}$  in Serpens.

The Bolocam surveys were designed to cover the same regions as mid- and far-infrared *Spitzer* IRAC and MIPS maps of Perseus, Serpens, and Ophiuchus completed as part of the “Cores to Disks” Legacy project. Combining the *Spitzer* and Bolocam surveys provides wavelength coverage from  $\lambda = 1.25 - 1100 \mu\text{m}$ , and enables the separation of prestellar and protostellar cores, as well as the construction of well-sampled spectral energy distributions (SEDs) for cold protostellar candidates. This unprecedented, complete census of the youngest star forming objects in three diverse molecular clouds includes 108 prestellar cores, 43 Class 0 sources and 94 Class I sources. It is complete for all Class 0 objects that have envelope masses  $M_{env} \gtrsim 0.2 M_{\odot}$ , and for all Class I objects that have  $M_{env} \gtrsim 0.1 M_{\odot}$ . This unique sample enables the following investigations of questions (1) through (4) outlined above:

1. Two simple observational tests can distinguish between magnetic fields and turbulence as the dominant physical processes controlling the formation, support, and collapse of dense cores in molecular clouds: the prestellar core lifetime, and the existence of an  $A_V$  threshold. Surprisingly, the results of these tests seem to suggest conflicting interpretations. In all three clouds the lifetime of dense prestellar cores is approximately equal to the entire time spent in the embedded protostellar phase,  $2 - 4 \times 10^5$  yr, or only a few free-fall timescales. Such a short prestellar core lifetime is inconsistent with the classic scenario of magnetic field support in which core evolution occurs on the ambipolar diffusion timescale of  $t_{AD} \sim 10^7$  yr (Nakano, 1998). Thus the measured prestellar core lifetime argues for a dynamic, turbulent core formation process in these clouds.

On the other hand, the fact that dense cores are found only at high cloud column densities ( $A_V \gtrsim 7$  mag) in all three clouds, and the observation of a true  $A_V$  threshold

in Ophiuchus at  $A_V \sim 17$  mag, suggests that magnetic fields must also play some role in the formation of prestellar cores. As discussed in chapter 1, column density thresholds for star formation arise naturally if core collapse is moderated by ambipolar diffusion (Shu et al., 1987; McKee, 1989), but are difficult to reconcile with a turbulent paradigm (Johnstone et al., 2004).

Scenarios in which both magnetic fields and turbulence are important have been explored with numerical simulations; Vázquez-Semadeni et al. (2005) suggest that strong magnetic fields in turbulent clouds decrease the star formation efficiency without increasing the prestellar core lifetime. The fraction of total cloud mass contained in dense cores, an upper limit to the instantaneous star formation efficiency, is less than 10% in all three clouds, lower than typically predicted in turbulent simulations without magnetic fields (e.g., Klessen et al., 2000). Taken together, my results argue for turbulence being the dominant physical process in molecular clouds, but in the presence of magnetic fields that are strong enough (i.e. marginally sub-critical) to prevent core formation in low column density regions, and to lower the star formation efficiency to  $< 10\%$ .

**2.** The prestellar core mass distribution (CMD) is an important diagnostic of initial conditions, in that it may reveal whether feedback, dynamical, or core fragmentation processes are responsible for the form of the stellar initial mass function (IMF). I constructed the prestellar CMD by utilizing the combined starless core samples from all three clouds. The best fitting power law to the prestellar CMD for  $M > 0.8 M_\odot$  has a slope of  $\alpha = -2.5 \pm 0.2$ , remarkably similar to recent measurements of the slope of the IMF for  $M \gtrsim 0.5 M_\odot$ :  $\alpha = -2.4 - 2.8$  (Reid et al., 2002; Scalo, 1986). While such a similarity cannot rule out the importance of feedback or competitive accretion in determining the final masses of stars, it provides support for the hypothesis that stellar masses are directly linked to the masses of their parent cores. Furthermore, given my conclusion above that turbulence dominates core formation, this result indicates that the shape of the IMF is determined during the turbulent fragmentation of cloud material into dense cores. The ratio of the characteristic masses of the CMD and

IMF places a lower limit on the efficiency of core collapse of 25%.

Measured angular deconvolved sizes of starless cores indicate that the majority have radial density profiles that are substantially flatter than  $\rho \propto r^{-2}$ , predicted by Shu et al. (1987) for cores on the verge of collapse. My results support recent research showing that most starless cores are consistent with density power law indices of  $p \lesssim 1.6$ , or with flattened inner profiles such as Bonnor-Ebert spheres (e.g., Di Francesco et al., 2007).

A comparison of the starless and protostellar core populations in each cloud indicates that dense starless cores are already spatially clustered, and occur in regions of high cloud column density. Therefore, the initial spatial distribution of cores is not significantly altered by protostellar formation. In contrast, the mass distribution widens considerably after the formation of a central protostar, as determined from a comparison of the prestellar CMD to the protostellar CMD. Starless cores in Perseus have larger sizes and lower densities on average than protostellar cores for a similar range of masses, providing a simple explanation of how protostellar cores might have evolved from the starless cores in that cloud, by becoming smaller and denser at a constant mass. In Serpens, however, it is not clear how the relatively massive protostellar cores could have evolved from the current population of compact, low mass starless cores, suggesting that the future generation of stars in that cloud will have lower mass than those of the currently forming protostars. By contrast, cores in Ophiuchus appear to evolve very little after the formation of a central protostar.

**3.** To study the early evolution of protostars, observed source properties are compared to protostellar evolutionary models using the bolometric temperature-luminosity ( $T_{bol}$ – $L_{bol}$ ) diagram, the protostellar equivalent of the H-R diagram (Myers et al., 1998). Neither models with a constant mass accretion rate (Young & Evans, 2005), nor those with an exponentially declining rate (Myers et al., 1998) fit the observed population of Class I sources. In particular, Class I sources display a large spread in  $L_{bol}$  of 2–3 orders of magnitude, and there is a substantial population of low-luminosity Class I objects that cannot be explained by the general model prediction that  $L_{bol}$  should

peak during the Class I phase. This result provides strong evidence for episodic accretion during the Class I phase. Based on the number of sources with  $L_{bol} < 0.1L_{\odot}$ , protostars must spend approximately 25% of their Class I lifetime in a quiescent state.

Corresponding low-luminosity Class 0 sources are not observed; most Class 0 sources can be explained by a constant accretion rate model and masses from 0.3 to  $3.0 M_{\odot}$ . I find approximately half as many Class 0 as Class I sources in Perseus and Serpens, implying a Class 0 timescale of  $1 - 2 \times 10^5$  yr. Thus there can be no very rapid early accretion truncating the Class 0 phase, as has been suggested by André & Montmerle (1994) and more recently by Froebrich et al. (2006). In fact, it appears unlikely that the *average* accretion rate drops by more than a factor of two from Class 0 to Class I. In Ophiuchus the fraction of Class 0 sources is much smaller:  $N_{Class0}/N_{ClassI} \sim 0.1$ . This difference may be due in part to overestimates of  $T_{bol}$  values derived without  $160\mu\text{m}$  flux measurements, but more likely either the Class 0 phase is considerably shorter, or the star formation history is much more temporally variable, in Ophiuchus than in the other clouds.

4. With a few important exceptions, large environmental differences are not observed for the dense core populations. The majority of 1.1 mm cores are consistent with power law density profiles, at least on scales larger than the  $31''$  Bolocam beam, and inferred power law indices are similar in each cloud ( $p \sim 1.4 - 1.7$ ). Spatial clustering properties are also similar for all three clouds, with some evidence that clustering remains strong out to larger scales in Perseus. There is a larger range of measured core sizes and densities in Perseus, reflecting a wider variety of physical conditions and more distributed star formation in that cloud. The relationship between dense cores and the local cloud column density does vary from cloud to cloud, as 1.1 mm cores are found at considerably higher column densities in Ophiuchus than in Perseus or Serpens. More than 75% of cores are found at visual extinctions of  $A_V \gtrsim 8$  mag in Perseus,  $A_V \gtrsim 15$  mag in Serpens, and  $A_V \gtrsim 20 - 23$  mag in Ophiuchus.

The measured core mass distributions (CMDs) display notable variations with environment. Cloud CMDs are well characterized by power law fits ( $dN/dM \propto M^{\alpha}$ )

above their empirically derived 50% completeness limits, resulting in slopes of  $\alpha = -2.1 \pm 0.1$  in Perseus,  $\alpha = -2.1 \pm 0.3$  in Ophiuchus, and  $\alpha = -1.6 \pm 0.2$  in Serpens. The slope predicted for turbulent fragmentation,  $\alpha \sim -2.4$  (e.g., Padoan & Nordlund, 2002), is similar to the measured slope for Perseus and Ophiuchus, but not for Serpens. Based on a two-sided Kolmogorov-Smirnov test, the core samples in Ophiuchus and Serpens are found to have a low probability (5%) being drawn from the same parent distribution of masses. Ballesteros-Paredes et al. (2006) argue that the shape of the CMD should depend on the turbulent properties of the cloud, with higher Mach numbers leading to a larger fraction of low mass cores. The relative shapes of the observed cloud CMDs, with the largest fraction of high mass cores in Serpens, the most turbulent cloud, are contrary to what would be expected from the simulations of Ballesteros-Paredes et al. (2006). While it seems likely turbulence is responsible for the formation of dense cores, and can explain the CMD in a general sense, the detailed dependence on Mach number is not well characterized by simulations.

The studies described in this thesis help to shed light on a number of problems in low mass star formation, while in turn raising new issues and highlighting the need for more precise, testable predictions from theory and simulations. Perhaps most surprising is the variation of core properties and protostellar evolution with environment for the three molecular clouds. In recent years much effort has gone into reproducing the short Class 0 lifetime originally measured in Ophiuchus, but the unprecedented sample assembled here suggests that Ophiuchus may be a special case, and the Class 0 lifetime is likely to be much longer in the majority of star-forming environments. While my results support the growing body of evidence that turbulence plays a very important role in the star formation process (e.g., Mac Low & Klessen, 2004), the distinction between magnetic fields and turbulence as the dominant physical forces in molecular clouds is not clear cut; apparently, the influence of magnetic fields must be accounted for in any complete model of turbulent star formation.

## 7.2 The Future

Closer collaboration between theorists, simulators, and observers is essential to fully understand the implications of the wealth of *Spitzer* data and large scale (sub)mm continuum and molecular line surveys made available in the last few years. In chapter 5, I compared core mass distributions from three molecular clouds to the results of turbulent fragmentation simulations, in order to test environmental dependencies and the agreement between simulations and observations. A straightforward method for compare other properties of the dense core populations to results from turbulent fragmentation simulations would be extremely useful. For example, the spatial distribution of cores could be compared using the two-point correlation function (e.g., §5.5.4), and the relationship between dense cores and the surrounding cloud density (e.g., §5.5.5). Having the ability to “observe” the output of simulations or models in the same way as real observations will provide a substantial step forward in our ability to constrain star formation models.

Another important area for improvement is the measurement of the starless core mass distribution to much lower masses, which is essential to further test the relationship between the IMF and the CMD. The CMD for dense 1.1 mm cores studied here begins to suffer from incompleteness at  $M \sim 0.8 M_{\odot}$ ; to directly compare to the IMF characteristic mass of  $0.25 M_{\odot}$  (Chabrier, 2005), more sensitive observations are needed. While the CMD of Alves et al. (2007) is complete to approximately  $0.4 M_{\odot}$ , the dust extinction method used traces structures with relatively low density, and their sample may be contaminated by unbound cores and other diffuse structures. The upcoming SCUBA2 bolometer array and the ALMA interferometer will revolutionize this field, making it possible to detect prestellar cores with  $M \ll 0.1 M_{\odot}$  over large scales and at high resolution. The coordination of these continuum data with molecular line observations to determine if observed cores are bound will enable a more detailed comparison between the CMD and the IMF.

In the remaining sections I outline in more detail a few projects inspired by the work in this thesis, which I intend to pursue in the next several years. Anticipated

lines of inquiry include the refinement of arguments made in this thesis, such as the lifetime of the Class 0 phase, and using the large sample compiled here to isolate unbiased subsets for more detailed study.

### 7.2.1 Main Accretion Phase Lifetime

The combination of *c2d Spitzer* maps and Bolocam 1 mm surveys made possible a calculation of the number of Class 0 sources in the Perseus, Serpens, and Ophiuchus molecular clouds, but in fact this analysis only begins to tie down the main accretion phase lifetime. A major source of uncertainty in this calculation is the treatment of close multiple sources, which are confused in the 31'' resolution Bolocam data. Thus follow-up observations are necessary, particularly at high resolution.

Observations of a sample of 19 multiple protostars not previously observed at high resolution are currently underway with the Combined Array for Millimeter-wave Astronomy (CARMA) interferometer. Targets are identified from Bolocam *Spitzer* *c2d* maps of Perseus, Serpens, and Ophiuchus as two or more  $24\mu\text{m}$  or  $70\mu\text{m}$  sources within the radius of a single Bolocam 1 mm core (e.g., figure 6.2, Pers-Bolo 49). These high-resolution 3 mm continuum observations will determine the fraction of millimeter flux associated with each source, thus clarifying their evolutionary state. A more accurate accounting of the relative number of Class 0 and Class I sources will enable a refinement of the Class 0 lifetime estimate. Simultaneous observations of outflow-tracing molecular lines will give further insight into the evolutionary state of each source.

### 7.2.2 Tracing Structure Near the Protostar

The data presented in this thesis are sensitive to deeply embedded protostars and their surrounding envelopes, but they cannot probe the envelope on scales smaller than the 31'' Bolocam beam. Very little is known about the small scale structure in most Class 0 sources, including whether they might be small-separation binaries. Directly resolving the structure around protostars on scales  $<100$  AU is difficult, but

the amount of flux escaping at  $\lambda \lesssim 50\mu\text{m}$  from deeply embedded sources strongly constrains their innermost structure. Recently, evidence for a hole in the inner envelope of IRAS 16293-2422 was found by comparing the observed IRS spectrum with detailed radiative transfer models (figure 7.1, left; Jørgensen et al. 2005). Those data revealed an inner cavity that is slightly larger than the separation of this Class 0 binary.

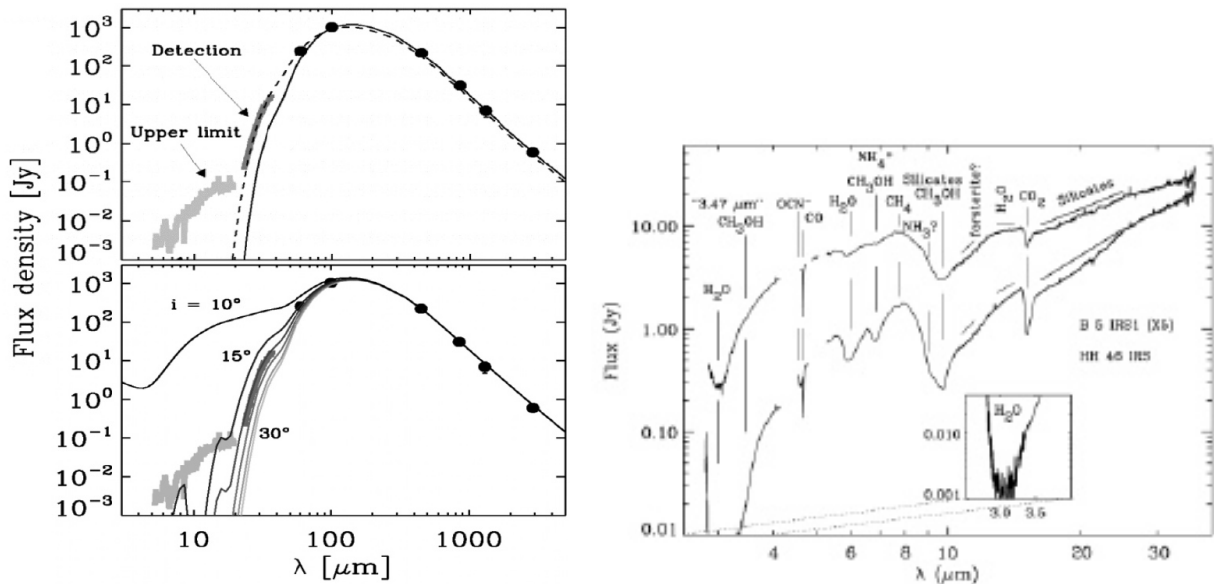


Figure 7.1 An example of using *Spitzer* IRS data to understand small scale structure in a Class 0 protostar. *Left top*: The SED of IRAS 16293-2422 from Jørgensen et al. (2005), compared to radiative transfer models with (dotted line) and without (solid line) a 600 AU inner cavity. The two models are only differentiated by the IRS spectrum (in dark gray). *Left bottom*: Similar, but showing the effects of an outflow cavity with varying inclination angle (all with opening angle  $30^\circ$ ). *Right*: *Spitzer* IRS spectra of two embedded protostars from Boogert (2004), showing the silicate absorption at  $10\mu\text{m}$  and other ice features.

The IRS spectrograph on *Spitzer* will be used to observe a sample of 25 Class 0 objects from Perseus, Serpens, and Ophiuchus, with the goal of determining the innermost envelope structure of deeply embedded protostars. IRS spectra will also reveal inner cavities in both binary and single sources, e.g., if the inner region has been cleared out, or flattened into a thin disk by rotation in the core. The sources to be observed are chosen from the Class 0 samples compiled in this thesis, and

include objects from a range of environments. A diverse sample like this one is very important, as only a few famous sources have been studied to date. To infer the innermost envelope structure, the spectral energy distribution (SED) from  $3.6$  to  $1100\mu\text{m}$  must be combined with radiative transfer modeling (Shirley et al., 2002). Model inputs include the envelope inner radius,  $T_{eff}$  of the central source, and the density distribution of the envelope. The first two are constrained by the SED, but the latter requires resolved (sub)mm observations. High-resolution millimeter maps of these targets will be obtained with CARMA to tightly constrain the envelope density profile.

IRS observations will also reveal the spectral details of Class 0 SEDs from  $7$  to  $37\mu\text{m}$ . Many of the Class 0 protostars identified here display a dip in the SED around  $10\mu\text{m}$ , which is likely a silicate absorption feature in the envelope (figure 7.1, right; Boogert 2004), but could also be related to a conical outflow cavity (figure 7.1, left). It is tempting to assign those sources with minima at  $10\mu\text{m}$  to a distinct phase within the Class 0 classification, but differences may simply be a function of cloud environment or outflow inclination angle. Correlations between observed source properties and evolutionary tracers such as  $T_{bol}$  will determine if the presence of a cavity, average cavity size, or spectral features from  $7-37\mu\text{m}$  change systematically with protostellar age.

### 7.2.3 Timescale for Disk Formation and the Disk Mass Fraction

Although disk-like structures have now been observed embedded within the envelopes of a few Class 0 sources, it is still not clear how soon after protostellar formation the disk appears. Separating the disk flux from that of the envelope is becoming more feasible with the improved uv coverage and sub-arcsecond resolution of current (sub)mm interferometers, which can resolve emission on small to large scales. Figure 7.2 shows an example of disentangling the disk and envelope contributions in a Class I protostar using the PdB Interferometer (from Harvey et al., 2003).

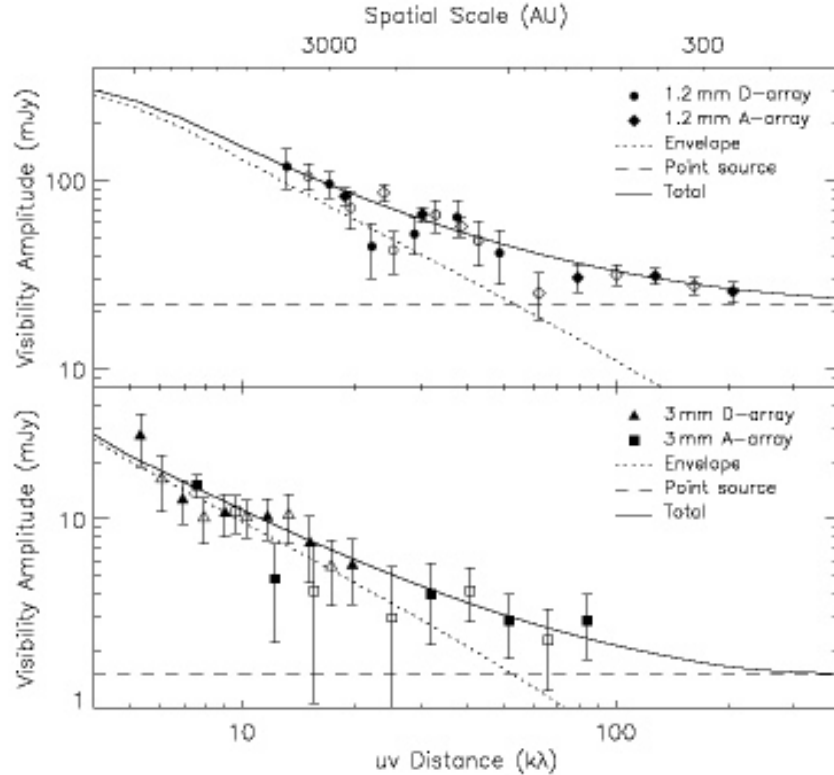


Figure 7.2 An example of separating disk and envelope contributions. IRAM PdBI interferometric observations at 1.2 and 3.0 mm are compared to a simple model consisting of a point-like disk (dashed line) and extended envelope (dotted line) (Harvey et al., 2003). CARMA observations will be sensitive to  $uv$  distances from 8.5 to 770  $k\lambda$  at 1.3 mm, sampling the region most sensitive to the disk.

CARMA will be used to search for disks in a sample of 30 Class 0 sources in Perseus, Serpens, and Ophiuchus. This represents a larger and more unbiased sample than previous studies, and includes main accretion phase protostars at a range of ages. Class 0 disks are thought to have sizes of order 100 – 300 AU (Chandler et al., 1995). Thus a resolution of at least 100 AU and  $uv$  coverage from  $\sim 10$  to  $\gtrsim 500$   $k\lambda$  are required to adequately sample disk and envelope structures, both of which are achievable with CARMA. Millimeter continuum observations detect emission from dust grains in the disk and envelope; assuming that this emission is optically thin at  $\lambda = 1 - 3$  mm, it provides a direct measure of mass. Mosaiced observations at 1–3 mm will attempt to determine the total mass in the envelope and disk components in Class 0 objects.. Although dust emission is stronger at shorter wavelengths, the

possibility of grain grown in the disk makes observations at longer wavelengths (7 mm–2 cm, e.g., with the VLA) desirable as well.

## Bibliography

- Alves, J., Lombardi, M., & Lada, C. J. 2007, *A&A*, 462L, 17
- André, P. & Montmerle, T. 1994, *ApJ*, 420, 837
- Ballesteros-Paredes, J., Gazol, A., Kim, J., Klessen, R. S., Jappsen, A-K., & Tejero, E., 2006, *ApJ*, 637, 384
- Boogert, A. C. A. 2004, *ApJ*, 154, 359
- Chabrier, G. 2005 in *The Stellar Initial Mass Function Fifty Years Later*, editors E. Corbelli, F. Palla, and H. Zinnecker, p. 41
- Chandler, C. J., Koerner, D. W., Sargent, A. I., Wood, D. O. S. 1995, *ApJ*, 449, 139
- Di Francesco, J., Evans, N. J., II, Caselli, P., Myers, P. C., Shirley, Y., Aikawa, Y., & Tafalla, M. 2007, in *Protostars and Planets V*, editors B. Reipurth, D. Jewitt, and K. Keil, p. 17
- Froebrich, D., Schmeja, S., Smith, M. D., & Klessen, R. S. 2006, *MNRAS*, 368, 435
- Harvey, D. W. A., Wilner, D. J., Myers, P. C., Tafalla, M. 2003, *ApJ*, 596, 383
- Johnstone, D., DiFrancesco, J., & Kirk, H. 2004, *ApJ*, 45, 611L
- Jørgensen, J. K., Bourke, T. L., Myers, P. C., Schöier, F. L., van Dishoeck, E. F., Wilner, D. J. 2005, *ApJ*, 631, L77
- Klessen, R. S., Heitsch, F., & Mac Low, M.-M. 2000, *ApJ*, 535, 887
- Mac Low, M.-M., & Klessen, R. S. 2004, *RevPhys*, 76, 125
- McKee, C. F. 1989, *ApJ*, 345, 782
- Myers, P. C., Adams, F. C., Chen, H., Schaff, E. 1998, *ApJ*, 492, 703
- Nakano, T. 1998, *ApJ*, 494, 587

- Padoan, P., & Nordlund, Å. 2002, ApJ, 576, 870
- Reid, I. N., Gizis, J. E., & Hawley, S. L. 2002, AJ, 124, 2721
- Scalo, J. M. 1986, Fundam. Cosmic Phys., 11, 1
- Shirley, Y. L., Evans, N. J., II, & Rawlings, J. M. C. 2002, ApJ, 575, 337
- Shu, F. H., Adams, F. C., & Lizano, S. 1987, ARA&A, 25, 23
- Vázquez-Semadeni, E., Kim, J., Shadmehri, M., & Ballesteros-Paredes, J. 2005, ApJ, 618, 344
- Young, C. H. & Evans, N. J., II 2005